Umut Türker
Özgür Eren
Eris Uygar   *Editors*

Sustainable Civil Engineering at the Beginning of Third Millennium

Proceedings of 15th International Congress on Advances in Civil Engineering (ACE2023)

Springer

Lecture Notes in Civil Engineering 481

Lecture Notes in Civil Engineering (LNCE) publishes the latest developments in Civil Engineering—quickly, informally and in top quality. Though original research reported in proceedings and post-proceedings represents the core of LNCE, edited volumes of exceptionally high quality and interest may also be considered for publication. Volumes published in LNCE embrace all aspects and subfields of, as well as new challenges in, Civil Engineering. Topics in the series include:

- Construction and Structural Mechanics
- Building Materials
- Concrete, Steel and Timber Structures
- Geotechnical Engineering
- Earthquake Engineering
- Coastal Engineering
- Ocean and Offshore Engineering; Ships and Floating Structures
- Hydraulics, Hydrology and Water Resources Engineering
- Environmental Engineering and Sustainability
- Structural Health and Monitoring
- Surveying and Geographical Information Systems
- Indoor Environments
- Transportation and Traffic
- Risk Analysis
- Safety and Security

To submit a proposal or request further information, please contact the appropriate Springer Editor:

- Pierpaolo Riva at pierpaolo.riva@springer.com (Europe and Americas);
- Swati Meherishi at swati.meherishi@springer.com (Asia—except China, Australia, and New Zealand);
- Wayne Hu at wayne.hu@springer.com (China).

All books in the series now indexed by Scopus and EI Compendex database!

Umut Türker · Özgür Eren · Eris Uygar
Editors

Sustainable Civil Engineering at the Beginning of Third Millennium

Proceedings of 15th International Congress on Advances in Civil Engineering (ACE2023)

Springer

Editors
Umut Türker
Department of Civil Engineering
Eastern Mediterranean University
North Cyprus, Türkiye

Özgür Eren
Department of Civil Engineering
Eastern Mediterranean University
North Cyprus, Türkiye

Eris Uygar
Department of Civil Engineering
Eastern Mediterranean University
North Cyprus, Türkiye

Preface

The quality of civil engineering directly impacts people's lives and personal safety, and it also has a significant impact on the advancement of society. Civil engineering and human life are intimately intertwined. To address the issues pertaining to the current state of civil engineering development, it is imperative that the field's advancement and development status be thoroughly examined. Hence, the proceedings book shares current trends in civil engineering including new technologies, methods, theories, and practices in all branches of civil engineering by bringing together researchers and experts worldwide. As a result, we obtained fascinating papers detailing recent developments in the field of civil engineering. We are optimistic that the papers included in the proceedings book will spark fruitful debate among scholars and enable us to increase our level of understanding, opening new avenues for the civil engineering profession.

The popular research topics in the book comprises: investigation in the areas of innovative materials in concrete production, recycling of waste in the construction industry, fiber reinforced and high strength concrete, soil stabilization, problematic soils of semi-arid and arid regions, deep foundations, staged construction modeling, repair and maintenance of reinforced concrete, earthquake engineering and seismic retrofitting, coastal and harbor engineering, water resources management, hydrology and hydraulics engineering, traffic engineering and urban transport, life cycle cost analysis, and decision making strategies. All these topics have been in the general context of the rising trends recently, as we advance into the third Millennium, the current outlook is such that they will continue to be as important as ever. With sustainability in mind, research and practice in the field of civil engineering will also continue to deliver societies' demand effectively.

Getting together with researchers and practitioners to share ideas and create future research partnerships was very pleasant. As the hosting organization, Eastern Mediterranean University appreciates everyone who participated in the congress by submitting, reviewing, and delivering papers.

Umut Türker

Contents

Geotechnics

Health and Safety

Hydraulics

Structures

x   Contents

Transportation

Building Materials

Influence of Short Polyethylene Terephthalate Fibres on Mechanical and Physical Properties of Cementitious Mortars

Can Özgün Sayı$^{(\boxtimes)}$, Necat Özaşık , and Özgür Eren

Civil Engineering Department, Eastern Mediterranean University, Famagusta, North Cyprus, Turkey
can.sayi@gmail.com, ozgur.eren@emu.edu.tr

Abstract. Commodity plastics are being used in many applications due to their low density, high durability, and relatively low cost. Their wide usage and degradable nature create environmental problems. Polyethylene terephthalate (PET) is the one of most used plastics and the second largest contributor to the global plastic waste. The scientific literature suggests a global effort for utilizing PET waste in building materials including concrete, mortars, and cementitious composites, in the form of granules, powder or fibres. This study aims to contribute to the knowledge about the material behavior of Recycled PET Fibre Reinforced Mortars (RPFRMs) by investigating the influence of fibres on some physical and mechanical properties of a cementitious render mortar.

Recycled-PET monofilaments with 0.45 mm diameter were chopped into fibres with 6 mm length. RPFRM mixtures with varying fibre volume fractions (0.5, 1.0 and 1.5%) were prepared and tested. The fresh properties were assessed by measuring the fresh density, and mean flow diameter. The influence of recycled PET fibres on the mechanical properties of render mortars were investigated using flexural strength and compressive strength. Furthermore, water absorption coefficient of the specimens was also measured for briefly investigating the influence of recycled-PET fibre addition on durability properties.

Keywords: PET fibre · mortar · compressive strength · flexural strength · water absorption coefficient

1 Introduction

Their relatively low price, density, availability and easy production, make plastics useful in many products, and they are being used in great amounts for various industries [1]. The global plastics production is increasing at a concerning rate, reaching 390.7 million tonnes in 2021 [2]. The plastic waste generated are either sent to landfills, incinerated, or recycled, where recycling in considered to be a more environmentally responsible method for disposal [3]. The recycled plastic waste can either be used as raw materials for plastics production. Another approach is the utilization of plastic waste in construction industry, in which the plastic waste can be used in insulation materials, as fillers [4],

concretes or cementitious mortars [5]. Polyethylene Terephthalate (PET) is a type of commodity plastic, which the usage amount is one of the highest [6] and constitutes the second largest fraction in plastic waste stream [5]. However, the recycling rate of PET waste is relatively lower than its production and the most of them end up in landfills or nature [4, 7]. Therefore, any effort for making use of PET waste contributes towards environmental sustainability. PET waste can be utilised as aggregate substitute, or as fibres in concretes and mortars [7]. In this study, mortars reinforced with recycled PET fibres will be focussed.

Depending on the dimensions, properties and the volume of fibres, the properties of matrix phase and the quality of bonding between fibre and the matrix phases, the fibres can affect the properties of cementitious materials [8]. For instance, a study by Oliveira et al. [5] reports significant increase (up to 33%) in the flexural strength of mortars when PET fibres were added at 1.5vol%, Francioso et al. [9] reports insignificant increase at same volume of PP fibres, and rather reduction at lower fibre volumes, probably due to poor adhesion which reduce the potential positive impact. In general, synthetic fibres with low elastic modulus such as PET fibres contribute to the control of shrinkage cracks via bridging mechanism [5]. Literature reports insignificant changes of compressive strength of cementitious mortars upon the addition of synthetic fibres made of PET and PP [5, 9, 10]. As the specific gravity of PET is lower than that of conventional aggregates used in cementitious mortars, the fresh and hardened density is expected to decrease slightly with PET fibre or PET granule addition, as reported in previous studies [5, 7]. There are conflicting views regarding the influence of PET fibres on the consistency and water absorption of cementitious mortars.

This study aims to contribute to the knowledge about the material behaviour of Recycled PET Fibre Reinforced Mortars (RPFRMs) by investigating the influence of fibres on some physical and mechanical properties of a cementitious render mortar. The physical properties of cementitious mortars were looked into, by measuring the fresh density, hardened density and consistency of render mortar samples with varying amounts of fibres, as well as non-fiberized mortar samples. Furthermore, the mechanical properties were also evaluated by investigating the compressive and flexural strength of the same set of mortar samples. Finally, the durability properties were also briefly discussed by investigating the water absorption.

2 Methodology

2.1 Materials

Type 1 (42.5) Ordinary Portland Cement complying with TS EN 197-1:2012 was used as the binder phase of the mortar mixes. The fine aggregate consisted of crushed limestone which was obtained from quarries in Beşparmak Mountains. The properties of fine aggregate and cement are presented in Table 1. Short fibres (Fig. 1) were produced by cutting monofilament threads made of recycled PET (Table 2).

Table 1. Chemical and physical properties of mortar constituents

Property	Cement	Fine Aggregate
SiO_2 (%)	19.17	1.67
Al_2O_3 (%)	4.51	0.53
Fe_2O_3 (%)	3.24	0.31
CaO (%)	63.29	84.51
MgO (%)	1.99	12.58
SO_3 (%)	3.21	0.06
Loss on Ignition	3.72	–
Insoluble Residue	0.66	–
Blaine Specific Area (cm^2/gr)	3700	–
Residue on 45μm sieve (%)	2.50	–
Specific Gravity (gr/cm^3)	3.15	2.71
Maximum Diameter (μm)	–	2000
Water Absorption (%)	–	2.55

Table 2. Physical properties of recycled PET fibres.

Diameter (mm)	Length (mm)	Aspect Ratio	Specific Gravity
0.45	30	67	1.61

Fig. 1. Short PET fibres with 0.45 mm diameter and 6 mm length.

2.2 Sample Preparation

The mix design for the non-fiberized cementitious mortar were adapted from the formulation of a commercial dry-mix render mortar, and the parameters were presented in Table 3. The constituents were weighed and mixed at room temperature. The recycled PET fibres were added at a volume of 0.5%, 1.0% and 1.5% of the non-fiberized mortar.

Table 3. Mix design of mortar

Constituent	Dosage (kg/m^3)
Cement	415
Fine Aggregate	1120
Water	335

2.3 Test Procedures

Fresh and hardened properties of cement-based mortars with and without fibers were briefly investigated. Related standards were followed to evaluate the behavior of mortar on specific properties of which the test procedures were explained below.

Density
Bulk density of samples was measured according to BS-EN 1015-6.

Mean Flow Diameter
Average mean flow diameter of cement-based mortar samples was investigated according to BS-EN 1015-3 standard. Freshly mixed mortar was filled into the cone placed on the flow table in two layers by stroking each layer at least ten times with tamper until the cone was completely full. The steel cone was later removed to leave samples free, and the handle was rotated fifteen times at approximately fifteen seconds to provide enough jolting of the flow table. Finally, the diameter of the fresh spread mortar was measured both in vertical and longitudinal dimensions to record the diameter in mm.

Mechanical Strength (Compressive and Flexural Strengths)
The specimens were prepared and tested according to BS EN 1015-11 standard in a hydraulic press with relevant test jigs (see Fig. 2). The test specimens were prisms with dimensions $160 \times 40 \times 40$ mm. For the compressive strength test, three prism specimens were broken down into two halves to provide six test samples to be tested at an age of 28 days. The machine with two supporting rollers and span length of 100 mm was used for flexural strength tests.
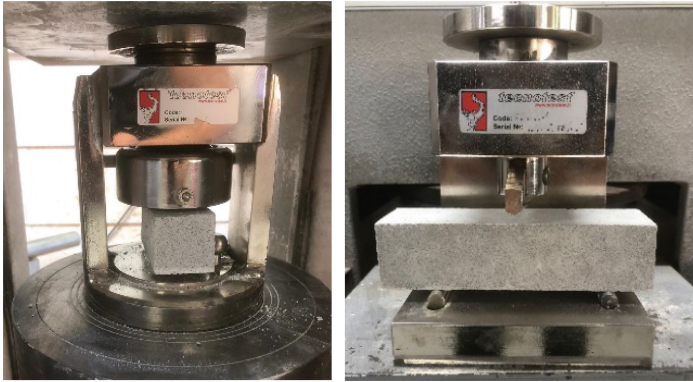
Fig. 2. RPFRM samples being tested for their compressive strength (left) and flexural strength (right)

Water Absorption Coefficient

The water absorption coefficient of control and fiber added cement-based mortar samples were measured according to BS EN 1015-18 standard. First of all, freshly prepared mortar was placed into molds covered with filter papers on both bottom and top surfaces. Then, cured for two days in the molds plus five days with the molds removed at 95% relative humidity, followed by 21 days at 65% relative humidity. After the curing period, four long sides of the specimens were sealed with wax material to prevent ingress of water from the sides and broken down into halves. On the day of testing, oven dried specimens were placed in the tray with broken surfaces downwards and immersed in water with a depth of 5 to 10 m. Weight of each specimen was recorded at 10 min and 90 min of immersion (Fig. 3).

Fig. 3. Control mortar samples being tested for water absorption coefficient.

3   Results and Discussion

3.1   Density

Fresh and hardened density measurements of control and RPFRM samples were performed, and the results are presented in Fig. 4. It can be seen that in both fresh and hardened states the recycled PET fibre addition decreased the density of mortars. In literature, small decrease in mortar density with PET fibre addition was previously reported [5]. Maximum density reduction (8.4% for fresh density and 10.4% for hardened density) was observed at highest fibre content (1.5vol%). The relatively lower density of PET fibres in comparison to that of the control mortar mix, could be contributing to the density reductions. Furthermore, the formation of voids around the fibres due to potential entanglements, or other imperfections in fibre dispersion could be other reasons for the reductions in density.
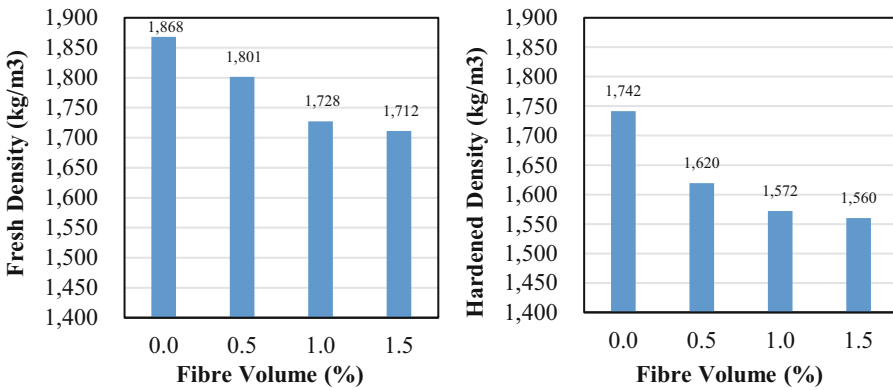
Fig. 4. Influence of PET fibres on the fresh (left) and hardened (right) density of mortars.

3.2   Mean Flow Diameter

Mean flow diameter measurements were performed for control and RPFRM samples and the results are presented in Fig. 5. It can be observed that fibre addition into mortar resulted in a steady decrease in the mean flow diameter of the mortars. The maximum reduction in the flow diameter was 3.4% and was observed at a fibre volume of 1.5%. Study of Bendjillali et al. [8] mentions that the mortar becomes less workable with the addition of synthetic fibres, due to higher surface area. However, Sposito et al. [7] reports increased workability with PET granule addition, due to lower absorption of PET surface, allowing free water which enhances the flow. This may suggest that the effect of PET fibre geometry could be dominating the effect of low absorption of PET.
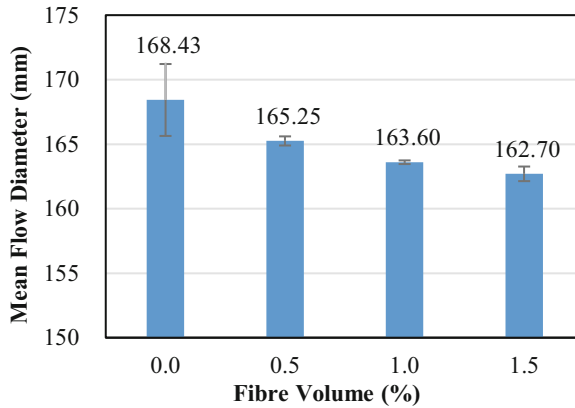
Fig. 5. Influence of PET fibres on the mean flow diameter of PFRMs.

3.3 Compressive Strength

Compressive strength tests were performed for control and RPFRM samples and the results are presented in Fig. 6. It can be observed that fibre addition into mortar resulted in insignificant variations in compressive strength, where the maximum increase compared to non-fiberized mortar was 2.2% and maximum reduction was 5.5%. Insignificant changes in compressive strength of cementitious mortars as a result of PET fibre addition was previously encountered in similar studies [5].
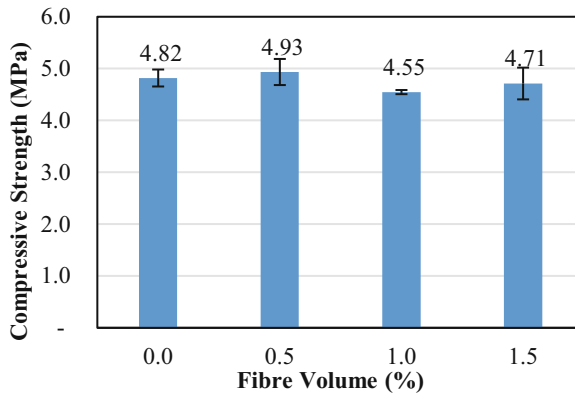
Fig. 6. Influence of PET fibres on the compressive strength of RPFRMs.

3.4   Flexural Strength

Flexural strength tests were performed for control and RPFRM samples and the results are presented in Fig. 7. It can be observed that recycled PET fibre addition resulted in a steady decrease in flexural strength of mortar. The maximum reduction was %22.6 and it was observed at a fibre content of 1.5 vol%.
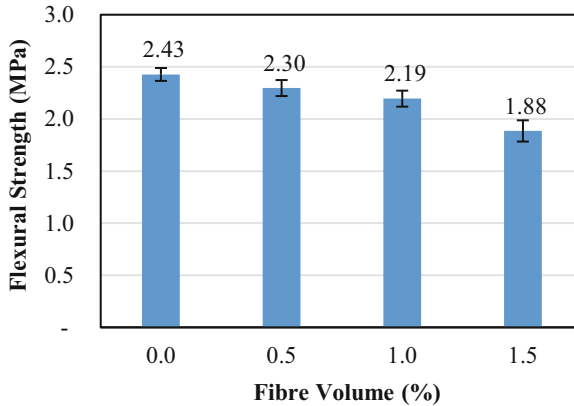
Fig. 7. Influence of PET fibres on the flexural strength of PFRMs.

3.5   Water Absorption Coefficient

Water absorption coefficient measurements were performed for control and RPFRM samples and the results are presented in Fig. 8. It can be observed that recycled PET fibre addition resulted in a slight increase in water absorption coefficient of mortar. The maximum increase was %5 at a fibre volume of 0.5 vol%. The increase in water absorption could be attributed to the potential void formations around the recycled PET fibres in the mortar specimens, which could increase the overall porosity which could allow water ingress. It was previously mentioned in the literature that the water resistance of PET could be deteriorating the adhesion and dispersion within cementitious materials, which could lead to receives that increase the water permeation at the interface between PET fibre and cement phases [11]. A non-linear increase of water absorption of mortars upon addition of PET granules was also observed in literature [7], which also supports such effect of PET. Further fibre addition resulted in water absorption coefficient values which were statistically the same as 0.5 vol%. In a similar study performed by Oliveira et al., the insignificant and irregular variations of water absorption at different fibre volumes were attributed to potential pullout of fibres at the fracture surface [5].
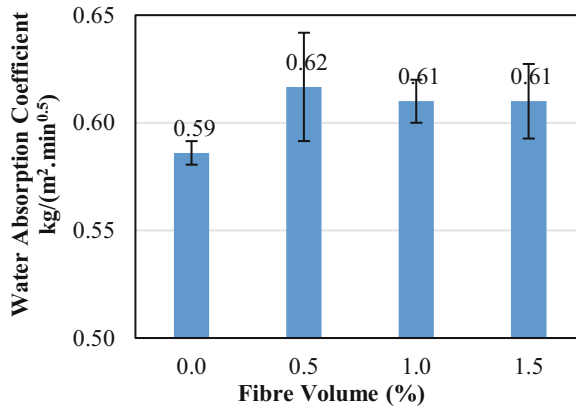
Fig. 8. Influence of PET fibres on the water absorption of PFRMs

4   Conclusions

Tests and measurements were performed in order to assess the mechanical and physical properties of recycled PET reinforced mortars. It was observed that:

- Density of mortars decreased with PET fibre volume, due to lower density of fibres and void formation,
- Mean flow diameter volume of RPFRMs decreased with addition of PET fibres. At 1.5% fibre volume, 3.4% reduction in the flow diameter was observed.
- The effect of PET fibres on compressive strength of mortar samples was insignificant. The maximum increase and decrease compared to control mortar were 2.2% and 5.5% respectively.
- A steady decrease was observed in flexural strength of mortar with PET fibre addition where maximum reduction was 22.6% with addition of 1.5% fibres.
- Water absorption coefficient of mortars were increased up to 5% when recycled PET fibres were added at a volume of 1.5%.

References

1. Siddique, R., Khatib, J., Kaur, I.: Use of recycled plastic in concrete: a review. Waste Manag. **28**(10), 1835–1852 (2008)
2. Association of Plastic Manufacturers, 'Plastics - the Facts 2022: An analysis of European plastics production, demand and waste data', Plastics Europe (2022). https://plasticseurope.org/knowledge-hub/plastics-the-facts-2022. Accessed 02 July 2023

3. Gholampour, A., Ozbakkaloglu, T.: Recycled plastic. In: New Trends in Eco-efficient and Recycled Concrete, Woodhead Publishing Series in Civil and Structural Engineering, pp. 59–85 (2019)

4. Awoyera, P.O., Adesina, A.: Plastic wastes to construction products: status, limitations and future perspective. Case Stud. Constr. Mater. **12** (2020)

5. Pereira de Oliveira, L.A., Castro-Gomes, J.P.: Physical and mechanical behaviour of recycled PET fibre reinforced mortar. Constr. Build. Mater. **25**(4), 1712–1717 (2011)

6. Foti, D.: Recycled waste PET for sustainable fiber-reinforced concrete. In: Use of Recycled Plastics in Eco-efficient Concrete, Woodhead Publishing Series in Civil and Structural Engineering, pp. 387–410 (2019)

7. Spósito, F.A., et al.: Incorporation of PET wastes in rendering mortars based on Portland cement/hydrated lime. J. Build. Eng. **32** (2020)

8. Bendjillali, K., Chemrouk, M., Boulekbache, B.: Performances of cementitious mortars containing recycled synthetic fibres under hot-dry climate. Euro. J. Environ. Civ. Eng. **23**(10) (2019)

9. Francioso, V., Moro, C., Castillo, A., Velay-Lizancos, M.: Effect of elevated temperature on flexural behavior and fibers-matrix bonding of recycled PP fiber-reinforced cementitious composite. Constr. Build. Mater. **269** (2021)

10. Silva, D.A., Betioli, A.M., Gleize, P.J.P., Roman, H.R., Gómez, L.A., Ribeiro, J.L.D.: Degradation of recycled PET fibers in Portland cement-based materials. Cem. Concr. Res. **35**(9), 1741–1746 (2005)

11. Won, J.P., Jang, C.I., Lee, S.W., Lee, S.J., Kim, H.Y.: Long-term performance of recycled PET fibre-reinforced cement composites. Constr. Build. Mater. **24**(5), 660–665 (2010)

Alkali Activation of Stabilized Rammed Earth Bricks: A State-of-the-Art Review

Maroan Elgallal[(✉)] and Ayse Pekrioglu Balkis

Civil Engineering Department, Cyprus International University, Nicosia, North Cyprus, Turkey
marwanelgallal@yahoo.com, apekrioglu@ciu.edu.tr

Abstract. The construction industry's increasing focus on sustainability has led to a growing interest in Stabilized Rammed Earth (SRE) as a low-carbon and affordable building material. However, SRE's widespread adoption has been hindered by its relatively low strength and durability. This review explores the potential of alkali activation to enhance the mechanical properties of SRE. Alkali activation involves using alkaline solutions to activate pozzolanic materials, such as fly ash, slag, or calcined clay, to form a hardened binder. The review compares the mechanical properties of traditional stabilized rammed earth with its alkali-activated counterparts, investigating the effects of alkali activation on structural integrity, durability, and overall performance. Various methodologies of alkali activation are discussed, along with an explanation of the underlying chemical reactions and mechanisms involved. Additionally, the review examines the use of lime-gypsum and cement additives to improve the compressive strength and durability of SRE. The incorporation of fibers, such as polypropylene, straw, plastic, and marble dust, is explored for further enhancing the mechanical properties. The findings highlight the potential of alkali activation in improving the mechanical properties of SRE. Optimal binder compositions, replacement percentages, and selection of alkali activators are crucial factors in achieving high-performance SRE structures. Further research is needed to fine-tune these parameters and fully unlock the potential of alkali-activated SRE for sustainable construction practices.

Keywords: Stabilized Rammed Earth · Alkali Activation · Mechanical Properties · Sustainable construction · environment

1 Introduction

The construction industry is facing increasing pressure to adopt sustainable practices in response to the growing concern about environmental degradation and the depletion of natural resources [1]. In this context, Stabilized Rammed Earth has emerged as a promising alternative to conventional building materials due to its low carbon footprint, abundance, and affordability [2]. SRE involves compacting a mixture of earth (containing a proportion of clay, aggregate such as gravel or sand), and a stabilizer such as cement or lime [3]. This mixture is rammed into place within temporary forms to create walls, and is often done in layers to create an aesthetically pleasing striped effect [3]. Although SRE has been used for centuries, its widespread adoption has been limited by its relatively

low strength and durability [4]. Recently, Alkali Activation has been identified as a potential solution to improve the mechanical properties of SRE [5]. Alkali activation is a process that uses alkaline solutions to activate silica-rich materials, such as fly ash, slag, or calcined clay to form a hardened binder [6]. This review aims to explore and compare the mechanical properties of traditional stabilized rammed earth and its alkali-activated counterparts, in order to elucidate the effects of the alkali activation process on its structural integrity, durability, and overall performance [7]. Furthermore, it discusses the diverse methodologies of alkali activation used in the field, and it outline the fundamental understanding of the underlying chemical reactions and mechanisms involved in the activation process.

2   Traditional Stabilized Rammed Earth Bricks

Traditional Stabilized Rammed Earth (TSRE) bricks are an innovative and sustainable material designed for construction that optimally combines strength, and durability [8]. The typical composition of TSRE bricks is made up of a carefully balanced blend of earthen materials, water and stabilizing agents [9]. Approximately 60–75% of these bricks are constituted by earthen materials, a composite mixture of clay and sand [9]. These materials give the bricks their inherent strength and natural insulation properties, as well as allowing them to be sourced locally in many regions, reducing their overall carbon footprint [10]. The clay, with its cohesive properties, binds the sand particles together, providing the raw material for the brick [11]. The sand contributes to the brick's structural integrity, preventing excessive shrinkage and cracking that can occur if the clay content is too high [12]. The remaining 25–40% of the brick consists of stabilizing agents and water, which further enhance the brick's structural integrity and weather-resistance [13]. This typically includes a mixture of lime, gypsum, or cement [13]. Lime, a calcium-based binder, reacts with the clay to create a hydraulic set, improving the brick's durability and resistance to water damage [14]. Gypsum acts similarly, aiding in binding the components together while also making the bricks more workable [15]. Alternatively, cement provides high compressive strength and increased durability, particularly in exposed conditions [16]. The specific blend of materials can vary based on the desired characteristics of the bricks and the local availability of resources, making TSRE bricks a versatile and adaptable option for sustainable construction [17].

2.1   Lime-Gypsum Additives

The use of a mixture of lime and gypsum as stabilizing agents in the composition of traditional Stabilized Rammed Earth (SRE) bricks has garnered attention and has been the subject of numerous studies due to its potential to improve the material's overall properties [18]. Research has shown that incorporating a small percentage of lime, usually not more than 2%, can significantly enhance the brick's compressive strength, while also contributing to its overall durability [19]. Moreover, gypsum is added in varying proportions, generally ranging between 3 and 10% [20, 21]. Gypsum serves to bind the brick's components together, making the bricks more workable and further improving their durability. The varying proportions of these two components allow for

flexibility in achieving the desired strength and durability of the bricks. The compressive strength ranged between 1 and 5.1 Megapascals after 28 days of curing [19–21].

2.2 Cement Additives

The application of cement as an additive in the composition of Traditional Stabilized Rammed Earth (TSRE) bricks has been extensively explored by researchers. Researchers have predominantly focused on analyzing the effect of cement content in the range of 2% to 12% in the composition of TSRE bricks. These investigations have revealed a direct, linear relationship between the cement content and the compressive strength of the bricks as shown in Fig. 1. This implies that as the proportion of cement in the TSRE bricks increases, the compressive strength of the bricks correspondingly increases. This linear correlation allows for flexibility and predictability in manipulating the physical characteristics of the bricks based on specific construction requirements. In a particular study by [22], they discovered that the bulk density of the TSRE bricks also had a significant effect on their compressive strength. They found that increasing the bulk density of the SRE bricks from 1.7 g/cm3 to 1.8 g/cm3 could enhance their compressive strength by 35–40%. This demonstrated that not only the composition but also the physical characteristics of the TSRE bricks, such as their bulk density, can be tuned to achieve desired strength levels, further endorsing the versatility of these sustainable construction materials.
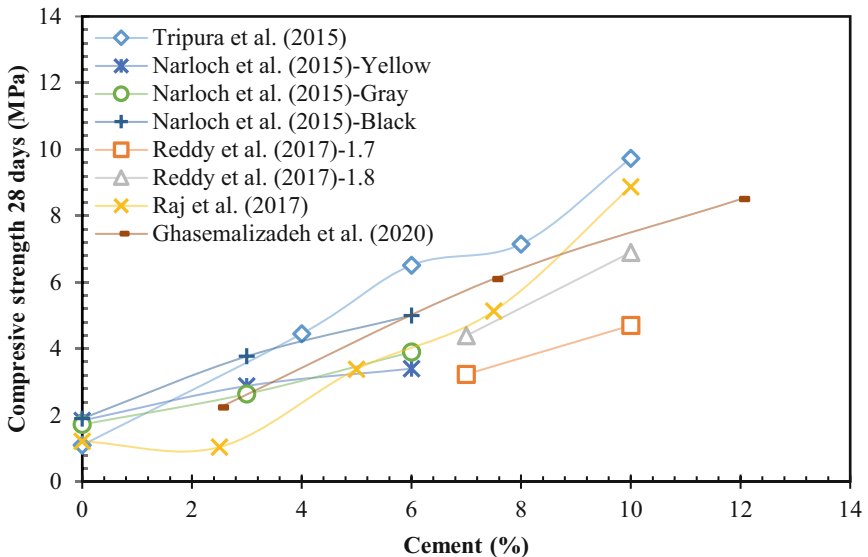
Fig. 1. Effect of cement content on the compressive strength of TSRE bricks.

2.3 Fiber Utilization in TSRE

To further enhance the mechanical properties of Traditional Stabilized Rammed Earth (TSRE) bricks, researchers have turned their attention towards incorporating various types of fibers into the TSRE matrix. This innovative approach aims to boost both compressive and flexural strength, two key parameters defining the robustness of these construction materials. Research by [20] demonstrated that incorporating polypropylene fiber, straw, and plastic fiber into the composition of Traditional Stabilized Rammed Earth (TSRE) bricks at varying percentages (0.5%, 2%, and 1% respectively) can significantly enhance the compressive strength of the resulting bricks. However, the flexural strength, another critical parameter, was found to remain unchanged. This revelation is of considerable significance as it suggests that these additive materials can contribute to producing more robust and resilient structures using TSRE bricks. Subsequent research, such as that conducted by [37], delved deeper into this aspect by experimenting with different concentrations of polypropylene fiber in the TSRE mixture, varying from 0.2% up to 1%. They discovered that both compressive and flexural strength of the TSRE bricks peaked at a polypropylene fiber concentration of 0.4%, beyond which both parameters began to decrease. The inclusion of marble dust in the TSRE bricks was also investigated by [19]. The study revealed that adding marble dust could enhance the compressive strength of TSRE bricks. On the other hand, the addition of polypropylene resulted in a decrease in compressive strength. Interestingly, flexural strength improved with the inclusion of 10% marble dust, but a higher concentration of 20% resulted in a decline. Polypropylene, in contrast, was seen to enhance flexural strength up to a concentration of 0.5%, but any increase beyond this concentration led to a reduction. [39] further investigated the impact of polypropylene fiber on TSRE bricks, incorporating it at concentrations of 0.25%, 0.5%, and 1%. Their findings indicated that the compressive strength of TSRE bricks increased up to a fiber concentration of 0.25%, after which it decreased. On the other hand, flexural strength was observed to improve across all mixtures, suggesting promising prospects for enhancing the mechanical performance of TSRE bricks. A more recent study by [38] explored the inclusion of Polyethylene terephthalate (PET) in TSRE bricks at concentrations of 0.5%, 1%, and 1.5%. Their research indicated that the compressive strength of TSRE bricks increased up to a PET concentration of 1%, after which the strength started to decline. Furthermore, the flexural strength was only found to increase for mixtures that included the lowest PET concentration.

3 Alkali Activation of SRE

Alkali activation is an innovative technique employed to enhance the mechanical properties and durability of construction materials including Stabilized Rammed Earth (SRE) bricks. It involves the utilization of alkaline substances to induce a reaction with pozzolanic materials, creating a robust and resilient binder that confers improved strength to the bricks. The principal components used in this process are fly ash, granulated blast furnace slag, and calcined clay. Fly ash, a by-product of coal combustion in power plants, contains a high proportion of silicon dioxide (SiO_2) and aluminum oxide (Al_2O_3), making it an excellent candidate for alkali activation. Granulated blast furnace slag, another industrial by-product derived from the ironmaking process, is also rich in SiO_2 and

Al2O3, along with calcium oxide (CaO). Calcined clay, in turn, serves as a readily available source of reactive silica. The alkaline activation is initiated by agents such as liquid sodium silicate, potassium hydroxide, and Portland cement. Sodium silicate and potassium hydroxide contribute sodium and potassium ions respectively, which act as the alkali component in the reaction. These substances dissolve the reactive silicate and aluminate species from the pozzolanic materials, leading to the formation of a complex aluminosilicate gel, often termed as geopolymer. This geopolymer gel hardens over time, providing the material with its binding strength. Portland cement plays a dual role in the process. Besides acting as an alkali activator, it also provides calcium ions. These calcium ions can react with the alumina present in the fly ash, slag, or clay to form additional calcium-alumino-silicate hydrate (C-A-S-H) phases. These C-A-S-H phases are similar to those formed in conventional cement hydration reactions, which contribute to the overall strength of concrete. Hence, the inclusion of Portland cement enhances both the binding capacity and the overall compressive strength of the SRE bricks. Alkali activation, therefore, provides a significant enhancement to the properties of SRE bricks. It facilitates the production of a more robust and sustainable building material, providing a potential avenue for the beneficial use of industrial by-products and reducing the environmental impact of construction.

3.1 Fly Ash Based SRE

Several studies have explored this domain, shedding light on various aspects of this process and its implications on SRE's compressive strength as shown in Table 1. [27] investigated the use of cementitious binders consisting of fly ash in combination with either lime or granulated blast furnace slag (GBFS) in a 50% by weight of dry soil ratio. Their results exhibited a significant difference in compressive strength based on the type of binder used. The fly ash and lime mixture resulted in a compressive strength of 7 MPa, while the combination of fly ash and GBFS yielded a superior result of 17.1 MPa. This significant strength disparity underscored the importance of the type of binder utilized with fly ash in the manufacture of SRE blocks. [28] focused on alkali-activated SRE bricks using class F (low calcium) fly ash as the binder and potassium hydroxide (KOH) as the activating agent. They noticed that the compressive strength was maximized at a 60% replacement of the clay-sand mixture with the binder, indicating that an optimal balance exists between the soil and binder proportions for strength enhancement. Without any replacement, the compressive strength was significantly registering 0.3 MPa only, underscoring the binder's role in strength augmentation. [29] studied the impact of composition variations on the compressive strength of alkali-activated SRE bricks. Their research suggested that increasing the molarity of sodium silicate and a higher proportion of GBFS in the binder generally yielded higher compressive strengths. However, a higher clay content typically led to reduced compressive strength, suggesting that an optimized soil composition is vital for strength performance. In a similar vein, [31] examined the effects of varying the replacement of the clay-sand mixture with Fly Ash (FA) on the compressive strength of alkali-activated SRE bricks. Their findings indicated that as the percentage of FA replacement increased, the compressive strength of the SRE bricks decreased, highlighting the importance of careful calibration of the binder quantity. In the absence of an alkali activator, the strength drastically reduced, demonstrating the

activator's crucial role in the alkali-activated SRE process. Alkali-activated SRE with fly ash exhibits promising results for sustainable construction applications. Still, its success largely depends on the careful optimization of various factors such as binder type, replacement ratio, and alkali activator use. Future research should focus on fine-tuning these parameters to optimize the strength and durability of alkali-activated SRE structures.

Table 1. Fly Ash Based SRE compressive strength at 28 days.

Researcher	Clay (%)	Sand (%)	Binder	Activator	Replacement (%)	Compressive Strength (MPa)
Rivera et al. (2020)	50	50	80% Fly ash and 20% Lime	Liquid sodium silicate (NaOH M = 10)	50	7
Rivera et al. (2020)	50	50	80% Fly ash and 20% GBFS	Liquid sodium silicate (NaOH M = 10)	50	17.1
Teing et al. (2019)	95	5	Class F fly ash	KOH	40–70	0.3–4.7
Toufigh et al. (2022)	7.5–22.5	92.5–77.5	75% FA and 25% GBFS, 25% FA and 75% GBFS	Liquid sodium silicate (NaOH M = 8–12)	15	1.68–16.03
Rios et al. (2016)	33	67	15–25% FA	Liquid sodium silicate (NaOH M = 7.5) or none	15–25	0.05–2.3

3.2   Fly Ash and Cement Based SRE

Two seminal studies conducted by [25, 26], which investigated the impact of different replacement percentages of binders (cement, and fly ash) on the compressive strength and elastic modulus of alkali activated SRE. In the study by [25], the authors highlighted the potential of cement and fly ash as binders in alkali-activated SRE. Their experimental setup kept a constant clay to sand ratio (67:33) while varying the replacement percentage

of the binder in the clay-sand mixture. The findings revealed that as the cement replacement percentage increased from 4% to 10%, there was a corresponding rise in the compressive strength from 4.45 MPa to 5.98 MPa, and the elastic modulus from 4 MPa to 5.55 MPa. However, when the fly ash replacement percentage increased in the absence of cement, both the compressive strength and the elastic modulus showed a decrease. Moreover, when both 7% cement and 1% to 4% fly ash simultaneously replaced the mixture, the performance decreased with an increase in the fly ash replacement percentage, even when cement was present. In contrast, [26] broadened the investigation by introducing calcium bentonite alongside cement and fly ash. Their study employed a different clay to sand proportion (28:72) and a wide range of binder replacement percentages. Echoing Narani et al.'s findings, an increase in cement replacement percentage led to an increase in both compressive strength and elastic modulus. However, as the replacement percentage of fly ash increased, an inconsistent pattern emerged in the compressive strength and elastic modulus, indicating a complex relationship between the two. Furthermore, the researchers found that when cement, fly ash, and calcium bentonite each replaced 15% of the mixture, the strength characteristics varied, underlining the importance of careful binder selection and proportioning. Both studies provide insightful observations on the complex interplay of binder types and replacement percentages in shaping the mechanical properties of alkali-activated SRE. The studies suggest that cement plays a critical role in enhancing the mechanical properties of SRE. However, the intricate performance trends observed with different percentages of fly ash and calcium bentonite underscore the need for further research to determine the optimal binder combinations and proportions.

3.3 Calcined Clay Based SRE

In recent years, there has been a growing interest in the potential of calcined clay as a binder in alkali-activated Stabilized Rammed Earth (SRE). The studies by [23, 30] provide valuable insights into the role of calcined clay and the alkali activator's molarity in enhancing the compressive strength of SRE. [23] concentrated on the impact of calcined clay as a binder on SRE's compressive strength, bulk density, and flexural strength, maintaining constant proportions of clay and sand at 65.1% and 34.9%, respectively. The experiment used liquid sodium silicate with a molarity of 8 (NaOH M = 8) as the activator. The study found that as the binder replacement percentage of calcined clay increased, significant improvements were observed in all parameters, notably in compressive strength. Particularly noteworthy were the results with a 20% binder replacement, which yielded the highest compressive strength (20.1 MPa), bulk density (1.81 g/cm3), and flexural strength (3.1 MPa). These findings underline the promising role of calcined clay as a binder in enhancing the mechanical properties of alkali-activated SRE. Simultaneously, [30] shed light on how the interplay between calcined clay and sodium hydroxide molarity (Fig. 2) can influence the compressive strength of alkali-activated SRE. The study varied calcined clay percentages in the SRE mixtures from 14% to 40%. Remarkably, even in the absence of an alkali activator, an increase in calcined clay percentage led to a significant improvement in compressive strength. The study further demonstrated that coupling sodium hydroxide and higher calcined clay percentages could considerably enhance compressive strength. Moreover,

[30] explored the impact of varying sodium hydroxide molarity, demonstrating a gradual increase in compressive strength as the molarity increased to 2 and 3. Intriguingly, a downward trend in compressive strength was observed beyond a molarity of 3, suggesting an optimal sodium hydroxide molarity for the activation process. The highest compressive strength was achieved with a sodium hydroxide molarity of 3 and a calcined clay percentage of 40%. Both studies confirm the valuable contribution of calcined clay as a binder in alkali-activated SRE. They underscore the importance of determining an optimal binder replacement percentage and sodium hydroxide molarity to achieve maximum compressive strength. The exploration of these parameters paves the way for the optimized use of calcined clay in the production of high-performance SRE.
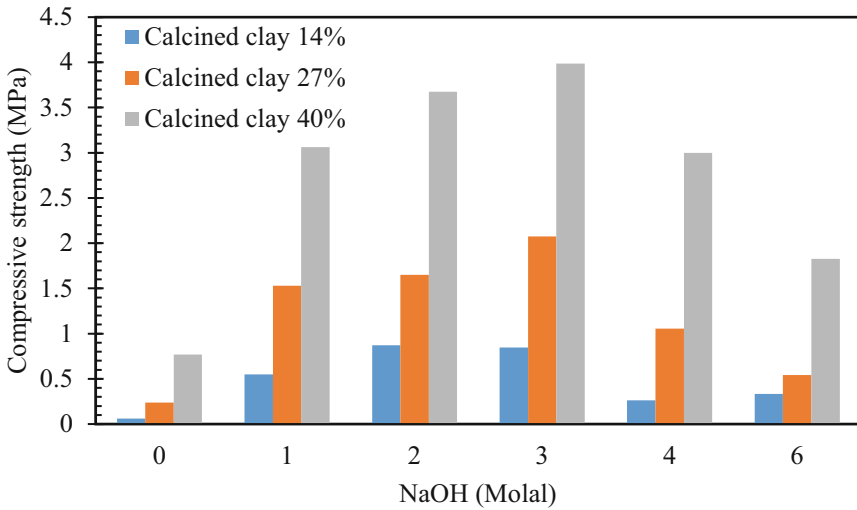
Fig. 2. Effect of NaOH molarity on the compressive strength of alkali activated calcined clay based SRE bricks.

4   Conclusion

In conclusion, this comprehensive review highlights the potential of alkali activation as a promising approach to enhance the mechanical properties of Stabilized Rammed Earth (SRE). The construction industry's increasing demand for sustainable practices has led to a renewed interest in SRE as a low-carbon and affordable alternative to conventional building materials. However, the widespread adoption of SRE has been limited by its relatively low strength and durability. Alkali activation, through the utilization of alkaline solutions and pozzolanic materials such as fly ash, slag, or calcined clay, offers a solution to overcome these limitations. By forming a hardened binder, alkali activation can significantly improve the structural integrity, durability, and overall performance of SRE. This review explored and compared the mechanical properties of traditional stabilized rammed earth and its alkali-activated counterparts, shedding light

on the effects of alkali activation on SRE. Moreover, the review discussed the diverse methodologies of alkali activation, including the use of different binders and activators, as well as the inclusion of additives such as lime, gypsum, cement, and fibers. These factors play a crucial role in optimizing the strength and durability of SRE, making it a versatile and adaptable option for sustainable construction. The findings underscore the importance of careful selection and calibration of binder compositions, replacement percentages, and activators to achieve high-performance alkali-activated SRE. Further research is needed to fine-tune these parameters and establish standardized guidelines for the industry. Overall, alkali activation holds significant potential for transforming SRE into a robust and environmentally friendly building material, contributing to the construction industry's sustainability goals. By enhancing the mechanical properties of SRE, alkali activation opens new avenues for widespread adoption and application of this innovative construction technique.

References

1. Akadiri, P.O., Chinyio, E.A., Olomolaiye, P.O.: Design of a sustainable building: a conceptual framework for implementing sustainability in the building sector. Buildings **2**(2), 126–152 (2012)
2. Onyegiri, I., Ugochukwu, I.B.: Traditional building materials as a sustainable resource and material for low cost housing in Nigeria: advantages, challenges and the way forward. Int. J. Res. Chem. Metall. Civ. Eng. **3**(2), 247–252 (2016)
3. Priyadharshini, P., Ramamurthy, K., Robinson, R.G.: Reuse potential of stabilized excavation soil as fine aggregate in cement mortar. Constr. Build. Mater. **192**, 141–152 (2018)
4. Abdullah, E.S.R., Mirasa, A.K., Asrah, H., Lim, C.H.: Review on interlocking compressed earth brick. In: IOP Conference Series: Earth and Environmental Science, vol. 476, no. 1, p. 012029 (2020)
5. Rivera, J., Coelho, J., Silva, R., Miranda, T., Castro, F., Cristelo, N.: Compressed earth blocks stabilized with glass waste and fly ash activated with a recycled alkaline cleaning solution. J. Clean. Prod. **284**, 124783 (2021)
6. Rakhimova, N.R., Rakhimov, R.Z.: Toward clean cement technologies: a review on alkali-activated fly-ash cements incorporated with supplementary materials. J. Non-Cryst. Solids **509**, 31–41 (2019)
7. Marvila, M.T., Azevedo, A.R.G.D., Vieira, C.M.F.: Reaction mechanisms of alkali-activated materials. Revista IBRACON de Estruturas e Materiais **14** (2021)
8. Meek, A.H., Beckett, C.T., Elchalakani, M.: Alternative stabilised rammed earth materials incorporating recycled waste and industrial by-products: durability with and without water repellent. Constr. Build. Mater. **265**, 120629 (2020)
9. Avila, F., Puertas, E., Gallego, R.: Mechanical characterization of lime-stabilized rammed earth: lime content and strength development. Constr. Build. Mater. **350**, 128871 (2022)
10. Akhil, U.V., Radhika, N., Saleh, B., Aravind Krishna, S., Noble, N., Rajeshkumar, L.: A comprehensive review on plant-based natural fiber reinforced polymer composites: fabrication, properties, and applications. Polym. Compos. (2023)
11. Dos Reis, G.S., et al.: Fabrication, microstructure, and properties of fired clay bricks using construction and demolition waste sludge as the main additive. J. Clean. Prod. **258**, 120733 (2020)
12. Labaied, I., Douzane, O., Lajili, M., Promis, G.: Bricks using clay mixed with powder and ashes from lignocellulosic biomass: a review. Appl. Sci. **12**(20), 10669 (2022)

13. Han, F., & Wu, L.: Comprehensive Utilization of Fly Ash. Industrial Solid Waste Recycling in Western China, pp. 207–304 (2019)
14. Mohammed, A.A., Nahazanan, H., Nasir, N.A.M., Huseien, G.F., Saad, A.H.: Calcium-based binders in concrete or soil stabilization: challenges, problems, and calcined clay as partial replacement to produce low-carbon cement. Materials **16**(5), 2020 (2023)
15. Losini, A.E., Grillet, A.C., Bellotto, M., Woloszyn, M., Dotelli, G.: Natural additives and biopolymers for raw earth construction stabilization–a review. Constr. Build. Mater. **304**, 124507 (2021)
16. Rosicki, Ł, Narloch, P.: Studies on the ageing of cement stabilized rammed earth material in different exposure conditions. Materials **15**(3), 1090 (2022)
17. Khadka, B.: Rammed earth, as a sustainable and structurally safe green building: a housing solution in the era of global warming and climate change. Asian J. Civ. Eng. **21**(1), 119–136 (2020)
18. Elahi, T.E., Shahriar, A.R., Islam, M.S.: Engineering characteristics of compressed earth blocks stabilized with cement and fly ash. Constr. Build. Mater. **277**, 122367 (2021)
19. Balkis, A.P.: The effects of waste marble dust and polypropylene fiber contents on mechanical properties of gypsum stabilized earthen. Constr. Build. Mater. **134**, 556–562 (2017)
20. Binici, H., Aksogan, O., Shah, T.: Investigation of fibre reinforced mud brick as a building material. Constr. Build. Mater. **19**(4), 313–318 (2005)
21. Onochie, K.K., Balkis, A.P.: Polypropylene fiber reinforced Alker as a structurally stable and sustainable building material. J. Clean. Prod. **279**, 123600 (2021)
22. Venkatarama Reddy, B.V., Suresh, V., Nanjunda Rao, K.S.: Characteristic compressive strength of cement-stabilized rammed earth. J. Mater. Civ. Eng. **29**(2), 04016203 (2017)
23. Idriss, E., et al.: Engineering and structural properties of compressed earth blocks (CEB) stabilized with a calcined clay-based alkali-activated binder. Innov. Infrastruct. Solut. **7**(2), 157 (2022)
24. Kosarimovahhed, M., Toufigh, V.: Sustainable usage of waste materials as stabilizer in rammed earth structures. J. Clean. Prod. **277**, 123279 (2020)
25. Narani, S.S., Zare, P., Abbaspour, M., Fahimifar, A., Siddiqua, S., Hosseini, S.M.M.M.: Evaluation of fiber-reinforced and cement-stabilized rammed-earth composite under cyclic loading. Constr. Build. Mater. **296**, 123746 (2021)
26. Naeini, A.A., Siddiqua, S., Cherian, C.: A novel stabilized rammed earth using pulp mill fly ash as alternative low carbon cementing material. Constr. Build. Mater. **300**, 124003 (2021)
27. Rivera, J.F., de Gutiérrez, R.M., Ramirez-Benavides, S., Orobio, A.: Compressed and stabilized soil blocks with fly ash-based alkali-activated cements. Constr. Build. Mater. **264**, 120285 (2020)
28. Teing, T.T., Huat, B.B., Shukla, S.K., Anggraini, V., Nahazanan, H.: Effects of alkali-activated waste binder in soil stabilization. GEOMATE J. **17**(59), 82–89 (2019)
29. Toufigh, V., Ghasemalizadeh, S., Karamian, M.: Experimental investigation of mixture design and durability performance of alkali-activated rammed earth. Int. J. Geomech. **22**(4), 04022029 (2022)
30. Cristelo, N., Glendinning, S., Miranda, T., Oliveira, D., Silva, R.: Soil stabilisation using alkaline activation of fly ash for self compacting rammed earth construction. Constr. Build. Mater. **36**, 727–735 (2012)
31. Rios, S., Cristelo, N., Viana da Fonseca, A., Ferreira, C.: Structural performance of alkali-activated soil ash versus soil cement. J. Mater. Civ. Eng. **28**(2), 04015125 (2016)
32. Tripura, D.D., Singh, K.D.: Characteristic properties of cement-stabilized rammed earth blocks. J. Mater. Civ. Eng. **27**(7), 04014214 (2015)
33. Beckett, C., Ciancio, D.: Effect of compaction water content on the strength of cement-stabilized rammed earth materials. Can. Geotech. J. **51**(5), 583–590 (2014)

34. Raj, S., Mohammad, S., Das, R., Saha, S.: Coconut fibre-reinforced cement-stabilized rammed earth blocks. World J. Eng. **14**(3), 208–216 (2017)
35. Narloch, P.L., Woyciechowski, P., Jęda, P.: The influence of loam type and cement content of the compressive strength of rammed earth. Arch. Civ. Eng. **61**(1), 73–88 (2015)
36. Ghasemalizadeh, S., Toufigh, V.: Durability of rammed earth materials. Int. J. Geomech. **20**(11), 04020201 (2020)
37. Donkor, P., Obonyo, E.: Earthen construction materials: assessing the feasibility of improving strength and deformability of compressed earth blocks using polypropylene fibers. Mater. Des. **83**, 813–819 (2015)
38. Ahmad, A., Balkis, A.P., Onochie, K.K.: The use of shredded plastic wastes in Alker production and its effect on compressive strength and shrinkage properties. Alex. Eng. J. **61**(2), 1563–1570 (2022)
39. Araya-Letelier, G., Concha-Riedel, J., Antico, F.C., Sandoval, C.: Experimental mechanical-damage assessment of earthen mixes reinforced with micro polypropylene fibers. Constr. Build. Mater. **198**, 762–776 (2019)

Some Mechanical Properties of Concrete Incorporating Plastic Wastes and Marble Dust Wastes

Mostafa Hamoleila and Özgür Eren(✉)

Department of Civil Engineering, Faculty of Engineering, Eastern Mediterranean University, Türkiye via Mersin 10, Famagusta, Turkey
`ozgur.eren@emu.edu.tr`

Abstract. This research investigates incorporating locally produced wastes which are marble dust waste (MDW) and shredded fibrous plastic wastes (SFPW) on the physical and mechanical properties of normal strength concrete. For this particular reason, testing program that involves 20 different mixtures of concrete is developed. MDW is utilized as a cement's replacement in concrete with the percentages of 0, 5, 10, 15, and 20. On the other hand, SFPW is used as an additive by means of the cement volumes with a proportion of 0, 2, 3 and 5%. The influence of these mixtures on the fresh concrete slump, compressive and splitting tensile strength, and flexural strength were studied. Results indicated that physical characteristics such as workability was affected slightly. On the other hand, the mechanical response does vary where it outperforms the control mixture at some replacement levels and underperform at high replacement levels. It is concluded that the optimal replacement levels of the MDW and SFPW is 5% and 2%, respectively.

Keywords: Concrete · Marble dust · Shredded fibrous plastic wastes · Construction waste

1 Introduction

As of the strategic location of Cyprus and its charming shores, people from all around the world are seeking to possess a real estate in the island. This causes sharp increase in the construction industries all over the island to overcome the massive demand. Most of the construction industries relays on traditional Portland cement concrete which increases the environmental and ecological footprint of the island. Another material that are extensively used in the construction industry are marble stones and polyvinyl chloride. However, during cutting, molding and polishing large amount of waste is produced which are not recycled and dumped in land fill. Incorporating these two materials in concrete to substitute the cement and its impact on the mechanical characteristics of concrete is rather ambiguous and requires further investigation.

The aim of this study is to produce a more environmentally friendly concrete by means of reutilizing largely produced wastes in the Northern Cyprus. These wastes include marble dust waste and shredded fibrous plastic waste that are largely produced

and does not decompose in a short period of time. The targeted mixture should perform better or in similar manner of the traditionally produced concrete.

1.1 Sustainability and Environmental Aspects of Traditional Concrete

To help improve living standards across the globe, environmental concerns must be considered in all aspects of life, including construction. According to the experts, the construction sector's primary objective is to participate in the implementation of ecological building structures through the use of technical and functional methods by reducing energy consumption of the construction material sector, minimizing embodied energy, and by reducing cost and environmental potential impact [1]. Researchers stated that it is critical to utilize environmentally sustainable construction materials which can contribute to the quality of the atmosphere within buildings. This is an important health concern that must be addressed [2]. Eco-friendly material production aims to enhance material management, eliminate waste, and produce materials with adequate physical and mechanical characteristics.

1.2 Local Wastes that can be Incorporated in Concrete

Marble Dust Waste (MDW)
MDW is considered as the main by-product in the building industry that is produced in large quantities in various countries. The large marble blocks are cut to smaller blocks to make the recommended flat figure. While cutting and polishing of marble, approximately 30% of marble is converted into dust, mainly consisting of Al_2O_3, SiO_2, Fe_2O_3 and CaO, with some secondary components such as Mg, K, Mn and Ti oxides. If not effectively treated before disposal, it can cause dangerous damages to the environment, such as pollution of the soil and ground water [3].

Shredded Fibrous Plastic Waste (SFPW)
In the most recent recorded year, 322 million tons of plastic were made worldwide, with Europe solely producing 58 million tons. Average production grew to 335 million tons in 2016, with Europe producing 60 million tons. According to the statistics, 31.1% of these were reprocess in 2016, 41.6% were utilized for energy retrieval, and 27.3% were landfilled internationally in 2016. However, by 2035, plastic manufacture is anticipated to triple, and by 2050, it is anticipated to quadruple [1].

1.3 Effect of the Local Wastes on the Fresh Properties of Concrete

Effect of MDW on Workability
The researchers discovered that when concrete comprises 0, 5, 10, 15, and 20% MDW as cement replacement by weight, and at a water/cement ratio of 0.43, MDW has a negative impact on slump. As an outcome, they concluded that as the MDW ratio grows from 0% to 20%, the slump tends to diminish, owing to the refinement of MDW [4]. Another research which is used MDW as partially cement and fine aggregate replacement found at various concrete mixes that as the amount of MDW increases the slump of concrete tend to decrease [5].

Research used MDW as partially cement replacement with percentages 5 and 10, shows a slight increase in the slump value for 5% substitution, however no considerable change was recorded for 10% MDW [6].

Effect of Plastic Waste (PW) on Workability
Several concrete characteristics containing plastic aggregate produced with strips were studied, having plastic aggregate substituting sand by 5%, 15%, 30%, 45%, 65%, and 85%. The results reveal that the slump value maintained steady until to 15% substitution, although it fell somewhat at 30% and 45%, but this impact was more pronounced at 65 and 85% of the integration ratio [7]. One research that utilizes fine plastic as a replacement for fine aggregate at 10, 15, and 20% indicates that as the proportion of substitute grows, the slump reduces, with a substantial drop at 20% substitution, which is about 95% when opposed to the reference mix. Additionally, the particle magnitude of plastic aggregates has a substantial influence on concrete's workability. At 10% and 20% replacements, survey was performed, and the findings revealed that mixes with a greater size of plastic aggregate had a lesser slump value [8].

1.4   Effect of the Local Wastes on the Mechanical Properties of Concrete

Effect of MDW on Compressive Strength
Numerous researches have analysed and inspected the advantages of utilizing MDW for enhancing the characteristics of concrete. A few of these research looked at whether utilizing MDW as a cement substitute at 0, 10, 15, and 20% in concrete with a water/cement ratio of 0.5 enhanced compressive strength marginally in comparison to a control mix. This small improvement occurred up to 10% cement substitution by MDW, but at 15% and 20% substitution, the trend was negative when compared to the control mix [9]. Other analysis looked at the compressive strength of concrete that included MDW as a partial substitute for cement by weight. The goal of those experiments was to substitute cement for MDW in attempt to create a more sustainable combination. According to the compressive strength data, the optimum ratio for substituting the cement with MDW was around 5% [10, 11]. Nonetheless, in another research, MDW had no influence on compressive strength at 10% and 15% substitution, but at 20% and 25% substitution, there was a decrease as MDW percentage increases [12]. A research was done by using MDW as partially cement replacement with percentages 5 and 10, the results at 28 days curing show as the marble dust content increases the compressive strength decrease for both substitution percentages, where around 18% reduction was recorded at 10% marble substitution [6]. Another research used MDW as cement replacement the substitution percentages were 5, 10, 15, and 20. The results show as the percentage of marble increase the compressive strength value also increase up to 10 marble substitution, however, a dramatical decrease in compressive strength was recorded at percentage 15 and 20 [9].

Effect of MDW on Flexural Strength and Splitting Tensile Strength
According to the flexural strength assessment results given by [13] as the marble dust increases the flexural strength also incceases up to 10% MDW replacement, with an adverse trend at 15% and 20% replacement. Another research [14] indicated a slight loss in flexural strength equal to 10% MDW substitute compared to the reference sample,

but a decline in flexural was identified at 15% afterwards, which maintained to flexural decline as the MDW percentage rose. This might be due to a leak in the delivery of cementitious materials.

The study conducted by [12] demonstrates that whenever the MDW substitute is 5%, the splitting tensile strength rises when in contrast to the reference mix; however, as the MDW substitution exceeds 5%, the splitting tensile strength begins to decline until it reaches 25% substitution. Another investigation found that when the MDW replacement increased, the splitting tensile decreased at 30% as MDW is replaced with cement, the splitting tensile is reduced by more than 20% when compared to the reference mix [15].

Effect of Plastic Waste on Compressive Strength

Research conducted by [7] shows an increment in compressive strength at 5% plastic waste replacement, at 10 and 15% replacement the compressive strength had slight decrease compare by control were at 45% replacement it decreases more than 50% compare by reference. As natural aggregate replacement a study carried by [16] shows a dramatic decrease in the compressive strength at 5% PW replacement, however, a steady decrease at 10, 15 and 20%. Last study which uses electronic plastic as natural aggregate replacement by 10, 20, 30 and 40%, in general the compressive strength decrease as the replacement percentage increases. At 10% replacement the compressive strength decreases, however, a slight enhance was found at 20% were a steady decrease at 30 and 40% replacement [17].

Effect of PW on Flexural Strength and Splitting Tensile Strength

As natural aggregate replacement a study carried by [16] shows a sudden drop in the flexural strength at 10% PW replacement, however, a steady decrease in flexural strength was detected at 15% PW substitute. Another study which uses PW powder as natural aggregate replacement was carried by [8] demonstrated that as the PW powder replacement rises the flexural strength decreases, steady decrement in flexural was obtained up to 10% were at 25% replacement more than 15% was lost compare with reference specimen.

One study shows that as the PW powder replacement percentage increases the splitting tensile strength decreases were at 25% replacement approximately 30% loss had observed [8]. Another study was carried out by [17] indicates a significant drop in splitting tensile strength 5% PW substitution, but a continuous decline at 10, 15, and 20%. In a previous study that used electronic plastic as a natural aggregate replacement by 10, 20, 30, and 40%, the splitting tensile strength decreased as the quantity of replacement amplified. The splitting tensile strength drops at 10% replacement, although there is a minor increase at 20% substitution and a continuous reduction at 30 and 40% substitute [7].

2   Materials and Experimental Methods

2.1   Materials

The cement used is CEM II/B-S 42.5 N.

Aggregate was crushed limestone obtained from Beşparmak Mountains of Cyprus with a maximum particle diameter of 20 mm. Classification of the used aggregate is conducted in accordance with ASTM C136/C136M-19 and ASTM C33/C33M – 18. Additionally, the physical characteristic of fine aggregate and coarse aggregate are evaluated as per ASTM C128-15 and ASTM C127-01, respectively (see Table 1).

Table 1. Physical properties of the aggregates used.

Physical properties	Fine aggregate	Coarse aggregate
Relative Density (Saturated surface dry)	2.76	2.74
Relative Density Oven Dry	2.68	2.70
Apparent Relative Density	2.92	2.81
Water absorption	3.09%	1.39%

The water which is used as mixing eater was ordinary tap fresh water. The amount of dissolved salts and pH level are measured using the multiprobe method as per ASTM 2976-71. Results indicate that the amount of dissolved salts is 179.8 part per million and a pH level of 6.91.

Shredded Fibrous Plastic Waste (SFPW) is obtained from the industrial region of Famagusta. The waste is generated as scraped material after production of doors and windows to desired sizes. The SFPW is extremely light in density that it can float on water, alcohol and gasoline. For this reason, available methods for measuring its specific gravity are not adequate as they involve submersing the material in water or any liquid. Thus, new testing methodology is developed to measure the specific gravity of the SFPW material. The test setup is composed basically of 1-L graduated cylinder which is equipped with a detachable wire mesh. The function of the wire mesh is to keep the SFPW submersed under water. The specific gravity is found to be 0.4143.

Marble dust waste (MDW) is obtained also from the industrial region of Famagusta. The waste is generated in sludge form as results of cutting and polishing the marble stones to make statues, decorative elements and grave monuments. Particle size distribution of MDW is conducted in accordance with ASTM C136/C136M – 19. The specific gravity of marble dust waste is evaluated using density bottle method (pycnometer) as per ASTM C110 where ethyl alcohol is used instead of water in 500 ml pycnometer. This is done, in order to prevent any reactions between the MDW and water from taking place. Results indicated that the specific gravity of the MDW is 2.64.

2.2   Experimental Methods

The design strategy is basically composed of 5 replacement percentages of the marble dust waste by means of the cement mass. These percentages are 0, 5, 10, 15, and 20%.

Also, the SFPW is introduced to the mix as an additive with an amount of 0, 2, 3, and 5% of the cement volume in the mix. After casting the samples, they are cured for periods of 7 and 28 days to evaluate the specimen's compressive strength. However, for the splitting tensile strength and flexural strength, samples are cured for 28 days.

The mix design is prepared by Building Research Establishment (BRE) method of mix design. The characteristic compressive strength is selected to be 30 MPa at 28 days as it covers wide range of site application (foundations, columns, and beams). Defective percentage of 10% is selected and the target strength was found to be 40 MPa. The water to cement ratio was fixed as 0.5 and cement content was 330 kg/m^3. So, based on these assumptions mix design table is generated which is shown in Table 2.

Table 2. The adopted testing mix design.

mixture*	cement (kg)	MDW (kg)	SFPW (g)	water content (kg)	crushed limestone aggregate (kg)			
					0– 5 (mm)	5–10 (mm)	10–15 (mm)	15–20 (mm)
S 0 M 0	330	0.0	0	205	925	350	350	350
S 0 M 5	314	16	0	205	925	350	350	350
S 0 M 10	297	33	0	205	925	350	350	350
S 0 M 15	281	50	0	205	925	350	350	350
S 0 M 20	264	66	0	205	925	350	350	350
S 2 M 0	330	0	882	205	925	350	350	350
S 2 M 5	314	16	882	205	925	350	350	350
S 2 M 10	297	33	882	205	925	350	350	350
S 2 M 15	281	50	882	205	925	350	350	350
S 2 M 20	264	66	882	205	925	350	350	350
S 3 M 0	330	0	1323	205	925	350	350	350
S 3 M 5	314	16	1323	205	925	350	350	350
S 3 M 10	297	33	1323	205	925	350	350	350
S 3 M 15	281	50	1323	205	925	350	350	350
S 3 M 20	264	66	1323	205	925	350	350	350
S 5 M 0	330	0	2205	205	925	350	350	350
S 5 M 5	314	16	2205	205	925	350	350	350
S 5 M 10	297	33	2205	205	925	350	350	350
S 5 M 15	281	50	2205	205	925	350	350	350
S 5 M 20	264	66	2205	205	925	350	350	350

*S (SFPW): Shredded fibrous plastic, and M (MDW): Marble dust waste

Preparation of Test Samples

Cubic plastic molds with a side dimension of 150mm are used for compressive and splitting tensile test. Prismatic steel mold with a length of 500 mm, width of 100 mm and height of 100 mm are used fort flexural strength test.

Immediately after casting the samples, they are shipped to curing room. Samples are kept in the curing room for an overnight period. Then, the samples are discharged from their mold into a curing tank that is filled with fresh water. Samples are kept in the curing tanks until the desired testing period is reached.

2.3 Testing Procedures

All the tests within this study are conducted in the Material of Construction Laboratory of the Civil Engineering Department at Eastern Mediterranean University. Testing procedures are conducted with the ASTM standards.

The compressive strength of the concrete specimen is conducted in accordance with C109/C109M-20b.

The flexural strength is obtained as provisioned by ASTM C1609/C1609M-19a.

3 Results and Discussion of Results

3.1 Slump

The results of slump test are depicted in Fig. 1. As shown the slump of the fresh concrete mix significantly dropped upon incorporating both MDW and SFPW. It is worth to mention that the relationship between slump level and the MDW replacement percentage is inversely proportional where replacement level of MDW of 20% resulted in reducing the slump to roughly 70% of the controlled mix slump, where a similar outcome obtained by [4, 5]. This can be related to the high surface area that the MDW possesses in addition to its high-water absorption capacity. Similarly, the SFPW percentage also negatively influenced the workability of the control mix where even 2% addition of SFPW resulted in reducing the slump to roughly 67% of the controlled mix slump. This can be attributed to the fact that SFPW acts as fibrous additive which usually reduces the slump of the concrete mixture.
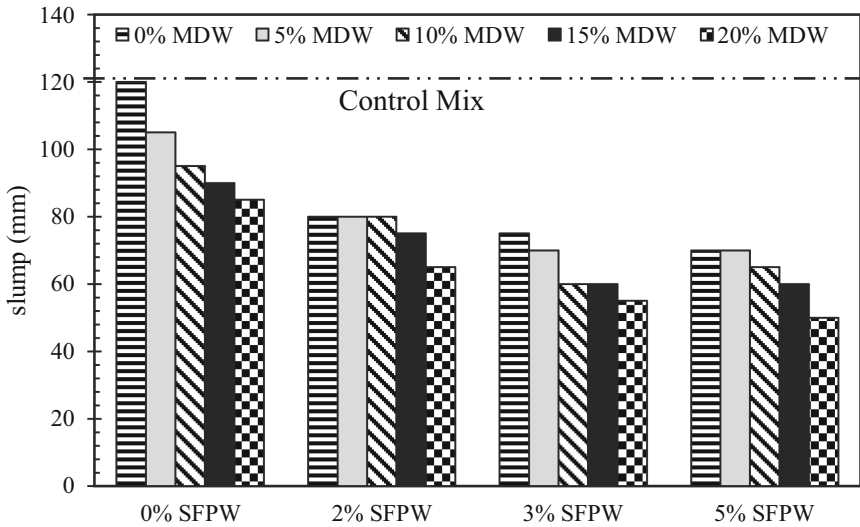
Fig. 1. Slump test results of concrete mixtures.

3.2 Compressive Strength

The early development of strength upon one weak of curing is evaluated for every single mixture. The compressive strength results are presented in Fig. 2. As illustrated the compressive strength at 7 days curing period is inversely proportional with the MDW replacement levels. For instance, 20% addition of marble dust resulted in a compressive strength that is roughly 27% lower when compared with reference, this is also obtained in previous study which done by [9, 10, 12]. It might be linked to the fact that, MDW does not possesses any pozzolanic activity and is rather an inert material which acts as filler only. However, including the SFPW indeed resulted in improving the compressive strength slightly (by 1.5%) at 2% SFPW addition with 5% MDW.

The samples that were crushed after 28 days of curing resulted in similar behavior with the samples cured after 7 days. This can be observed in Fig. 3 which present the testing outcomes in a bar chart form. As illustrated as the MDW percentage increases beyond 5% dramatic reduction in the compressive strength is attained, where replacing the cement by 20% MDW resulted in a compressive strength that is roughly 20% lower than the control sample, moreover, same results was discovered by previous studied which is done by [10, 11]. On the contrary, SFPW percentage has almost no significant effect on the compressive strength where the rate of change did not exceed ±2%. For the composite mixtures that includes both of MDW and SFPW it gives an optimal performance with 5% MDW and 2% SFPW replacement levels where the compressive strength improved by 4%.
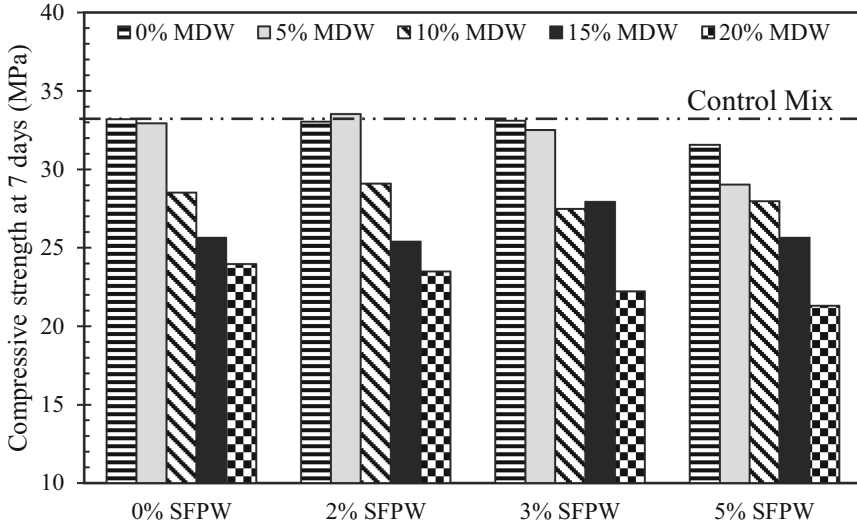
Fig. 2. Compressive strength at 7 days of curing.
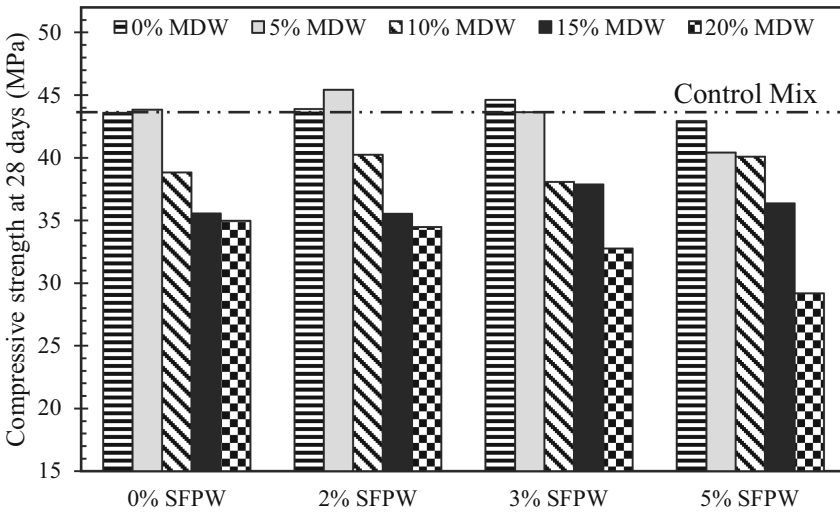
Fig. 3. Compressive strength at 28 days of curing.

As depicted the compressive strength of the cured samples reduces as the MDW percentage increases beyond 5%, for instance, 20% MDW that was used as substitute of the cement resulted in a compressive strength that is roughly 22% lower than the reference sample, similarly was recorded by a study which done by [10]. Alternatively, the effect of SFPW percentage is almost insignificant regarding the compressive strength where the rate of change did not exceed ±2%. Ultimately, optimal performance for mixtures including both of MDW and SFPW is achieved at 5% MDW and 2% SFPW replacement levels where the compressive strength increased by 2.37%.

3.3   Splitting Tensile Strength

The tensile strength of the produced materials is evaluated indirectly by means of the splitting tensile strength test. Results are shown in Fig. 4. It is observed that SFPW has no influence on the splitting tensile strength. Unlike the MDW which generally reduces the splitting tensile strength for replacement levels larger than 5%, this is also reported by the previous studies which done by [12, 15]. However, incorporating both wastes lead to dramatic decrease of the splitting tensile strength. Where 20% MDW with 5% SFPW resulted a splitting tensile strength that is 36% less than the reference mix. This can be linked to the information that both of MDW and SFPW lack any cementitious materials.
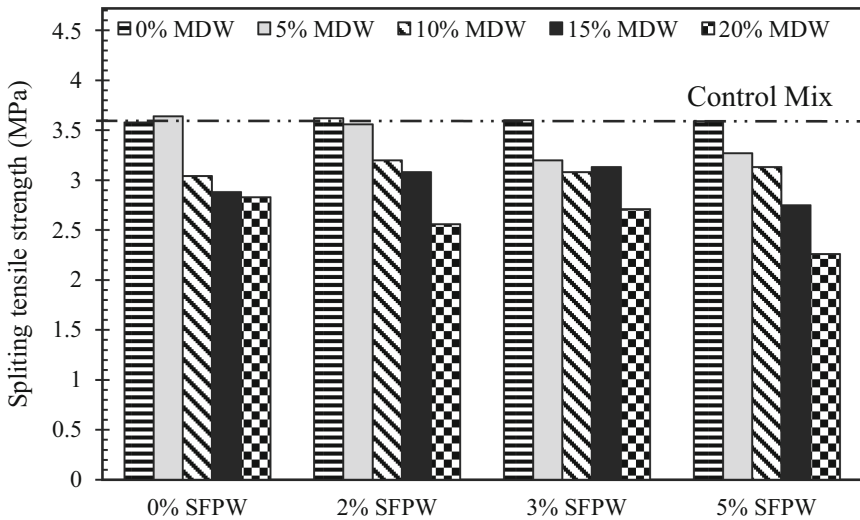
Fig. 4. Splitting tensile strength at 28 days of curing.

3.4   Flexural Strength

Flexural strength is an essential property as it measures the resistance of a material to deformation by means of modulus of rapture. Outcomes of flexural strength are displayed in Fig. 5. As shown, the flexural strength of concrete significantly improved upon adding SFPW, where 5% of SFPW has flexural strength 13% larger than the control mix. On the other hand, MDW tends to reduce the flexural strength for replacement levels larger than 5% as MDW does not initiate any pozzolanic activities, additionally, similar results for 5% MDW substitution was reported by [14]. On the contrary, considering both of MDW and SFPW it is found that the optimum mixture is 5%MDW and 2% SFPW increased the flexural strength by roughly 10% in comparison with the controlled mix.
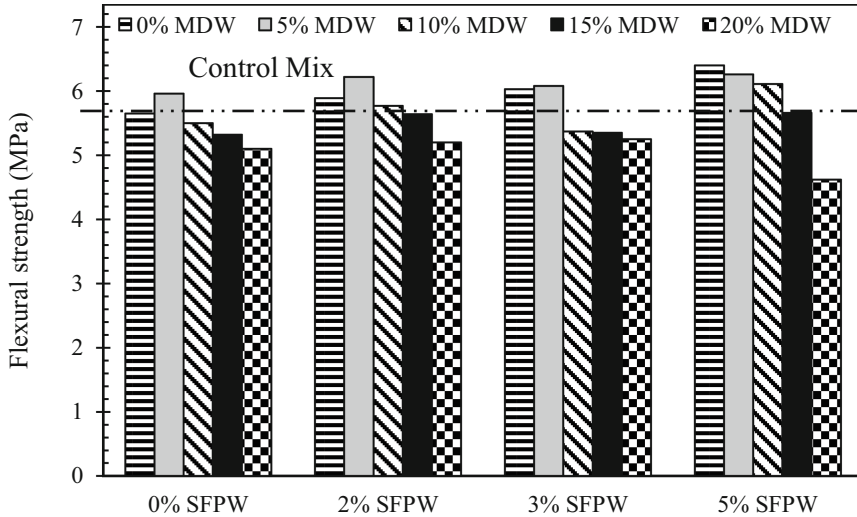
Fig. 5. Flexural strength at 28 days of curing.

4 Conclusions

1. The slump of the mixture dropped from high to medium workability. The most crucial element on the workability is replacing the cement by the marble dust as it has very large surface area and requires more water to cover its particles surfaces.
2. The compressive strength is evaluated over two periods of curing which are: 7 and 28 days. However, the behavior with respect to the control samples remained similar regardless of the curing periods. The optimal percentage of using the MDW and SFPW is found to be 5% and 2% respectively. This proportion achieved higher compressive strength in comparison with the controlled mix.
3. Regarding the indirect tensile strength, the MDW replacement levels significantly reduced the tensile strength. In contrast, the addition of SFPW has no significant effect. The optimal mix that causes no decrease in the indirect tensile strength using the MDW and SFPW is found to be 5% and 2% respectively.
4. Flexural strength is impacted significantly by means of the MDW replacement levels. However, the SFPW enhanced the flexural strength so slightly. The optimal probation of the MDW and SFPW is found to be 5% and 2–5% respectively.

References

1. Bahij, S., Omary, S., Feugeas, F., Faqiri, A.: Fresh and hardened properties of concrete containing different forms of plastic waste–a review. Waste Manag. **113**, 157–175 (2020)
2. Aciu, C., Ilutiu-Varvara, D.A., Manea, D.L., Orban, Y.A., Babota, F.: Recycling of plastic waste materials in the composition of ecological mortars. Procedia Manuf. **22**, 274–279 (2018)
3. Dhanapandiana, S., Shanthib, M.: Utilization of marble and granite wastes in brick products. J. Ind. Pollut. Control. **25**(2), 145–150 (2009)

4. Kumar, S.K., Kumar, R.: Partial replacement of cement with marble dust powder. Int. J. Eng. Res. Appl. **5**(8), 106–114 (2015)

5. Sharma, N., Kumar, R.: Use of waste marble powder as partial replacement in cement sand mix. Int. J. Eng. Res. Technol. **4**(5), 501–504 (2015)

6. Bostanci, S.C.: Use of waste marble dust and recycled glass for sustainable concrete. J. Clean. Prod. **251** (2020)

7. Mohammed, A.A., Mohammed, I.I., Mohammed, S.A.: Some properties of concrete with plastic aggregate derived from shredded PVC sheets. Constr. Build. Mater. **201**, 232–245 (2019)

8. Babafemi, A.J., Šavija, B., Paul, S.C., Anggraini, V.: Engineering properties of concrete with waste recycled plastic: a review. Sustainability **10**(11) (2018)

9. Shirule, P.A., Rahman, A., Gupta, R.D.: Partial replacement of cement with marble dust powder. Int. J. Adv. Eng. Res. Stud. **1**(3), 15 (2012)

10. Arel, H.Ş: Recyclability of waste marble in concrete production. J. Clean. Prod. **131**, 179–188 (2016)

11. Singh, M., Srivastava, A., Bhunia, D.: An investigation on effect of partial replacement of cement by waste marble slurry. Constr. Build. Mater. **134**, 471–488 (2017)

12. Vardhan, K., Goyal, S., Siddique, R., Singh, M.: Mechanical properties and microstructural analysis of cement mortar incorporating marble powder as partial replacement of cement. Constr. Build. Mater. **96**, 615–621 (2015)

13. Ali, M.M., Hashmi, S.M.: An experimental investigation on strengths characteristics of concrete with the partial replacement of cement by marble powder dust and sand by stone dust. Int. J. Sci. Res. Dev. **2**(7), 360–368 (2014)

14. Rana, A., Kalla, P., Csetenyi, L.J.: Sustainable use of marble slurry in concrete. J. Clean. Prod. **94**, 304–311 (2015)

15. Shaaban, M.: The effects of marble dust on the rheological and mechanical properties of shotcrete. Eng. Technol. Appl. Sci. Res. **10**(5), 6344–6348 (2020)

16. Merlo, A., Lavagna, L., Suarez-Riera, D., Pavese, M.: Mechanical properties of mortar containing waste plastic (PVC) as aggregate partial replacement. Case Stud. Constr. Mater. **13** (2020)

17. Evram, A., Akçaoğlu, T., Ramyar, K., Çubukçuoğlu, B.: Effects of waste electronic plastic and marble dust on hardened properties of high strength concrete. Constr. Build. Mater. **263** (2020)

Eco-friendly vs Fire Safe? Conceptualising Fire Risk for Construction Systems Incorporating Waste and Biomass

Richard Walls[(✉)] , Yohannes Shewalul , Adewumi John Babafemi ,
and Natalia Flores-Quiroz

Department Civil Engineering, Stellenbosch University, Stellenbosch, South Africa
{rwalls,yshewalul,ajbabafemi,nataliaflores}@sun.ac.za

Abstract. There is an international push to incorporate materials such as waste plastic, rubber and biomass, amongst other products, into construction systems to enhance sustainability and reuse waste. This paper investigates the fire risk associated with incorporating (a) continuous-, (b) macro- (large, distinct fuel packages), and (c) micro-encapsulated (small, dispersed pieces) combustible materials, along with (d) biomass into construction systems. Heat release rates, fire growth rates, smoke production, fire resistance ratings, firefighting requirements and general building safety can be influenced when these materials are used. Fire risk cannot be ignored and may be one of the biggest barriers to various sustainable construction systems. A challenge to be overcome is to define what level of smoke and energy release is considered safe. Many of the systems will readily obtain a standard fire resistance rating and pass reaction-to-fire tests, meaning that they are permitted according to building codes. Of the systems considered, plastered masonry systems with micro-encapsulation are likely to present a low fire risk, with continuously-encapsulated waste plastic systems presenting a high fire risk. Outer plaster layers, which function as passive protection, are often essential in protecting combustible internal materials.

Keywords: Sustainable construction · waste plastic · fire risk · eco-friendly · construction systems

1 Introduction

In recent decades there has been a massive drive to enhance sustainability. Various materials have been incorporated into construction systems including waste plastic, waste glass, recycled tire rubber, typical concrete extenders such as fly ash and ground granulated blast-furnace slag, bottles filled with non-recyclable waste (ecobricks), biomass and various other systems [1–5]. However, synthetic materials, such as plastic, are oil-based materials with energy contents comparable to petrol, and also produce noxious fumes when they burn [6]. Rubber does not ignite easily but has a high heat release rate after ignition [7]. Biomass systems (e.g. hemp) are also combustible and may contribute

to fire spread, albeit typically less severely than hydrocarbon-based materials. Additionally, there has been a significant resurgence in the use of natural materials, especially timber [8]. One of the reasons for the widespread adoption of timber in applications for which it was previously considered unsuitable, e.g. high-rise buildings, has been significant advancements in structural fire engineering. Research and better characterisation of the behaviour of timber at elevated temperature, along with the ability to engineer safety systems to accommodate the risk (e.g. detection, suppression, passive protection), has permitted this [9].

The influence of fire safety on sustainable building practices has started gaining significant attention as the combustion of materials can produce large amounts of greenhouse gases, result in contaminated firefighting water and can endanger people [10]. Fire safety can be a major barrier to introducing materials that may improve thermal performance (e.g., low conductivity plastics), result in carbon capture (e.g., timber) or permit the reuse of waste (e.g. recycled rubber tires). As an example of the sort of disaster that can occur when fire safety is not considered, the aluminium composite panels used on the Grenfell Tower were good for thermal performance and aesthetics, but resulted in a rapidly spreading fire that killed 72 people [11].

This paper discusses the risks associated with the incorporation of waste and biomass into construction systems. Initially the requirements of products in fire are presented as an overview of the required performance of materials, but this is also used to highlight areas where some modern codes may not be suitable. Thereafter typical geometrical arrangements and systems are discussed in relation to their potential influence on fire behaviour. The paper concludes with an analysis of important factors that must be addressed to advance the use of waste and biomass materials without compromising fire safety. This paper is conceptual in nature through discussing various fire safety considerations that must be addressed, and highlights where certain systems may fail or should be used with caution.

2   Fire Requirements and System Considerations

2.1   Codified Requirements for Construction Systems

Structural systems typically are assigned a *fire resistance rating* based on the length of time that they withstand the ISO 834 standard time-temperature fire curve [12]. Failure is based on the time at which (i) structural resistance (ability to carry load), (ii) insulation (ability to prevent heat transfer based on limiting temperatures on the unexposed face) and/or (iii) integrity (ability to prevent smoke and flame from passing through) criteria are exceeded [13]. A fire resistance rating is more applicable for the fully-developed stage of a fire, i.e., post-flashover. Combustible materials, such as timber, can obtain a fire rating provided that they have sufficient thickness to ensure that they do not burn through. However, such systems will contribute to the total heat release rate (HRR) in a real building and result in fires lasting longer. HRR has been acknowledged as the most important parameter for quantifying the severity of a fire [14]. Furthermore, when materials burn, especially synthetic materials, they can release a variety of noxious fumes which hinders evacuation of occupants [15]. Figure 1(a) illustrates an ecobrick

wall sample at the end of a standard fire test where the fuel packages have ignited and remain burning after the furnace has stopped.

Reaction-to-fire tests measure how easily a material ignites and flames spread across its surface. Reaction-to-fire tests are more important for ensuring that the rate of fire development in the early stage is limited, i.e., pre-flashover. Figure 1(b) illustrates the ignition of biomass material when studying the HRR under a cone calorimeter. Figure 1(c) shows how significant quantities of smoke can be released from samples during the course of a test, where the images apply to RESIN8 bricks radiatively heated at 30 kW/m^2. For a discussion on the various fire tests available refer to [16].

Since most structural systems are rated purely based on fire resistance tests, their contribution to fuel load, HRR, and rate of fire spread may not be considered (depending on the country and requirements). Some codes placed a limit on the contribution of insulation or walling systems to fuel loads, which may result in many of the systems discussed in this paper from being automatically excluded [17]. However, this will vary from country to country.

| 1 min | 2 min | 3 min | 5 min | 10 min | 30 min |

Fig. 1. Consideration of fire behaviour showing (a) flaming ecobricks within a wall after standard furnace testing [5] (each flame occurs in front of an ecobrick), (b) ignition of biomass under a cone calorimeter [18], and (c) smoke emissions from a bricks incorporating RESIN8 [19].

2.2 Encapsulation of Combustibles in Construction Systems

The configuration of typical waste and biomass systems will now be discussed in relation to Fig. 2. In this work, a differentiation is made between (a) continuous-, (b) macro- and (c) micro-encapsulation of combustibles within a construction system, and then (d) biomass systems, which is typically a form of one of the preceding categories. Encapsulation refers to how a combustible material is enclosed, and in this paper, with specific reference to non-combustible materials surrounding it.

Continuous-encapsulation refers to when there is a contiguous placement of combustible fuel packages, typically with a non-combustible plaster layer on the outside. The plaster layer may be anchored to a frame and have a lightweight mesh within it. An example of this system is vertically orientated ecobricks placed side-by-side within a wall with plaster on the outsides. Ecobricks are typically 2 L cooldrink bottles filled with non-recyclable waste materials [20]. Numerous schools have been built with such walling systems. The behaviour of ecobricks in fire has been studied in [5]. Other examples of continuous-encapsulation include tire walls [21], and plastered hay bale walls. If the material encapsulated has a low charring rate, and is not highly reactive, e.g., dense hay, the risk is far lower and may be acceptable.

Macro-encapsulation refers to the placement of larger distinct fuel packages within the system, but with non-combustible materials between each fuel package. An example is ecobricks placed horizontally with layers of plaster between each brick, or bricks with polystyrene on the inside but mortar between bricks. Such systems will typically require significantly more mortar and time to construct than the continuously-encapsulated system. If tire walls are filled with sand, they can be considered as either having continuous- or macro-encapsulated geometries.

Micro-encapsulation refers to the mixing of small combustibles into a cementitious mix resulting in distributed materials within a non-combustible matrix. The quantity of combustible material may range from 5% to 50%, or even more. An example of such systems is the use of RESIN8, an aggregate made of recycled plastic [22]. The behaviour of RESIN8 concrete exposed to fire conditions has been studied in [19, 23].

Biomass systems may take on a variety of forms depending on the nature of the material used, the size of materials used and the construction system. Mass timber could be considered as an example, but will not be considered in this work due to extensive treatment in the literature [9]. However, the use of biomass within masonry systems is becoming popular with the rise of materials such as hemp bricks or hempcrete. Hemp is mixed with lime (used as a cementitious binder), and formed in brick moulds. In Cape Town, South Africa, the world's tallest building incorporating hempcrete was recently constructed [24]. In this paper, distributed biomass within a cementitious matrix will be discussed, i.e. biomass with a micro-encapsulated arrangement.

Figure 2(a) to (d) illustrates the aforementioned categories utilized in this paper, providing illustrations of each along with key considerations.
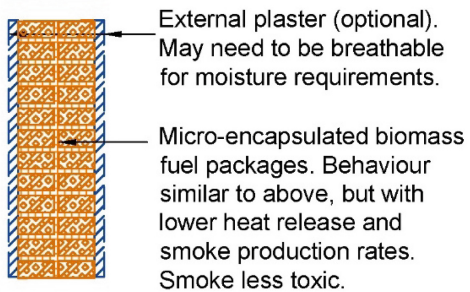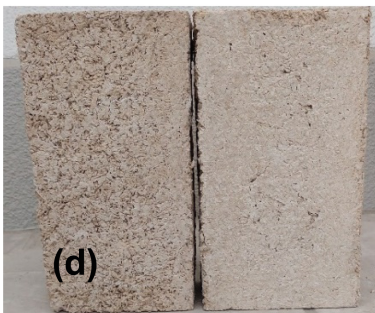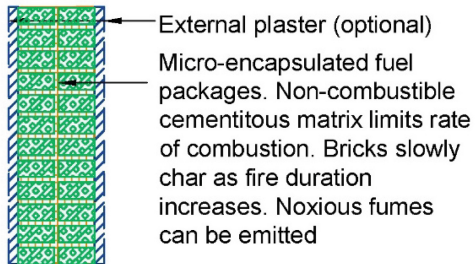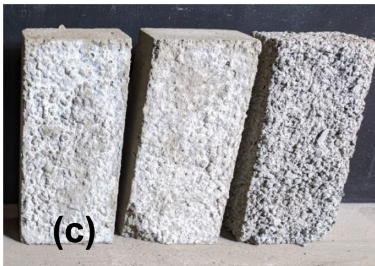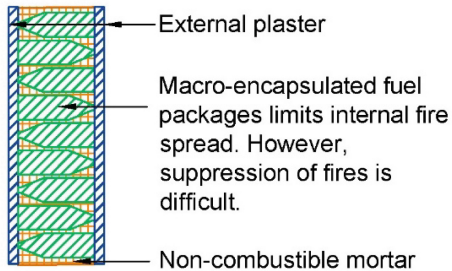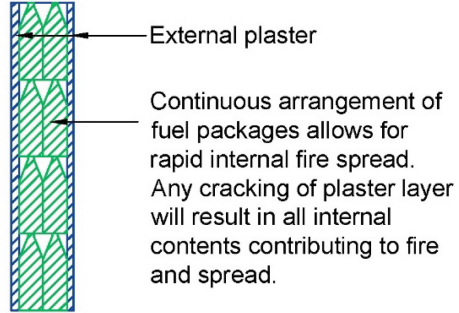
Fig. 2. Important considerations regarding fire safety for various construction systems. (a) Continuous encapsulation of fuel packages, (b) macro-encapsulation, (c) micro-encapsulation (showing RESIN8 bricks), and (d) hempcrete masonry systems.

3   Evaluation of Fire Resistance

3.1   Overview

This section assesses the fire performance of the systems considered in the paper. Assessments are based on a variety of experimental tests in the literature and the application of engineering principles. Significant additional testing will be required to assess the many systems available, and generally only over-arching concepts and considerations are provided here.

The plaster layer provided on the outside of any combustible system is key for providing fire resistance. A low conductivity material with good stability in fire can prevent heat from reaching the internal materials, thereby mitigating the chance of combustion and smoke production. The inclusion of a steel mesh can increase the ductility of the plaster and reduce the chance of cracks opening. Through heat transfer finite element modelling the thickness required to limit internal materials to specific temperatures can be determined [25]. However, the cracking of materials is far more complex to predict and is influence by the materials used, construction tolerances, moisture content, rate of drying, localized hot spots during testing and more. This typically has to be assessed through experimental testing [26].

3.2   Continuous Encapsulation

If a robust plaster layer is provided that does not fail during the required fire duration, and keeps internal temperatures below thresholds for producing smoke or igniting, continuously encapsulated systems can achieve a fire rating. However, such systems pose the highest risk for fire spread and collapse. If the plaster layer is compromised in any way (e.g., localised cracking, poor construction, modifications by users, through penetrations in walls such as pipes, etc.) fires will be able to access and travel through a continuous fuel bed.

The internal waste fuel packages are typically not rigid and provide limited support to the plaster. Hence, the plaster will need to span between the anchor points of any frame. As layers heat up during fire exposure the lack of support, or greater distances between support, will lead to more rapid cracking than macro-encapsulated systems. However, plaster layers will provide resistance for reaction-to-fire systems. As noted above, these tests assess early-age fire spread phenomena, and with a non-combustible external plaster skin no fire spread will occur during such tests.

Once a fire has ignited inside the wall it will be almost impossible for the fire services to suppress the fire without demolishing large sections. Furthermore, if ventilation is limited the fire could smoulder for hours unnoticed, and flame up at a later stage. Smoke may be emitted either back into the fire compartment, or to the unexposed face, if cracking on the back of the wall occurs. It is currently not clear if a pressure build-up could occur, due to the smoke, that could result in explosive spalling.

Testing on ecobrick walls with a continuous vertical orientation highlighted how such configurations failed the fastest of those tested [5]. As noted above, tire walls may also behave in this way. If the tires are filled with sand, the fire will progress far more slowly, and, in some instances, the sand may even suppress the fire. If tire walls are not

filled it will result in internal chimneys leading to very rapid spread over the height of the structure, and lead to extreme fire hazards [27].

3.3 Macro-encapsulation

From a fire safety perspective macro-encapsulation is still problematic, but poses a reduced risk relative to continuous-encapsulation as fuel packages are isolated from each other. As per the previous section, plaster layers are key for providing passive protection. However, localized fire and cracking of the plaster is less serious as the fire should typically stay within a small area and affect a limited number of fuel packages. Depending on the nature of the fuel packages this may, or may not, be considered acceptable. If smoke or flames are emitted on the unexposed face it will result in an integrity and insulation failure of the wall.

Once a building utilizing such a construction system has experienced a severe fire it will be extremely difficult to ensure that fires have been fully suppressed, and demolition may be necessary to access fuel packages within walls. Figure 1(a) illustrates the flaming of ecobricks within a wall at the end of a standard fire test. As per continuous encapsulation, smouldering of fires could continue for hours after a fire has been suppressed if the fire services has not been able to get water into each fuel package.

3.4 Micro-encapsulation

Micro-encapsulation presents the arrangement with the lowest fire risk, depending on the mix design used. For waste plastic materials contained within a matrix of lime or concrete a suitable fire resistance rating can be readily achieved, with the level of smoke emission experienced varying. At high replacement values in mixes for materials such as plastic and rubber, e.g. above 20% by volume, noxious smoke production will occur and there will be an increase in HRR, which can start becoming quite problematic. Figure 1(c) illustrates such a phenomena. Standard fire resistance tests do not assess smoke production and contribution to HRR.

Experimental reaction-to-fire testing is required to assess the behaviour of masonry systems incorporating high replacement levels of combustibles. However, preliminary testing in [19] tends to indicate that the rate of pyrolysis gas production will be sufficiently low, such that even at 50% RESIN8 replacement fire spread over the surface of unplastered walls will not occur. It is likely that a higher incident heat flux will be required to create a combustible gas mixture than those provided from a transient flame.

The addition of a non-combustible plaster layer will significantly enhance fire resistance, and in some cases mitigate poor fire performance altogether. If a plaster layer was to stand adhered throughout a fire test it will significantly decrease the temperature of the combustible materials, potentially to below ignition temperatures. The latter would be especially true for a 30-min standard fire rating requirement (i.e., typically the lowest requirement for structures).

3.5 Biomass Systems

As noted above, this paper only considers biomass systems where the biomass has been mixed into a cementitious matrix, rather than solid biomass systems (e.g. timber).

Biomass inherently has a much lower HRR than synthetic products, with timber having a HRR or around 100–200 kW/m^2, whilst plastics can have a HRR over 1000 kW/m^2 [28]. Furthermore, smoke emitted from biomass is typically less noxious, although can still be dangerous to humans in sufficient quantities.

Extensive testing is required to quantify the HRR, smoke emissions, fire resistance and fire spread rates of masonry systems incorporating combustible biomass. It is estimated that for systems such as hempcrete, due to the presence of cementitious binders, especially those which undergo an endothermic reaction, good fire resistance ratings can be achieved. Reaction-to-fire tests will only be a problem at very low binder contents where raw biomass, especially thin particles, are directly exposed on the surface of walling systems.

Hence, overall, these systems typically do not present a high fire risk. They may char slowly and need to be repaired or replaced after a severe fire, but are unlikely to severely increase fire risk in terms of life safety and evacuation considerations.

4   Conclusions

This paper has discussed the influence of various sustainable construction practices on fire risk. A variety of systems with different ways of encapsulating combustible contents have been discussed.

It is shown that systems with continuous encapsulation of fuel packages pose the greatest fire risk. Once internal materials have ignited fires can spread rapidly within the wall of a structure. Firefighting efforts will be extremely difficult, and walls could collapse onto firefighters during operations. It is concerning to note that large numbers of schools have been built with recycled products in this way. Macro-encapsulation may also have fuel packages that can ignite, but internal flame spread is somewhat mitigated and plaster layers are better supported making them more robust. Micro-encapsulated systems with plaster present a very low risk if the plaster remains intact. If no plaster layer is present a fire resistance rating can be achieved, but smoke emission and increases in compartment HRR will occur. Further research is required to quantify this. Biomass systems in a cementitious matrix are likely to provide a good fire resistance, release less smoke and provide lower HRRs. Plastered biomass bricks are likely to have a negligible negative influence on fire risk. Biomass systems such as mass timber have not been addressed in this paper, but are considered in the literature extensively.

There is limited data providing categorical pass/fail criteria for construction systems, meaning that significant additional research and the development of suitable codes is required. Contemporary research on mass timber buildings could potentially be adopted to guide what area of combustible material can be left exposed before fire risks become unacceptable. There are no simple answers to the problems posed, and sustainability should be encouraged, but often fire risks are ignored when combustible materials are included in walls, floors, insulation systems and general homes. Smoke emissions and increases in HRR will need limits placed on them to not impact evacuation and building fire severity.

References

1. Babafemi, A.J., Šavija, B., Paul, S.C., Anggraini, V.: Engineering properties of concrete with waste recycled plastic: a review. Sustainability **10** (2018). https://doi.org/10.3390/su10113875

2. Oosthuizen, J.: 3D printing of eco-friendly concrete incorporating recycled plastic waste (RESIN8) as fine aggregate, Stellenbosch University, Masters Thesis (2022). http://hdl.handle.net/10019.1/125958

3. Govender, T., Barnes, J.M., Pieper, C.H.: The impact of densification by means of informal shacks in the backyards of low-cost houses on the environment and service delivery in Cape Town, South Africa. Environ. Health Insights. **5**, 23–52 (2011). https://doi.org/10.4137/EHI.S7112

4. Supit, S.W.M., Priyono.: Utilization of recycled PET plastic waste as replacement of coarse aggregate in pervious concrete. Mater. Today Proc. **66**, 2990–2995 (2022)https://doi.org/10.1016/j.matpr.2022.06.573

5. Sander, Z.: Fire behaviour of plastic bottle ecobricks as an infill building material. Stellenbosch University (2022)

6. Drysdale, D.: An Introduction to Fire Dynamics (2011).https://doi.org/10.1016/0379-7112(86)90046-9

7. Wang, Y., Bertrand, C., Beshir, M., Kahanji, C., Walls, R., Rush, D.: Developing an experimental database of burning characteristics of combustible informal dwelling materials based on South African informal settlement investigation. Fire Saf. J. **111**, 102938 (2020). https://doi.org/10.1016/j.firesaf.2019.102938

8. van der Westhuyzen, S., Walls, R., de Koker, N.: Fire tests of South African cross-laminated timber wall panels: fire ratings, charring rates, and delamination. J. South African Inst. Civ. Eng. **62**, 33–41 (2020). https://doi.org/10.17159/2309-8775/2020/v62n1a4

9. Buchanan, A., Östman, B.: Fire Safe Use of Wood in Buildings: Global Design Guide (2022)

10. Meacham, B.J., McNamee, M.: Handbook of Fire and the Environment. Springer, Cham (2023).https://doi.org/10.1007/978-3-030-94356-1

11. Guillaume, E., Dréan, V., Girardin, B., Benameur, F., Fateh, T.: Reconstruction of Grenfell tower fire. Part 1: lessons from observations and determination of work hypotheses. Fire Mater. **44**, 3–14 (2020). https://doi.org/10.1002/fam.2766

12. ISO, ISO 834 Fire-resistance tests - Elements of building construction. Parts 1–12, International Organization for Standardization, Geneva (1999)

13. Buchanan, A.H., Abu, A.K.: Structural Design for Fire Safety, 2nd edn. John Wiley & Sons, LTD (2017)

14. Babrauskas, V., Peacock, D.R.: Heat release rate: the single most important parameter in fire hazard. Fire Saf. J. **18**, 255–272 (1992)

15. SFPE, SFPE Guide to Human Behavior in Fire, 2nd (ed.). Springer, Cham (2019). https://doi.org/10.1007/978-3-319-94697-9

16. Whitehead, M.: Comparative analysis of fire test standards applicable to building materials. MEng thesi, Stellenbosch University (2022). http://hdl.handle.net/10019.1/124619

17. SABS, SANS 10400-T:2020 - The application of the National Building Regulations Part T: Fire Protection, South African Bureau of Standards (2020)

18. Oguaka, A., Quiroz, N.F., Walls, R.: Fire parameters, behaviour, and comparative thermal hazard of food grains based on the cone calorimeter tests. Process Saf. Environ. Prot. (2023). https://doi.org/10.1016/j.psep.2023.03.078

19. Botha, A.: Behaviour of masonry systems incorporating waste plastic subjected to fire. Stellenbosch University (2022). http://hdl.handle.net/10019.1/124748

20. Global Ecobrick Alliance, 10 Step Guide to Making an Ecobrick | Ecobricks.org, Ecobrick.Org. (2020)
21. Xu, Y., Zhuge, Y., Karim, M.R., Hassanli, R., Rahman, M.M., Freney, M.: Structural analysis of a 3D dry-stack tyre wall by finite-discrete element method. Eng. Struct. **281**, 115787 (2023). https://doi.org/10.1016/j.engstruct.2023.115787
22. Babafemi, A.J., Sirba, N., Paul, S.C., Miah, M.J.: Mechanical and durability assessment of recycled waste plastic (Resin8 & PET) eco-aggregate concrete. Sustainability **14**, 1–15 (2022). https://doi.org/10.3390/su14095725
23. Botha, A., Walls, R., Babafemi, A.: Behaviour of masonry systems incorporating waste plastic subjected to fire - Data Repository - MEng Thesis Ayden Botha, SUN Scholar Data (2022). https://doi.org/10.25413/sun.16902802.v1
24. Construction World, The world's tallest building constructed with hempcrete is in Cape Town, Crown Publ. (2022). https://www.crown.co.za/construction-world/projects-and-contracts/21412-the-world-s-tallest-building-constructed-with-hempcrete-is-in-cape-town. Accessed 29 May 2023
25. Shuttleworth, S.M., De Koker, N., Walls, R.S.: Insulation resistance time reference curves for specifying passive fire protection for modular structures from shipping containers. Fire Technol. **58**, 133–147 (2022). https://doi.org/10.1007/s10694-021-01143-9
26. Marx, H., Walls, R.: Thermal behaviour of a novel non-composite cellular beam floor system in fire. J. Struct. Fire Eng. **10** (2019). https://doi.org/10.1108/JSFE-10-2018-0032
27. Gratkowski, M.T.: Burning characteristics of automotive tires. Fire Technol. **50**, 379–391 (2014). https://doi.org/10.1007/s10694-012-0274-9
28. Hurley, M.J.: SFPE Handbook of Fire Protection Engineering, 5th (ed.). Springer, New York (2016)

Comparing the Effects of Two Binders, Sulfur and Portland Cement on the Permeability and Corrosion Rate of Reinforced Concrete

Omid Deldar [ORCID], Behnam Rafie [ORCID], Khaled Hamed Marar[(✉)] [ORCID], and Tülin Akçaoğlu [ORCID]

Department of Civil Engineering, Eastern Mediterranean University, Famagusta, via Mersin 10, North Cyprus, Turkey
khaled.marar@emu.edu.tr

Abstract. Permeability plays a crucial role in determining the durability of concrete structures, particularly their susceptibility to corrosion. This study explores the potential of sulfur concrete as a protective insulator for concrete surfaces. A comparative analysis is conducted to assess the permeability of sulfur concrete (SC), conventional concrete covered with 1 mm sulfur cover (CC-SC), and conventional Portland cement concrete (CC). The investigation includes evaluations of water absorption, void percentage, and accelerated corrosion tests. The time taken for crack initiation and propagation to reach a 1 mm width is recorded. The results demonstrate that sulfur concrete exhibits lower porosity and water absorption, highlighting its waterproof properties and ability to reduce permeability. Significantly, sulfur concrete effectively blocks current flow in the accelerated corrosion test, acting as an insulating barrier. Additionally, cracks in the Portland cement concrete specimens appear after 6 and 9 days for initial crack formation and a 1 mm crack width, respectively. However, when a 1 mm sulfur layer is applied to the surface of the Portland cement concrete, the first crack occurs after 7 days, with a 1 mm crack width observed after 12 days. This indicates that the sulfur cover provides protection for the reinforced concrete and delays the corrosion process. It is important to note that although the sulfur cover delays corrosion in Portland cement concrete, it does not entirely prevent it. Further research and the implementation of additional preventive measures are recommended to address this limitation and enhance corrosion resistance.

Keywords: Sulfur Concrete · Corrosion Resistance · Porosity

1 Introduction

Concrete is a widely used composite material in construction, offering excellent resistance to compressive stress [1, 2]. However, it is weak in tensile and flexural strength. To address this limitation, reinforcement bars, typically made of steel, are added [3, 4]. Nevertheless, steel bars are prone to corrosion when exposed to water and oxygen [5, 6]. Corrosion causes volume expansion, resulting in internal stresses that lead to cracks within the concrete. These cracks propagate and reach the surface, accelerating corrosion rates and ultimately leading to the deterioration of the concrete [7–11]. Numerous

studies have been conducted to tackle this issue, including methods such as increasing the concrete cover, applying epoxy resin, and using bitumen coatings [12–15]. In this study, we investigate the effects of sulfur cover as a potential solution for preventing steel bar corrosion in Portland Cement concrete. Since sulfur is known for its nonabsorbent properties, sulfur concrete mixtures are cast and compared to Portland cement concrete mixtures to evaluate its protection against corrosion. A notable advantage of sulfur concrete is its exceptional durability, particularly in environments prone to acidity and salinity, which often lead to premature degradation and failure of Portland cement concrete [16–18]. In highly corrosive acidic environments, sulfur concrete offers significant benefits for construction. Although the exact lifespan and durability of sulfur concrete in various applications have yet to be fully determined, substantial evidence supports its corrosion resistance and long-lasting nature, surpassing that of other construction materials used in corrosive environments [16, 19]. This study aims to assess the corrosion rate of steel bars in reinforced sulfur concrete and a Portland cement concrete coating by sulfur layer and comparing the results with reinforced Portland cement concrete leading to gain a comprehensive understanding of the topic.

2 Materials and Methods

2.1 Cement and Sulfur

In the present study, CEM II/B-S Portland slag cement of class 42.5 N was employed. The properties of the cement align with the specified limits set by ASTM C150 [20], ensuring its suitability for use. Table 1 provides a comprehensive overview of the physical properties and chemical composition of the cement, showcasing its key characteristics for reference [20].

Table 1. Physical and chemical properties of cement

Property	Value	Property	Value
CaO	60.88%	Al_2O_3	2.19%
SiO_2	19%	Loss on Ignition	0.98%
Fe_2O_3	2.89%	Specific Gravity	2995 kg/m^3
SO_3	2.55%	28-day Compressive Strength	42.5 MPa
MgO	2.27%	Initial Setting Time	190 ± 30 min

Sulfur with 99% purity is utilized as a binder for sulfur concrete specimens as well as cover layer applications on Portland cement concrete specimens. Its properties illustrated in Table 2.

Table 2. Physical and chemical properties of sulfur

Allotropes	Atomic number	Density (kg/m^3)	Temperature (°C)	Melting point
Rhombic (α)	16	2.08	<96	119
Monoclinic (β)	16	1.98	>96	119

2.2 Fine and Coarse Aggregates

The fine aggregate utilized in this study consisted of crushed limestone aggregate sourced from Besparmak Mountain, with a maximum diameter of 5 mm. To evaluate the particle size distribution, a sieve analysis was conducted in accordance with ASTM C136 [21]. The obtained results were then compared to the specifications outlined in ASTM C33 [22]. In addition to the particle size analysis, the physical properties of the fine aggregate were determined following the guidelines provided by ASTM C128 [23]. The relative density of the fine aggregate in the saturated surface-dry (SSD) condition was measured at 2.74. Furthermore, the water absorption rate was found to be 1.38%. The sieve analysis results indicated that 43% of the fine aggregate particles passed through the 600μm sieve. [24–26]. Figure 1 displays the graphical representation of the sieve analysis results for the fine aggregate.
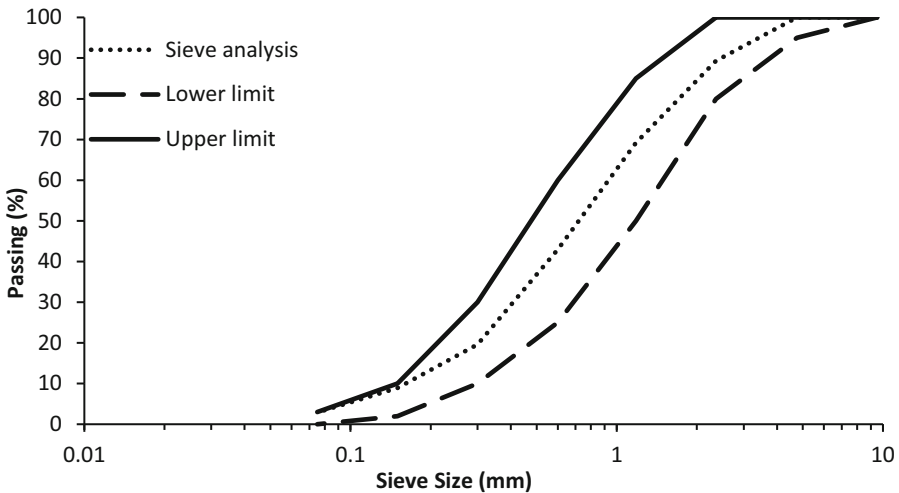
Fig. 1. Sieve analysis of fine aggregate

The coarse aggregate employed in this study was obtained from Besparmak Mountain and consisted of crushed limestone aggregate with varying sizes of 10 mm and 14 mm. To determine the appropriate proportions for each size, a sieve analysis was conducted based on ASTM C136 [21]. According to the results, the optimal proportion was determined using ASTM C33 [22], resulting in a composition of 35% for 10 mm aggregate and

65% for 14 mm aggregate. To assess the properties of the coarse aggregate, such as relative density and water absorption, experimental investigations were conducted for each aggregate size, adhering to the specifications outlined in ASTM C127 [27]. The findings indicated that the average relative density in the saturated surface-dry (SSD) condition was measured at 2.70, while the average water absorption rate was determined to be 0.91%, with the sieve analysis of the coarse aggregate presented graphically in Fig. 2.
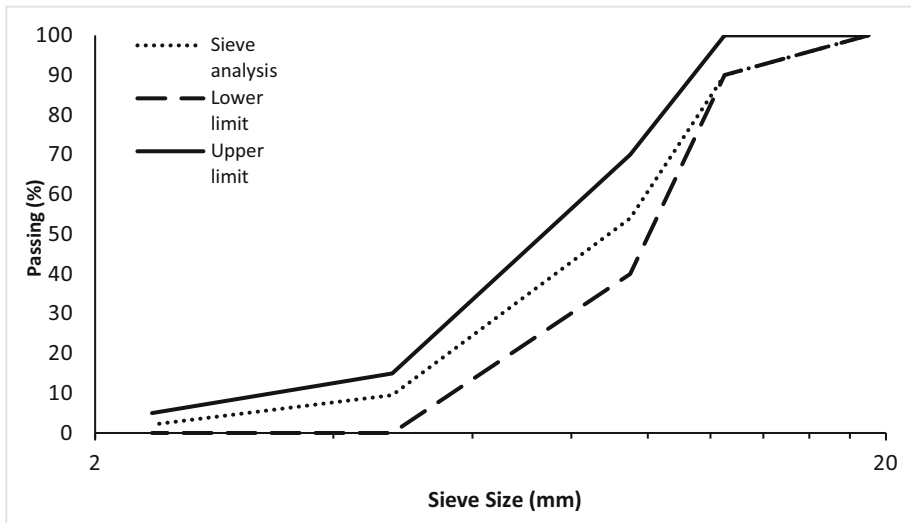
Fig. 2. Sieve analysis of coarse aggregate

Rebars. For the purpose of this experimental study, ordinary construction steel rebars were chosen, characterized by a density of 7.85 g/cm^3 and a diameter of 12 mm. Table 3 presents the characteristics of the rebars utilized in the study. Initially, the rebars were cut to a length of 30 cm and subjected to a thorough brushing procedure to remove any external impurities and eliminate rust formation. To further enhance their cleanliness, an acetone washing process was employed to eliminate any remaining oil residues. Following this cleaning procedure, the rebars were air-dried and subsequently weighed to determine their precise mass.

Water. Tap water was utilized for the mixing and curing of cement concrete specimens in this experimental study. Table 4 presents the chemical and physical properties of the tap water, which were assessed to determine its suitability for the experimental procedures. The obtained results were compared against the criteria outlined in ASTM C1602 [28]:

Table 3. Characteristics of rebars

No.	Length (cm)	Weight of rebar (gr)	No.	Length (cm)	Weight of rebar (gr)
1	29.7	272.8	6	30.3	279.6
2	29.8	276.3	7	29.9	279.3
3	29.5	275.5	8	30.1	280.6
4	30.0	281.3	9	29.4	268.3
5	29.5	273.5			

Table 4. Chemical and physical properties of water

Parameter	Tap Water	ASTM C1602 [28]
pH	8.18	-
Electrical Conductivity (EC) (μS/cm)	242.1	-
Total solids (TS) (mg/l)	124	<50,000
Salinity (ppm)	120	-
Chloride (Cl^-) (mg/l)	24.6	<500
Sulfate ($SO4^{2-}$) (mg/l)	4.2	<3,000

3 Experimental Methods

3.1 Concrete Mixture Groups

To meet the objectives of this study, three distinct groups of concrete mixtures were prepared:

- Group I: Cement Concrete (CC)
- Group II: Sulfur Concrete (SC)
- Group III: Cement Concrete with a Sulfur Cover (CC-SC)

A total of 21 specimens were fabricated, following the guidelines outlined in the ASTM C192 [29]. The cement concrete specimens were subjected to curing for a duration of up to 28 days and in case of sulfur concrete there is no need for curing, this type of concrete will reach up to 90% of its strength just after 24 h. The specimens included the following:

- 6 cylindrical specimens with 100×200 mm dimensions for compressive strength test.
- 6 cubic specimens with $100 \times 100 \times 100$ mm dimensions for porosity test.
- 9 cylindrical specimens with 100×200 mm dimensions and a 12 mm rebar for accelerated corrosion test.

3.2   Mix Design

In this study, the mix design was developed by BRE method, as described in [30]. The primary objective was to achieve a 25 MPa concrete with a slump value of 10 cm, while maintaining a water-to-cement ratio of 0.6. Through a trial-and-error process, the optimal quantities of each ingredient were determined as it presented in Table 5. For sulfur concrete, the aggregate quantities were kept constant, while the amount of sulfur is determined through a trial-and-error process in order to achieve the same compressive strength as that designed for Portland cement concrete.

Table 5. Concrete mix design for different specimen groups

Concrete group	W/C	Binder (kg/m^3)	Fine aggregate (kg/m^3)	Coarse aggregate (kg/m^3)		Water (kg/m^3)
			5 mm	10 mm	14 mm	
CC	0.5	375	860	320	600	225
CC-SC	0.5	375	860	320	600	225
SC	-	550	860	320	600	-

4   Results and Discussion

4.1   Permeability

The permeability of concrete is a critical factor affecting its long-term durability, particularly in reinforced concrete structures, as the porosity directly impacts the permeability, corrosion rate, and overall lifespan of the structure. This study focused on determining the void percentage (porosity) of concrete specimens by following the guidelines outlined in ASTM C642 [31]. To avoid potential complications arising from the low melting point of sulfur concrete, the traditional boiling step was omitted, and instead, the void content was determined by measuring the mass of the specimens after immersion. The experimental results presented in Table 6 clearly demonstrate that sulfur concrete exhibits significantly lower water absorption and void percentages compared to cement concrete. These findings underscore the water-resistant characteristics of sulfur concrete and reinforce its efficacy as an effective insulating material.

Table 6. Physical properties of CC and SC specimens based on ASTM C642

Specimen	Absorption after immersion %	Apparent density	Voids %
CC	7.35	2.56	12.45
SC	2.42	2.18	5.32

4.2 Accelerated Corrosion Test by Impressed Voltage (ACTIV)

This experimental study introduces a novel methodology for assessing the corrosion resistance of different concrete specimens. The durability and corrosion resistance of these specimens were evaluated using an accelerated corrosion test with impressed voltage. This technique allows for the simulation and acceleration of the natural corrosion process, which typically takes several years to occur. By employing this method, the analysis becomes significantly more time efficient. In this investigation, a persistent 12-V DC voltage was applied to the concrete specimen. The specimen was partially submerged in a solution with a sodium chloride concentration of 5% relative to the weight of water. Additionally, copper was used as the cathode in the electrical current, as illustrated in the Fig. 3.
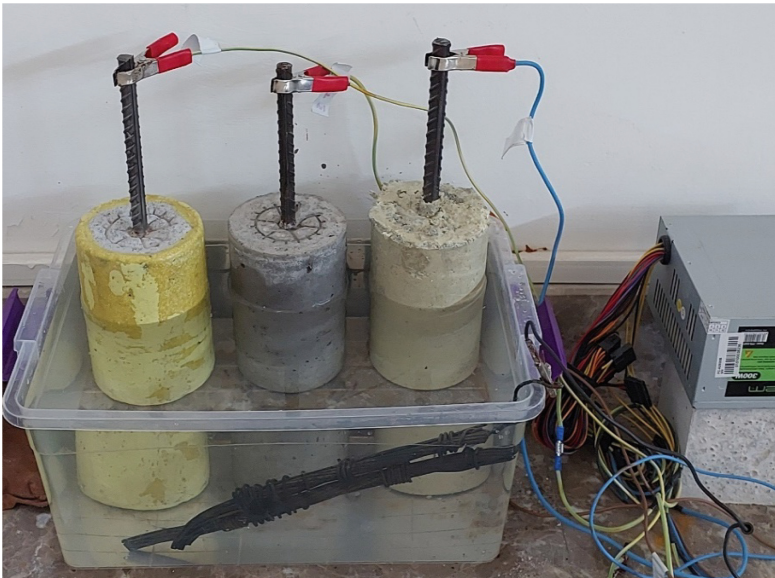
Fig. 3. The used accelerated corrosion test setup

This experimental setup replicates the adverse conditions commonly associated with the corrosion of reinforced concrete structures. The electrical current flowing through the circuit was carefully recorded at 24-h intervals. The initiation of the first visible crack was noted, and the test was continued until the crack expanded to a width of 1 mm as depicted in Fig. 4-a. This meticulous monitoring and observation enabled the assessment of the corrosion process and the determination of the concrete specimens' resistance to corrosion. Figure 4-b illustrates the specimens after the corrosion test.

The rate of corrosion was determined based on the amount of current passing through the circuit over time. This method allowed us to observe the start and the progression of cracks on the concrete surface due to corrosion, which provided a more direct way to compare the relative durability of different concrete mixtures. The electrochemical reactions underpinning this setup are as follows:

At the anode (steel rebar), iron undergoes oxidation, meaning it loses electrons and transforms into iron ions:

$$Fe \rightarrow Fe^{2+} + 2e^- \tag{1}$$
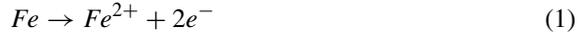
On the other hand, at the cathode (copper), the reduction process takes place. Here, the electrons generated at the anode are consumed, typically leading to the reduction of hydrogen ions in the electrolyte to form hydrogen gas:

$$H_2O + 1/2\,O_2 + 2e^- \rightarrow 2(OH)^- \tag{2}$$

And the complete reaction is:

$$Fe + 1/2\,O_2 + H_2O \rightarrow Fe(OH)_2 \tag{3}$$

In the present study, Faraday's Second Law of electrolysis was employed to calculate the corrosion rate. This law postulates that the mass of a substance altered at an electrode during electrolysis is directly proportional to the quantity of electrical charge passed through the cell. This relationship can be mathematically expressed as:

$$W = Q \times (M/zF) \tag{4}$$

where: M is the molar mass of iron, (M = 55.845 g/mol), z is the number of electrons involved in oxidation of iron, (z = 2), F is Faraday's constant (approximately 96485 C/mol), and the quantity of charge (Q) was calculated by integrating the current over the time of the test [32].

To convert the calculated mass loss into a corrosion rate, according to ASTM G1–03 [33]we used:

$$C.R.(mm/y) = ((K \times W)/(A \times D \times T)) \tag{5}$$

where W is the mass loss during the accelerated corrosion test (gr), K is a conversion factor, approximately 8.76×104 in this case, A is the total exposed area of the steel (cm2), D is the density of iron (7.85 g/cm^3), and T is the duration of the test (hr).

The derived formula allowed for the determination of the average rate at which the steel corroded over the duration of the test.

Fig. 4. a) Crack width measurements, b) CC and CC-SC specimens after corrosion

The results obtained from the comparative analysis of the accelerated corrosion test on reinforced concrete across different concrete groups, as depicted in Fig. 5 and Table 7, reveal significant findings. Notably, the SC specimens exhibited zero current flow during the test, indicating that the molten sulfur adhered to the rebars during casting and acted as an effective insulator, thereby protecting them from corrosion. In the CC specimen group, the appearance of the first visible crack occurred after 6 days, with the crack width reaching 1 mm after 9 days. The corresponding mass loss during the corrosion test was measured at 24.92 gr, resulting in a corrosion rate of 25.26 mm/year. In the CC-SC specimen group, where a 1 mm sulfur layer was applied to the surface of the CC specimens, the first crack was observed after 7 days, and it took 12 days for the crack to widen to 1 mm. The associated mass loss was recorded as 28.28 gr, resulting in a corrosion rate of 21.5 mm/year. These findings show that the utilization of sulfur as a cover can effectively delay the corrosion mechanism. Figure 5 illustrates the initial currents for the CC and CC-SC specimens, with the former measuring approximately 0.2 A and the latter recording 0.09 A. This discrepancy further supports the insulating behavior of sulfur.
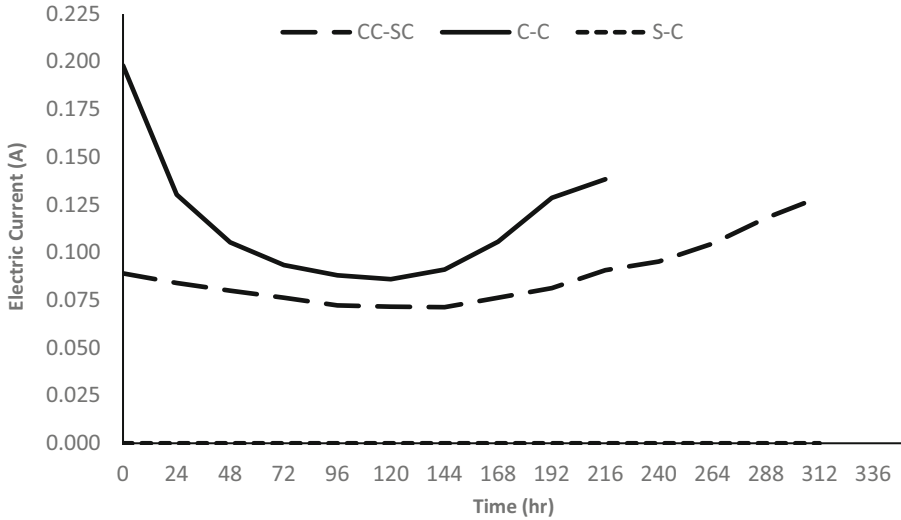
Fig. 5. Electric current (A) versus time (hr) for different concrete groups

Table 7. Corrosion characteristics of reinforced concrete

Concrete group	Time to initial crack (hr)	Time to 1 mm crack (hr)	Mass loss to 1mm crack (gr)	Corrosion rate up to 1 mm crack
SC	0	-	-	-
CC	144	216	24.92	25.26
CC-SC	168	288	28.28	21.50

5   Conclusion

Sulfur concrete (SC) demonstrated excellent corrosion protection capabilities: The SC specimens exhibited zero current flow during the accelerated corrosion test, indicating that the molten sulfur used in the concrete acted as a highly effective insulator. This insulation provided robust protection to the rebars, preventing corrosion, and enhancing the durability of the concrete structure.

Sulfur cover delayed the onset of cracks: When a 1 mm sulfur cover was applied to the surface of cement concrete (CC-SC group), the appearance of the first crack and 1 mm crack was delayed by 1 day and 3 days respectively compared to the CC group without sulfur cover. This indicates that the sulfur layer acted as a protective barrier, slowing down the initiation and propagation of cracks in the concrete, thereby enhancing its overall structural integrity.

Corrosion rates were lower in the CC-SC group compared to the CC group: The CC-SC specimens exhibited a lower corrosion rate (21.5 mm/year) compared to the CC group (25.26 mm/year). This suggests that the sulfur cover provided additional corrosion

resistance, reducing the degradation of the reinforced concrete, and increasing its service life.

Additionally, the results of the porosity test revealed that sulfur concrete exhibited lower porosity and water absorption compared to conventional cement concrete (CC) specimens. This underscores the waterproof properties of sulfur concrete, which contributed to a decrease in the initial current observed in the CC-SC specimens compared to the CC specimens.

References

1. Shoukry, S.N., William, G.W., Downie, B., Riad, M.Y.: Effect of moisture and temperature on the mechanical properties of concrete. Constr. Build. Mater. **25**(2), 688–696 (2011)
2. Neville, A.M.: Properties of Concrete, 5th edn. Pearson Education Ltd, England (2004)
3. Malvar, L.J.: Review of static and dynamic properties of steel reinforcing bars. ACI Mater. J. **95**(5), 609–616 (1998)
4. Zhang, Z., Shao, X.-D., Zhu, P.: Direct tensile behaviors of steel-bar reinforced ultra-high performance fiber reinforced concrete: effects of steel fibers and steel rebars. Constr. Build. Mater. **243**, 118054 (2020)
5. Royani, A., Prifiharni, S., Nuraini, L., Priyotomo, G., Purawiardi, I., Gunawan, H.: Corrosion of carbon steel after exposure in the river of Sukabumi, West Java. In: IOP Conference Series. Materials Science and Engineering, vol. 541 (2019)
6. Xu, X., Liu, S., Smith, K., Cui, Y., Wang, Z.: An overview on corrosion of iron and steel components in reclaimed water supply systems and the mechanisms involved. J. Clean. Prod. **276**, 124079 (2020)
7. Rodriguez, J., Ortega, L.M., Casal, J.: Load carrying capacity of concrete structures with corroded reinforcement. Constr. Build. Mater. **11**(4), 239–248 (1997)
8. Almusallam, A.A.: Effect of degree of corrosion on the properties of reinforcing steel bars. Constr. Build. Mater. **15**(8), 361–368 (2001)
9. François, R., Khan, I., Dang, V.H.: Impact of corrosion on mechanical properties of steel embedded in 27-year-old corroded reinforced concrete beams. Mater. Struct. **46**(6), 899–910 (2013)
10. Fang, C., Lundgren, K., Chen, L., Zhu, C.: Corrosion influence on bond in reinforced concrete. Cem. Concr. Res. **34**(11), 2159–2167 (2004)
11. Castel, A., François, R., Arliguie, G.: Mechanical behaviour of corroded reinforced concrete beams - Part 1: experimental study of corroded beams. Mater. Struct. **33**(9), 539–544 (2000)
12. Bertolini, L., Elsener, B., Redaelli, E., Polder, R.: Corrosion of Steel in Concrete: Prevention, Diagnosis, Repair, 2nd edn. Wiley, Germany (2013)
13. Topçu, İB., Uzunömeroğlu, A.: Properties of corrosion inhibitors on reinforced concrete. J. Struct. Eng. Appl. Mech. **3**(2), 93–109 (2020)
14. Tabatabai, H., Pritzl, M.D., Ghorbanpoor, A.: Evaluation of select methods of corrosion prevention, corrosion control, and repair in reinforced concrete bridges. https://minds.wisconsin.edu/handle/1793/53046. Accessed 08 June 2023
15. Rodrigues, R., Gaboreau, S., Gance, J., Ignatiadis, I., Betelu, S.: Reinforced concrete structures: a review of corrosion mechanisms and advances in electrical methods for corrosion monitoring. Constr. Build. Mater. **269**, 121240 (2021)
16. Vlahovic, M.M., Martinovic, S.P., Boljanac, T.D., Jovanic, P.B., Volkov-Husovic, T.D.: Durability of sulfur concrete in various aggressive environments. Constr. Build. Mater. **10**(25), 3926–3934 (2011)

17. Mohamed, A.M.O., El-Dieb, A., El Sawy, K.M., El Gamal, M.M.: Durability of modified sulfur concrete in sewerage environment. Environ. Geotech. **2**(2), 95–103 (2015)
18. Dehestani, M., Teimortashlu, E., Molaei, M., Ghomian, M., Firoozi, S., Aghili, S.: Experimental data on compressive strength and durability of sulfur concrete modified by styrene and bitumen. Data Brief **13**, 137–144 (2017)
19. Gillott, J.E., Jordaan, I.J., Loov, R.E., Shrive, N.G.: Durability studies of sulfur concrete. In: Sereda, P.J., Litvan, G.G. (eds.) Durability of Building Materials and Components 1980, pp. 594–599, ASTM, STP-691, Philadelphia (1980)
20. ASTM C150: Standard Specification for Portland cement (2018)
21. ASTM C 136–06: Standard Test Method for Sieve Analysis of Fine and Coarse Aggregates (2006)
22. ASTM C33/C33M – 16: Standard Specification for Concrete Aggregates 1 (2016)
23. ASTM C128: Standard Test Method for Relative Density (Specific Gravity) and Absorption of Fine Aggregate (2022)
24. ASTM C136: Standard test method for sieve analysis of fine and coarse aggregate (2019)
25. ASTM C33: Standard specification for concrete aggregate (2018)
26. ASTM C128: Standard Test Method for Relative Density (Specific Gravity) and Absorption of Fine Aggregate (2015)
27. ASTM C127: Standard Test Method for Density, Relative Density (Specific Gravity), and Absorption of Coarse Aggregate (2004)
28. ASTM C 1602/C 1602M – 06: Mixing water used in the production of hydraulic cement concrete (2006)
29. ASTM C192/C192M-19: Standard Practice for Making and Curing Concrete Test Specimens in the Laboratory (2019)
30. Teychenné, D.C., Franklin, R.E., Erntroy, H.C., Marsh, B.K.: Design of normal concrete mixes, 2nd (edn). Building Research Establishment, England (1997)
31. ASTM C 642–97: Standard Test Method for Density, Absorption, and Voids in Hardened Concrete (1997)
32. Broomfield, J.P.: Corrosion of Steel in Concrete, Understanding, Investigation and Repair, 3rd edn. CRC Press, England (2023)
33. ASTM G1–03: Standard Practice for Preparing, Cleaning, and Evaluating Corrosion Test Specimens (2017)

Performance Comparison Between Synthetic and Natural Fiber Reinforced Wood Ash Cement Composite Pastes

Sevket Can Bostanci[(✉)] and Hasan Dilek

Civil Engineering Department, Faculty of Engineering Northern Cyprus, European University of Lefke, TR-10 Mersin, Turkey

{sbostanci,21170039}@eul.edu.tr

Abstract. Fibers use in cement-based composites have drawn interest of scientific community due to its contribution to flexural performance and other engineering properties. Contribution to environmental impact is considered as minor but cost of these materials is the major challenge for the production of cost-effective approaches. Polypropylene fiber (PF) and dog hair (DH) were used to, proportion of 0.25% of total binder content, in this study to reinforce cement pastes produced with Portland cement (PC) and wood ash (WA) cements. WA was used to replace PC with proportions of 5 and 10% in aiming to promote cleaner production. Composite pastes were tested for slump, flow table, fresh and hardened densities, compressive and flexural strengths. Environmental and economic sustainability of composites pastes were further investigated.

Results suggest that engineering properties were influenced by chemical and physical aspects of the materials used. PF and DH utilized WA cement pastes had lower fresh properties. Strength values were improved at 14d and beyond through pozzolanic reactions. Synthetic and natural fibers had quite similar performances. Results also suggest that both PF and DH could be used to promote sustainable approaches.

Keywords: Natural fiber · Composites · Sustainability

1 Introduction

Weak tensile property of cement-based materials is the major challenge from the structural perspectives. Fiber use has become a common approach to overcome this deficiency. Synthetic fibers are widely used and enhance engineering properties of these materials [1, 2]. Varying types of fibers with different lengths, diameter and length are currently available [3, 4]. However, higher cost of these materials is against the principles of sustainable development for the production of cost-effective materials and one of the biggest challenges when circular economy is considered [5]. Even though they do no contribute to environmental impact, the use of these materials could increase cost reasonably. Animal hairs are used to mitigate this issue and promote cleaner production [6]. The use of these materials are quite new in the literature and there is no clear agreement regarding to the effect of these materials.

Waste incorporation for the sustainable production has become a widespread trend to lower environmental impact of composites [7, 8]. The use of these materials may lower the mechanical properties at early ages [9] but increase at longer ages through pozzolanic reactions [10]. Wood ash (WA) is one of the local wastes in Cyprus that is mostly generated in winter seasons. There is no disposal facility of WA and it is mostly sent to landfill which undermines the sustainable development due to reducing the available virgin lands. In addition, solid waste disposal is a public concern due to limited facilities. Use of WA has been studied earlier [11, 12]. It was observed that fresh characteristics are adversely influenced through its porous nature [12, 13]. An earlier study [14] suggest that WA replacement for optimum performance should be 5% while few other studies [15, 16] claimed 10% when strength parameters are taken into account. For sustainability parameters, there is a single study [15] which investigated the environmental emissions of WA-cement concrete. There have been no cost related studies available in the literature for WA-cement composites.

Fibers are considered potentially to compensate early performance loss and improve weaker tensile properties. Natural fibers are recently preferred due to their low cost and potential to enhance mechanical properties [17]. Animal fibers are waste materials and their disposal could lead to environmental problems. However, there is a very limited data regarding to use of pig hair and cow hair in composite materials but there is no available literature on the use of dog hair in composites production.

This study aims to compare engineering and sustainability performances of wood ash cement pastes reinforced with polypropylene (PF) and dog hair (DH) as synthetic and natural fibers respectively. Wood ash (WA) was used to lower environmental impact and it was sieved through 150 and 300μm sieves. WA was used to replace Portland cement (PC) with proportions 5 and 10%. Polypropylene and dog hair was further used with proportion of 0.25% of the total cementitious content. Composites were then tested for mini slump, fresh and hardened density, compressive and flexural strengths and porosity. Environmental and economic sustainability of these mixes were also performed.

2 Materials and Test Methods

2.1 Materials and Mix Proportioning

Nine composites mixes were studied in this study. Mixes were designed with constant water/binder ratio of 0.38. Two cementitious materials were used throughout the study. Initially, CEM I, PC 42.5R, was used for control mix. WA, that was used through 150 and 300 μm sieves, was used to replace PC with contents of 5 and 10%. Two mixes were denoted as 150 indicating WA sieved through 150 μm sieve while 300 indicating WA sieved through 300 μm sieve. 5 and 10 for WA represent WA replacement level. Chemical compositions for PC and WA were given in Table 1.

Table 1. Mix proportion percentages

Sieved WA	Mix name	Cementitious proportions (%)		Fiber proportions (%)	
		PC	WA	PF	DH
-	100PC	100	-	-	-
150	95PC-5WA-PF	95	5	0.25	-
	90PC-10WA-PF	90	10	0.25	-
	95PC-5WA-DH	95	95	-	0.25
	90PC-10WA-DH	90	10	-	0.25
300	95PC-5WA-PF	95	5	0.25	-
	90PC-10WA-PF	90	10	0.25	-
	95PC-5WA-DH	95	95	-	0.25
	90PC-10WA-DH	90	10	-	0.25

Two different fiber types used for this study. PF fiber was introduced as synthetic fiber while DH was utilized as natural fiber. Both fiber contents were kept the same as 0.25% of the total cementitious content. Fiber types were labelled with abbreviations for PF and DH respectively. Available information on the fiber characteristics are revealed in Table 2. DH fiber diameter was predicted from the existing literature [18] (Table 3).

Table 2. Chemical compositions of cementitious materials

Chemical compound	Cementitious materials	
	PC	WA
SiO_2	21.2	18.1
CaO	64.7	44.4
Al_2O_3	5.1	3.3
Fe_2O_3	2.5	2.8
MgO	0.9	2.8
SO_3	1.5	0.9
K_2O	0.2	5.2
LOI	2.5	22.1

Table 3. Fiber properties.

Property	PF	DH
Tensile strength (MPa)	350	N/A
Modulus of elasticity (GPa)	-	N/A
Length (mm)	6	N/A
Specific gravity (gr/cm^3)	0.91	N/A
Fiber diameter (μm)	18–22	60
Melting point (°C)	165–170	N/A

2.2 Test Methods

Fresh testing was performed through mini slump and and flow table tests conforming to ASTM C143/C143M-20 and ASTM C230M/C230M-14 respectively. Fresh and hardened tests were also noted for these mixes. Strength tests were performed at 7, 14 and 28d. Compressive strength values were established through 50 mm × 50mm × 50 mm cubic moulds according to C109/C109M-21 while flexural strength was obtained through 40 mm × 40 mm × 160 mm prisms conforming with ASTM C348–21.

2.3 Sustainability Assessment

Sustainability assessment includes environmental and economic performances of composites. Figure 1 gives the system boundaries adopted for the calculations. Values used to calculate sustainability assessment were obtained through author's previous study [7] and collaboration with the Kascon Ltd. European University of Lefke was considered as construction site and values were determined accordingly.
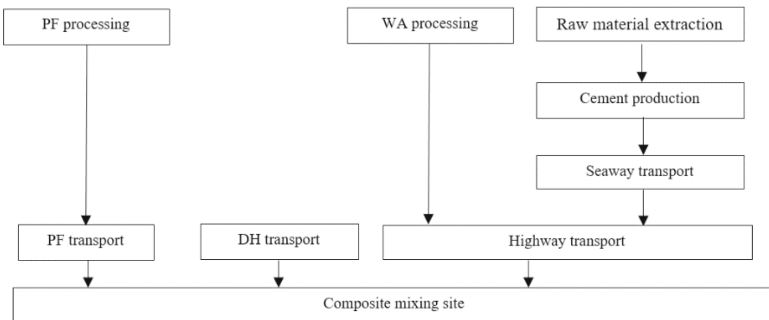
Fig. 1. Sustainability assessment factors

3   Results and Discussion

3.1   Fresh Properties

Fresh properties of composite pastes are revealed in Fig. 2. Results showed that WA addition decreased fresh properties regardless to the type of fibers. This is in line with earlier studies [12, 13]. 150-WA mixes had lower values compared to 300-WA mixes as smaller particle size with higher surface area demanded more water to coat its surface. It was also observed that both fiber addition had air-entraining effect. There is no clear trend observed between PF and DH. Synthetic and natural fiber composite mixes had similar fresh characteristics.
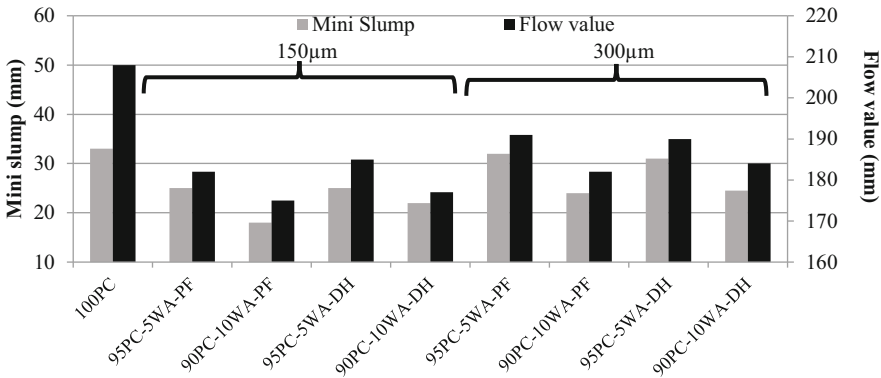
Fig. 2. Fresh properties of composite pastes

Table 4. Fresh and hardened densities of composite pastes

Sieved WA	Mix Name	Fresh density (kg/m^3)	Hardened density (kg/m^3)
-	100PC	2122	2034.7
150	95PC-5WA-PF	2087.1	1974.4
	90PC-10WA-PF	2041.6	1908.9
	95PC-5WA-DH	2134.8	2026.3
	90PC-10WA-DH	2112.5	2003.3
300	95PC-5WA-PF	2082.3	1994.8
	90PC-10WA-PF	2069.4	1939.7
	95PC-5WA-DH	2132.9	2013.1
	90PC-10WA-DH	2105.7	1989.1

3.2 Density Properties

Fresh and hardened densities of composite paste are shown in Table 4. Results are in line with fresh properties that indicated WA mixes had lower densities due to absorbing characteristics of WA. Densities were lowered as WA content increased. This was expected due to lower specific gravity of WA. In addition, PF-utilized mixes had lower fresh and hardened densities compared to DH mixes. This is believed to be both PF had water absorbing property and DH had hydrophobic nature. Thus, absorbing characteristics influenced the densities of composite pastes.

3.3 Strength Properties

Compressive Strength
Compressive strengths of composite pastes are revealed in Fig. 2. Results showed that fiber incorporated WA composite mixes had lower strengths at 7d and 14d. This is believed to be due to WA addition reduced the hydration products. In addition, porous nature of WA led to increased pore structure which may have weakened the matrix. Strength losses were observed to be lower at 28d. This may be linked with WA addition led to pozzolanic reaction and improved strength reasonably. This is also reported earlier [19]. In addition, water stored in the pores introduced by PF and DH fibers addition may have reacted with Calcium hydroxide and produced secondary Calcium silica hydrate. 150-95PC-5WA-PF and 150-95PC-5WA-DH mixes had slightly higher compressive strengths at 28d while other composite mixes had either similar or slightly lower strength values. 150-WA mixes had higher strengths compared to 300-WA mixes due to pore refinements of these mixes (Fig. 3).
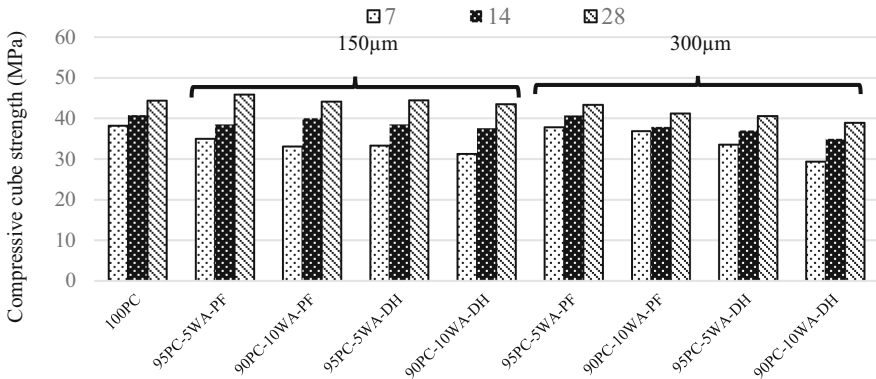
Fig. 3. Compressive strengths of composite pastes

Flexural Strength

Flexural strength results of composite pastes are given in Fig. 4. Similar trend as compressive strength was observed. Lower strength values were noted at 7 and 14d. Similar or higher values were noted at 28d. This is believed to linked with both chemical and physical factors. Initially, composite mixes had improved pore refinement through pozzolanic reactions generated by WA. In addition, both PF and DH addition had bridging effect which consequently improved the flexural strength. Even though DH had water-repellent characteristics, improvement is believed to be linked with water stored in the pore matrix was consumed for hydration process and thus this led to better bonding with DH and the matrix. 150-WA mixes had slightly improved strengths due to better particle packing led to improved matrix.
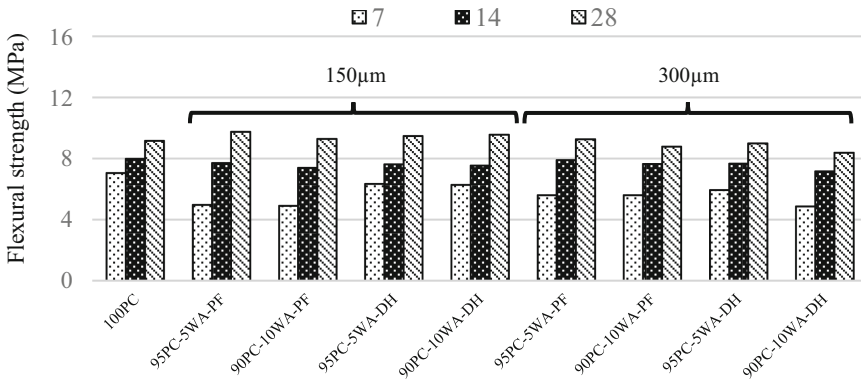
Fig. 4. Flexural strengths of composite pastes

3.4   Sustainability Assessment

Environmental Sustainability

Environmental impact of the composite pastes is seen in Table 4. It is clear that WA utilized PF and DH mixes had lower emissions compared to control mix. This was expected due to lower PC content of these mixes. Emissions were lowered as PC content decreased. It is important to note that emissions were established based on fresh densities reported for this study. For this reason, PF mixes had lower eCO_2 emissions than DH mixes. Even though DH processing and transportation related emissions are lower, higher emissions of these mixes could be linked with higher water absorption of PF reduced density compared to water-repellent DH mixes and thus reduced the materials per cubic meter which consequently reduced emissions. Results suggested that PF and DH utilized mixes can reduce the environmental impact and be used for environmentally-friendly applications.

Table 5. Environmental sustainability of composite pastes.

WA sieve size	Mix name	PC		WA		PF		DH		Total emissions (eCO$_2$ kg/m^3)
		P	T	P	T	P	T	P	T	
-	100PC	1046.9	56.8	0	0	0	0	0	0	1151.1
150	95PC-5WA-PF	1003.6	54.5	4.9	9.4	11.3	18.0	0	0	1101.9
	90PC-10WA-PF	945.4	51.3	9.7	9.4	11.3	18.0	0	0	1045.0
	95PC-5WA-DH	1047.0	56.9	5.1	9.4	0	0	0	9.4	1127.7
	90PC-10WA-DH	1002.5	54.4	10.3	9.4	0	0	0	9.4	1085.9
300	95PC-5WA-PF	1017.9	55.3	1.2	9.4	11.5	18.0	0	0	1113.3
	90PC-10WA-PF	958.3	52.0	2.5	9.4	11.4	18.0	0	0	1051.5
	95PC-5WA-DH	1042.6	56.6	1.3	9.4	0	0	0	9.4	1119.2
	90PC-10WA-DH	995.6	54.1	2.6	9.4	0	0	0	9.4	1071.0

Economic Sustainability

Economic sustainability of composite paste is provided in Table 5. It is seen from the results that all fiber-included composites mixes had lower cost except 150-95PC-5WA-PF mix due to production and transportation related costs of PF. Similar trend as environmental sustainability was reported for economic sustainability assessment. Even though DH had no production related emissions, higher cost of these mixes were due to the higher densities of DH-added mixes compared to PF mixes. Cost is one of the most important indicators for feasible application of a material. Thus, both PF and DH utilization in

Table 6. Costs of composite pastes

WA sieve size	Mix name	PC		WA		PF		DH		Total cost ($/m^3)
		P	T	P	T	P	T	P	T	
-	100PC	278.58	13.91	0	0	0	0	0	0	305.80
150	95PC-5WA-PF	280.89	14.76	0.17	3.67	4.15	7.09	0	0	310.74
	90PC-10WA-PF	271.23	14.25	0.36	3.67	4.15	7.09	0	0	289.51
	95PC-5WA-DH	278.63	14.64	0.17	3.67	0	0	0	3.67	300.79
	90PC-10WA-DH	266.79	14.02	0.35	3.67	0	0	0	3.67	288.51
300	95PC-5WA-PF	273.81	14.39	0.04	3.67	4.23	7.09	0	0	291.92
	90PC-10WA-PF	262.38	13.79	0.09	3.67	4.21	7.09	0	0	279.93
	95PC-5WA-DH	277.44	14.58	0.04	3.67	0	0	0	3.67	299.42
	90PC-10WA-DH	264.97	13.92	0.09	3.67	0	0	0	3.67	286.33

low carbon cement applications could be a promising approach when sustainability is concerned (Table 6).

4   Conclusions

WA composite pastes reinforced with PF and DH were investigated in this study. It was aimed to compare the influence of synthetic and natural fiber incorporation on engineering and sustainability performances of composite pastes. Results suggested that PF use mixes were more prone to absorb water compare to DH mixes. DH showed water-repellent property. In overall, fresh properties were adversely effected. 150-WA mixes with finer particle size increased the water demand and reduced the fresh properties. Densities were decreased due to lower specific gravity of WA and also air-entraining effect of both PF and DH. PF mixes had lower values than DH mixes due to increased water absorption. Strength values suggested that fiber incorporation did not contribute to compressive strength. Lower strength values are believed to be mostly associated with WA addition reduced the hydration products. Moreover, both, PF and DH, are believed to act as reservoirs and provided extra hydration products to the composite mixes. Flexural strength values were lower compared to control mix at 7d and had improved values at 14d and 28d. PF and DH addition showed bridging effect and improved flexural strength. For DH utilization, water conserved in the pores introduced contributed to pozzolanic reactions and thus, DH had better and smoother bonding with the paste matrix. 150-WA mixes had higher strengths compared to 300-WA due to better particle packing of these mixes. Sustainability assessments suggest that PF and DH incorporation could be a promising approach to produce environmentally-feasible and cost-effective mixes. Natural fibers could achieve similar properties as synthetic fibers in general. It could be recommended that composite pastes should be further investigated for increased contents of fibers. Durability properties should be also evaluated to reveal the performance of these mixes under several exposure mechanisms.

References

1. Hanafi, M., Aydin, E., Ekinci, A.: Engineering properties of basalt Fiber-reinforced bottom ash cement paste composites. Materials **13**(8), 1952 (2020)
2. Alrawashdeh, A., Eren, O.: Mechanical and physical characterization of steel fibre reinforced self-compacting concrete. Results Eng. **13**, 100335 (2022)
3. Özaşık, N., Eren, O.: Influence of recycled polyethylene terephthalate fibres on plastic shrinkage and mechanical properties. Front. Struct. Civ. Eng. **16**(6), 792–802 (2022)
4. Onochie, K.K., Balkis, A.P.: Polypropylene fiber reinforced Alker as a structurally stable and sustainable building material. J. Clean. Prod. **279**, 123600 (2021)
5. Thomas, S., Rouxel, D., Jose, S.: Green composites: material for a sustainable world. Emergent Mater. **5**, 601–602 (2022)
6. Ali, H., Rohit, K., Dixit, S.: Fabrication and characterization of eco-friendly natural human hair fiber reinforced polyester composite. J. Nat. Fibers **20**(1), 2181268 (2023)
7. Bostanci, S.C., Kew, H., Ajogi, I.E.: Waste coal cement concrete for sustainable production. Eur. J. Environ. Civ. Eng. (2023)

8. Gencel, O., et al.: The use of waste marble for cleaner production of structural concrete: a comprehensive experimental study. Constr. Build. Mater. **361**, 129612 (2022)
9. Bostanci, S.C.: Engineering properties and sustainability assessment of recycled glass sand concrete. Eur. J. Sci. Technol. **17**, 117–130 (2019)
10. Rodier, L., Bilba, K., Onesippe, C., Arsene, M.A.: Study of pozzolanic activity of bamboo stem ashes for use as partial replacement of cement. Mater. Struct. **50**, 87 (2017)
11. Ekinci, A., Hanafi, M., Aydin, E.: Strength, Stiffness, and Microstructure of Wood-Ash Stabilized Marine Clay. **10**, 796 (2020)
12. Hamid, Z., Rafiq, S.: An experimental study on behaviour of wood ash in concrete as partial replacement of cement. Mater. Today Proc. **46**, 3426–3429 (2021)
13. Rissanen, J., et al.: The effect of peat and wood fly ash on the porosity of mortar. Constr. Build. Mater. **223**, 421–430 (2019)
14. Chowdury, S., Mishra, M., Suganya, O.: The incorporation of wood waste ash as a partial cement replacement material for making structural grade concrete: an overview. Ain Shams Eng. J. **6**(2), 429–437 (2015)
15. Pavlikova, M., et al.: Volarization of wood chips as eco-friendly mineral admixture in mortar design. Waste Manage. **80**, 89–100 (2018)
16. Stolz, J., Boluk, Y., Bindiganavile, V.: Wood ash as a supplementary cementing material in foams for thermal and acoustic insulation. Constr. Build. Mater. **215**, 104–113 (2019)
17. Ahmad, J., Zhou, Z.: Mechanical properties of natural as well as synthetic fiber concrete: a review. Constr. Build. Mater. **333**, 127353 (2022)
18. Cadar, M.E.: SEM study of hair cuticle in some canidae breds. Bull. UASVM Anim. Sci. Biotechnol. **72**(2), 127–130 (2015)
19. Bostanci, S.C.: Alternative sustainable binder for concrete construction: wood ash as a cement replacement. Eur. J. Sci. Technol. **31**, 594–608 (2021)

Civil Engineering Education

Enhancing Students' Comprehension in Building Structures: An Experimental Exploration of Augmented Reality Applications

Salman Azhar[(⊠)] [iD] and Guangyan Shao [iD]

McWhorter School of Building Science, Auburn University, Auburn, AL, USA
{salman,gzs0035}@auburn.edu

Abstract. In the modern era, technological devices have become an indispensable aspect of students' lives. However, effectively engaging these students, who are well-versed in technology, and catering present preferred learning styles, presents a significant challenge. The discrepancies in teaching and learning methods have resulted in issues such as student disengagement, decreased learning aptitude, and limited knowledge retention. Augmented Reality (AR), a visualization technology, provides promising opportunities to involve these students in a dynamic, collaborative, and socially interactive learning environment. By employing 3D AR models for various structural exercises, both building science and architecture students can experience an immersive and meaningful learning journey, thereby greatly stimulating their interest in the subject matter. The objective of this study is to empirically measure the improvements in students' comprehension of building structures through the utilization of AR applications. The research methodology employs a mixed-methods approach for comprehensive data collection. The outcomes of the study demonstrate a significant enhancement in students' learning outcomes and knowledge retention when integrating AR technology into the learning process. It is expected that the findings of this study will provide valuable insights for educators seeking to effectively implement advanced visualization technologies in their courses, ultimately enhancing students' learning experiences and facilitating better knowledge retention in the subject matter.

Keywords: Augmented Reality · Building Structures · Visualizations · Virtual Fieldtrips

1 Introduction

The current generation of tech-savvy students is transforming the higher education landscape. Having grown up with widespread internet access and a strong affinity for technology, including active participation on social media platforms, these students possess a high level of proficiency in digital environments [1]. They are particularly attracted to social learning environments that provide hands-on experiences and direct involvement in the learning process. Being digitally native, these students expect a seamless integration of digital learning tools into their educational journey. However, effectively

engaging these technologically savvy students and catering to their preferred learning styles pose notable challenges. Differences in teaching and learning approaches can result in issues such as student disengagement, reduced learning effectiveness, and diminished knowledge retention [2].

Students enrolled in building science and architecture programs are tasked with analyzing designs for building projects and planning their construction. This process typically involves reviewing and understanding 2D project drawings. However, the interpretation of these 2D drawings by students can vary based on factors such as their educational background, previous practical experience, and visualization capabilities [2]. Despite the availability of 3D and 4D digital models for certain projects, higher education often relies on limited advanced visualization techniques. Fortunately, recent advancements in visualization technologies have opened up new possibilities for student education. It is now feasible to educate students using digital immersive environments that provide a 3D/4D full-scale virtual model of a construction project. These advanced visual communication tools can significantly enhance students' comprehension, learning, and experience in reviewing designs for constructability and planning the construction of complex building projects [3].

In recent years, the applications of Augmented Reality (AR) have witnessed significant growth, providing diverse perspectives on the integration of virtual and real worlds throughout the construction process, from planning to completion. Several research studies have demonstrated the positive impact of AR as an educational tool in Architecture, Engineering, and Construction (AEC) environments, aiming to make a lasting impression on students' learning experiences [2, 3]. These studies effectively conveyed learners' perception of AR technology. However, they did not analyze whether the learning outcomes using AR technology would surpass those of traditional methods, nor did they fully explore how the presentation of class content would impact the outcomes.

This paper presents results of an experimental study by integrating Augmented Reality (AR) and Building Information Modeling (BIM) technologies to assist in architecture and construction education. The primary objective of this research is to assess students' understanding of building structures in the context of their courses through the use of AR applications. The study addresses three key questions: (1) What are the differences in students' comprehension of building structures when utilizing 2D drawings compared to 3D models in AR mode? (2) How do learners perceive the pedagogy of Augmented Reality (AR) in the context of building structures education? (3) What factors influence students' performance in comprehending building structures through the use of AR applications? The research hypothesis is as follows "As a result of using AR technology, there will be a significant improvement in students' comprehension of building structures courses". The research specifically focuses on third-year undergraduate students who are enrolled in the Building Science and Architecture programs at Auburn University.

2 Literature Review

Augmented Reality (AR) technology has emerged as a promising tool in the fields of construction, civil engineering, and architecture education. By overlaying virtual information onto the real world, AR enhances learning experiences, visualization, and practical skills [2]. This brief literature review examines the applications of AR technology in these domains, highlighting its impact on education and identifying key research studies.

AR technology has been successfully integrated into construction education, providing students with interactive and immersive learning experiences. Ahmed demonstrated that AR-based visualizations improved students' understanding of construction sequencing and site logistics [4]. Similarly, Le et al. developed an AR-based training system that enhanced students' construction skills and safety awareness [5]. In a study conducted by Azhar et al., the potential of AR technology as an educational tool was investigated in the context of Construction Communications and Construction Safety classes [6]. The students were tasked with constructing a basic mock bathroom using both 3D holograms and traditional 2D paper-based drawings. Additionally, they engaged in a virtual walkthrough of a construction site where they identified potential hazards [6]. The findings demonstrated that AR technology is highly valuable in simulating real-life construction scenarios, enabling students to learn about jobsite planning, organization, safety measures, and risk identification without the necessity of visiting an actual construction site [6].

AR technology offers innovative applications in civil engineering education, providing students with enhanced visualization and analysis capabilities. Dib and Adamo developed an AR-based platform for structural behavior analysis, allowing students to visualize and interact with virtual structural models [7]. Additionally, Rehman developed an AR-based geotechnical engineering education system that improved students' understanding of soil mechanics concepts [8]. Similarly, AR technology has transformative applications in architecture education, facilitating design exploration, visualization, and collaboration. Milovanovic et al. developed an AR-based platform that allowed students to visualize and assess design options in real-time [9]. Similarly, Alp et al. explored the integration of AR in architecture design studios, highlighting its potential for enhancing students' spatial cognition and design comprehension [10].

AR technology facilitates collaborative learning and communication in construction, civil engineering, and architecture education. Ko and Chang developed an AR-based collaborative platform that enabled students and industry professionals to co-create and visualize designs [11]. Additionally, Vergas et al. explored the use of AR in interdisciplinary design education, highlighting its potential for enhancing communication and teamwork among students from different disciplines [12]. While AR technology offers numerous advantages, it is important to note that research indicates its use may lead to cognitive overload, potentially affecting task performance negatively. A study by Abbas et al. emphasizes the significance of thoroughly evaluating and considering the cognitive demands imposed by mobile AR applications to maximize their effectiveness in AEC tasks [13].

3   Research Design and Methodology

Figure 1 illustrates the research design adopted in this study, and the subsequent paragraphs elaborate on each step of the design.
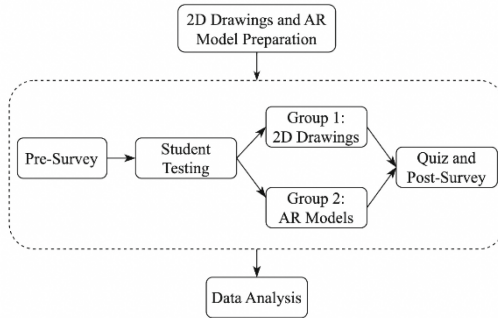
Fig. 1. Research design.

3.1   2D Drawings and AR Model Preparation

In this study, a selection of 8 structural steel, wood, and concrete assemblies was made. These chosen assemblies encompass intricate structural elements found in standard steel, wood, concrete, and composite connections. A 2D drawing and a corresponding 3D model were developed for each assembly using Autodesk Revit®. These 3D models were subsequently exported to an augmented reality (AR) application called Augment®, allowing them to be viewed within an AR environment using a Tablet or a smart phone. Figure 2 depicts the 2D drawing alongside its accompanying 3D AR model.
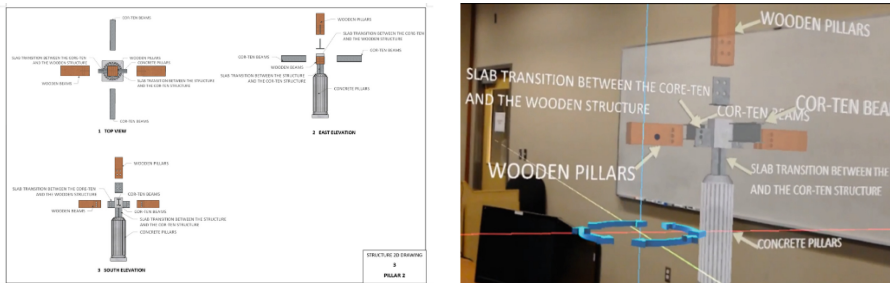
Fig. 2. (Left) 2D drawing of a composite column-beam connection, (Right) 3D AR model of the same assembly.

3.2 Pre-survey

The study involved third-year undergraduate architecture and building science students as participants. To better comprehend the participants' background, a pre-survey questionnaire was distributed to their email addresses. The questionnaire aimed to gather information about their familiarity with Augmented Reality (AR) and their understanding of the concepts related to the Structures of Buildings course. Furthermore, it sought insights into their expectations regarding the utilization of AR technology for interpreting drawings, in comparison to traditional 2D drawings. Taking into consideration the survey feedback and the students' current academic grades in the Structures of Buildings class, they were divided into two distinct groups: the Control Group (Group 1) and the AR Group (Group 2). Group 1 comprised 14 students, while Group 2 had 13 students. Each group consisted of students with diverse academic performance levels and varying degrees of familiarity with AR technology.

3.3 Student Testing and Quiz

On the testing day, each group received a 45-min lecture on structural assemblies, delivered either through 2D drawings or 3D AR models. Following the lecture, the participants were required to complete an online quiz consisting of 18 multiple-choice questions. The quiz aimed to assess their knowledge acquisition and retention, with approximately 2–3 questions dedicated to each structural assembly. The time taken by each student to complete the quiz as well as quiz score were recorded. Following the completion of the quiz, Group 1 was provided with an additional briefing on the AR system, which included several demonstrations to familiarize them with its functionality and features.

3.4 Post Survey

To assess and compare students' understanding of structural systems using the two methods, an online post-survey questionnaire was distributed to participants via email. The questionnaire was aimed to gather participants' feedback on their experiences and future expectations regarding the utilization of AR technology as compared to traditional 2D drawings. Prior to distributing the survey, both groups were provided with a comprehensive presentation that offered a comparison between the two testing methods: 2D drawings and 3D AR technology. This ensured that participants had sufficient understanding to effectively complete the survey. Building upon the findings of the literature review, several potential influencing factors for using AR in a structures class were identified. Participants were given the opportunity to rank these factors and suggest any additional factors they deemed relevant.

3.5 Data Analysis

Quantitative data analysis in this study involved the use of descriptive and inferential statistics, allowing for a comprehensive examination of the data. On the other hand, qualitative data was analyzed through content analysis, enabling a deeper understanding of the themes and patterns present. The subsequent section presents a concise overview of the data analysis conducted and highlights the main findings derived from the study.

4   Results and Main Findings

4.1   Participants Background

The study involved the participation of 27 third-year undergraduate students enrolled in BSCI 3440: Structures of Buildings-II course. Out of these participants, 15 students (56%) were majoring in Building Science, while 12 students (44%) were majoring in Architecture. Among all the participants, 11 students (41%) had prior experience using AR apps similar to Augment® on personal devices, while 16 students (59%) did not have any previous AR experience. In addition, participants were requested to rate their level of comprehension in the Structures of Buildings class on a scale of 1 to 10, where 1 represented "Least Knowledgeable" and 10 indicated "Very Knowledgeable". The results, presented in Table 1, reveal a mean score of 6.74, suggesting that the participants possessed above-average knowledge in the subject matter.

Table 1.   Results of participants' level of comprehension in the Structures of Buildings class.

Minimum	Maximum	Mean	Median	Std Deviation	Variance	Count
3	9	6.74	7	1.51	2.27	27

The participants were surveyed regarding their preferred method of viewing structural assembly models. The findings revealed that the majority of students (64%) favored 2D drawings over the AR models (36%). The primary reason cited for this preference was familiarity, as students were accustomed to working with 2D drawings. Additional reasons provided by participants in support of their preferred viewing method are listed in Table 2.

Table 2.   Reasons for preferring 2D drawings and augmented reality (AR) model before testing.

2D drawings		Augmented reality (AR) model	
Reason	Count	Reason	Count
More prior experience	7	Better visualization	6
Simple and easy to use	5	Manipulate model (turn or move)	3
Less training required	3	Easier and more portable	2
Less disturbance	2		
Rich and detailed content	2		

4.2   Quiz Results

Table 3 presents the results of the online quiz, which consisted of 18 multiple-choice questions, each carrying a value of 1 point. The mean, minimum, maximum, and median

percentage scores achieved by building science and architecture students are listed. The maximum time allocated for completing the quiz was 25 min. Additionally, the table displays the average time taken by students to finish the quiz.

Table 3. Scores and time taken by student groups for completing the online quiz.

	Group 1: 2D drawings		Group 2: AR model	
Program	Building science	Architecture	Building science	Architecture
Mean score	66%	60%	81%	73%
Low score	42%	32%	48%	35%
High score	84%	76%	96%	82%
Median Score	73%	65%	78%	71%
Mean Completion Time (minutes)	25	25	21	23

The results of the quiz clearly demonstrate that Group 2, which utilized the 3D AR models, outperformed Group 1, which relied on 2D drawings. Furthermore, Group 2 exhibited a shorter average completion time compared to Group 1. These findings suggest that the use of 3D AR models helped to enhance students' knowledge retention and productivity. It is worth noting that the performance of building science students was slightly superior to that of architecture students. This distinction could be attributed to their greater familiarity with construction drawings and practical experience gained through field internships. In order to assess the statistical significance between the two groups, a t-test was conducted on the average test scores. The outcomes of this analysis are presented in Table 4.

Table 4. T-test results for mean quiz score for group 1 (2D drawings) and group 2 (AR).

	Group 1 (2D drawings) v. Group 2 (AR)
Sample size (N)	14 and 13
Std. Error mean	0.7797
t-value	-1.0282
Sig. (2-tailed)	0.3191

The findings demonstrate a substantial disparity in the performance of the two student groups. This supports the acceptance of the alternative hypothesis, which states that the utilization of AR technology leads to a significant enhancement in students' understanding of building structures courses, while rejecting the null hypothesis. More discussion on the results is available in Sect. 4.4.

4.3 Post-survey Results

Upon finishing the quiz, all students were given a post-survey to gather insights into their perceptions regarding both visualization methods. During this phase, a presentation was delivered to the students, elucidating the advantages and disadvantages of each visualization method. Consequently, students had a comprehensive understanding of both methods and were well-informed before providing their feedback.

In the survey, the initial question inquired about the preferred method, either 2D drawings or 3D AR models, if participants had to undertake the lecture and quiz again. Among the submitted answers, AR received 19 votes, while 2D drawings received 7 votes. One student did not provide any answer. These results indicate a clear preference among participants for using AR technology to comprehend structure drawings.

After conducting the literature review, several advantages and limitations of employing AR technology in building structure classes were identified. Participants were asked to rank these advantages and limitations from their perspective which are listed in Table 5. The top advantages include the provision of an interactive learning environment, integration with various AEC (Architecture, Engineering, and Construction) courses, better visualization of complexity for enriched content, and the ability to accurately depict real-life scenarios. These findings highlight the significant benefits of AR in enhancing the learning experience for students in building structure classes. The leading limitations were identified as follows: cognitive overload, attention disturbance from lectures, reduced coordination among students, and the high cost of hardware and software. Notably, participants expressed significant concern regarding cognitive overload, which aligns with previous research [13]. This research has indicated that an overwhelming amount of information can lead to cognitive overload, ultimately impacting task performance in a negative manner.

Table 5. Top advantages and limitations of the AR technology from students' perspective.

Rank	Advantage	Limitation
1	Interactive learning environment	Cognitive overload
2	Integrate with various AEC courses	Disturb attention from lecture
3	Visualize complexity for rich content	Less students' coordination
4	Accurate depiction of real-life scenarios	High cost on hardware and software
5	Accelerate task completion	Motion sickness
6	Interested and motivative for gamification	Extra training
7	Relived students' safety risk on jobsite visit	Immature technology

4.4 Discussion on Results

The findings presented numerous compelling justifications for preferring the adoption of 3D Augmented Reality (AR) technology over conventional 2D drawings. Firstly, 3D

AR models provide a more immersive and interactive learning experience. Students can visualize and explore complex structures in three dimensions, allowing for a deeper understanding of spatial relationships and design principles. This hands-on approach promotes active engagement and boosts comprehension. Secondly, 3D AR technology offers a realistic representation of objects and structures, bridging the gap between the virtual and physical worlds. Students can manipulate and interact with virtual objects in real-time, enabling them to examine various design aspects and make informed decisions. This enhances their problem-solving skills and fosters creativity in architectural and construction processes. Furthermore, 3D AR models provide a dynamic and adaptable learning tool. Students can view structures from different angles, toggle between different design options, and even simulate real-time construction processes. This flexibility facilitates better decision-making and enables students to explore design alternatives and assess their impact. Lastly, the use of 3D AR technology aligns with industry trends and prepares students for the modern workforce. Many architectural and construction firms are increasingly incorporating AR into their workflows. By familiarizing students with this technology, educational institutions equip them with valuable skills that are in high demand in the professional realm.

While there are several advantages to utilizing 3D augmented reality (AR) technology, it also has certain limitations when compared to 2D drawings. Firstly, AR technology often provides users with a wealth of visual and auditory information simultaneously. This abundance of stimuli can overwhelm the cognitive system, making it challenging for users to focus on relevant information and filter out distractions. Processing excessive information can lead to cognitive overload, hindering learning and task performance. AR experiences often require users to simultaneously engage in multiple tasks, such as navigating the virtual environment, interpreting visual cues, and interacting with digital objects. Switching between these tasks and managing the cognitive load associated with each can strain working memory and cognitive resources, potentially leading to decreased performance and increased errors.

Secondly, AR technology relies on the availability of compatible devices and reliable network connections. In some settings, students may not have access to the necessary devices or internet connectivity, limiting their ability to engage with AR-based learning materials. In contrast, 2D drawings are independent of such technological requirements and can be easily accessed and used in various learning environments. Additionally, AR technology may present a steeper learning curve for both students and instructors. Mastering the skills and techniques involved in navigating and interacting with 3D AR models may require additional time and training. On the other hand, 2D drawings have a more straightforward and familiar format, making them easier to understand and work with for individuals of different skill levels.

5 Conclusions and Recommendations

The research results support the use of augmented reality (AR) technology in architecture and building science education. In particular, AR technology offers numerous advantages in Structures of Buildings classes. It provides an immersive and interactive learning environment that enhances comprehension of complex structures and spatial relationships. AR technology integrates well with various AEC courses, offering a versatile

tool for visualizing and exploring building designs. It also allows for accurate depictions of real-life scenarios, aiding in practical understanding. However, it is important to consider the limitations of AR technology, such as the higher cost of implementation, technological dependencies, learning curve challenges, and the potential for cognitive overload. Despite these limitations, when used strategically and with appropriate support, AR technology can greatly benefit students by enhancing their learning experiences and preparing them for the demands of the modern architecture and construction industry. This research study has a few limitations that should be acknowledged. Firstly, the sample size used for testing was limited, which may affect the generalizability of the findings. Additionally, the testing time allocated to participants was relatively short, potentially constraining the depth of exploration and evaluation of AR technology. The study did not include an examination of social and collaborative experiences, missing an opportunity to assess the potential benefits and challenges of using AR in such contexts. Future research should consider addressing these limitations to provide a more comprehensive understanding of the implications and effectiveness of AR technology in educational settings.

References

1. Smetana, L.K., Bell, R.L., Jansen, H.: Visualizations in science education: the influence of prior knowledge and cognitive load on student learning and engagement. J. Sci. Educ. Technol. **28**(1), 65–80 (2019)
2. Liao, Y.K., Chen, C.Y., Chen, H.C., Huang, P.K.: The application of augmented reality in higher education: a systematic literature review and conceptual framework. Educ. Technol. Soc. **21**(4), 195–216 (2018)
3. Hartless, J., Chalhoub, J., Ayer, S.K.: Mixed reality to enable construction design comprehension for digital natives. In: AEI 2019: Integrated Building Solutions - The National Agenda, pp. 166–173 American Society of Civil Engineers, Reston, VA (2019)
4. Ahmed, S.: A review on using opportunities of augmented reality and virtual reality in construction project management. Organ. Technol. Manage. Constr. Int. J. **10**(1), 1839–1852 (2018)
5. Le, Q.T., Pedro, A.K.E.E.M., Lim, C.R., Park, H.T., Park, C.S., Kim, H.K.: A framework for using mobile based virtual reality and augmented reality for experiential construction safety education. Int. J. Eng. Educ. **31**(3), 713–725 (2015)
6. Azhar, S., Kim, J., Salman, A.: Implementing virtual reality and mixed reality technologies in construction education: students' perceptions and lessons learned. In: ICERI 2018 Proceedings, pp. 3720–3730. IATED (2018)
7. Dib, H.N., Adamo, N.: An augmented reality environment for students' learning of steel connection behavior. In: Computing in Civil Engineering, pp. 51–58 (2017)
8. Rehman, Z.U.: Trends and challenges of technology-enhanced learning in geotechnical engineering education. Sustainability **15**(10), 7972 (2023)
9. Milovanovic, J., Moreau, G., Siret, D., Miguet, F.: Virtual and augmented reality in architectural design and education. In: 17th International Conference, CAAD Futures (2017)
10. Alp, N.C., Yazici, Y.E., Oner, D.: Augmented reality experience in an architectural design studio. Multimed. Tools Appl. 1–19 (2023)
11. Ko, C.H., Chang, T.C.: Evaluation and student perception of augmented reality based design collaboration. Management **6**(6), 6 (2011)

12. Vargas, Y.A.M., Rojas, E.E.M., Castillo, V.S.: Application of augmented reality as a means of interdisciplinary learning. Sci. Tech. **24**(3), 479–489 (2019)
13. Abbas, A., Seo, J., Kim, M.: Impact of mobile augmented reality system on cognitive behavior and performance during rebar inspection tasks. J. Comput. Civ. Eng. **34**(6), 04020050 (2020)

Construction Management

Digital Quality Management System for Construction: The Role of Smart Cameras

Zanyar Abdullah[1] , Tahir Çelik[1(✉)] , and Tolga Celik[2]

[1] Civil Engineering Department, Cyprus International University, Adana, Northern Cyprus, Turkey
tcelik@ciu.edu.tr
[2] Civil Engineering Department, Eastern Mediterranean University, Gaziantep, Northern Cyprus, Turkey
tolga.celik@emu.edu.tr

Abstract. This review paper synthesizes the existing literature on the integration of smart cameras within digital quality management systems (QMS) for the construction industry. It provides an overarching perspective on how digital QMS, enhanced by smart camera technology, addresses key challenges in construction quality, safety, and efficiency. The paper begins by exploring the general benefits of digital QMS in construction, emphasizing the role of smart cameras in automating process monitoring and issue detection. It then categorizes the literature on various types of smart cameras and their broad capabilities, such as image recognition and real-time analysis, in the context of construction. The review highlights the prevalent themes in the application of smart cameras in construction, such as site safety monitoring and progress assessment, drawing on common findings from existing studies. Further, it identifies the main challenges highlighted in the literature, including cost implications, privacy concerns, and the need for technical expertise. The paper underscores the gaps in current research, particularly in the integration of smart cameras with other emerging technologies like drones and wearable devices. It concludes by emphasizing the need for continued research and development to enhance the effectiveness and usability of smart cameras in digital QMS for construction, suggesting areas for future investigation.

Keywords: Smart Camera · Digital Quality Management · Quality Management System · Automation in Construction

1 Introduction

Digital quality management systems (QMS), as part of the broader movement towards automation in the construction industry, have demonstrated significant benefits, including improved quality control, reduced rework, and enhanced productivity [1–3]. Recent innovations in information technology, such as Building Information Modeling (BIM) [4, 5] and Big Data [6], have further optimized digital QMS, providing more efficient ways to manage the complexities of construction projects. However, these systems still face considerable implementation challenges, including cost, privacy concerns, and the need

for specialized expertise [7–9]. Smart cameras, as a key technology in these systems, offer a novel approach to addressing these issues. They provide automated monitoring of construction processes, enabling real-time analysis, object tracking, and image recognition, which are instrumental in identifying potential issues before they escalate into substantial problems [10, 11]. Studies have shown that smart cameras can be utilized in various construction applications, such as monitoring site safety [12], tracking worker activity [13], and assessing progress [14]. The integration of smart cameras into digital QMS in construction is relatively recent, and the effectiveness of this technology has been evidenced in several studies [15, 17]. However, the adoption of smart cameras in construction still requires thorough examination, as there are significant challenges associated with their use, such as privacy concerns, cost, and the need for training [7, 18]. Moreover, the potential for integrating smart cameras with other emerging technologies, such as drones and wearable devices, is becoming a new frontier for enhancing the effectiveness of digital QMS in construction [19]. Despite the growing body of research in this field, further investigations are necessary to fully understand the implications and potential of these integrations. In light of these considerations, this review paper examines the role of smart cameras in the digital quality management system for construction, discussing their benefits, challenges, and potential integrations with other technologies. Additionally, it explores strategies for overcoming implementation challenges, with insights drawn from the latest research and case studies. The ultimate goal is to provide a comprehensive perspective on the use of smart cameras in digital QMS for construction, contributing to the ongoing discussion on improving quality, safety, and efficiency in the construction industry.

2   Construction Quality Management Systems in the Digital Era

2.1   Overview of Digital QMS

Quality management systems have been indispensable in the construction industry, influencing the efficiency and success of construction projects [3]. Traditionally, these systems focused on a series of checks and balances, documented on paper and enforced through regular audits and site inspections. However, with the advent of the digital era, the traditional methods of maintaining and enforcing QMS have been radically transformed. The onset of the digital era brought about the development and integration of digital tools into QMS, turning these systems into digital QMS. Building information modeling is an advanced tool that allows for building model visualization, simulation, and analysis. This technology has improved the ability of architects, engineers, and builders to coordinate their work, leading to fewer mistakes and reworks, thus improving construction quality [5, 20, 21]. The IoT and big data have also found a place in the construction industry. IoT devices, such as sensors and cameras, collect vast amounts of data that can be used to monitor construction processes, ensure safety standards, and track project progress [13, 22]. Big data, on the other hand, enables the analysis of these data, providing insights that lead to better decision-making and improved quality [6].

2.2 Benefits of Digital QMS

Digital QMS provides a plethora of benefits to the construction industry. Firstly, it increases efficiency by streamlining quality control processes. Digital technologies such as BIM allow for early detection and correction of design issues, reducing the likelihood of costly reworks [5]. Digital QMS also improves communication and collaboration among project stakeholders. Project team members can access and update information through shared digital platforms in real-time, enhancing coordination and reducing errors [9, 23]. Moreover, digital QMS contributes to better decision-making. Big data analytics provide actionable insights about project performance, enabling project managers to make data-driven decisions that enhance construction quality [13].

2.3 Importance of Digital QMS in Construction

The construction industry is fraught with complexities that range from ever-changing building codes and regulations to the intricate interplay between various professions. These complexities, coupled with the inherent variability and risk in construction projects, make quality management a crucial part of the construction process [1, 2]. Implementing digital QMS in construction projects can improve construction quality considerably. For instance, using BIM has been shown to improve cost and time control in construction, thereby enhancing overall project quality [24]. Moreover, the integration of IoT devices and big data into QMS provides real-time monitoring and advanced analytics that facilitate swift detection and resolution of quality issues, contributing to the successful completion of projects [6, 13]. Despite the aforementioned benefits, implementing digital QMS in construction also faces challenges. These include cost, privacy concerns, and the need for specialized expertise [7]. As the industry navigates these challenges, the importance of the continued evolution of digital QMS cannot be overstated. Emerging technologies, such as smart cameras, are expected to play a crucial role in advancing digital QMS, improving construction quality, and enhancing the overall productivity and safety of the construction industry [11]. Overall, the digital QMS is pivotal in improving quality and productivity in the construction industry. It signifies a substantial shift from traditional quality management methods towards a more automated and efficient approach. The role of smart cameras in enhancing these systems is of high interest, providing promising avenues for further research and development.

3 Role of Smart Cameras in Digital QMS

3.1 Types of Smart Cameras

Smart cameras, often referred to as intelligent cameras, have become essential components of digital QMS in the construction industry. Unlike conventional cameras, smart cameras possess internal processing capabilities that enable them to analyze the visual data they capture. Different types of smart cameras are categorized based on their specific features and functionalities. On a basic level, there are standalone smart cameras, which are single units that include the lens, image sensor, and processing unit. They perform image processing independently and can perform simple tasks such as motion

detection and object tracking. More advanced types include networked smart cameras. These devices are connected via wired or wireless networks and can work together to analyze visual data on a larger scale, for example, in a construction site where multiple cameras can cover a wider area. AI-empowered smart cameras are another significant development. These cameras leverage AI technologies, such as machine learning and deep learning, to intelligently analyze the captured visual data. They can recognize patterns, classify objects, and even predict future events based on past data.

3.2   Capabilities of Smart Cameras

Smart cameras, also known as intelligent cameras, have gained significant attention in recent years for their ability to extend beyond the typical functions of conventional cameras. Equipped with advanced capabilities, smart cameras have been widely adopted in various industries, including construction, to enhance monitoring and quality management [11]. One of the main capabilities of smart cameras is their ability to process images on the device itself. This starkly contrasts traditional cameras that merely capture images and require an external device for processing. The integrated processing capability in smart cameras makes them particularly beneficial in applications where real-time decision-making is crucial. The construction industry is one such sector where real-time decision-making can significantly affect project outcomes. Smart cameras can be used in construction projects for quality control, safety monitoring, and progress tracking [11]. The onboard processing capabilities of smart cameras allow them to analyze the images they capture, recognize patterns, identify potential safety hazards, and detect deviations from project plans. Another key capability of smart cameras is their ability to connect to the Internet, which places them within the broad category of IoT devices [13]. This connectivity allows smart cameras to transmit the data they capture and process to other devices or systems in real time. In the construction context, this can facilitate immediate corrective action in the face of potential safety hazards or quality issues. Integrating smart cameras with other digital technologies, such as BIM, provides additional capabilities. For instance, images captured by smart cameras can be compared against the 3D models in a BIM system to monitor construction progress and ensure adherence to design specifications [20]. Moreover, the capability of smart cameras to collect data continuously allows them to feed into big data systems, where the data can be further analyzed for in-depth insights. These insights can guide project managers in making data-driven decisions, leading to improved construction quality [13]. However, using smart cameras also raises several concerns, such as privacy and data security. Given their ability to capture and transmit data continuously, smart cameras can potentially infringe upon the privacy, especially in public or semi-public spaces [7]. Additionally, the data transmitted by smart cameras can be vulnerable to cyber-attacks, necessitating robust data security measures.

3.3   Applications of Smart Cameras in Construction

The deployment of smart cameras in construction presents myriad applications that have the potential to revolutionize various aspects of the industry. These applications include quality control, safety monitoring, and progress tracking. In terms of quality control,

smart cameras can play an instrumental role. Using integrated image processing capabilities, they can detect deviations from design specifications in real-time. The images captured by the cameras can be compared against the design plans, thus identifying any non-conformities. When such deviations are detected, alerts can be sent out immediately to facilitate corrective action. This rapid detection and response can significantly improve construction quality and reduce costly rework. Smart cameras can also contribute significantly to safety monitoring in construction sites. Construction sites are often fraught with potential hazards such as falling objects, unsafe scaffolding, or machinery accidents. With their ability to analyze images and identify patterns, smart cameras can detect these potential safety threats and alert site managers in real time. The immediate awareness provided by smart cameras can prevent accidents and promote a safer working environment [11]. Furthermore, integrating facial recognition technologies with smart cameras can control site access, ensuring that only authorized personnel are permitted within the premises [7]. In terms of progress tracking, smart cameras paired with BIM can be remarkably beneficial. The images captured by the cameras can be compared against the 3D models in the BIM system to monitor construction progress accurately. This enables project managers to keep track of the project schedule and promptly address any delays. Moreover, it can aid in identifying areas where productivity can be improved, ultimately contributing to the overall efficiency of the construction process [20]. Additionally, smart cameras can serve as a crucial element in the broader context of construction site surveillance. By leveraging their internet connectivity, smart cameras can transmit the images they capture to remote locations in real-time. This allows project managers and stakeholders to monitor construction activities from anywhere, providing flexibility and convenience. This can also facilitate improved coordination and communication among project teams, as any issue can be visually presented and discussed. The use of smart cameras also extends to asset tracking on construction sites. With their ability to continuously collect data, smart cameras can monitor the movement and usage of construction equipment and materials. This can help in preventing theft or loss of valuable assets and ensure efficient utilization of resources. Finally, the data collected by smart cameras can feed into big data systems for further analysis. The continuous flow of data can yield insights into construction processes, safety measures, productivity, and even predictive analytics. These data-driven insights can support decision-making at various levels of the construction project, thus enhancing its success potential [13]. However, it is crucial to bear in mind that the application of smart cameras in construction also entails several challenges. Key among these are privacy concerns and data security issues. Robust measures need to be in place to ensure the appropriate use of smart cameras and the secure transmission and storage of the data they capture [7].

4 Challenges in Implementing Digital QMS and Smart Cameras in Construction

4.1 Cost

Cost is the first significant barrier to implementing digital QMS and smart cameras in construction [18]. Developing and deploying such systems can be expensive, particularly for small and medium-sized construction firms that may lack the resources for significant

capital investment [25]. Moreover, the benefits of digital QMS, while considerable, may not be immediately apparent, making it challenging to justify the investment to stakeholders [5]. Additional costs may also arise from the need to maintain and upgrade the system, further adding to the total cost of ownership [14].

4.2 Privacy Concerns

Privacy issues represent a significant hurdle for the adoption of smart cameras in construction [7]. The use of surveillance technology in the workplace can be seen as intrusive and may lead to resistance from workers who feel their privacy is being infringed upon [15]. Similarly, there are potential legal issues related to data protection and the use of personal data collected by smart cameras, particularly in regions with strict data protection laws, such as the European Union [10]. Therefore, the challenge is finding a balance between the need for surveillance to ensure safety and quality control and workers' rights to privacy and dignity in the workplace.

4.3 Need for Specialized Expertise

Finally, implementing digital QMS and smart cameras in construction requires specialized expertise [8]. Construction firms may lack the necessary technical skills to develop and operate these systems, requiring them to invest in training or hire additional personnel. This could potentially increase project costs and lead to resistance from existing staff [26]. The deployment of smart cameras, in particular, requires knowledge of computer vision techniques and the ability to interpret the data collected [11]. This lack of expertise may hinder the effective use of digital QMS and smart cameras and limit their potential benefits [17].

5 Strategies for Overcoming Challenges

5.1 Use of Open-Source Software

In the digital age, adopting open-source software could be a potential solution to many challenges in the construction sector. Open-source software refers to software whose source code is available for modification or enhancement by anyone. This can reduce costs, enhance flexibility, and foster innovation. Building information modeling is an example of such software and has proven to be beneficial for managing time and cost control in the construction sector [24]. BIM is a digital representation of a facility's physical and functional characteristics. It serves as a shared knowledge resource for information about a facility, forming a reliable basis for decisions [5]. In addition, technologies like Unmanned Aerial Vehicles (UAVs) and IoT are revolutionizing the construction sector, offering solutions for remote sensing and logistics management [19, 27].

5.2 Collaboration Between Stakeholders

The construction industry encompasses a wide array of stakeholders, such as architects, engineers, builders, contractors, and clients. Successful projects often result from effective communication and collaboration among these stakeholders [28]. A culture of collaboration can help prevent construction delays, reduce conflicts, and ensure quality control [1]. A study by Leong et al. [3] confirmed that a well-implemented quality management system could improve productivity and customer satisfaction in the construction industry. Moreover, with advancements in technology, it is possible to enable better communication and collaboration. For instance, electronic document management systems can streamline collaboration and information sharing [23].

5.3 Training for Workers

Given the industry's dynamic nature and technological advancements, the importance of training cannot be overstated. A study by Ahn et al. [26] highlights the importance of competencies for construction graduates, signifying the need for education and training in the construction industry. Incorporating safety training, especially with the use of modern technologies such as computer vision and intelligent video surveillance systems, can significantly reduce accident rates and improve worker safety [10, 11]. Furthermore, continuous education can keep workers up-to-date with the latest technologies, building codes, and best practices in the industry [29]. Addressing the lack of knowledge in the local workforce and encouraging continuous professional development can also lead to the growth of indigenous contractors and improve the overall productivity of the construction sector [30].

6 Future Directions for Digital QMS and Smart Cameras in Construction

As mentioned before, digital QMS and smart cameras are transforming the construction industry, paving the way for enhanced productivity, quality, and safety. These technologies are expected to become even more deeply embedded in construction processes, offering a wealth of opportunities for further innovation and improvement. Digital QMS in construction is pivotal in improving operational efficiency, reducing waste, and ensuring compliance with safety and quality standards. Future enhancements to digital QMS are likely to focus on greater integration with other digital tools and systems. One promising avenue is the fusion of QMS with BIM, allowing for more thorough and real-time tracking of quality management parameters. Also, with the increasing trend of digitalization and IoT in construction, QMS could be further refined and automated, leading to even more efficient operations and higher quality outputs. Smart cameras, capable of recording and analyzing data, are becoming indispensable in construction, particularly for safety and security management. With their ability to monitor construction sites continuously, smart cameras can help identify potential safety hazards and prevent accidents before they occur. In the future, advancements in machine learning and computer vision technologies will likely lead to even smarter cameras with improved capabilities

for analyzing complex scenes and detecting potential risks. Moreover, integrating smart cameras with digital QMS could revolutionize how construction projects are monitored and managed. For example, smart cameras could capture real-time data on the construction process and feed this information directly into the QMS. This would allow for a much more dynamic and responsive approach to quality management, with potential issues being identified and addressed almost as soon as they arise. However, the future application of digital QMS and smart cameras also raises several issues, particularly regarding data privacy and ethical considerations. Thus, robust guidelines and regulations will need to be put in place to ensure these technologies are used responsibly and ethically.

7   Conclusion

This paper has explored the integration of digital QMS and smart cameras in the construction industry, elucidating their current applications, inherent challenges, strategies to overcome these challenges, and potential future directions. The findings indicate that digital QMS and smart cameras significantly enhance the efficiency, quality, and safety of construction projects. Digital QMS contributes to operational efficiency and adherence to safety and quality standards, while smart cameras bolster security and hazard detection. The implications of these technologies for the construction industry are profound. With the integration of digital QMS and smart cameras, companies can achieve a more efficient and dynamic approach to quality management. Real-time data collection and processing allow for immediate identification and mitigation of potential issues, improving project outcomes. However, deploying these technologies also calls for a revamp in traditional construction practices, necessitating open-source software, collaboration among stakeholders, and adequate training for workers to effectively utilize these tools. While this study provides valuable insights into the role of digital QMS and smart cameras in construction, certain limitations suggest avenues for future research. The study mainly focused on the positive implications of these technologies, leaving room for further exploration of potential challenges, especially those associated with data privacy and ethical considerations. Moreover, as technology continues to evolve, it will be crucial to study the impact of upcoming advancements on the construction industry. Future research could delve into the integration of other emerging technologies, such as artificial intelligence and robotics, with digital QMS and smart cameras. Also, additional studies could focus on developing comprehensive guidelines and regulations to ensure these technologies' ethical and responsible use in construction.

References

1. Luo, H., Lin, L., Chen, K., Antwi-Afari, M.F., Chen, L.: Digital technology for quality management in construction: a review and future research directions. Dev. Built Environ. **12**, 100087 (2022)
2. Egwunatum, S.I., Anumudu, A.C., Eze, E.C., Awodele, I.A.: Total quality management (TQM) implementation in the Nigerian construction industry. Eng. Constr. Archit. Manag. **29**(1), 354–382 (2022)

3. Rwelamila, P.D.: Quality management in construction projects in developing countries—where to, from current body of knowledge? In: Building a Body of Knowledge in Project Management in Developing Countries, pp. 261–294. (2023)

4. Hall, A.T., Durdyev, S., Koc, K., Ekmekcioglu, O., Tupenaite, L.: Multi-criteria analysis of barriers to building information modeling (BIM) adoption for SMEs in New Zealand construction industry. Eng. Constr. Archit. Manag. **30**(9), 3798–3816 (2023)

5. Barlish, K., Sullivan, K.: How to measure the benefits of BIM—a case study approach. Autom. Constr. **24**, 149–159 (2012)

6. Veras, P.R., Suresh, S., Renukappa, S.: The adoption of big data concepts for sustainable practices implementation in the construction industry. In: 2018 IEEE/ACM International Conference on Utility and Cloud Computing Companion (UCC Companion), pp. 349–352 (2018)

7. Patel, T., Patel, V.: Data privacy in construction industry by privacy-preserving data mining (PPDM) approach. Asian J. Civ. Eng. **21**(3), 505–515 (2020)

8. Aleksandrova, S.V., Vasiliev, V.A., Alexandrov, M.N.: Integration of quality management and digital technologies. In: 2019 International Conference "Quality Management, Transport and Information Security, Information Technologies", pp. 20–22 (2019). IEEE

9. Dudgikar, C.S., Kumthekar, M.B., Khot, S.R.: Development of ERP module for quality management in construction industry. Int. J. Electron. Commun. (IJEC) **1**(1), 29–40 (2012)

10. Guo, S., Li, J., Liang, K., Tang, B.: Improved safety checklist analysis approach using intelligent video surveillance in the construction industry: a case study. Int. J. Occup. Saf. Ergon. **27**(4), 1064–1075 (2021)

11. Seo, J., Han, S., Lee, S., Kim, H.: Computer vision techniques for construction safety and health monitoring. Adv. Eng. Inform. **29**(2), 239–251 (2015)

12. Park, M.W., Brilakis, I.: Construction worker detection in video frames for initializing vision trackers. Autom. Constr. **28**, 15–25 (2012)

13. Guo, S.Y., Ding, L.Y., Luo, H.B., Jiang, X.Y.: A Big-Data-based platform of workers' behavior: observations from the field. Accid. Anal. Prev. **93**, 299–309 (2016)

14. Yan, R.J., Kayacan, E., Chen, I.M., Tiong, L.K., Wu, J.: QuicaBot: quality inspection and assessment robot. IEEE Trans. Autom. Sci. Eng. **16**(2), 506–517 (2018)

15. Mabrouk, A.B., Zagrouba, E.: Abnormal behavior recognition for intelligent video surveillance systems: a review. Expert Syst. Appl. **91**, 480–491 (2018)

16. Rao, A.S., et al.: Real-time monitoring of construction sites: Sensors, methods, and applications. Autom. Constr. **136**, 104099 (2022)

17. Arabshahi, M., et al.: Review on sensing technology adoption in the construction industry. Sensors **21**(24), 8307 (2021)

18. Zhou, Z., Irizarry, J., Li, Q.: Applying advanced technology to improve safety management in the construction industry: a literature review. Constr. Manag. Econ. **31**(6), 606–622 (2013)

19. Guan, S., Zhu, Z., Wang, G.: A review on UAV-based remote sensing technologies for construction and civil applications. Drones **6**(5), 117 (2022)

20. Lu, W., Peng, Y., Shen, Q., Li, H.: Generic model for measuring benefits of BIM as a learning tool in construction tasks. J. Constr. Eng. Manag. **139**(2), 195–203 (2013)

21. Woo, J., Wilsmann, J., Kang, D.: Use of as-built building information modeling. In: Construction Research Congress 2010: Innovation for Reshaping Construction Practice, pp. 538–548 (2010)

22. Bibri, S.E.: The IoT for smart sustainable cities of the future: an analytical framework for sensor-based big data applications for environmental sustainability. Sustain. Cities Soc. **38**, 230–253 (2018)

23. Björk, B.C.: Electronic document management in construction – research issue and results. Electron. J. Inf. Technol. Constr. ITcon **8**, 101–113 (2003)

24. Haron, A.N., Alias, N.A., Mohammed, I.B., Baba, D.L.: Improving cost and time control in construction using building information model (BIM): a review. TQM J. (2018)
25. Kar, D., Basak, S., Bhattacharya, A.K.: Implementation of construction projects on schedule—a challenge to the developing world. J. Econ. Int. Finance **1**(4), 088–092 (2009)
26. Ahn, Y.H., Kwon, H., Pearce, A.R., Shin, H.: Key competencies for US construction graduates: an exploratory factor analysis. In: ASC Proceedings of the 46th Annual Conference (2010)
27. Jianli, S.: Design and implementation of IOT-based logistics management system. In: 2012 IEEE Symposium on Electrical & Electronics Engineering (EEESYM), pp. 603–606 (2012)
28. Irfan, M., Thaheem, M.J., Kaka Khel, S.S., Faizan Ul Haq, M., Saeed Zafar, M., Ehtsham, M.: Development of comprehensive coursework of quality management in universities pertinent to the construction industry: a case of Pakistan. TQM J. **33**(6), 1100–1122 (2021)
29. Ugochukwu, S.C., Onyekwena, T.: Participation of indigenous contractors in Nigerian public sector construction projects and their challenges in managing working capital. Int. J. Civ. Eng. Constr. Estate Manag. **1**(1), 1–21 (2014)
30. Abdullah, A.A., Mukmin, M.N., Samad, Z.A.: Application of project management methods in the construction of bungalow house project: a case study in Kuala Terengganu, Malaysia. Int. J. Econ. Manag. Sci. **1**(2), 42–58 (2011)

Cost Overrun Analysis in Road Projects: Insights from ADB's Funded Projects

Iman Youssefi[✉] 🆔 and Tolga Celik 🆔

Civil Engineering Department, Eastern Mediterranean University, Famagusta, Northern Cyprus, Turkey

{iman.youssefi,tolga.celik}@emu.edu.tr

Abstract. This study aims at investigating cost overruns in road construction, rehabilitation, and/or improvement projects that are financed partially or entirely by the Asian Development Bank (ADB). A dataset comprising 70 completed road projects that experienced cost overrun in the course of the year 1990 to 2015 is generated using their project completion reports. The dataset was developed using a variety of project characteristics including starting date of the project, completion report date, country, operation type, type of road access provision, length of the road, total project delay, total project cost overrun, civil work-related cost overrun, cost overrun causes related to civil works. Furthermore, different statistical analyses including descriptive analysis, frequency analysis, and cross-tabulation analysis are first performed to describe the dataset while other inferential analyses such as deferential and correlational hypothesis testing aimed at exploring the differences and relationships between various project characteristics and cost overrun. The results from hypothesis testing revealed that there are meaningful differences among different project operation and road access provision types. Focusing on the examination of the causes and consequences of the cost overruns in road construction projects funded by ADB, the results of this study could be an indication of enhancing project planning, project monitoring, improved risk response plan, and identification of the project characteristics that could assist prevention of the cost overruns. Eventually, the outcomes provide valuable insights for project managers, policymakers, and other stakeholders involved in the road construction industry.

Keywords: Cost Overrun · Descriptive Analysis · Hypothesis Testing

1 Introduction

The construction industry heavily relies on the transportation sector, which contributes significantly to a country's gross domestic product (GDP) [1, 2]. Road networks play a crucial role in economic and social development, connecting construction projects and important facilities such as ports, airports, and factories [3, 4]. The efficiency of road network construction is essential for cost savings and sustainable GDP growth [5].

Cost overruns, which refer to the amount by which actual expenditures exceed the planned cost, remain a major issue in construction projects and significantly impact

project success rates [6]. Road projects, due to their high investment, large-scale nature, long duration, and specific site conditions, are exposed to higher risks than traditional construction projects [6]. Factors such as project length, size, ownership, unexpected soil conditions, weather events, changes in scope and design, and funding dependencies can contribute to cost overruns in road projects [7–10]. Identifying and managing these risks is a critical aspect of the risk management process in construction projects (Cooper et al., 2005). However, previous studies on cost overruns in road projects have limitations. Many of these studies rely on biased questionnaires to collect data and focus on general causes of cost overruns throughout the project lifecycle. Additionally, these studies are often limited to specific regions, making their findings less applicable to large-scale projects worldwide. To address these gaps, this study focuses on large-scale road projects partially or fully funded by ADB that have experienced cost overruns. The study aims to identify cost overrun causes directly associated with road project civil works and their relation to project characteristics. The findings of this study can contribute to a better understanding of cost overrun causes in mega road projects, inform risk mitigation strategies, and assist policymakers and funding agencies in resource allocation. Furthermore, the study can serve as a benchmark for future research and the development of more accurate cost estimation models for road projects.

2   Literature Review

Infrastructure projects, particularly road projects, are considered complex and precarious due to their multifaceted impact on a country's economy and quality of life [11]. The demand for infrastructure projects, including roads, has significantly increased [12]. Global investment in infrastructure construction and maintenance accounted for an average of 1.1% of countries' GDP in 2020, with China having the highest share at 5.8% and Portugal the lowest at 0.17% [13]. Among 33 OECD countries, road project investments in 2021 averaged 24.77 billion Euros, with China having the highest investment at 626.83 billion Euros and Israel the lowest at 104.31 billion Euros [14]. Road projects face numerous challenges, such as design changes, financial instability, unpredictable weather and soil conditions, labors and material shortages, all of which can have cost implications and pose challenges for accurate cost prediction [15, 16]. Given the substantial investment involved, the failure of infrastructure projects can have severe economic consequences [17]. A study examining cost overruns in large-scale infrastructure projects across 20 nations and 5 continents found that cost overruns ranged from 20.4% to 44.7%, with 90% of projects experiencing cost overruns worldwide [18]. Other examples that investigated the average cost overrun using real-case road projects namely were included, [19] conducted a study in the USA, investigating 2,668 road projects, and found an average cost overrun of 9.0%. [20] examined 620 road projects in Norway, with an average cost overrun of 8%. [21] focused on Australia, studying 49 road projects and reporting an average cost overrun of 13.55%. Finally, [22] conducted a study focusing on Germany by examining 20 road projects worldwide, and reported an average cost overrun of 30%.

Altogether, these findings contribute to the understanding of cost overruns in road projects globally and highlight that road projects are prone to cost overruns, and the impact of these overruns can have severe negative consequences on society and the economy. Therefore, accurate cost estimation and cost management throughout the project's

lifecycle, along with a well-developed risk response plan, are crucial for project success. Several studies have investigated the identification of critical cost overrun causes in road projects through extensive literature reviews. However, variations in data collection methodologies and analysis techniques contribute to disparities among these studies. The primary data collection approaches can be categorized as either survey administration or real-case scenario investigation. Studies utilizing questionnaire administration follow a similar procedure, involving the identification of potential causes through literature reviews, interviews, or case studies, and designing and conducting surveys based on these identified causes and eventually performing analysis on collected data for further interpretation. For example in a recent study [10] conducted a survey in Oman, investigating 18 causes of cost overrun using the Relative Importance Index (RII). The top three causes identified were delay in payment, incomplete design at the time of tender, and design errors. Another study by [9] investigated cost overruns in India, through the administration of a questionnaire developed by 30 causes of cost overrun using the average index analysis. The top three causes reported were inadequate planning, frequent design changes, and financial difficulties faced by the client.

Among all the studies that were performed by conducting surveys different analysis methods such as the RII, weighted average index, risk matrix, severity, frequency, and importance indices were utilized for analysis purposes. However, it is worth mentioning that while a questionnaire is a commonly used approach, it could introduce bias in the data collection process. As [23] stated that biases can occur during questionnaire design and administration, potentially leading to inaccurate data and affecting research results negatively. In addition to survey administration, another approach toward cost overrun analysis is to collect data on the causes of cost overruns in road projects through the investigation of real case scenarios. These studies also differ in terms of their evaluation approach and the specific regions they focus on. For instance, [24] conducted a study in Ethiopia, analyzing 10 projects using frequency analysis. The primary causes of cost overruns were found to be financial problems, improper planning, and land acquisition. Also, [25] conducted a worldwide study using data envelop analysis and examined 63 projects. The analysis identified fluctuation and escalation in prices, changes in exchange rates, and underestimated or inaccurate appraisals as the key causes of cost overruns. Apart from these two research types, there are some exceptions in terms of data collection and analysis approaches. For instance, a study by [26] in Nigeria utilized a semi-structured interview approach with clients, contractors, and consultants as the data collection method. The study employed inductive thematic analysis and saliency analysis and identified delays in work progress, political instability, and adverse weather as key drivers of cost overruns. Similarly, in a study conducted in Turkey by [27], a focus group was used for data collection. The researchers employed the Fuzzy Analytic Hierarchy Process (FAHP) and identified occupational accidents, integration between design and construction phases, and excessive design variations as the most influential causes of cost overruns in road projects in Turkey.

3 Methodology

This study utilized a qualitative research design, which involves examining the subject matter in a natural and interpretive manner. This entails observing the subject matter within its authentic environment and trying to comprehend the patterns and behaviors associated with it. A descriptive and statistical analysis is performed on the archival data retrieved from ADB projects' completion reports. The acquired information from completion reports was further analyzed using descriptive analysis such as frequency analysis, cross-tabulation analysis accompanied with chi-square test, and descriptive statistics. Among all the possible combinations of variables, those with a P-value less than 0.05 were selected for cross-tabulation analysis. Furthermore, statistical tests including differential and associational hypothesis testing utilized, and finally, the outcomes were interpreted. All the analyses in this study were performed using IBM Statistics version 26 software.

4 Results and Discussions

4.1 Data Collection Approach

Through an extensive search in the ADB document archive from the year 2000 to 2021, 343 available completion reports related to road and transportation projects were identified. Among these 343 projects, 205 of them were identified to be directly associated with road operations such as construction, rehabilitation, improvement, reconstruction, or maintenance, and subsequently 138 projects were discarded. Hence, from the total of 205 retrieved projects 70 of them (approximately 34.14%) were subjected to cost overrun. The starting date of these projects fell within the year 1990 to 2015. From the completion reports, for those projects that were subjected to cost overrun, the projects' specifications including length of the road, road accessibility class, operation type, country, project estimated and actual duration of the project, total estimated and actual cost of the project, civil work estimated and the actual cost of the project and the cost overrun causes related to civil works were identified. Accordingly, using the aforementioned information a dataset has been developed.

4.2   Cost Overrun Causes

From the completion reports 18 causes of the cost overrun have been identified for civil work in road projects. Table 1 presented the description of civil work cost overrun causes.

Table 1. Classification of the cost overrun causes

Cause ID	Cause Descriptions
C1	Unpredicted cost of police forces to maintain law
C2	Unforeseen security incidents
C3	Unexpected costs related to unforeseen adverse weather conditions
C4	Unexpected costs related to the unforeseen adverse geological condition
C5	Underestimation of civil works costs in appraisal
C6	Scarcity of materials
C7	Price escalation for material, labor, and/or equipment
C8	Governmental disputes during the implementation phase
C9	Fluctuation of exchange rate
C10	Floating of bids based on only conceptual designs
C11	Design change in civil work led to additional and/or unexpected civil work quantity
C12	Delay in the project implementation phase
C13	Contract violation by sub-contractors
C14	Change in project scope led to additional and/or unexpected civil work quantity
C15	Change in governmental rules and regulation
C16	Change in contracts by contractors
C17	Lack of contractors' experience
C18	High bidding price

4.3   Project and Road Types

This study identified four major types of operations among 70 road projects including construction, improvement, rehabilitation, and maintenance. The roads in current research are also classified based on their accessibility provision standpoint into three groups including high accessibility including expressways and highways, medium accessibility including national, regional, provincial, and primary roads and lastly low accessibility provision roads such as county, inter-county, secondary, rural, trunk, feeder, ring, and core roads.

4.4 Descriptive Statistics

Table 2 presents descriptive statistics for key variables related to a project, including the total length of the road, estimated and actual durations, delays, estimated and actual total costs, total cost overruns, and civil work costs. The project's length ranges from 32.90 km to 3784.20 km, with a mean of 575.79 km. Estimated duration ranges from 24.00 to 114.00 months, and actual duration from 29.00 to 192.00 months, with means of 54.86 and 79.39 months, respectively. Delays range from 44 months of early project completion to 120.00 months of delay, with an average of 24.54 months. Estimated total cost ranges from 12.50 to 1753.00 million dollars, actual cost from 13.31 to 1998.20 million dollars, with average overruns of 77.02 million dollars. Civil work cost estimates range from 4.93 to 1412.90 million dollars, and actual costs from 6.29 to 1791.53 million dollars, with average overruns of 85.93 million dollars. These statistics provide an overview of the project's length, duration, delays, and cost performance.

Table 2. Descriptive statics results

Variables	Range	Minimum	Maximum	Mean	Std. Deviation
Total Length (Km)	3751.30	32.90	3784.20	575.79	608.21
Estimated duration (Month)	90.00	24.00	114.00	54.86	13.90
Actual duration (Month)	163.00	29.00	192.00	79.39	24.70
Delay (Month)	164.00	-44.00	120.00	24.54	23.31
Total Estimated Cost (Million $)	1740.50	12.50	1753.00	340.64	385.37
Total Actual Cost (Million $)	1984.89	13.31	1998.20	417.66	474.97
Total Cost Overrun (Million $)	570.83	0.17	571.00	77.02	122.18
Civil work estimated cost (Million $)	1407.97	4.93	1412.90	246.57	287.53
Civil work actual cost (Million $)	1785.24	6.29	1791.53	332.50	376.30
Civil work cost overrun (Million $)	418.01	1.19	419.20	85.93	107.40

4.5 Frequency Analysis

A set of frequency analyses has been performed. Table 3 presented the results from frequency analysis of the countries in which the projects have taken place. The results indicated these projects were taken place in 27 different countries. Among them, China

Table 3. Frequency analysis of the countries

Country	Frequency	Relative frequency (%)	Cumulative relative frequency (%)
China	23	32.9	32.9
India	6	8.6	41.4
Sri Lanka	6	8.6	50.0
Kyrgyzstan	3	4.3	54.3
Afghanistan	2	2.9	57.1
Bangladesh	2	2.9	60.0
Bhutan	2	2.9	62.9
Cambodia	2	2.9	65.7
Indonesia	2	2.9	68.6
Kazakhstan	2	2.9	71.4
Laos	2	2.9	74.3
Solomon Islands	2	2.9	77.1
Viet Nam	2	2.9	80.0
Armenia	1	1.4	81.4
Azerbaijan	1	1.4	82.9
Bhutan	1	1.4	84.3
Fiji	1	1.4	85.7
Kiribati	1	1.4	87.1
Mongolia	1	1.4	88.6
Pakistan	1	1.4	90.0
Papua New Guinea	1	1.4	91.4
Philippines	1	1.4	92.9
Tajikistan	1	1.4	94.3
Timor-Leste	1	1.4	95.7
Tonga	1	1.4	97.1
Uzbekistan	1	1.4	98.6
Vanuatu	1	1.4	100.0
Total	70	100.0	

hosted the highest number of projects with 23 projects equivalent to approximately 33% of total projects with cost overrun.

Frequency analysis of road accessibility provision and operation type (Tables 4–5) revealed that 38.89% of the projects that were subjected to cost overrun were from the

low accessibility class while the dominant type of operation was road improvement (51.85%).

Table 4. Frequency analysis of the road accessibility provision

Accessibility type	Frequency	Relative frequency (%)	Cumulative relative frequency (%)
Low accessibility	42	38.89	38.89
Medium accessibility	30	27.78	66.67
High accessibility	36	33.33	100
Total	108	100	

Table 5. Frequency analysis of the operation types

Operation type	Frequency	Relative frequency (%)	Cumulative relative frequency (%)
Construction	27	25.00	25.00
Improvement	56	51.85	76.85
Maintenance	5	4.63	81.48
Rehabilitation	20	18.52	100
Total	108	100	

Table 6 provided the distribution of investment sizes for projects, which are classified into four categories based on their investment size: small investments (less than $82.5 million), medium investments (between $82.5 million and $264 million), large investments (between $264 million and $744 million), and very large investments (over $744 million).

Table 6. Frequency analysis of the investment size

Investment size	Frequency	Relative frequency (%)	Cumulative relative frequency (%)
Small	21	30.0	30.0
Medium	19	27.1	57.1
Large	14	20.0	77.1
Very large	16	22.9	100.0
Total	70	100.0	

According to the findings, the majority of projects (around 30%) had small investments of less than $82.5 million, whereas large investment projects accounted for the

smallest share (20%) of the total projects. Since the major focus of this study is on cost overrun causes of the projects' civil work, therefore, following Tables 7–8 presented the frequency analysis of the cost overrun in these projects. For both the total and civil works' cost overrun four different categories are defined where <5% cost overrun is considered as minor, between 5% to 10% as moderate, 10% to 15% as high, 15% to 20% as very high, and finally above 20% considered to have an extreme cost overrun.

Table 7. Frequency analysis of the civil works cost overruns

Civil work cost overrun	Frequency	Relative frequency (%)	Cumulative relative frequency (%)
Minor	16	22.86	22.86
Moderate	13	18.57	41.43
High	8	11.43	52.86
Very High	3	4.29	57.15
Extreme	30	42.86	100
Total	70	100	

Table 7 showed that 42.86% of the projects experienced cost overruns exceeding 20% of the total project cost, while only 4.29% of the projects had extremely high-cost overruns. However, when considering cost overruns specifically for civil works, the majority of projects (64%) had cost overruns that exceeded the maximum allowable threshold, with only 7% of the projects having cost overruns below 5% (Table 8).

Table 8. Frequency analysis of the total cost overruns

Total cost overrun	Frequency	Relative frequency (%)	Cumulative relative frequency (%)
Minor	5	7	7
Moderate	3	4	11
High	8	11	23
Very High	9	13	36
Extreme	45	64	100
Total	70	100	

The outcome of the frequency analysis for cost overrun causes in civil works revealed that price escalation for material, labor, and/or equipment (C7), a design change in civil work led to additional and/or unexpected civil work quantity(C11), Fluctuation of the exchange rate (C9), delay in the project implementation phase (C12), and unexpected cost related to the unforeseen adverse geological condition (C4) were existing in 80% of the project as responsible cost overrun causes (Table 9).

Table 9. Frequency analysis of the cost overrun causes

Cost overrun causes	Frequency	Relative frequency (%)	Cumulative relative frequency (%)
C7	39	25.49	25.49
C11	35	22.88	48.37
C9	21	13.73	62.09
C12	14	9.15	71.24
C4	14	9.15	80.39
C5	11	7.19	87.58
C14	5	3.27	90.85
C16	3	1.96	92.81
C13	2	1.31	94.12
C1	1	0.65	94.77
C10	1	0.65	95.42
C15	1	0.65	96.08
C17	1	0.65	96.73
C18	1	0.65	97.39
C2	1	0.65	98.04
C3	1	0.65	98.69
C6	1	0.65	99.35
C8	1	0.65	100.00
Total	153	100	

4.6 Cross-Tabulation Analysis

In this section, a comprehensive analysis was conducted to explore the relationship between total and civil work cost overruns and various characteristics of the projects. Cross-tabulation was performed to investigate the associations between these variables. Additionally, a chi-square analysis was employed to determine the statistical significance of these associations. A significance level of 0.05 was chosen for hypothesis testing. If the obtained p-value from the chi-square test is less than 0.05, it indicates a failure to reject the null hypothesis (H_0) that assumes independence between the variables. Consequently, there is not enough evidence to support a significant relationship between the two variables. Accordingly, the subsequent results present the cross-tabulation analysis of these related variables across all possible combinations.

The results from the chi-square test revealed that the total cost overrun has a significant association with investment size (P-value = 0.000), road accessibility (P-value = 0.016), delay (P-value = 0.000), and civil work cost overrun (0.000). For the aforementioned associations the cross-tabulation analysis provided in Tables 10, 11, 12 and 13. On the other hand, apart from the relationship between total and civil work cost overrun, as presented in Table 14 civil work cost overrun only demonstrated a significant association

with the investment size of the project (P-value = 0.000). Regarding the cost overrun causes, the results of the chi-square test indicate no significant association between cost overrun causes and other characteristics of the projects in the dataset.

Table 10. Cross-tabulation analysis between the investment size and total cost overrun

		Investment size				
		Small	Medium	Large	Very Large	Total
Total cost overrun	Minor	6	5	4	1	16
	Moderate	6	4	1	2	13
	High	2	2	2	2	8
	Very High	1	0	1	1	3
	Extreme	6	8	6	10	30
	Total	21	19	14	16	70

Table 11. Cross-tabulation analysis between the road accessibility provision and the total cost overrun

		Road Accessibility			
		Low	Moderate	High	Total
Total cost overrun	Minor	10	10	5	25
	Moderate	2	9	6	17
	High	3	1	7	11
	Very High	3	0	2	5
	Extreme	24	10	16	50
	Total	42	30	36	108

4.7 Hypothesis Testing

In the final stage of the analysis, both differential and associational hypothesis testing were conducted. The main objectives firstly were to assess the differences in total and civil work cost overruns among different groups based on operation type, accessibility provision, and investment size. Additionally, the aim was to examine the correlation between the percentage of total cost overrun, civil work cost overrun, and project delays. Prior to hypothesis testing to select the required test for the aforementioned purposes for each project characteristic a normality test has been performed to determine whether or not the normality assumption is violated. The results from both the Kolmogorov-Smirnov test and the Shapiro-Wilk normality test unitedly indicated that the null hypothesis of the normality test (H_0 = The data are normally distributed) for all the variables are violated

Table 12. Cross-tabulation analysis between the delay and the total cost overrun

| | | Delay | | | | | | |
		On-Time	Minor	Moderate	High	Very High	Extreme	Total
Total cost overrun	Minor	3	0	5	0	0	17	25
	Moderate	0	2	1	0	2	12	17
	High	0	0	0	0	1	10	11
	Very High	0	1	2	2	0	0	5
	Extreme	7	1	0	2	2	38	50
	Total	10	4	8	4	5	77	108

Table 13. Cross-tabulation analysis between the civil work cost overrun and the total cost overrun

| | | Civil work cost overrun | | | | | |
		Minor	Moderate	High	Very High	Extreme	Total
Total cost overrun	Minor	5	3	9	8	0	25
	Moderate	1	1	0	3	12	17
	High	0	0	1	1	9	11
	Very High	0	0	0	2	3	5
	Extreme	1	0	1	0	48	50
	Total	7	4	11	14	72	108

Table 14. Cross-tabulation analysis between the civil work cost overrun and the investment size

| | | Investment size | | | | |
		Small	Medium	Large	Very Large	Total
Civil work cost overrun	Minor	0	2	2	1	5
	Moderate	0	3	0	0	3
	High	4	2	2	0	8
	Very High	4	1	2	2	9
	Extreme	13	11	8	13	45
	Total	21	19	14	16	70

since the P-value was 0.000 and therefore the required tests needed to be selected from non-parametric test's group. To perform differential hypothesis testing for the percentage of the total cost overrun causes and civil work cost overruns across different groups

among investment size, road accessibility provision, and operation type, the Kruskal-Wallis H test is employed. The null hypothesis for the Kruskal-Wallis H test indicated that the distribution of the percentage of the total and civil work cost overrun across all the groups of investment size, accessibility provision, and operation type is the same. Hence, if the acquired p-value is larger than 0.05 we fail to reject the null hypothesis.

The results from the Kruskal-Wallis H test revealed that the distribution of both the percentage of total cost overrun and the percentage of civil work cost overrun across all the groups is the same. It is because all the obtained P-values are larger than 0.05, Therefore, there is no significant difference between the percentage of total cost overrun and percentage of civil work cost overrun among all the existing groups of investment size, operation types, and accessibility provision types (Table 15).

Table 15. Differential hypothesis testing results

	Test statistics	Degree of freedom	P-value
Total cost overrun (percentage)			
Investment size types	6.309	3	0.097
Operation types	1.294	3	0.729
Accessibility provision types	3.627	2	0.163
Civil work cost overrun (percentage)			
Investment types	3.038	3	0.386
Operation types	2.788	3	0.425
Accessibility provision types	0.634	2	0.729

As far as the associational hypothesis testing is concerned due to the violation of the normality assumption Spearman rank-order correlation was adopted to statistically test the association between the percentage of total cost overrun, civil work cost overrun, and the delay among all the projects. The results indicated (Table 16) that as expected there is a positive significant correlation between the percentage of total cost overrun and civil work cost overrun. However, no significant correlation between either type of cost overrun and the delay in the projects is not detected.

Table 16. Associational hypothesis testing results

		Total cost overrun (%)	Civil work cost overrun (%)	Delay (%)
Total cost overrun (%)	Spearman rho	1.000	0.698**	0.116
	Sig. (2-tailed)		0.000	0.340
Civil work cost overrun (%)	Spearman rho	0.698**	1.000	0.055
	Sig. (2-tailed)	0.000		0.653
Delay (%)	Spearman rho	0.055	0.116	1.000
	Sig. (2-tailed)	0.653	0.340	

5   Conclusion

This study aimed to perform different statistical analyses on the causes and characteristics of cost overruns in road and transportation projects based on completion reports from the Asian Development Bank (ADB) document archive. A dataset of 70 road projects with cost overruns was developed, and various analyses were conducted to examine the patterns and relationships within the dataset, and the following conclusions were withdrawn from the analyses.

- Approximately 34.14% of the total road projects funded by ADB experienced cost overruns.
- The results from frequency analysis revealed that price escalation, design changes, exchange rate fluctuations, project delays, and adverse geological conditions were identified as the main causes of the cost overrun that more frequently occurred among others.
- Road improvement among other operation projects accounted for the majority (51.85%) of the projects with cost overruns.
- China hosted the highest number of projects with cost overruns (32.9% of the total).
- Projects with low accessibility provisions had the highest frequency (38.89%) of cost overruns.
- Over 42% of the projects experienced cost overruns exceeding 20% of the total project cost.
- The results revealed that there were significant associations between the total cost overrun and investment size, road accessibility, delay, and civil work cost overrun. While the total cost overrun demonstrated association with aforementioned projects' characteristics, except for the investment size there was not enough evidence regarding the relationship between other projects' characteristics and civil work cost overrun.

In conclusion, this study sheds light on the causes and characteristics of cost overrun in road projects and provides valuable insights for project planning and management.

The identified causes can help project stakeholders anticipate and address potential cost overrun risks. The findings emphasize the importance of considering factors such as price escalation, design changes, exchange rate fluctuations, and geological conditions during project planning and implementation. Furthermore, the analysis of project characteristics and their associations with cost overruns highlights the need for effective monitoring and control mechanisms, particularly for projects with low accessibility and large investments. By understanding the factors contributing to cost overruns and considering them in project management practices, stakeholders can improve the cost performance of road projects and enhance their overall success.

References

1. Berk, N., Biçen, S.: Causality between the construction sector and GDP growth in emerging countries: the case of Turkey. Athens J. Mediterr. Stud. **4**(1), 19–36 (2017). https://doi.org/10.30958/ajms.4-1-2

2. Kebede, S.D., Tiewei, Z.: Public work contract laws on project delivery systems and their nexus with project efficiency: evidence from Ethiopia. Heliyon **7**(3), e06462 (2021). https://doi.org/10.1016/j.heliyon.2021.e06462

3. Klarenberg, G., Muñoz-Carpena, R., Campo-Bescós, M.A., Perz, S.G.: Highway paving in the southwestern Amazon alters long-term trends and drivers of regional vegetation dynamics. Heliyon **4**(8), e00721 (2018). https://doi.org/10.1016/j.heliyon.2018.e00721

4. Shi, G., Shan, J., Ding, L., Ye, P., Li, Y., Jiang, N.: Urban road network expansion and its driving variables: a case study of Nanjing city. Int. J. Environ. Res. Public Health **16**(13), 1–16 (2019). https://doi.org/10.3390/ijerph16132318

5. Akal, A.Y.: Mapping the causes of time, cost overruns and quality shortfall in Egyptian Public Highway Projects. Eur. Bus. Manag. **3**(6), 120 (2017). https://doi.org/10.11648/j.ebm.20170306.14

6. Ammar, T., Abdel-Monem, M., El-Dash, K.: Risk factors causing cost overruns in road networks. Ain Shams Eng. J. **13**(5), 101720 (2022). https://doi.org/10.1016/j.asej.2022.101720

7. Flyvbjerg, B., Skamris Holm, M.K., Buhl, S.L.: What causes cost overrun in transport infrastructure projects? Transp. Rev. **24**(1), 3–18 (2004). https://doi.org/10.1080/0144164032000080494a

8. Sohu, S., Abdullah, A.H., Nagapan, S., Jhatial, A.A., Ullah, K., Bhatti, I.A.: Significant mitigation measures for critical factors of cost overrun in highway projects of Pakistan. Eng. Technol. Appl. Sci. Res. **8**(2), 2770–2774 (2018). https://doi.org/10.48084/etasr.1916

9. Sohu, S., Abdullah, A.H., Nagapan, S., Rind, T.A., Jhatial, A.A.: Controlling measures for cost overrun causes in highway projects of Sindh Province. Eng. Technol. Appl. Sci. Res. **9**(3), 4276–4280 (2019). https://doi.org/10.48084/etasr.2749

10. Al Adawi, O.S., Yahia, H.: Causes of costs overrun in road construction project in Oman. J. Student Res. (2021). https://doi.org/10.47611/jsr.v10i3.1295

11. Mills, A.: A systematic approach to risk management for construction. Struct. Surv. **19**(5), 245–252 (2001). https://doi.org/10.1108/02630800110412615

12. Al Hosani, I.I.A., Dweiri, F.T., Ojiako, U.: A study of cost overruns in complex multi-stakeholder road projects in the United Arab Emirates. Int. J. Syst. Assur. Eng. Manag. **11**(6), 1250–1259 (2020). https://doi.org/10.1007/s13198-020-00979-8

13. Statista: Global investments on the construction and maintenance of infrastructure as share of GDP in 2020 (2023). https://www.statista.com/statistics/566787/average-yearly-expenditure-on-economic-infrastructure-as-percent-of-gdp-worldwide-by-country/

14. OECD: Infrastructure investment. OECD data (2023). https://data.oecd.org/transport/infrastructure-investment.htm

15. Rehak, D., Senovsky, P., Slivkova, S.: Resilience of critical infrastructure elements and its main factors. System **6**(2), 21 (2018). https://doi.org/10.3390/systems6020021

16. Song, Y., et al.: Segment-based spatial analysis for assessing road infrastructure performance using monitoring observations and remote sensing data. Remote Sens. **10**(11), 1696 (2018). https://doi.org/10.3390/rs10111696

17. Lee, E., Alleman, D.: Ensuring efficient incentive and disincentive values for highway construction projects: a systematic approach balancing road user, agency and contractor acceleration costs and savings. Sustainability **10**(3), 701 (2018). https://doi.org/10.3390/su10030701

18. Flyvbjerg, B., Skamris, M.K., Buhl, S.L.: Transport reviews: a transnational how common and how large are cost overruns in transport infrastructure projects? Transp. Rev. A Transnatl. Transdiscipl. J. **23**(1), 71–88 (2003). https://doi.org/10.1080/01441640309904

19. Bordat, C., McCullouch, B.G., Labi, S., Sinha, K.: An analysis of cost overruns and time delays of INDOT projects (2004). http://docs.lib.purdue.edu/jtrp/11

20. Odeck, J.: Cost overruns in road construction - what are their sizesand determinants? Transp. Policy **11**(1), 43–53 (2004). https://doi.org/10.1016/S0967-070X(03)00017-9

21. Love, P.E.D., Sing, C.-P., Carey, B., Kim, J.T.: Estimating construction contingency: accommodating the potential for cost overruns in road construction projects. J. Infrastruct. Syst. **21**(2), 1–10 (2015). https://doi.org/10.1061/(asce)is.1943-555x.0000221

22. Kostka, G., Fiedler, J.: Large Infrastructure Projects in Germany: Between Ambition and Realities, pp. 1–206. Palgrave Macmillan, Cham (2016). https://doi.org/10.1007/978-3-319-29233-5

23. Choi, B.C.K., Pak, A.W.P.: A catalog of biases in questionnaires. Prev. Chronic Dis. **2**(1), 1–13 (2005)

24. Durdyev, S., et al.: Factors influencing time and cost overruns in road construction projects: Addis Ababa, Ethiopian scenario: review paper. Eng. Constr. Archit. Manag. **2**(2), 393–406 (2017). https://doi.org/10.1108/ECAM-02-2020-0137

25. Ahbab, C., Daneshvar, S., Çelik, T.: Cost and time management efficiency assessment for large road projects using data envelopment analysis. Tek Dergi/Technical J. Turkish Chamb. Civ. Eng. **30**(2), 8937–8959 (2019). https://doi.org/10.18400/tekderg.375664

26. Mahmud, A.T., Ogunlana, S.O., Hong, W.T.: Key driving factors of cost overrun in highway infrastructure projects in Nigeria: a context-based perspective. J. Eng. Des. Technol. **19**(6), 1530–1555 (2021). https://doi.org/10.1108/JEDT-05-2020-0171

27. Aladağ, H., Işık, Z.: Design and construction risks in BOT type mega transportation projects. Eng. Constr. Archit. Manag. **26**(10), 2223–2242 (2019). https://doi.org/10.1108/ECAM-08-2018-0351

Geotechnics

Dynamic Response of Shallow Mat Footings on Coir Geotextile Reinforced Sand Under Cyclic Loading

Mohamad Hanafi[1] and Abdullah Ekinci[2(✉)]

[1] Faculty of Engineering, Department of Civil Engineering, Aalto University, Espoo, Finland
Mohamad.hanafi@aalto.fi

[2] Civil Engineering Program, Middle East Technical University, via Mersin 10, Northern Cyprus Campus, Kalkanli, Guzelyurt, North Cyprus, Turkey
ekincia@metu.edu.tr

Abstract. The use of shaking table tests to investigate the dynamic behavior of soil-structure interaction dates back several decades. In this study the response of a laboratory scale mat foundation constructed on well-graded fine sand under cyclic loading conditions was examined. The study also sought to evaluate the impact of geotextile reinforcement on the dynamic behavior of the mat foundation. Six tests were conducted under both unsaturated and saturated conditions, with and without geotextile reinforcement. The results of the tests revealed that incorporating geotextile into both unsaturated and saturated sand resulted in a decrease in the acceleration of the model foundation. These findings highlight the potential of geotextile reinforcement as an effective means of improving the performance of mat foundations on fine-grained soils subjected to cyclic loading. The results may have implications for the design and construction of mat foundations in real-world applications, particularly in earthquake-prone regions where cyclic loading is a major concern.

Keywords: Coir · geotextile · cyclic load · shake table

1 Introduction

Evaluating seismic hazards is an important aspect of geotechnical engineering, as these can induce plenty of ground hazards. In clean sand deposits, large settlements can be induced by the action of the dynamic loading applied by the earthquake, especially when liquefaction is triggered [1] due to the increase in the pore water pressure between sand grains. These settlements can have great damaging effects on structures such as foundations or utilities [2]. Consequently, many studies have been conducted on the seismically induced settlement of both saturated and unsaturated sand deposits, and researchers were able to correlate this settlement to other parameters such as the SPT-N value or the relative density [1]. However, most of these studies were conducted in the lab on small specimens. While the lab experiments can produce relatively reliable data, it does not take into account some important factors such as the on-site effective strength

or the boundary conditions [3]. For that reason, shaking table test, where large soil specimens can be placed and earthquake loading scenarios can be reproduced, has been adopted to better simulate the field conditions under more realistic testing arrangements [4, 5]. Since then, the shaking table test has been used extensively to evaluate the various seismic hazards on soil stratum [6], and despite the extensive studies conducted in this field, many uncertainties remain around the soil behaviour under dynamic loading [7].

Among the many available ground improvement techniques, reinforcing the soil with geotextiles is considered one of the oldest and most effective methods to improve the soil prosperities [8]. Therefore, geotextiles have been widely used in various geotechnical engineering applications such as buildings, roads, bridges, landfills, and slopes stability [9–12]. In their study, Al-Subari et al. [13] found that reinforcing the soil with geotextiles significantly enhanced the bearing capacity of the sand and resulted in a higher interface friction when conducting direct shear test.

A common way to counteract the damaging effects of earthquake on the soil is by reinforcing the soil with geotextiles. Using geotextiles as a reinforcing material can increase both the shear strength of the soil, and its resistance to the cyclic loading, and therefore, improve the liquefaction resistance [14]. Many studies have investigated the dynamic behaviour of geotextiles-reinforced soil [15–17]. Krishnaswamy and Issac [18] studied the seismic behaviour of sands with different types of reinforcement. They reported significant improvement on the liquefaction resistance when including geosynthetics. Moreover, they found that coir resulted in an increase in the resistance when used as a natural fibre. Srilatha et al. [16] studied the seismic response unreinforced and reinforced soil slopes using shaking table tests. Authors observed that the increase in frequency results in increase in displacement of all the slopes in the unreinforced samples. However, the increase in the frequency did not have a significant effect on the reinforced samples. Authors also concluded that the reinforced slopes experience less displacement at all frequency levels. Vieira et al. [26] studied the behaviour of silica sand combined with high strength geotextile, subjected to static and cyclic loading. Authors observed increase in the stiffness during the first loading cycles and slight improvement on the shear and damping ratio. In addition, the cyclic loading did not cause a degradation of the post peak shear strength. Wang et al. [19] also studied the behaviour of geotextile-reinforced embankments during earthquake by the means of centrifuge model tests. Authors found that the geotextile significantly reduced the deformation of the embankments and prevented slide failures. In another study, Naeini and Gholampoor [20] evaluated the behaviour of geotextiles reinforced sand under cyclic loading and performed a series of cyclic triaxial tests on dry silty sand with the inclusion of the geotextiles, and found that the geotextile inclusion increased the axial modulus and decrease the cyclic ductility of the dry sand. Maheshwari et al. [17] studied the effects of geosynthetic fibres and natural coir on the liquefaction resistance of Solani sand by incorporating geogrid sheets, and reported a significant improvement on the dynamic behaviour of the sand. In another study, Bahadori et al. [21] used the shaking table to assess the effects of geosynthetics in a liquefiable soil and found that the geosynthetics effectively reduced the settlement due to their impervious characteristics.

In this study, six shaking table tests were conducted on a mat foundation model underlaid by well graded unsaturated and saturated geosynthetics-reinforced sand in

order to evaluate the effects of the geosynthetics on the liquefaction resistance. A novel testing setup have been developed to directly relate the effects of the chosen geotextiles to the dynamic behaviour of the sand.

2 Materials

2.1 Sand

This study was conducted on a standard commercial sand. The physical properties of the sand were assessed through some basic tests such as, the specific gravity test (ASTM D854-14 [22]) and sieve analysis test (ASTM D6913/D6913M-17 [23]). Those properties are shown in Fig. 1, along with its particle size distribution. The sand is classified with accordance to the Unified Soil classification System (USCS) as well-graded sand (SW). The specific gravity of the sand is 2.62, and its particles are angular in shape.

   This sand was used in two states, unsaturated and saturated. The unsaturated sand was calculated according to the desire density and comprised in the tank without the addition of water. On the other hand, in the saturated state, the sand was saturated up to 95 saturation degree (S = 95%), and the amount of water was calculated correspondingly.

Soil Properties	Value
D10 (mm)	0.13
D30 (mm)	0.39
D60 (mm)	0.85
coefficient of curvature	1.38
coefficient of uniformity	6.54
specific gravity	2.62
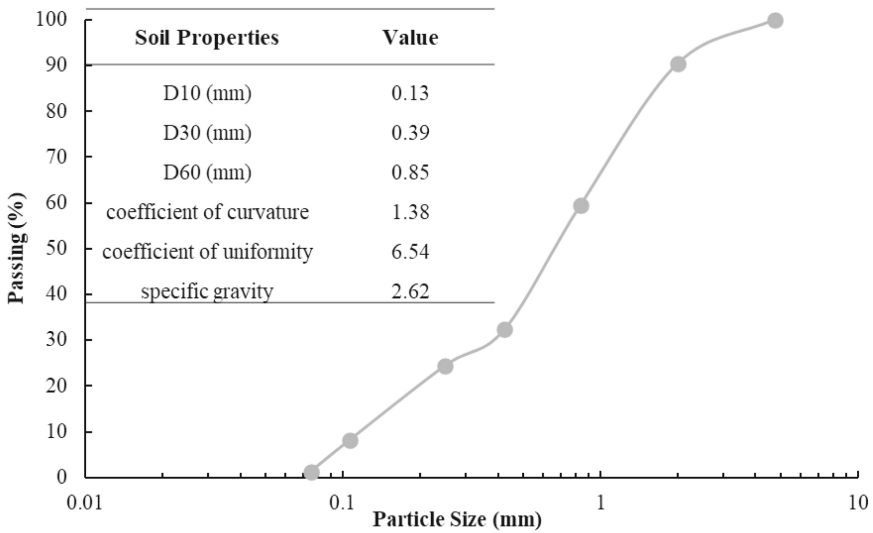
Fig. 1. Particle size distribution and physical properties of the sand

2.2 Geotextiles

Coir geotextile (shown in Fig. 2) was used as a reinforcement to the sand in order to evaluate its effect on dynamic response. For this purpose, a piece of coir of the dimensions

20 cm × 20 cm was cut and used under the foundation. Grab breaking load according to (ASTM D4632-08 [24]) was conducted on this geotextile and its tensile strength was found as 0.84 kN Geotextiles mass per unit area was also found as 237g/m^2. The coir has opening size of 0.2 mm.

Fig. 2. Coir geotextiles used as a reinforcement in the study

3   Experimental Setup

In this study, a computer controlled shaking table "Quanser Shake Table II" has been used to induce dynamic loading on a model foundation. The shaking table has the ability of producing waves with up to 2.5 g acceleration, 5 Hz frequency and 2.5 cm amplitude.

A rigid container with the dimensions of 46 cm × 46 cm, and 40 cm in height was manufactured from 1 cm of plexiglass sheets and attached on top of the shaking platform. Figure 3 shows a schematic set-up of the tank and the shaking table.

Foundation used in this model was designed from several plates of plexiglass, each plate is 10 × 10 cm, and 1 cm in thickness. An accelerometer was mounted on top of the foundation model in order to record the motions produced by the base (Fig. 4). Another accelerometer was connected to the base of the shaking table in order to compare the seismic waves produced at the base and at the top of the soil.

The sand was filled in the tank in three equal layers to a total height of 10 cm. First, the targeted dry density was calculated by spraying the sand from a constant height
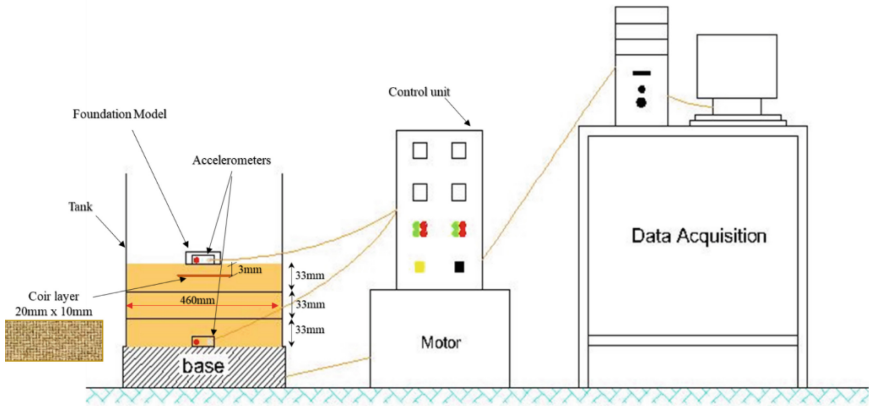
Fig. 3. Schematic diagram of the testing setup
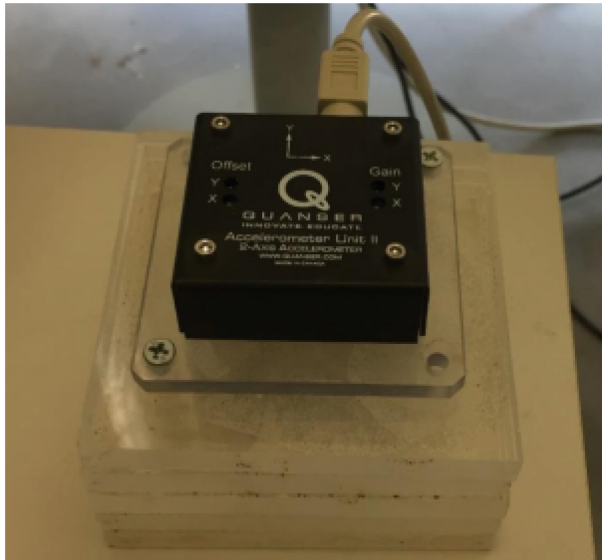
Fig. 4. The foundation Model with the accelerometer mounted on top

into a container with a known volume. In the case of the unsaturated condition (dry sand), the sand was placed into the tank without the addition of water. In the saturated condition, the saturated density to get the sand to a saturation degree of 95% (S = 95%) was calculated, and the corresponding water content was determined. The sand and water were then mixed thoroughly for each layer until a homogeneous condition is achieved. The calculated amount of the sand was directly placed in the tank without any compaction efforts. A pre-calculated amount that corresponds to 1 cm of the height of

the last layer was removed, and a coir mat, 20 cm × 20 cm was placed in the middle of the tank. The remaining sand was then used to cover the geotextile layer. After laying the sand layers, the foundation model, which is connected to an accelerometer, was placed on top of the surface.

The testing program consisted of two tests on unsaturated sand, two tests on geotextile-reinforced unsaturated sand, a test on unreinforced saturated sand, and a test on geotextile-reinforced saturated sand. As can be seen on Table 1, all of the test schemes consisted of periodic sinusoidal waves with the 1 cm amplitude and variant frequency.

Table 1. Details of tests prosperities

	sand status	geotextiles	Applied wave	Amplitude (cm)	Frequency (Hz)
Test 1	unsaturated	–	sinusoidal	1	1
Test 2	unsaturated	Coir	sinusoidal	1	1
Test 3	unsaturated	–	sinusoidal	1	2
Test 4	unsaturated	Coir	sinusoidal	1	2
Test 5	saturated	–	sinusoidal	1	2
Test 6	saturated	coir	sinusoidal	1	2

4 Results

4.1 Unsaturated Sand

Four tests have been conducted on the unsaturated sand, two without reinforcement and two with reinforcement, to observe any effects of the addition of geotextiles on the soil. Figure 5 shows the amplitude for one cycle for each of the four tests. It is clear from the figure that there is a delay in the acceleration between the table and the foundation, which is expected. It is also evident that this delay increases with increase of the frequency (Figs. 5c and 5d). The figure also shows almost identical results for the same frequencies for the reinforced and unreinforced sand.

Figure 6 shows the acceleration for one cycle as measured on the base and on the foundation surface for each of the four tests. The effects of the geotextile can be clearly seen when comparing Figs. 6a and 6b for the 1 Hz frequency. It can be seen that the acceleration curve for the foundation has been flattened in many areas as an effect of the geotextile reinforcement. Similar but less pronounced effect can be observed on Figs. 6c and 6d for the tests where 2 Hz frequency was applied. Figure 6c, shows that the foundation did not cope with the acceleration of the base, and foundation sliding is observed especially on the sharp edges of the figure where the direction of motion is changed. This behavior was not observed in the reinforced test.
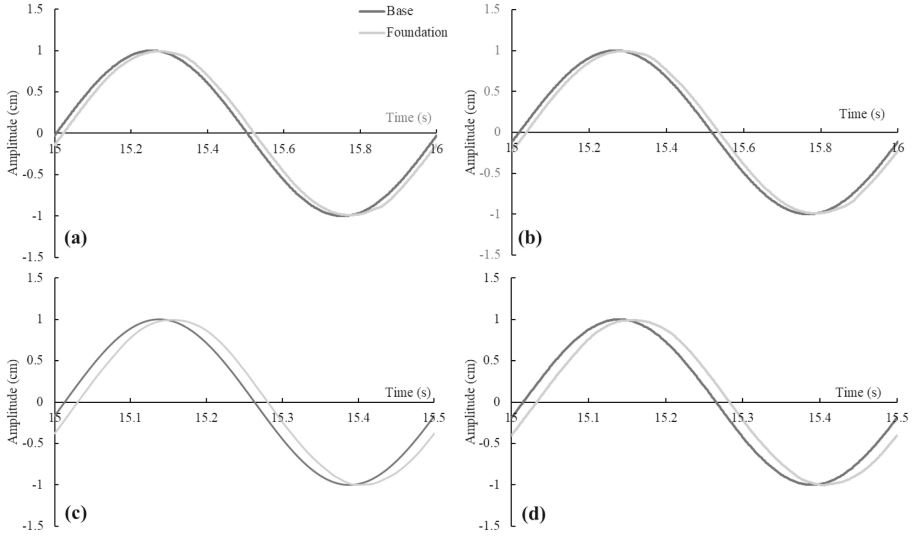
Fig. 5. The amplitude for one cycle for unsaturated sand: **a)** 1 Hz without geotextiles, **b)** 1 Hz with geotextiles, **c)** 2 Hz without geotextiles, **d)** 2 Hz with geotextiles
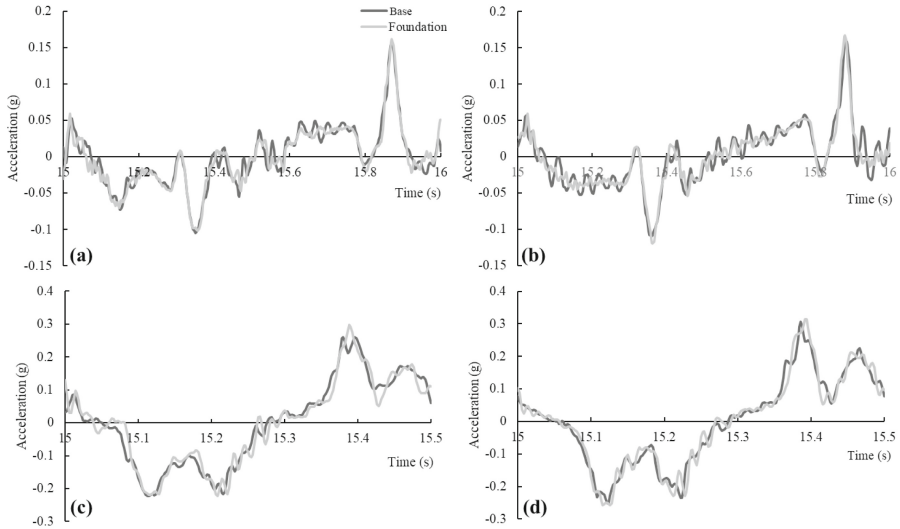
Fig. 6. The acceleration for one cycle for the unsaturated sand: **a)** 1 Hz without geotextiles, **b)** 1 Hz with geotextiles, **c)** 2 Hz without geotextiles, **d)** 2 Hz with geotextiles

4.2 Saturated Sand

In the first test, the saturated sand was subjected to 1 cm amplitude and 2 Hz frequency sinusoidal waves for 1.5 min. Figure 7 below shows one cycle of acceleration at two

different times. Figure 7a shows the cycle between 15 and 15.5 s, and Fig. 7b shows the cycle between 75 and 75.5 s. It can be seen that as the cyclic loading progresses, the sudden movements of the table lose their initial effect on the foundation. When compared to the unsaturated conditions (Fig. 6), it can be observed that the foundation exceeded the acceleration of base plate, which indicates the sliding of the foundation due to the load.
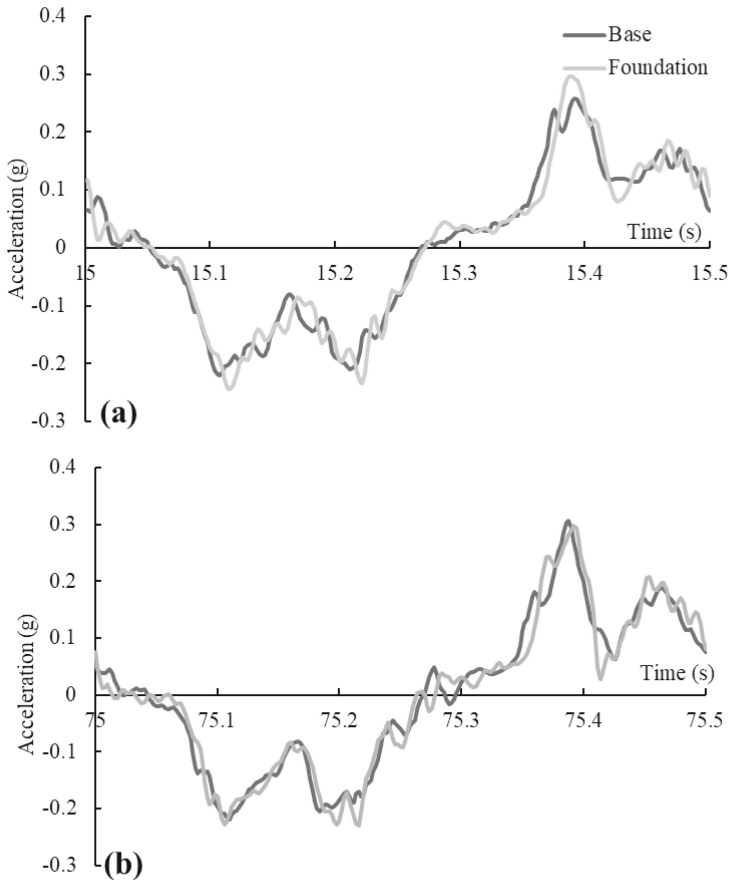
Fig. 7. One cycle acceleration for the 2 Hz test on saturated sand: **a)** the cycle 15 s–15.5 s, **b)** the cycle 75 s–75.5 s

On the other hand, Fig. 8 shows the one cycle acceleration plots for the saturated geotextile-reinforced sand at the seconds 15–15.5 and 75–75.5. It can be seen that the addition of geotextile reinforcement layer resulted in a reduction in the acceleration of the foundation when compared to the unreinforced condition. This effect is observed both at the beginning of the test (Fig. 8a) and further later on the test (Fig. 8b). Similar results

were reported from other findings on the effectiveness of geotextiles on the dynamic response of the soil [17, 25].
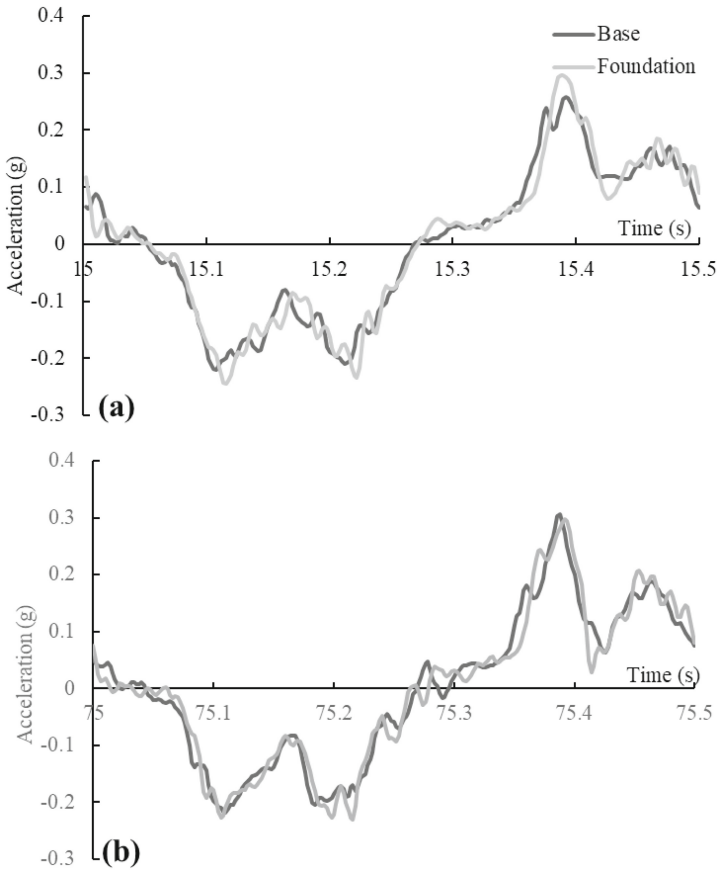
Fig. 8. One cycle acceleration for the 2 Hz test on geotextile-reinforced saturated sand: **a)** the cycle 15 s–15.5 s, **b)** the cycle 75 s–75.5 s

5 Conclusion

In this study, the dynamic behaviour of geotextile-reinforced and unreinforced fine sand was investigated using a plexiglass tank that was connected to a shaking table. A specific designed foundation model with an accelerometer mounted on top was placed on top of sand layer with and without geotextile reinforcement and tested in saturated and unsaturated condition. The study concluded the following:

- When testing the unsaturated sand, a delay in the acceleration was observed between the base and the foundation, this delay was higher when increasing the frequency.

- The inclusion of the geotextiles resulted in a softening in the acceleration response of the foundation model when compared to the unreinforced sand. This softening was less pronounced when increasing the frequency of the wave.
- As the dynamic loading progress in the saturated sample, the sudden movements of the table lose their effects on the foundation, which was extensively settle down due to the liquefaction effects.
- The effects of the dynamic loading in the reinforced saturated sample were not as prominent as the unreinforced sample, which shows the effectiveness of the coir geotextiles in resisting the damaging effect on the foundation.
- The results demonstrate that the use of geotextile can effectively reduce the liquification potential in fine sand, and softens the acceleration induced by the dynamic strength on the foundation.
- It is recommended to perform a full scale field test to allow for a more comprehensive assessment of the performance of mat foundations on fine-grained soils under cyclic loading, taking into account the variability and heterogeneity of natural soils. Additionally, field tests could provide a better understanding of the long-term durability and effectiveness of geotextile reinforcement in improving the performance of foundation systems.

References

1. Ueng, T.S., Wu, C.W., Cheng, H.W., Chen, C.H.: Settlements of saturated clean sand deposits in shaking table tests. Soil Dyn. Earthq. **30**, 50–60 (2010)
2. Hwang, J.-H., Yang, C., Chen, C.-H.: Investigations on soil liquefaction during the Chi-Chi earthquake. Soils Found. **43**, 107–122 (1994)
3. Lee, C.J., Wei, Y.C., Kuo, Y.C.: Boundary effects of a laminar container in centrifuge shaking table tests. Soil Dyn. Earthq. **34**, 37–51 (2012)
4. Van Laak, P.A., Taboada, V.M., Dobry, R., Elgamal, A.W.: Earthquake centrifuge modeling using a laminar box. In: Dynamic Geotechnical Testing II ASTM International (1994)
5. Taylor, C.A., Dar, A.R., Crewe, A.J.: Shaking table modelling of seismic geotechnical problems. In: Proceedings of the 10th European Conference on Earthquake Engineers, pp. 441–446 (1995)
6. Zayed, M., Ebeido, A., Prabhakaran, A., Kim, K., Qiu, Z., Elgamal, A.: Shake table testing: a high-resolution vertical accelerometer array for tracking shear wave velocity. Geotech. Test. J. **44**(4), 1097–1118 (2021)

7. Chiou, J.S., Huang, T.J., Chen, C.L., Chen, C.H.: Shaking table testing of two single piles of different stiffnesses subjected to liquefaction-induced lateral spreading. Eng. Geol. **281**, 105956 (2021)
8. Goodarzi, S., Shahnazari, H.: Strength enhancement of geotextile-reinforced carbonate sand. Geotext. Geomembr. **47**, 128–139 (2019)
9. Kalpakci, V., Bonab, A.T., Özkan, M.Y., Gülerce, Z.: Experimental evaluation of geomembrane/geotextile interface as base isolating system. Geosynth. Int. **25**, 1–11 (2018)
10. Kermani, B., Xiao, M., Stoffels, S.M., Qiu, T.: Reduction of subgrade fines migration into subbase of flexible pavement using geotextile. Geotext. Geomembr. **46**, 377–383 (2018)
11. King, D.J., Bouazza, A., Gniel, J.R., Rowe, R.K., Bui, H.H.: Serviceability design for geosynthetic reinforced column supported embankments. Geotext. Geomembr. **45**, 261–279 (2017)
12. Saran, R.K., Viswanadham, B.V.S.: Centrifuge model tests on the use of geosynthetic layer as an internal drain in levees. Geotext. Geomembr. **46**, 257–276 (2018)
13. Al-Subari, L., Hanafi, M., Ekinci, A.: Effect of geosynthetic reinforcement on the bearing capacity of strip footing on sandy soil. SN Appl. Sci. **2**, 1–11 (2020)
14. Liu, J., Wang, G., Kamai, T., Zhang, F., Yang, J., Shi, B.: Static liquefaction behavior of saturated fiber-reinforced sand in undrained ring-shear tests. Geotext. Geomembr. **29**, 462–471 (2011)
15. Koseki, J.: Use of geosynthetics to improve seismic performance of earth structures. Geotext. Geomembr. **34**, 51–68 (2012)
16. Srilatha, N., Madhavi Latha, G., Puttappa, C.G.: Effect of frequency on seismic response of reinforced soil slopes in shaking table tests. Geotext. Geomembr. **36**, 27–32 (2013)
17. Maheshwari, B.K., Singh, H.P., Saran, S.: Effects of reinforcement on liquefaction resistance of Solani sand. J. Geotech. Geoenviron. Eng. **138**, 831–840 (2013)
18. Krishnaswamy, N.R., Thomas Isaac, N.: Liquefaction potential of reinforced sand. Geotext. Geomembr. **13**, 23–41 (1994)
19. Wang, L., Zhang, G., Zhang, J.M.: Centrifuge model tests of geotextile-reinforced soil embankments during an earthquake. Geotext. Geomembr. **29**, 222–232 (2011)
20. Naeini, S.A., Gholampoor, N.: Cyclic behaviour of dry silty sand reinforced with a geotextile. Geotext. Geomembr. **42**, 611–619 (2014)
21. Bahadori, H., Motamedi, H., Hasheminezhad, A., Motamed, R.: Shaking table tests on shallow foundations over geocomposite and geogrid-reinforced liquefiable soils. Soil Dyn. Earthq. **128**, 105896 (2020)
22. ASTM D854-14, Standard Test Methods for Specific Gravity of Soil Solids by Water Pycnometer. ASTM International, West Conshohocken (2014). www.astm.org
23. ASTM D6913/D6913M-17, Standard Test Methods for Particle-Size Distribution (Gradation) of Soils Using Sieve Analysis. ASTM International, West Conshohocken (2017). www.astm.org
24. ASTM D4632-08, Standard Test Method for Grab Breaking Load and Elongation of Geotextiles. ASTM International, West Conshohocken (2017). www.astm.org
25. Senapati, S., Maheshwari, B.K.: Effects of geogrid on dynamic strength characteristics of solani sand. Indian Geotech. J. **42**, 287–293 (2012)
26. Vieira, C.S., Lopes, M.D.L., Caldeira, L.M.: Sand-geotextile interface characterisation through monotonic and cyclic direct shear tests. Geosynth. Int. **20**, 26–38 (2013)

Utilization of Recycled Concrete Sand in Soil Stabilization

Victor Temiloluwalase Ojotisa$^{(\boxtimes)}$ and Shihab Ibrahim

Civil Engineering Department, Cyprus International University, Nicosia, Northern Cyprus, Turkey

ojotisavictor@gmail.com, sibrahim@ciu.edu.tr

Abstract. In this research, the efficacy of recycled concrete sand (RCS), a by-product of demolished concrete structures, as an alternative to traditional lime for soil stabilization was investigated. The study examined RCS from four different categories of parent concrete, sorted based on their original compressive strengths (30–39 MPa, 40–49 MPa, 50–59 MPa, and 60–69 MPa), applied to lean clay soil. Hydrated lime and natural sand were used as comparative references. Key assessments were performed using Unconfined Compressive Strength (UCS) test to investigate the mechanical property of the stabilized soils after 28 days of curing. The study observed an increase in pH values due to calcium hydroxide leaching from RCS, resulting in improved soil strength. A direct correlation was found between the parent concrete strength and the 7th-day strength of the stabilized soil, revealing higher strength in the soil stabilized with RCS derived from stronger parent concrete. Additionally, the physical shape of the RCS, due to the impact crushing method, facilitated better interlocking and binding mechanisms. The research concludes that RCS has potential for soil stabilization, enhancing its mechanical properties. However, further investigations on durability are needed to fully comprehend the potentiality of RCS in this application. This study contributes to the expanding body of knowledge regarding sustainable and cost-effective alternatives in the construction industry.

Keywords: Recycled Concrete Sand · Soil Stabilization · Sustainability

1 Introduction

Soil stabilization represents a cornerstone technique within the realm of civil engineering and construction, primarily used to bolster the engineering properties of soil, leading to a more stable and sturdy base for construction [1, 2]. The process involves manipulating soil properties to improve its shear strength, reduce compressibility, and lower permeability to water, among other enhancements. The result is a stronger soil base capable of supporting load-bearing structures such as roads, buildings, and bridges while reducing soil erosion and increasing overall durability [2].

The use of certain materials is pivotal to soil stabilization, which are typically added to alter soil properties. Among the materials used are cement, lime, fly ash, and bitumen, or often, a combination of these. These materials interact with the soil in various ways to

improve its load-bearing capacity, density, and resistance to water and erosion. Notably, lime has found extensive application in soil stabilization [1, 3, 4].

Lime, or calcium oxide (CaO), reacts exothermically with water to produce calcium hydroxide (Ca(OH)2), a process known as slaking. This reaction results in a significant release of heat, turning the lime into a fine powder that can be mixed with soil. The use of lime in soil stabilization has a long-standing history, dating back to ancient civilizations [5, 6]. When introduced to the soil, lime initiates several chemical reactions. First, the lime reacts with the soil moisture to form calcium hydroxide. The calcium ions (Ca2+) from this reaction then interact with clay particles in the soil. In a process called ion exchange, these calcium ions replace exchangeable ions like sodium and magnesium, leading to the deflocculation or dispersion of clay particles. As a result, the soil's physical properties undergo transformation, enhancing its compaction and load-bearing capacity [7]. Lime-based soil stabilization, however, is not without its challenges. One primary concern lies in the sustainability of lime production. The extraction and processing of lime involve the thermal decomposition of limestone, a process that emits a substantial quantity of carbon dioxide (CO2). Given the urgent need to reduce greenhouse gas emissions, this carbon-intensive process poses a significant sustainability issue [8].

Natural sand, another commonly used material in soil stabilization, lends the soil improved compaction, strength, and workability. When mixed with soil, sand particles fill the voids between larger soil particles. This process increases the soil's density, lowers the void ratio, and results in a more compact and stable base [9, 10]. Over time, builders and engineers have relied on natural sand due to its availability and its impressive results in soil stabilization [11]. Despite these advantages, the extraction of natural sand, especially from rivers and other water bodies, carries severe environmental implications. Large-scale sand extraction can lead to biodiversity loss, riverbed degradation, and even alter the course of rivers. Beyond environmental harm, this practice can also result in the lowering of the water table and increase in salinity in certain regions, thus presenting severe sustainability issues [12].

The construction sector is perceived as a significant contributor to environmental degradation and is linked to substantial generation of construction and demolition (C&D) waste [13–16]. Defined as a mix of various materials, including inert waste, non-inert non-hazardous waste, and hazardous waste, C&D waste originates from construction, renovation, and demolition activities [13]. Notably, natural disasters such as earthquakes, floods, hurricanes, and tsunamis also contribute to sudden spikes in C&D waste [15]. The quantity and composition of C&D waste can vary widely, influenced by factors such as regional planning, construction industry practices, and legislation. Both internal factors (e.g., building age, type, construction materials, construction technologies) and external factors (e.g., demolition technologies, population growth) affect the quantity and quality of C&D waste [14, 15]. Recycled concrete aggregates (RCAs) obtained from C&D waste have found applications in soil stabilization. When mixed with soil, RCAs behave similarly to natural aggregates, providing bulk, enhancing compaction, and increasing the overall strength of the soil base. The interactions between RCAs and soil can vary based on various factors, including the properties of the original concrete, such as its compressive strength [17]. Current data suggests that in the EU, approximately 333 million tons of C&D waste (excluding soils) were produced in 2014, while in the USA,

534 million tons of C&D waste were generated in the same year [14]. These substantial volumes illustrate the vast potential of C&D waste as a source of recycled materials for construction applications, including soil stabilization.

In light of this, the focus of the present study lies in examining the utility of recycled concrete sand from different strength classes, specifically 30–39 MPa, 40–49 MPa, 50–59 MPa, and 60–69 MPa, in soil stabilization. Each strength class provides a unique range of aggregate properties, which allows for an exploration of how these variations influence the stabilization process and the final stabilized soil product. This approach offers a potential solution for a more sustainable method of soil stabilization, making use of a widely available waste product while reducing the industry's dependence on virgin natural resources.

2   Materials and Methods

2.1   Soil

The soil used in this research was sourced from Haspolat, Nicosia, Cyprus. Various tests were conducted to determine its properties, such as specific gravity, Atterberg Limits, hydrometer and sieve analysis, and Standard Proctor test. The test results are presented in Table 1. The compaction curve for the soil done without any additives using standard Proctor. The result of XRF is presented in Table 2. Based on the Unified Soil Classification System (USCS), the soil was classified as CL.

Table 1. Soil physical properties

Soil properties	Values
Specific gravity (Gs)	2.71
Liquid limit (%)	45%
Plastic limit (%)	23.90%
Plasticity index (%)	21.10%
Sand (%)	3.84%
Silt (%)	65.85%
Clay (%)	30.31%
Standard Proctor test:	
Maximum dry unit density (g/cm^3)	1.64
Optimal moisture content (%)	20.36%

Table 2. Soil chemical composition

Oxide	SiO_2	Al_2O_3	Fe_2O_3	CaO	MgO	Na_2O	K_2O
%	32.0%	11.30%	6.90%	23.30%	7.10%	1.10%	2.10%

2.2 Hydrated Lime

Commercially available hydrated lime used in this research.

2.3 Natural Crushed Sand

Natural crushed sand, obtained from a quarry Levent Mozaik Ltd, was used in this research. Essential properties such as specific gravity, water absorption, and sieve analysis were performed and are tabulated in Table 3.

2.4 Recycled Concrete Aggregates

Recycled Concrete Aggregates (RCA), categorized into four classes based on the parent concrete's compressive strength (30–39 MPa, 40–49 MPa, 50–59 MPa, 60–69 MPa), were provided by the Chamber of Civil Engineers-Mehmet Göze (Asi) laboratory. Then they were manually crushed with an impact hammer, then sieved accordingly. Samples passing through the sieve size 4.75 m. Properties such as specific gravity, water absorption, pH and sieve analysis were assessed. The properties are tabulated in Table 3. The sieve analysis results are shown in Fig. 1.

Table 3. Physical properties of sands

Properties	Natural Sand (NS)	30–39 RCS	40–49 RCS	50–59 RCS	60–69 RCS
Specific Gravity	2.65	2.13	2.30	2.37	2.47
Water Absorption %	1.50	8.50	9.79	12.15	12.06
pH Value	8.32	10.59	10.66	10.56	10.45

2.5 Mixture

The mix proportions employed in this study will be documented in Table 4. Each mixture's name has S (stand for soil) followed by either L (stand for lime), NS (stand for natural sand), or RCS (recycled concrete sand) based on the parent material strength. The percentage of the additives are limited to 10%. According to the literature, the percentage of lime typically ranges from 3 to 8% [2]. However, for this study, 10% is chosen to maintain the amount of clay within the mixes, in comparison to the mixes containing sand.
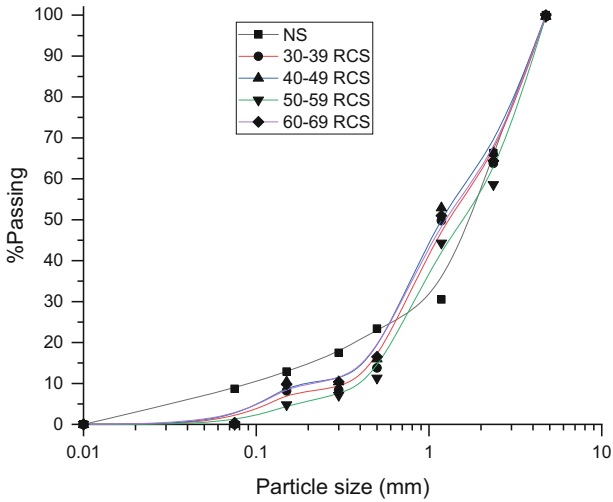
Fig. 1. Sieve analysis for the sands

Table 4. Mix proportions

Mix	Soil	Lime	Sand					Water
			Natural Sand	30–39 RC.Sand	40–49 RC.Sand	50–59 RC.Sand	60–69 RC.Sand	
S/L	90%	10%	0	0	0	0	0	20.36%
S/NS	90%	0	10%	0	0	0	0	20.36%
S/30-39RCS	90%	0	0	10%	0	0	0	20.36%
S/40-49RCS	90%	0	0	0	10%	0	0	20.36%
S/50-59RCS	90%	0	0	0	0	10%	0	20.36%
S/60-69RCS	90%	0	0	0	0	0	10%	20.36%

2.6   Sample Preparation

For sample preparation, mixing at optimum moisture content was performed, and then compaction was conducted in three separate layers within a 38×76 mm mold using small hammer applying 25 blows per layer. It should be mentioned that the optimum moisture content used is based on the soil without additive. Once compacted, the samples were sealed within plastic bags to maintain the moisture content and were left to cure until the days of testing, either on the 7th or 28th day.

2.7   Density and Moisture Content

The size and mass of the samples were measured on the 7th and 28th days to determine their densities. Following the unconfined compressive strength tests, the moisture content of all samples was analyzed.

2.8   Unconfined Compressive Strength (UCS)

Unconfined Compressive Strength tests were conducted using the UTEST multiplex device, having 1 N load sensitivity with 0.001 mm displacement sensitivity according to AST standard with pace rate of 1 mm/min. The samples were checked to have a flat surface to insure proper load distribution on the surface area. Load applied until 10% of axial strain.

3   Result and Discussion

3.1   Effect of Density and Moisture Content on UCS

Density and moisture content are two crucial parameters that influence the Unconfined Compressive Strength (UCS) result. An increase in dry density represents a lower void ratio, i.e., a more compacted soil skeleton, which results in an increased UCS. Despite careful measures to ensure similar dry densities during the compaction process, samples displayed differences in dry densities between 4 and 7% on the testing date. Figure 2 depicts the maximum UCS result for each mix. To mitigate the effect of density, normalized UCS was calculated, as shown in Fig. 3.

On the other hand, the effect of moisture content on the day of testing is more critical due to its impact on the compressive strength, as dictated by pore water pressure. The Soil Water Characteristic Curve (SWCC), aided by the Soil Suction Characteristic Curve (SSCC), can be utilized to calculate metric suction due to available water and subsequently, the effective UCS. In this research, however, the aforementioned calculation was omitted. Figure 4 illustrates the relationship between UCS and moisture content on the day of testing.
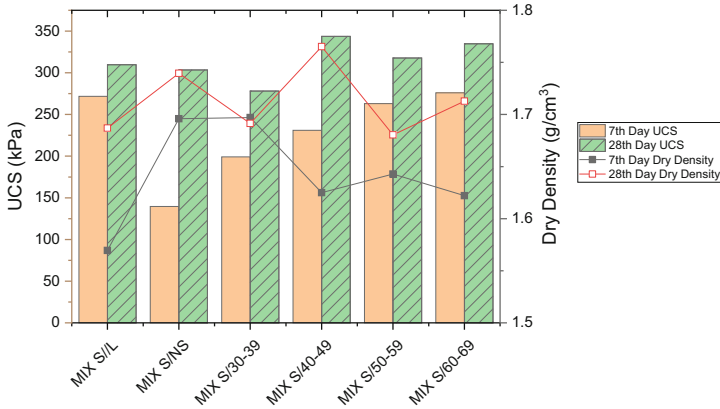
Fig. 2. UCS and dry density results before normalization
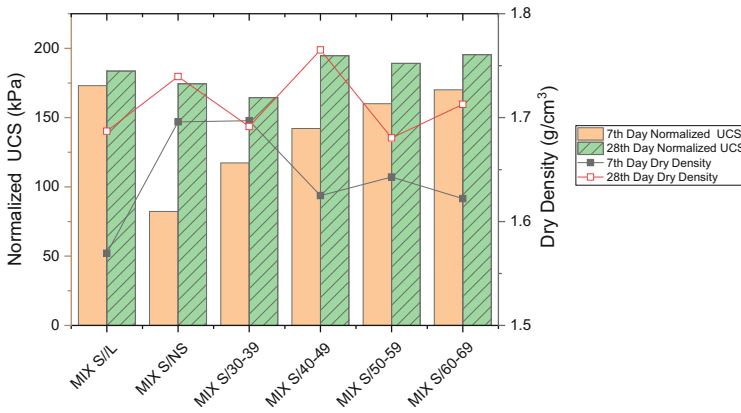
Fig. 3. UCS and dry density results after normalization

Various samples were observed, and it was noted that their moisture content on the 7th day was fairly similar, indicating a comparable effect of pore water pressure on the Unconfined Compressive Strength (UCS) results. By the 28th day, however, a distinct decrease in moisture content was found in the MIX S/40-49RCS mix compared to the other mixes.
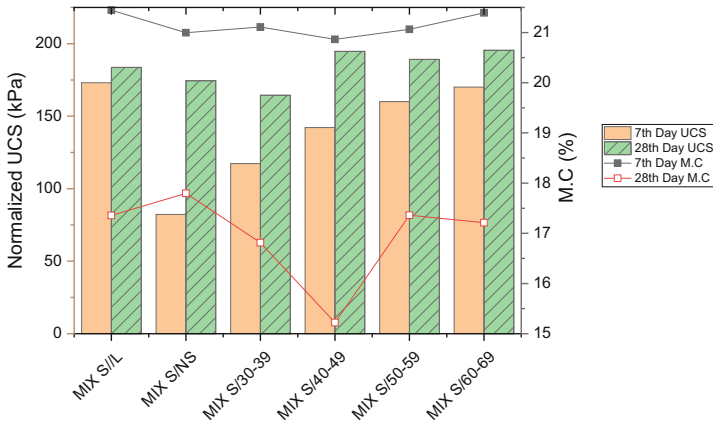
Fig. 4. UCS and moisture content of the stabilized soil

A detailed analysis of UCS changes over time was conducted. A minor increase in the UCS from the 7th to the 28th day was noticed in the mix stabilized with lime, suggesting that the majority of the leaching occurs within the initial 7-day period. On the contrary, in the mix stabilized with natural sand, a two-fold increase in UCS between these days was noted. This increase is believed to be related to the stabilization mechanism, a process that is amplified by the angularity of the crushed natural sand used, which boosts interlocking and shear strength. However, it's crucial to mention that an adequate improvement in chemical bonding is hindered due to the mix's insufficiently strong pH value. Over the 28-day period, a reduction in moisture content was observed, which led to an improvement in friction between sand particles and soil.

For the Recycled Concrete Aggregates (RCSs), a dual mechanism of stabilization was identified. The first involves the enhanced angularity resulting from the type of crushing process, and the second is associated with the chemical stabilization effect due to a rise in pH to higher alkalinity levels.

According to our study, a direct correlation between the strength of parent materials and UCS was established—higher UCS is associated with stronger parent materials. This is attributed to the strength of parent materials influencing the bonding between the cement paste and parent aggregate, a finding that aligns with the results of [17], which also found weaker parent materials to be linked to a weaker interfacial zone between the cement paste and parent aggregate.

In the final observation, the UCS of 40–49, 50–59, and 60–69 RCSs was found to surpass that of the mixes stabilized with lime and natural sand, highlighting the significance of the type and strength of materials used in determining the final compressive strength of the mix.

3.2 Stress and Strain Diagram

The results of the non-normalized stress-strain diagrams are presented in Figs. 5 and 6. The 7-day results display a bell-shaped curve for the mix stabilized with lime and natural

sand. For the mixes stabilized with Recycled Concrete Aggregates (RCSs), there is a steeper drop-off in stress evident in the 7-day results. The moisture content across all samples was similar, attributed to the excessive absorption rate of the RCS. A reduction in water between the soil and sand particles lessens the lubrication effect, resulting in sharp peaks in the stress-strain curves and more brittle failure.

By the 28th day, all the samples exhibited similar behavior, likely due to the reduction in moisture content across all mixes. The water entrapped in the voids of the RCS will be the last to evaporate.
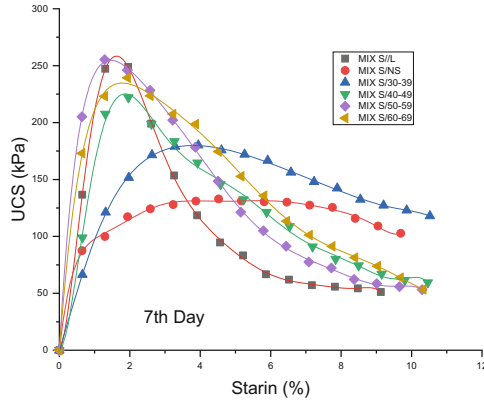
Fig. 5. Stress-Strain curves for 7 days curing
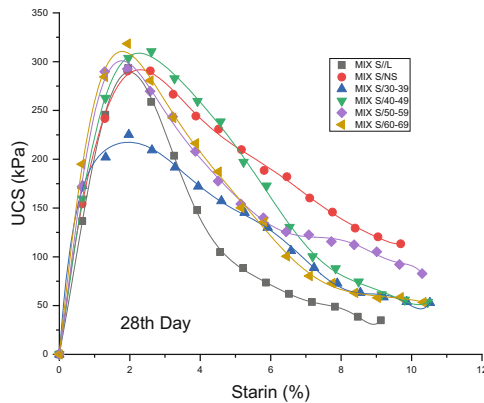
Fig. 6. Stress-Strain curves for 28 days curing

4   Conclusions and Recommendation

The result of the experiments shows that mechanical properties of soil stabilized with recycled concrete sands are comparable/higher that the soil stabilized with lime or natural sand. The pH value of the mix with RCS are above 10 provides an alkaline media for

leaching and chemical stabilization. The higher the strength of the parent material for the RCS, the higher the strength of the stabilized soil. Due to high rate of absorption the stabilized soil with RCS shows brittle failure mode in stress-strain diagrams. Over all usage of RCS shows not just a positive impact in soil stabilization by the dual affect, chemical and mechanical interlocking, but also serves in sustainability manner by using waste materials and limiting the use of lime and natural sand to protect the environment. Further research must be done to address the durability of the stabilized soil.

References

1. Afrin, H.: A review on different types soil stabilization techniques. Int. J. Transp. Eng. Technol. **3**(2), 19–24 (2017)
2. Zuber, S.S., Kamarudin, H., Abdullah, M.M., Binhussain, M.: Review on soil stabilization techniques. Aust. J. Basic Appl. Sci. **7**(5), 258–265 (2013)
3. Sherwood, P.: Soil Stabilization with Cement and Lime (1993)
4. Firoozi, A.A., Guney Olgun, C., Firoozi, A.A., Baghini, M.S.: Fundamentals of soil stabilization. Int. J. Geo-Eng. **8**, 1–6 (2017)
5. Negi, A.S., Faizan, M., Siddharth, D.P., Singh, R.: Soil stabilization using lime. Int. J. Innov. Res. Sci. Eng. Technol. **2**(2), 448–453 (2013)
6. Jawad, I.T., Taha, M.R., Majeed, Z.H., Khan, T.A.: Soil stabilization using lime: advantages, disadvantages and proposing a potential alternative. Res. J. Appl. Sci. Eng. Technol. **8**(4), 510–520 (2014)
7. Diamond, S., Kinter, E.B.: Mechanisms of soil-lime stabilization. Highway Res. Rec. **92**(303), 83–102 (1965)
8. Gutiérrez, A.S., Van Caneghem, J., Martínez, J.B., Vandecasteele, C.: Evaluation of the environmental performance of lime production in Cuba. J. Clean. Prod. **1**(31), 126–136 (2012)
9. Mishra, S., Sachdeva, S.N., Manocha, R.: Subgrade soil stabilization using stone dust and coarse aggregate: a cost effective approach. Int. J. Geosynthetics Ground Eng. **5**, 1 (2019)
10. Firat, S., Khatib, J.M., Yilmaz, G., Comert, A.T.: Effect of curing time on selected properties of soil stabilized with fly ash, marble dust and waste sand for road sub-base materials. Waste Manag. Res. **35**(7), 747–756 (2017)
11. Cömert, A., Firat, S., Yilmaz, G., Mansur, S.: The effect of fly ash marble dust and waste sand on the CBR and permeability of the road subbase filling materials (2010)
12. Rentier, E.S., Cammeraat, L.H.: The environmental impacts of river sand mining. Sci. Total. Environ. **10**(838), 155877 (2022)
13. Yuan, H., Shen, L.: Trend of the research on construction and demolition waste management. Waste Manag. **31**(4), 670–679 (2011)
14. Menegaki, M., Damigos, D.: A review on current situation and challenges of construction and demolition waste management. Curr. Opin. Green Sustain. Chem. **1**(13), 8–15 (2018)
15. Yeheyis, M., Hewage, K., Alam, M.S., Eskicioglu, C., Sadiq, R.: An overview of construction and demolition waste management in Canada: a lifecycle analysis approach to sustainability. Clean Technol. Environ. Policy **15**, 81–91 (2013)
16. Coelho, A., De Brito, J.: Influence of construction and demolition waste management on the environmental impact of buildings. Waste Manag. **32**(3), 532–541 (2012)
17. Tavakol, M., Hossain, M., Tucker-Kulesza, S.E.: Subgrade soil stabilization using low-quality recycled concrete aggregate. In: Geo-Congress 2019: Geotechnical Materials, Modeling, and Testing, pp. 235–244. American Society of Civil Engineers, Reston (2019)

Thermal Modeling of the Buffer Around Nuclear Waste Repository

Esra Güneri[1,2(✉)] 📵 and Yeliz Yükselen Aksoy[2] 📵

[1] Civil Engineering Department, İzmir Demokrasi University, İzmir, Turkey
esra_cetinorgu@hotmail.com
[2] Civil Engineering Department, Dokuz Eylul University, İzmir, Turkey
yeliz.yukselen@deu.edu.tr

Abstract. The safe and rapid disposal of radioactive is an issue of great importance. The leakage from radioactive wastes should be prevented. In the storage of nuclear wastes (radionuclides), the wastes are regularly placed in a sealed, gas and water-free copper container called a canister. In order to prevent the canister from being damaged by a movement in the bedrock or by dangerous substances that may be present in the groundwater, it is covered with a buffer material. Some countries use multiple barrier systems to isolate the waste. Here comes the bedrock that acts as the primary buffer, followed by the engineered barrier system that surrounds it. While the primary buffer material here is the bedrock itself, the secondarily engineered barrier system is the materials positioned between the canister and the bedrock consisting of bentonite or sand-bentonite mixture. In this study, 10% bentonite-90%sand mixture was chosen and the thermal modeling of sand-bentonite mixture as a buffer material around the nuclear waste landfill was performed using the Code Bright Program. In order to use in the analyses, the thermal conductivity values of the mixture and other necessary thermal parameters were measured. At the end of the analysis with 100-years final interval value, it was determined that the temperature in the canister reached 197.96 °C, and 111.48 °C in a part of the green colored zone where the 10B-90S mixture was used as a buffer.

Keywords: Buffer · Nuclear waste · Sand-bentonite · Temperature

1 Introduction

With increase in number and type of energy geo-structures, the interaction of soils with temperature increases and changes in engineering properties were observed. Depending on the temperature increase in cohesive soils, the decrease in shear strength and volume deformation [1, 2] or change in the liquid-plastic limit values were reported [3]. Optimizing these changes is possible with materials that can maintain their resistance against high temperatures. One of the main energy structures is nuclear waste storage repositories. After nuclear waste is disposed of, they begin to decompose, emitting radiation and heat [4]. Nuclear waste is buried underground at a depth of 400–500 m, where

the usually canister are covered with bentonite. The material to be selected as a buffer must have some criterias [4]. For example, it must have very low hydraulic conductivity and maintain its properties throughout its service life. Bentonite acts as a buffer by transmitting the heat it receives from the heat source towards the bedrock. Increase in temperature causes the water to evaporate and a process occurs that affects each other from a thermal-hydraulic and mechanical even chemical point of view [5]. In this study, sand-bentonite mixture was preferred to be used as a buffer around the heat source. Thermal analyses were performed and thermal parameters for analyses were measured for the mixture.

2   Materials and Methods

2.1   Materials

The Na-bentonite and sand used in this study. The materials were used after drying in the oven (Fig. 1). Table 1 gives the physico-chemical properties of the materials. Approximately 20.7% of the sand passed through No.200 sieve.

Fig. 1.   The materials used in the tests

Table 1.   Physico-chemical properties of materials

	Bentonite	Sand
Specific gravity	2.70	2.63
Liquid limit (%)	476	–
Plastic limit (%)	70	–
pH	9.5	–

2.2   Methods

The abbreviated name of the mixture is given as 10B-90S for the 10% bentonite-90% sand mixture. Compaction tests of the mixtures were carried out according to ASTM D698–12. The optimum water content and maximum dry unit weight values of the mixture were obtained. Thermal conductivity measurements were performed in order to thermal modeling of the sand-bentonite mixture. The samples were compacted before the tests according to the compaction parameters which were obtained from the compaction tests. Thermal conductivity measurements were made with the Tempos instrument. The thermal conductivity and volumetric heat capacity values were measured using different probes (Fig. 2). In this context, host rock size was chosen as 60×60 m, buffer diameter and canister diameter of 6 m and 1 m, respectively. All required data for modeling for the 10B-90S was obtained from the experiments of this study.

Fig. 2. The thermal conductivity measuring equipment

3   Results

According to the Standard Proctor test results, the optimum water content of the 10B-90S mixture was determined as 15.5% and the maximum dry unit weight value was determined as 16.7 kN/m^3. The data for the thermal analyses were determined as a result of performed measurements and experiments. Thermal conductivity measurements were made with the Tempos instrument. Thermal conductivity and volumetric heat capacity were determined using different probes. The unit is converted from volumetric heat capacity to heat capacity. The specific heat value was determined by the ratio of heat capacity to unit volume weight (Table 2). The hydraulic conductivity value was obtained from the test results (Guneri, 2022).

The time for half of the amount of a radioactive element decay is called as half-life, and this time varies depending on the structure of the nucleus. In the present study, the half-life was taken as 100-years.

Table 2. Properties of the materials used in the model

Mixtures	Thermal Conductivity (w/mK)	Vol. Heat Capacity (MJ/m^{3}K)	Heat Capacity (J/m^{3}K)	γ_n (kg/m^3)	Specific Heat (J/kgK)	Hydraulic Conductivity (m/s)
10B-90S	1.877	2.260	2260000	1875	1205	8.2×10^{-7}
Rock*	3.000	–	–	2500	800	–

The temperature change from canister to host rock at the end of this period is shown in Fig. 3. At the end of the 100-years final interval value, it was determined that the temperature in the canister reached 197.96 °C, and 111.48 °C in a part of the green colored zone where the 10B-90S mixture was used as a buffer. The decreased conduction of the temperature from the canister to the bedrock was supplied with the help of the primary buffer bedrock and the secondary buffer sand-bentonite mixture.
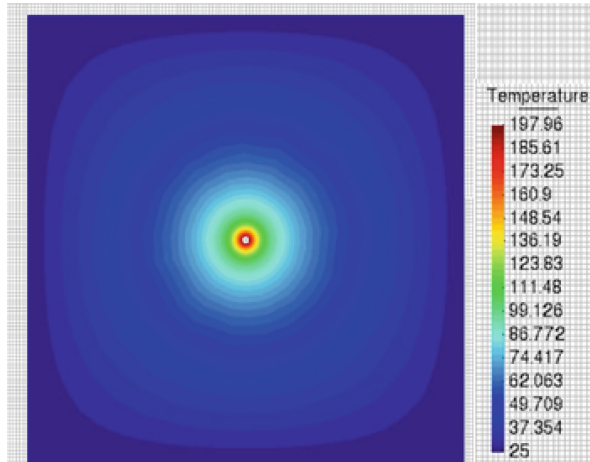
Fig. 3. Contour fill of temperature representation in the presence of 10B-90S buffer mixture at the end of the time

Figure 4 shows the variation of temperature with respect to distance from the axis of the canister. It shows that decrease in temperature of the canister based on the distance of 30 m from the center of the canister to the bedrock.
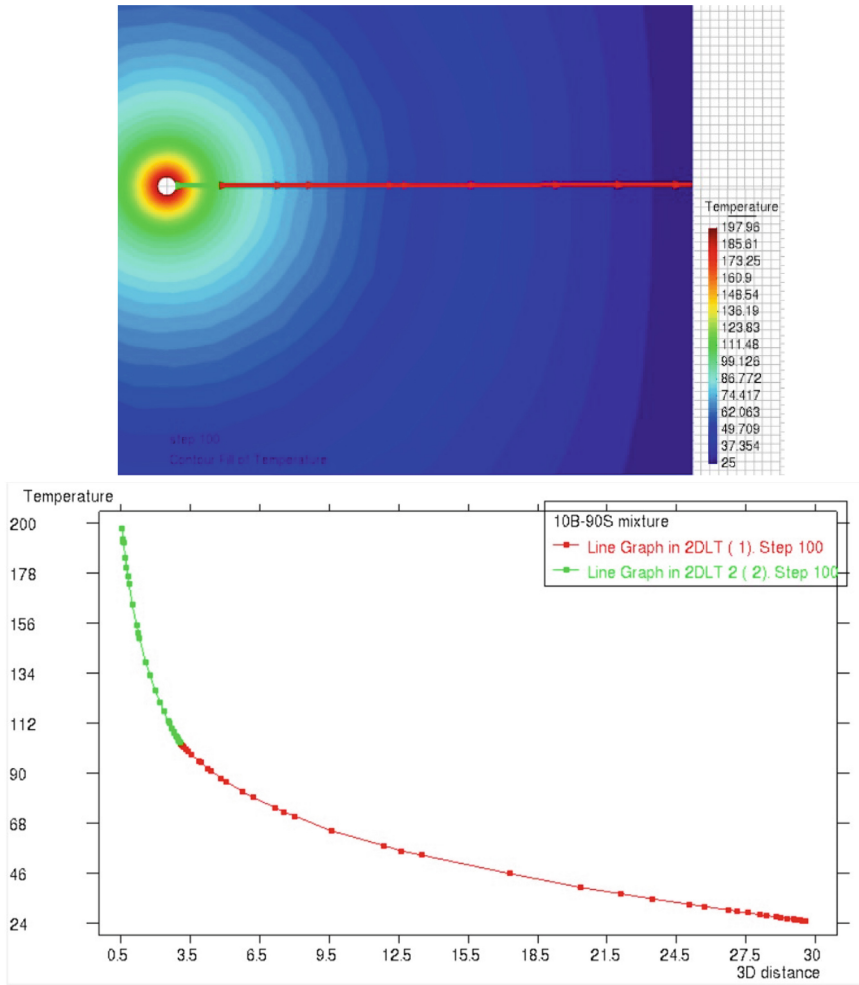
Fig. 4. Temperature vs. distance relationship

Figure 5 indicates that the heat conducted from the canister can be distributed from the 10% bentonite-90% sand mixture, which means that this mixture can act as a buffer. For a selected point (10 isochrone), the temperature of the canister (red zone-line) was determined to be approximately 160 °C, in the buffer zone (green zone-line) 100 °C, and close to the boundary zone of the bedrock (blue zone-dark green line) approximately 40 °C.
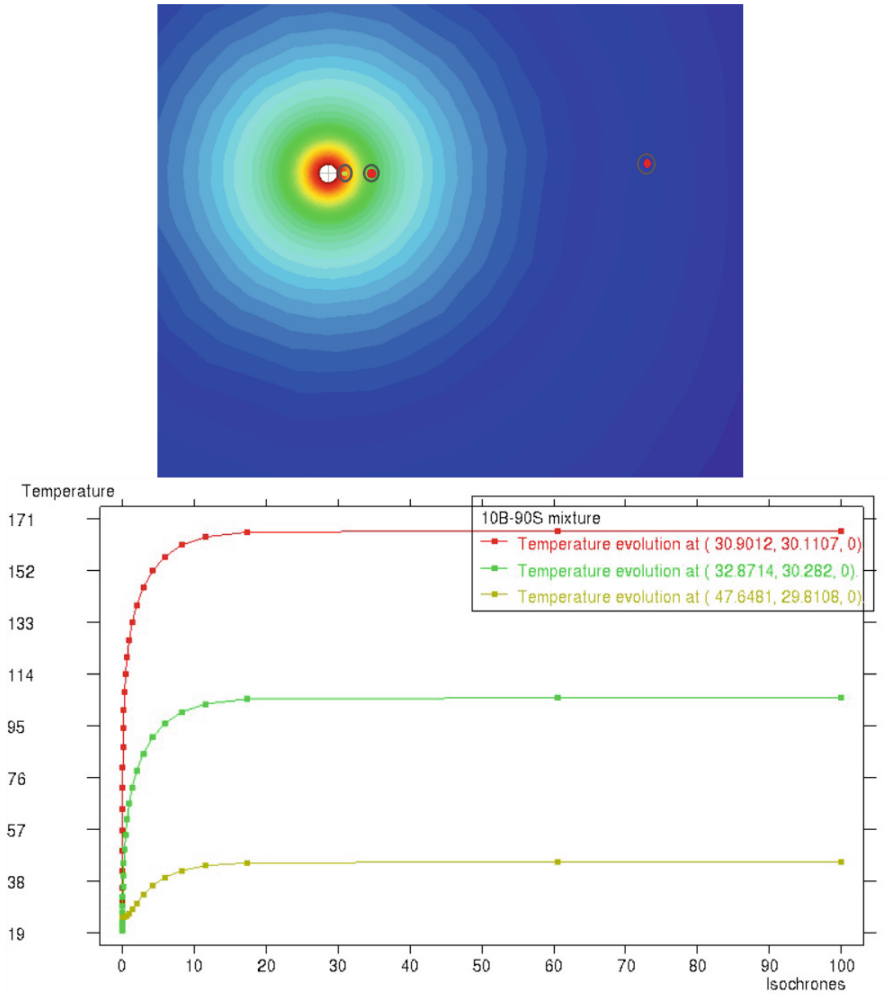
Fig. 5. Point temperature evaluation

4   Conclusions

Within the scope of this study, thermal conductivity measurements and thermal modeling of sand-bentonite mixture were performed. As a result of the thermal analyses made in the Code Bright Program, it was determined that the temperature value of the 10B-90S mixture selected as a barrier in the nuclear waste landfills will be 111.48° at the end of the 100-years final interval period. In addition, it was observed that the temperature value decreases as one moves from the canister, which is the heat source, to the bedrock. It can be concluded that sand-bentonite mixture can be used as a buffer material in nuclear waste repositories in terms of thermal analyses. However, other parameters such as swelling potential and hydraulic conductivity should be checked considering the design criterias.

References

1. Gray, H.: Progress report on research on the consolidation of fine-grained soils. In: Proceedings of the International Conference on Soil Mechanics and Foundation Engineering, Harvard University, vol. 2, pp. 138–141 (1936)
2. Paaswell, R.: Temperature effects on clay soil consolidation. J. Soil Mech. Found. Div. **93**, 9–22 (1967)
3. Youssef, M.S., Sabry, A. El Ramli, A.H.: Temperature changes and their effects on some physical properties of soils. In: Proceedings of the Fifth International Conference on Soil Mechanics and Foundation Engineering, Paris, vol. 2, pp. 419–421 (1961)
4. Sellin, P., Leupin, O.X.: The use of clay as an engineered barrier in radioactive-waste management - A review. Clays Clay Miner. **61**(6), 477–498 (2013)
5. Gens, A., et al.: HM and THM interactions in bentonite engineered barriers for nuclear waste disposal. Int. J. Rock Mech. Min. Sci. **137**, 104572 (2021). https://doi.org/10.1016/j.ijrmms.2020.104572

Undrained Spherical Expansion Analysis for Clay

Vincenzo Silvestri[(✉)] [iD] and Claudette Tabib

Civil Engineering Department, Polytechnique Montreal, Montreal, QC, Canada
`vincenzo.silvestri@polymtl.ca`

Abstract. The application of cavity expansion methods in geotechnical engineering has been extensively developed in the last six decades and has resulted in solutions of great interest, such as in situ soil testing and pile foundations. This paper presents a large-strain analytical solution which allows obtaining the constitutive properties of clay from the pressure-expansion curve of a spherical cavity. The theory applies to the interpretation of static cone penetration tests, which are often modelled as spherical expansion processes in an unbounded medium. Shear stress-strain curves of clay are found from experimental pressure-expansion relationships, without making assumptions regarding the constitutive properties of the material, i.e., elastic and elastic-plastic. The only assumptions made are that the expansion takes place under undrained conditions and an initial hydrostatic stress field. For illustration purposes, the theory is applied to the determination of clay properties from two idealized spherical expansion relationships which are known to yield strain-hardening and strain-softening responses. The solution is also obtained for the case when the expansion takes place in a clay medium of finite outer radius.

Keywords: Spherical Cavities · Expansion · Clay

1 Introduction

In situ cylindrical expansion tests, such as pressuremeter and dilatometer tests, are often carried out to obtain soil properties for design purposes. For undrained clay response, exact interpretation procedures were independently derived by [1–3]. Another in-situ test is the quasi-static cone penetration test. Recent interpretation procedures regarding this test have taken three complementary directions: the deep bearing capacity approach (See, for example, [4–6]), the spherical cavity expansion approach (See, for example, [7–9]), and the fluid flow approach (See, for instance, [10–12]).

The present paper addresses limitations of the expansion of spherical cavities and demonstrates, similar to the case of cylindrical cavities, that is possible to deduce stress-strain curves from pressure-expansion relationships. This was achieved by considering that the expansion occurred under initial hydrostatic pressure and undrained conditions.

The large-strain procedure developed in the paper deals with spherical cavity expansions both in an unbounded medium and in a clay medium of finite outer radius. The proposed approach applies to expansion tests performed in clay characterized by idealized nonlinear strain-hardening and strain-softening responses.

2 Theoretical Development

2.1 Large Strain

A spherical coordinate system (r, θ, ψ) is retained for the analysis, and tensile stresses and strains are considered positive. The principal stresses are σ_r, σ_θ, σ_ψ. Because large strains are used in the paper, a choice had to be made between the various definitions of such strains. The logarithmic definition was found particularly attractive due to its simple physical interpretations for problems with no rotation [13, 14]. The corresponding principal logarithmic strains are ε_r, ε_θ, ε_ψ. In addition, because the spherical expansion takes place under an initial isotropic pressure p_o, then $\sigma_\theta = \sigma_\psi$ and $\varepsilon_\theta = \varepsilon_\psi$ for symmetry. The logarithmic radial and tangential strains are:

$$\varepsilon_r = \ln\left(\frac{dr}{dr_0}\right) \tag{1a}$$

$$\varepsilon_0 = \ln\left(\frac{r}{r_0}\right) \tag{1b}$$

In this case, it is necessary to distinguish the polar distance r_o of a point in the original unstrained condition and the corresponding distance r of the same material element in the strained condition, and similarly the inner radius of the spherical cavity a_o before and a after the distortion has occurred.

The undrained condition retained in the analysis implies that the volumetric strain ε_v is zero during the expansion. This leads to:

$$\varepsilon_v = \varepsilon_r + \varepsilon_\theta + \varepsilon_\psi = \varepsilon_r + 2\varepsilon_\theta = 0 \tag{2a}$$

from which

$$\varepsilon_r = -2\varepsilon_\theta \tag{2b}$$

Thus, the shear strain which is defined as:

$$\gamma = \varepsilon_\theta - \varepsilon_r \tag{3a}$$

reduces to:

$$\gamma = 3\varepsilon_\theta = \ln\left(\frac{r}{r_0}\right)^3 \tag{3b}$$

from Eqs. 1b and 2b.

From the equation of equilibrium

$$\frac{d\sigma_r}{dr} = \frac{2(\sigma_\theta - \sigma_r)}{r} \tag{4a}$$

it follows that:

$$\frac{dr}{r} = \frac{d\sigma_r}{4\tau} \tag{4b}$$

where $\tau = (\sigma_\theta - \sigma_r)/2$ is the principal shear stress. Now, because the spherical expansion is undrained, the volume of an expanding spherical shell remains constant, implying that:

$$4\pi r^2 dr = 4\pi r_0^2 dr_0 \tag{5}$$

Then, combining the above equation with Eq. 3b yields:

$$\frac{dr}{r} = \frac{d\gamma}{3(1 - e^\gamma)} \tag{6}$$

Substitution of Eq. 6 into the equation of equilibrium, either Eq. 4a or Eq. 4b, gives:

$$d\sigma_r = -\frac{4}{3}\frac{\tau d\gamma}{(e^\gamma - 1)} \tag{7}$$

Equation 7 allows determination of the shear stress mobilized at the wall of the cavity for which $r = a$, that is

$$\tau_a = \frac{3}{4}(e^{\gamma a} - 1)\frac{dp_a}{d\gamma_a} \tag{8}$$

where $\tau_a = (\sigma_{\theta a} - \sigma_{ra})/2$, $\gamma_a = 3\varepsilon_\theta$, $p_a = -\sigma_{ra}$. The last equation shows that the stress-strain curve of the clay may be easily obtained from the derivative of the experimental pressure –expansion relationship as function of the shear stain mobilized at the wall of the cavity.

Integration of Eq. 7 permits finding the expansion pressure p, that is,

$$p = -\sigma_r = p_0 + \frac{4}{3}\int_0^{\gamma_a} \frac{\tau d\gamma}{(e^\gamma - 1)} \tag{9}$$

where p_o is the initial pressure acting throughout the soil.

2.2 Almansi Strain

If the Almansi tangential strain α, which is defined as in Eq. 10,

$$\alpha = \frac{1}{3}\left(\frac{r^3 - r_0^3}{r^3}\right) \tag{10}$$

α is used instead of the logarithmic shear strain γ, then Eq. 7 can be rewritten as Eq. 11:

$$\frac{d\sigma_r}{d\alpha} = -\frac{4}{3}\frac{\tau}{\alpha} \tag{11}$$

Therefore, from Eq. 11, the mobilized shear stress at the cavity wall can be obtained as highlighted in Eq. 12:

$$\tau_a = \frac{3}{4}\alpha_a\frac{dp}{d\alpha_a} \tag{12}$$

where $\alpha_a = \frac{1}{3}\left(\frac{a^3 - a_0^3}{a^3}\right)$. Consequently, the expansion pressure is given by:

$$p = p_0 + \frac{4}{3}\int_0^{\gamma_a} \frac{\tau d\alpha}{\alpha} \tag{13}$$

2.3 Small Strain

Large-strain theory is complex and whenever possible small strain is used to model cavity expansion because it becomes possible to obtain closed-form solutions [14]. In addition, as the tangential strain $\varepsilon_\theta = (r - r_o)/r_o$ in a small-strain assumption, then Eqs. 8 and 9 reduce respectively to

$$\tau_a = \frac{3}{4}\gamma_a \frac{dp}{d\gamma_a} \tag{14a}$$

and

$$p = p_0 + \frac{4}{3}\int_0^{\gamma_a} \frac{\tau \, d\gamma}{\gamma} \tag{14b}$$

2.4 Bounded Medium

When the spherical expansion takes place in a medium of finite outer radius b_o, before expansion and b, after expansion, then differentiation of Eq. 9 yields

$$\frac{dp}{d\gamma_a} = \frac{4}{3}\left[\frac{\tau_a}{e^{\gamma_a} - 1} - \frac{\tau_b}{e^{\gamma_b} - 1}\right] \tag{15}$$

where τ_b and γ_b represent respectively the shear stress and the shear strain mobilized at the outer radius. In addition, by letting:

$$q = \left(\frac{a}{a_0}\right)^3 \tag{16a}$$

and

$$\beta = \left(\frac{a_0}{b_0}\right)^3 \tag{16b}$$

substitution of these parameters into Eq. 15 gives

$$\frac{dp}{dq} = \frac{4}{3(q-1)}\left[\frac{\tau_a}{q} - \frac{\tau_b}{1 - \beta + \beta q}\right] \tag{17}$$

where $1 - \beta + \beta q = (b/b_o)^3$. Note also that when the medium is of infinite extent, $\tau_b = 0$ and Eq. 17 reduces to:

$$\tau_a = \frac{3}{4}q(q-1)\frac{dp}{dq} \tag{18}$$

which may be shown to be equivalent to Eq. 8.

3   Application to Idealized Responses

As mentioned previously, the expansion of the spherical cavity is assumed to take place under an initial isotropic stress $\sigma_{ro} = -p_o$, acting everywhere in the soil, and undrained conditions. The solutions presented above belong to a type of problem that has been termed the inverse cavity expansion procedure [14]. To this problem also belong the solutions obtained by [1–3], in the case of the pressuremeter test in clay.

In the inverse cavity expansion, the problem becomes one of determining the actual soil stress-strain curve as well as stress and displacement fields for a given pressure-expansion curve. However, for obtaining closed-form expressions for the stress-strain curves, a small-strain approach is used, i.e., Eqs. 14a and 14b. In addition, for calculation purposes, it is assumed that the experimental pressure-expansion curves may be approximated by idealized expressions which are known to yield strain-hardening and strain-softening responses, with the following assumptions made for the clay behavior [14–16]:

3.1   Strain Hardening

If the net pressure-expansion curve can be represented by an expression of the form

$$p - p_0 = \frac{4}{3} S_u \ln\left(\frac{D + \gamma}{D}\right) \tag{19}$$

application of Eq. 14a yields the following relation:

$$\tau = \frac{\gamma S_u}{D + \gamma} \tag{20}$$

for the shear stress τ. This equation is a simple hyperbolic strain-hardening expression, in which S_u is the ultimate undrained shear strength and D is a material parameter. It may be shown that the parameter $D = S_u / G$, where G is the initial shear modulus.

For illustration purposes, calculations were performed by assuming $S_u = 100$ kPa and $D = 0.004$, resulting in $G = 250\, S_u$. Figure 1 presents the results of the simulation for the net pressure-expansion, $p - p_o$, and the deduced shear stress τ, as function of the shear strain γ. For example, the curves show that when the net expansion pressure reaches 525 kPa at $\gamma = 0.2$, the shear stress equals 99 kPa.
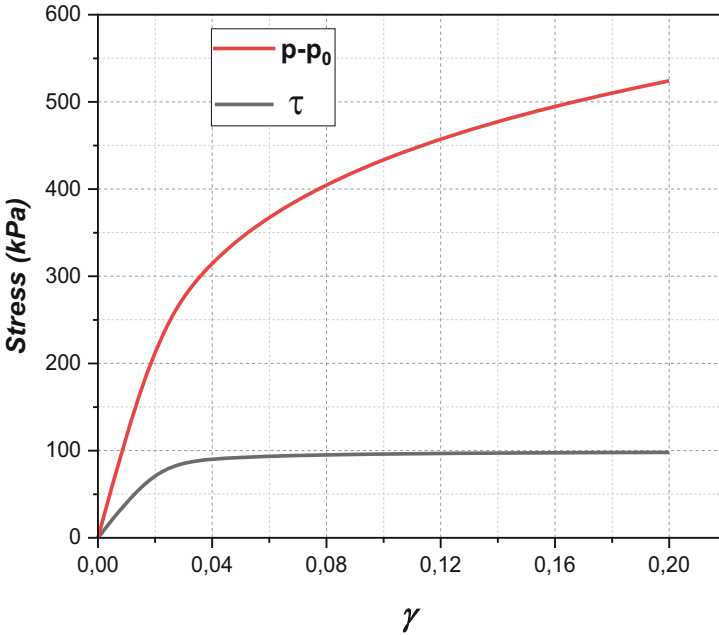
Fig. 1. Strain-hardening response.

3.2 Strain Softening

If the experimental net pressure-expansion curve can be represented by the expression

$$p - p_0 = \frac{4}{3}\frac{AB}{C}\ln\left(C\gamma^2 + 1\right) + \frac{4}{3}\frac{A}{\sqrt{C}}\tan^{-1}(C\gamma) \tag{21}$$

application of Eq. 14a gives:

$$\tau = A\gamma\left(\frac{B\gamma + 1}{C\gamma^2 + 1}\right) \tag{22}$$

where A, B, and C are material constants and the shear strain γ is expressed as a percentage. Equation 22 represents a strain-softening stress-strain curve. The constants are such that: (i) the peak shear strength $S_u = S_{up}$ occurs at $\gamma = \gamma_p = (B + (B^2 + C)^{1/2})/C$, (ii) the slope $d\tau/d\gamma = A$ at $\gamma = 0$, and (iii) the residual shear strength $S_{uresid} = AB/C$ at $\gamma = \infty$.

For illustration purposes, calculations were carried out for values $A = 500$, $B = 1.2$, and $C = 12$, resulting in $S_{up} = 101.4$ kPa at $\gamma = 0.4055$, and $S_{uresid} = 50$ kPa at $\gamma = \infty$. Figure 2 presents the net expansion pressure, $p - p_o$, and the shear stress τ as function of the shear strain γ. For example, when the net expansion pressure reaches 490 kPa at $\gamma = 5\%$, the shear stress τ equals 58 kPa.
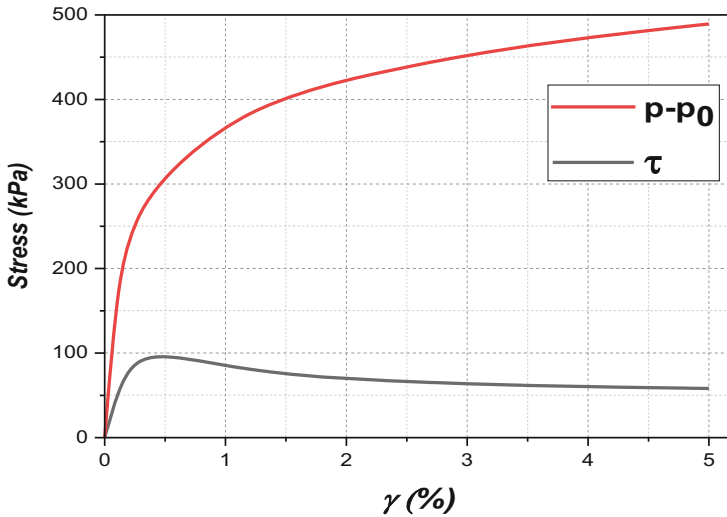
Fig. 2. Strain-softening response.

4 Conclusions

The following conclusions are drawn based on the contents of the present paper:

1) It is possible to obtain the stress-strain curve of clay from the pressure-expansion relationship of a spherical cavity in an unbounded medium by assuming undrained conditions in an initial isotropic stress field.
2) It is also possible to determine the stress-strain curve of clay when the expansion takes place in a medium of finite extent.
3) The solution obtained for the case of the unbounded medium was applied to idealized strain-hardening and strain-softening responses. Closed-form expressions were found for a small-strain approach.
4) Expressions for the net expansion pressure and the shear stress were given for the case of the Almansi tangential strain approach.

References

1. Baguelin, F., Jezequel. J.-F., Lemee, E., Le Mehaute, F.: Expansion of cylindrical probes in cohesive soils. ASCE JSMFD **98**(SMII), 1129–1142 (1972)
2. Ladanyi, B.: In situ determination of undrained stress-strain behavior of sensitive clays with the pressuremeter. Can. Geotech. J. **9**(3), 313–319 (1972)
3. Palmer, A.C.: Undrained plane-strain expansion of a cylindrical cavity in clay: a simple interpretation of the pressuremeter test. Geotechnique **22**(3), 451–457 (1972)

4. Meyerhof, G.G.: Bearing capacity and settlement of pile foundations. ASCE JGED **102**(GT3), 195–228 (1976)
5. Bustamante, M., Gianeselli, L.: Pile bearing capacity predictions by means of static penetrometer CPT. In: Verruijit, A., Beringen, F.L., de Leeuw, E.H. (eds.) ESOPT II, vol. 2, pp. 493–500. Routledge, Amsterdam (1982)
6. Meigh, A.C.: Cone penetration testing, CIRIA, Butterworth, London (1987)
7. Ladanyi, B.: Expansion of a cavity in a saturated sand medium. ASCE JSMFD **89**(SM4), 127–161 (1963)
8. Vesic, A.S.: Expansion of cavities in infinite soil mass. ASCE JSMFD **98**(SM3), 265–290 (1972)
9. Collins, I.F., Pender, M.J., Wang, Y.: Cavity expansion in sands under drained conditions. Int. J. Num. Anal. Meth. Geomech. **16**(1), 3–33 (1992)
10. Baligh, M.M.: Strain path method. ASCE JGED **111**(GT9), 1108–1136 (1985)
11. Teh, C.I., Houlsby, G.T.: An analytical study of the cone penetration test in clay. Geotechnique **41**(1), 17–34 (1991)
12. Yu, H.-S., Hermann, L.R., Boulanger, R.W.: Analysis of steady cone penetration in clay. ASCE JGGE **125**(7), 594–605 (2000)
13. Silvestri, V.: On the determination of the stress-strain curve of clay from the undrained plane-strain expansion of hollow cylinders: a long-forgotten method. Can. Geotch. J. **35**(2), 360–363 (1998)
14. Yu, H.-S.: Cavity Expansion Methods in Geomechanics. Cambridge University Press, Cambridge (2000)
15. Prevost, J.-H.: Undrained stress-strain-time behavior of clays. ASCE JGED **102**(GT12), 1245–1260 (1976)
16. Prapaharan, S., Chameau, J.-L., Holtz, R.D.: Effect of strain rate on undrained strength derived from pressuremeter tests. Geotechnique **39**(4), 615–624 (1989)

An Experimental Study on the Usability of Reclaimed Asphalt Pavements or Waste Bricks in the Stone Columns

Talha Sarici[1](✉) , Bahadir Ok[2] , Nurullah Akbulut[3] ,
and Ahmet Haydar Cenk[3]

[1] Department of Civil Engineering, Inonu University, Malatya, Turkey
`talha.sarici@inonu.edu.tr`
[2] Department of Civil Engineering, Adana Alparslan Turkes Science and Technology University, Adana, Turkey
`bahadirok@atu.edu.tr`
[3] Department of Civil Engineering, Hasan Kalyoncu University, Gaziantep, Turkey
`nurullah.akbulut@hku.edu.tr`

Abstract. This study presents experiments to find out if recycled asphalt pavements (RAP) or waste bricks (WB) can be used instead of natural aggregates (NA) in the stone columns that are used to increase bearing capacity and speed up consolidation settlement. The first step in this research was to get RAP, WB, and NA, then figure out a suitable gradation and unit weight for stone columns, and lastly do tests in the lab, such as pycnometer, minimum and maximum dry unit weights, water absorption, California bearing ratio (CBR), aggregate impact value (AIV), and large-scale direct shear tests. In order to perform CBR, AIV, and large-scale direct shear tests, it was necessary to find the unit volume weight in the stone column. Therefore, the model tests were conducted in a steel tank. The tank was filled with cohesive soil, so that soft soil conditions were created. And then, the stone columns with a diameter of 5 cm were built using RAP, WB, and NA in the middle of the soft soil. Thus, the unit weight values of RAP, WB, and NA were determined according to the amount of material used for the stone column. The results show that RAP and WB could be an alternative to NA for the stone column, although their strengths were lower than those of NA according to the shear strength parameters. However, it was thought that these waste aggregates should be used by improving their insufficient properties, such as water absorption and crushing behavior.

Keywords: Geotechnics · Recycled Asphalt Pavements · Waste Bricks · Stone Column

1 Introduction

If the soil doesn't have the geotechnical characteristics necessary to support a footing, either the soil's geotechnical characteristics could be improved or the foundation's design could be altered. Engineers have been working on different ways to improve the soil for

a long time so that buildings can be built on it [1]. Since the 1970s, the stone column method has been used in many countries around the world. This is because it is easy to build stone columns and can solve problems with settlement and low stability in soft soil [1–3]. In the stone column method, a group of cylinder-shaped columns improves the soil. These columns generally are built by filling them with natural aggregates and compacting them. Researchers did both experimental and numerical studies on stone columns to figure out how they work and improve them [1–6].

Many researchers looked into whether construction and demolition wastes such as recycled concrete aggregates (RCA), recycled asphalt pavements (RAP), and waste bricks (WB) could be used as filler instead of natural aggregates (NA) in geotechnical applications [7–17]. They reported that many types of recycled aggregates could be used as fillers. Therefore, stone columns could be a great way to use recycled aggregates [18–21]. Since a lot of natural aggregates are needed to build a lot of stone columns, it makes sense to use recycled materials in stone columns in places where there aren't enough of those aggregates to go around. Also, reusing and recycling the debris produced during construction and demolition will help with waste management. However, Zukri and Nazir [20] reported that there haven't been many studies on using recycled materials in stone columns, so more research is needed. Shahverdi and Haddad [21] tested stone columns with recycled bricks and recycled concrete in the lab. As a result, they mentioned that recycled aggregates worked well but that more research should be done on the subject. They also reported that different recycled materials could be investigated.

It has been seen from the literature that the researches on the use of waste aggregates in stone column construction are limited. This study looks into whether or not RAP or WB can be used instead of NA to build stone columns. First, RAP and WB were obtained from a local government municipality. After that, NA supplied from a quarry. To figure out the geotechnical properties of aggregate specimens, tests like pycnometer, minimum and maximum dry unit weights, water absorption, California bearing ratio (CBR), aggregate impact value (AIV) and large-scale direct shear tests were done in the lab. The outcomes of the sieve analyses carried out on the RAP, WB, and NA determined a suitable gradation for stone columns. The maximum and minimum unit weight of RAP, WB, and NA with this gradation, which were usable for stone columns, were found. For this purpose, a series of model tests in a test tank with a 30 cm diameter and 30 cm height was carried out to determine the unit weight values of aggregates when a stone column is built with the RAP, WB, or NA. In the model tests, soil from a nearby quarry was used to fill the tank and create soft soil conditions. In the middle of the soft soil, stone columns made of RAP, WB, and NA and 5 cm in diameter were put in place. The quantities of materials used to make the stone columns determined the unit weights values. After that, CBR, AIV and direct shear tests were done on RAP, WB, and NA, which had their unit weights already determined with the model tests. The test results from RAP and WB were presented in comparison with those of NA.

2   Material and Method

2.1   Supply of Aggregates

In this study, two different construction and demolition waste materials were preferred. These were recycled asphalt pavement (RAP) and waste brick (WB). The RAP was obtained from the waste formed due to the renovation of a road in Malatya/Türkiye that had served for more than 20 years. The WB was taken from a building roof in Malatya/Türkiye, which reached the end of its useful life as after being used for more than 25 years. In order to compare the usage of the RAP and WB supplied within the scope of this study in the stone column, the experiments were also carried out on the natural aggregate (NA). For this reason, the NA was obtained from a quarry in Malatya province.

2.2   Grain Sizes of Aggregates

The supplied aggregates were crushed with the help of a jaw crusher, and thus test samples in the diameter range of 2–6 mm were obtained. It was seen that this range was used in the literature for stone column construction [22]. Care was taken to ensure that the grain size distributions of all aggregates (RAP, WB and NA) were quite similar. Because it was thought to be a very important criterion in order to compare the results of the experiments on these aggregates with each other. After crushing was completed, sieve analysis tests were performed on all aggregates. ASTM D 422–63 was taken into account while performing the sieve analysis tests. All aggregate samples were classified as SP (poorly-graded sand) according to the unified soil classification system (ASTM D 2487–11). The gradation curves obtained as a result of the sieve analyses are presented in Fig. 1. The images of the aggregates used in this study are given in Fig. 2.
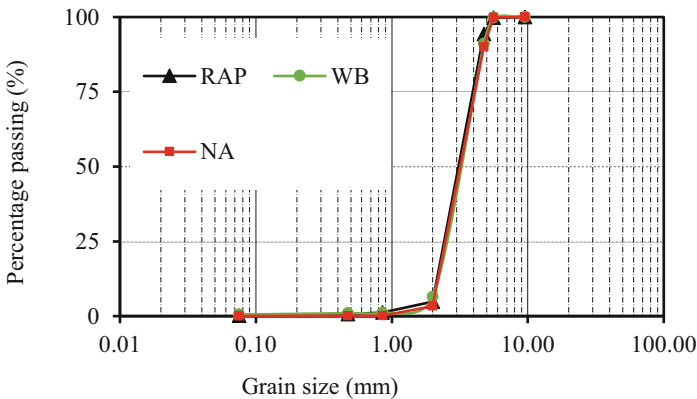
Fig. 1.   Gradation curves of the aggregate samples.

2.3 Tests on Aggregate Samples

In order to determine the physical and mechanical properties of the aggregates, pycnometer, minimum and maximum dry unit weights, water absorption, California bearing ratio (CBR), aggregate impact value (AIV), and large-scale direct shear tests were carried out.

The pycnometer test to find the specific gravity of the aggregates was carried out in accordance with ASTM C 127–12 standards. In order to determine the minimum and maximum dry unit weights and the water absorption values of the aggregates, tests were carried out according to ASTM D 4253 and D 4254 standards.
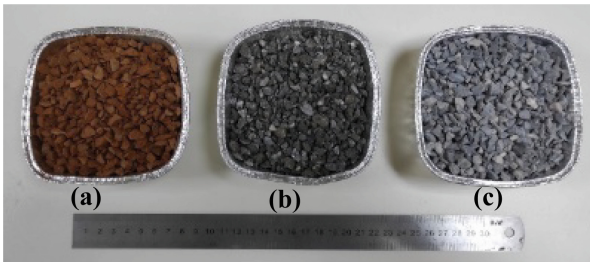
Fig. 2. Images of the WB (a), RAP (b), and NA (c).

Before performing the other tests, model stone columns were built with these aggregates in weak soil. Thus, the unit weight values required for other tests were determined. The undrained shear strength, water content, and soil classification of the weak soil on which the stone column was built were determined to be 50.5 kPa, 32%, and MH (high-plasticity silt), respectively. Figure 3a shows a photograph of the model stone column. In stone column construction, firstly, the weak soil was placed layer by layer into a 30 cm diameter and 30 cm height steel tank. While placing the weak soil, the water content and strength values of each layer were checked. To assess the moisture content of individual layers, soil samples were collected and subsequently dried in an oven to determine their water content. Furthermore, a hand penetrometer was used to ascertain the undrained shear strength of each layer, providing an evaluation of their respective strength values. After that, a hole with a diameter of 5 cm was drilled in the center of the steel tank. After the drilling was complete, the aggregate samples were placed in the hole, layer by layer. In the preparation process of the stone column, a special designed hammer was utilized to aid in compacting the aggregates. This hammer shares some similarities with the standard Proctor hammer. Prior to the construction of the model stone column, a preliminary test was carried out to compact the aggregate samples at predetermined relative density values. Then, the energy required for compacting the samples was determined. At the end of this process, the unit weights of the aggregates were determined by dividing the weight of the aggregate, which was the stone column material, by the volume of the hole. The determined unit weights of the aggregates were 15.11, 12.12, and 16.15 kN/m^3 for the RAP, WB, and NA, respectively.

The CBR tests were applied to determine the load-displacement behavior of the aggregates. According to ASTM D1883–99, the CBR tests were performed by penetrating a cylindrical piston approximately 50 mm in diameter into the samples in a mold at a rate of 1.27 mm/min. To conduct the CBR test, aggregates were carefully arranged in layers within the CBR mold, which had a diameter of approximately 152.4 mm, following the guidelines outlined in ASTM D1883–99. The unit weight aimed for during this process matched the unit weight obtained from the stone column model tests. After the CBR tests were completed, both load-displacement curves were plotted, and percentage values were calculated relative to the reference value given in ASTM D1883–99.

The AIV tests were performed to determine a relative measure of aggregates' resistance to sudden shock or impact (Fig. 3b). First of all, the aggregate, which was prepared at the unit weight determined in the model stone column test, was compacted in a steel mold in accordance with the standard. After compaction was complete, a series of standard impacts were applied to the aggregate test specimen by means of a falling weight (a mass of 4 kg falling from a height of 38 cm was repeated 15 times). At the end of the impact process, the aggregate sample was sieved through a 2.36-mm test sieve. The AIV number was determined by dividing the tested aggregate mass by the aggregate mass passing through the sieve (BS 812–112:1990).

The direct shear test is generally used to determine the internal friction angle and cohesion values, which are the shear strength parameters of soils. Generally, a small-scale (traditional) direct shear test device is used to determine the shear strength parameters of soils. However, the small size of this experimental setup has some limitations. For a test box, the minimum width shall be 5 cm and not less than ten times the maximum grain size. However, the minimum initial thickness of the test box shall be 1.3 cm and not less than six times the maximum grain size. (ASTM-D 3080–04). To overcome this limitation and to determine the shear strength parameters of aggregates more realistically, large-scale direct shear tests were performed in this study. Figure 3c shows the large-scale direct shear test device. The aggregates samples prepared for the tests were placed in a large-scale direct shear box of 30 cm x 30 cm x 20 cm (width x length x height). The aggregates samples were placed in the mold layer by layer. It was ensured that the unit weight of the aggregate in the mold was the same as that determined during the model stone column construction. After placing the aggregate sample into the mold, the mold was placed in the test setup and subjected to shear stresses: 50 kPa, 100 kPa, and 200 kPa.
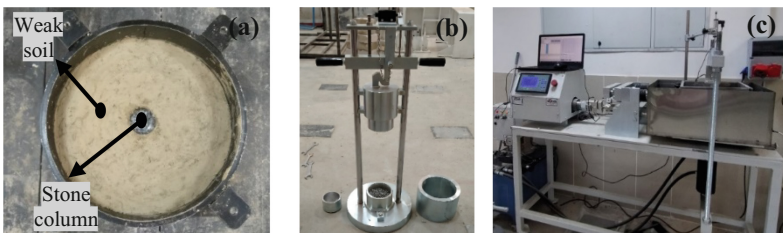
Fig. 3. Model stone column (a), AIV test device (b), and large-scale direct shear test device (c).

3   Results and Discussion

3.1   Pycnometer Tests

The specific gravity values (G_s) obtained as a result of the pycnometer tests performed on the aggregates are shown in Fig. 4. When the studies in the literature [8–10, 23, 24] were examined, it was seen that the specific gravity value was between 2.53 and 2.76. The obtained values in this study were found to be in this range. In addition, it was observed that the specific gravities of natural aggregates and waste aggregates were different from each other. The reason for this was thought to be the difference in microstructure. To clarify, the specific density value of the aggregate was influenced by the characteristics of the individual grains that composed it. For example, in the case of WB aggregate, the grains were lighter in weight compared to the other aggregates, resulting in the lowest specific density value for WB.
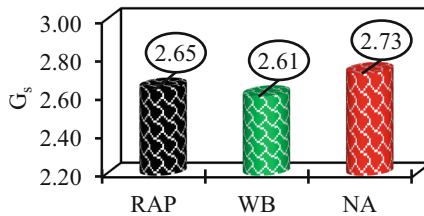
Fig. 4. Specific gravity values of the aggregates.

3.2   Minimum and Maximum Dry Unit Weights Tests

The minimum and maximum dry unit weight values (γ_{dmin} and γ_{dmax}), as well as the unit weight values (γ) found by the model stone column tests, are presented in Fig. 5. From these results, it was seen that the lightest aggregate was the WB and the heaviest aggregate was the NA. While the NA was in the expected state, it was thought that the high void ratio of the WB caused this situation. In addition, the unit weight values found from the model stone column tests were between the minimum and maximum unit weight values. However, the fact that the unit weight values were very close to the maximum dry weight values indicated that the stone columns were properly compacted.
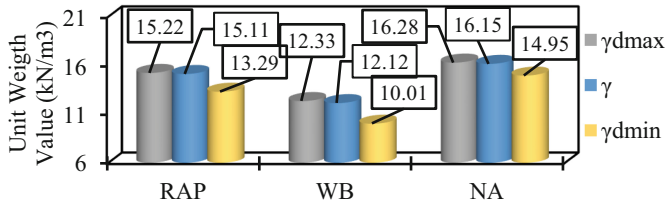
Fig. 5. Minimum and maximum dry unit weights of the aggregates.

3.3   Water Absorption Tests

Figure 6 shows the water absorption values of the aggregates. It is clearly seen from this figure that the highest and lowest water absorption values belong to the WB and the RAP, respectively. It was estimated that the clay, etc., in the WB increased the water absorption potential. Given these values, it could be problematic if drainage is the primary purpose of using WB in stone column construction. However, the reason for this behavior in the RAP was thought to be the very low water absorption potential of bitumen, etc. in it.
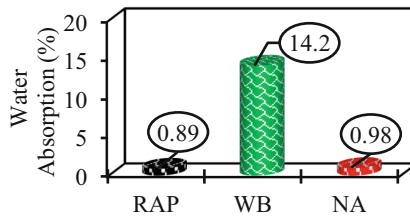
Fig. 6. Water absorption values of the aggregates.

3.4   CBR Tests

The load-displacement behaviors of the aggregates determined as a result of CBR tests are shown in Fig. 7. Besides, as a result of these tests, CBR values were calculated as 10.42%, 14.91%, and 25.01% for RAP, WB, and NA, respectively. As seen from these test results, the NA is the best and the RAP is the worst in terms of CBR values. These results show that these waste aggregates may not be suitable for use in filling. Furthermore, the specimens' poorly graded grain size distribution suggests that they would not be appropriate as fill material.
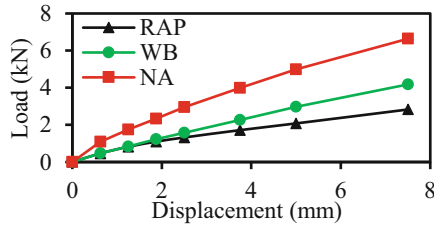
Fig. 7. Load-displacement behavior of the aggregates.

3.5   Aggregate Impact Value Tests

The aggregate impact values (AIV) of the aggregates are shown in Fig. 8. The results clearly show that the aggregate with the highest resistance to crushing and abrasion was the NA, while the WB was the least resistant. In addition, it was predicted that the RAP-built stone column would be more durable against crushing and abrasion than the WB-built stone column.
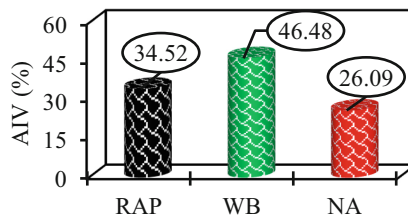
Fig. 8. AIV of the aggregates.

3.6   Large-Scale Direct Shear Tests

Figure 9 shows the curves of the shear force (T)-horizontal displacement (ΔL) behavior from the large-scale direct shear tests. The failure envelopes determined as a result of this test are also presented in Fig. 10. According to Figs. 9 and 10, it was seen that the aggregate with the highest shear strength was NA. While the shear strength of the WB was higher than that of the RAP, the shear strength of both was close to that of the NA. The cohesion (c) values of the RAP, the WB, and the NA were determined as 9.9 kPa, 14.7 kPa, and 1.6 kPa, respectively. The internal friction angle (φ) values of the RAP, the WB, and the NA were also determined as 39.5°, 41.0°, and 47.8°, respectively.

One of the most important parameters affecting the behavior of the stone column is the shear strength parameters of the aggregate from which it is made. Therefore, it was thought that the WB and the RAP may be sufficient in terms of shear strength parameters for stone column construction. However, it would be better to improve the shear strength parameters of the WB and the RAP by various methods, making them similar to those of the NA. In addition, as seen in Fig. 9, the least displacement is required for the NA to

reach the peak shear force, while the most displacement is required for the RAP. It may give an idea if they are used in stone columns.
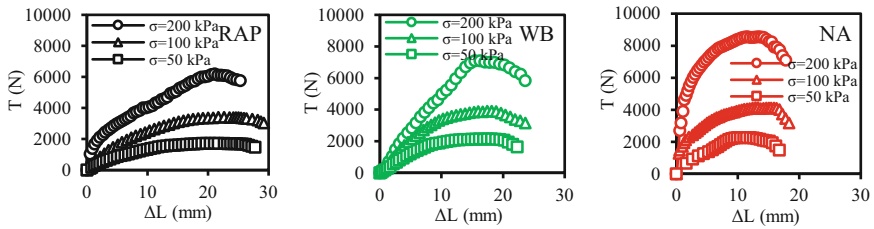
Fig. 9. Shear force-horizontal displacement behavior of the aggregates.
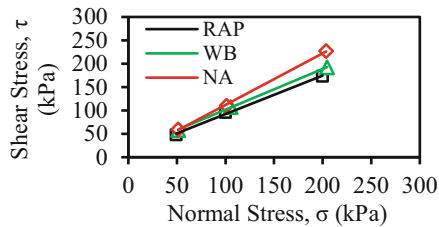
Fig. 10. Failure envelopes of the aggregates.

4   Conclusions

In this study, some properties of two different waste aggregates (RAP and WB) planned to be used in stone columns were examined, and then their properties were compared with those of NA. The results obtained as a result of this study are summarized below:

- First of all, regardless of all the results found, building stone columns with waste aggregates was just like building with natural aggregate. In other words, no difficulties were encountered during the construction phase.
- It has been determined that the specific gravity values of the waste aggregates were within the range described in some studies in the literature.
- Comparing waste aggregates revealed that WB aggregates were lighter than RAP aggregates.
- Due to the differences in grains present in WB and RAP, it was found that WB had a highwater absorption, while RAP had a relatively lower water absorption. As a result, it could be recommended that WB not be used as a fill material for stone columns that are built to offer drainage.
- It was determined that the aggregate with the highest resistance to crushing and abrasion among the waste aggregates was RAP. Therefore, it was predicted that the stone column constructed with RAP could be more resistant to abrasion and crushing than the one constructed with WB.

- In terms of shear strength parameters, it was thought that WB and RAP could be sufficient for stone column construction. Because the shear resistance parameters of these waste aggregates were determined to be close to those of the natural aggregate. However, it is recommended that all insufficient properties of waste aggregates should be improved in order to make stone columns with waste aggregates.
- Reusing waste aggregates will contribute to nature and the economy. Therefore, it is important to use waste aggregates in stone column construction. However, before using waste aggregates, it is essential to determine all their properties. Therefore, as a continuation of this study, the bearing capacity and settlement behavior of stone columns should be determined. In addition, geosynthetics could be used to improve the behavior of stone columns built with waste aggregates.

References

1. Demir, A., Sarici, T.: Bearing capacity of footing supported by geogrid encased stone columns on soft soil. Geomech. Eng. **12**(3), 417–439 (2017). https://doi.org/10.12989/gae.2017.12.3.417
2. Isaac, D.S., Girish, M.S.: Suitability of different materials for stone column construction. Electro. J. Geotech. Eng. **14**, 2–12 (2009)
3. Demir, A., Sarici, T.: Bearing capacity and bulging behavior of geogrid encased stone columns. Selçuk Üniversitesi Mühendislik, Bilim Ve Teknoloji Dergisi **4**(2), 131–144 (2016). https://doi.org/10.15317/Scitech.2016218525
4. Han, J., Ye, S.L.: A theoretical solution for consolidation rates of stone column-reinforced foundations accounting for smear and well resistance effects. Int. J. Geomech. **2**(2), 135–151 (2002). https://doi.org/10.1061/(ASCE)1532-3641(2002)2:2(135)
5. Andreou, P., Papadopoulos, V.: Modelling stone columns in soft clay. In: Proceeding of the 6th European Conference on Numerical Methods in Geotechnical Engineering, Graz, Austria, pp. 777–780 (2006)
6. Ambily, A.P., Gandhi, S.R.: Behavior of stone columns based on experimental and FEM analysis. J. Geotechn. Geoenviron. Eng. **133**(4), 405–415 (2007). https://doi.org/10.1061/(ASCE)1090-0241(2007)133:4(405)
7. Arulrajah, A., Piratheepan, J., Aatheesan, T., Bo, M.W.: Geotechnical properties of recycled crushed brick in pavement applications. J. Mater. Civ. Eng. **23**(10), 1444–1452 (2011). https://doi.org/10.1061/(ASCE)MT.1943-5533.0000319
8. Arulrajah, A., Piratheepan, J., Disfani, M.M., Bo, M.W.: Geotechnical and geoenvironmental properties of recycled construction and demolition materials in pavement subbase applications. J. Mater. Civ. Eng. **25**(8), 1077–1088 (2013). https://doi.org/10.1061/(ASCE)MT.1943-5533.0000652
9. Arulrajah, A., Piratheepan, J., Disfani, M.M.: Reclaimed asphalt pavement and recycled concrete aggregate blends in pavement subbases: laboratory and field evaluation. J. Mater. Civ. Eng. **26**(2), 349–357 (2014). https://doi.org/10.1061/(ASCE)MT.1943-5533.0000850
10. Gabr, A.R., Cameron, D.A.: Properties of recycled concrete aggregate for unbound pavement construction. J. Mater. Civ. Eng. **24**(6), 754–764 (2012). https://doi.org/10.1061/(ASCE)MT.1943-5533.0000447
11. Sangiorgi, C., Lantieri, C., Dondi, G.: Construction and demolition waste recycling: an application for road construction. Int. J. Pavement Eng. **16**(6), 530–537 (2013). https://doi.org/10.1080/10298436.2014.943134

12. Saribas, I., Ok, B.: Seismic performance of recycled aggregate–filled cantilever reinforced concrete retaining walls. Adv. Mech. Eng. **11**(4), 1–11 (2019). https://doi.org/10.1177/1687814019838112

13. Saribas, I., Ok, B.: The numerical simulation of soil–structure interaction containing sustainable materials. In: Proceedings of the Institution of Civil Engineers – Engineering Sustainability (2022). https://doi.org/10.1680/jensu.22.00062

14. Geckil, T., Sarici, T., Ok, B.: Model studies on recycled whole rubber tyre reinforced granular fillings on weak soil. Revista de la construcción **21**(2), 264–280 (2022). https://doi.org/10.7764/rdlc.21.2.264

15. Ok, B., Sarici, T., Talaslioglu, T., Yildiz, A.: Geotechnical properties of recycled construction and demolition materials for filling applications. Transp. Geotech. **24**, 100380 (2020). https://doi.org/10.1016/j.trgeo.2020.100380

16. Ok, B., Sarici, T., Demir, A., Talaslioglu, T., Yildiz, A.: Investigation of construction and demolition materials reinforced by geosynthetics. In: Proceedings of the Institution of Civil Engineers – Engineering Sustainability (2023). https://doi.org/10.1680/jensu.22.00077

17. Sarici, T., Ok, B., Mert, A., Çömez, Ş.: The resilient modulus of hybrid construction and demolition wastes reinforced by a geogrid. Acta Geotechnica Slovenica **19**, 2–14 (2023). https://doi.org/10.18690/actageotechslov.19.2.2-14.2022

18. Egan, D., Slocombe, B.C.: Demonstrating environmental benefits of ground improvement. Proc. Inst. Civil Eng. – Ground Improv. **163**(1), 63–69 (2010). https://doi.org/10.1680/grim.2010.163.1.63

19. Demir, S., Mokarram, F.R., Ozener, P.: The sustainable design of granular columns based on laboratory model tests. In: De, A., Reddy, K.R., Yesiller, N., Zekkos, D., Farid, A. (eds.) Geo-Chicago 2016, pp. 893–903. ASCE, Chicago, IL, USA (2016). https://doi.org/10.1061/9780784480144.089

20. Zukri, A., Nazir, R.: Sustainable materials used as stone column filler: a short review. In: IOP Conference Series: Materials Science and Engineering, vol. 342, p. 012001 (2018). https://doi.org/10.1088/1757-899X/342/1/012001

21. Shahverdi, M., Haddad, A.: Use of recycled materials in floating stone columns. Proc. Inst. Civil Eng. – Constr. Mater. **173**(2), 99–108 (2019). https://doi.org/10.1680/jcoma.18.00086

22. Deb, K., Samadhiya, N.K., Namdeo, J.B.: Laboratory model studies on unreinforced and geogrid-reinforced sand bed over stone column-improved soft clay. Geotext. Geomembr. **29**(2), 190–196 (2011). https://doi.org/10.1016/j.geotexmem.2010.06.004

23. Cerni, G., Cardone, F., Bocci, M.: Permanent deformation behaviour of unbound recycled mixtures. Constr. Build. Mater. **37**, 573–580 (2012). https://doi.org/10.1016/j.conbuildmat.2012.07.062

24. Park, T.: Application of construction and building debris as base and subbase materials in rigid pavement. J. Transp. Eng. **129**, 558–563 (2003). https://doi.org/10.1061/(ASCE)0733-947X(2003)129:5(558)

Seismic Site Response Analysis of the Famagusta Region: Investigation of Amplification and Attenuation Characteristics of the Local Soil Strata

Hamza Saeed[✉] , Eris Uygar , and Zalihe Nalbantoglu

Civil Engineering Department, Eastern Mediterranean University, Famagusta, Northern Cyprus, Turkey
{hamza.saeed,eris.uygar,zalihe.nalbantoglu}@emu.edu.tr

Abstract. Seismic site response analysis is crucial for geotechnical engineers as it defines the dynamic behaviour of soils and rocks subjected to earthquake-induced ground motion. In this research work, an extensive site response analysis of the Famagusta region located in the eastern part of Cyprus, known for its seismic activity, is conducted to investigate the amplification and attenuation characteristics of the local site conditions. One-dimensional equivalent linear analysis is conducted using PROSHAKE software consisting of multiple soil layers with varying properties, ranging from soft to stiff alluvial deposit formations. The ground motion input consists of a suite of recorded earthquakes embedded in the software. The analysis also includes the effect of ground motion input along with varying soil conditions. The analysis results indicated that the local soil strata properties significantly influenced seismic waves' amplification and attenuation characteristics. The soft alluvial shallow deposits amplified seismic waves and relatively higher displacements. In contrast, the stiff, deep alluvial deposits showed attenuated high-frequency waves. The analysis also highlighted the significance of seismic-induced ground displacement, primarily linked with selecting ground motion and soil parameters. The results of this research work can be utilised to carry out the seismic hazard assessment of the region and earthquake engineering design, which will contribute to the local community's safety.

Keywords: Earthquake engineering · Equivalent linear analysis · Seismic waves · Site response analysis

1 Introduction

In geotechnical engineering, seismic site response analysis plays a crucial role in understanding the soil and rock behaviour subjected to seismic waves. The key aspect in site response analysis is to evaluate the dynamic characteristics of the strata and the amplification and attenuation of seismic waves propagating through soil layers and their potential seismic hazard. The key analysis involves the potential of amplifying or deamplification of seismic waves through different soil layers and estimating ground motion

at the ground surface. In addition, in the case of the amplification of waves, the dominant frequency also plays a critical role in designing structures to minimise the resonance effects. For sites with granular media, the liquefaction susceptibility is also assessed and identified to minimise the risk. Since the ground motions and their corresponding seismic design parameters play a critical role in structural design, such site response analysis can generate the ground motion time history, and various seismic design parameters, such as peak ground acceleration and response spectra, can be obtained.

Famagusta Bay in Northern Cyprus is located in an active earthquake region surrounded by six active fault lines, namely Florence Rise (west), Paphos Fault (southwest), Cyprian Arc (south and extending to the northeast), Ovgus fault (north), East Anatolian fault (northeast), and Dead Sea fault (east). Famagusta Bay coastlines are well-known for their historical earthquakes as the ancient city of Salamis is still buried under the sand due to seismic induced liquefaction phenomenon [1, 2]. In addition, the laboratory testing also showed the potential of liquefaction susceptibility of Famagusta coastlines as the granular deposits are deposited in a loose state [3, 4]. In this research work, a detailed seismic response analysis of two sites in the Famagusta region is analysed to evaluate the potential seismic hazards of the region subjected to various seismic waves.

2   Research Methodology

The research methodology comprises two selected sites in the Famagusta region, as illustrated in Fig. 1-a and the borehole data indicating the standard penetration test results are highlighted in Fig. 1-b. The seismic response analysis is carried out as a one-dimensional equivalent linear in PROSHAKE software. The soil strata are primarily composed of soft to stiff clay layers and sand layers sandwiched in between. A range of ground motions embedded within the PROSHAKE software were utilised. Deterministic Seismic Hazard Analysis (DSHA) was performed beforehand to analyse which ground motions are applicable in this study. The primary reason for DSHA is to obtain the attenuation relationships of the site based on the fault lines located nearby for accurate analysis rather than just applying the set of ground motions in the software.

3   Results and Discussions

This section presents the findings of the seismic site response analysis, in which the DSHA results are discussed first. The DSHA analysis provides insights into the seismic hazard analysis of the two aforementioned sites, and the attenuation relationships was further utilised in analysing the 1-D equivalent linear seismic site response analysis using PROSHAKE software.

3.1   Deterministic Seismic Hazard Analysis

Deterministic seismic hazard analysis (DSHA) is a method considered to estimate the potential ground shaking and seismic hazards for specified locations. This method involves a deterministic approach considering predefined seismic events or scenarios
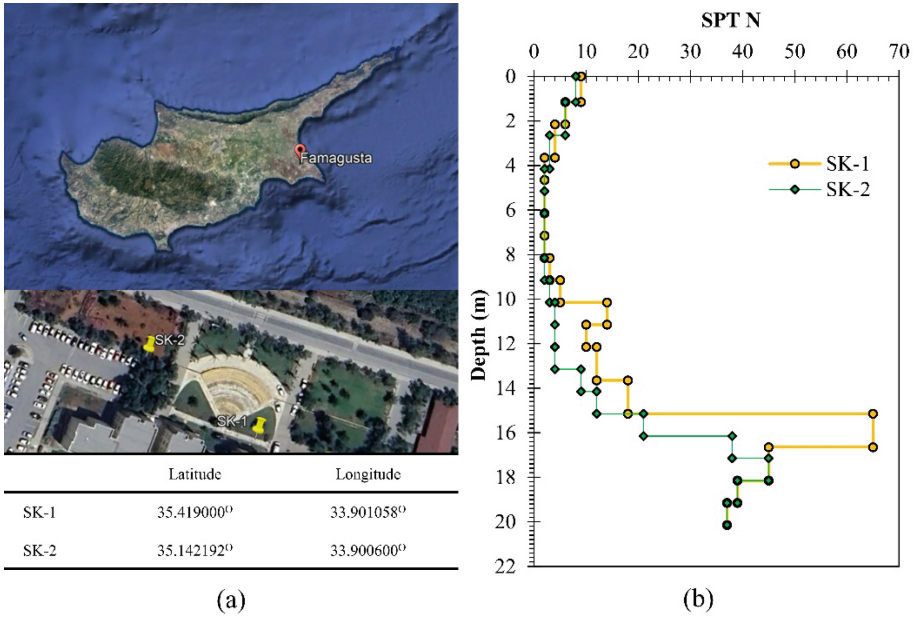
Fig. 1. Seismic site response analysis (a) site location and (b) SPT borehole data.

with specific characteristics. These characteristics involve earthquake magnitude and source-to-site distance. A combined effect of geological, geophysical, and geotechnical data is used in DSHA to model the propagation of seismic waves, taking into account the local site conditions.

Figure 2 illustrates the identification and characterisation of all seismic sources capable of producing ground motion [5–7]. In addition, in Fig. 3 (b-d), the shortest distances from the source to the site are illustrated, obtained through plotting the concentric circles of an equal incremental radius of approximately 10 kms. Figure 3 shows that the critical seismic sources for both sites are Ovgus and Cyprian Arc faults, as the sites are located relatively closer. The proximity of the Ovgus and Cyprian Arc faults can significantly impact the seismic hazard levels for both sites. Since the attenuation relationships are correlated with the source-to-site distance, these faults will generate stronger ground motions than others. Based on the data in Fig. 3 (h), the attenuation relationships calculated for all sites are tabulated in Fig. 4 (c) and were evaluated using Eqs. 1 [8] and 2 [9]. Since both Eqs. 1 and 2 are also a function of earthquake magnitude, two scenarios were adopted. The first case is the observed maximum magnitude in the seismic sources, as illustrated in Fig. 2, and second case is estimation of maximum magnitude a fault can generate based on Wells and Coppersmith [10] empirical relationship (Eqs. 3 and 4).

$$ln\ PHA(gals) = -4.141 + 0.868M - 1.09ln\left(R + e^{0.7M}\right) \tag{1}$$

$$ln\ PHA(gals) = 6.74 + 0.859M - 1.80ln(R + 25) \tag{2}$$

$$M_w = 5.16 + 1.12 log(L) \left[Strike\ Slip \right] \qquad (3)$$

$$M_w = 5.00 + 1.32 log(L) [Normal] \qquad (4)$$

where, PHA is the peak horizontal acceleration, M is the magnitude, R is the source-to-site distance, and L is the length of the fault.
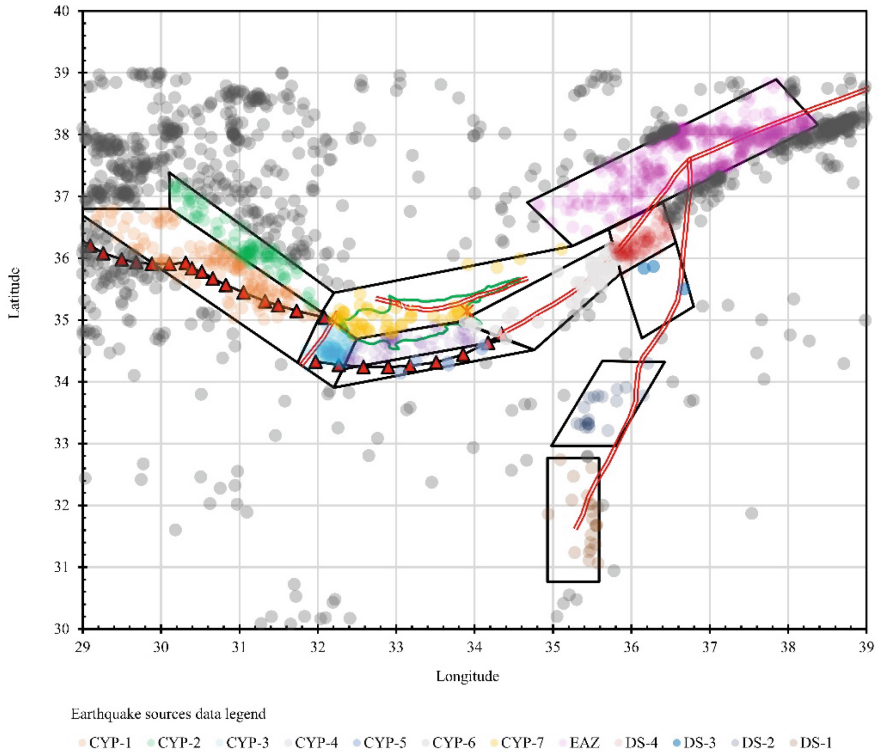
Fig. 2. Identification and characteristics of seismic sources and earthquake data [5–7].

From Fig. 4 (a, b), the magnitude calculated using empirical relationship clearly generated higher earthquake magnitude compared to the observed earthquakes, which might be illogical. Nevertheless, the recent earthquake in Turkey in 2023 showed the importance of DSHA analysis, where the magnitude obtained through DSHA analysis is 8.3, whereas the actual earthquake magnitude was recorded as 7.8, which was not anticipated of this high magnitude. In this aspect, the probabilistic seismic hazard analysis (PSHA) is required to assess the probability of that earthquake magnitude obtained from DSHA. The DSHA is considered as an extreme case scenario; therefore, the PSHA analysis of the selected sites is omitted in this research work. Similarly, Fig. 4 (c) illustrates the PHA
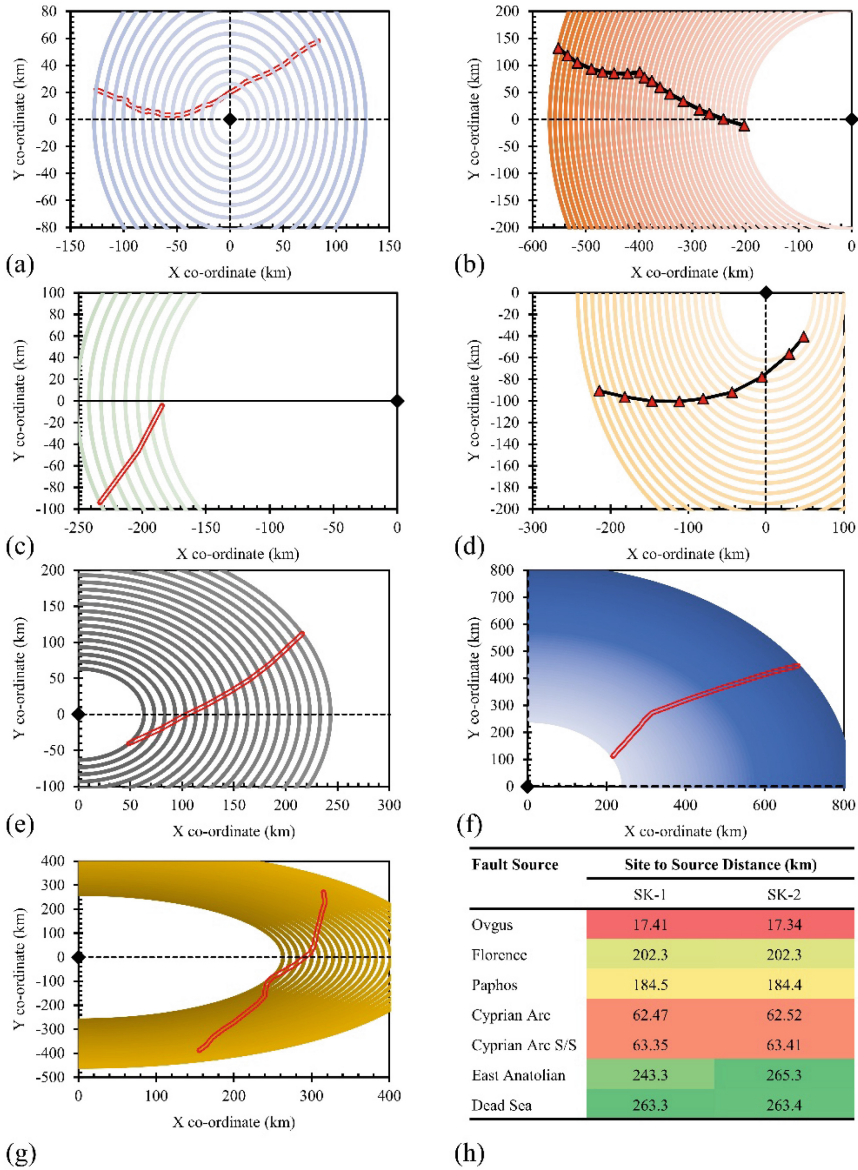
Fig. 3. Source to site (SK-1 & SK-2) distances (a) Ovgus fault, (b) Florence Rise fault, (c) Paphos fault, (d) Cyprian Arc fault, (e) Cyprian Arc strike-slip fault, (f) East Anatolian fault, (g) Dead Sea fault, and (h) distance numeric values.

Fault Source	Site to Source Distance (km)	
	SK-1	SK-2
Ovgus	17.41	17.34
Florence	202.3	202.3
Paphos	184.5	184.4
Cyprian Arc	62.47	62.52
Cyprian Arc S/S	63.35	63.41
East Anatolian	243.3	265.3
Dead Sea	263.3	263.4

values of the corresponding earthquakes shown in Fig. 4 (a,b). The general perception observed is that Eq. 1 resulted in higher PHA values. Another aspect of Eqs. 1 and 2

is that they possess certain limitations as Campbell's [8] equation is only applicable for source-to-site distance within 50 km, and for Cornel et al. [9], the distance is between 20 to 200 kms.
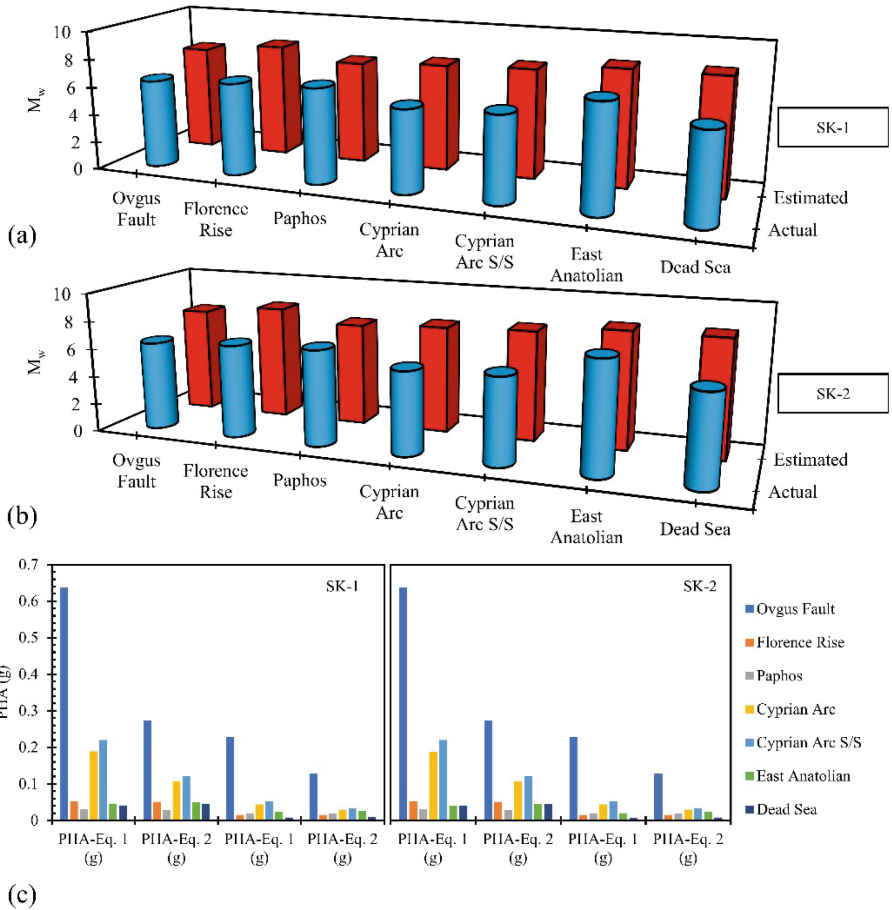
Fig. 4. Peak horizontal acceleration for SK-1 and SK-2 for all fault lines.

3.2 Seismic Site Response Analysis

The shear wave velocity (V_s) is calculated for cohesionless and cohesive layers through SPT (N) values given in Eqs. 5 and 6 [11], respectively.

$$V_s = 100.3 \ N^{0.338} \tag{5}$$

$$V_s = 94.4 \ N^{0.379} \tag{6}$$

The depth to bedrock is considered where N values are approximately 40 in both SK-1 and SK-2 borehole data. For SK-1 and SK-2, the bedrock depth is 19.15 m. The SK-1 borehole is divided into 13 layers, whereas the SK-2 is divided into 12. Based on the obtained parameters from correlations, the modulus reduction curves for SK-1 are illustrated in Fig. 5 (a) based on Ishibashi & Zhang's criteria. In this work, for comparison between methods, Vucetic & Dobry model is also evaluated (Fig. 5-b). In correspondence with Vucetic & Dobry, criteria yielded higher shear stress values for the top layer. In comparison with Fig. 5 (a), for layers 4 and 5, after 1% shear strain amplitude γ, strain hardening is observed. Whereas strain softening behaviour is observed afterwards (Layers 7–12). A point to be noted here is that in these layers, sand is present, and from such observed behaviour, these layers (10.5–15.5 m) can be considered critical layers, which can cause ground deformation as large volumetric strains will be accumulated beneath the strain hardening layers. Similarly, modulus reduction curves for SK-2 are illustrated in Fig. 5 (e) based on Ishibashi & Zhang and Vucetic & Dobry criteria are presented in Fig. 5 (f). The shear stress corresponding to the modulus reduction curve for both methods for SK-2 is illustrated in Fig. 5 (g,h). As observed from the soil profile, the soil composition and SPT values are not differing too much. Similar behaviour is observed for the SK-2 borehole regarding strain hardening and softening behaviour (Fig. 5-c,d). In terms of ground motions, seven earthquake records are utilised (Loma Prieta-GM1, El Centro-GM2, Petrolia/cape Mendocino-GM3, Taft Kern county-GM4, Northridge earthquake-GM5, Treasure Island Loma Prieta-GM6, Yerba Buena island Loma Prieta-GM7).

Figure 6 (a,b) illustrates the relative peak displacement occurring due to ground motions (GM1 – GM7) in SK-1 strata. Excessive displacements are observed in middle soil layers when GM-2 and GM-3 ground motion is simulated; in these earthquakes, the PGA values are higher at 0.344 g and 0.422 g. Such behaviour is due to low soil shear strength as observed in SPT values for mid layers approximately 4.5–10 m where the displacements are occurring. In addition, a PGA of 0.422 g resulted in the collapse of the soil model at the same depth. In comparison, Vucetic & Dobry model parameters yielded a complete distortion of strata for layers composed of sandy soil (10–13.7 m) hence again directing towards considering the said layer as a critical layer. The spectral acceleration of SK-1 strata is shown in Fig. 6 (c, d). The peak accelerations are amplified approximately 4.5 times more than PGA for GM3 and 5.2 times increase in GM-2 ground motions considering Ishibashi & Zhang model parameters. Whereas the Vucetic & Dobry model yielded lower amplification compared to 1.04 times for GM-3 and 1.5 times for GM-2, whereas GM6 and GM-5 yielded amplified accelerations. In contrast with the previous statement, the amplified acceleration results from Fast Fourier Transform show that dominant frequencies for GM-3 are 1.53 Hz and 1.82 for GM-3 and GM-2, respectively, whereas 1 Hz for GM-3 and 0.43 Hz for GM-2 are observed for Vucetic & Dobry model. For GM-7, the dominant frequency is 1.7 Hz (Fig. 6-e,f). In Fig. 6 (e), the amplification of ground motions compared to surface motion yielded higher wave application of GM-7 at multiple frequencies. The first peak of amplification (Fig. 6-e) and peak values of spectral acceleration (Fig. 6-c) are occurring in the range of 1.5–2.5 Hz. The peak amplification values are occurring as 2.4, 1.6, 1.5, 2.2, 2.1, 2.2, and 2.5 Hz for GM 1–7, respectively. Similarly, for Vucetic & Dobry model, the first peak of amplification (Fig. 6-f) and peak

values of spectral acceleration (Fig. 6-d) are occurring in the range of 0.5–2.4 Hz. The peak amplification values are occurring as 0.2, 2.2, 0.8, 0.5, 1.9, 1.8, 1.5, and 2.4 Hz for GM1–7, respectively. In comparison, the peak amplitudes occur under the same ground motions at lower frequencies for Vucetic & Dobry model parameters. In the SK-2 case, more severe and critical results are obtained, whereas a similar pattern is observed.
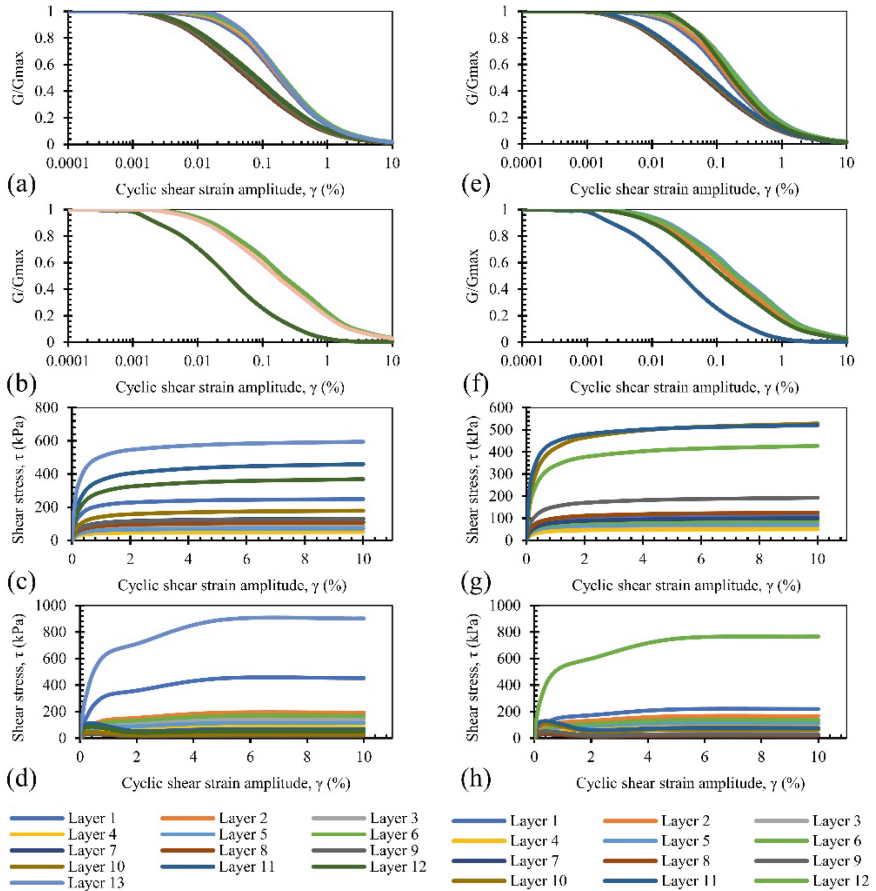
Fig. 5. SK-1 and SK-2 (a, b, e, f) modulus reduction curves and (c, d, g, h) backbone curves
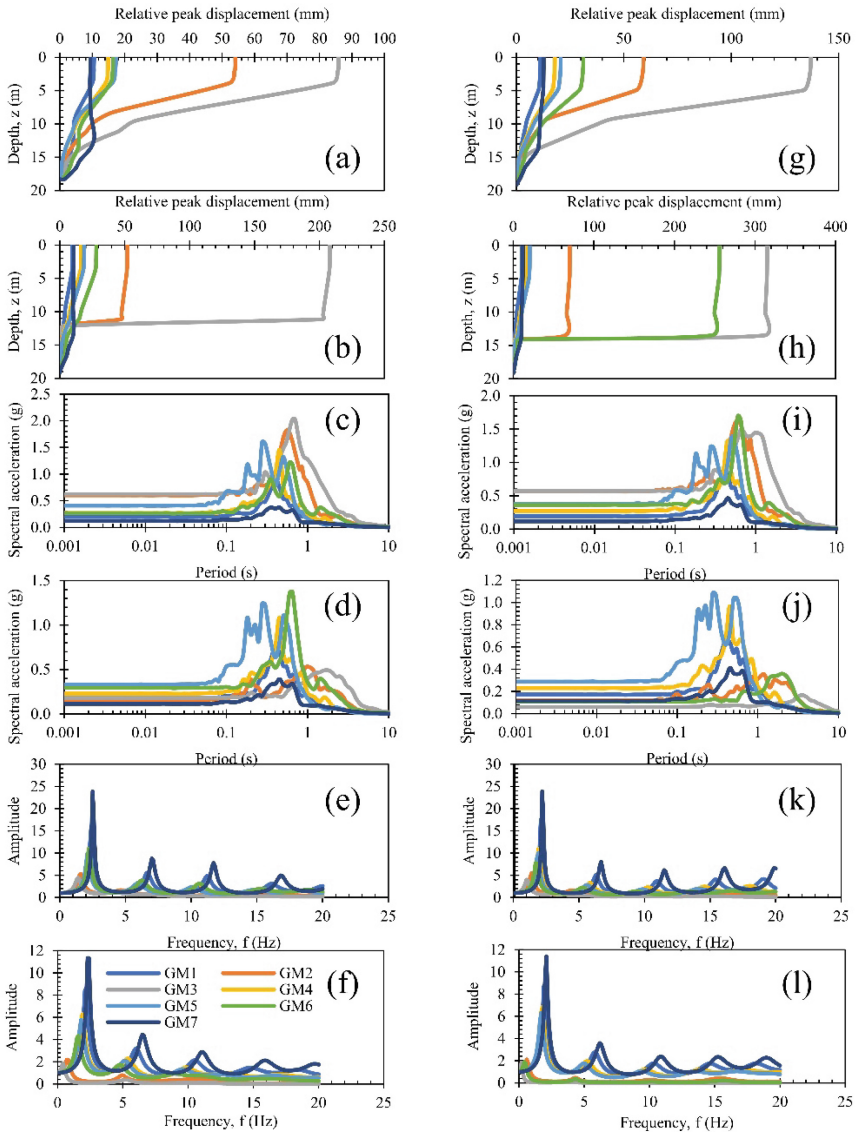
Fig. 6. SK-1 and SK-2 (a, b, g, h) relative peak displacement, (c, d, i, j) spectral acceleration, and (e, f, k, l) response spectra.

4 Conclusions

The following are the fundamental aspects concluded from this study:

- The seismic site response analysis is conducted to investigate the seismic hazard and site-specific effects at the two sites. The DSHA analysis revealed important insights into the seismic hazard of the sites. The Ovgus and Cyprian arc fault lines generated the critical scenario for the selected sites in Famagusta.
- The seismic site response analysis indicated that soft deposits, as determined by the soil profile and SPT data, led to significant displacements.
- Furthermore, the analysis demonstrated that the peak accelerations experienced at the sites were amplified compared to the actual ground motions.
- The frequency ranges obtained for sites are significant as it indicates that the site exhibits a higher vulnerability to seismic activity. This aspect suggests that the specific sites might experience a higher ground motion level than the reference ground motion.

References

1. Papadopoulou, A.I., Tika, T.M.: The effect of fines plasticity on monotonic undrained shear strength and liquefaction resistance of sands. Soil Dyn. Earthq. Eng. **88**, 191–206 (2016)
2. Öğretmen, N., Cosentino, D., Gliozzi, E., Cipollari, P., Iadanza, A., Yildirim, C.: Tsunami hazard in the eastern Mediterranean: geological evidence from the Anatolian coastal area (Silifke, southern Turkey). Nat. Hazards **79**, 1569–1589 (2015)
3. Saeed, H., Nalbantoglu, Z., Uygar, E.: Liquefaction susceptibility of beach sand containing plastic fines. Mar. Georesour. Geotechnol. **41**(1), 1–13 (2023)
4. Saeed, H., Uygar, E., Nalbantoglu, Z.: Critical state behaviour of carbonate sand containing plastic fines. In: 16th International Conference on Geotechnical Engineering, Lahore, Pakistan (2022)
5. Cagnan, Z., Tanircan, G.B.: Seismic hazard assessment for Cyprus. J. Seismolog. **14**, 225–246 (2010)
6. Harrison, R.W., et al.: Tectonic framework and late Cenozoic tectonic history of the northern part of Cyprus: implications for earthquake hazards and regional tectonics. J. Asian Earth Sci. **23**(2), 191–210 (2004)
7. Papaioannou, C.: A model for the shallow and intermediate depth seismic sources in the eastern Mediterranean region. Bollettino Di Geofisica Teorrica Ed Applicata **42**, 57–74 (2001)
8. Campbell, K.W.: Near-source attenuation of peak horizontal acceleration. Bull. Seismol. Soc. Am. **71**(6), 2039–2070 (1981)
9. Cornell, C.A., Banon, H., Shakal, A.F.: Seismic motion and response prediction alternatives. Earthq. Eng. Struct. Dynam. **7**(4), 295–315 (1979)
10. Wells, D.L., Coppersmith, K.J.: New empirical relationships among magnitude, rupture length, rupture width, rupture area, and surface displacement. Bull. Seismol. Soc. Am. **84**(4), 974–1002 (1994)
11. Kirar, B., Maheshwari, B.K., Muley, P.: Correlation between shear wave velocity (Vs) and SPT resistance (N) for Roorkee region. Int. J. Geosynthetics Ground Eng. **2**, 1–11 (2016)

Health and Safety

Occupational Health and Safety Practices in North Cyprus

Murude Celikag[1](✉) , Serife Bozkir[1] , and Fatma Cellatoglu[2]

[1] Department of Civil Engineering, Faculty of Engineering, Eastern Mediterranean University, Famagusta, Mersin 10, North Cyprus, Turkey
murude.celikag@emu.edu.tr

[2] Department of Labour, Ministry of Labour and Social Security, Nicosia, Mersin 10, North Cyprus, Turkey

Abstract. Occupational Health and Safety (OHS) is a field that has always existed from past to present, constantly renewing and developing itself with the needs of working life and the use of technological developments. For the successful implementation of internationally accepted OHS rules it is important to consider the working environment, workforce planning, development level and cultural structure of the country. In this article, the recent historical developments of the OHS laws, regulations and practices in North Cyprus and the effective factors are conveyed, the current situation and the plans are shared. The production of North Cyprus OHS Law and the related Regulations has considered the relevant European Union Directives, Laws and Regulations of the Republic of Turkey and country's condition. Despite present OHS laws and regulations in the North Cyprus, the implementation is insufficient since the OHS culture has not yet been established and the system has not been formed sufficiently. It is important for the state to improve the preventive inspection/audit quality with a continuous improvement perspective, not only to ensure the implementation of laws and regulations, but also to regulate the working life of society, to protect the employer by protecting its employees, to ensure continuity of work and increase efficiency, and to make the right contribution to the economy. Appropriate use of technological development by the Labour Department and workplaces will have a significant impact on the implementation of OSH laws and regulations. Addressing the following issues will make important contributions to the OHS practices to come to the right point: Reviewing the legal regulations related to Turkish and other third country nationals, who make up a significant proportion of those working in the TRNC, registering the employees, finding a solution to the language problem.

Keywords: EU directives · foreign employees · technology · preventive inspection

1   Introduction

1.1   Occupational Health and Safety (OHS) Definition

OHS is an inseparable part of daily life, which includes all aspects of society and concerns all segments of society, particularly, health and safety of employees, operational, production, and service safety, etc. The common definition of occupational health, which was adopted in 1950 by the Joint Occupational Health Committee of the International Labor Organization (ILO) and the World Health Organization (WHO), and revised in 1995, is given below [1]. The following three objectives are the main focal points of the occupational health:

  i. Developing and maintaining workers' health and working capacity.
 ii. Improving the working environment to make it suitable for OHS.
iii. Developing work organizations and working cultures in a way that supports occupational health and safety, promoting a positive social climate and smooth working, and increasing the productivity of enterprises.

The concept of work culture, in this context, means a reflection of the core value systems adopted by the undertaking concerned. Such a culture is reflected in management systems, personnel policy, participation principles, training policies and the quality management of the enterprise [1].

For the successful implementation of internationally accepted OHS rules it is important to consider the working environment, workforce planning, development level and cultural structure of the country. In this article, the recent historical developments of the OHS laws, regulations and practices in North Cyprus and the effective factors are conveyed, the current situation and the plans are shared.

To have a better understanding of the current stand of OHS in North Cyprus one needs to look at the brief history of OHS in the world. While doing that the concentration will be on the countries that are best regarding the application of OHS. This would help to better apprehend the developments and achievements in this country.

1.2   A Brief History on OHS

In the TRNC, there are several laws and regulations that regulate, implement and control OHS in workplaces. Before going into details about TRNC, it is necessary to understand why, when, and how OHS started to be implemented, developed, and to what point it has now reached in the countries like UK, USA, European Union, and Turkey, as being the main point of contact for TRNC. This will help to better analyze the situation in TRNC.

The foundations of OHS were laid in the United Kingdom (UK), the United States (USA) and in Turkey around 1800. Safety records of the UK and USA are among the best in terms of OHS applications and the fatality rates. The first OHS related laws and regulations were in sectors that involved in hazardous work related to miners and factory workers. In general, Laws and Regulations related to OHS date back to the 1960s. Even in some developed countries, laws came into force in the 1990s. 1966 Canada, 1967 Turkey, 1970 United States of America, 1974 United Kingdom, 1989 European Union, 1993 South Africa, 1994 Malaysia, 2002 People's Republic of China.

a) **United Kingdom (UK):** OHS legislation was prepared and enacted by the Health and Safety Executive (HSE) and local councils under the Act 1974 [2, 3]. OHS processes in the UK are proceeding in the form of risk assessment-based management rather than rulemaking.

b) **United States of America (USA):** With the OHS Law enacted in 1970, three agencies were created to manage it [4]. These are the OSH Administration (OSHA), the National OSH Institute and the OSH Review Commission [5]. Established in 1971, OSHA was mandated to regulate private employers in all 50 states, the District of Columbia, and other territories [6]. OSHA is an agency of the Department of Labor whose purpose is to create safe and healthy workplaces in the United States. It implements 5-year plans to achieve this goal. Within these plans, it conducts free or very low fees, audits and training and prepares publications [6].

c) **European Union (EU):** Member states of the EU have established competent authorities for the fulfillment of basic legal requirements regarding OSH. In 1996, the European Agency for Occupational Health and Safety (EU OSHA) was established. The European Commission created the first OSH European strategy in 2007–12 followed by the Strategic OHS framework for 2014–2020. The aim was to ensure that the EU continues to play a leading role in promoting high standards of work, both in Europe and internationally, in line with the Europe 2020 Strategy [7, 8].

d) **Turkey:** Turkey is very close to TRNC geographically, culturally, and politically. Hence developments in Turkey would become an example for TRNC to follow. OHS laws came into force in 2003 in Turkey [9]. Since then, numerous regulations related to OHS have been prepared and put in force. At the same time there is continuous update to the existing regulations. After Turkey's enforcement of OHS law TRNC followed in 2008 [10]. This followed by ensuring the harmonization of regulation with EU and Turkey. TRNC is a young and unrecognized state. However, considering the start date of the OHS law in 2008, and the developments happened since then the current situation cannot be underestimated. Nevertheless, there is still a long way to go. Further improvements and OHS achievements in TRNC will only be possible with the support of all workplaces, employees, and the state. The following section covers the OHS in TRNC.

2 OHS in Turkish Republic of Northern Cyprus

2.1 Brief Introduction to OHS in TRNC

Occupational Health and Safety (OHS) in Northern Cyprus was first addressed with the Factories Law, which came into force on April 02, 1957. There are two separate sections in this law, health, and safety. Under the health section, it discusses topics such as heat, ventilation, lighting, drainage of surfaces, while under the safety section, topics such as energy and transmission engines, protective parts of machines are discussed. However, this law included only production-oriented workplaces that were included in the definition of factory where raw materials are processed [11].

With the enactment of Labor Law No. 22/1992 in 1992, the Factories Law was repealed, and occupational health and safety began to be carried out within the scope of this law. With the Labor Law, the concept of "Workplace", which describes the place where the work is done, was introduced. With this Law,

- every employer is obliged to take the necessary measures to ensure the health and work safety of the workers working at the workplace, to provide the necessary conditions and to keep the tools and equipment in good order.
- employees are obliged to comply with the rules of occupational health and safety.
- work accidents, occupational diseases and dangerous events should be reported to the Labor Office within 2 working days.
- it was mentioned that working conditions should be determined for dangerous works, and that these articles (conditions) should be applied in all workplaces, including construction works.

Depending on this Law, some rules regarding the precautions to be taken in the related sectors have been determined with the 1992 Work (Occupational Health and Safety in Factories and Workplaces) Regulation, which came into force in 1992, and the Occupational Health and Safety Regulation in Construction, which entered into force in 1998. Until 2008, the occupational health and safety legal provisions, which were partially determined within the scope of the labor law and the relevant regulations created under this law, were tried to be implemented in the country [12–14].

The TRNC legal authority studied the OHS related developments in the world and particularly in the EU countries over the past years. With specific consideration of the EU directives, the Occupational Health and Safety Law was prepared by experts, unanimously approved by the Turkish Republic of Northern Cyprus Assembly, and entered into force on 14.07.2008. This law points to the establishment of an OHS organizational structure, in which the roles of employer, employee and department are determined in OHS practices prepared in accordance with the EU directive. Within the scope of this law, 12 Regulations, which constitute the technical total basis for the implementation of the Law, have been established and entered into force until 2019, considering the EU directives and the legal regulations of the Republic of Turkey. Since 2019, due to the gaps in practice and technical deficiencies, the Regulation on Certification of Persons Providing Occupational Health and Safety Services and Authorization of Organizations and Risk Assessment Principles in Workplaces [15] have been revised with a perspective based on continuous improvement and efficiency control.

Under the OHS Law, especially for the legislation created or revised in recent years, the approach was based on the management system perspective and the goal of continuous improvement. Improvements have been made in the following and many similar issues compared to the previous legislation [16].

- How to carry out occupational health and safety studies,
- To what extent and by whom the specialist and workplace training will be provided,
- Determining the criteria and content of the trainings given,
- Profession determination of experts,
- Creation of risk assessment report template
- Bringing the content of the risk assessment report to a proactive approach with the legal compliance table and action plan

2.2   OHS Accident Records Between the Years 2000 and 2022

This section provides statistical data obtained from available records of TRNC Labour Department. Most of the records kept are not electronic and hence data collection is a

very difficult, time-consuming job and open to mistakes too. On the other hand, due to the absence of regulations and its enforcement not all accidents have been reported and the records do not necessarily reflect all accidents and injuries. However, fatalities are correct particularly if it is related to work-related accidents. Therefore, one can see some discrepancies in kept records as an example those for the year 2007 [17]. Irrespective of such inconsistencies the following are the analysis made by considering the records and the OHS developments in the country between the years 2000–2022.

Table 1 gives the total number of reported accidents and fatalities between the years 2007 and 2022 for main groups of economic activity. Considering the number of accidents, those in construction works, manufacturing works, hotels and restaurants account for around 23%, 20% and 17% of all accidents, respectively. However, the fatality rates for the same activities were around 45%, 15% and 7% of all fatalities, respectively. This shows that construction works have the highest risk among the economic activity in TRNC. On the other hand, looking at the rate of fatality with respect to the number of accidents in each activity, construction works, agriculture, farming, forestry and real estate, rental, business activities have the highest rate, ranging between 4.2 to 4.7%.

Figure 1 shows how accidents in construction works and other main economic activities varied between the years 2007 and August 2022. Figures 1 and 2 indicate a general trend of fluctuating data and overall drop in the number of accidents, particularly, construction work related accidents between the years 2007–18. In the early years, between 2000 and 2007, due to the absence of regular visits by senior inspectors and lack of regulations to force employees to report accidents and injuries, there were less accidents reported (Fig. 2). Besides, in those years the construction activities were mainly building housing and around 4 stories high apartment type buildings. The volume of construction was less than what it is in recent years where more multi story buildings are being constructed. This leads to more construction work with complicated and dangerous activities.

OHS Law was approved in 2008. The first batch of OHS experts received their certificates and started to work in the market in 2011. Twelve OHS Regulations have been established and entered into force until 2019. All these developments were part of the reason for the reduction in accidents until 2018. During the last quarter of year 2018 and throughout 2019 there has been high publicity on OHS, Labour Department carried out serious controls and tried to enforce the law. This led to more accidents being reported and the sudden increase in number of accidents in 2019. Due to accident records being reflected late in the statistics the high accident numbers continued into the year 2020.

The years 2001, 2006 and 2007 saw the number of fatalities peak at 6, 5 and 7, respectively [17, 18] (Fig. 3). Since 2007 construction work fatalities have dropped and the numbers have fluctuated between 0 and 5 each year. From 2000–07, an average of 2.75 fatalities per year and from 2008–22, an average of 2.1 fatalities per year have been recorded. The total number of construction workers ranges from 8079 to 14,694 between the years 2004 to 2022.

Using the statistics obtained from [19] the construction works fatality numbers per 100,000 construction workers were obtained between the years 2004 and August 2022 (Fig. 4). It was highest in 2007 and 6.8 in 9 months of 2022. Comparing the UK fatality

Table 1. Total number of reported accidents and fatalities between the years 2007 and 2022 for main groups of economic activity.

Main groups of economic activities with high accidents and fatalities	2007–2022	
	Accidents	Fatalities
Construction Work	858	37
Manufacturing Works (Production)	750	12
Hotels and Restaurants	632	6
Wholesale/Retail Trade, Motor Vehicle, Household Goods Repair	519	7
Transport, Storage and communication	218	5
Agriculture, Farming, Forestry	128	6
Other	584	10
Total	**3689**	**83**
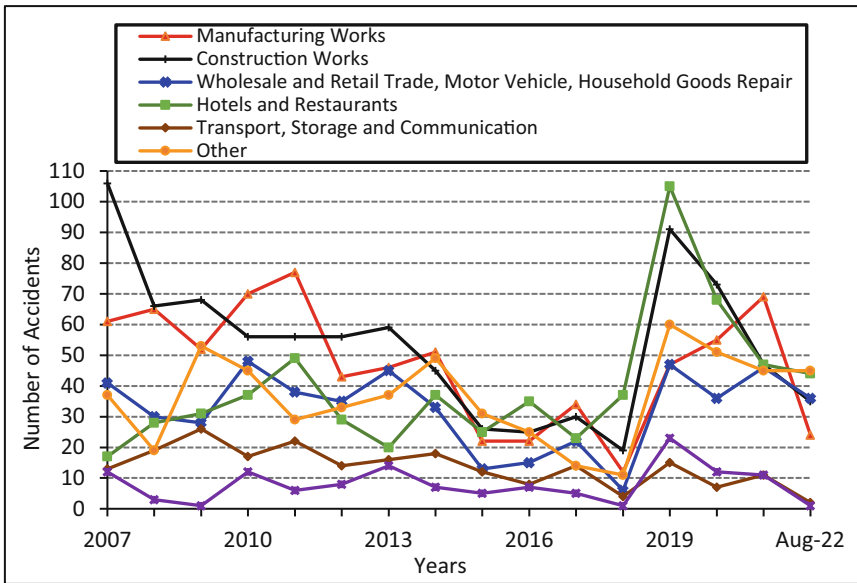
Fig. 1. Total number of reported fatalities between the years 2007 and August 2022 for main groups of economic activity.

numbers per 100,000 workers in construction works with TRNC, in 2022/23 UK was 2.1 TRNC was 6.8 and during the last 5 years UK was 1.72 whilst TRNC was 17.42. Hence, TRNC rates are around 3 to 8 times more than UK [20].

The common reasons for injury and fatalities can be seen in Table 2 between the years 2000 and September 2017. Yearly records indicate that "falling from height" has been the major cause for majority of accidents and fatalities, followed by traffic related
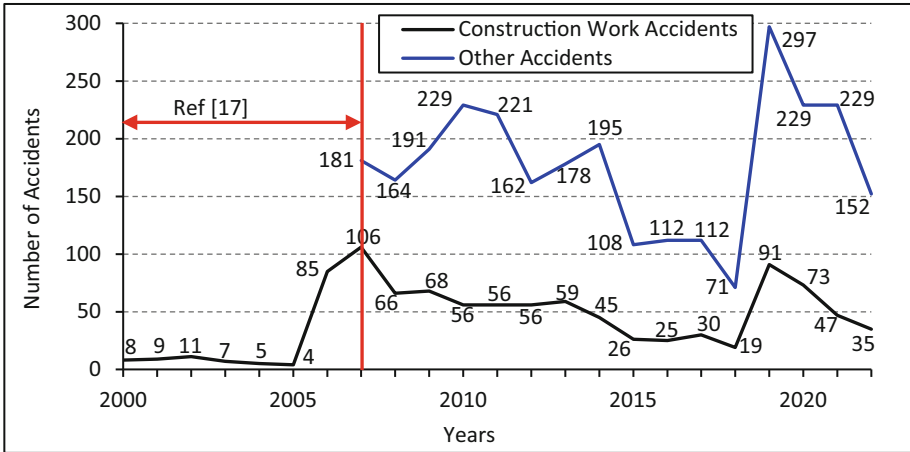
Fig. 2. Construction work reported accidents versus total reported accidents for the other main groups of economic activity for each year from 2007 to August 2022.
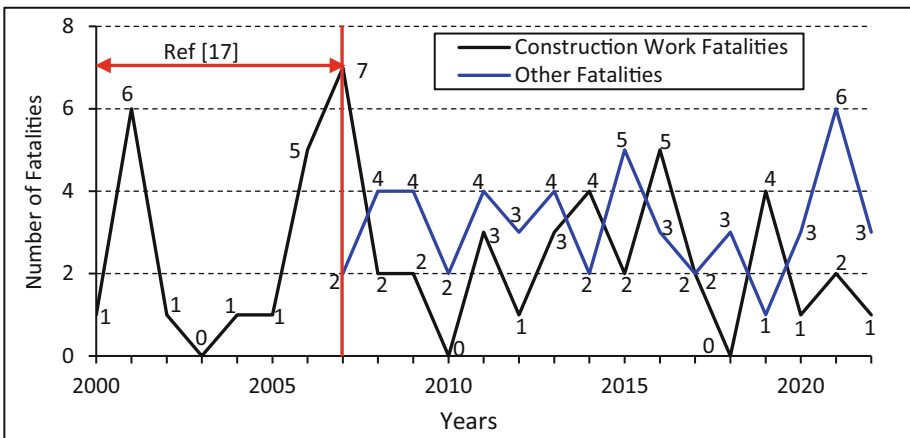
Fig. 3. Construction work fatalities versus total fatalities for the other main groups of economic activity for each year from 2007 to August 2022.

accidents and fatalities, electricity and chemicals related accidents and fatalities, etc. It is important to highlight that despite "Contact with moving machinery", "Struck by moving object" and "falling from the same level" are among the high accident records these accidents have considerably lower fatality rate. Hence a clause is introduced in the relevant OHS regulations enforcing that those workers that are expected to work at height should go through more rigorous health checks and OHS training.

Furthermore, use of non-standard material, lack of design and erection methods for scaffolding have been the main reasons for falling from height. Recent amendments in relevant regulations enforce the import of scaffolding made according to EU standards and prevent the use of locally produced non-standard scaffolding. While the fatalities due
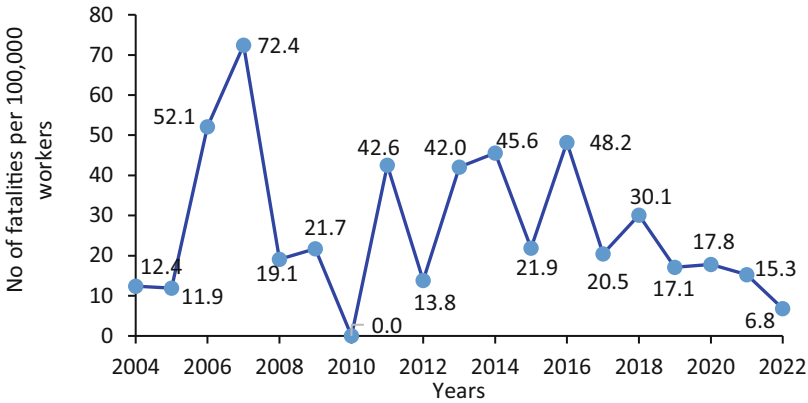
Fig. 4. Construction works fatalities per 100,000 construction workers, 2004- Aug 2022.

Table 2. Construction works Causes of Accidents, 2000-Aug 2016 [17, 18].

Causes of Accidents	Accidents	Fatalities
Falling from a height	630	32
Struck by moving vehicle	439	13
Contact with moving machinery	383	2
Trapped between objects	333	8
Struck by moving object	296	5
Electricity, chemicals, etc	236	14
Falling from the same level	235	1
Other	201	11

to working at height in 2001 and 2006 were 4 and 5, since 2007 it has fluctuated between zero and three. This suggests that despite the increasing number of multi-story buildings, their associated complications and risks the fatality numbers decreasing. There have been problems related to foreign labour that may be unskilled for the job, not registered with the Labour Department and have communication problems due to language. Hence the Labour Department needs to introduce new regulations to better control and minimize or eliminate such problems.

2.3   Digitalization in Turkish Republic of Northern Cyprus

Industry 4.0 was first emerged in Germany, and it has started to show its effect worldwide by making production and service environments smarter, enabling us to produce complex products in a shorter time and at the highest quality. Developing technologies with Industry 4.0 is applied in the OHS field, and new technologies that protect employee health and safety have evolved [21]. In TRNC, the transition to Industry 4.0 is observed

with projects that are supported by the EU and UNDP but not yet within the construction sector and certainly OHS services.

BIM (Building Information Modeling/ Management) applications [22] are observed to be implemented in large projects. This collaborative process that makes it possible for stakeholders to plan, design and construct a structure within a single 3D model is not yet used together with OHS in TRNC. The state has no need analysis and long-term strategic plan for investors and economic activity areas, such as, construction works. This has a knock-on effect on all sub-sectors that are related to main economic activities. In general, the structure and working system of construction sector lack the professionalism required in developed countries. When the absence of state law enforcement combines with the high ratio of unskilled labour use, external demand for properties and high profit margins then this wrong approach becomes the strategic plan for the sector. On one side this has a clear negative effect on the management of OHS in construction works and on the other side it has positive economic rewards. However, in the long term, it causes chaotic social and environmental problems for the country.

Since late 2018, the benefits of introducing software for the management of OHS related matters in Labour Department has been discussed. There are ready software packages available and custom-made ones can be prepared. When the introduction of such a digital tool is coupled with law enforcement of Labour Department the OHS audit on site and the management of related paperwork would become faster and more accurate with the use of less staff. For achieving efficiency in management also requires other stakeholders to have digital systems that are in communication with the main system at necessary points.

Unfortunately, short-term plans are being made, and both governments and businesses are trying to save the day. There are mostly small-scale enterprises within the system, but the situation is also not different for the large enterprises. Hence, despite the many benefits it brings, due to lack of interest and effort by governments and enterprises, unfortunately it is too early to talk about digitalization in construction related works.

3 Conclusions

This article covered the developments and improvements in the management of OHS, particularly in construction works in TRNC. The following are the conclusions:

1. Since the introduction of OHS in construction in 1998, there has been a noticeable increased awareness and improvement in OHS applications in the sector. This was particularly accelerated after the OHS Law entered into force in 2008 and the OHS experts started to do risk analysis in 2011.
2. Despite the increase in population, workforce in all economic sectors, also the processes are getting more complicated and riskier the total number of accidents and fatalities are continuously dropping in recent years for all sectors including.
3. Digitalization, which helps in the management of complex operations, makes the work environment more efficient and less risky, is very important for all sectors and should urgently be implemented.
4. Labour Law needs to be updated to include the emerging new trends in work life.

References

1. International Labour Organization Homepage. https://www.ilo.org/global/lang--en/index.htm. Accessed 26 July 2023
2. Health and Safety at Work etc. Act 1974 (1974.c37). https://www.legislation.gov.uk/ukpga/1974/37/contents. Accessed 6 Aug 2023
3. Health and Safety Executive. A Guide to Health and Safety Regulation in Great Britain (2013). https://www.hse.gov.uk/pubns/hse49.htm. Accessed 6 Aug 2023
4. Reflections on OSHA's History, U.S. Department of Labor, Occupational Safety and Health Administration, OSHA 3360 (2009)
5. Della-Giustina, D.E.: Developing a Safety and Health Program. CRC Press, Boca Raton (2010)
6. U.S. Department of Labor Homepage, OSHA. http://www.osha.gov. Accessed 6 Aug 2023
7. EU OHS Directives. https://osha.europa.eu/en/legislation/directives/workplaces-equipment-signs-personal-protective-equipment. Accessed 6 Aug 2023
8. European Agency for Safety and Health at Work. https://oshwiki.osha.europa.eu/en/themes/general-principles-eu-osh-legislation. Accessed 6 Aug 2023
9. Sariyer OSGB Homepage, İş Sağlığı ve Güvenliğinin Türkiye'deki Tarihsel Gelişimi, http://www.sariyerosgb.com.tr/is-sagligi-ve-guvenliginin-turkiye-deki-tarihsel-gelisimi/. Accessed 28 July 2023
10. KKTC Çalışma Dairesi Müdürlüğü Homepage, Çalışma Dairesi'nin Yasa, Tüzük ve Yönetmelikleri. http://calisma.gov.ct.tr/e-MEVZUAT. Accessed 6 Aug 2023
11. Chapter 134 (Amended with the law no. 27/1978), Factories Act (1957)
12. Department of Labour, Labor Law (1992)
13. Department of Labour, Work (Occupational Health and Safety in Factories and Workplaces) Regulation (1992)
14. Department of Labour, Occupational Health, and Safety Regulation in Constructions (1998)
15. Department of Labour, Regulation on Certification of Persons Providing Occupational Health and Safety Services and Authorization of Organizations and Risk Assessment Principles in Workplaces (2019)
16. Department of Labour, OHS Law (2008)
17. Celikag, M., Ozbilen, M.: Health and safety matters in construction industry in North Cyprus. In: Proceedings of the 8th International Congress on Advances in Civil Engineering, ACE2008, 15–17 September 2008, Gazimagusa, North Cyprus (2008)
18. Department of Labour Monthly/Annual activity report (2017)
19. KKTC İstatistik Kurumu, Hanehalkı İşgücü Anketi 2014 to 2022. https://istatistik.gov.ct.tr/TEMEL-İSTATİSTİKLER/İSTİHDAM-VE-İŞSİZLİK. Accessed 6 Aug 2023
20. Work-related fatal injuries in Great Britain, 2023, Data up to March 2023, Annual statistics, 6 July 2023, HSE. https://www.hse.gov.uk/statistics/pdf/fatalinjuries.pdf. Accessed 5 Aug 2023
21. Topaloğlu, I., Şahin, M.E.: Endüstri 4.0'ın İş Sağlığı ve Güvenliğine Katkıları ve Hata Türü ve Etkileri Analizi (FMEA) Risk Değerlendirme Metoduyla Ambulansta Bir İnceleme. Takvim-i Vekayi **9**(2), 66–94 (2021)
22. Akçay, C., Giran, Ö.: İnşaat Projelerinde Yapı Bilgi Modelleme İle İş Güvenliği Tedbirleri ve Maliyetlerinin Örnek Bir Vaka Üzerinden İncelenmesi. Kent Akad. **14**(4), 950–960 (2021)

Hydraulics

Evaluating Urban Runoff in a Catchment of Güzelyurt: A Comparative Analysis of Traditional and LID Approaches

Mirza Mohammed Abdul Basith Baig[1] and Bertuğ Akıntuğ[2(✉)]

[1] Sustainable Environment and Energy Systems Graduate Program, Middle East Technical University, Northern Cyprus Campus, Kalkanlı, 99738 Güzelyurt, Mersin 10, Turkey
mirza.baig@metu.edu.tr

[2] Civil Engineering Program, Middle East Technical University, Northern Cyprus Campus, Kalkanlı, 99738 Güzelyurt, Mersin 10, Turkey
bertug@metu.edu.tr

Abstract. Global warming and climate change have become pressing environmental challenges, primarily caused by human activities such as burning fossil fuels and deforestation. These activities release greenhouse gases into the atmosphere, disrupting the natural balance of radiation and leading to rising global temperatures. The consequences of global warming include more frequent and severe heatwaves, changes in precipitation patterns, and increased risks of urban flooding. This research focuses on sustainable stormwater management as a strategy to mitigate urban flooding and adapt to climate change. The study area is the city of Güzelyurt in Northern Cyprus, characterized by a flat topography and limited stormwater infrastructure. The existing stormwater network is insufficient and prone to failures during rainfall events. The research compares the effectiveness and efficiency of two approaches: a traditional approach that involves resizing conduits, and a sustainable approach that implements Low-Impact Development (LID) strategies. LID strategies aim to mimic natural hydrological processes and include measures such as green infrastructure, permeable pavements, rainwater harvesting systems, and vegetative swales. By implementing these strategies, stormwater runoff can be controlled, mitigating the risk of flooding, improving water quality, promoting groundwater recharge, and reducing the demand for freshwater resources. The study utilizes the Storm Water Management Model (SWMM) software to design the existing stormwater management network and simulate different scenarios. Through the evaluation of performance and analysis of results, the research results demonstrate that the implementation of LID strategies effectively doubled the existing rainfall handling capacity of the stormwater drainage system from 20 mm/h to 40 mm/h.

Keywords: Climate Change · Urban Flooding · SWMM · LID

1   Introduction

Global warming has become widely recognized as one of the most significant environmental challenges of our time. It is commonly understood as the impact of human activities, particularly the burning of fossil fuels (coal, oil, and gas) and large-scale deforestation. These activities have significantly increased since the industrial revolution, resulting in the annual release of approximately 7 billion tons of carbon dioxide, along with substantial quantities of methane, nitrous oxide, and chlorofluorocarbons (CFCs), into the atmosphere [1]. Global warming is directly impacting climate change by altering weather patterns and environmental conditions. The increased concentration of greenhouse gases in the atmosphere is causing a rise in global temperatures, leading to various consequences for the climate. One significant effect is the intensification of heatwaves, which are becoming more frequent and severe. These extreme heat events have detrimental effects on human health, agriculture, and ecosystems, resulting in illnesses, reduced crop yields, and ecological stress. Changes in precipitation patterns are also observed due to global warming. Some regions experience heavier rainfall and an elevated risk of flooding, while others face extended periods of drought and water scarcity, affecting agriculture, water resources, and ecosystems [2]. Additionally, global warming alters precipitation patterns, leading to changes in the frequency and distribution of rainfall. Some regions may experience more frequent and intense rainfall, while others may suffer from prolonged dry spells and droughts. These changes in precipitation patterns further challenge urban areas, as they must adapt to the increased uncertainty in rainfall events.

Urban environments, with their vast expanses of impervious surfaces such as roads, buildings, pavements, and parking lots, exacerbate the effects of heavy precipitation. These impermeable surfaces prevent natural infiltration of rainwater into the ground, resulting in rapid surface runoff that overwhelms drainage systems. As a consequence, urban areas are more prone to flash floods and urban flooding [3]. The combination of intensified rainfall events and altered precipitation patterns due to climate change heightens the risk of urban flooding. This necessitates a comprehensive approach to urban planning and stormwater management that considers the projected impacts of climate change. Implementing measures such as improved drainage infrastructure, green infrastructure, and sustainable stormwater management practices can help to mitigate the adverse effects of climate change on urban flooding. It is crucial to consider the long-term implications of climate change in urban planning and infrastructure development to ensure the safety and well-being of urban populations in the face of increasing precipitation extremes.

1.1   Sustainable Stormwater Management

In recent years, there has been an increasing recognition of the significance of stormwater as a valuable resource that should be considered in urban planning and development. This shift in perspective has been driven by several factors, such as population growth, higher water demand, growing environmental awareness, the heightened risk of storm damage due to climate change, and the expansion of urban areas and impervious surfaces. This global trend has given rise to more sustainable approaches to urban stormwater

management which is known as Water-Sensitive Urban Design (WSUD) in Australia, Sustainable Urban Drainage Systems (SuDS) in Britain, and Low-Impact Development (LID) in North America [4]. Unlike traditional drainage methods that view stormwater as a problem to be quickly removed from urban areas, sustainable stormwater management recognizes it as a versatile resource with numerous potential societal and environmental benefits if managed effectively [5].

The implementation of sustainable stormwater management involves a range of measures at various levels, starting from urban and regional planning, which considers the appropriate location of different land uses based on topographical and hydrological factors, to the construction of specific installations or Low impact Development Strategies (LIDs) [6]. These LIDs are designed to retain, detain, convey, and preserve stormwater flow, promote groundwater recharge, provide water for irrigation, mitigate topsoil erosion, and filter out pollutants and sediments [7]. These strategies aim to mimic natural hydrological processes and minimize the adverse impacts of urban development on water resources. Bioretention basins, also known as rain gardens, are designed to capture and treat stormwater runoff. They consist of vegetated depressions that collect runoff, allowing it to infiltrate into the soil, where natural filtration processes remove pollutants. Permeable pavement systems are specifically designed to facilitate water infiltration through the pavement surface and into the underlying soil [8]. These systems utilize porous materials like pervious concrete or permeable pavers, which allow stormwater to percolate through, reducing runoff and promoting groundwater recharge. Permeable pavements are effective in reducing surface runoff, mitigating the risk of flooding, and improving water quality by filtering pollutants. Rainwater harvesting systems capture and store rainfall for later use. These systems collect rainwater from rooftops, which is then stored in tanks or cisterns. The collected rainwater can be used for non-potable purposes such as irrigation, toilet flushing, or car washing. Rainwater harvesting reduces the demand for freshwater resources, eases pressure on municipal water supply systems, and helps to mitigate urban flooding by reducing stormwater runoff. Other LID strategies include green roofs, vegetative swales, infiltration trenches, and rain barrels. These LID strategies offer multiple benefits, including reducing stormwater runoff volume, improving water quality, enhancing groundwater recharge, mitigating urban heat island effects, and promoting biodiversity in urban areas. By incorporating these strategies into urban planning and design, cities can effectively manage stormwater and minimize the impact of urbanization on water resources and the environment [9].

This research focuses on the implementation of sustainable stormwater management practices, specifically the investigation of best management practices within a selected study area. The study begins by assessing the existing stormwater management network, which is designed to handle regular rainfall events but may experience challenges during critical events leading to flooding. In response, two approaches are considered: a traditional approach involving resizing conduits to increase the network's capacity to handle runoff, and a sustainable approach involving the application of LID strategies. The traditional approach involves modifying the existing system by resizing conduits and making necessary adjustments. On the other hand, the sustainable approach emphasizes the implementation of LID strategies, which focus on controlling and managing runoff in a more environmentally friendly and sustainable manner. These strategies can

include the use of green infrastructure, rain gardens, permeable pavements, and other nature-based solutions. The research aims to compare the effectiveness and efficiency of these two approaches. By evaluating their performance and analyzing the results, valuable insights can be gained regarding the advantages and limitations of each approach in terms of flood mitigation, environmental impact and long-term sustainability.

The subsequent sections of this research paper provide further details. Section 2 presents the study area, providing relevant information about its geographical and hydrological characteristics. Section 3 describes the methodology employed, including data collection methods, modeling techniques, and criteria for performance evaluation. Section 4 presents the application of both the traditional and sustainable approaches, highlighting the results obtained and comparing the outcomes. Finally, the conclusion section summarizes the findings, draw conclusions, and discuss the implications and potential for future research in the area of sustainable stormwater management.

2   Study Area

Cyprus, situated in the Mediterranean Sea, is the third largest island in the region, positioned south of Turkey and west of Syria. The study focuses on the city of Güzelyurt, located in Northern Cyprus, which is the fourth major city in Northern Cyprus, following Nicosia, Famagusta, and Kyrenia. Güzelyurt is geographically located at a longitude of $32° 59'$ and a latitude of $35° 12'$ N. With a population of 30,037 according to the 2011 population census, Güzelyurt accounts for approximately 10.4% of the total population in Northern Cyprus. Over the five-year period from 2006 to 2011, the population of Güzelyurt experienced a 2.6% growth, increasing from 29,264 to 30,037 [10], the Fig. 1 shows the location of the Study area.

| (a) | (b) | (c) |

Fig. 1. Location of the study area and city plan (a) Location of Island, (b) Location of Güzelyurt, (c) Ground layout of the Town [11].

Güzelyurt, with a reported area of 381 km^2, consists of an urbanized area spanning approximately 3–4 km^2, which is surrounded by agricultural lands and fruit gardens. The topography of the region is relatively flat, sloping steadily towards the river bed situated on the north side of the city. The Serrahi river bank remains dry at all times due

to the construction of a number of dams upstream, ensuring to store water for agricultural purposes in the area of Güzelyurt [12]. Güzelyurt experiences a Mediterranean and semi-arid climate, characterized by hot and dry summers with minimal rainfall during June, July, and August. The urban design of Güzelyurt reflects its age, featuring high-density residential areas in the central part of the city. The existing pipe system in the urban area does not cover all the streets, leading to the need for rainwater runoff to flow over the surface of streets with no drainage system. This often results in water accumulation and flooding at street junctions. Additionally, the stormwater network system has insufficient capacity, causing failures even during regular rainfall events. Due to the lack of available maps or detailed documents, the municipality was contacted to gather information about the locations and sizes of the existing pipes.

The identification of catchments in this research area was conducted manually by examining the road elevation map provided by the municipality. The process involved analyzing the directions of flows and the differences in elevations to determine distinct catchment areas. By closely studying the map and considering the natural topography, the boundaries of each catchment were delineated based on the observed flow patterns and elevation changes. This approach allowed for a comprehensive understanding of the drainage characteristics within the study area and facilitated the accurate representation of catchments in the analysis. The areas are classified as A, B, C and D and the areas for catchments are 0.54, 0.16, 0.29 and 0.10 km^2, respectively. The exit point for all the catchments is the riverbed of Serahis river as shown in Fig. 2.
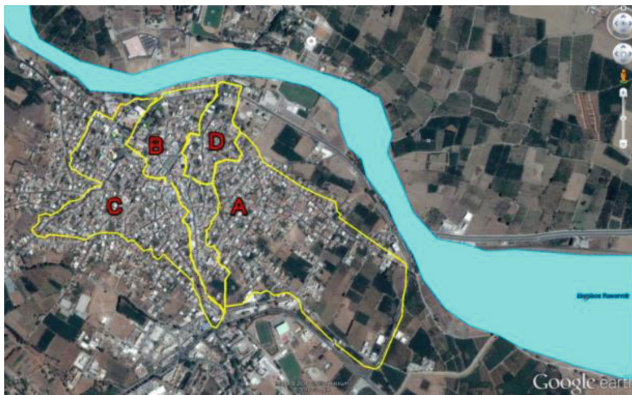
Fig. 2. Major stormwater drainage catchments of Güzelyurt [13].

Among the identified catchments, Catchment-B exhibits the highest percentage of impervious surface, as indicated in Table 1. The presence of a greater impervious surface in a region implies an increased likelihood of high runoff volumes and the potential for urban flooding. Consequently, Catchment-B has been selected as the focal area for this research study. By focusing on this catchment, we can investigate the impacts of impervious surfaces on stormwater runoff and explore strategies to mitigate urban flooding within this particular region.

Table 1. General characteristics of catchments [13].

Catchment	Number of Sub-areas	Total area (m^2)	Impervious (%)
A	35	550,371	27
B	26	149,735	64
C	60	291,374	62
D	9	79,319	51

3 Methodology

The first step in this study was to design the existing stormwater management network for Catchment-B in Güzelyurt. To accomplish this, the SWMM (Storm Water Management Model) software, developed by the Environmental Protection Agency (EPA) was utilized. SWMM is a widely-used software tool for simulating urban stormwater runoff drainage systems, and water quality. It provides a comprehensive platform for designing, analyzing, and optimizing stormwater management strategies.

SWMM allowed us to input various parameters such as land use characteristics, topography, and rainfall data to create a representation of the existing stormwater network [14]. By using the software's capabilities, we were able to accurately model the flow of stormwater through the network and assess its performance under different scenarios. This information served as a baseline for further analysis and comparison with alternative stormwater management strategies. The SWMM software played a crucial role in this study by enabling us to evaluate the performance of the existing stormwater management network and explore potential improvements. The advantages of utilizing SWMM include its ability to simulate various hydrologic processes, such as infiltration, evaporation, and runoff generation, considering different land use types and surface conditions. The software also allows for the evaluation of different stormwater management strategies and their impact on flow patterns, water quality, and flood risk. By utilizing SWMM, we were able to analyze and compare alternative design scenarios and integrating LIDs into the catchment, enabling us to identify the most effective stormwater management measures for Catchment-B in Güzelyurt. Furthermore, SWMM's user-friendly interface and robust simulation capabilities facilitated the visualization of complex hydraulic processes and provided valuable outputs for decision-making.

3.1 Low Impact Development (LID) Strategies Implementation

LID consist of a variety of approaches that aim to address the negative impacts of urbanization by minimizing the runoff produced from impermeable surfaces. Three LID techniques, namely bio-retention basins, permeable pavement, and rainwater harvesting systems, were chosen for implementation in the study. These LIDs were selected based on their potential effectiveness in controlling stormwater runoff and mitigating urban flooding. The placement of these LIDs within the study area was strategically determined to optimize their flood control capabilities. Designing these LIDs is possible using the SWMM software, In the design process of LIDs using SWMM software, several crucial

parameters are entered to accurately model and simulate the behavior of LIDs within the stormwater management system. These parameters include defining the geometry and dimensions of LIDs, such as the size, shape, and dimensions of bio-retention basins, permeable pavements, and rainwater harvesting systems. Soil properties like infiltration rate, porosity, and hydraulic conductivity are specified to determine the LIDs capacity to absorb and retain stormwater runoff. Rainfall data, such as intensity, duration, and frequency, are incorporated to simulate various storm events and assess the effectiveness of LID performance. Moreover, the software allows for configuring runoff control settings like infiltration rates, storage capacities, and flow routing options to govern the behavior of LIDs and their ability to control and attenuate stormwater runoff. The typical design system provided in SWMM software is given in the Fig. 3, where (a) is Bioretention Unit, (b) is a Permeable pavement system and (c) is Rainwater harvesting tank.
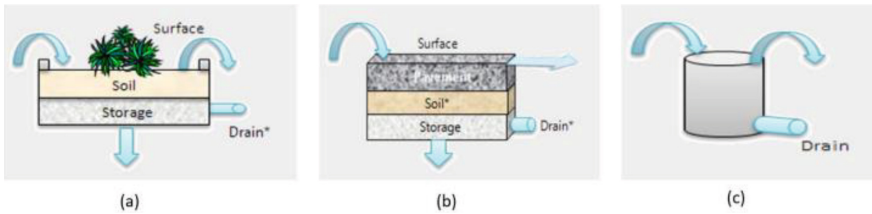
Fig. 3. LID design in SWMM (a) Bioretention Basin, (b) Permeable Pavement, (c) Rainwater Harvesting [14].

Following the design of LIDs, each LID is strategically implemented in different sub-areas of Güzelyurt Catchment-B. To evaluate the effectiveness of these LIDs in reducing stormwater runoff, a simulated rainfall event is conducted. By subjecting the catchment to this rainfall simulation, the resulting runoff volumes can be observed and analyzed. This assessment allows for the comparison of runoff volumes before and after the implementation of LIDs, providing valuable insights into the extent of reduction achieved. By examining the observed reduction in runoff volume, the performance and effectiveness of each LID can be assessed, helping to determine their contribution to mitigating stormwater runoff in the catchment.

4   Results and Discussions

Upon completion of the design of the existing stormwater management network in Güzelyurt Catchment-B, the next step involved simulating various design rainfalls (5 mm/h, 10 mm/h, 15 mm/h …) to determine the critical rainfall threshold event that leads to urban flooding. Through this analysis, it was revealed that the system handles a rainfall event of 20 mm/h without causing urban flooding. However, when the design rainfall was exceeded 20 mm/h, the system experienced flooding, as evidenced by the observations presented in Table 2. These findings highlight the sensitivity of the system to higher intensity rainfall events and emphasize the need for further measures to effectively manage stormwater and mitigate the risk of urban flooding in the catchment.

Table 2. Flooding under various rainfall simulations

Rainfall Intensity (mm/hr)	Flooded Junctions	Surcharged Conduits	Peak Outfall Flow (m³/s)
20	–	–	0.706
22	J24	C22	0.777
24	J16, J24, J33	C16, C22, C32	0.794

The design rainfall considered for this study is a varying rainfall, distribution of rainfall intensity is divided into distinct time intervals to replicate real-world conditions more accurately. In the initial 15 min of the rainfall event, only 20% of the total rainfall accumulates, indicating a relatively lower intensity period. Subsequently, between 15 and 30 min, the rainfall intensity experiences a substantial increase, peaking at 40% of the total rainfall. This peak occurs during the second quarter of the rainfall event, leading to a more concentrated period of intense precipitation, followed by 30% and finally from 45 to 60 min 10% of total rainfall is considered.

The traditional approach for increasing the rainfall handling capacity of the system is resizing the conduits. Initially, the system successfully managed a 20 mm/h rainfall event without any flooding issues. However, problems arose when the rainfall intensity increased to 22 mm/h, affecting conduits and junctions. As a first step towards improvement, the troubled conduits and junctions were replaced with larger pipes, enabling the system to function without problems during a 22 mm/h rainfall event. However, flooding occurred in certain conduits (C32, C22, and C16) when the intensity reached 24 mm/h. Further modifications, including the replacement of multiple conduits with larger pipes, were performed iteratively until the system effectively handled a 40 mm/h rainfall event.

In addition to the modifications made to the existing stormwater drainage network, an alternative solution was explored to enhance the system's capacity without altering conduit sizes or making direct modifications. This involved the strategic placement of LIDs in various locations within Catchment-B. By implementing LIDs such as bioretention basins, permeable pavement, and rainwater harvesting systems, the overall rainfall handling capacity of the existing system was increased to 40 mm/h as shown in Table 3. These LIDs effectively controlled and managed runoff, mitigating the risk of urban flooding. The strategic placement of LIDs played a crucial role in optimizing the system's performance and providing a sustainable approach to stormwater management within the catchment.

Table 3. Flooding after application of LIDs

Rainfall Intensity (mm/hr)	Flooded Junctions	Surcharged Conduits	Peak Outfall Flow (m^3/s)
40	–	–	0.605
42	J24, J33	C22, C32	0.674
44	J24, J33	C22, C32	0.738
46	J15, J16, J17, J24, J33	C15, C16, C17, C22, C32	0.796

5   Conclusion

The study area of Güzelyurt in Northern Cyprus was analyzed to assess the existing stormwater management network and explore the effectiveness of traditional approaches versus sustainable approaches. The existing piping network in Güzelyurt was found to be insufficient and prone to failures, especially during regular rainfall events. The identification of catchments and the selection of Catchment-B, with the highest percentage of impervious surface, allowed for a focused analysis of the impacts of impervious surfaces on stormwater runoff. The methodology employed the SWMM software to design the existing stormwater management network and simulate its performance. SWMM provided a comprehensive platform to evaluate the hydraulic behavior of the system and assess its capacity to handle stormwater runoff effectively. Low Impact Development (LID) strategies, such as bio-retention basins, permeable pavement systems, and rainwater harvesting, were implemented to mitigate urban flooding and promote sustainable stormwater management. The comparison between the traditional approach and the sustainable approach revealed that sustainable stormwater management practices, including LID techniques, showed promising results in terms of flood mitigation, environmental impact, and long-term sustainability.

In conclusion, this research emphasizes the importance of sustainable stormwater management practices in mitigating the impacts of climate change, particularly urban flooding. By implementing LID strategies and integrating nature-based solutions into urban planning and design, cities can effectively manage stormwater, minimize the adverse effects of urbanization on water resources and the environment, and build resilience to changing precipitation patterns.

References

1. Houghton, J.: Reports on Progress in Physics, vol. 68, p. 6, 1343. IOP Science (2005)
2. IPCC. Climate Change 2014: Synthesis Report. Contribution of Working Groups I, II and III to the Fifth Assessment Report of the Intergovernmental Panel on Climate Change. Cambridge University Press (2014)
3. Kundzewicz, Z.W., et al.: Flood risk and climate change: global and regional perspectives. Hydrol. Sci. J. 1–28 (2014)

4. Fletcher, T.D., et al.: SUDS, LID, BMPs, WSUD and more – the evolution and application of terminology surrounding urban drainage. Urban Water J. 525–542 (2015)
5. Mitchell, B.: Integrated water resource management, institutional arrangements, and land-use planning. Environ. Plann. A **37**, 1335–1352 (2005)
6. Carmon, N., Shamir, U.: Water-sensitive urban planning: protecting groundwater. J. Environ. Plann. Manage. **40**(4), 413–434 (1997)
7. Barbosa, A.E., Fernandes, J.N., David, L.M.: Key issues for sustainable urban stormwater management. Water Res. Spec. Issue Stormwater Urban Areas **46**, 6787–6798 (2012)
8. Han M.Y., Mun J.S.: Operational data of the star city rainwater harvesting system and its role as a climate change adaptation and a social influence. Water Sci. Technol. 2796–2801 (2011)
9. Roy, A.H., et al.: Impediments and solutions to sustainable, watershed-scale urban stormwater management: lessons from Australia and the United States. Environ. Manage. 344–359 (2008)
10. Hatay, M.: TRNC general population and housing unit census, pp. 25–29. Peace Research Institute Oslo, Cyprus (2011)
11. REAP, Climate responsive planning, Guzelyurt, Northern Cyprus. Technical Report, Resources Efficiency in Architecture and Planning Graduate Program, HafenCity University, Hamburg, Germany (2016)
12. Ergil, M.E.: The salination problem of the Guzelyurt aquifer, Cyprus. Water Res. **34**(4), 1201–1214 (2000)
13. Elham, J.: Investigating the applicability of water sensitive urban design techniques for Güzelyurt, Northern Cyprus. MSc thesis, Middle East Technical University, Northern Cyprus Campus (2017)
14. Storm Water Management Model (SWMM) version 5.1 User's Manual | US EPA (2022). https://www.epa.gov/water-research/storm-water-management-model-swmm-version-51-users-manual

Analysis of the Influencing Factors of Variation in Sediment Concentration in the Lower Değirmendere Basin, Trabzon, Türkiye

Osman Tuğrul Baki[1(✉)], Betül Mete[2], and Ömer Yüksek[2]

[1] Department of Civil Engineering, Karadeniz Technical University, 61830 Trabzon, Turkey
tbaki@ktu.edu.tr

[2] Department of Civil Engineering, Karadeniz Technical University, 61080 Trabzon, Turkey
{betulmete,yuksek}@ktu.edu.tr

Abstract. This study aimed to investigate the variation of total suspended sediment concentration (TSS, mg/L) from upstream to downstream as well as its variation during the sunrise and mid-day periods. The Lower Değirmendere Stream Basin was selected as the study area. Sampling and monitoring studies were conducted weekly, four times a month, from December 2021 to May 2022. Samples were taken on four gauging stations upstream to downstream. Sunrise samples were taken between 06.00–07.00 a.m. and mid-day samples were taken between 12:00 a.m.–01:00 p.m. Over the 24-weekly sampling period, the variation TSS were characterized. The samplings and laboratory experiments were used to evaluate TSS. The results have indicated that TSS increases from upstream to downstream and the TSS values at mid-day were 20–75% higher than at sunrise. It has been shown that anthropogenic activities in the Lower Değirmendere Stream Basin cause an increase in TSS concentration. The fact that anthropogenic activities in the Basin is low at night has resulted in low mixing into the stream and therefore low TSS concentrations.

Keywords: Stream Management · Total Suspended Sediment Dynamics · Eastern Black Sea Basin · Trabzon

1 Introduction

Water quality is of paramount importance both the stream ecology and human health. Suspended sediment (SS) is an important parameter determining water quality in streams. This parameter refers to the concentration of inorganic and organic substances transported in streams. SS, which determine the physical and chemical properties of streams, are affected by many factors, such as discharge, sedimentation rate, erosion, anthropogenic activities, and vegetation cover. SS transport varies due to both natural and anthropogenic influences. Natural impacts include rainfall regime, erosion, dissolution, karst formations and volcanic activities. Human-induced impacts are caused by many factors such as agricultural activities, industrial wastes, mining, construction activities and urban wastes. Increasing SS concentrations may adversely affect both chemical and

physical properties of streams. The transported materials may contain harmful substances such as nutrients, heavy metals, pesticides, and organic pollutants. These substances can pose a threat to both human health and the aquatic ecosystem [1, 2].

The total suspended sediment (TSS) is an important variable in determining the water quality and ecological health of streams, as pollutants can attach to TSS particles and be transported through the stream to distant points. The presence of high TSS concentrations in the stream pollutes the accessible clean water resources, damages soil and plants when used for irrigation in agricultural areas, damages equipment in wastewater treatment plants and hydroelectric power plants when used for water supply, accumulates in the stream section and dam reservoirs, reduces the economic life of hydraulic structures, and increases the operating costs of hydraulic structures. Therefore, monitoring, controlling, and reducing the transport of TSS in streams is of great importance for water quality and the sustainability of water resources [3–5].

These factors have led to the degradation of the natural ecological environment, with semi-daily/daily fluctuations in TSS concentrations and deteriorating water quality. Suspended sediment, an important carrier of nutrients and pollutants, has a direct impact on the aquatic environment under the influence of human-induced activities and terrestrial inputs. Therefore, the analysis of the temporal and spatial variation and distribution of the SS concentration in marine ecosystem is of great research importance [6].

In streams with excessive amounts of SS, accurate determination of TSS concentration and total sediment volume is critical. Sediment rating curves are often used to estimate suspended sediment loads where sampling is insufficient to define a continuous record of TSS concentration [7, 8]. Up-to-date, frequent, and real-time monitoring of TSS data is becoming increasingly important to meet environmental, drinking water and public health needs. The temporal variation of TSS is the key to understanding the sediment dynamics in coastal areas. For these reasons, continuous and frequent monitoring of TSS has important implications for many disciplines [4, 9].

Many studies have been conducted worldwide on the seasonal and diurnal variability of TSS monitoring and estimation in stream basins [10]. In this study, raw stream water samples were taken at sunrise and mid-day to determine the TSS concentration in order to monitor the changes in TSS transport during the day and to determine the possible effects of human-induced activities on TSS transport in streams. For this purpose, the Lower Değirmendere Basin in Trabzon province was selected as the study area. These criteria were considered in the location of the gauging stations.

2 Material and Methods

2.1 Study Area

Turkey consists of 25 hydrological basins. With a recharge area of 24,077 km^2 and a surface water potential of 16.46 billion cubic meters, the Eastern Black Sea Basin (Fig. 1) is one of the most important basins in Turkey and, together with the Çoruh and Aras basins, forms an important part of the Caucasus ecoregion [11].

The Değirmendere Stream Basin in north-eastern Turkey is one of the most important basins in Trabzon Province, supplying drinking and industrial water as well as major settlements. Located approximately 4 km east of Trabzon city center, the basin rises from
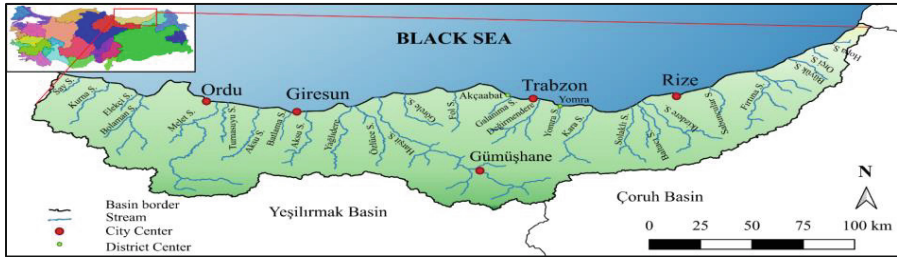
Fig. 1. The location of Eastern Black Sea Basin

the mountain peaks in the south and meets the Black Sea in the north. The basin covers an area of 1,042 km^2 and basin is formed by the main Değirmendere Stream and many important tributaries (Fig. 2). The Atasu Dam, which supplies the drinking and industrial water needs of Trabzon province, and the Esiroğlu Drinking Water Treatment Plant, which provides drinking water treatment, are in this basin. There are also numerous run-of-river hydroelectric power plants in the basin, which produce 117.5 GWh of energy per year [12, 13]. Hydrometric observations in the lower basin are available at the D22A086 Öğütlü Stream Gauging Station which is operated by the General Directorate of State Hydraulic Works (DSI).

In order to determine the variation in the TSS concentration along the basin, four gauging stations were determined from the upstream to the downstream. The locations of the sediment gauging stations were determined by considering the stream gauging station, the tributary confluence, pollutant sources, topography, and the density of settlements and industrial units. Sediment gauging stations were located from D1 to D4 from upstream to downstream. The D1 gauging station is located just upstream of the stream gauging station where there are few settlements and industrial units, the D2 gauging station is located downstream of the stream gauging station and the confluence of the Galyan tributary, D3 gauging station is located in an area with dense residential and industrial areas. And the D4 gauging station is located at the outlet of the basin where there are dense residential and industrial areas. The locations of the gauging sites are shown in Fig. 2.

2.2   Determination of Total Suspended Sediment Concentration

The TSS monitoring study in the Lower Değirmendere Stream Basin were conducted for six-months between December 2021 and May 2022. Sampling was conducted in weekly periods at sunrise (06.00–07.00 a.m.) and mid-day (12.00 a.m.–01.00 p.m.) periods. The locations of the gauging stations were determined according to the criteria described in the previous section. In addition to the variation of TSS from upstream to downstream, samples were also taken at sunrise and mid-day to determine its variation at different times of the day.

The procedure, including sampling, preservation, and delivery of the stream water samples to the laboratory, was conducted in accordance with APHA [14]. At the gauging sites, samples were taken from the middle of the stream by closing the lid so that there
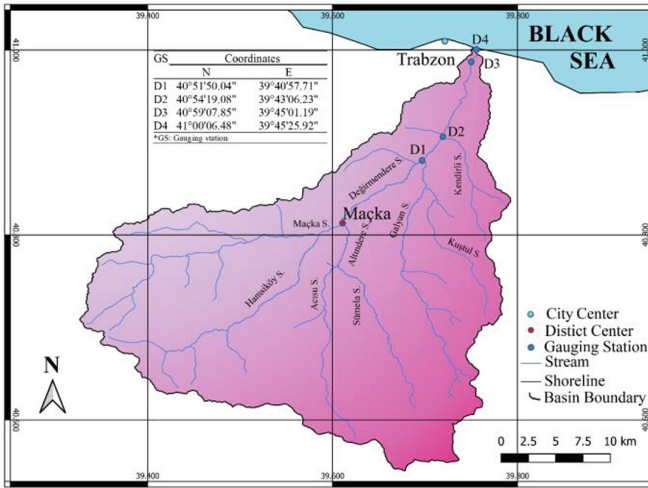
Fig. 2. The Değirmendere Stream Basin and locations of gauging stations

was no air space in the sampling bottle. The samples were transported to the laboratory in transport containers with ice cassettes.

The TSS determination was performed according to TS EN 872 [15]. The glass microfiber filters through which the water samples were filtered were soaked in distilled water before filtration and dried in an oven at 105 ± 2 °C for 1 h before filtration and 4 h after filtration. The TSS concentration (mg/L) was determined by dividing the difference obtained by subtracting the initial weight from the final weight by the sample volume.

The TSS concentration was determined by collecting water samples from December 2021 to May 2022 through field surveys followed by laboratory analysis. Water samples were collected under a range of atmospheric and flow conditions to reflect conditions that may influence the variability of TSS concentrations and loads.

3   Findings

The average TSS concentration (mg/L) obtained from the gauging stations in the Lower Değirmendere Stream Basin are interpreted. TSS concentration data were obtained from 24 field studies conducted twice a day (sunrise and mid-day) on a weekly basis between December 2021 and May 2022. The TSS concentration are plotted as a box plot and shown in Fig. 3 and time series scatter is also shown in Figs. 4, 5, 6 and 7. These graphs are used to interpret the results of the upstream to downstream variation of TSS concentration and the sunrise and mid-day variation of TSS concentration. In the box plot (Fig. 3) and the time series plots, the sunrise data are labelled with the S index, while the mid-day data are labelled with the M index. When drawing the box plots, data coinciding with the extreme flow period and construction works in the stream section were excluded from the data set as they distort the general trend. A box plot shows the minimum, first quartile, median, third quartile maximum and mean values. A box plot provides an overview of parameters such as kurtosis, skewness, and standard deviation,

as well as showing the central tendency (median), interquartile range and outliers of the data set.

The box plot shows that the TSS concentration tends to increase from upstream to downstream. In the sunrise study it was found that the average TSS concentrations determined at D1 and D2 gauging stations were approximately the same. It was determined that the TSS concentrations determined at D3 and D4 gauging stations were approximately the same, and that the concentrations at D4 gauging station were higher than D3 gauging station.
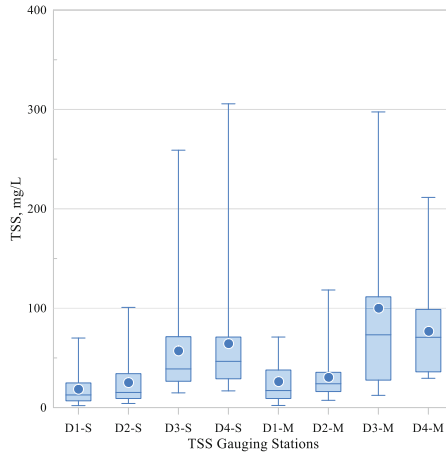
Fig. 3. Average TSS (mg/L) box plot

Considering the mid-day concentrations in the box plot, it was understood that the TSS concentration increased from upstream to D3 gauging station. It was noted that the concentration tended to decrease at D4 gauging station. The peak TSS concentrations were monitored at sunrise at D4 gauging station, at mid-day at D3 gauging station.
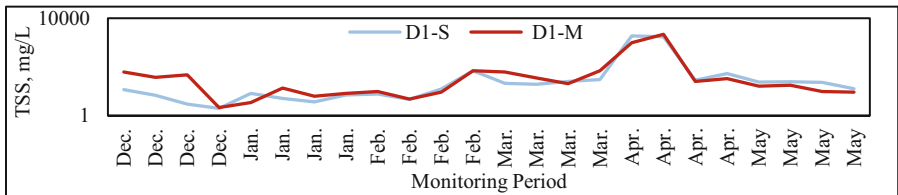
Fig. 4. Time series of TSS at D1 gauging station in the sunrise and mid-day periods

Based on the six months of sunrise and mid-day TSS values at station D1 in Fig. 4, the mid-day concentrations in December were higher than the sunrise concentrations, the sunrise concentrations in May were higher than the mid-day concentrations, and although there were fluctuations in the remaining concentrations during the day, they

generally fluctuated around values close to each other. The highest TSS values were recorded in April and the lowest in December.
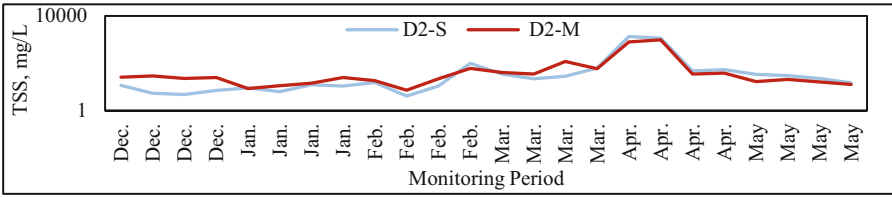
Fig. 5. Time series of TSS at D2 gauging station in the sunrise and mid-day periods

According to the results of the sunrise and mid-day TSS monitoring for six months at station D2 in Fig. 5, the mid-day concentrations were higher than the sunrise concentrations up to April, after April the sunrise concentrations were higher than the mid-day concentrations, the highest TSS values were recorded in April, the lowest TSS values in February.
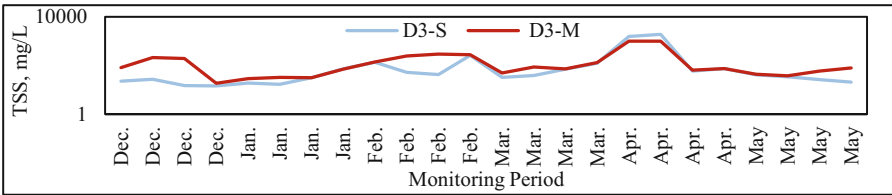
Fig. 6. Time series of TSS at D3 gauging station in the sunrise and mid-day periods

Results of sunrise and mid-day TSS monitoring for six months at station D3, shown in Fig. 6, indicate that mid-day concentrations are higher than sunrise concentrations. It is noticeable that the TSS concentration for April is higher than the other five months. The lowest TSS values were recorded in December.
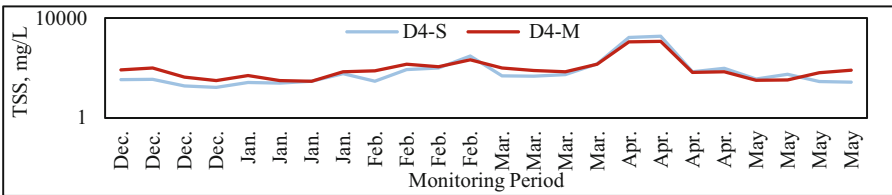
Fig. 7. Time series of TSS at D4 gauging station in the sunrise and mid-day periods

The time series of TSS concentrations obtained from 24 monitoring studies at the D4 gauging station, located at the outlet of the basin, is shown in Fig. 7. From this graph it can be observed that the mid-day concentrations are generally higher than the sunrise

concentrations. It was also noted that TSS concentrations were higher in April compared to other months. The lowest TSS concentrations values were recorded in December.

TSS is a parameter that varies from day to day. In addition to the conditions in the basin, atmospheric events can also cause an increase in the concentration of SS [10]. The time series of the variation of the TSS determined at the gauging stations are shown in Fig. 4, 5, 6 and 7. It is clear from these graphs that the TSS is higher in April than at any other time of the observation period. This peak increase is probably due to the melting of snow masses in the upper parts of the basin as a result of the heavy precipitation. At some of the gauging stations the transported TSS was found to have increased by a factor of 10 during this period. In addition, the discharges recorded at the D22A086 stream gauging station during the six-month monitoring period in the Lower Değirmendere Stream Basin are visualized in Fig. 8. It can be seen from this graph that the discharge reached its maximum in April.
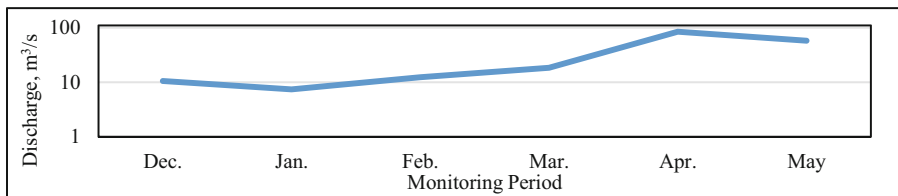
Fig. 8. The average discharges recorded at D22A086 SGS

It was found that the melting of snow masses in the upper parts of the basin with the warming of the weather and the spring rainfall had an increasing effect on the stream flow in April and May.

4   Results and Discussion

In order to observe the upstream and downstream changes in TSS concentration in the Lower Değirmendere Stream Basin during a six-month monitoring period, TSS samples were taken at four gauging stations at weekly intervals for 24 weeks. Furthermore, to determine the impact of anthropogenic activities on TSS (mg/L), variation of TSS concentration was analysed with samples collected during minimum (sunrise, 6.00 a.m.– 07.00 a.m.) and maximum (mid-day, 12.00 a.m.–01.00 p.m.) human activity periods.

The D1 and D2 gauging stations are in the upper parts where residential and industrial facilities are very sparse, the D3 gauging station is located in a place where residential and industrial facilities are dense, and the D4 gauging station is located at the outlet point of the basin where residential and industrial facilities are dense.

Figure 9 shows the upstream to downstream variation of the mean TSS concentrations obtained over the six-month observation period with respect to station location for both the sunrise and mid-day surveys. This graph is plotted on a logarithmic scale.

It is clear from this graph that the TSS concentration increases from upstream to downstream in both time periods. It is also understood that the TSS concentrations
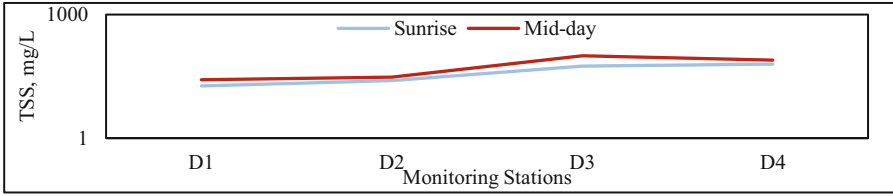
Fig. 9. Variation of the average TSS from upstream to downstream in sunrise and mid-day periods

determined at mid-day are higher than the TSS concentration at sunrise. The increase in TSS concentration at mid-day compared to the sunrise can be interpreted as an effect of human activities. The fact that the D3 gauging station is closer to the denser residential and industrial facilities compared to the D1 and D2 gauging stations has also caused the TSS concentration change during the day to be higher. It was found that the mid-day concentration change at station D4 was expected to be higher due to its proximity to denser residential and industrial facilities but was lower than at D3 gauging station. The decrease in TSS concentration at D4 gauging station compared to D3 gauging station was attributed to TSS accumulation because of widening of the stream cross-section, decrease in stream bed slope and decrease in flow velocity.

In addition to the sunrise and mid-day variation of TSS concentration, the scatter plot of the monthly average concentration is shown in Fig. 10. In this graph, the vertical axis is prepared on a logarithmic scale to better determine the scattering of the data.
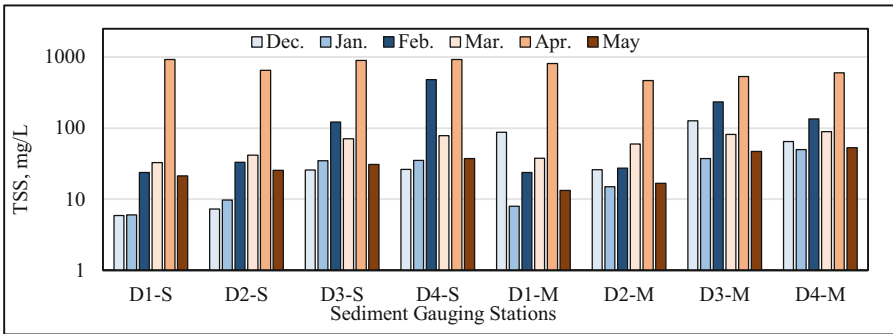
Fig. 10. Monthly variation of TSS concentration

It was found that the concentrations determined during the sunrise studies in the December, January, and February were lower than the concentrations determined during the March, April, and May. It was observed that the peak values were recorded in April at all stations. The highest TSS transport was determined at D3 and D4 gauging stations in both time periods. This is considered to be a consequence of the proximity of the D3 and D4 gauging stations to dense residential and industrial areas.

In the mid-day studies, no clear interpretation could not be made for the monthly changes, except for the increase from upstream to downstream. Because in addition to natural factors, the effects of continuous human-induced activities in the direction

of increasing the TSS concentration caused the inability to make a precise monthly interpretation. Peak values in the mid-day studies were also recorded in April.

According to the TSS concentrations obtained at sunrise and mid-day, it was found that the TSS concentration increased from upstream to downstream. The TSS concentrations from the mid-day study were found to be higher than the sunrise concentrations, with increases up to 40, 20, 75%, and 19% at D1, D2, D3, and D4 gauging stations, respectively. In the Lower Değirmendere Stream Basin, it is understood that there is an increase in mid-day TSS concentrations even in regions where agricultural land, wooded and semi-natural areas are dominate, residential areas are sparse and there are no manufacturing activities. This situation has resulted in more intensive TSS transport by the stream because of the intensive agricultural activities in the relevant area and the erosion-enhancing effect of irrigation. Therefore, in addition to residential areas and production activities, agricultural activities and the structure of the basin were found to have an impact on TSS transport during the day.

Although there are exceptions where higher values are observed than mid-day TSS concentrations due to precipitation during sunrise hours, it has been understood that mid-day TSS concentrations are generally higher than sunrise TSS concentrations.

5   Conclusion

The variation of total suspended sediment (TSS) concentration from upstream to downstream and the variation during different time periods of the day (sunrise and mid-day) in the Lower Değirmendere Stream Basin were investigated during a six-month monitoring period. In order to determine the impact of human-induced activities on TSS (mg/L), the TSS variation was analyzed with samples taken during the periods when the activities were considered to be minimum and maximum.

The TSS data were obtained from 24 field studies on a weekly basis during the sunrise (06.00–07.00 a.m.) and mid-day (12.00 a.m.–01.00 p.m.) periods. In addition to the changes from the upstream to the downstream, the variation in TSS concentration over different time periods were also examined.

- TSS concentration increased from upstream to downstream in both the sunrise and mid-day periods.
- During the six-month monitoring period, the highest TSS concentration throughout the Basin was determined in the April and the lowest in December and February.
- At all stations included in the study, mid-day TSS concentrations were found to be higher than sunrise TSS concentrations.
- Increasing temperatures in spring, melting of snow masses in the upper parts of the basin and spring precipitation have also had an increasing effect on TSS.
- It has been found that more intensive TSS transport occurs in areas where residential and industrial areas are dense. The TSS concentration varies depending on factors such as wastewater discharged from settlements, agricultural activities, erosion, precipitation, industrial activities and stream bed regulation works.
- The results show that TSS (mg/L) are also low during periods when anthropogenic and production activities are sparse (sunrise) and that the increase in anthropogenic and production activities during the day affects the increase in TSS concentrations.

- As a result of rising temperatures in spring, melting of snow masses in the upper parts of the basin and spring precipitation, TSS (mg/L) increased at all gauging stations.
- In order to study the impact of human activities on water quality in more detail, it will be possible to monitor other water quality parameters in the future.
- By identifying the exact location of the pollutants, measures can be taken to reduce TSS in the basin.
- Monitoring TSS is difficult and time-consuming, which prevents easy sampling. In the future, studies on TSS determination may be carried out using remote sensing or sensors. It is also thought that these methods may be useful for continuous sampling.

References

1. Hu, Y., et al.: Tidal-driven variation of suspended sediment in Hangzhou Bay based on GOCI data. Int. J. Appl. Earth Observ. Geoinf. **82** (2019). https://doi.org/10.1016/j.jag.2019.101920
2. Wu, W., Yang, Z., Tian, B., Huang, Y., Zhou, Y., Zhang, T.: Impacts of coastal reclamation on wetlands: loss, resilience, and sustainable management. Estuar. Coast. Shelf Sci. **210**, 153–161 (2018). https://doi.org/10.1016/j.ecss.2018.06.013
3. Moatar, F., Person, G., Meybeck, M., Coynel, A., Etcheber, H., Crouzet, P.: The influence of contrasting suspended particulate matter transport regimes on the bias and precision of flux estimates. Sci. Total. Environ. **370**, 515–531 (2006). https://doi.org/10.1016/j.scitotenv.2006.07.029
4. Khosravi, K., Mao, L., Kisi, O., Yaseen, Z.M., Shahid, S.: Quantifying hourly suspended sediment load using data mining models: case study of a glacierized Andean catchment in Chile. J. Hydrol. (Amst). **567**, 165–179 (2018). https://doi.org/10.1016/j.jhydrol.2018.10.015
5. Owens, P.N., et al.: Fine-grained sediment in river systems: environmental significance and management issues. River Res. Appl. **21**, 693–717 (2005). https://doi.org/10.1002/rra.878
6. Eom, J., et al.: Spatiotemporal variation in suspended sediment concentrations and related factors of coastal waters based on multispatial satellite data in Gyeonggi Bay, Korea. J. Coast. Res. **333**, 653–667 (2017). https://doi.org/10.2112/JCOASTRES-D-16-00012.1
7. Walling, D.E.: Assessing the accuracy of suspended sediment rating curves for a small basin. Water Resour. Res. **13**, 531–538 (1977). https://doi.org/10.1029/WR013i003p00531
8. Meybeck, M., Laroche, L., Dürr, H.H., Syvitski, J.P.M.: Global variability of daily total suspended solids and their fluxes in rivers. Glob. Planet Change **39**, 65–93 (2003). https://doi.org/10.1016/S0921-8181(03)00018-3
9. Duvert, C., Gratiot, N., Némery, J., Burgos, A., Navratil, O.: Sub-daily variability of suspended sediment fluxes in small mountainous catchments & ndash implications for community-based river monitoring. Hydrol. Earth Syst. Sci. **15**, 703–713 (2011). https://doi.org/10.5194/hess-15-703-2011
10. Mano, V., Nemery, J., Belleudy, P., Poirel, A.: Assessment of suspended sediment transport in four alpine watersheds (France): influence of the climatic regime. Hydrol. Process. **23**, 777–792 (2009). https://doi.org/10.1002/hyp.7178
11. DSI, DSI 2020 official water resources statistics (2020). https://www.dsi.gov.tr/sayfa/detay/1499
12. Directorate General of Environmental Impact Assessment Permit and Inspection, Trabzon ili 2020 yılı çevre durum raporu, 20210616135008.Pdf (2021)
13. Satılmış, U.: A study on spatial and temporal variation of surface water quality in the Stream Değirmendere Watershed (Trabzon), MsC. thesis, KTU The Graduate School of Natural and Applied Sciences (2015)

14. APHA, Standard methods for the examination of water and wastewater, 18th edn., American Public Health Association (APHA), American Water Works Association (AWWA) and Water Pollution Control Federation (WPCF), Washington DC (1992)

15. Turkish Standards Institution, Su kalitesi - Askıdaki katı maddelerin tayini - Cam elyaf süzgeçler kullanılarak süzme yöntemiSu kalitesi- Askıdaki katı maddelerin tayini- Cam elyaf süzgeçler kullanılarak süzme yöntemi (TS EN 872), Ankara (2007)

Extremely High and Average Climate Forecast: Impact on Thermal Performance in Urban Areas

Berk Adali[(✉)] and Yigit Can Altan

Department of Civil Engineering, Ozyegin University, İstanbul, Turkey
berk.adali@ozu.edu.tr, yigitcan.altan@ozyegin.edu.tr

Abstract. This research aims to compare the extreme and monthly average weather conditions in an urban area model, designed in accordance with Yesilkoy/Istanbul, and examine the effect of mitigation strategies. To achieve this, five urban designs are developed using different geometries (aspect ratio) and materials (albedo level). These configurations were analyzed using Computational Fluid Dynamics software (ANSYS) along with two different meteorological data. Models were simulated using data from 29th July 2020 for the hottest day and monthly average of July 2020 data. Also, in the study, TS 825 standards are used with a basic model as an evaluation parameter to check the effect of the weather boundary conditions. The outputs aim to enlighten the impact of weather data on the most suitable geometric configuration and best thermal performance design for the given climate projections. The advantages and disadvantages of extreme and average weather data are presented. As a result of the studies, the highest average wall surface temperature observed among the five scenarios using monthly average weather data is 42.12 °C at 2 pm. In contrast, the highest average building surface temperature value observed in the five analyses using extreme weather data reaches 48.7 °C at 11 am.

Keywords: Urban Microclimate · CFD · Different Climate Forecast

1 Introduction

The average global temperature is increasing, leading to more frequent extreme weather events that negatively impact the health of living things and building energy consumption in urban areas. Especially, the expansion of cities and the use of construction materials have caused a significant rise in average temperatures. In examining the connection between urbanization and temperature increase, researchers have explored various aspects, including building energy use, heat waves, and human health [1–4]. The difference in average temperature in the urban area with respect to rural areas is known as the Urban Heat Island (UHI) effect. Today, mitigation strategies are applied to solve UHI problems to prevent the negative effects of energy use in buildings and uncomfortable living conditions for human health.

Mitigation strategies aim to decrease the adverse effects by changing the material and geometric properties of the buildings. These strategies can focus on various parameters such as aspect ratio [5], albedo level [6], and urban design [7]. Various types of

computational studies can be found in the literature for simulating the thermal environment of urban areas. Toparlar et al. separated simulations into categories such as scale, configuration type, considered parameters, time solver, and validation [3]. In this investigation, transient analysis is made on a 3D generic urban area on a microscale by evaluating the consolidated short-wave radiation gain, enhanced long-wave radiation gain from the sky, reduced long-wave radiation loss, increased heat storage, evapotranspiration, and reduced turbulent heat transport were evaluated. Although time-dependent analysis requires more computational power than steady-state analysis, transient simulations are capable of modeling dynamic conditions such as urban heat islands and wind flow patterns. In line with the time solver type and aim of the study, real meteorological data which are obtained from Turkish State Meteorological Service (TSMS) (Yesilkoy/Istanbul) are preferred instead of parametric meteorological data such as constant wind speed or temperature as input [8]. To mitigate the UHI effect, the thermal performance of the urban area is analyzed, and strategies are quantified.

Proper selection of weather conditions is essential for determining mitigation strategies' efficiency, energy conservation, and recovery. There are two primary approaches for selecting a database for the computational domain. If the aim is modeling and analyzing the intense weather conditions, extreme weather data from the selected location can be used. Alternatively, if the goal is to acquire a general idea about environmental thermal performance for the chosen area, the average weather data can be used for the analysis. This study focuses on the assessment of differences between these two approaches. Thereupon, five different geometrical urban areas or building blocks are created and modeled with extreme (hottest) and average weather data. Results are evaluated according to buildings' surface temperature and streets' wind velocity values. The remaining sections of the study explain the problem statement, details of urban areas and describe the methodology part. Following those, results and discussions are presented, and conclusions are given.

2 Problem Statement and Urban Area

2.1 Problem Statement

In this study, comparisons of two different weather conditions on the thermal performance of the building environment are assessed for the selected urban area. These analyses aided in identifying the optimal geometrical design and material selection for both average and extreme climatic projections by examining the effects of weather forecast over the outcomes. These analyses enable us to reduce the adverse impacts on the environment and climate for urban area analysis and help us comprehend the impact of meteorological conditions on the microclimate. Various urban areas with diverse geometries, construction materials, and average and extreme weather events are modeled to understand the effects. ANSYS Fluent, a commercial Computational Fluid Dynamics (CFD) package, is used to analyze the generated urban area models. In accordance with the purpose of this study, the weather conditions data for 29th July 2020 (the hottest day of the year) and the average weather conditions of July in the same year are investigated for five different configurations based on the height of the buildings and the buildings' surface albedo. Table 1 summarizes the specifications of the studied cases.

Table 1. Summary of the studied parameters for different scenarios.

Number of Case	Albedo Value	H/W	Weather Condition	Number of Case	Albedo Value	H/W	Weather Condition
Case I	0.25	1	Extreme	Case VI	0.25	1	Average
Case II	0.4	1	Extreme	Case VII	0.4	1	Average
Case III	0.6	1	Extreme	Case VIII	0.6	1	Average
Case IV	0.6	1.5	Extreme	Case IX	0.6	1.5	Average
Case V	0.6	0.75	Extreme	Case X	0.6	0.75	Average

2.2 Location-Specific Information

Oke [9] mentioned that there is a relationship between population and temperature in urban areas. As the population rises, an average temperature increase is observed in the urban area. Istanbul is selected as a reference location to investigate the significant correlation between population growth and its impact on the future. With a current population of 15.5 million, urgent action is required to mitigate potential challenges that may arise. However, modeling the wind profile and gathering the meteorological data is not straightforward. In the urban microclimate or thermal environment analysis, the logarithmic wind profile is used actively to create a realistic domain to evaluate the urban design. Therefore, selecting the station where the data are received is important.

Meteorological data from the Atatürk Airport station located in Yesilkoy/Istanbul, with coordinates of 40°58′34″N 28°48′51″E and where it is known to be very rough on davenport class due to the number of floors of buildings [10]. Throughout this paper, care is taken to ensure that the height values chosen are near the already-existing structures in the area. Average building surface temperature, temperature in urban areas, and wind velocities are evaluation parameter attributes used to investigate the basic urban area with 16 structures. Also, the monthly cooling cost is used as an evaluation parameter for the solution approaches.

3 Methodology

3.1 Computational Domain and Mesh Details

Octagonal prism which has 206.7 m edge length, 100 m domain height, 200 m shortest distance between the buildings and outlet surfaces, and 498.9 m distance between two opposite edges, is preferred to create a fundamental urban area with an aspect ratio equal to one. The specifications of the domain are determined in accordance with the study by Abu-Zidan et al. [11]. With the aid of an octagonal prism, there is no need to modify or recreate the domain for extreme and monthly average analysis. The bottom surface is separated into two parts with one circular sub-domain with a 60 m radius. This circular sub-domain located around the buildings is created at the center of the domain. There are a total of 16 same building blocks with 10-15-7.5 m height, and these buildings block are located symmetrically as a rectangular base area with 70x70 m. Moreover,

structures outside of the circular sub-domain are not modeled explicitly. One of the most significant parameters which can affect the accuracy of analysis is the blockage ratio. This ratio is calculated with the relationship between the domain's cross-section and the cross-sectional area of buildings and streets. In light of the given physical information of the domain, the blockage ratio equals 1.4%, which is in the safe zone compared to the recommended value of 3% [12]. Details of the mesh design are changed depending on the location. While fine cells with 0.25 m are used on the surface of the buildings and with 0.1 m are used around the buildings with boundary layer, coarser cells are used for the rest. However, the increase in mesh size is limited to a 1.1 growth rate, which is below the recommended value of 1.3 [12]. Furthermore, another boundary layer is added to the domain's bottom surface to fix the model's first cell height.

3.2 Boundary Conditions
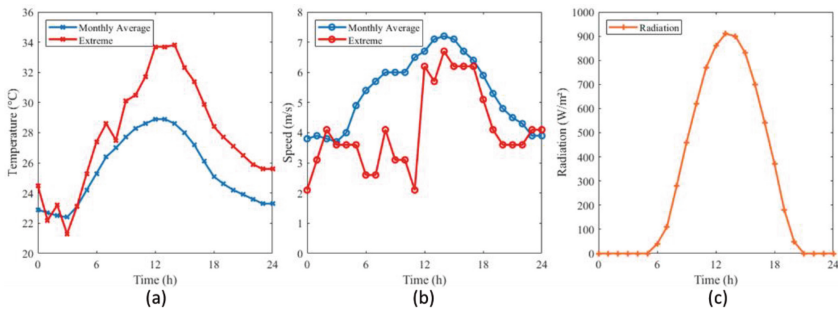
Fig. 1. Meteorological data for (a) temperature, (b) wind velocity, and (c) solar radiation with hour

Hourly meteorological data provided by TSMS are obtained, and these data are adapted to a user-defined function (UDF) for extreme (29th July 2020) and average (July 2020) climate modeling. Wind speeds, wind directions, and air temperature values are modified based on scenarios. While wind which is obtained for the extreme scenario, comes from the north direction, otherwise in the average scenario, the wind comes from the north-east direction with generally higher speed than the extreme scenario. Furthermore, wind speed differences between hours are critical because the wind speed change is smoother in average scenario data. When the temperature value is examined, air temperature values of extreme scenarios are found to be higher than the average scenario from 4 am to the end of the day, as shown in Fig. 1.

Also, the maximum temperature differences between the two cases increase to 5.2 °C at 2 pm. Direct and diffuse radiation values are used the same in both scenarios since amounts of radiation data are not adequate to modify to the average scenario. In this circumstance, only wind speed, wind direction, and air temperature are specified as weather parameters. The logarithmic profile for wind speed (U (m/s)) is used and defined as [3];

$$U_{(Z)} = \frac{u^*}{\kappa} \ln(\frac{z + z_0}{z_0}) \tag{1}$$

The roughness length ($z_0 = 0.5$ m) is chosen based on the location's davenport class and has a critical role in the calculation of the U (m/s) value. Another parameter is atmospheric boundary layer friction velocity ($u*$) and calculated as shown in Eq. (4). Most stations, according to TSMS [13], measure wind at an altitude of 10 m, and the reported values for meteorological stations measuring at various elevations are adjusted to this altitude. After that, other wind speed values are calculated related to this reference value at 10 m height. Therefore, near the U (m/s) value, turbulent kinetic energy (k (m^2/s^2)) and turbulence dissipation rate (ε (m^2/s^3) are determined for inlet and outlet boundary conditions, and these parameters are calculated with Eq. (2) and Eq. (3) like shown the study by Toparlar et al. [3];

$$k = \frac{u^{*2}}{\sqrt{C_\mu}} \tag{2}$$

$$\varepsilon(z) = \frac{u^{*3}}{\kappa(z + z_0)} \tag{3}$$

$$u^* = \frac{\kappa \times U_{ref}}{ln(\frac{z_{ref}+z_0}{z_0})} \tag{4}$$

In Eqs. (1–5), height is represented by the z (m) height coordinate, the von Karman (κ) constant is equal to 0.41, and the constant C_μ is equal to 0.09. As mentioned before, outside of the sub-domain is not modeled explicitly. For that reason, the standard wall function is used in this part of the bottom surfaces of the domain. The first cell mesh design on the domain's bottom surface depends on the roughness height (k_s) parameter.

$$k_s = \frac{9.793 \times z_0}{C_s} \tag{5}$$

According to the davenport classification given in [10], the z_0 value is considered as 0.5 m for determining the roughness height parameter. On the other hand, urban areas' roughness constant (C_s) value is defined to be 7. The roughness height (k_s) parameter is derived from Eq. (5) using the information provided regarding the aerodynamic roughness length and roughness constant, and it is found to be 0.7. However, the ground plane is modeled as $z_0 = 0$ m in the sub-domain, which is the domain's center.

In addition to the inlet wind boundary conditions set in the urban area, thermal and physical conditions adjustments are also made on the building and domain surface. The ground layer of the domain is not modeled explicitly. It is modeled as a thin wall with a 10 m thickness, and 10 °C constant temperature is added at 10 m below ground. Also, heat flux values are used actively in the bottom surface of the domain to model the evapotranspiration effect, which is generated from the green part of the urban area. These heat flux values are not defined as constant but are updated with time and radiation effects. For instance, surface heat flux increases to 246 W/m^2 at maximum sun's rays, and then it starts to decrease with the sun's moves. Internal air temperature is also assumed to be a constant parameter at 24 °C. On the buildings' surface, brick material with a thickness of 0.4 m is used for modeling thin walls. Since windows and other openings are not considered in the study. It is assumed that the convection type is natural convection, and the heat transfer coefficient value is used at 20 W/m^2K [14] inside buildings. The thermophysical properties of materials are provided in Table 2.

Table 2. Thermophysical material properties

Materials	Density (kg/m^3)	Specific Heat (J/kgK)	Thermal Conductivity (W/mK)	Absorptivity			Emissivity
Wall	1400	900	1.7	0.4	0.6	0.75	0.88
Earth	1150	650	1.5	0.6			0.9

3.3 Other Computational Parameters in Solver Settings

To simulate urban microclimate, 3D URANS (Unsteady Reynolds-Averaged Navier-Stokes) equations are solved with the realizable k-turbulence model, and a standard wall function is chosen for near-wall treatment in the domain surface. In addition, the solar radiation P1 model is used, and the sun direction vector is generated using the solar calculator included in the ANSYS Fluent user interface, based on the global position. The pressure-velocity coupling is solved by the SIMPLE algorithm, and pressure interpolation is adjusted to second order. Furthermore, second-order upwind is used to achieve spatial discretization of momentum, turbulent parameters, and energy. The Least Squares Cell Based approach is employed for gradient discretization, and the second-order implicit method is used for time integration. Transient simulations run in fifteen-minute steps, with a total time step of 96 (24 h) daily. Furthermore, the simulation is not terminated until all residuals' criteria reach the minimum value and it converges. Finally, the following minimum values for various scaled residuals are obtained: 10^{-3} for continuity, 10^{-4} for u - v - w velocities, 10^{-4} for k and ε, and 10^{-7} for energy and radiation.

4 Result and Discussion

In Fig. 2, the highest average buildings' surface temperature values on the extreme and average scenarios are 48.7 °C and 42.12 °C, respectively. The peak hours of the highest temperatures differ between the two scenarios, with the extreme scenario showing the critical hour at 11 am, whereas in the average scenario, the hottest time of the day is 2 pm. Also, the average buildings' surface temperature differences are 5.38 °C at 2 pm.

Moreover, by examining the minimum average temperature values during the critical hours of 11 am and 2 pm in both scenarios, the results showed respective values of 45.8 °C and 40.02 °C. In light of these results, temperature differences between the two scenarios are 6.5 °C and 5.8 °C in maximum and minimum average building surfaces' values.

In addition to that, when the temperature values are compared between two scenarios, for extreme weather conditions, the average surface temperatures remained higher than the maximum average temperature value of monthly average conditions for up to 5 h. With these evaluations, the effect of the weather boundary conditions can be observed clearly. Maximum and minimum average surface temperature values are shown in the same cases with high albedo level and 1.5 H/W ratio (IV and IX), and low albedo and 1.0 H/W ratio (I and VI) in both scenarios are depicted in Fig. 3.
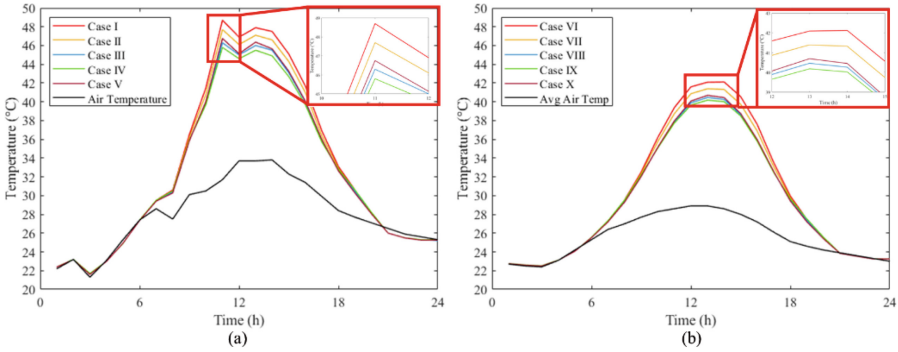
Fig. 2. Average temperature on buildings' surfaces in (a) extreme and (b) average
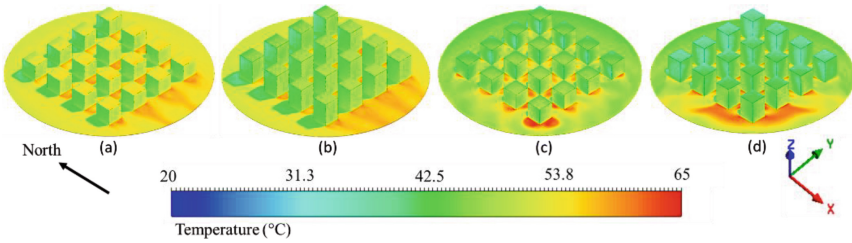
Fig. 3. Surface temperature on cases (a) I and (b) IV at 11 am, (c) VI and (d) IX at 2 pm

Another comparison parameter to evaluate the effect of the meteorological data is the TS 825 Thermal Insulation Requirements in Buildings (the obligatory standard). Using this approach, the cases with the highest average surface temperature values (I and VI) in both weather conditions were selected, and their cooling costs were calculated. Cooling cost ratios related to five calculations are illustrated in Fig. 4.
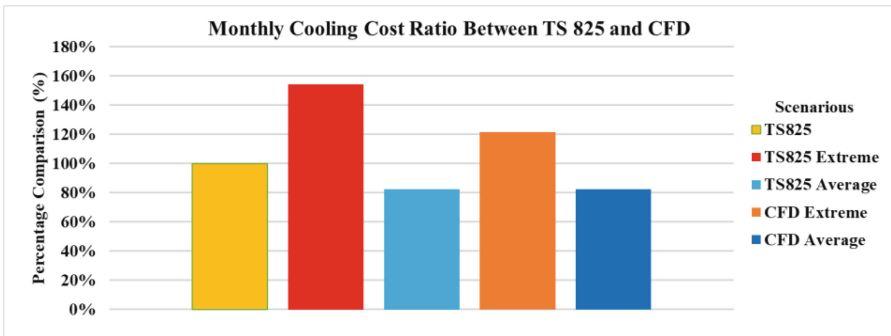
Fig. 4. Cooling cost ratios

Firstly, the cooling cost of the 10-m-high building is calculated according to the reference value given in TS 825 formulations, with the tables and data given in the standard. The wall's thermophysical properties given in Table 2 are used to calculate the reference scenario, "TS 825" case. In addition, 19 °C, which is the reference monthly average indoor temperature in TS 825, is used as the indoor temperature of the building, while the outdoor temperature values are determined as 24.9 °C for the second zone value reached in the guide. Similarly, other parameters such as solar radiation intensity, shading factor, and solar energy transmission factor are selected per the guide and the building. In the second and third scenarios, TS825 Extreme and Average, monthly average outdoor temperatures increase to 33.8 and 28.65 °C due to TSMS. Also, the monthly average inside temperature parameter is increased to 24 °C as in ANSYS simulations. According to the results, while the cooling cost ratio increased by almost 54% in "TS 825 extreme" scenario, the cooling cost decreased 18% in "TS 825 average" scenario. In further analysis, the monthly cost of CFD Extreme and CFD Average are computed by determining the wall heat flux values per cell on the building surfaces using simulation results. As seen in the extreme and average analysis results, cooling cost increased 21% and decreased 18%.

As a result, the monthly cooling cost value is almost equal in the average scenarios. However, there is a huge difference between the monthly cooling cost value of extreme scenarios in TS 825 and CFD calculations. The cost value obtained from TS 825 Extreme is computed to be 27% higher than the value acquired from CFD Extreme. The reason for these differences in the investigations of cost analysis is the solution details of CFD Analysis and TS 825 Guide. While TS 825 guide uses average weather conditions and locations, CFD simulations can use specific weather conditions, boundary conditions, and locations with actual modeling of the wind flow and heat transfer. The wind speed values obtained at 14:00 are shown with contour maps in Fig. 5. Wind direction has a critical role in wind speeds that occur in an urban configuration. In the extreme scenario, while the wind can enter the corridors in the x direction without being blocked, this does not occur in the average scenario. That's why, as seen in Fig. 5, unlike the TSMS data, the wind speed is generally lower in corridors in the average scenario. In the average scenario, the wind slows down as it enters the corridors and is ineffective in cooling the building surfaces. Since convective heat transfer is directly related to the temperature difference and velocity of the fluid, convection heat transfer values in the urban area are also affected by wind speed and temperature changes. These analyses of the wind models of the two situations allow for a more detailed interpretation of external effects in CFD simulations. Together with the external factors examined, more accurate solutions can be developed for the urban heat island problem in the region.
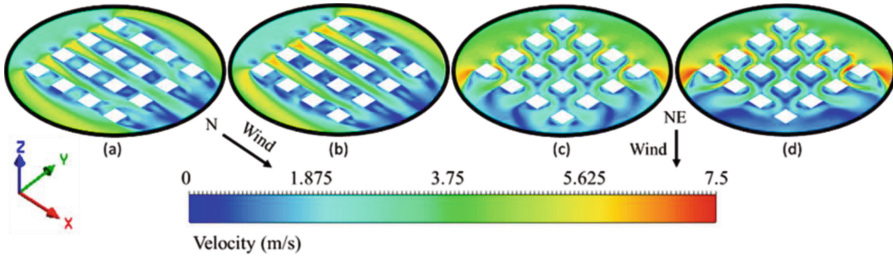
Fig. 5. Wind velocity values at 2 pm on cases (a) I, (b) IV, (c) VI, and (d) IX at 1.5 m height

5   Conclusion

This study presents the results of different scenarios calculated using unsteady CFD simulations and TS 825 regulation for comparing the cooling costs of buildings in the Yesilkoy/Istanbul region. The CFD analysis is simulated using the 3D URANS approach and the realizable k-ε turbulence model performed on a high-resolution grid, considering wind flow and heat transfer (conductivity, convection, and radiation). The simulations used factors affecting the urban climate, such as short and long-wave radiation, wind speed, evapotranspiration, and heat storage, excluding the effect of anthropogenic heat sources. Positive and negative advantages of scenarios are interpreted by calculating the cooling cost as a percentage with two different examination approaches. It has been observed that results obtained from buildings with a height of 10 m and low albedo levels, the order made for monthly cooling expenses can be listed as "CFD Average", "TS 825 Average", "TS 825", "CFD Extreme", and "TS 825 Extreme" from lowest to highest. The results show that using CFD simulations to model the urban area with average weather conditions is not more efficient than the results from the TS 825 cases due to computational power. The TS 825 guide is more advantageous for the average scenario because of CFD methods' high computation cost and simulation time. For instance, when the value obtained in the original TS 825 scenario is considered 100 units, the cost in the average TS 825 and CFD models is the same. However, in extreme cases, CFD simulations have critical differences related to wind and heat transfer modeling in 3D configurations. Even so, this does not mean that the values obtained from CFD simulations are definitely more accurate because there are certain limitations in the models created. Accordingly, CFD simulations created with guidelines provide low cooling costs for urban areas in extreme weather events. Considering the value obtained in the original TS 825 scenario as 100 units, the cost calculated in the TS 825 extreme scenario is approximately 33 units more than in the CFD extreme scenario. As a future study, further comparison for population growth can be used as a parameter with the increase in the number of buildings will be a good way to examine the effect of the number of buildings in the city on the approaches. Besides, wind direction can be updated at each step by using a dynamic model for wind angle to better examine the effect of wind angle and improve results in CFD analysis.

References

1. Scott, M.J., Wrench, L.E., Hadley, D.L.: Effects of climate change on commercial building energy demand. Energy Sour. **16**(3), 317–332 (1994)
2. Xu, P., Huang, Y.J., Miller, N., Schlegel, N., Shen, P.: Impacts of climate change on building heating and cooling energy patterns in California. Energy **44**(1), 792–804 (2012)
3. Toparlar, Y., et al.: CFD simulation and validation of urban microclimate: a case study for Bergpolder Zuid, Rotterdam. Build. Environ. **83**, 79–90 (2015)
4. Haines, A., Kovats, R.S., Campbell-Lendrum, D., Corvalan, C.: Climate change and human health: impacts, vulnerability and public health. Public Health **120**(7), 585–596 (2006)
5. Ali-Toudert, F., Mayer, H.: Numerical study on the effects of aspect ratio and orientation of an urban street canyon on outdoor thermal comfort in hot and dry climate. Build. Environ. **41**(2), 94–108 (2006)
6. Mirzaei, P.A., Haghighat, F.: A procedure to quantify the impact of mitigation techniques on the urban ventilation. Build. Environ. **47**(1), 410–420 (2012)
7. Allegrini, J., Dorer, V., Carmeliet, J.: Coupled CFD, radiation and building energy model for studying heat fluxes in an urban environment with generic building configurations. Sustain. Cities Soc. **19**, 385–394 (2015)
8. Allegrini, J., Dorer, V., Defraeye, T., Carmeliet, J.: An adaptive temperature wall function for mixed convective flows at exterior surfaces of buildings in street canyons. Build. Environ. **49**(1), 55–66 (2012)
9. Oke, T.R.: Boundary Layer Climates, 2nd edn. Routledge, London (2002)
10. Stewart, I.D., Oke, T.R.: Local climate zones for urban temperature studies. Bull. Am. Meteor. Soc. **93**(12), 1879–1900 (2012)
11. Abu-Zidan, Y., Mendis, P., Gunawardena, T.: Optimising the computational domain size in CFD simulations of tall buildings. Heliyon **7**(4), e06723 (2021)
12. Franke, J., Hellsten, A., Schlünzen, H., Carissimo, B.: Best practice guideline for the CFD simulation of flows in the urban environment. Doctoral dissertation, COST European Cooperation in Science and Technology (2007)
13. TSMS. https://www.mgm.gov.tr/genel/ruzgar-atlasi.aspx. Accessed 06 July 2022
14. Kosky, P., Balmer, R., Keat, W.D., Wise, G.: Exploring Engineering: An Introduction to Engineering and Design, 3rd edn. Academic Press, Elsevier (2012)

The Capacity of Coastal Gravel Beaches in Absorbing the Storm Wave Energy

Umut Türker[1]([✉]) [iD] and M. Sedat Kabdaşlı[2] [iD]

[1] Civil Engineering Department, Eastern Mediterranean University, Famagusta, North Cyprus, Turkey
umut.turker@emu.edu.tr
[2] Engineering Faculty, İstanbul Technical University, İstanbul, Turkey
kabdaslis@itu.edu.tr

Abstract. Four series of laboratory experiments were conducted to observe the effect of storm waves on the morphologic changes of coastal bed profile. The aim was to interpret the relationship between the offshore bar and foreshore erosion profiles under the effect of storm waves and calculate the damage generated over the bed profile by the storm waves. The beach material was one of the most important factors on the short-term morphological changes of cross-shore bed profile, and the size of the bed material was composed of gravel. The relationship between the wave characteristics and post-storm bed profiles at different gravel sizes were analyzed and dimensionless parameters representing the event were discussed. Depending on the size of the gravels, the damage level over the profile exhibit variations where the damage level was characterized by the length measured in between the center of masses of offshore bar and foreshore erosion. Dimensionless parameters like damage parameter, resistance parameter and steepness parameter were effective in defining the damage. It was observed that the damage of coastal region increases as the beach profile gradient increases and the effective static stability was reached by increasing the size of the gravel particles or increasing the magnitude of dimensionless shore resistance parameter.

Keywords: Wave Height · Dynamic Stability · Damage parameter · Coastal Profile · Gravel

1 Introduction

The use of natural or man-made coastal defense habitats and structures is rapidly increasing in order to maintain the static and dynamic stability of coastal ecosystems. In this respect, constructing low-crested and submerged hard coastal defense structures [1–3] and plantation of coastal vegetation at coastal zones [4, 5] are highly used and recommended. However, it is vital to understand the behavior of coastal morphology before initiating any project based on coastal defense. For such purposes, in the past, coastal cross-shore beach profile morphodynamic models have been well assembled for sandy [6–8], mixed sand/gravel [9, 10] and gravelly beaches/barriers [11]. Further to such

developments on the beach morphology, morphological changes and their consequences over the subareal beach profiles are recently evaluated for sandy profiles [12]. Among the above mentioned models, non-uniform gravel beach models are lacking laboratory investigations, static and dynamic stability analysis based on material sorting and the evidence base for developing a generic understanding than their sand-only, uniform gravel-only and mixed sand/gravel counterparts.

In general gravel beaches have steeper slopes than the sandy beaches, with overall slopes (β) typically more than 5°, thus have steep slopes and often inclined up to 1:5 gradients. The main factors yielding steep beach morphology is the local wave climate and larger angle of repose due to large sediment size [13, 14]. The main criteria separating gravelly beaches from its counterparts is their geometric convex shape. Pertinent literature suggests and proves that profile responses of gravel beaches are cyclic (seasonal variations are evident) and related to the wave energy in which loss of material reduces the overall beach profile under storm waves and builds back up the profile under lower energy waves. Hence, the energy released during wave breaking and the location and type of breaking of coastal waves turn out to be an important factor for the morphologic changes of gravel beaches. Kabdaşlı and Türker [15] examined the amount of wave energy dissipation at coastal regions and find out that the plunging type of breaking dissipates the highest energy. Over the gravel beaches, the steep face makes shores to be more reflective, and this reflection grounds the breaking of waves to break within the close vicinity of shoreline [16].

Polidoro et al. [17] carried out a laboratory work to clarify the effect of storm waves on gravel beaches. In this study a new parametric model was developed to propose morphological changes of gravel beaches under the storm waves. The morphological changes were mostly associated with the erosion of beach faces and small bar formations at the close vicinity of shoreline, closer than the sandy and mixed sand-gravel beaches. Even though many work have been developed to generate empirical models for predicting morphological changes for cross-shore sandy beach profiles [18–21] and subareal beach profiles [12], it has been discovered by Poate et al., [22], that their findings are invalid on gravel beaches.

For the last decade numerical models have been developed to simulate the run-up and overwashing characteristics over the gravel beaches [23] and [24]. However, these studies were limited to the hydrodynamic interaction of sea waves and the gravel beaches without concentrating on the sediment transport processes. Lately, Pollard et al. [25] simulated the effect of storm waves over the gravel beaches by means of morphological parameters. Also, Ions et al. [26] developed a model by the help of XBeach-G and predict changes in gravel beach morphology. Nevertheless, the validity of previous empirical and numerical models displayed good results but the majority of them still needs greater exploration for better understanding the gravel beach morphodynamics.

In this study, four series of laboratory experiments were conducted to observe the resilience of gravel beach profiles to storm waves. The aim was to interpret the relationship between the onshore erosion and foreshore bar under the effect of storm waves and calculate the damage generated on the bed profile. The beach material, gravel was one of the most important factors on the short-term morphological changes of cross-shore bed profile. The relationship between the wave characteristics and post-storm bed profiles

at different gravel sizes were analyzed and dimensionless parameters representing the event were delineated.

2 The Damage Parameter

Storm waves approaching perpendicular to the gravel coast erodes the fore-beach until the dynamic stability of the shore is attained. As the erosion process initiates, the eroded gravel material is transported towards the offshore direction to initiate the formation of offshore bar. As the water depth above the offshore bar gets shallower enough to break the incoming storm waves, the waves break and dissipates their energy. Together with the energy dissipation of storm waves, the erosion over the foreshore terminates and the static stability of the gravel beach profile is attained. The damage over the beach front generated by storm waves until the static stability is reached can be defined as coastal erosion or scour. This seasonal variations on the morphology of the coastal zone is therefore depends on the incoming wave height and period, the initial slope angle, sorting properties of the gravel beach, and the amount of erosion at the beach front and the amount of accretion at the offshore of the coast. The distance (Ω) between the center of gravity of eroded region and the offshore bar formation is also an important variable for defining the damage over the beach profile. Therefore, the damage parameter for non-uniform gravel beaches can be written as given in Eq. (1).

$$S_c = f(\Omega, H_o, T_o, \phi_{85}, \phi_{15}, A_e, A_b, tan\alpha, g) \tag{1}$$

Here, H_o and T_o represents the deep water wave height and period. The particle size where 85 percent of the total sample is finer is represented by ϕ_{85} and the particle size where 15 percent of the total sample size is finer is represented by ϕ_{15}. The amount of erosion at the beach face is given by A_e and the corresponding bar area somewhere offshore is termed as A_b. The original slope of the beach is represented by $tan\alpha$. The g term is gravitational acceleration.

As a novelty, in order to represent the damage as a function of the distance between the center of gravity of eroded region and the bar formation dimensional analysis model is employed with the variables given in Eq. (1). The resultant dimensionless parameters are as follows:

$$S_c = \frac{\Omega}{H_o} \tag{2}$$

$$\mu = \frac{A_e}{L^2} \tag{3}$$

$$\Delta = \frac{A_e}{A_b} \tag{4}$$

$$\xi = \frac{\phi_{85}}{\phi_{15}} \tag{5}$$

$$m = tan\alpha \tag{6}$$

$$F = \frac{H_o}{gT_o^2} \tag{7}$$

The dimensionless damage parameter, S_c, defined by Eq. (2) is related to the movement of the gravel particles due to energy dissipated as the wave breaks. The ratio between the eroded area and the incoming wave length, μ defines the dimensionless erosion area. The fraction of the erosion area and the offshore bar area defines the dimensionless sediment transport parameter, Δ. Dimensionless shore resistance parameter, ξ, on the other hand, indicates the resilience capacity of coastal region to the external forces. The slope of the coastal region before being exposed to the storm waves is represented as, m. The steepness parameter F is defined in Eq. (7) and is the ratio of incoming wave height to the wave length.

Based on the derived parameters it can be observed that the damage of coastal region increases as the gradient increases. An effective static stability can be reached by increasing the size of the gravel particles or increasing the magnitude of dimensionless shore resistance parameter. The growth of coastal erosion and offshore bar continues until the dynamic stability is reached. At the beginning of the growth process the damage parameter increases. As the dynamic stability progresses the rate of growth of coastal erosion and offshore bar decreases and finally ends. Even though the previous modelling studies, either flume tests or numerical, contributed to the developments on understanding the behavior of gravel coastal morphodynamics, their validity is limited. Therefore, the relationship between the above mentioned six parameters and their effect on the failure of gravel coastal beaches will be tested through flume tests and empirical analysis.

3   Experimental Setup and Results

The experiments were conducted in a flume that was 22.5 m long. The width of the flume was 1 m and the maximum depth capacity was 0.5 m. The initial slope of the gravel barrier was 1:5. The test codes, numbers, material properties and test results for different material compositions are given in Table 1.

The duration of each experiment was limited to 20–25 min which was long enough to observe the evolution of dynamic equilibrium over the profile. The wave properties such as significant wave height and period were determined by recording each wave passing over a fixed point. At the end of each experiment, the profile change over the slope, were recorded. The offshore bar formation and coastal erosion over the profile were recorded and digitally stored. The resultant similar profiles recorded after each experiment are given in Fig. 1, 2 and 3. In each of these figures, the wave properties (wave height and period) of each experiment were selected to be close to each other but with different shore resistance parameters. Then, the distance between the center of gravity of eroded region and the offshore bar formation (Ω) were measured. The results were representing the magnitude of damage of each profile at the end of each experiment.

As the initial beach slope was constant, the influence of variable slopes on the dimensionless damage parameter, dimensionless sediment transport parameter, dimensionless shore resistance parameter and the dimensionless erosion area were not accurately defined and analyzed, which is the main limitation of this study. In addition, different

Table 1. The summary of experimental results under regular wave conditions

Exper. code	Exper. No	Significant wave height H_s (cm)	Wave period T_s (sec)	Dynamic Equilibrium distance Ω (cm)	$\varphi_{85}/\varphi_{15}$
F	1–10	3.71–9.36	0.54–1.09	25.45–75.70	18.62
G	11–19	4.94–9.04	0.60–1.08	27.81–63.50	26.67
H	20–28	4.78–8.10	0.57–1.09	33.57–77.75	70
I	29–37	4.78–8.10	0.57–1.09	30.28–54.79	48.07
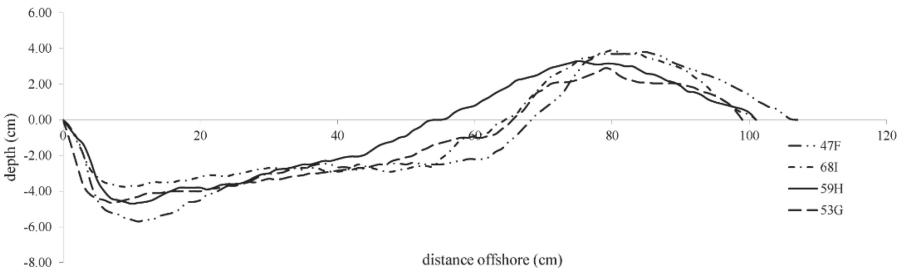
Fig. 1. The resultant profiles of experiments 47F, 68I, 59H and 53G.

sized gravel was used throughout all the experiments and blended with different sized pebble particles to obtain non-uniform beach materials.
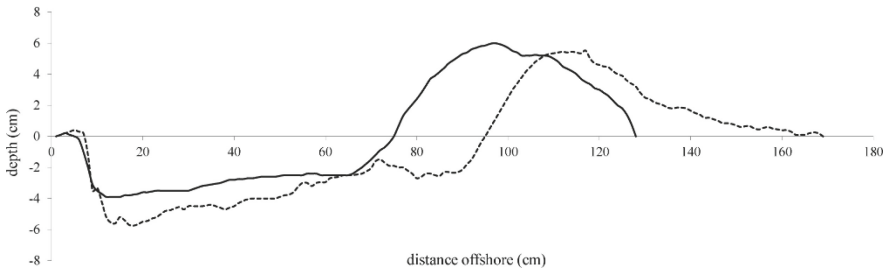
Fig. 2. The resultant profiles of experiments 40F and 50G.
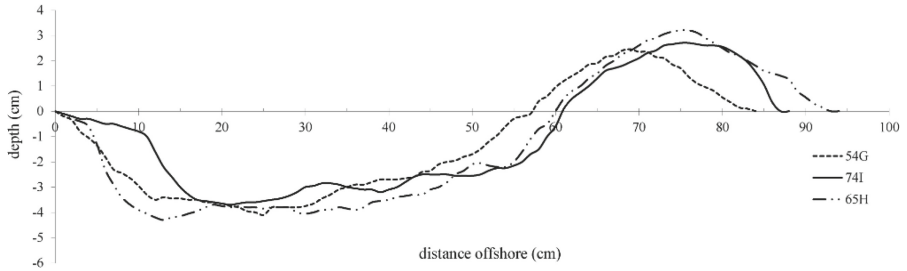
Fig. 3. The resultant profiles of experiments 74I, 65H and 54G

4 Analysis and Discussions

In all the experiments, it is observed that the space between the center of mass of eroded region and the offshore bar formation (Ω) was directly proportional to the incident wave height. As the wave height increase, the energy dissipation due to the wave breaking enlarged. Increase in the amount of energy dissipation commenced the transport of more materials towards offshore to accelerate the evolution of an offshore bar. Therefore, by definition, more energy loss through wave breaking process decrease the resilience of profiles and increase the risk of failure of gravel beaches with severe damage occurrences. Figure 4 shows how does damage enlarged over each profile as the wave height (wave energy) increases.
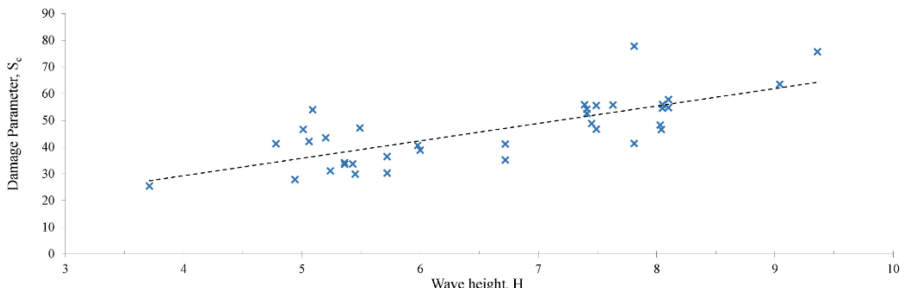
Fig. 4. The variations of damage over the gravel profiles with respect to incident wave height.

The results also indicated that the dimensionless damage parameter, S_c increases as the wave height increase. However, this is not valid for the wave period and the resistance parameter. As both increase the damage over the profile diminishes, increasing the risk for reaching the dynamic equilibrium. On the other hand, it is not possible to propose a definite relationship between the offshore bar area and the erosion area. It was observed that in sequential experiments, the damage that occurred in the previous experiment had a slight effect on the initial erosion area in the following experiment. Considering the interactions of the above parameters that directly and indirectly affect the coastal

damage, the damage parameter can be defined as follows.

$$\frac{\Omega}{H_o} \alpha \frac{H\tan\alpha}{\xi g T^2} \tag{8}$$

The two primary dimensions—length and time—are the primary determinants of the five variables listed in Eq. (8). As a result, a distinct equation representing the relationship between the dimensionless damage parameter and the dependent variables can be formed. Consequently, the damage parameter is

$$\frac{\Omega}{H_o} = a\left(\frac{H\tan\alpha}{\xi g T^2}\right)^b \tag{9}$$

The magnitude of the constants a, and b can be written with the relationship established in Fig. 6. The magnitudes of these constants based on the dimensionless shore resistance parameter are given in Table 2. Based on Fig. 6 reduction on coastal damage can be obtained by increasing the resistance, while, the effect of wave period, wave height and beach slope kept constant. Likewise, to increase the damage, it is understood that the sand dune material over the coastline should be uniform and free from pebbles and gravels. As the combined effect of shore resistance parameter, wave steepness and the slope increase, the magnitude of the change parameter decreases. Hence, as the size of gravels that built up the profile increase, the stability of the beach profiles get stronger. As the dimensionless shore resistance increase, the performance of beach to withstand the expected changes for static stability increases. Therefore, increasing the resistance capacity of profiles minimizes the variations over the profile indicating stronger profiles (Fig. 5).
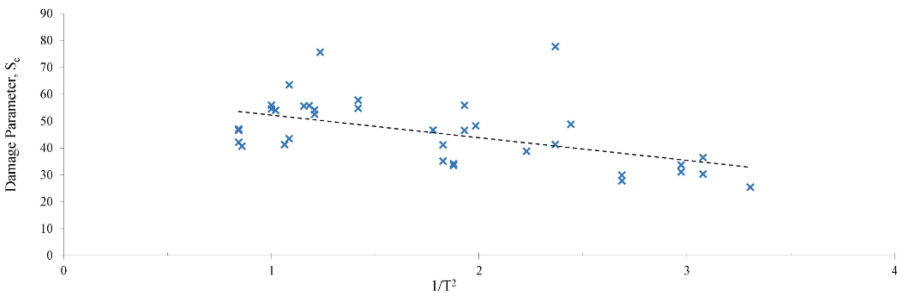
Fig. 5. The damage reduction over the gravel profile with respect to the square of wave period

On the other hand, in relation to the amount of energy dissipation, the sediment size sorting over the beach profile displays a pattern-wise distribution. The sorting was observed starting over the berm with large diameter materials to the smaller sizes as the position gets closer to the offshore bar. In particular, the bar formed at the farthest distance from the shore was assembled with the smallest diameter materials completely separated from larger diameter materials. The sorting of various size materials on different locations based on the dissipated energy of waves is directly related with the distance between the
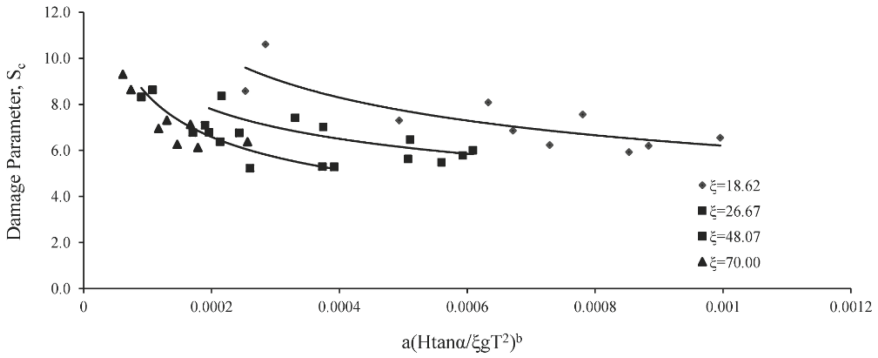
Fig. 6. The variations in dimensionless damage parameter with respect to related variables

center point of offshore bar and the assembled trough centroid, indicating the average distance travelled by sediment particles with respect to dissipated energy [27]. It is clear that the amount of energy dissipated by the breaking of the wave can carry the smallest material to the furthest and the largest material to the closest distance.

Table 2. Magnitude of constants a and b for various material distributions

Exper. Code	a	b	R^2	ξ
F	0.6936	−0.3172	0.70	0.0537
G	0.8491	−0.2603	0.64	0.0375
H	0.3289	−0.3519	0.87	0.0142
I	0.5347	−0.2902	0.81	0.0208

5   Conclusion

In this study, the morphological changes that can occur on gravel coastal zones under regular storm wave conditions were examined. The dimensionless damage parameter is described with the help of variables that contributes to morphological changes. The increase in wave height on such shores retards the formation of dynamic equilibrium and grounds more damage until equilibrium is reached. The experimental results depicted that there is a random relationship between the volumes of eroded and barred profiles, whereas, the length between the center of masses of two volumes is in harmony with the morphological change.

The results show that, the necessary energy required to initiate the sediment transport process and transport the sediment particles from onshore to offshore should be sufficient to generate dynamic equilibrium after the formation of offshore bar. Sometimes the energy necessary to initiate sediment transport can be less than the required energy. In such cases the resistance of the coastal zone approaches a value close to static stability.

References

1. Tsiaras, A.C., Karambas, T., Koutsouvela, D.: Design of detached emerged and submerged breakwaters for coastal protection: development and application of an advanced numerical model. J. Waterw. Port Coast. Ocean Eng. **146**(4), 04020012 (2020)

2. Schoonees, T., et al.: Hard structures for coastal protection, towards greener designs. Estuaries Coasts **42**, 1709–1729 (2019)

3. Türker, U.: Excess energy approach for wave energy dissipation at submerged structures. Ocean Eng. **88**, 194–203 (2014)

4. Zhang, W., et al.: The role of seasonal vegetation properties in determining the wave attenuation capacity of coastal marshes: implications for building natural defenses. Ecol. Eng. **175**, 106494 (2022)

5. Rosenberger, D., Marsooli, R.: Benefits of vegetation for mitigating wave impacts on vertical seawalls. Ocean Eng. **250**, 110974 (2022)

6. Riazi, A., Türker, U.: Equilibrium beach profiles: erosion and accretion balanced approach. Water Environ. J. **31**(3), 317–323 (2017)

7. Rotnicka, J., Dłużewski, M., Dąbski, M., Rodzewicz, M., Włodarski, W., Zmarz, A.: Accuracy of the UAV-based DEM of beach–foredune topography in relation to selected morphometric variables, land cover, and multitemporal sediment budget. Estuaries Coasts **43**, 1939–1955 (2020)

8. Lapietra, I., et al.: A potential beach monitoring based on integrated methods. J. Marine Sci. Eng. **10**(12), 1949 (2022)

9. Ortega-Sánchez, M., Bergillos, R.J., López-Ruiz, A., Losada, M.A.: Morphodynamics of Mediterranean Mixed Sand and Gravel Coasts. Springer, Cham (2017). https://doi.org/10.1007/978-3-319-52440-5

10. MacDonald, K.E., Hart, D.E., Pitman, S.J.: Geomorphic responses of uplifted mixed sand and gravel beaches: combining short-term observations from Kaikōura, New Zealand with longer-term evidence. NZ J. Geol. Geophys. **66**(2), 228–243 (2023)

11. López, I., Aragonés, L., Villacampa, Y.: Analysis and modelling of cross-shore profile of gravel beaches in the province of Alicante. Ocean Eng. **118**, 173–186 (2016)

12. Riazi, A., Türker, U., Slovinsky, P.A.: Subaerial beach profiles: the application of erosion and accretion balanced approach in southwestern Maine, USA. Estuaries Coasts **45**(7), 1983–1998 (2022)

13. Reeve, D.E., Chadwick, A., Fleming, C.: Coastal Engineering: Processes, Theory and Design Practice, p. 542. CRC Press, London (2018)

14. Türker, U., Kabdaşlı, M.S.: The effects of sediment characteristics and wave height on shape-parameter for representing equilibrium beach profiles. Ocean Eng. **33**(2), 281–291 (2006)

15. Kabdaşlı, M.S., Türker, U.: The wave breaking phenomena as a tool for environmental friendly shore protection. Water Sci. Technol. **46**(8), 153–160 (2002)

16. Austin, M.J., Masselink, G.: Observations of morphological change and sediment transport on a steep gravel beach. Mar. Geol. **229**(1–2), 59–77 (2006)

17. Polidoro, A., Dornbusch, U., Pullen, T.: Improved maximum run-up formula for mixed beaches based on field data. In: From Sea to Shore–Meeting the Challenges of the Sea: (Coasts, Marine Structures and Breakwaters 2013, pp. 389–398. ICE Publishing (2014)

18. Lorang, M.S.: Predicting the crest height of a gravel beach. Geomorphology **48**(1–3), 87–101 (2002)

19. Stockdon, H.F., Holman, R.A., Howd, P.A., Sallenger, A.H.: Empirical parameterization of setup, swash, and runup. Coast. Eng. **53**(7), 573–588 (2006)

20. Türker, U., Kabdaşlı, M.S.: Verification of sediment transport rate parameter on cross-shore sediment transport analysis. Ocean Eng. **34**(8–9), 1096–1103 (2007)

21. Türker, U., Yagci, O., Kabdasli, M.S.: Impact of nearshore vegetation on coastal dune erosion: assessment through laboratory experiments. Environ. Earth Sci. **78**, 1–14 (2019)
22. Poate, T.G., McCall, R.T., Masselink, G.: A new parameterisation for runup on gravel beaches. Coast. Eng. **117**, 176–190 (2016)
23. McCall, R.T., et al.: Modelling storm hydrodynamics on gravel beaches with XBeach-G. Coast. Eng. **91**, 231–250 (2014)
24. Almeida, L.P., Masselink, G., McCall, R., Russell, P.: Storm overwash of a gravel barrier: field measurements and XBeach-G modelling. Coast. Eng. **120**, 22–35 (2017)
25. Pollard, J.A., Christie, E.K., Spencer, T., Brooks, S.M.: Gravel barrier resilience to future sea level rise and storms. Mar. Geol. **444**, 106709 (2022)
26. Ions, K., Karunarathna, H., Reeve, D.E., Pender, D.: Gravel barrier beach morphodynamic response to extreme conditions. J. Marine Sci. Eng. **9**(2), 135 (2021)
27. Türker, U., Kabdaşlı, M.S.: Average sediment dislocation analysis for barred profiles. Ocean Eng. **31**, 1741–1756 (2004)

Assessment of Reanalysis and Satellite Precipitation Products over the Dead Sea Region, Jordan

Youssef Kassem[1,3,4(✉)], Hüseyin Gökçekuş[2,3,4], and Nour Alijl[2,5]

[1] Department of Mechanical Engineering, Engineering Faculty, Near East University, via
Mersin 10, 99138 Nicosia, Cyprus, Turkey
`youssef.kassem1986@hotmail.com, yousseuf.kassem@neu.edu.tr`
[2] Department of Civil Engineering, Civil and Environmental Engineering Faculty, Near East
University, via Mersin 10, 99138 Nicosia, Cyprus, Turkey
`huseyin.gokcekus@neu.edu.tr`
[3] Energy, Environment, and Water Research Center, Near East University, via Mersin 10, 99138
Nicosia, Cyprus, Turkey
[4] Engineering Faculty, Kyrenia University, via Mersin 10, 99138 Kyrenia, Cyprus, Turkey
[5] International Designers Company, Amman, Jordan

Abstract. The extensive application of satellite-based data and reanalysis-based precipitation has significantly assisted hydro-meteorological research in locations with limited precipitation observations. Despite their inherent inaccuracies, which vary with distinct temperature zones, seasonal cycles, and land surface characteristics, the applicability of such precipitation products must be carefully considered before implementation in particular basins; moreover, precipitation products have never been examined in Jordan's Dead Sea area. In addition to the scarcity of precipitation station gages and limited timescales, In this work, precipitation products derived from satellite data and reanalysis precipitation datasets were evaluated using statistical metrics based on the observed data, which was collected from 2015–2020. The results reveal that precipitation based on reanalysis is better quality than precipitation based on satellite. With ER, actual precipitation is most accurately captured, and the MR performed well compared to the remaining products. Then, a correction method for precipitation data (ERA-Ag and MERRA-2) was implemented. The findings reveal that the quality of rectification of ERA-Ag corrected is considerably improved, has the most excellent quality, and outperforms corrected MERRA-2. Besides, various statistical metrics were implemented to assess the performance of the HEC-HMS model. It is found that R-squared values are more than 0.5 in the calibrated and simulated (actual and ERA-Ag) models, indicating strong performance across all basins. ER represents satellite-based precipitation products, which have been frequently employed in hydrological models.

Keywords: Satellite-based precipitation · Reanalysis-based precipitation · Error correction · Runoff simulation · Dead Sea · Model calibration

1   Introduction

According to the Emergency Database, precipitation is a critical component in the perceptual reflection of climate change. Precipitation is the principal atmospheric output flow and the primary component driving hydrological processes. Accurate precipitation measurement is crucial to simulating a basin's hydrologic cycle, comprehending water balance, and forecasting extreme weather conditions and natural disasters like floods and landslides [1].

Since its excessive unpredictability can substantially influence human civilization, the natural environment [2], and historical and cultural values [3, 4]. The frequency and intensity of flash floods are expected to increase due to climate change [4]. The need for more precipitation station locations, uneven regional distributions, restricted timelines, and sensitivity to climatic and human variables makes it impossible to ensure the reliability and accuracy of precipitation data. The fast development of sophisticated technology data integration and remote sensing in the current period has resulted in high-quality reanalysis/satellite-basedipitation products widely utilized in hydrological modelling and flood forecasting [5]. The accuracy of precipitation data varies by location, even though precipitation products are widely used. Climate zoning, seasonal fluctuations, and underlying surface conditions all produce mistakes in precipitation. Jordan is vulnerable to extreme rainfall events as a result of population growth and uncontrolled urbanization; however, very few studies, if any, have been conducted in Al Hasa, Dead Sea, Wadi Wala, Jordan Rift Valley, Petra, Yarmouk River, Wadi Dhuliel, Wadi al-Arab, and Wadi Mousa on the characteristics of observed and future changes in flood and rainfall extremes. Most studies [6, 7] are based on hydrological flow regimes, which do not provide comprehensive knowledge of flood hazards for contingency planning and mitigation techniques.

Furthermore, Jordan has never previously assessed precipitation products. In addition to the lack of precipitation) station gages and the constrained timeframes, only the GSMP (Global Satellite Mapping of Precipitation dataset was used to analyze precipitation rates across the Wadi Dhuliel desert watershed [8].

Therefore, the aim of this study is twofold. The first part seeks to evaluate the appropriateness of reanalysis-based precipitation data (ER, MR, and ND) and satellite-based precipitation data (CH, NP, and NC). Following this assessment, the most suitable data will be selected and rectified. The second section involves evaluating the observed daily precipitation used to power the hydrological model, examining the selected and adjusted SPD, and assessing the applicability and accuracy of the runoff simulation results. Additionally, the study aims to evaluate the efficiency of correcting the adjusted precipitation data. Figure 1 illustrates the suggested analytical procedure employed in this work.
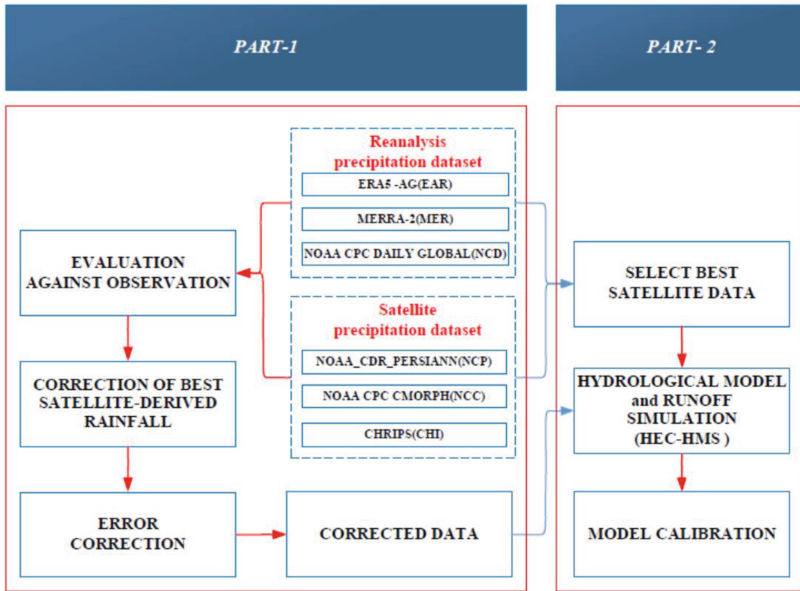
Fig. 1. Technical framework flow chart used in the present study.

2 Material and Methods

2.1 Study Area

The Dead Sea (DS) is located in a geological depression at the lowest elevation on the continents (433 m below mean sea level is its surface elevation), as shown in Fig. 2. According to Ref. [9], the watershed includes the Mediterranean and Saharan desert climatic zones.

The northern and central-western watersheds of the DS have Mediterranean climates (hot/warm summer Hagen classification), whereas the southern and eastern regions have hot semi-arid to hyper-arid desert climates. Previous research [10, 11] in DS indicates that the watershed receives the most precipitation between December and February, with the rainy season lasting from October to May. Rainfall is uncommon during the summer months (June to September), when large-scale atmospheric subsidence dominates the region. The average annual rainfall varies greatly, with lowlands receiving 100 mm and altitudes receiving 450 mm. The average yearly temperature is 22 degrees Celsius. Meteorological data for the study region is acquired from two weather stations.

Moreover, the heavy rainstorms frequently cause flash floods in the region. They cause infrastructure damage and have the potential to be fatal. On October 25, 2018, flash floods killed 21 people in two distinct locations, and a bridge collapsed. Most energy released during such cataclysmic occurrences is eliminated through incisions into weak mud deposits. Jordan is vulnerable to several natural disasters and dangers. The frequency and intensity of other present severe hazards in Jordan, such as flash floods and drought, are anticipated to rise as a result of climate change. It endangers Jordan's economic and human growth. Since 2018, Jordan has seen unusually high localized flash

floods. They are uncommon yet extremely dangerous to people, national ecosystems, and infrastructure.
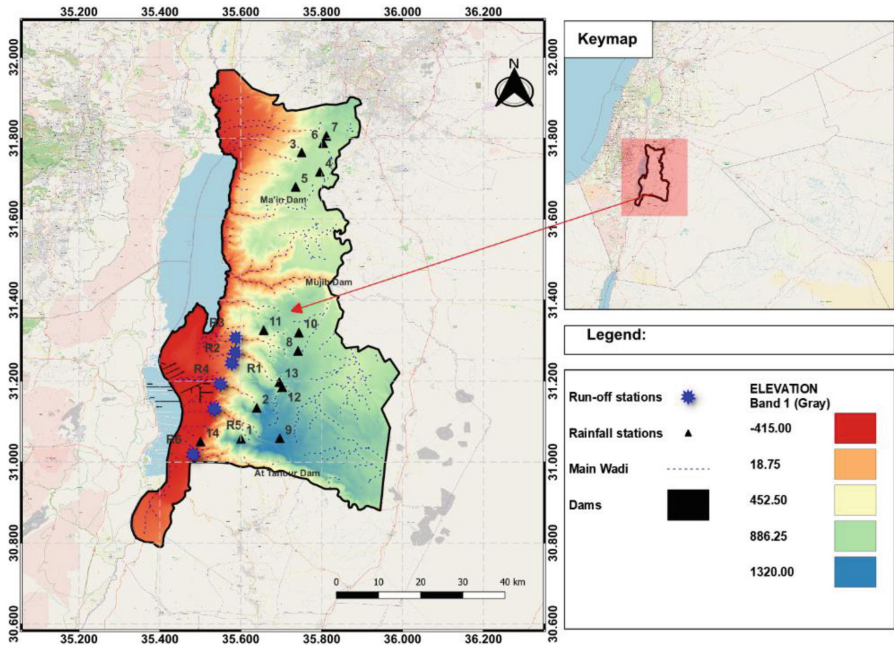
Fig. 2. Location and elevation of DS region.

2.2 Dataset

The Ministry of Water and Irrigation has provided rainfall data observed daily at DS region gauge stations (as shown in Table 1) from 2011 to 2022. The altitude of the stations varies from 343 m to 1278 m, with most of them situated in the middle and lower latitudes (refer to Fig. 2). Due to the limited number of years of station rainfall data available in the DS region, precipitation information with spatial resolution from the climate engine during 1979–2022 was retrieved and utilized.

Moreover, Reanalysis has numerous applications in the atmospheric sciences, not the least of which is in operational weather centres. There, it can be applied to evaluate forecast-error anomalies, gauge the impact of observing system changes, and obtain state-of-the-art climatology to assess progress in modeling and assimilation capabilities. Because of the restricted gauge stations in the Ds area, this study chose ER, MR, and ND (reanalysis-based precipitation) in addition to CH, NP, and NC (satellite-based precipitation). Table 2 lists the specifications of SPD.

Table 1. DS region gauge stations Information

Station ID	Station name	Latitude [N°]	Longitude [E°]	Elevation [m]
1	Khanzira (taiybat el-karak)	31.057	35.601	997
2	Aiy	31.133	35.640	898
3	Mountain_nibo	31.764	35.751	791
4	Madaba	31.716	35.796	799
5	Ma'in	31.679	35.736	865
6	Mushaqqar evap. St	31.787	35.804	859
7	Hisban	31.805	35.812	875
8	Rabba_evap	31.274	35.742	958
9	Mazar	31.058	35.697	1278
10	Qasr	31.319	35.744	940
11	Sirfa	31.325	35.657	870
12	Karak	31.184	35.703	1031
13	Ain_al-bsas	31.197	35.696	720
14	Ghores-Safi	31.050	35.501	−343

Table 2. Significant characteristics of SPD used in the study.

Type	ID	Product	Resolution	Period
Reanalysis	ER	ERA-AG	1/10°	1979-present
	MR	MERRA-2	1/10°	1980-present
	ND	NOAA CPC DAILY GLOBAL		1979-present
Satellite	CH	CHIRPS	1/20°	1981-present
	NP	NOAA_CDR_PERSIANN	1/4°	1983-present
	NC	NOAA CPC CMORPH		1998-present

2.3 Evaluation Metrics

Three statistical metrics are utilized in this work to quantify the data quality of numerous precipitation products: RMSE (root mean square error), R^2 (coefficient of determination, or R-squared), and MAE (mean absolute error). Table 3 tabulates mathematical expression for the selected statistical metrics.

2.4 Correction of Satellite-Derived Rainfall

The rainfall and precipitation numbers supplied by SPD are either exaggerated or underestimated, exhibiting inaccuracy owing to inadequate parameterization methodologies. Due to regionally prominent atmospheric components, this underestimating or overestimation is referred to as Bias. Using gauged R/P data, bias correction methods can enhance the estimated R/P values. Table 4 summarizes previous studies [12–18] that offer different techniques based on measure-correlated prediction, linear adaptation, cumulative distribution functions, and model output statistics. The explanation for the correction methods is found in Ref. [18].

Table 3. Statistical metrics.

Index	Mathematical expression	Eq. No.
R^2	$R^2 = 1 - \dfrac{\sum_{i=1}^{n} \left(a_{a,i} - a_{p,i}\right)^2}{\sum_{i=1}^{n} \left(a_{p,i} - a_{a,ave}\right)^2}$	1
RMSE	$RMSE = \sqrt{\dfrac{1}{n} \sum_{i=1}^{n} \left(a_{a,i} - a_{p,i}\right)^2}$	2
MAE	$MAE = \dfrac{1}{n} \sum_{i=1}^{n} \left|a_{a,i} - a_{p,i}\right|$	3

2.5 HEC-HMS Model

The US Army Corps of Engineers' HEC-HMS 4.1 simulation software was utilized in this work to replicate dendritic watershed systems' precipitation-runoff processes [19]. The semi-distributed HEC-HMS conceptual hydrological model simulates runoff. The HEC-HMS model setup [19] requires daily precipitation, long-term average monthly potential evapotranspiration, basin runoff flow (for calibration and validation), and basin geographical information [20]. In addition to the basin and meteorological models, time series data and control specifications must be simulated. The description of the ARIMA models is given in Ref. [21].

Moreover, Hydrological modeling relies heavily on sensitivity analysis and calibration. Sensitivity analysis can assist uncover factors that substantially influence hydrological simulation and enhance hydrological simulation efficiency, bringing simulation results closer to gauge-observed data [22]. Three criteria were chosen for calibration:

Table 4. Correction methods.

Method	Equation	Parameters index	Eq. No.
Measure Correlate Predict (MCP)	$R_{ce,i} = \frac{\overline{R_m}}{\overline{R_e}} \times R_{e,i}$	• Correct estimated rainfall data ($R_{ce,i}$) • Mean gauged rainfall data ($\overline{R_m}$) • Mean estimated r/p data provided by spp ($\overline{R_e}$) • SPP supplied approximated R/P statistics ($R_{e,i}$)	4
Linear Adaptation (LA1)	$R_{e,i} = m_1 R_{m,i} + c_1$	• New estimated R/P with negligible Bias ($R_{ne,i}$) • Slope (m_1) and the intercept (c_1)	5
	$R_{ne,i} = R_{e,i} - \left[(m_1 - 1)R_{m,i} + c_1 \right]$		6
Linear Adaptation (LA2)	$R_{ne,i} = m_2 R_{e,i} + c_2$	• Slope (m_2) • Intercept (c_2)	7
	$R_{ce,i} = m_2 R_{e,i} + c_2$		8

the CN, imperviousness, and lag time. The observed peak discharges in the DS area increased the disparity between the served and the simulated discharge. The calibrating procedure is explained in Ref. [21].

The calibration results are then evaluated using R^2, RMSE, Sutcliffe efficiency coefficient (NSE), and BIAS, and the calibration is repeated until the three indications are no longer increased.

3 Results and Discussions

3.1 Evaluation of Multi-precipitation Products Based on Gauge-Observed Data

The SPD products (ER, MR, CH, ND, NP, and NC) were compared to the actual daily rainfall for each station. For instance, the daily scale data at station 05 in the DS region, as shown in Fig. 3, exhibits an unsatisfactory correlation and unimodal pattern, with the peak daily rainfall of 52.90 appearing in January 2016 for CH, NP, NC, ND, and Station; meanwhile, ER and MR show a satisfactory correlation with values 19.85 and 24.84, respectively. Additionally, the same indications were present when the flood event occurred in October 2018, when the actual daily peak was 46.70, and the precipitation values on the same date were 0,0,0,0, 12.94,22.41, for ND, CH, NP, NC, ER and MR, respectively.

Table 5 depicts the statistical comparison based on the R2, MAE, and RMSE, respectively. Acceptable R^2 values are more significant than 0.5, whereas the obtained R^2 values for most gauge stations for CH, NP, NC, and ND are approaching to zero, suggesting unacceptable predictive model values.

Additionally, the obtained MAE values for CH, NP, NC, and ND at most stations are more significant than one, indicating poor agreement with observed data, whereas
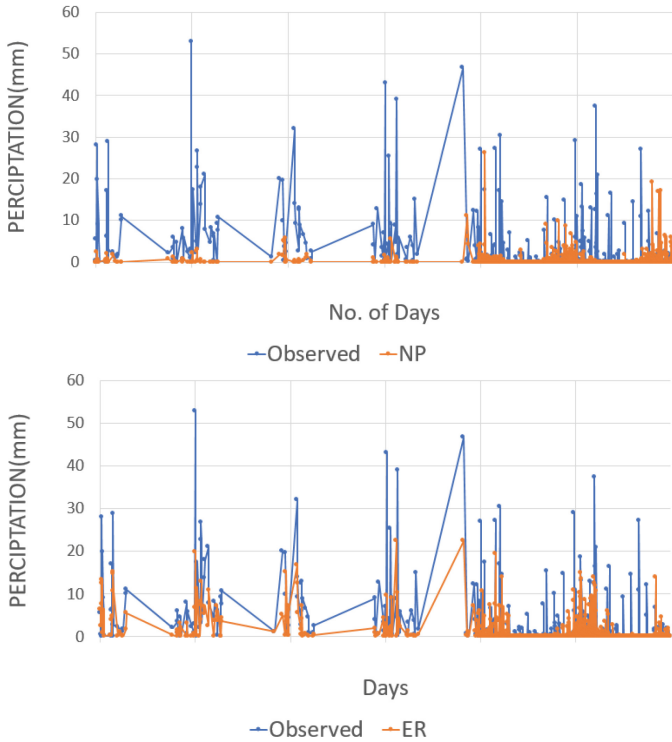
Fig. 3. Evaluation of multi-precipitation products based on gauge-observed data at station 05.

MAE values for ER and MR at stations 3,4,7 and 8 are less than one, meaning an acceptable value correction for MR and ER data to improve MAE values. The resultant RMSE values were more than one for SPD products, suggesting that the adjustments can considerably reduce SPD product overestimation and that precipitation products are unable to reflect actual precipitation occurrence effectively.

Table 5. The values of R^2, MAE, and RMSE statistical index for all stations.

Sta.	MAE						RMSE					
	CH	NP	NC	ER	MR	ND	CH	NP	NC	ER	MR	ND
1	2.47	2.09	7.8	1.67	2.17	1.94	7.57	6.33	17.3	5.16	6.38	6.2
2	2.54	2.05	7.76	1.66	2.24	2.04	7.58	6.03	17.2	4.98	6.56	5.97
3	3.84	7.22	0.8	0.73	0.87	0.28	18.1	17.7	2.66	2.61	3.08	1.79
4	1.32	1.27	4	0.89	0.83	1.32	5.68	4.6	20	3.63	3.65	4.8
5	2.63	2.13	5.78	1.72	1.75	2.36	8.24	5.96	26.9	4.71	4.86	6.32

(*continued*)

Table 5. (*continued*)

Sta.	MAE						RMSE					
	CH	NP	NC	ER	MR	ND	CH	NP	NC	ER	MR	ND
6	3.02	2.45	5.31	1.94	1.84	2.51	10.3	7.52	18.7	6.07	5.82	7.54
7	1.18	4.86	1	1.03	1.42	0.81	3.85	27.4	3.19	3.22	4.45	3.52
8	1.24	0.97	5.85	0.7	1.29	0.86	4.68	3.28	13.3	2.68	4.64	3.49
9	1.05	5.16	0.75	0.8	0.87	0.67	4.1	15.3	3.78	3.84	3.91	3.85
10	1.21	5.08	0.86	1.24	1.05	0.73	4.1	15.8	3.18	4.81	3.75	3.51
11	2.63	2.39	31.5	2.02	2.43	2.37	7.35	6.82	64	5.55	6.53	6.79
12	1.13	6.81	0.83	1.24	0.83	0.76	4.7	17.2	4.27	5.25	4.27	4.44
13	1.28	8.48	1	1.52	1.22	0.92	4.5	4.5	18.6	3.58	5.04	4.31
14	0.63	7.03	0.34	1.05	0.33	0.17	2.52	17.5	1.33	4.48	1.43	1.15

Sta.	R^2											
	CH	NP	NC	ER	MR	ND						
1	0.01	0	0	0.3	0.24	0						
2	0.01	0	0.05	0.18	0.21	0						
3	0	0	0	0.02	0.01	0						
4	0.01	0	0	0.21	0.2	0						
5	0	0	0	0.29	0.24	0						
6	0	0	0	0.25	0.34	0						
7	0	0	0	0.18	0.16	0						
8	0	0	0	0.17	0.04	0						
9	0.01	0	0	0.13	0.16	0						
10	0	0	0	0.16	0.05	0						
11	0.05	0	0	0.33	0.3	0						
12	0	0	0	0.06	0.05	0.06						
13	0	0	0	0.21	0.07	0						
14	*	0	0	0.05	0.01	0						

There is no CHRIPS (CH) for station gauge number 14, and no data is provided

As indicated in earlier research [23–26], precipitation is overestimated by NP, NC, and ND, particularly ND, which has a poor performance for forecast Purposes and the data still need to be calibrated. The findings demonstrate that the CH's applicability in a ride region is inferior to that of the DS region. A reference for the use of ER in hydrological applications was also provided by ER rainfall, demonstrating its value as an alternative to observations in data-poor areas in the DS region, which permits the calibration of such hydrological models on a larger scale for operational flood modeling and forecasting [27, 28]. Although MR still has some ambiguities [29], it still performed

well in the DS region when compared with ER precipitation products. Nevertheless, consumers and data creators should pay attention to MR, as well.

3.2   Error Correction

The numerous precipitation product assessment findings show that ER quality is good and well associated with observed gauge data, whereas MR performs best compared to other datasets. The slope (m, m_1, m_2) and intercept (c, c_1, c_2) of the best-fit line, which represents proportional and constant systematic error were estimated using scatter plots for each gauge station. To quantify the correction quality of the ER AND MR dataset, the R^2 for the daily precipitation of ER and MR before and after correction relative to observed data was determined. The adjusted ER R^2 at gauge stations 2, 4, and 12 was 0.81, 0.79, and 0.94, respectively, whereas the corrected MR was 0.50, 0.77, and 0.56. The findings reveal that the quality of corrected ER is considerably improved at the gauge stations specified, has the best quality, and outperforms corrected MR.

3.3   Evaluation of Hydrological Simulation

Table 6 summarizes basin metrics acquired using GIS technologies, including basin area, stream length, lowest and highest elevations for streams, and slopes. Figure 4 depicts these catchments as they are represented within the watershed.

In general, Curve numbers (CN) are calculated for each basin based on hydrologic soil groups, land use, and soil types [21]. The lag and concentration times values were displayed in Table 6. The control was chosen based on a historical occurrence in 2018 following severe rainfall, the first such rain on October 25th, 2018; records for peak discharge were obtained for most gauge stations within the research region. Following the initial HEC-HMS simulation, Table 9 shows the discrepancy between the peak discharge observed for the event year 2018 and the simulated (actual and ER data set). Table 7 shows that in basins 0, 3, and 14, the simulated actual peak discharge is greater than the simulated ER and observed. The simulated hydrograph underestimates the peak discharge at basin 5; the simulated peak discharge for real precipitation is 95.40 m^3/s, and ER is 60.60 m^3/s; nevertheless, the observed peak discharge is about 120.00 m^3/s. The same observations were made on October 25th, 2018, for the actual ER and observed peak discharges at basins 8 (52.10, 40.6, and 60.00) and basin 4 (63.80, 40.6, and 120).

Following the initial simulation using HEC-HMS, Table 7 shows the discrepancy between the peak discharge calibrations and seeks to find the parameters whose alteration creates a substantial change in the model's outputs. To improve the disparity between the observed and simulated discharge hydrograph, the measured runoff of every gauge station is utilized in the calibration of the simulation created for this study.

Table 8 shows the performance model. The Bias reveals how closely the gauge mean and meanR2 values for the actual simulated model at all basins are more significant than 0.5, indicating satisfactory performance, consistent with the results obtained in the calibrated model and era 5 simulations at basins 1,24,5,6, and 7. In contrast, ER results at stations 8, 9, 10, 11, 12, 13, and 14 are less than 0.5, indicating unsatisfactory performance. The R2 values for calibration and validation were 0.82, 0.83, 0.87, and 0.88 for stations 1, 2, 5, and 7, respectively, near 1 for the HMS model to validate the

correctness, indicating the model's accuracy. Correspondingly, 0.5, 0.4, and 0.4 are the RMSE values for basins 4, 5, and 9's actual simulated model.

Table 6. DS basins parameters.

ID	Basin Area [km²]	Upper stream Elev.	Downstream Elev.	length of stream [Km]	Slope	CN.	Initial abstraction	Tc (Min.)	Tlag (Min.)
1	141.71	−193.96	−360.5	9.71	1.71%	90.92	5.07	361.4	216.84
2	167.08	700.65	−374.5	31.29	3.44%	91.52	4.71	225.61	135.37
3	131.64	531.26	−398	23.05	4.03%	91.52	4.71	197.97	118.78
4	159.99	449.07	−394.5	12.57	6.71%	91.62	4.65	179.33	107.6
5	239.95	745.45	−397	38.65	2.96%	90.8	5.15	266.14	159.69
6	63.88	830.88	800.5	3.45	0.88%	90.72	5.2	505.5	303.3
7	596.64	591.05	−395.5	45.56	2.17%	91.57	4.68	396.48	237.89
8	96.34	783.62	−385.65	17.65	6.62%	91.43	4.76	144.19	86.52
9	178.26	790.1	−398.36	24.78	4.80%	91.43	4.76	197.05	118.23
10	226.75	1180.49	−397	50.61	3.12%	91.38	4.79	257.09	154.25
11	257.58	694.56	−381	24.46	4.40%	91.43	4.76	230.71	138.42
12	507.08	1055.31	−382.5	24.73	5.81%	91.48	4.73	251.52	150.91
13	107.04	661.43	39.5	10.7	5.81%	91.5	4.72	172.74	103.65
14	330.58	1119.2	893.52	26	0.87%	91.5	4.72	557.78	334.67
15	707.27	1169.13	559.5	50.78	1.20%	91.5	4.72	554.49	332.7

Tc: time of concentration; Tlag: lag time; CN: Curve number

It is found that In basin 2, the calibrated models' values (Bias) are 0.5, 0.4, 0.5, 0.5, 0.5 and 0.5 improved to be more accurate. For the ER dataset, the values are 0.50, which is less than 0.5, and show good performance. As with the calibrated model in the same basins as well as basins 3, 11, 12, 13, 14, and 15 and ER5 simulations at basins 2,4 and 5, the NSE values for the actual simulated model for basins 2,1,4,5, 8, and 9 are more significant than 0.5, indicating good performance. he actual simulated model's average inclination BIAS values for basins 2, 4, 5, 8, and 9 are 0.19, −0.19, 0.05, −0.18, and 0.19, respectively, and are nearly zero, indicating a good model. The calibrated model in basins 2,3,4,5,8, and 10 yielded the same findings as the ER data set at basins 2,3,5 and 9: −0.16, −.03, −0.05, and 0.05, respectively. The calibrated model in basins 0,9,11,13,14 and 15, as well as the actual simulated model in basins 3,7,10,11,12,13,14, and 15, all have positive values of Bias, suggesting that the model is understated. In addition to the calibrated model in basins 6, 7, 8, 12, 13, 14, and 15, negative Bias values were discovered in the actual simulated model in basin 1.
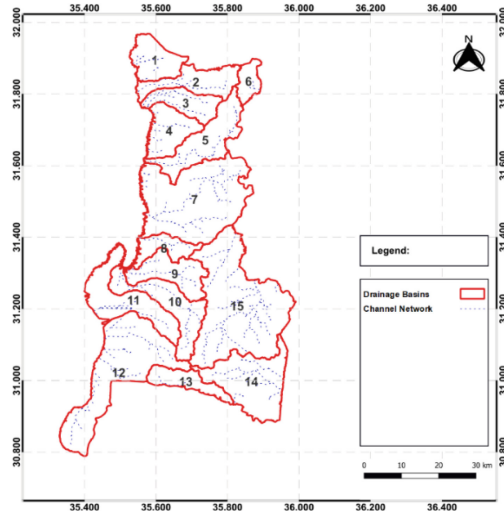
Fig. 4. Extracted basins for the study area.

Table 7. Simulated, observed and optimized peak discharge (actual and ER data set).

BASIN	Peak Discharge [m³/s]				Volume [mm]			
	Simulated Runoff		Observed Runoff	Optimized Runoff	Simulated Runoff		Observed Runoff	Optimized Runoff
	Actual	ER			Actual	ER		
1	56.4	35.8	120	56.7	252.79	196.3	321.4	257.77
2	66.6	66.6	120	66.7	254.3	254.3	272.47	254.33
3	37.6	30	25.2	25.2	162.39	144.9	79.93	98.86
4	63.8	40.6	120	63.8	254.56	198	284.66	255.53
5	95.4	60.6	120	90.3	252.48	196	189.87	221.29
6	25.4	16.1	120	25.7	252.27	195.8	712.78	266.01
7	237.8	151.4	120	180.3	254.43	197.8	76.33	163.87
8	52.1	40.6	60	53.2	236.28	225.4	225.84	252.12
9	96.8	75.4	60	97.4	252.48	229.7	98.61	244.53
10	123.1	92	35.9	62.5	241.47	229.6	48.89	119.31
11	65.2	39.5	41.7	43.6	180.79	106.4	62.15	110.9
12	128.3	73.3	78.3	85.7	177.97	89.41	84.3	108.98

(*continued*)

Table 7. (*continued*)

BASIN	Peak Discharge [m³/s]				Volume [mm]			
	Simulated Runoff		Observed Runoff	Optimized Runoff	Simulated Runoff		Observed Runoff	Optimized Runoff
	Actual	ER			Actual	ER		
13	27.1	15.5	16.5	18.1	178.01	89.45	57.34	109.21
14	83.7	47.8	71	56	187.01	89.45	66.95	109.22
15	179	102.3	109.2	118.4	178.01	89.45	60.17	108.09

Table 8. Performance model parameters.

BASIN	R^2			RMSE			NSE			Bias		
	Act	ER	Opt	Act	ER	Opt	Act	ER	Opt	Act	ER	Opt
1	0.83	0.6	0.82	0.6	0.8	0.6	0.67	0.4	0.68	−0.29	−0.44	−0.28
2	0.83	0.83	0.83	0.6	0.5	0.5	0.67	0.75	0.75	0.05	−0.16	−0.16
3	0.71	0.03	0.73	0.9	1.3	0.5	0.23	−0.8	0.73	0.58	−0.03	−0.03
4	0.83	0.6	0.82	0.5	0.7	0.5	0.73	0.45	0.73	−0.19	−0.36	−0.19
5	0.83	0.6	0.87	0.4	0.6	0.4	0.82	0.58	0.85	0.19	−0.05	0.05
6	0.83	0.6	0.79	0.8	0.9	0.8	0.28	0.11	0.29	−0.68	−0.75	−0.66
7	0.83	0.6	0.88	1.7	1.2	0.8	−1.97	−0.53	0.37	2	1.38	0.93
8	0.69	0.02	0.72	0.6	1.1	0.6	0.65	−0.23	0.69	−0.18	−0.55	−0.12
9	0.65	0.02	0.65	0.4	1.3	0.6	0.82	−0.72	0.64	0.19	0.05	0.29
10	0.53	0.03	0.36	1.3	2	0.8	−0.74	−2.84	0.34	1.55	1.1	0.17
11	0.69	0.06	0.57	1	1.5	0.7	0	−1.26	0.51	1.45	0.13	0.52
12	0.67	0.02	0.59	0.9	1.1	0.7	0.23	−0.3	0.58	1.06	−0.54	0.26
13	0.77	0.01	0.66	1.2	1.1	0.7	−0.42	−0.27	0.5	1.88	−0.47	0.77
14	0.8	0.01	0.76	0.8	1.1	0.5	0.29	−0.2	0.7	1.48	−0.54	0.52
15	0.77	0.01	0.65	1.1	1.1	0.7	−0.26	−0.26	0.54	1.79	−0.47	0.69

4   Conclusions

The Precipitation is the principal atmospheric output flow and the primary component driving hydrological processes. Precipitation measurement precision is crucial for understanding water balance, recreating a basin's hydrologic cycle and forecasting severe weather and natural disasters (such as landslides and floods). Jordan is vulnerable to several natural calamities. The frequency and intensity of other catastrophic catastrophes in Jordan, particularly in the DS area, are expected to rise due to climate change. The

feasibility of CH, NP, NC ND, ER and MR in the DS region was initially assessed. Afterwards, a correction model is built using the correlations between the observations and precipitation products to adjust for the deviation in the precipitation products (MR and ER). Eventually, multi-source precipitation data was used to calibrate the hydrological runoff simulation. The following are the primary conclusions:

(1) The quality of precipitation products derived from satellite data is inferior than that of precipitation products derived from reanalysis data on a daily time frame. NP, NC, and ND all overestimate the precipitation, particularly ND, which performs appallingly when making predictions. More blatantly, CH overestimates precipitation.

(2) The ER and MR performed well compared to other precipitation dataset products. Furthermore, all other precipitation products show an even more significant departure from the observation. The best capacity to record actual precipitation is found in ER.

(3) A correction approach for precipitation data (ER and MR) was proposed. These techniques considerably increased the accuracy of the data by correcting the precipitation data for each of the chosen years independently. R^2 was calculated to assess the quality of correction in selected datasets. The findings demonstrate that the quality of ER correction has significantly increased at the gauge stations in question, is of the highest caliber, and outperforms corrected MR.

(4) The performance of the HMS model was assessed using R2, RMSE, NSE, and Bias techniques.
    a. R^2 values greater than 0.5 in simulated (actual and ER) and calibrated models indicate good performance.
    b. RMSE values for the calibrated models in basins 2,3,4,5, and 14 have been enhanced to be more accurate.
    c. NSE values for the actual simulated model operate adequately.
    d. The calibrated model at basins 2, 3, 5, 8, and 10, the ER 5 data set at basins 2, 3, 5, and 9, and the actual simulated model at basins 2, 4, 5, 8, and 9 all have BIAS values that are very near to zero, indicating the model's exceptional performance.

In conclusion, while satellite-based precipitation products represented by ER are commonly utilized in hydrological models, the data quality of these products is necessarily influenced by observational bias, geographic scale, and retrieval technique. To maximize the hydrological simulation findings and clarify the water cycle process in the basin, additional in-depth study on regional variations among numerous precipitation products and the application of hydrological simulations is required.

References

1. Tan, X.H., Yong, B., Ren, L.L.: Error features of the hourly GSMaP multi-satellite precipitation estimates over nine major basins of China. Hydrol. Res. **49**(3), 761–779 (2018)
2. Limsakul, A., Singhruck, P.: Long-term trends and variability of total and extreme precipitation in Thailand. Atmos. Res. **169**, 301–317 (2016). https://doi.org/10.1016/j.atmosres.2015.10.015
3. Jonkman, S.N., Vrijling, J.K.: Loss of life due to floods. J. Flood Risk Manag. **1**(1), 43–56 (2008). https://doi.org/10.1111/j.1753-318x.2008.00006.x

4. Rahman, M.S., Di, L., Yu, E., Lin, L., Zhang, C., Tang, J.: Rapid flood progress monitoring in cropland with NASA SMAP. Remote Sens. **11**(2), 191 (2019). https://doi.org/10.3390/rs11020191

5. Zhang, Y., Ma, N.: Spatiotemporal variability of snow cover and snow water equivalent in the last three decades over Eurasia. J. Hydrol. **559**, 238–251 (2018)

6. Gökçekuş, H., Kassem, Y., Alijl, N., Tawalbeh, M.: Flash flood risk mitigation plan: Zarqa Ma'in Basin, along the Dead Sea in Jordan. Int. J. Sci. Technol. Res. **9**(3), 4089–4095 (2020)

7. Obeidat, M., Awawdeh, M., Al-Hantouli, F.: Morphometric analysis and prioritization of watersheds for flood risk management in Wadi Easal Basin (WEB), Jordan, using geospatial technologies. J. Flood Risk Manag. **14**(2), 1–19 (2021). https://doi.org/10.1111/jfr3.12711

8. Abushandi, E., Merkel, B.: Modeling rainfall runoff relations using HEC-HMS and IHACRES for a single rain event in an arid region of Jordan. Water Resour. Manag. **27**(7), 2391–2409 (2013). https://doi.org/10.1007/s11269-013-0293-4

9. Kottek, M., Grieser, J., Beck, C., Rudolf, B., Rubel, F.: World map of the Koppen- Geiger climate classification updated. Meteorol. Z. **15**, 259–263 (2006). https://doi.org/10.1127/0941-2948/2006/0130

10. Tyrlis, E., Lelieveld, J., Steil, B.: The summer circulation over the eastern Mediterranean and the Middle East influences the South Asian monsoon. Clim. Dyn. **40**, 1103–1123 (2013). https://doi.org/10.1007/s00382-012-1528-4

11. Kushnir, Y., Dayan, U., Ziv, B., Morin, E., Enzel, Y.: The climate of the Levant: phenomena and mechanisms. In: Enzel, Y., Ofer, B.-Y. (eds.) Quaternary of the Levant: Environments, Climate Change, and Humans, pp. 31–44. Cambridge University Press, Cambridge (2017)

12. Schumann, K.: Gridded results of swath bathymetric mapping of Disko Bay, Western Greenland, 2007–2008 (preview maps) (2011). http://doi.pangaea.de/10.1594/PANGAEA.770250

13. Gueymard, C.A., Gustafson, W.T., Bender, G., Etringer, A., Storck, P.: Evaluation of procedures to improve solar resource assessments: optimum use of short-term data from a local weather station to correct Bias in long-term satellite-derived solar radiation time series. In: World Renewable Energy Forum Conference Proceedings, pp. 13–17 (2012)

14. Cebecauer, T., Šúri, M.: Correction of satellite-derived DNI time series using locally-resolved aerosol Data. In: Proceedings of the Solar PACES Conference, Marrakech, Morocco (2012)

15. Kankiewicz, A., Dise, J., Wu, E., Perez, R.: Solar 2014: reducing solar project uncertainty with an optimized resource assessment tuning methodology. In: American Solar Energy Society Annual Conference (2014)

16. Polo, J., et al.: Integration of ground measurements to model-derived data: a report of IEA SHC Task 46 Solar Resource Assessment and Forecasting. International Energy Agency: Paris, France (2015)

17. Polo, J., Martín, L., Vindel, J.M.: Correcting satellite-derived DNI with systematic and seasonal deviations: application to India. Renew. Energy **80**, 238–243 (2015)

18. Asim, M., Azhar, M., Moeenuddin, G., Farooq, M.: Correcting solar radiation from reanalysis and analysis datasets with systematic and seasonal variations. Case Stud. Therm. Eng. **25**, 100933 (2021)

19. HEC: Hydrological Modelling (HEC-HMS) user's Manual, US Army Corps of Engineers (2006)

20. Feldman, A.D.: Hydrologic Modeling System HEC-HMS. Technical Reference Manual. US Army Corps of Engineers (USACE), Hydrologic Engineering Center, HEC. Davis, CA, USA (2000)

21. Kassem, Y., Gökçekuş, H., Alijl, N.: Gridded precipitation datasets and gauge precipitation products for driving hydrological models in the Dead Sea Region, Jordan. Sustainability (Switzerland) **15**(15) (2023). https://doi.org/10.3390/su151511965

22. Cunderlik, J., Simonovic, S.P.: Calibration, verification and sensitivity analysis of the HEC-HMS hydrologic model. Department of Civil and Environmental Engineering, The University of Western Ontario (2004)
23. Gebremicael, T.G., et al.: Evaluation of multiple satellite rainfall products over the rugged topography of the Tekeze-Atbara basin in Ethiopia. Int. J. Remote Sens. **40**, 4326–4345 (2019)
24. Saidah, H., Saptaningtyas, R.S., Hanifah, L., Jaya Negara, I.D.G., Widyanty, D.: NOAA Satellite performance in estimating rainfall over the Island of Lombok. In: IOP Conference Series Earth Environmental Science, vol. 437, p. 012035 (2020)
25. Mosaffa, H., et al.: Spatiotemporal variations of precipitation over Iran using the high-resolution and nearly four decades satellite-based PERSIANN-CDR dataset. Remote Sens. **12**, 1584 (2020)
26. Prat, O.P., Nelson, B.R., Nickl, E., Leeper, R.D.: Global evaluation of gridded satellite precipitation products from the NOAA Climate Data Record program. J. Hydrometeorol. **22**, 2291–2310 (2021)
27. Cantoni, E., et al.: Hydrological performance of the ERA reanalysis for flood modeling in Tunisia with the LISFLOOD and GR4J models. J. Hydrol. Reg. Stud. **42**, 101169 (2022). https://doi.org/10.1016/j.ejrh.2022.101169
28. Jiang, Q., et al.: Evaluation of the ERA reanalysis precipitation dataset over Chinese Mainland. J. Hydrol. **595** (2021)
29. Arshad, M., Ma, X., Yin, J., Ullah, W., Liu, M., Ullah, I.: Performance evaluation of ERA-5, JRA-55, MERRA-2, and CFS-2 reanalysis datasets, over diverse climate regions of Pakistan. Weather Clim. Extremes **33**, 100373 (2021). https://doi.org/10.1016/j.wace.2021.100373

Structures

Cost Estimation of Reinforced Concrete Buildings Using Neural Network and Multi Regression Analysis

Mohamad Abou Rajab[(✉)] and Giray Özay

Civil Engineering Department, Eastern Mediterranean University, Famagusta, North Cyprus, Turkey
{21601004,giray.ozay}@emu.edu.tr

Abstract. In this study, an Artificial Neural Network and Multi Regression Analysis have been used to evaluate the strengthening cost and total cost of reinforced concrete buildings. To obtain strengthening cost, 377 reinforced concrete buildings which have been designed according to the 1975, 1997 and 2007 Turkish Earthquake Codes have been checked and strengthened according to the new code 2018 Turkish Earthquake Code. After that, to obtain the total cost (rough total construction cost) of the buildings according to the new code, 84 different reinforced concrete buildings have been designed according to the 2018 Turkish Earthquake Code. The professional program Sta4CAD has been used to model, analyze and strengthening those reinforced concrete buildings. When the old buildings are checked according to the new code, they may not satisfy the conditions of the code since the new code has more general rules. According to that, those old buildings will need strengthening. Section enlargement method, addition of shear wall and other methods have been used so that the old buildings can satisfy the new code provisions. For strengthening cost of Reinforced Concrete buildings, 13 parameters have been chosen accordingly. The output parameter for the study is the strengthening cost, which are in Turkish Lira according to the unit prices of materials in Turkey. For rough total cost according to TEC 2018 8 parameters have been used. According to the study, the prediction accuracy of the Artificial Neural Network that has been trained, was found to be 94% accuracy for the strengthening cost. However in the regression analysis method, 71% accuracy has been found. For total cost, Artificial Neural Network gave 97% accuracy and for regression analysis method 95% accuracy has been found.

Keywords: Artificial Neural Network · Strengthening · Cost · Earthquake · Regression Analysis

1 Introduction

Artificial neural networks are commonly used to solve the problems that may be complicated or there are difficult in modeling by using other techniques like mathematical modeling. Multi regression analysis is an extension of simple linear regression. It is commonly used to estimate the value of a variable based on the value of two or more other

variables. Multi regression requires two or more predictor variables, and this is why it is called multi regressions. Cost is one of the major criteria in decision making at the early stages of a building design process. Strengthening of building is also very important in the construction life. If the structure is strong enough then the peoples or others that are using that structure are at safe position. During past earthquakes, many reinforced concrete (RC) buildings have either collapsed or suffered distinct degrees of damage [1]. Safety is also one of the most important considerations which should be taken before any construction project gets underway. Buildings are legally required to meet certain codes and rules that set minimum safety standards. These codes are important because when it gets applied, the building will be safer [2].

In the study of Alshaer [15], ANN have been developed for evaluation the collapse vulnerability of RC buildings. In his study, 260 RC buildings were chosen with 16 input parameters. ANN has been used and the outputs of the system represent the performance of the structures. As a result, 90% accuracy has been found for nonlinear analysis and 89% accuracy for linear analysis.

In the study of Arslan [16], a total of 256 RC buildings with between 4 and 7 floors were modeled. Modal analysis and pushover analysis have been applied to each of the capacity curves for each structure. 2007 Turkish earthquake code have been used in the analyzing of data. The effect and importance of each parameter have been tested in his study and he found that short column formation and shear wall ratio are the most important structural component that affects the performance of the structures. As a result the performance of ANN founds to be 91.68% and 98.47% depending on the parameters of the model.

Furtado (2014) study is to prepare a numerical analysis and possible solutions to strengthen existing reinforced concrete buildings and to have the full potential governed by soft-story mechanisms. In their study they use concrete buildings which are located in the South European countries. They use different techniques for strengthening such as RC column jacketing, addition of RC shear wall and steel bracing. Finally they compared the strengthened buildings results with original structures and detect about the improvement in the performance of each type of strengthening technique.

The objective of this study is to prepare a Neural Network and Multi Regression analysis software for quick strengthening cost estimation of buildings with different structural systems. The buildings has been designed according to 1975, 1997, 2007 and 2018 Turkish Earthquake codes. After that the buildings have be strengthened according to the last earthquake code which is 2018 and strengthening has been done according to those old buildings that are not satisfying the standards of the new code. Another ANN and MRA have been created to calculate the total cost of the structures according to 2018 TEC. The input parameters of the study have been sorted accordingly to the importance. The study aims to provide all the reinforced concrete buildings in the most economical way without affecting their strength and sustainability.

2 ANN and MRA

Artificial neural networks are a system of many artificial nerve cells consists together as in the biological system. Multiples of data input to artificial neural cell are transmitted. The outputs of those generated data are obtained after the processing method is activated [1].

Multi regression analysis is a technique that is used to estimates a single regression model with more than one outcome variable. The parameter that is used to measure the dependent variable or consequence is known as the independent variable. The coefficient of determination (R-squared) is a statistical metric for determining how much difference in the independent variables can be explained by variation in the result. As a result, R-squared alone cannot be used to determine which predictors should be included and which should be omitted from a model. R-squared can only be between 0 and 1, with 0 indicating that none of the independent variables can predict the outcome and 1 indicating that the independent variables can predict the outcome without error [11].

3 Methodology

3.1 Background

Different types of reinforced concrete buildings will be considered with their input parameters. The buildings will be designed according to 1975, 1997 and 2007 Turkish Earthquake Code and those buildings will be checked according to TEC 2018. Since old buildings usually do not satisfy the 2018 Turkish earthquake standards, strengthening will be done. After strengthening, the performance of the building will be improved and the structure will become safer than before. In the case studies buildings with 4 and 5 floors will be considered. After the strengthening done and the buildings start to satisfy the new code, cost of strengthening will be considered for every building. Then an artificial neural network and multi regression analysis system will be used in order to find the efficiency with strengthening of building with the lowest price. Finally the input parameters will be sorted accordingly to the importance.

3.2 Plans for Buildings

(See Fig. 1).
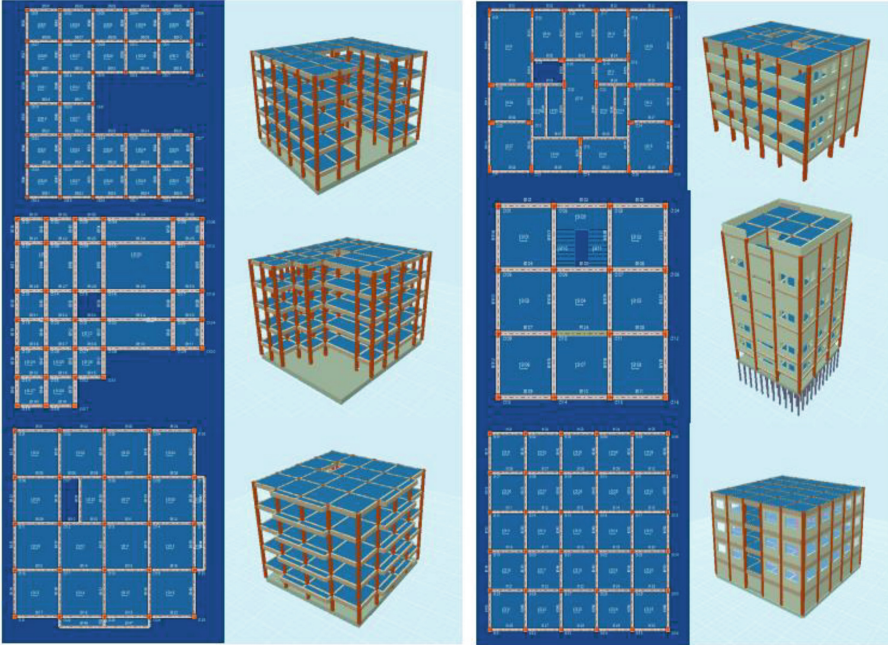
Fig. 1. Different plans of building models used in this study.

4   Earthquake Codes

Building structures are totally made out of earthquake resistant starting from the foundation. Throughout this way, after an earthquake happen, the buildings are likely to experience the least damage. The earthquake code is the system of laws that guarantee the design of buildings in an earthquake-resistant condition. Within that way, from the start to the finish, the structures are guaranteed to abide with the earthquake requirements. To meet this process, audits are always made accordingly. In order to ensure that the buildings or structures to be designed in areas defined as unsafe within the scope of the earthquake are immune to earthquakes, the measurement takes into account all considerations such as calculations, construction stages, construction laws, the value of buildings and structures and local ground conditions. This situation is called earthquake regulation.

5   Case Study

5.1   Parameters

For the strengthening cost of RC buildings several parameters has been considered. The commercial program Sta4cad is used for modeling and analyzing the buildings which are designed according to 1975, 1997 and 2007 Turkish Earthquake Code. Those building will be analyzed according to the last code which is 2018 code and which is the last and the current code in use.

Parameters considered in the study are number of story, concrete class, steel class, area, shear wall ratio, column ratio, earthquake code, weak column-strong beam, soil type, earthquake zone, stirrup spacing, torsional irregularity and soft story.

For total cost according to TEC 2018 8 parameters have been used. Those parameters are: Plan Area (A), Number of Story (N), Concrete Class (C), Steel Class (S), Shear Wall Ratio (SWR), and Column Ratio (CR).

5.2 Analysis

Linear static analysis is dependent on strength analysis when the elastic potential of structural elements exceeds the demands of loading situations. Response spectra are used as a common seismic study for design purposes. It has the potential to speed up time by demonstrating only the full answer without having to justify it.

The aim of non-linear analysis methods is to determine the structural strength and retrofitting analysis of existing buildings under the influence of seismic loads. The member's and the building's structural efficiency levels are assessed.

5.3 Details for Strengthening

Since the conditions of every structure are different, the price is changing. But in the structures there are some common properties. The columns strengthened with concrete cover of 10 cm–15 cm with 1.4 cm for the longitudinal reinforcement. In the study the concrete class was 16 and 20. For strengthening method, minimum of C25 have been used.

5.4 Methods of Strengthening Used in the Study

Section enlargement method is happen where the section (column, beam etc.) of the building is increasing so that the building will meet the requirements. In the study, for the columns jacketing have been added for strengthening of the buildings which have weak column size. In the study 10 cm or 15 cm thickness jacketing have been added to these columns to make them strong enough.

On the other hand for the buildings with torsional irregularities since on one side of the structure the column sizes are bigger or there are more columns on one side of the building.

After that in the case study, there are some cases where the buildings have weak column and strong beam. Here the columns sizes are also increases by jacketing method so that the columns will become strong enough. Because in the past earthquakes, it can be obviously seen that building collapse like pancake and one of the reason is that the columns are very weak. This method is also possible for the case where there is soft story. Due to stores that are at the bottom floor of the structures, soft story may occur. Prevention of this is to increase the column size at the bottom floor since there are less windows and more opening in this floor. All the weight of the building is on that floor.

The most important strengthening element against earthquakes is the shear wall. The last element to collapse during an earthquake is the shear wall. For the strengthening shear wall should be more than 200 cm. In this study external shear walls have been added to the structures. In the cases where jacketing is not enough and where the performance of the building is poor, 88 shear wall is added.

5.5 Strengthening Cost of Buildings

First of all, 377 different models have been analyzed according to earthquake codes. After that 61 of those models have been chosen and analyzed according to gravity load design. Strengthening cost for earthquake design and gravity loaded design has been calculated separately. Then the percentage of the strengthening cost to the total cost of buildings according to 2018 have been found for both earthquake and gravity load design. From the results it have been seen that the average for the strengthening cost with earthquake codes divided by total cost of that buildings found as 18.92%. However the average for the gravity loaded design divided by the total cost has been found as 23.70%. This means that the strengthening cost with gravity force is 25% more expensive than the strengthening against earthquakes codes.

6   Results and Discussion

From this comparison it is obvious that the cost calculation for the structures is in a good agreement with 94% accuracy found in the program. Another neural network has been created for the total cost of each building. From this comparison it has been found an accuracy of 97% (Figs. 2, 3, 4 and 5).
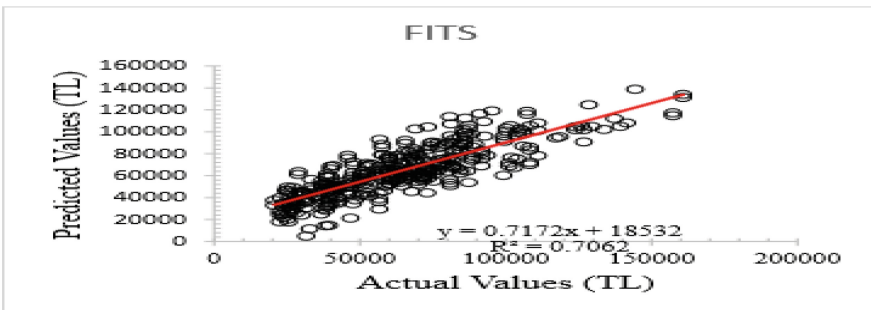
Fig. 2. Multi regression analysis for strengthening cost of buildings.
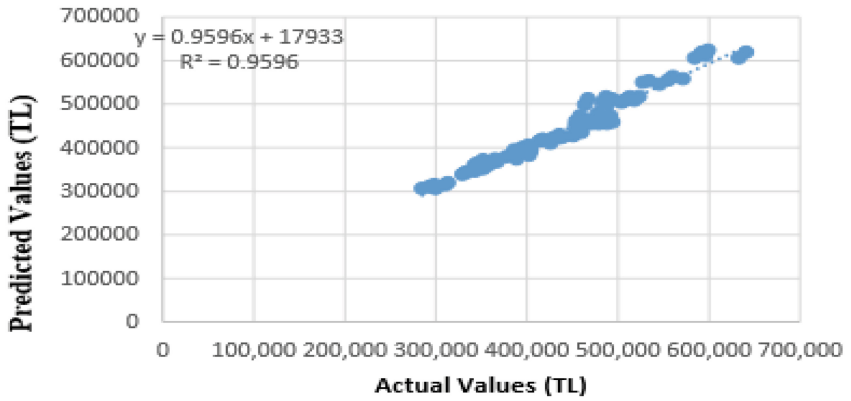
Fig. 3. Multi regression analysis for total cost of buildings.
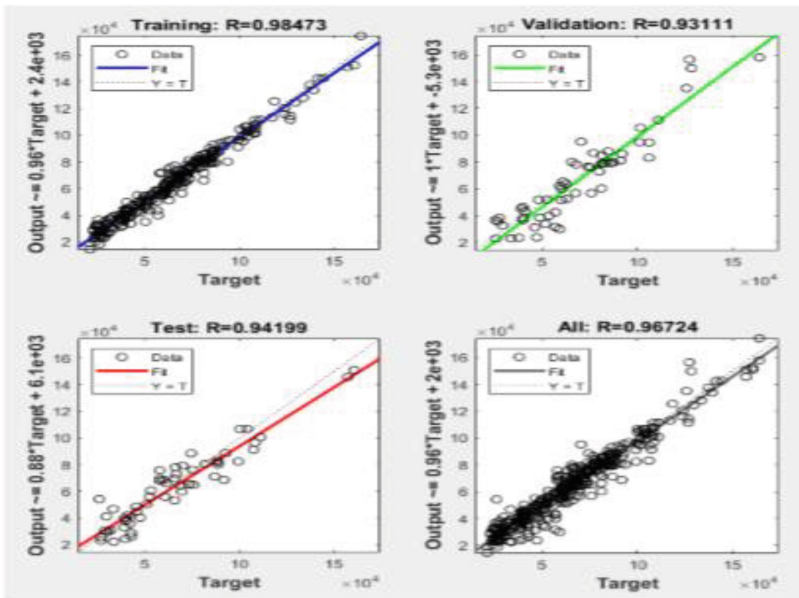
Fig. 4. Performance of ANN for the strengthening cost.
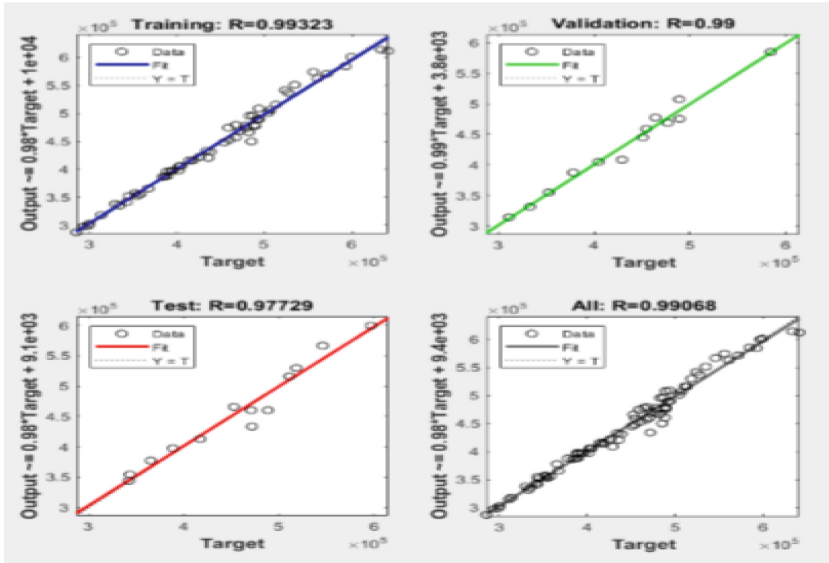
Fig. 5. Performance of ANN for the total cost.

6.1 Sorting of the Input Parameters

After sorting the input parameters, by adding of shear wall and by increasing the section which is calling jacketing, increase the strength and the performance of the structures. Performance decreases and strengthening cost increases when torsional irregularities exist in the structure. Also where there is weak column strong beam, the cost of strengthening is also high because more columns need to get enlarged. The average column ratio which was one of the input parameters in the study has a significant effect on the performance of the project together with the shear wall ratio. Structures that have high column and shear wall ratio will cost less for strengthening. By increasing the strength and concrete class, the cost of strengthening is decreasing. The reason is that the new and high classes have more ability to perform more. For the new materials, the strengthen cost of the structures is affected directly. For the structures which are checked according to the 1st and 2nd earthquake zone which are the less effective places for earthquake costs less for strengthening. But for the 3rd and 4th zones, the strengthening cost is higher since more added shear wall and better section enlargement method is needed because the earthquake will appear more dangerous in this place.

7   Conclusion

This research explored the use of artificial neural networks to estimate the cost of reinforced concrete buildings for strengthening. Using the available test data of 377 RC buildings that have been modeled with the commercial software STA4cad, an artificial neural network model was designed according to 1975, 1997 and 2007 and strengthened according to 2018 regulations. After that 84 RC buildings have been tested to calculate

the total cost according to 2018. 61 of those buildings have been designed according to gravity load design. The percentage of the different between earthquake code and gravity load design have been discussed and have been found that gravity loaded design is 25% more expensive than earthquake code design.

The neural network model that have been created predict the strengthening cost of the buildings with 94% accuracy and for the total cost according to 2018 of each building the accuracy was about 97% in the system.

In neural network, the accuracy for the study has been found 94% for strengthening cost and 97% for total cost. While in multi regression analysis this result became around 71% for strengthening cost and 95% for total cost.

References

1. Günaydın, H.M., Doğan, S.Z.: A neural network approach for early cost estimation of structural systems of buildings. Int. J. Project Manag. **22**(7), 595–602 (2004)
2. ElSawy, I., Hosny, H., Razek, M.A.: A neural network model for construction projects site overhead cost estimating in Egypt. arXiv preprint arXiv:1106.1570 (2011)
3. Matel, E., Vahdatikhaki, F., Hosseinyalamdary, S., Evers, T., Voordijk, H.: An artificial neural network approach for cost estimation of engineering services. Int. J. Constr. Manag. 1–14 (2019)
4. Elhag, T.M.S., Boussabaine, A.H.: An artificial neural system for cost estimation of construction projects. In: Proceedings of the 14th ARCOM Annual Conference (1998). ACE2023 http://www.ace2023.emu.edu.tr. Accessed 18 Mar 2023
5. Hong, Y., Hammad, A.W., Akbarnezhad, A., Arashpour, M.: A neural network approach to predicting the net costs associated with BIM adoption. Autom. Constr. **119**, 103306 (2020). ACE2023 http://www.ace2023.emu.edu.tr. Accessed 18 Mar 2023
6. El-Sawalhi, N.I., Shehatto, O.: A neural network model for building construction projects cost estimating. J. Constr. Eng. Project Manag. **4**(4), 9–16 (2014). ACE2023 http://www.ace2023.emu.edu.tr. Accessed 18 Mar 2023
7. Mijwel, M.M.: Artificial neural networks advantages and disadvantages (2018). LinkedIn: https://www.linkedin.com/pulse/artificial-neuralnetworks-advantages-disadvantages-maad-m-mijwel. ACE2023 http://www.ace2023.emu.edu.tr. Accessed 18 Mar 2023
8. Roxas, C.L.C., Ongpeng, J.M.C.: An artificial neural network approach to structural cost estimation of building projects in the Philippines. In: Proceedings of the DLSU Research Congress (2014). ACE2023 http://www.ace2023.emu.edu.tr. Accessed 18 Mar 2023
9. Juszczyk, M., Leśniak, A., Zima, K.: ANN based approach for estimation of construction costs of sports fields. Complexity **2018** (2018). ACE2023 http://www.ace2023.emu.edu.tr. Accessed 18 Mar 2023
10. Lazarevska, M., Knezevic, M., Cvetkovska, M., Trombeva-Gavriloska, A.: Application of artificial neural networks in civil engineering. Tehnički vjesnik **21**(6), 1353–1359 (2014). ACE2023 http://www.ace2023.emu.edu.tr. Accessed 18 Mar 2023
11. Manning, T., Sleator, R.D., Walsh, P.: Biologically inspired intelligent decision making: a commentary on the use of artificial neural networks in bioinformatics. Bioengineered **5**(2), 80–95 (2014). ACE2023 http://www.ace2023.emu.edu.tr. Accessed 18 Mar 2023
12. Okakpu, A., Ozay, G.: A comparative study of building strengthening methods to have an efficient and economical solution. Case study in Famagusta, Cyprus. Int. J. Civil Struct. Eng. **5**(2), 165–176 (2014)
13. Ünsal, M.A., Aydinli, S., Oral, E.: Cost Estimation of Reinforced Concrete Structural System via Artificial Neural Networks Model (2017)

14. Furtado, A., et al.: Assessment and strengthening strategies of existing RC buildings with potential soft-storey response. In: 9th International Masonry Conference (IMC), Portugal (2014)
15. Arslan, M.H.: An evaluation of effective design parameters on earthquake performance of RC buildings using neural networks. Eng. Struct. **32**(7), 1888–1898 (2010)
16. Alshaer, I.M.: Collapse vulnerability of reinforced concrete buildings using neural networks. Master's thesis, Eastern Mediterranean University (EMU)-Doğu Akdeniz Üniversitesi (DAÜ) (2016)
17. Rodriguez, M., Park, R.: Repair and strengthening of reinforced concrete buildings for seismic resistance. Earthq. Spectra **7**(3), 439–459 (1991)
18. Kaplan, H., Yilmaz, S., Cetinkaya, N., Atimtay, E.: Seismic strengthening of RC structures with exterior shear walls. Sadhana **36**(1), 17 (2011)
19. Alashkar, Y., Nazar, S., Ahmed, M.: A comparative study of seismic strengthening of RC building by steel bracings and concrete shear walls. Int. J. Civil Struct. Eng. Res. **2**(2), 24 (2015)
20. Adar, K.: Comparison of 2007 earthquake regulation with 2018 earthquake regulation and differences in earthquake load account (2019)

Effect of Steel Braces on Progressive Collapse Using Applied Element Method

Laith Hafez[(✉)] and Mehmet Cemal Genes

Civil Engineering Department, Eastern Mediterranean University, Famagusta, North Cyprus, Turkey
{21508730,cemal.genes}@emu.edu.tr

Abstract. It is widely common to see terrorist attacks nowadays happening around the globe. In this study bracing effect on progressive collapse will be discussed. To start with, this study will analyze the collapse mechanism, due to explosive load on an average height building, which mimics important buildings like government buildings, ministries, hospitals, etc. Explosive loads are the loads coming from the explosion of a certain amount of TNT with respect to the standoff distance from the explosion. So, any terrorist attacks will target the columns at the ground floor to maximize the damage imposed on the structure achieving the highest number of casualties. As a result, this study covers the load transfer mechanism to prevent a progressive collapse in case of column loss scenario, which occurs in a terrorist attacks or earthquakes. Moreover, this study discusses multiple technologies to counteract and resist column removal. First of all, constructing tensile steel braces at one of the stories which can be used to transfer the load coming from upper stories to ground floor. Secondly, this study will discuss the effect of column removal location on the total deflection of the structure and the axial loads imposed on the nearby columns.

Keywords: Applied Element Method (AEM) · Progressive Collapse · Braces · Extreme Loading on Structures (ELS)

1 Introduction

Progressive collapse failure has been a topic of interest for many researchers in the past years, especially when terrorist attacks are growing more worldwide as in Oklahoma City bombing in 1995, Ronan point building failure in 1968 and world trade center in 2001 as in Fig. 1. By understanding the behavior of reinforced concrete moment frame under progressive collapse a lot of safety guidelines have been developed such as UCF and GSA to guide designers and engineers to design structures against progressive collapse or sudden column removal. This study aims to simulate multiple scenarios of column removal to examine the effectiveness of lateral bracing system to reduce and control the potential risks of column removal on 3D model. Other studies were modelled using 2D models on SAP2000 and ETABs, but a 2D model is not accurate enough compared with a 3D model cause in a 2D model the collapsed column is connected to only 2 side columns,

which is not the case in a 3D model. Additionally, the effect of steel bracing location will be assessed on the deflection of the top node of the removed column and to get higher accuracy results the progressive collapse analysis is performed using Applied Element Method (AEM), which is a high-fidelity program used to reduces the computational power required to analyze and simulate any structural system under different loading conditions, because In AEM each element has a six nodes 3 for translation movement and 3 for rotational movement, while the FEM (finite element method) or DEM (discrete element method) has 8 nodes for each element. In the upcoming Sect. 3 main models will be created and analyzed using non-linear dynamic analysis to compare the effectiveness of each lateral bracing system on progressive collapse for the first model it is a control model a simple 8 story moment frame with no masonry infill walls or partition an no lateral bracing system and for the second model a similar structure with one X-eccentric steel bracing on the top floor and for the third model a similar structure with a shear wall as a bracing system.

| Ronan Point, 1968- London, gas explosion | Skyline Plaza, 1973 – USA, Formwork removal | Khobar, 1996 – KSA, Terrorist Attack | WTC Center, 2001- USA, Terrorist Attack |

Fig. 1. Failed structures due to explosion [1]

2 Literature Review

2.1 Effect of Bracing Systems on Progressive Collapse

A lot of studies and experimental research have been done in recent years on progressive collapse of a reinforced concrete frame, so in this section review of other researchers work and results will be presented. To start with, according to Kai Qian et al. (2019) concluded that applying bracing system to a concrete frame reduces the vertical displacement after column loss, also he studied the effect of bracing design on progressive collapse, where he concluded that X-eccentric bracing is the most efficient design, because it can withstand a side column collapse or a middle column failure, since that steel braces buckle easily under compression but have a good load bearing capacity under tensile forces. Moreover, a study done by Feng Fu (2009) investigated the behavior of a 20-story steel structure with different lateral bracing system under progressive collapse and he noted that the results using ABAQUS, and the parameters recorded were, vertical displacement of the top node of the removed column, axial load on the neighboring columns, acceleration contour of the whole structure and the shear force on the beams in the following figures. Also, bracing story location has a little to no effect on the overall deflection of the structure, but according to Jun Yu et al. (2020) the most favorable place to construct the

bracing is the top story, because the improvement become more evident if the column failure occurs at the top floors (Fig. 2) [2, 5].

(a)   (b)
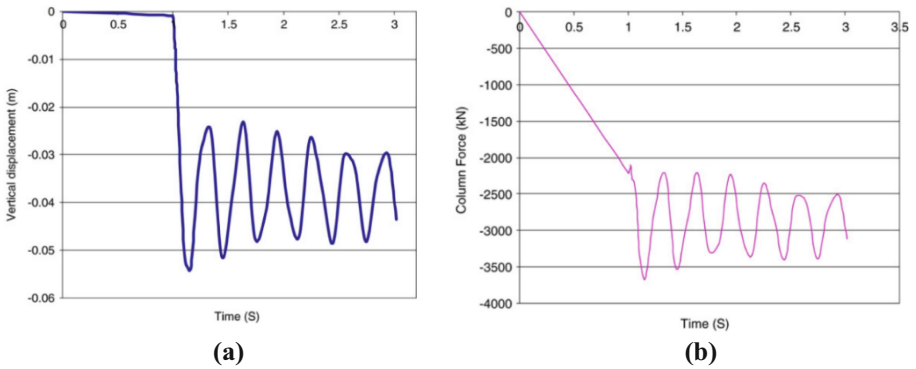
Fig. 2. a) vertical displacement with respect to time. b) column force with respect to time for the top node of the removed column [2].

2.2 Applied Element Method in Progressive Collapse

A lot of studies were done on progressive collapse using Applied Element Method in the last decade, due to its high reliability and accuracy. A study conducted by Ahmed Amir
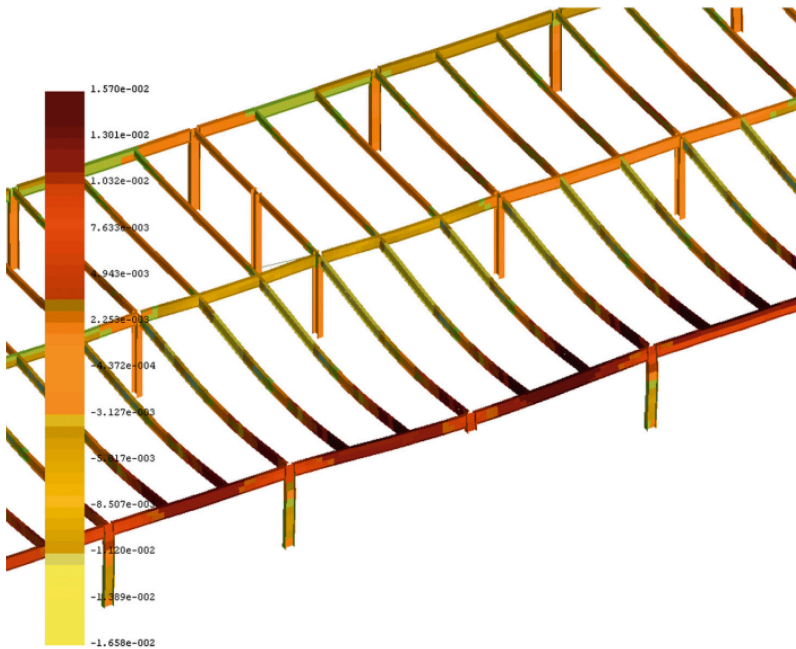
Fig. 3. Beam flexural rotations [3]
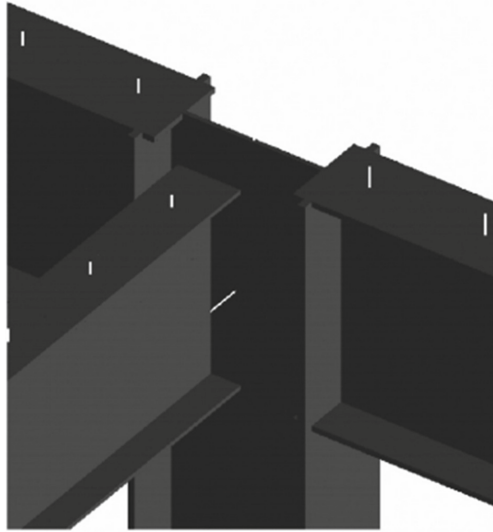
Fig. 4. Steel connection modelling [3]

Khalil (2011) about the enhanced modelling for steel structure for progressive collapse analysis using applied element method, where he designs 3 models one model without slabs and the other 2 models slabs are considered, so he concluded that the usage of AEM in non-linear dynamic analysis proven a higher accuracy than FEM is achieved cause slab contributions and steel connection modelling are considered as in Fig. 3 and 4. Also, another study done Mohammed El-Desoqi et al. (2020) about using AEM on
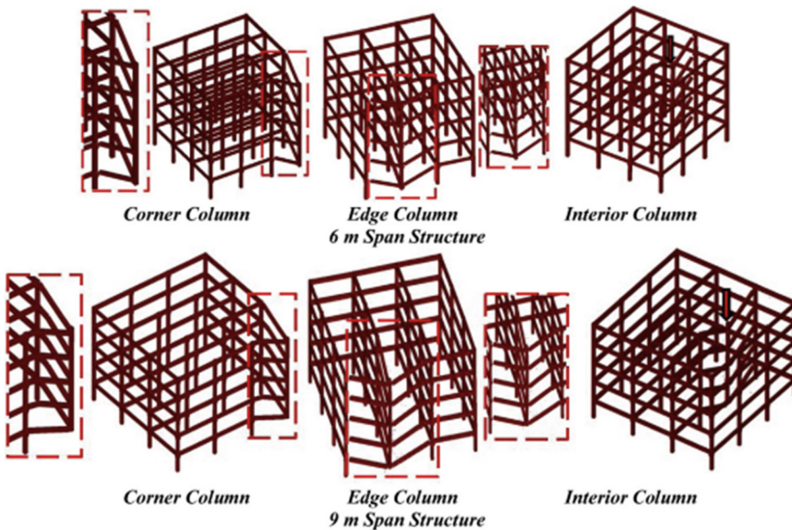
Fig. 5. Collapse scenarios [4]

progressive collapse assessment for precast reinforced beams. So, the multiple collapse scenarios were set as in Fig. 5. Moreover, the deflection of the column removed based on span, column rotations and beam rotations were also recorded using ELS program to study the relation between the span length and progressive collapse as in Figs. 6 and 7.
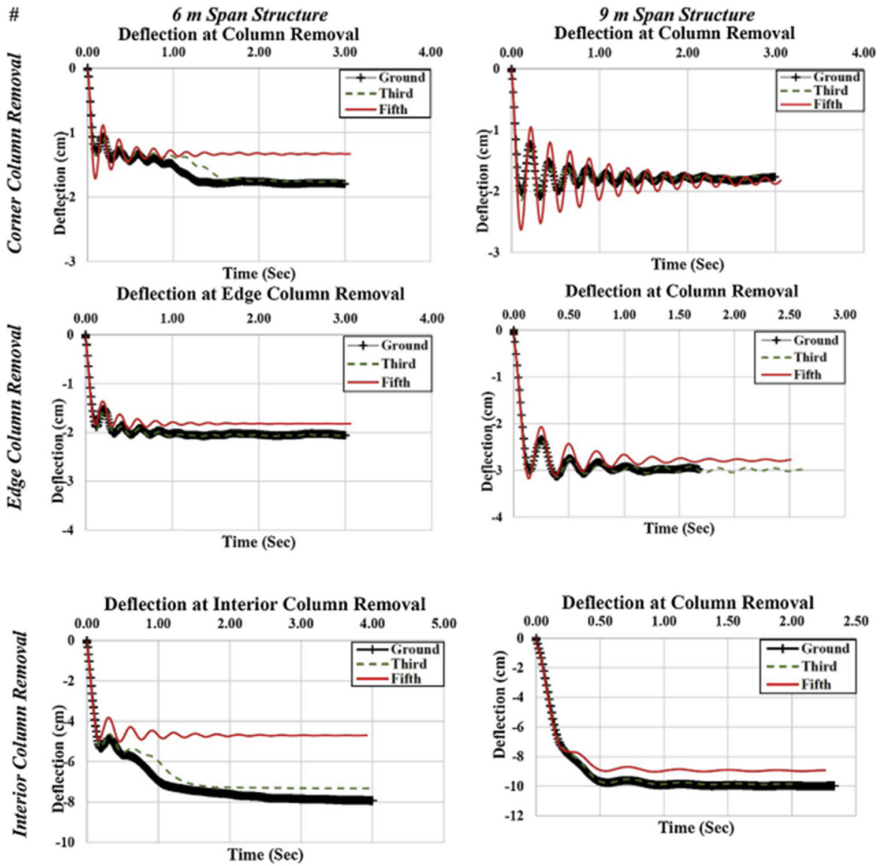
Fig. 6. Column deflection [4]

3 Methodology

3.1 Case Study Design

An 8-story structure is designed according to the Turkish design standard TS-500 is used as a case study for a progressive collapse scenario. To start with, the model is designed using ELS software with the consideration of reinforcement for columns, beams, and slabs also one of the advantages of using ELS software is that the beam-column connections are automatically considered. Also, the beam-slabs connections are also considered, which highly improves the post-collapse response accuracy, so in Figs. 7 and 8 the structure plan view and 3D model are shown respectively [9].
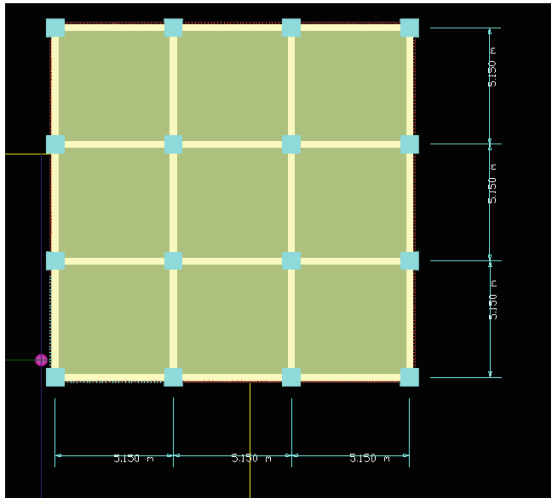
Fig. 7. Plan view.
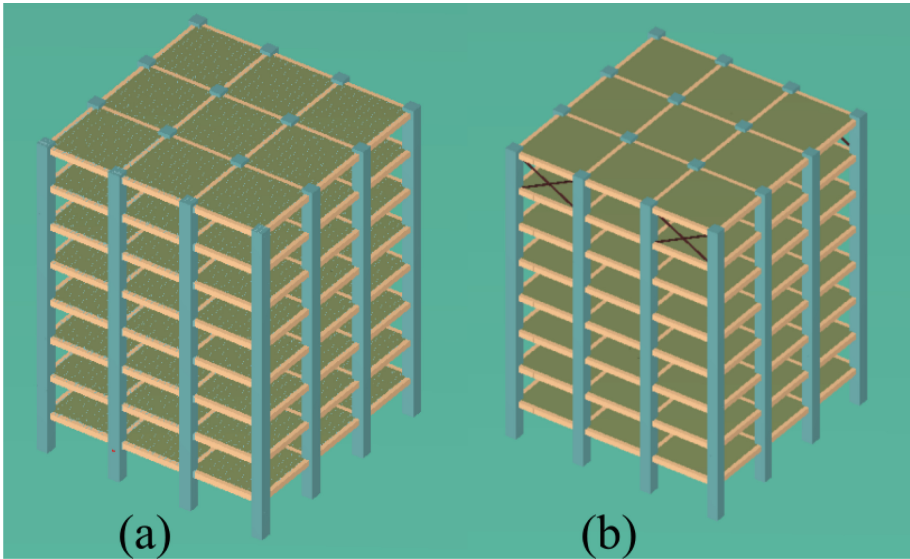
Fig. 8. a) Control model b) Braced model.

3.2 Load Assignment and Scenario

The load application and assignment are done according to the GSA (2013) and UFC (), where the load assigned for the non-linear dynamic analysis is (1.2 Dead load + 0.5 Live Load), so the load is assigned by multiplying the specific weight of the slabs with the above-mentioned factors. Moreover, the progressive collapse is simulated by assigning a demolish scene to the primary columns (B1, C1) at the ground floor [7, 8].

3.3 Study Procedure

As mentioned earlier the study will include 2 main models, one is a control model and the braced model. The results obtained will show the effect of adding braces to a structural system against progressive collapse. Moreover, the structure's behavior will be simulated for 2 s to obtain some representable data. Consequently, the analysis results will include the displacement of the top node of the removed column (mm) with respect to time, 3D rotation contour in radians in the Y-axis and the axial load on the adjacent column after the collapse for both braced and unbraced model.

4 Analysis Results

4.1 Analysis Results for the Unbraced System

For the unbraced system both B1 top node and C1 top node have the same results; Hence, only column B1 results values will be presented to avoid any unnecessary redundancy.
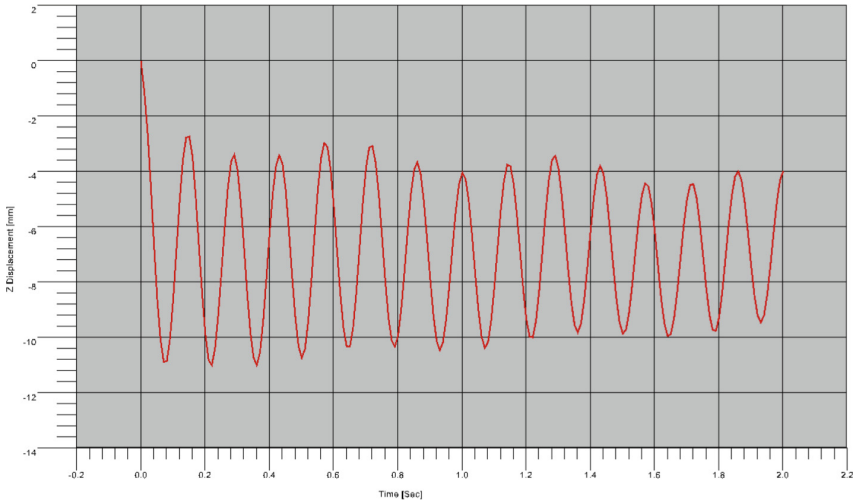
Fig. 9. B1 displacement with respect to time
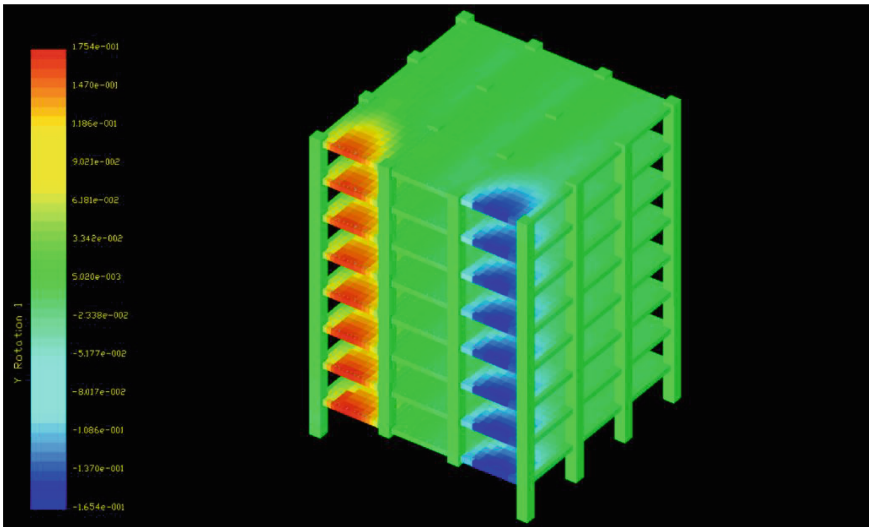
Fig. 10. Y-axis rotation

4.2 Analysis Results for Braced System

For the braced model, the braces used are British steel circular hollow section with a cross section code of CHCF 273 × 12.5 and the braces are located at the top story at the bay above the removed column as in Fig. 8b.
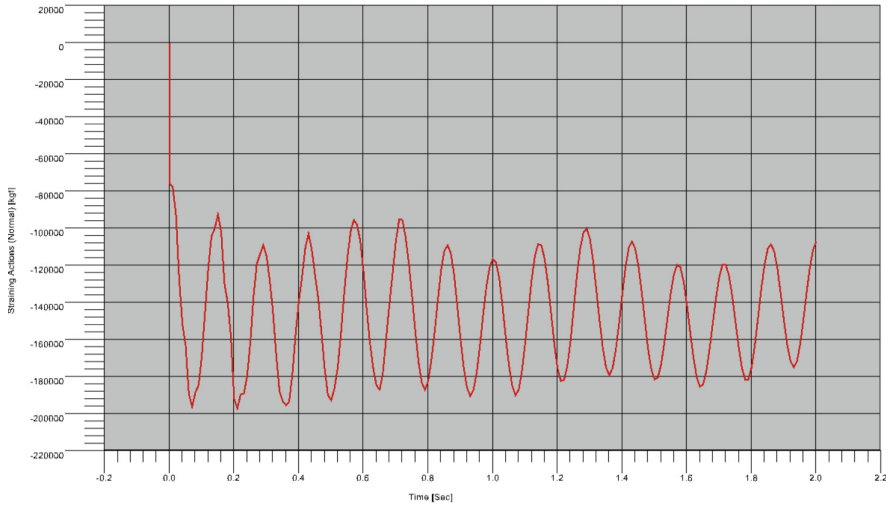
Fig. 11. A1 axial load
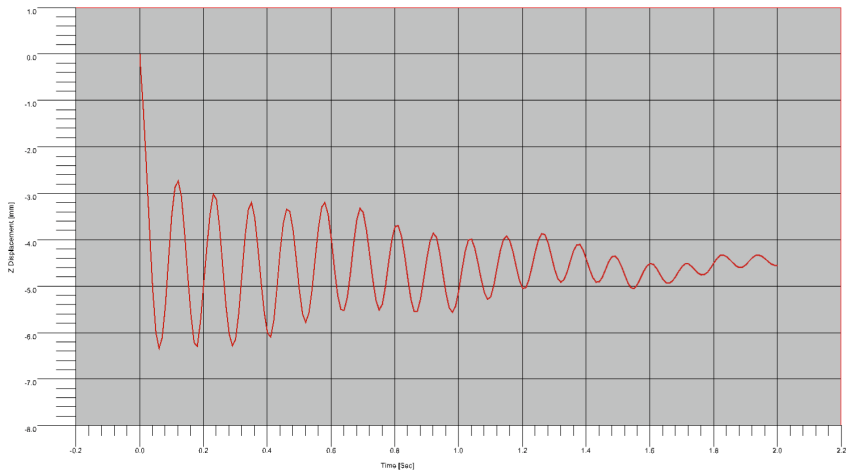
Fig. 12. B1 top node displacement against time

4.3   Results Comparison

This section will include some key points from the analysis results listed as follows:

Unbraced Model:

1. The maximum displacement for the unbraced model is approximately 12.5 mm.
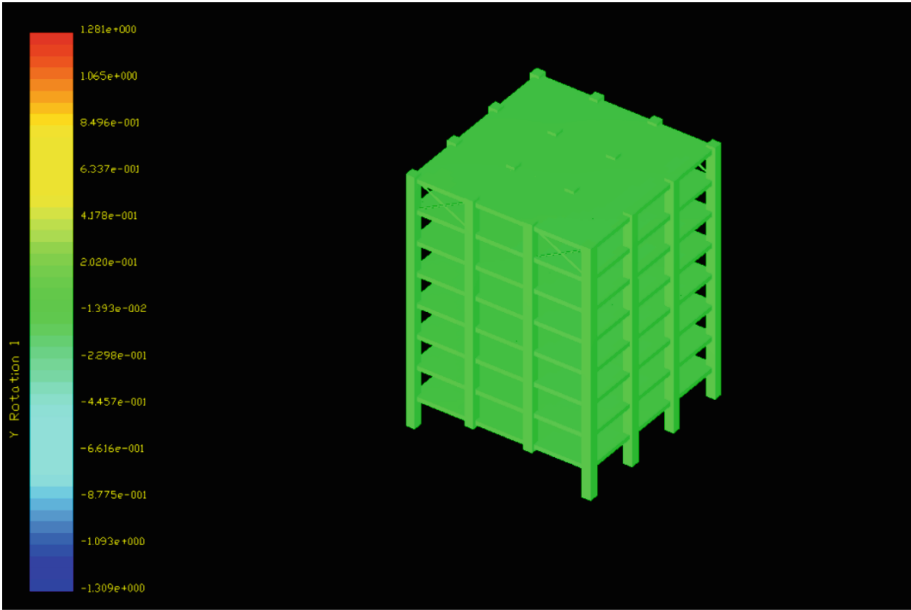
Fig. 13. Y-axis rotation
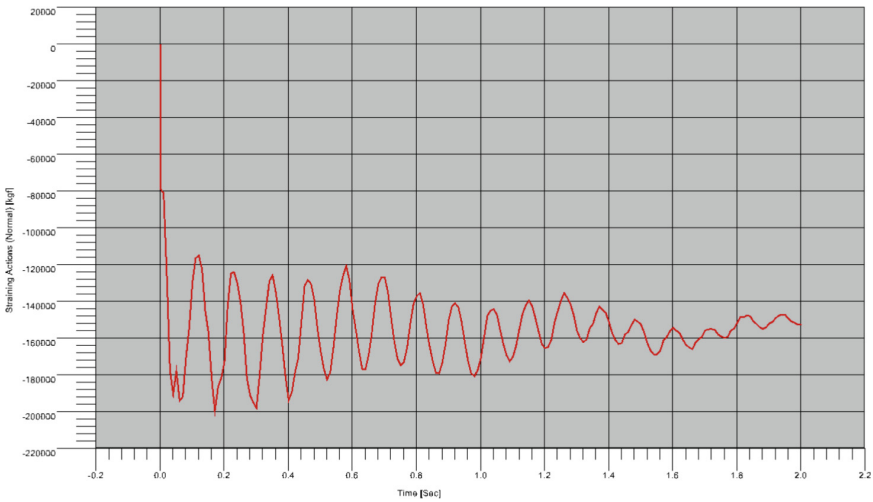
Fig. 14. A1 axial load

2. From Fig. 10, the first bay and third bay have an approximate similar rotation value
   with the red as the maximum positive 0.175 rad and blue as the maximum negative
   −0.165 rad, so the values are almost similar and rotates in opposite directions.
3. The maximum axial force is 195000 Kgf in the unbraced model.

Braced Model:

1. The maximum displacement for braced model is 6.2 mm.
2. From Fig. 12 the oscillation and vibration die out as time passes after the collapse reaching a stability unlike the unbraced model, where the structure keeps on vibrating and the oscillation dies out in a much slower pace as in Fig. 9.
3. The axial load on the adjacent column A1 exhibits a very similar behavior as the displacement, where the axial force reaches a maximum value of 200000 Kgf and then the load on the column diminishes as time passes as in Fig. 14, because of the bracing redistributing the force and absorbing the tensile load.
4. The rotation about Y-axis in the bays above the removed column exhibited a much more stable behavior with less rotations in the slabs itself with a value of -0.0139 rad as in Fig. 13, while for the unbraced model the rotation was much more noticeable as in Fig. 10.

5   Conclusion

In conclusion, the addition of steel braces in any structural system greatly improves its performance against progressive collapse or a sudden column removal, because braces provide a much higher lateral stability and redistribute the load to other undamaged members.

References

1. Abdelwahed, B.: A review on building progressive collapse, survey and discussion. Case Stud. Constr. Mater. **11**, e00264 (2019)
2. Fu, F.: Progressive collapse analysis of high-rise building with 3-D finite element modeling method. J. Constr. Steel Res. **65**(6), 1269–1278 (2009)
3. Khalil, A.A.: Enhanced modeling of steel structures for progressive collapse analysis using the applied element method. J. Perform. Constr. Facil. **26**(6), 766–779 (2012)
4. El-desoqi, M., Ehab, M., Salem, H.: Progressive collapse assessment of precast reinforced concrete beams using applied element method. Case Stud. Constr. Mater. **13**, e00456 (2020)
5. Yu, J., Gan, Y.P., Ji, J.: Behavior and design of reinforced concrete frames retrofitted with steel bracing against progressive collapse. Struct. Des. Tall Spec. Build. **29**(12), e1771 (2020)
6. Qian, K., Weng, Y.H., Li, B.: Improving behavior of reinforced concrete frames to resist progressive collapse through steel bracings. J. Struct. Eng. **145**(2), 04018248 (2019)
7. Guide, U.F.: Unified Facilities Criteria (UFC). Change **3**, 18 (2021)
8. GSA (General Services Administration). Alternate path analysis & design guidelines for progressive collapse resistance. General Services Administration (2013)
9. TS500, T.S.: Requirements for design and construction of reinforced concrete structures. Institute of Turkish Standard, Ankara (2000)

Wind Tunnel Study of the Rooftop of a New Railway Station

Roberto Gomez[(✉)] , Raul Sanchez , and J. Alberto Escobar

Institute of Engineering, UNAM, Mexico City, Mexico
rgomezm@iingen.unam.mx

Abstract. A new main infrastructure work and sustainable tourism project in the south-southeast region of Mexico is in progress. This project will provide a freight and passenger rail service linking the main cities and tourist areas of the South East of Mexico. The project involves the construction of a passenger terminal within the international airport area.

Given the importance and architectural design of the terminal, the designer, requested a wind tunnel study to evaluate wind local effects on the roof of the terminal and revise some wind design hypotheses, since these could be conservative and consequently the current design of this terminal could result in excessive construction costs.

This paper presents the results of wind tunnel tests of a rigid scale model of the railway terminal, as well as the statistical analysis to simulate the mean wind speeds and turbulence characteristics of the wind flow in the wind tunnel. The tests included the representation of the roughness characteristics of the terrain around the new terminal, and the construction of an instrumented scale model which was exposed to different wind flow directions to record pressures in the model. The recording system of the wind tunnel allows obtaining pressure histories at each sensor placed on the model. From these histories, average, maximum and minimum pressure coefficients are derived, which can be used to review the design of the structural elements of the new terminal. Results are compared to those provided in the current Wind Design Manual of Mexico, and those obtained in similar structures, as well.

Keywords: Wind Tunnel · Large Roofs · Railway Terminal

1 Introduction

Currently, wind design standards for buildings do not provide specific pressure coefficients for the design of special roofs such as the train passengers terminal project presented herein. Generally, medium pressure coefficients are used for structures with curved roofs or geometries with simple cone shapes, which are not entirely appropriate for the type of roof presented herein. Wind tunnels tests under boundary layer conditions provides more accurate aerodynamic information.

In this paper, we investigate wind-induced pressures on the roof of a new train terminal building for a full range of wind directions including the effects of the surrounding

topography. The study includes testing a rigid pressure model of a prototype of the train station in its final design. A scaled model was designed and built, replicating the geometric properties of the prototype structure, particularly the roof, including the platforms, plaza and mezzanine. Testing of the model was performed in a turbulent boundary layer flow, which is representative of the wind conditions at the site, and with the topography of the adjacent terrain considering nearby buildings or structures that could modify the flow. Given the importance of the structure, a statistical wind model was also developed for the site where the terminal train will be located; historical records of a nearby weather station were used (Fig. 1).

Fig. 1. A render view of the terminal building.

During the development of the wind tunnel tests, pressures were measured on the roof at strategically predefined points in conjunction with the designer to provide a complete estimate of the differential pressures on the surface of the roof itself or selected elements; the effect of a possible flexibility of the cover or roof of the train terminal was not considered.

This paper presents some aspects of the construction and instrumentation of the scale model for the representation and study of the new terminal building. Roughness characteristics of the surrounding terrain and a proximity model that generically replicates the geometry of the surrounding structures were considered. The procedure used for the simulation of the boundary layer in the wind tunnel (the mean wind profile and its turbulent characteristics) is presented as well.

The scale model was subjected to different wind incidence directions and for each direction the resulting pressures in the model were recorded using the pressure sensors. The recording system allows to obtain pressure histories of each sensor placed in the building. These histories are used to calculate average, maximum and minimum values of pressure coefficients.

Finally, we present the conclusions of this study. It should be clarified that we did not verify the structural design of the building.

2   Wind Climate

In order to consider the most recent wind data, a statistical analysis of the wind was performed using the records of a weather station located at the nearby airport. We present the results of this analysis and compares them with the recommendations of the Civil Works Design Manual of the Federal Electricity Bureau in the chapter of Wind [1]. The aforementioned station has wind data since 1974, so it is ideal to use it for an acceptable statistic of the wind climate.

2.1   Statistical Analysis of Wind

Data from a nearby weather station were obtained from the National Oceanic and Atmospheric Association [2] (NOAA, 2021) and processed according to the procedure recommended by the World Meteorological Organization [3] (WMO, 2008). Wind velocities are normalized to represent speeds at 10 m height for a category 2 terrain (open field terrain) that corresponds to the terrain type at the site and with an average time of 3 s. Figure 2 shows a histogram of the annual maximum velocities determined with the historical records and the normalization process. Using the normalized wind speeds, a statistical analysis of extreme values was performed in order to determine the wind speeds associated with different return periods.
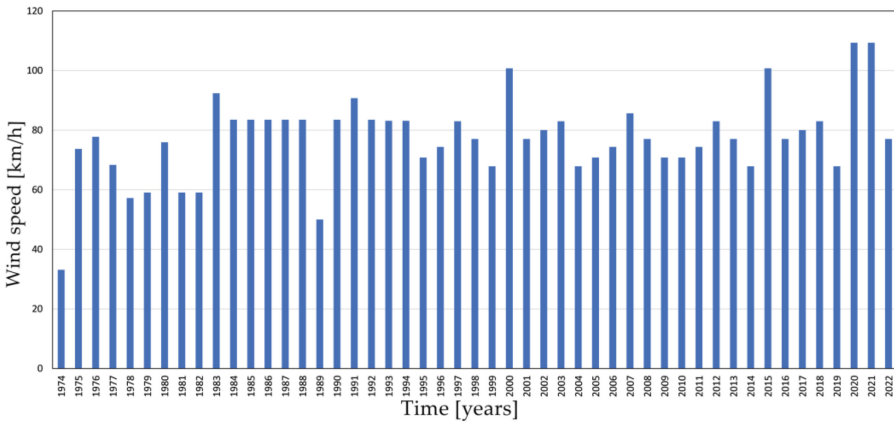
Fig. 2. Histogram of maximum annual wind speeds.

Table 1 shows a summary of the wind speeds predicted with the statistical model developed for return periods of 10, 50, and 200 years. We also present the regional wind speeds indicated in reference [1]. A study of directionality of the annual and monthly wind, providing the dominant directions was also carried out.

Table 1. Wind speeds for different return periods.

Return period years	Model, IIUNAM km/h [m/s]	MOC-CFE-2020 km/h
10	182 [51]	131
50	216 [60]	200
200	244 [68]	245

3   Construction and Instrumentation of the Model

3.1   Design and Elaboration of the Scale Model

Based on the information provided by the client, a 1:100 scale rigid model of the terminal was developed, using 5 types of materials: Acrylic (polymethylmethacrylate), ABS (Acrylonitrile Butadiene Styrene), PVC foamed (Polystyrene), MDF (High Density Cardboard Compressed Board) and aluminum (Fig. 3). The acrylic, polystyrene and MDF elements were manufactured using laser cutting technology to preserve the precision required by the geometry of the project. The parts with more complex geometry were manufactured with additive manufacturing technology, thick enough to preserve the stiffness during the wind tunnel tests. The following figures show some details of the construction process carried out for the manufacture of the model.

Fig. 3. Construction of the rigid model.

3.2   Model Instrumentation

In order to measure pressures in the model as well as wind speed during boundary layer simulation, in this section we describe the different measuring instruments and their

locations. Taps were placed strategically; their location was defined in accordance with the designer. Location of the taps match the points where the results will be shown.

The simulation of the boundary layer inside the wind tunnel must be representative (in statistics) of the study zone; the aim is to reproduce the aerodynamic parameters of the ground, wind speeds, and turbulence intensities [4]. For this purpose, the installation of passive elements (ground roughness and spires) is used to generate the required boundary layer thickness and wind turbulence levels. Figure 4 shows the distribution of the turbulence-generating elements used in this study.

To measure wind speeds at different heights, a hot wire anemometer is used, as it allows to measure turbulent wind speeds with a high sampling frequency (up to 10 kHz if required), and to check compliance with scaling laws. The hot wire specimen is mounted on a robotic arm, in order to perform the measurements more efficiently.

Fig. 4. Roughness elements in the test section of the wind tunnel.

4 Boundary Layer Simulation and Analysis Directions

4.1 Boundary Layer Simulation

For the study of structures, simulation of wind in a wind tunnel requires reproducing a scale wind gradient similar in statistics (mean speed and turbulence intensity) to the characteristics of the neutral boundary layer of the site of interest. In order to reproduce the profile of mean wind speed and turbulence intensity, widely known experimental results in meteorology and wind engineering are used. In [5–15], among others, state of the art, recent advances and recommendations are presented.

The simulated wind in the wind tunnel (with the roughness and vorticity-generating elements, such as those shown in Sect. 3.2) must be representative of the type of terrain

that is required to be simulated and is generally a function of the aerodynamic length of roughness of the z_0 soil [5] expressed in the logarithmic law (Eq. 1) or the power α of the power law (Eq. 2); both equations describe the wind speed profile with height.

$$u(z) = \frac{u^*}{\kappa} ln\left(\frac{z}{z_0}\right) \qquad (1)$$

where is $u(z)$ the mean wind speed at a height z, z_0 is the aerodynamic length of surface roughness and is the Von Karman κ constant ~0.41.

$$u(z) = u_{ref}\left(\frac{z}{z_{ref}}\right)^{\alpha} \qquad (2)$$

where is a u_{ref} wind speed at a height z_{ref} (usually 10 m) and α is a power exponent that depends on the roughness of the terrain.

On the other hand, turbulence intensity is a measure of the magnitude of turbulent velocity compared to the mean velocity at the same height. In [11], the following equation is proposed to estimate the intensity of turbulence as a function α of the power law parameter:

$$I_u(z) = 0.1\left(\frac{z}{z_g}\right)^{-\alpha-0.05} \qquad (3)$$

where z_g is the gradient height of the boundary layer.

Figure 5 shows the simulated mean wind speed and turbulence profiles in the wind tunnel for the tests. The characteristics corresponding to parameter α of the power law of ~0.22 (or $z_0 = 0.16$), which according to the classification of terrain types made by Davenport [5] corresponded to a rough open terrain, little rugged terrain or forest. With this, we simulate the aerodynamic characteristics of the terrain near the location of the railway terminal.

4.2   Wind Incidence

Because the direction of wind is uncertain and the pressures induced by wind depend on the wind, the model was studied in a range of 0° to 180° with increments of 10° (Fig. 6). Measurements at 10° intervals are adequate to describe the azimuthal variation of façade pressures, since turbulent flow fluctuations cause momentary changes in wind direction above 10° and therefore smaller angles do not substantially alter the predicted pressures and suctions.
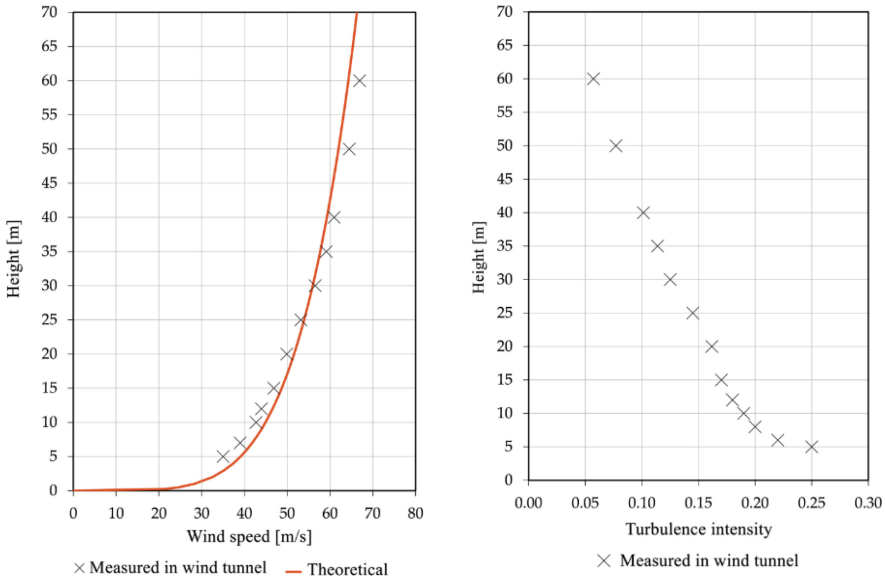
Fig. 5. Mean wind speed and turbulence profiles
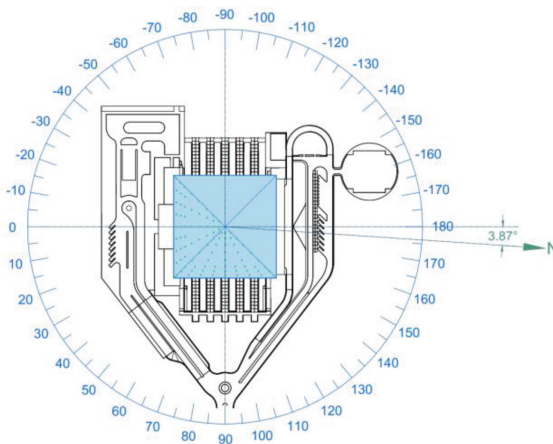
Fig. 6. Wind incidence angles considered in the tests, the TTMCUN model is shown as a reference.

5 Results of Experimental Tests

Below, we present some pressure coefficients obtained for the different directions considered (Fig. 7). These coefficients are obtained by normalizing the pressures measured in the model with the average dynamic pressure measured at a reference height, usually selected in the downstream free current of the boundary layer or at the height of the model being studied. The pressure coefficients for each measuring point are therefore defined as follows:

Mean pressure coefficient:

$$C_{\bar{p}} = \frac{\frac{1}{T}\int_0^T p(t)dt}{q} \tag{4}$$

RMS pressure coefficient:

$$\sigma_{C_p} = \frac{\sqrt{\frac{1}{T}\int_0^T (p(t)-\bar{p})^2 dt}}{q} \tag{5}$$

Maximum pressure coefficient:

$$C_{\hat{p}} = \frac{p_{max}}{q} \tag{6}$$

Minimum pressure coefficient:

$$C_{\underset{p}{\smile}} = \frac{p_{min}}{q} \tag{7}$$

Net pressure coefficient:

$$C_{p,net} = \frac{p_{top}(t) - p_{bot}(t)}{q} \tag{8}$$

where $p(t)$ is the instantaneous surface pressure measured with respect to the reference mean static pressure; σ_{C_p} is the RMS value of for the sampling period; p_{max} is the maximum value of for the sampling period; p_{min} is the minimum value of for the sampling period; $p_{top}(t)$ is the pressure measured at the top of the roof; $p_{bot}(t)$ is the pressure measured at the bottom of the roof; t is time; T is the sampling period; $q = \frac{1}{2}\rho\bar{u}^2$ is the reference dynamic pressure; ρ is the density of air; and $\bar{u}$ is the mean reference speed, measured at the height of the rail terminal.

It is important to mention that the instantaneous pressure can be positive or negative. The net pressure coefficient (for open rooftops) has a negative sign if it acts upward (suction) and positive sign if it acts downward (pressure). Figure 7 shows the mean net pressure coefficients, both maximum and minimum.
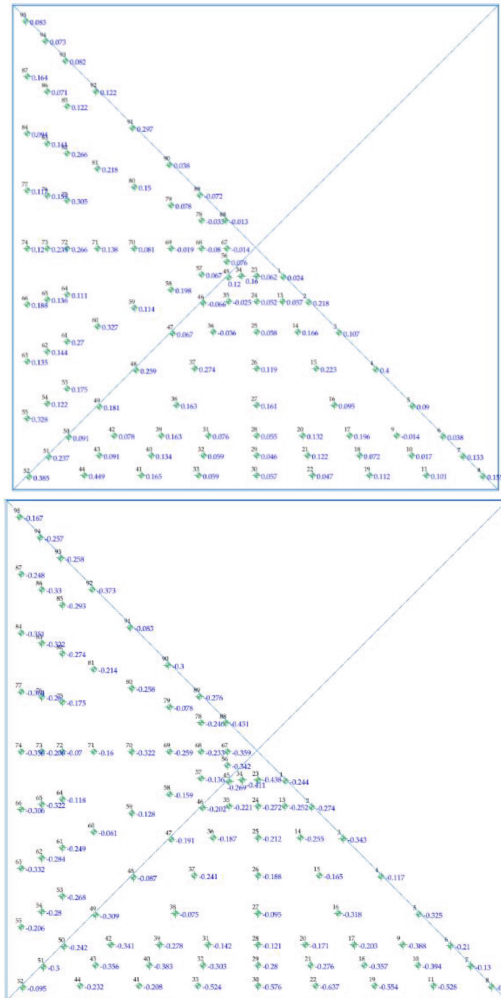
Fig. 7. Mean net pressure coefficients: above, maximum and below, minimum.

6 Final Comments

In this paper, the results of the study of the pressure model of a new train terminal were presented. From the construction of the model to the simulation of the boundary layer in the tunnel and instrumentation, including the statistical study of the wind climate to determine the properties of the wind to be simulated. The above in order to expose the experimental method used.

Although the analysis of historical records shows the existence of dominant wind directions, it is advisable for structural design purposes to analyze the structures in a complete range of directions (360° to every 10°); therefore, the results for each of these directions are included (in digital format).

For open decks, net pressure coefficients were determined for an overall review of each deck; however, the local pressure coefficients at each instrumented point of the roof were also presented.

References

1. MDOC-CFE. Manual of Civil Works, Wind Design. Federal Bureau of Electricity (2020). (in Spanish)
2. National Oceanic and Atmospheric Association (NOAA, 2021)
3. Organización Meteorológica Mundial "Guía de Instrumentos y Métodos de Observación Meteorológicos" (2008)
4. Martín Rodríguez, P., Rodríguez, E., Loredo-Souza, A., Camano-Schettini, E.: Utilización de anemómetro de hilo caliente a temperatura constante para mediciones de velocidad de aire en túnel de viento. RIELAC, vol. XXXV 1/2014, pp. 78–92 (2014). ISSN 1815-5928
5. Wieringa, J.: Updating the davenport roughness classification. J. Wind Eng. Ind. Aerodyn. **41**(1), 357–368 (1992). https://doi.org/10.1016/0167-6105(92)90434-0
6. Stull, R.B.: An Introduction to Boundary Layer Meteorology (1988 Edition), 666 p. Kluwer Academic Publishers. Dordrecht (1988)
7. Kaimal, J.C., Finnigan, J.J.: Atmospheric Boundary Layer Flows. Oxford University Press, Oxford (1994)
8. ESDU 82026. "Strong winds in the atmospheric boundary layer Part 1: hourly-mean wind speeds", ESDU International, Item No. 82026, London, 1986, revised 2002 (1982)
9. ESDU 85020. "Characteristics of atmospheric turbulence near the ground. Part II: Single point data for strong winds (neutral atmosphere)", ESDU International, Item No. 85020, London, 1985, revised 2001 (1985)
10. ESDU 86010. "Characteristics of atmospheric turbulence near the ground. Part III: Variations in space and time for strong winds (neutral atmosphere)", ESDU International, Item No. 86010, London, 1986, revised 2001 (1986)
11. Tominaga, Y., et al.: AIJ guidelines for practical applications of CFD to pedestrian wind environment around buildings. J. Wind Eng. Ind. Aerodyn. **96**, 1749–1761 (2008). https://doi.org/10.1016/j.jweia.2008.02.058
12. Simiu, E., Scanlan, R.: Wind Effects on Structures, 3a edn. Wiley, New York (1996)
13. Burton, T., Sharpe, D., Jenkins, N., Bossanyi, E.: Wind Energy Handbook, 4th edn. Wiley, Hoboken (2004)
14. Holmes, J.D.: Wind Loading of Structures, 2nd edn. Routledge, Taylor & Francis (2007)
15. Dyrbye, C., Hansen, S.O.: Wind Loads on Structures. Wiley, Hoboken (1997)

When a Silo Burns for a Month: Structural Assessment of a Severely Damaged Concrete Agricultural Structure

Richard Walls[1(✉)] , Anene Oguaka[1] , and Gareth Jones[2]

[1] Department of Civil Engineering, Stellenbosch University, Stellenbosch, South Africa
{rwalls,aoguaka}@sun.ac.za
[2] Synevo, Johannesburg, South Africa
gareth.jones@synevo.co.za

Abstract. Internationally there are tens of thousands of concrete silos storing millions of tons of agricultural produce. However, most biomass is combustible and when ignited there is sufficient fuel to burn for an extended period of time, up to months. This paper presents a structural fire assessment of a large-scale concrete silo which experienced a severe fire that eventually led to it being condemned. After an initial ignition, firefighting efforts resulted in a steam cloud being produced that pressurised the silo and caused a portion of the roof to blow off. The fire continued to smoulder for almost a month resulting in a constant, but relatively low, temperature at the base of the silo. Significant conduction up the walls of the silo, influenced by the heavy rebar in the walls, led to a high level of thermal expansion which was far beyond that initially anticipated. This resulted in severe cracking and damage for more than 5 m above the level of the fire. Based on concrete core tests, it was found that the strength had severely reduced, which appears primarily to have been driven by thermally-induced microcracking. Temperatures of around 100–200 °C caused the level of damage normally seen on structures experiencing temperatures of over 500–900 °C due to the high level of thermal penetration into samples.

Keywords: Structural fire engineering · assessment · cracking · agriculture · silo · demolish · concrete

1 Introduction

A silo is a large storage vessel that can be made from reinforced concrete, steel, wood, stone, or other materials. They are commonly used for storing granular materials such as coal, pebbles, food grains, biomass, cement, sand, and various other products. There have been several incidents around the world in which fires or explosions have occurred in or around silos. The fire ignition source could be external or internal [1]. Internal ignition sources include self-heating, silo dust explosion, friction, hot work, and electrical faults etc. External sources include accidents, adjacent conveyor belts overheating or possibly wildland fires. In some cases, these incidents have led to structural damage

to the silos themselves. Several studies have approached silo fires from experimental, numerical or computational studies [2, 3] to address different aspects of silo safety. These include studies on ignition and explosion prevention, instrumentation, fire detection and suppression [4], silo structures and construction materials response to heat, fire, and explosion [5], filling and emptying of silo contents [6], etc. The propensity of different grains and foodstuffs to ignite will vary [7], but ultimately every biomass is combustible and has a calorific value. High levels of moisture will reduce propensity to ignite and decrease flame spread rates.

Since the World Trade Centre disaster, there has been extensive research conducted to understand structural mechanics in fire [8] and also to predict the capacity of heated building elements. Numerical models have highlighted how very complex stress and strain states are created in elements when exposed to elevated temperatures [9]. As structural materials are heated their strength and stiffness decrease. However, a more dominant effect is that expanding elements can result in high forces being induced when they are not free to expand, i.e. restrained thermal expansion occurs [10]. The interaction between adjacent structural elements typically governs real building structural collapse [11].

This paper presents an overview of a fire incident and analysis of the structural response of a large agricultural silo. Findings from the work will assist in future work to protect silos from fires, analyse incidents and repair such structures. Unfortunately, the structure considered in this work had to be demolished as the damage was so extensive. The purpose is to describe and discuss the physical observations, laboratory test results of failed structural elements, and mechanisms of failure from fire and structural engineering perspectives.

2 Incident Analysis

2.1 Silo Characteristics

Figure 1 presents images of the fire damaged silo, whilst Fig. 2 presents a cross-section of the structure and details that will be discussed in the sections that follow. For privacy reasons only limited technical details are provided in this paper.

The silo contained 3000 t of maize and was approximately full at the time of the incident. The structure is a normally reinforced concrete silo, with a circular wall fixed to a thick base slab. The approximate dimensions of the silo are: outer diameter = 15.7 m, height of cylinder = 19.1 m, and wall thickness = 0.2 m. The sloped roof of the silo was formed from precast concrete panels. A transfer gantry housed a conveyor that fed maize to the silo at the top. At the bottom an outlet fed grain onto a conveyor in a transfer tunnel below the concrete.

2.2 Fire Incident

In this section the incident is discussed in relation to Fig. 2 with the numbers corresponding to the labels provided. (1) The fire was ignited at the top and was detected through visual observations. Exact details of the ignition will not be addressed. However, such fires can be readily started from conveyor belt operations, overhead lights,

workers smoking and electrical faults. The maize started flaming and produced significant quantities of smoke. (2) Once the maize had ignited the operators responded by emptying the bulk of the contents of the silo out, which saved a significant amount of material. Around 100 t of material was left after this action.

(3) Using a small hatch in the wall of the silo suppression activities were undertaken through the application of a water from a hose. Such a response is not necessarily incorrect and would have suppressed the fire. However, the problem was that since there was only a small opening at the top the rate of water application resulted in a steam cloud that pressurized the silo. The pressure was sufficient to blow the precast concrete panels of the top of the roof. Had a large vent been present, or the water had been applied slowly, this may not have occurred.

(4) Once the roof had been compromised response teams were concerned about safety of firefighters in the vicinity of the structure, in case further concrete panels fell off. Since a relatively small amount of material was left it was decided that it would be safer to allow the fire to continue burning at the slow rate that it was (based on observations through the side hatch). It was hoped that the fire would self-extinguish. With the remaining 100 t of material the fire continued to burn for almost a month. Limited flaming occurred and it was primarily a smouldering fire. Glowing red embers and a certain level of small flames could be observed through the side hatch.

(5) Heat was transferred from the smouldering maize into the silo walls around the perimeter. The exact temperature and thermal exposure are unknown. Combustion continued for almost a month until the fire burnt out.

(6) The heated concrete expanded and induced high compressive stresses, due to the radial action and restraint from the base slab. This will be discussed below.

2.3   Tests and Investigations

After the incident a detailed assessment of the silo was undertaken. This consisted of: (a) a high-resolution scan by a drone to map cracking and material degradation, (b) testing of concrete cores, and (c) visual assessments.

Concrete cores were extracted at 4 levels from the base of the cylinder (0.5 m, 1.5 m, 3 m and 5 m). At each height 12 cores were extracted (except 4 samples at 3.0 m could not be done due to restricted access), resulting in 44 samples being taken. Cores were 75 mm in diameter and tested according to SANS 5885. The coring specialists identified the rebar as consisting of Y16-75 horizontally (16 mm diameter high tensile bars at 75 mm spacing) and Y10-100 vertically. Of the 44 samples extracted:

1. 16 disintegrated during coring,
2. 6 had major structural cracks within them,
3. 4 had extensive microcracking,
4. 4 had significant microcracking,
5. 3 had a reasonable level of microcracking, and
6. 11 were competent to obtain a test result. Compressive strengths ranged from 30 to 52 MPa with an average of 38.5 MPa.

Hence, of the samples only 25% had sufficient integrity to yield a compressive strength result (i.e. categories 1 to 5 above could not be tested). Thus, in the lower 5 m of

Fig. 1. Images of the fire damaged silo showing: (a) external view of the silo, (b) view of the roof from inside, (c) roof and transfer structure, (d) internal charred material and smouldering fire, (e) precast concrete panels which were propelled by steam off the roof, and (f) example of cracks in the walls when viewed from the outside.
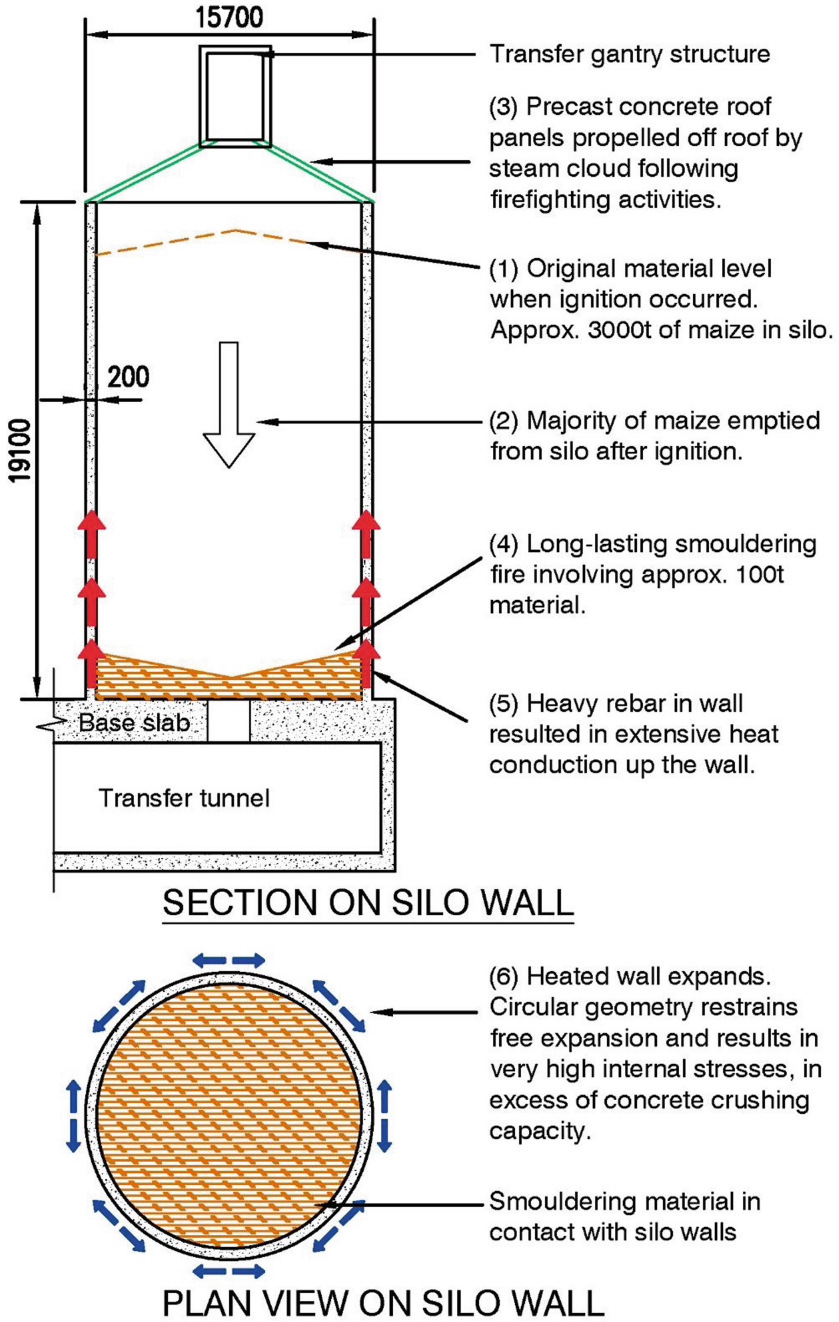
Fig. 2. Structural response of the silo showing incident timeline and development of internal stresses.

the silo around 75% of the concrete had been severely compromised and had negligible residual strength.

The drone survey and visual observations highlighted that horizontal and vertical cracks were present in the silo. A number of large horizontal cracks opened up as shown in Fig. 2(f). However, visual observations were unable to identify the extensive nature of internal cracking and material degradation that occurred, and this was only identified after the concrete cores had been tested. Initially it was hoped that the silo could be saved by repairing and strengthening the lower 2 m to 4 m of the silo walls. Unfortunately, the extent of degradation resulted in this not being achievable.

3 Thermo-Mechanical Structural Response

3.1 Fire and Thermodynamic Behaviour

It is difficult to accurately determine the temperatures experienced by the concrete wall. Within a compartment fire temperatures of 600–1200 °C typically occur (with the miniscule combustion flame zone being up to 2000 °C) [12]. For a smouldering fire the maximum temperature of a burning cellulosic material in the charred zone is around 600 °C, and occurs at the position where the production of visible products stop but the glowing of materials is present [13]. As the fire progressed a char layer would have formed up against the concrete wall, providing an insulating layer.

Heat would have been released (a) through conduction into the walls and base slab, (b) through convection of hot gases vertically, and (c) through radiation from the surface. The heat release rate (HRR), $\dot{Q}_c$, can be approximated by considering the mass loss, $\dot{m}$, where it is assumed that 100 t burn uniformly over a period of one month. The calorific value, ΔH_c, of cellulosic materials is around 20 MJ/kg with wood having a value of around 17 MJ/kg [14]. Here a conservative value of 17 MJ/kg will be applied, accounting for a limited amount of moisture. The combustion factor, χ, is taken 0.8 for cellulosic materials. Hence, the HRR is calculated as [15]:

$$\dot{Q}_c = \dot{m}\chi\,\Delta H_c = 525\,\text{kW} \tag{1}$$

A typical post-flashover compartment fire will be in the order of 5 MW, highlighting this is a relatively small fire. The heat release rate per unit (HRRPUA) area of the surface of the 15.3 m inner diameter of the silo is:

$$\dot{q}_c'' = \frac{\dot{Q}_c}{A} = 2.9\,\text{kW/m}^2 \tag{2}$$

There are significant uncertainties with regards to this value in terms of the total mass lost, calorific value and exact time period. However, it is sufficient to show that the rate of burning was low over the surface, but sufficient for localized glowing and smouldering to be sustained. Even if the majority of combustion had occurred in the first 2 weeks it would lead to a HRRPUA of around 5 kW/m² which is far below the rate of typical flaming fires (e.g. 100–200 kW/m² for flaming timber).

Silos contain a significant amount of rebar, and it is hypothesized that the reinforcing steel conducted heat up the walls. Steel has a much higher thermal conductivity than

concrete, being about 46 and 1.0 W/mK respectively [13]. The outer concrete would have insulated the steel from the ambient air temperatures, leading to an increase in temperature many meters from the fire. With the duration of the fire being around a month, steady-state heat transfer conditions would have approximately been achieved.

3.2 Determination of Internal Stresses

A question to be addressed now is: what temperature increase was required to cause crushing of the concrete, as the concrete had lost the majority of its capacity? This will be discussed in relation to Fig. 2 which illustrates the structural mechanics. At around 1000 °C concrete has around 4% of its residual strength, with 0% strength only being attained at 1200 °C [16]. However, much lower temperatures were attained based on site observations.

Based on fundamental structural mechanics the total strain of a material is the summation of the thermal (θ), mechanical (σ), creep (cr) and transient (tr) strains:

$$\epsilon_{total} = \epsilon_\theta + \epsilon_\sigma + \epsilon_{cr} + \epsilon_{tr} \tag{3}$$

Many codes, e.g. Eurocode 1992-1-2 [16], implicitly account for the latter two terms in the stress-strain model and, thus, are neglected. At the base of the silo the walls would have been restrained by both the base slab and the circular nature of the wall. Hence, as the wall was heated it would have expanded against itself, and the adjacent concrete, resulting in negligible deformation. Thus, the total strain would have been approximately zero. This gives:

$$\epsilon_\theta = -\epsilon_\sigma \tag{4}$$

The thermal strain, or elongation, of a heated siliceous concrete is given by:

$$\epsilon_\theta = -1.8 \times 10^{-4} + 9 \times 10^{-6}\theta + 2.3 \times 10^{-11}\theta^3 \tag{5}$$

where θ is the temperature (°C). The mechanical strain in a uni-axially loaded member is given by:

$$\epsilon_\sigma = \frac{f}{E_\theta} \tag{6}$$

where f is the stress in the element (MPa), and E_θ is the Young's Modulus (MPa) at temperature θ. It has been assumed that the failure stress of the concrete was 50 MPa (likely for such silos), and based on core tests above, and E_θ is 33 GPa. Based on this the temperature required to cause compressive crushing of the concrete is 175 °C. This value is approximately within the range where E_θ can be assumed constant.

A failure temperature of around 175 °C is feasible considering the magnitude of the HRR and HRRPUA calculated above, and the initial flaming observed. Hence, this highlights how thermal restraint has driven the failure mechanism, which is consistent with past findings [17]. Had the silo walls been able to move outwards the internal stresses would have quickly dissipated and damage would have been much reduced. However, the very nature of a silo typically precludes the option of having a sliding connection at the base. It is highly likely that the majority of the damage occurred within the first few days of the incident, but without a detailed thermal history within the silo this is difficult to accurately define.

4 Conclusions

This paper has presented a case study on an agricultural silo fire that caused extensive damage and resulted in the structure being condemned. A long-lasting fire caused extensive micro-cracking within the concrete due to restrained thermal expansion. The cylindrical nature of the silo, and the linking of the silo to the thick base slab, prevented the cylinder from expanding when heated. At a temperature of around 175 °C concrete crushing would have occurred, based on simplified calculations provided. Such a temperature could readily have occurred. Based on approximate assumptions regarding combustion a heat release value of 0.5 MW occurred over a period of one month.

Such fires do not commonly occur in silos. Furthermore, the fact that this incident lasted for around one month is an anomaly. Hence, engineers should not necessarily seek to provide additional passive protection to silos to accommodate such long-lasting fires. Rather, standard operating procedures for preventing these fires, and suppressing them when they do occur, should be adopted. However, some countries, such as Poland, have introduced fire resistance requirements for crop silos to protect them [1]. It may be possible to line the lower section of a silo, or increase concrete cover, to provide additional fire resistance. Furthermore, it is possible that the majority of the damage occurred within the first few days of the incident, meaning that the amount of damage that occurred during the latter days was limited.

Since agricultural silos are often located in remote areas where municipal fire departments may not be available (or functional), the organisations managing such facilities may need to provide the suppression systems required. It may be possible to install detection and suppression systems to allow for a more rapid response to these fires. However, the internal conditions of silos may not be suitable for various electronic systems, and systems are also not easy to access for regular inspection, testing and maintenance. Mobile firefighting units may be suitable to protect a number of silos, but will likely require a significant period of time to arrive at a remote location, depending on the number of vehicles, availability of trained staff and area covered. Further research is required to quantify the length of time available for a mobile unit to respond before significant damage is required. This will depend on the rate of fire spread, and rate of heat transfer into the walls.

If water is used to suppress such fire it is necessary to provide an area for steam and smoke to be vented from these confined spaces. Also, the rate at which water is supplied should be kept relatively low. Such facts will often not be immediately apparent to staff, or firefighters, when attending to such an event meaning that training is essential.

References

1. Roszkowski, P., Kimbar, G.: Full-scale external fire test of free-standing steel silo. Fire Saf. J. **120** (2021). https://doi.org/10.1016/j.firesaf.2020.103123
2. Villacorta, E., et al.: Onset of smoldering fires in storage silos: susceptibility to design, scenario, and material parameters. Fuel **284** (2021). https://doi.org/10.1016/j.fuel.2020.118964
3. Krause, U., Schmidt, M., Lohrer, C.: A numerical model to simulate smouldering fires in bulk materials and dust deposits. J. Loss Prev. Process Ind. **19**, 218–226 (2006). https://doi.org/10.1016/j.jlp.2005.03.005

4. Krause, U.: Fires in Silos: Hazards, Prevention, and Fire Fighting. Wiley, Hoboken (2009)

5. Ogle, R.A., Dillon, S.E., Fecke, M.: Explosion from a smoldering silo fire. Process. Saf. Prog. **33**, 94–103 (2014). https://doi.org/10.1002/prs.11628

6. Fernandez-Anez, N., Meyer, A.K., Elio, J., Kleppe, G., Hagen, B.C., Frette, V.: Behaviour of smoldering fires during periodic refilling of wood pellets into silos. J. Loss Prev. Process Ind. **72**, 104565 (2021). https://doi.org/10.1016/j.jlp.2021.104565

7. Oguaka, A., Flores Quiroz, N., Walls, R.: Fire parameters, behaviour, and comparative thermal hazard of food grains based on the cone calorimeter tests. Process Saf. Environ. Prot. (2023). https://doi.org/10.1016/j.psep.2023.03.078

8. McAllister, T.P., et al.: Structural analysis of impact damage to world trade center buildings 1, 2, and 7. 615–642 Fire Technol. (2012). https://doi.org/10.1007/s10694-012-0286-5

9. Walls, R., Viljoen, C., De Clercq, H.: Parametric investigation into the cross-sectional stress-strain behaviour, stiffness and thermal forces of steel, concrete and composite beams exposed to fire. J. Struct. Fire Eng. **11**, 100–117 (2019). https://doi.org/10.1108/JSFE-10-2018-0031

10. LaMalva, K., Hopkin, D.: International Handbook of Structural Fire Engineering. Springer, Cham (2021). https://doi.org/10.1007/978-3-030-77123-2

11. Beitel, J., Iwankiw, N.: Analysis of Needs and Existing Capabilities for Full-Scale Fire Resistance Testing, Nist Gcr 02-843-1. 1, 86 (2008). http://www.bfrl.nist.gov/866/pubs/NISTGCR02-843.pdf

12. Quintiere, J.G., Karlsson, B.: Enclosure Fire Dynamics, 1st edn. CRC Press, Boca Raton (2002). https://doi.org/10.1016/s0379-7112(01)00031-5

13. Drysdale, D.: An Introduction to Fire Dynamics (2011). https://doi.org/10.1016/0379-7112(86)90046-9

14. CEN, EN 1991-1-2:2002: Eurocode 1: Actions on structures - Part 1–2: General actions - Actions on structures exposed to fire, British Standard Institution (BSI), London (2002)

15. Quintiere, J.G.: Principles of fire Behavior. Alar Elken, New York (2011)

16. BSI, BS EN 1992-1-2:2005: Eurocode 2: Design of concrete structures – Part 1–2: General – Structural fire design, British Standards Institute, London (2005)

17. Usmani, A.S., Rotter, J.M., Lamont, S., Sanad, A.M., Gillie, M.: Fundamental principles of structural behaviour under thermal effects. Fire Saf. J.Saf. J. **36**, 721–744 (2001). https://doi.org/10.1016/S0379-7112(01)00037-6

Analysis of Stress Induced Deformation and Evaluation of Performance of Tunnel Boring Machine in Extraordinary Geological Conditions Encountered During Excavation of Longest Head Race Tunnel in Himalaya: A Case Study

Mainak Ghosh Roy[1]([✉]) [iD], Sajan Moideen[1], Nirmal Singh[1], and Biswajit Basu[2]

[1] Parbati Hydroelectric Project-II, NHPC Ltd., Nagwain, Himachal Pradesh, India
`mainakghosh@nhpc.nic.in`
[2] Corporate Office, NHPC Ltd., Faridabad, Haryana, India

Abstract. The paper reviews major geological problems encountered during construction of the longest Head Race Tunnel (HRT) of length 31.5 km in the hydropower projects of India through Tunnel Boring Machine (TBM). Major tunneling hindrances encountered in the TBM face include rock bursting, shear zone with groundwater ingress, high cutter consumption due to abrasive nature of rockmass and frequent detachment of rockmass above cutter head of TBM causing overbreak. The remedial measures adopted to successfully overcome these challenges are discussed. The paper also back analyzes magnitude of in-situ stresses in rock bursting zones using numerical modelling to determine role of depth of overburden and field stress ratio in causing rock bursting. The result indicates that yielding zones increase with depth of overburden and decrease in field stress ratios. TBM performance was evaluated using QTBM (Barton, 2000) parameters and the observed penetration rate (PR) during boring in quartzite, granite gneiss and chlorite schist. An empirical relationship developed between QTBM and PR indicates exponential increase of penetration rate with QTBM under stress induced conditions.

Keywords: Rock Bursting · Groundwater ingress · In-situ stress · TBM performance

1 Introduction

Parbati hydroelectric project-II, presently under construction by NHPC Ltd, is a run of river scheme located in Lesser Himalayas in Himachal Pradesh, India on the river Parbati, a tributary of Beas river. Major part of the project area falls within a tectonic window in close proximity to Jutogh thrust which is a part of Main Central Thrust (MCT). Project mainly comprises construction of 85 m high Concrete Gravity Dam, 31.5 km long, 6.0 m

diameter Head Race Tunnel, two inclined pressure shafts of 3.5 m diameter and a surface power house. This inter-basin transfer type project involves diversion of water of Parbati river into Sainj river, both being tributaries of river Beas. The discharge has been further augmented by diverting five intermediate streams namely Jigrai nala, Manihar nala, Pancha nala, Hurla nala and Jiwa nala by constructing Trench weirs, Feeder tunnels, Desilting Chambers and Drop Shafts. The power house utilizes a gross head of 862 m and will have installed capacity of 800 MW. The most critical area identified during investigation was a 13 km long segment of HRT which has to be negotiated with only two faces out of which 9.05 km is to be excavated through TBM from Face-4. Layout plan of Parbati hydroelectric project-II is shown in Fig. 1(a). Geological section along HRT Face-4 with zones of rock bursting is shown in Fig. 2(a).
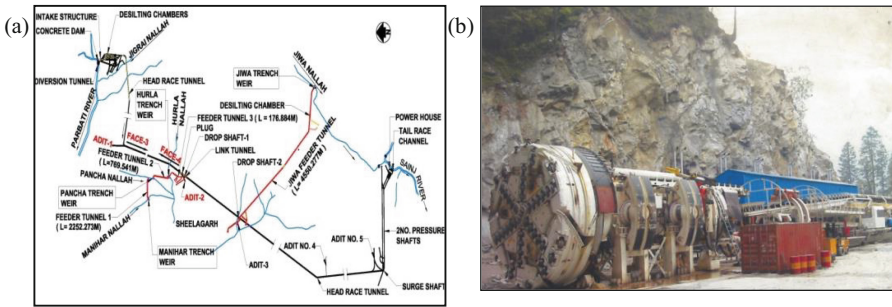
Fig. 1. (a) Layout plan of Parbati hydroelectric project-II **(b)** Open shield Tunnel Boring Machine used in HRT of Parbati-II project
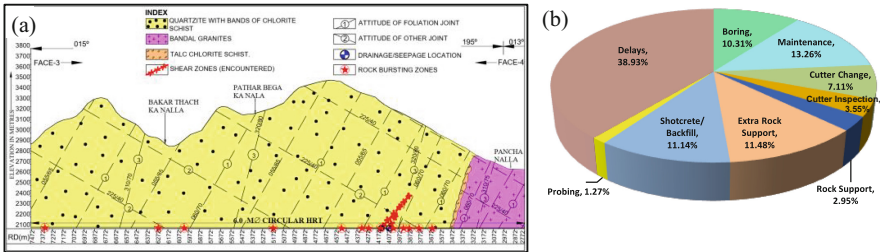
Fig. 2. (a) Geological section along HRT Face-4 **(b)** Utilization Chart of TBM

2 Major Hindrances Encountered in TBM Tunneling

The study area selected is a 9.05 km long segment of 31.5 km long HRT in Parbati hydroelectric project-II presently being excavated by TBM from Face-4. Balance length remaining for excavation is around 200 m. Major rock types encountered so far comprise of Granitic gneiss and Quartzite with bands of Chlorite schist. As tunnel entered into brittle and hard quartzite, incidences of frequent detachment of rockmass above cutter

head of TBM causing overbreak, high cutter consumption due to abrasive nature of quartzite, shear zone with ingress of silt laden groundwater and popping/spalling/rock bursting were experienced leading to major delay in TBM excavation causing both time and cost overrun as detailed in the following sections.

2.1   Frequent Detachment of Rockmass Above the Cutter Head of TBM

TBM used in HRT is a 6.8m diameter open shield TBM of Atlas Copco Jarva MK 27model as shown in Fig. 1(b). Due to lack of provision of any kind of rock support measures ahead of the cutterhead, intersection of opposite dipping major joint sets and their unfavourable orientation making an angle of 25º–40º with the tunnel axis cause wedge failure and sliding along the dip planes leading to the formation of cavity around the cutter head area as shown in Fig. 3(a) and 3(b). The failed blocks of rockmass accumulate and cause jamming of the cutter head. In one instance, a cavity of considerable dimension was created due to the failure of approximately 750 m^3 of muck equivalent to the excavation of 21 m length of tunnel.
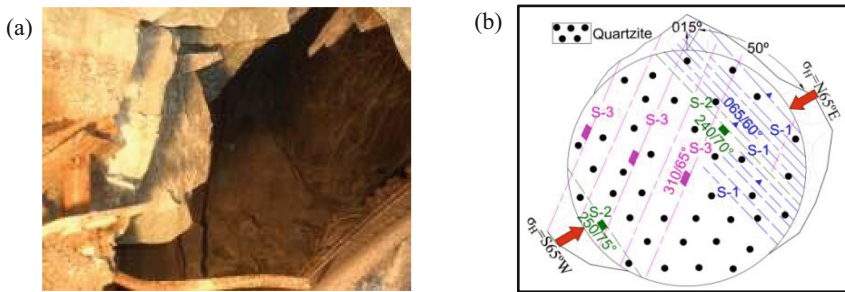
Fig. 3. (a) Cavity formation in the cutter head area of TBM **(b)** Sketch of Face log in quartzite showing orientation of major joint sets, major stress orientation and cavity profile

To overcome the problem of jamming of cutter head and formation of cavity above the cutter head due to sliding and wedge failure, McNally roof support system over the cutter head was developed in conjunction with steel plates/channels, wire mesh and rock anchors at suitable spacing as shown in Fig. 4(a) and 4(b). In the McNally system, a curved assembly of pockets with rectangular cross-sections extend axially from the rear side of the cutterhead through the cutterhead support in the area where roof drills could work as shown in Fig. 4(a).

2.2   Cutter Consumption

The hard rock tunnel boring is a form of crushing and chipping of rockmass with disc cutter applied against the rock surface with brute force (Dodeja et al., 2007). The factors involved in cutting the hard rock are mostly rock mass strength, elastic properties, abrasiveness, degree and type of discontinuities and insitu stress. Four types of cutters were used during excavation viz. CTS cutters, Robbins normal cutters, Robbins heavy duty

cutters and Palmieri cutters with the similar bore of 286 mm, thickness of 76 mm and outer dia of 17 in. Cutters of tip width of ½ inch and ¾ inch were used for less abrasive and jointed rock while 1 inch tip width was used for more abrasive rock.

A comparative analysis of the cutter consumption vis-à-vis rate of penetration during excavation of TBM in granite gneiss and quartzite is shown in Fig. 5(a). The average penetration rate in Granite Gneiss rock is 2.56 m/h which drastically reduces to 0.95 m/h in Quartzite. Further it could be seen in the TBM utilization chart in Fig. 2(b) that the cutter inspection and cutter change time was about 10.66% of total machine utilization time. The high rate of cutter consumption in quartzite is due to the high abrasivity of mineral components in quartzite as shown by Cerchar Abrasivity Index (CAI) value of 4.53 to 5.13 in comparison to granite gneiss (CAI value of 2.82 to 2.87).
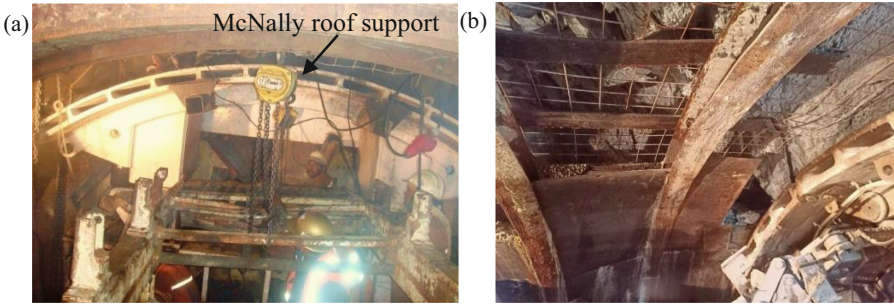
Fig. 4. **(a)** McNally roof support system **(b)** Erection of steel plates, channels and wiremesh
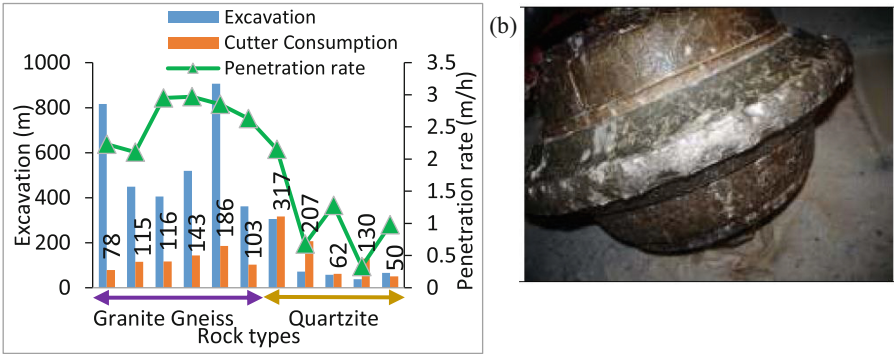
Fig. 5. **(a)** Comparison between cutter consumption and rate of penetration in Granite gneiss and quartzite **(b)** Wear of cutter due to high abrasivity in quartzite

2.3   Encounter of Shear Zone with Ingress of Groundwater

Due to the complex geology exhibited in the HRT area, a number of shear zones of varying thickness with ingress of groundwater were encountered during excavation.

Two major shear zones of length 20 m and 25 m with ingress of silt laden groundwater were encountered in HRT F-4 at RD $\pm$ 4057 m and RD $\pm$ 4124 m respectively which led to partial burying of TBM as shown in Fig. 2(a), 6(a) and (b).

Following ground treatments were carried out for the stabilization of the shear zones:

a) Prognostication of length and disposition of the shear zones ahead of the face were carried out by Tunnel Seismic Prediction (TSP) techniques, Seismic Tomography and probe holes through core drilling.
b) Ground consolidation for stabilization of rockmass around TBM and ahead of face at RD $\pm$ 4057 m were taken up by pre-grouting (Fig. 7a) and forepoling.
c) Consolidation work for shear zone treatment at RD $\pm$ 4124 m was carried out by excavating a 45 m long side tunnel at 17 m behind the face on the left side which is detailed in the following section.

Shear Zone Treatment at RD $\pm$ 4124 m. Initially shear/fractured zone of approx. 16 m length was anticipated by drilling two nos. Geognostic core holes of length 84.49 m and 59.18 m on both sides of main tunnel. Based on the assessment of length and orientation of the shear zone, excavation of side tunnel of 4 m dia was carried out parallel to main tunnel for a length of 45 m i.e. upto 26 m ahead of HRT face as shown in Fig. 7(b).

(a)   (b)
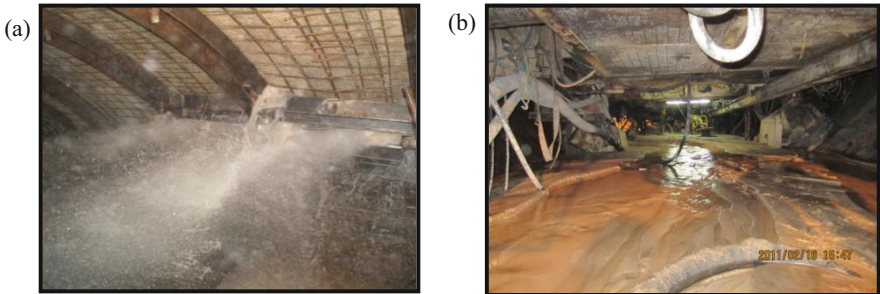
Fig. 6. Huge silt laden water ingress and burial of TBM at **(a)** RD 4057 m and **(b)** RD 4124 m

To facilitate drainage of ingress water and reduce hydraulic load, a niche of dimension 4 m $\times$ 5 m $\times$ 4 m was excavated on the right side of the main tunnel for drilling of eight no. 89 mm dia SIDRA drains (Fig. 7b). Chemical grouting was carried out from side tunnel towards main HRT in order to create a curtain/ impermeable barrier for the cement grout. Extensive consolidation grouting was then carried out with ordinary Portland and microfine cement through perforated PVC pipes from the side tunnel towards the main tunnel face to build a grout canopy and stabilize the shear zone as shown in Fig. 8(a). Geological plan of the anticipated shear zone based on probe drilling and TSP and encountered shear zone is shown in Fig. 8(b).

After stabilization of the shear zone, boring was carried out alongwith concurrent support erection of steel rib @ 0.4 and 0.8 m spacing with concrete backfill.
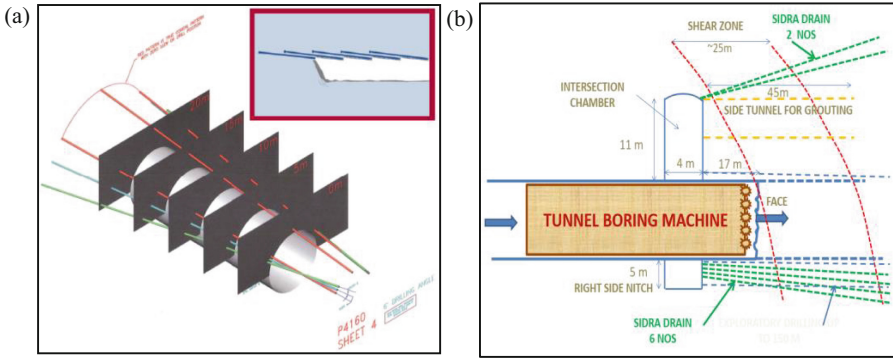
Fig. 7. (a) Grout canopy for shear zone treatment at RD ± 4057 m (b) indicative sketch of shear zone treatment carried out from side tunnel at RD ± 4124 m

2.4 Encounter of Popping/Spalling/Rock Bursting

As the tunnel passes under a high superincumbent cover of 750–1400 m through hard and brittle Manikaran quartzite, frequent stress related problems have been witnessed so far. Popping, spalling and rock bursting have been noticed in quartzite in both high (>1000 m) as well as relatively low cover zones (~750 m). The rock bursting was generally associated with sound and at places manifests failure of rock mass around the cutter head and shield area of TBM resulting into rockfalls in overt/crown portion as shown in Fig. 9(a). In many occasions it was observed that the rockmass appearing firm and massive at the time of excavation started showing popping and spalling after the face advanced for 10 to 15 m. As the pressure is applied by gripper pads on tunnel wall for holding the TBM in float mode during excavation and again released for realigning at a forward location for successive strokes, stresses get redistributed. In such cases, detachment of rock blocks and release of wedge mostly take place from the gripper area/spring line area as shown in Fig. 9(b). Guide/stress relief holes were drilled at regular interval to reduce the effect of rock bursting by transferring the peak stress deep into the surrounding rock, thereby dissipating accumulated elastic strain energy in advance (Chen et al., 2011). Dissipation of elastic energy increase plastic area which provides displacement space for deformation of rockmass preventing sudden failure. On the basis of rock bursting events already experienced in quartzite in HRT F-4, back analysis of magnitude of in-situ stresses in rock bursting zones was carried out using finite element modelling (Phase 2.0, ver. 8.0) to determine the role of strength, elastic properties of the rockmass and field stress ratio in causing rock bursting. Stress and deformation values at two different stress ratios corresponding to overburden cover of 800 m and 1400 m was determined using numerical method.

In-situ vertical stress σ_V was calculated from the equation

$$\sigma_V = \gamma.Z \tag{1}$$

where γ = density of the rock, Z = superincumbent cover above the tunnel section.
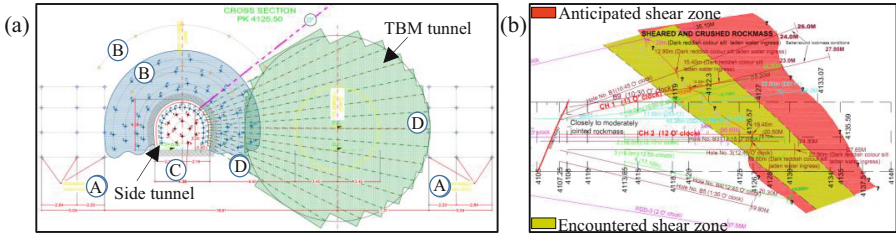
Fig. 8. (a) Cross section of side and main tunnel at RD ± 4124 m showing injection grouting pattern; A-Drainage hole, B-Contour grouting in side tunnel, C-Face injection from side tunnel, D-Contour and Face injection from side tunnel towards TBM tunnel (b) Geological plan at RD ± 4124 m showing anticipated and encountered shear zone
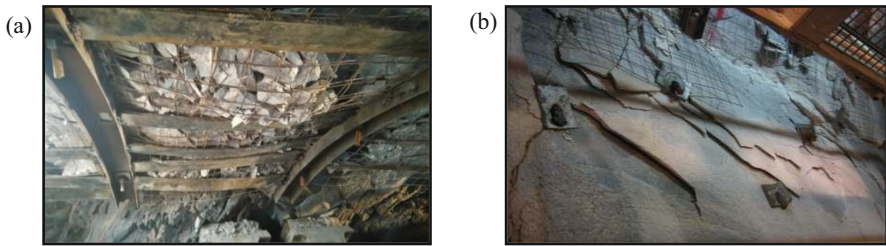
Fig. 9. (a) Rock bursting observed at crown (b) Spalling in the springline area in quartzite

In-situ horizontal stress σ_H was calculated from Hoek and Brown (1980) equation:

$$K_0 = 0.4 + \frac{800}{Z} \tag{2}$$

where K_0 is the field stress ratio defined by the equation

$$K_0 = \frac{\sigma_H}{\sigma_V} \tag{3}$$

In this study, the rockmass inside the tunnel has been considered homogeneous, perfectly plastic material subjected to uniform near field stresses. Generalized Hoek and Brown failure criterion was adopted for calculation of deformation parameters. Geotechnical parameters of the rockmass considered for study is shown in Table 1.

From Fig. 10, it can be interpreted that with decrease in field stress ratio, K_0 or with increase in in-situ stresses, σ_H and σ_V due to increase in depth of overburden, the values of principal stress, σ_1 and deformation, ε increase leading to the decrease in strength factor, S_f (<1.5) in both the crown and springline area of the tunnel. The yielding due to shear also concentrates more at lower field stress ($K_0 = 0.97$) in both crown and SPL while the yielding due to tension concentrates more in the area of intersection of the strike of the major joints with the tunnel axis (Fig. 10a, b). The magnitude of the principal stress, σ_1 also increases upto 1.5 times after excavation as determined from the numerical modelling and shown in Fig. 11. Based on World Stress Map (2016), in-situ horizontal stress, σ_H is aligned at N065°E near the study area. HRT Face-4 is aligned

Table 1. Geomechanical parameters of rockmass considered for the study

Rock type	Geomechanical parameters of rockmass									Stresses		
	Z (M)	GSI	UCS (MPa)	γ (MN/m³)	mi	Φ (°)	C (MPa)	ν	Ei (GPa)	K_0	σ_V	σ_H
Quartzite	800	70	150	0.027	20	48.5	30	0.2	60	1.4	22	30
	1400	70	150	0.027	20	48.5	30	0.2	60	0.97	38	37

in the direction of N15ºE and thus σ_H is oriented at an angle of 50º to HRT direction as shown in Fig. 3(b). Dip direction of the major discontinuity sets (045º–065º/55º–65º) in quartzite are also oriented almost parallel to the direction of σH (N065ºE) (Fig. 3b).

The above analysis indicates that the tunnel alignment and orientation of the major discontinuity sets w.r.t direction of in-situ stresses together with the increase in magnitude of the principal stresses after excavation are the major governing factors causing popping/spalling and rock bursting in hard and brittle quartzite which were experienced in the study area and as shown by the numerical model.
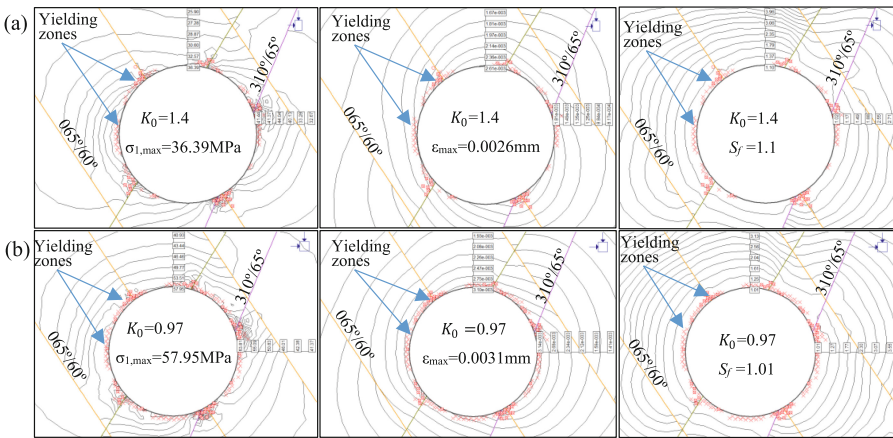
Fig. 10. Stress contours showing Principal stress (σ_1), displacement (ε) and strength factor (S_f) values at crown for two different stress ratios **(a)** $K_0 = 1.4$, **(b)** $K_0 = 0.97$ in study area

2.5 Evaluation of Performance of TBM Using QTBM

The QTBM method proposed by Barton (2000) is based on an expanded Q-system of rock mass classification, in which the average cutter force, abrasive nature of the rock, and rock stress level is accounted for (Goel, 2008). The new parameter QTBM is a function of 16 basic parameters given below.

$$Q_{TBM} = \frac{RQD_0}{J_n} \times \frac{J_r}{J_a} \times \frac{J_w}{SRF} \times \frac{\sigma_{cm}\,or\,\sigma_{tm}}{F^{10}/20^9} \times \frac{20}{CLI} \times \frac{q}{20} \times \frac{\sigma_\theta}{5} \qquad (4)$$
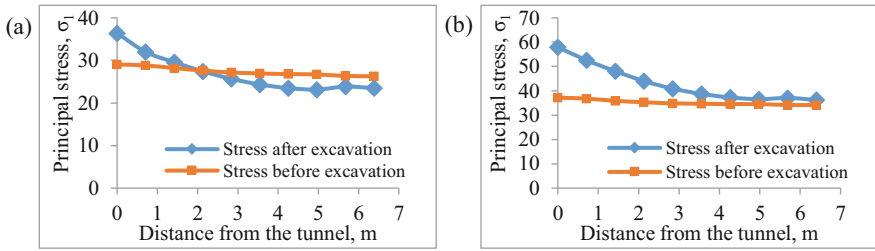
Fig. 11. Behaviour of principal stress, σ_1 away from the tunnel section at crown before and after excavation at **(a)** $K_0 = 1.4$ and **(b)** $K_0 = 0.97$

where RQD_0 is the conventional RQD interpreted in the tunneling direction; J_n, J_r, J_a, J_w and SRF are unchanged from conventional Q; σ_{cm} and σ_{tm} are the rock mass strength for unfavourable and favourable joint orientation respectively; F is the average cutter load (tnf); CLI is the cutter life index; q is the quartz content (in percentage); σ_θ is the average biaxial stress on tunnel face (in MPa).

From the analysis of numerous projects (145 cases), Barton derived a relationship between penetration rate and Q_{TBM} given as:

$$PR = 5(Q_{TBM})^{-0.2} \tag{5}$$

which predicts a power increase of penetration with decreasing of Q_{TBM}.

From Table 2 and Fig. 12(a) and (b), it is definite that in Q_{TBM} classification, rock quality depends not only on the strength and discontinuity characteristics of the rockmass but also on the machine parameters like Average cutter load (F) and Cutter Life Index (CLI) under stress induced conditions. Average cutter load increases due to increase in machine thrust leading to decrease in Q_{TBM} value as experienced in quartzite. Based on the experience of tunneling in three different rock masses in HRT Face-4, a comparative chart of TBM performance in these rock types under high stress conditions is prepared and shown in Fig. 12(a). Figure 12(a) shows that tunneling becomes tough in quartzite due to high cutter consumption and very low penetration rate (av. PR ~ 0.95 m/h) which drastically increase the boring time of TBM. In comparison, fair to good TBM performance has been witnessed in chlorite schist and granite gneiss rockmass respectively due to low cutter consumption and higher penetration rate which reduced boring time and increased progress rate. Per cutter boring rate in granite gneiss encountered for a length of 3480 m was 4.85 m which drastically reduced to 0.88 m during excavation in quartzite. Average thrust value of TBM increased from 4000 kN in chlorite schist and 8000 kN in granite gneiss to almost 10000 kN in quartzite. All these factors reduced the performance of TBM in quartzite encountered in HRT F-4.

Comparative analysis between average penetration rate and Q_{TBM} value shown in Fig. 12(a) indicates that penetration rate increases with increase in Q_{TBM} values. Increase of PR shows an exponential and logarithmic relationship with Q_{TBM} and Q respectively as shown in Fig. 12(b). Rock bursting and machine parameters are mainly responsible for low Q_{TBM} values in quartzite in comparison to chlorite schist and granite gneiss. Q_{TBM} values in the range of 30–300 in quartzite was most problematic during tunneling which experienced rock bursting, high cutter consumption, overbreak and problem of

Table 2. Estimation of Q_{TBM} in the study area

Parameter	Granite Gneiss	Chlorite schist	Quartzite
RQD_0	70	30	60
J_n	12	15	15
J_r	3	1	1
J_a	1	2	1
J_w	0.66	0.66	0.66
SRF	5	5	15
$Q=(RQD/J_n)(J_r/J_a)(J_w/SRF)$	2.31	0.132	0.176
σ_c (av.) (MPa)	90	25	115
γ (g/cc)	2.6	2.3	2.6
$\sigma_{cm}(MPa) = 5\gamma(Q.\sigma_c/100)^{1/3}$	16.55	3.73	7.63
F (tnf)	15	7.69	17
CLI	17	70	4
q(%)	40	15	93.5
$\sigma_\theta(MPa) = 2\gamma(MN/m^3) * rock\ cover\ in\ m$	52	46	52
Q_{TBM}	830.63	685.12	82.91
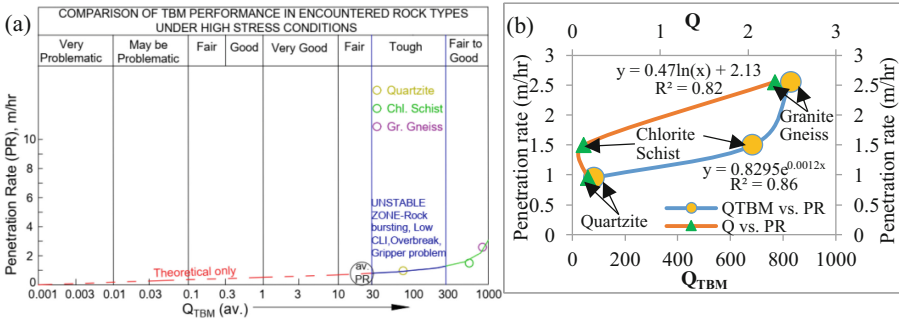
Fig. 12. (a) Comparison of TBM performance in encountered rock types under high stress conditions (modified after Barton, 1999) **(b)** Empirical relation between penetration rate & Q_{TBM}

resting of gripper pad due to slabbing of rockmass in springline area of the tunnel. Based on the TBM performance experienced in the three different rock types under high stress conditions, an empirical relation between penetration rate (PR) and Q_{TBM} is developed in high stress conditions as shown in Fig. 12(b) and given below:

$$PR = 0.83e^{0.001Q_{TBM}}, R^2 = 0.86 \tag{6}$$

3 Conclusions

The main conclusions drawn from the paper are as follows:

a) Modification in TBM was done by introducing McNally support system to overcome kinematically induced failure and cavity formation in the cutterhead region.

b) High abrasivity of quartzite greatly reduced the rate of advancement of TBM due to high cutter consumption and low penetration rate.

c) Two major shear zones with heavy groundwater ingress encountered in quartzites at RD $\pm$ 4059 m and RD $\pm$ 4124 m of HRT F-4 were successfully negotiated by adopting extensive geological and geophysical prognostication measures and ground consolidation measures such as pre-grouting, long drainage holes, excavation of side tunnels and chemical and consolidation grouting of main tunnel from the side tunnel.

d) Frequent incidences of rock bursting were encountered in hard and brittle quartzite due to readjustment of principal stresses with excavation. Stress analysis shows that both yielding and deformation increase with decrease in field stress ratio. Drilling of stress relief holes, installation of McNally plates with wiremesh and steel plates/channels tied with the rock wall through rock anchors at crown and springline area were the remedial measures adopted to tackle rock bursting.

e) Performance of TBM in terms of QTBM and penetration rate shows that PR increases with increase in QTBM values under high stress conditions leading to slight deviation from Barton (1999) Eq. (5). An empirical relation between Penetration rate and QTBM in the study area shows exponential increase of PR with QTBM.

f) Overall, the paper outlined the major geotechnical problems encountered during construction of the longest HRT in hydropower projects in Himalaya through TBM and remedial measures adopted to successfully negotiate the problems. Inspite of the adverse geological conditions, around 7.5 km of tunneling has been excavated till now through TBM with maximum boring of 539 m in a month in granite gneiss. The experience of TBM tunneling in the study area which is well documented for reference and information can be used as an impetus for future study.

References

Barton, N.: TBM performance estimation in rock using Q$_{TBM}$, pp. 41–48. Tunnels and Tunnelling International, Milan (1999)

Barton, N.: TBM Tunnelling in Jointed and Faulted Rocks, p. 173. A.A. Balkema (2000)

Dodeja, S.K., Mishra, A.K., Virmani, R.G.: Performance of tunnel boring machine in manikaran quartzite with special reference to construction of HRT at Parbati H.E. Project, Stage-II, NHPC, Distt- Kullu, H.P. India, Water and Energy Abstracts, pp. 1–14 (2007)

Chen, G., Su, G., Li, T.: Prevention logic of rock burst for brittle rock under high geo-stress. Adv. Mater. Res. **261–263**, 1484–1488 (2011)

Goel, R.K.: Evaluation of TBM performance in a Himalayan tunnel. In: World Tunnel Congress-Underground Facilities for Better Environment and Safety– India, pp. 1522–1532 (2008)

Hoek, E., Brown, E.T.: Underground Excavations in Rock. The Institute of Mining and Metallurgy, London (1980)

Effect of Column-to-Beam Strength Ratio Distribution on the Seismic Behavior of Reinforced Concrete Frame Structures

Fırat Sondilek[1]([✉]) [ID], Egemen Sönmez[2] [ID], and Ali Şahin Taşlıgedik[3] [ID]

[1] Sustainable Environment and Energy Systems, Middle East Technical University Northern Cyprus Campus, Güzelyurt, North Cyprus, Turkey
sondilek.firat@metu.edu.tr

[2] Civil Engineering Department, İzmir University of Economics, İzmir, Turkey
egemen.sonmez@ieu.edu.tr

[3] Civil Engineering Program, Middle East Technical University Northern Cyprus Campus, Güzelyurt, North Cyprus, Turkey
sahintas@metu.edu.tr

Abstract. Seismic design codes are the standards that provide resistance for the structures against the potential seismic forces that the structure may face. One of the provisions in the seismic design codes is the strong column-weak beam (SCWB) requirement. It suggests that at that the sum of the flexural strength of the columns at a joint should be greater than those of the beams at the same joint. This requirement aims to prevent column yielding during an earthquake and avoid story mechanisms in moment frames. Although the seismic design codes suggest a minimum column-to-beam strength ratio, previous research has shown that this ratio may not be sufficient to provide desired collapse mechanisms for all conditions. Also, it has been observed that the column-to-beam strength ratio distribution along the height of the frame structures affects the understory and damage distribution. This study investigated the effect of different column-to-beam strength ratio distributions on the drift distribution of the reinforced concrete moment frames. For this purpose, different frames were considered with different numbers of stories and bays. OpenSeesPy framework was used for numerical modeling. To evaluate the seismic response of the model frames, nonlinear time history, and nonlinear static analyses were used. The results showed that the column-to-beam strength ratio distribution significantly affects the distribution of inter-story drift ratios. An effective column-to-beam strength ratio distribution was proposed at the end of the study.

Keywords: Seismic design · Strong column-weak beam · Drift distribution

1 Introduction

The 1908 Messina earthquake brought attention to the significance of seismic design in improving the performance of structures during earthquakes. Further research has deepened the understanding of how structures behave under seismic actions and has provided

valuable design approaches to enhance their earthquake resistance. This knowledge is vital for professionals as they try to achieve to construct resilient and safe structures in earthquake-prone areas. The capacity design method, one of these approaches, has been integrated into seismic design codes since 1968 [1]. During seismic events, structural elements undergo elastic and plastic deformations. Plastic deformations in the members of the frame structures tend to concentrate at specific locations known as plastic hinge zones. To mitigate this concentration, a design concept should be followed, which aims to distribute the occurrence of plastic hinge locations throughout the structure instead of localizing them in a specific story.

To comprehensively comprehend the seismic response, the inter-story drift ratio (IDR) serves as a practical and effective indicator. IDR quantifies the relative horizontal displacement between consecutive floors during an earthquake, providing valuable insights into the distribution of lateral deformations and structural damage within the structure. Hence, analyzing the IDR behavior of structures proves to be an effective tool for understanding their response to seismic activity.

The design concept commonly known as the strong column-weak beam design approach is widely acknowledged in seismic design codes. It entails reinforcing columns to be significantly stronger than the beams they support. This design philosophy aims to enhance the seismic resistance of a structure by promoting ductile behavior during earthquakes, as the stronger columns are better equipped to withstand lateral forces, while the weaker beams can undergo controlled deformation. By prioritizing strength in the columns and allowing controlled flexure in the beams, the strong column-weak beam design concept helps prevent sudden failure and promotes the redistribution of plastic deformations, thereby improving the overall structural integrity during seismic events. While TBDY-2018 and ACI 318 [4] suggest that the ratio of the sum of the columns' flexural strength and beams' flexural strength should be at least 1.2, Eurocode-8 [5] suggested that the ratio is 1.3.

However, recent studies have highlighted that the suggested minimum ratio of flexural strengths may not be sufficient for column yielding in all scenarios. Therefore, further investigation and clarification of the design requirements could be investigated to ensure the prevention column yielding.

Ghorbanzadeh et al. [3] conducted a study to investigate the collapse probabilities of buildings with varying column-to-beam strength ratios (CBSRs) ranging from 1.2 to 3.0 in 4-, 8-, and 12-story structures. In their research, a constant CBSR was employed uniformly in elevation throughout each model. The findings revealed that severe damage occurred when column yielding took place, particularly on the lower floors. The analysis results indicated that the suggested minimum CBSR values of 1.2 (ACI 318) or 1.5 (Indian Seismic Code) [6] specified by regulations were insufficient in all cases.

Another study conducted by Surana et al. [7] investigated the effects of CBSRs on the collapse mechanism in low- and mid-rise reinforced concrete moment frames were examined. In the conducted research, four different structures have been examined. Two of them are four-story buildings, while the other two are eight-story buildings. The research focused on the Indian seismic design code and considered two highly seismic zones. Two designs were evaluated, one adhering to the strong column-weak beam design concept and the other not meeting this criterion. The analysis results demonstrated that

column yielding occurred when a collapse mechanism was observed. However, the design employing a 1.4 CBSR was effective in changing the collapse mechanism from column failure to beam failure for all cases. This transition into failure mode enhanced the ductility and collapse capacity of the structures. The authors suggested that increasing the CBSR may be sufficient to prevent collapse and proposed investigating a variable distribution of CBSR throughout the elevation, in addition to a constant ratio.

Considering relevant studies, the column-to-beam strength ratios (CBSRs) emerge as a significant parameter for controlling the location and distribution of plastic deformations in moment-frame structures. Although seismic design codes propose minimum ratios for CBSRs, they may not be adequate in all cases. Hence, comprehensive investigations are necessary to explore the effects of different CBSRs on seismic performance. This study aims to examine various distributions of CBSRs in elevation to understand their effect on the seismic behavior of structures. The assessment of structural performance will consider the IDR and damage indices. Notably, unlike previous studies, this research will consider varying CBSRs throughout the height of the structures.

2   Methodology

2.1   Buildings Under Investigation

A planar 10-story moment-frame building was selected as a model structure for this study. This planar model frame was assumed to be extracted from an interior axis of a three-dimensional building. Loads originating from the beams, slabs, and infill walls in the transverse direction were evaluated and incorporated into the planar model using the tributary area approach. The model frame is designed with a bay length of 5 m and a story height of 3 m, with four bays.

In this study, C30 concrete and S420 steel were used. The column dimensions were set to 60 cm × 60 cm, while the beam dimensions were defined as 60 cm × 30 cm.

During the determination of loads on the model frame, the regulations of TBDY-2018 [2], TS498 [8], and TS500 [9] were followed. The model also considered the presence of walls for all bays, with the wall height at the roof level assumed to be 0.8 m. Slabs of 12 cm thickness were assumed on all floors.

Nine differently detailed models of the same frame were examined for the study. An initial model following the minimum requirements of TBDY-2018 and TS500 was designed first. This model is referred to as "CodeBased" in the text. Subsequently, a design called "TriangularCBSR" was developed, featuring a linearly decreasing CBSR distribution towards the roof. Another design involved a model with a CBSR of approximately 1.8 throughout the structure, referred to as the "1.8CBSR" model. Similarly, a model was created with a CBSR of 2.2 throughout the structure, named the "2.2CBSR" model. Additionally, a model that resulted in a balanced distribution of inter-story drift ratios (IDR) was designed based on the analysis results and named the "BalancedIDR" model.

Apart from these, two sets of frames were designed to achieve the target CBSRs. One of them shows a different column reinforcement ratio to achieve those desired values, while beam reinforcement ratios are kept constant. In the other model, desired

CBSR values were achieved by changing the beams' reinforcements while keeping the columns' reinforcement constant.

The target CBSR at a joint can be obtained by modifying the column strengths and/or the beam strengths. To investigate the effect of these modifications, the target CBSR distributions in the TriangularCBSR, 1.8CBSR, 2.2CBSR, and BalancedCBSR were obtained in two ways: (i) by keeping the beam reinforcement ratios constant and modifying the column reinforcement ratios, (ii) by keeping the column reinforcement rations constant and modifying the beam reinforcement ratios. As a result, four pairs of models were obtained. The models in which the column reinforcement ratios were kept constant were named with the suffix "C", and those in which the beam reinforcement ratio was kept constant were named with the suffix "B". The CBSR distribution of the models can be seen in Fig. 1. One notable aspect of the graph is the difference in values among the TriangularCBSR models. When columns are kept fixed, and beam capacities are reduced, the obtained CBSR values are lower compared to the model where beams are fixed and columns are changed. This is because the change in column capacities is greater than that of beams, thus affecting the values to a greater extent. Another noteworthy observation is the values of the CodeBased model. As shown in the graph, starting at 4.4, the CBSR value decreases gradually due to the decreasing capacity of columns in the upper floors where there are no changes in material geometry, eventually reaching a value of 1.3.
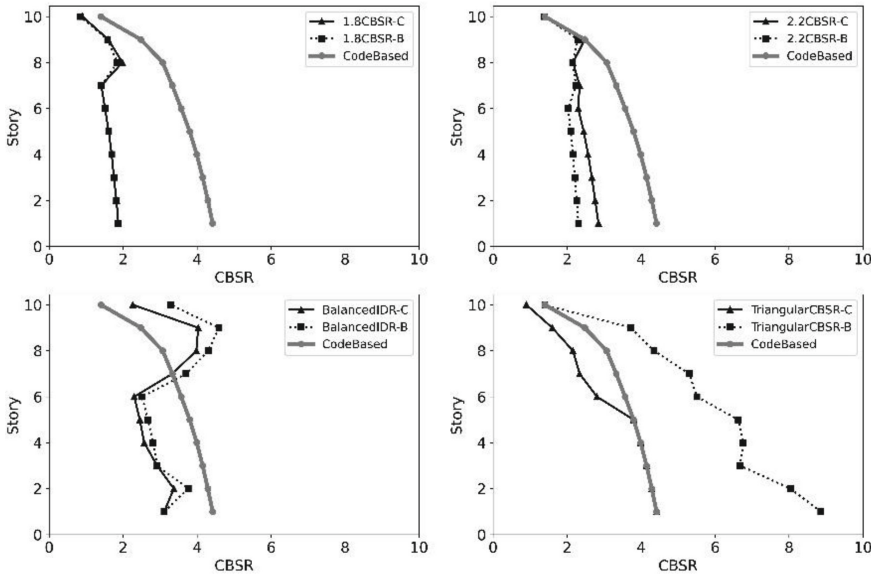
Fig. 1. CBSR for all models

2.2 Numerical Modeling

The numerical modeling of the models was performed using the OpenSeesPy [10] framework. The preliminary designs of the models were evaluated using the CSI SAP2000 [11] software.

To capture the behavior of plastic hinges, a lumped plasticity model was employed in this study. OpenSeesPy provides a convenient implementation of this model, enabling to define and analyze plastic hinges accurately. Material models are employed to describe the mechanical properties and behavior of different construction materials. In this study, two primary material models were utilized: Concrete01 and Steel02, which are available in OpenSeesPy.

The Concrete01 model was chosen to represent the concrete material, which is used to construct a uniaxial Kent-Scott-Park [12] concrete material without ignoring the tensile strength. This model accounts for both confined and unconfined concrete behavior, which is essential in capturing the response of structural elements under different loading conditions.

For the steel material, the Steel02 model was employed, which is used to construct a uniaxial Giuffre-Menegotto-Pinto [13] steel material object. This model accounts for the strain hardening and strain rate effects, providing a comprehensive representation of the steel material behavior.

Slabs were incorporated into the gravity system and modeled as rigid diaphragms. Using the OpenSeesPy framework, employing the equalDOF command.

To accurately capture the behavior of columns, fiber section models were employed at the element ends. These models divide the cross-section of the column into numerous fibers and consider their individual contributions to the overall structural response by using fiber section modeling.

In the analysis of beams, the combination of a rigid diaphragm assumption with fiber-reinforced sections has been observed to result in the generation of artificial axial loads within the beams. To overcome this challenge, an alternative approach utilizing a "hysteretic" model is proposed. By replacing fiber-reinforced sections with the "hysteretic" model, the occurrence of these undesired axial loads can be effectively prevented.

2.3 Nonlinear Dynamic Analyses

In this study, each model was subjected to nonlinear dynamic analysis in order to assess their seismic performances. While implementing the dynamic analyses, the TBDY-2018 [2] regulation was followed. According to regulation, a minimum of 11 ground motion records should be employed for modeling, and when selecting the ground motions, a maximum of three different records could be utilized for the same earthquake. For this research, only maximum of two different records were used for the same earthquake to ensure the limitation of regulation. The mean spectrum of the selected and scaled ground motion records should not fall below the design spectrum for a specified period range ($0.5T$ to $1.5T$ where T is the fundamental period of the structure considered). The design spectrum in TBDY-2018 varies based on the earthquake level, soil type, and geographical location of the building. In this study, the DD-2 spectrum of TBDY-2018 was chosen which represents an infrequent earthquake ground motion with a 10% probability of

exceedance in 50 years which corresponds to a recurrence period of 475 years (i.e., design-basis earthquake). For the soil class, the ZD soil class, which refers to shear wave velocity as 180 to 360 m/s, representing dense sand, gravel, or soft-solid clay layers, was selected. The investigation location selected as Izmir, Türkiye. Considering these choices, 12 earthquake records that satisfy the specified criteria were selected from the PEER NGA-West2 Strong Motion Database [14]. The following limitations were considered during the selection of earthquake records:

- Magnitude (M_w): 5.5–8.5,
- Fault type: Strike-slip,
- Distance to rupture surface (R_{rup}): >15 km,
- Shear wave velocity (V_{s30}): 180–360 m/s,
- Duration: >10 s.

To ensure that the selected ground motion records remain above the design spectrum for a specific period range, an amplitude scaling method was employed. However, to prevent unrealistic acceleration values, the scaling factors were limited to a range of 0.5 to 3.0. Scaled ground motions shown in Fig. 2. The uniform thick line represents the target spectrum where the ununiform thick line represents the design spectrum.
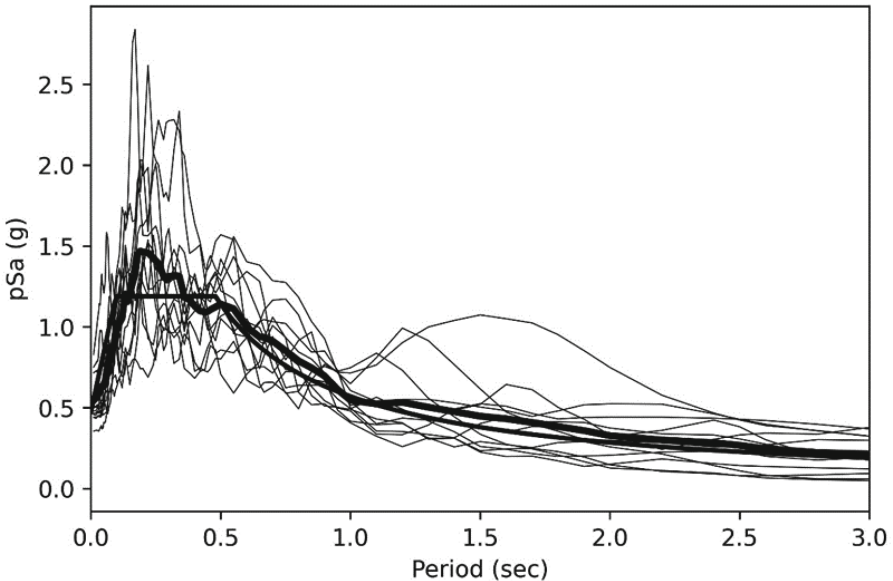
Fig. 2. Linear acceleration response spectra of the scaled ground motion records

3   Results and Discussion

3.1   Results

Following the completion of nonlinear dynamic analyses, the mean IDR and damage index values were determined for all the models under investigation. The mean IDR distributions of the models are presented in Fig. 3. In almost all designs, the IDR concentrates around the lower parts of the frames. The CodeBased frame has the highest IDR amongst all designs (2.4%), except the TriangularCBSR-C. Also, the overall drift is the highest for the CodeBased frame. The BalancedIDR yields the best result among all, having a well-distributed IDR profile between 1.5% and 2.0%.
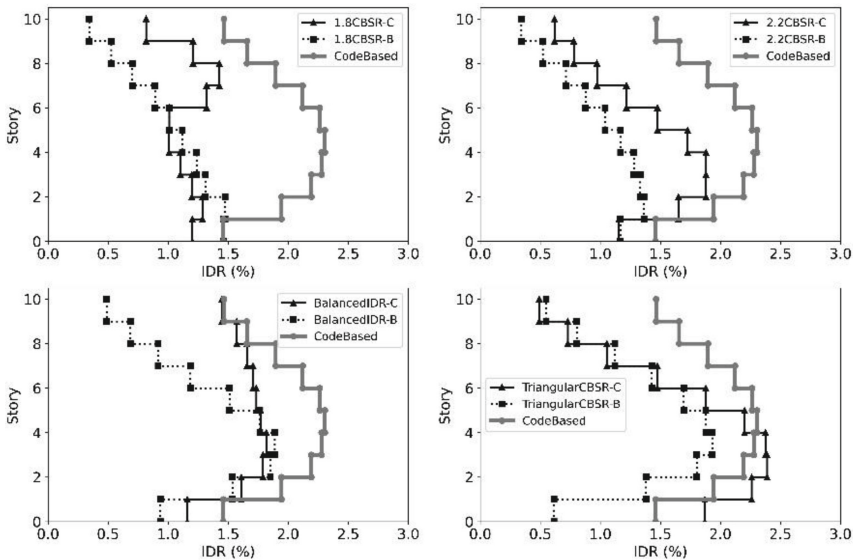
Fig. 3. IDR for all models

The mean damage index values of the models are illustrated in Fig. 4, revealing similar remarks with the IDR results. Notably, except for the TriangularCBSR-B model, the highest damage index value is observed on the first floor. This observation indicates a concentration of structural damage at the lower levels of the building, as indicated by the damage index analysis. The mean overall damage index values for all models are shown in Table 1. The TriangularCBSR and the BalancedIDR models have relatively lower overall damage, but the damage is distributed better in the BalancedIDR-C design.

Table 1. Overall damage index values for all models

Model	Overall Damage Index
CodeBased	0.23
1.8CBSR-C	0.24
1.8CBSR-B	0.28
2.2CBSR-C	0.2
2.2CBSR-B	0.25
TriangularCBSR-C	0.12
TriangularCBSR-B	0.165
BalancedIDR-C	0.18
BalancedIDR-B	0.14
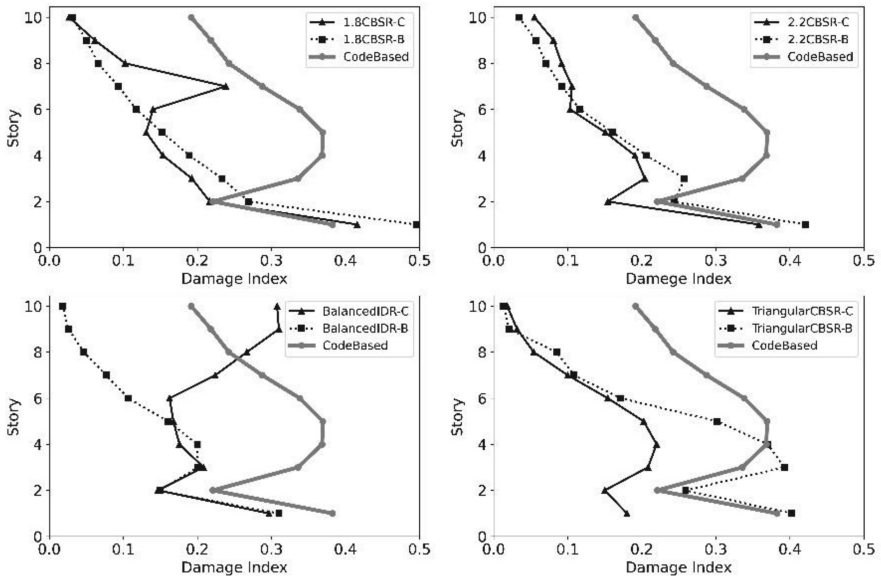
Fig. 4. Damage index values for all models

3.2 Discussion

Among the nine models analyzed in total, the first noteworthy result is the seismic performance demonstrated by the CodeBased model, which meets the minimum requirements specified by TBDY-2018. This result can be considered sufficient. According to the analysis, the first floor shows the highest damage index value of 0.37, indicating repairable damage [15]. When compared with the IDR graph, the model's damage index distribution is similar. Both show an increase up to a certain floor and then a decrease towards the roof level, denoting a damage concentration at the lower half.

Upon evaluating the results of the TriangularCBSR model, it can be observed that both the IDR distribution and the damage index distribution are similar to the CBSR distribution (Fig. 1). Although no collapse mechanism is observed based on the damage index values at any floor, it is evident that the damage demand is concentrated on the lower floors as the damage is not distributed along the structure. Another notable aspect of these models is that while the structural behavior remains unchanged, the IDR and damage index values differ based on column and beam reinforcement. As indicated by the analysis results, when there are changes in column reinforcement, the structure's damage index values increase. However, changes in beam reinforcement result in lower damage index values. Therefore, it can be inferred that for this study, an increase in beam capacity has a more significant impact on damage compared to an increase in column capacity.

When examining the results of the models with a constant CBSR along the structure, except for the 1.8CBSR-C model, similar IDR, and damage index distributions were observed in all models. While the CBSR distribution remains consistent along the structure, the IDR and damage index distributions exhibit an increasing trend toward the bottom of the frames. As expected, this indicates that there are columns and beams with the same capacity ratios throughout the average building height, while the expected damage and axial load demand vary along the structure. The damage incurred by structures with the same capacity shows a decreasing trend along the building height. Among these models, the highest damage index value was observed, particularly on the first floor of the 1.8CBSR-B model, as 0.48. Furthermore, changing the reinforcement of columns and beams in these models led to the same results as the TriangularCBSR models.

As a result of the obtained findings, a model (BalancedIDR) has been designed that ensures a balanced IDR distribution throughout the building height. The goal of this model is to achieve well-distributed damage along the building height. Therefore, based on the results of the BalancedIDR models, the desired behavior is achieved only in the model where the column reinforcements are kept constant. This can be attributed to the situation discussed when interpreting the results of the TriangularCBSR models. Instead of a decreasing damage index distribution towards the roof level, which is observed in all models, a distribution is obtained where the damage index decreases until the middle floors and then increases. The BalancedIDR-C model was designed while ensuring compliance with the beam reinforcement limits specified by TBDY-2018, even though they fell below the limits set by TS500. These beams were used on the last two floors, and the increase in damage index observed on these floors can be attributed to this factor. However, overall, when considering the entire structure, the obtained damage index values are within an acceptable range along the building height. In addition to the other models, the lowest damage index value per floor is observed on the ninth floor, which is the lowest value among the nine models, with a value of 0.32. This indicates that with the attainment of a uniform IDR distribution along the building height, the damage is distributed throughout the structure instead of being concentrated on a particular portion, leading to improved seismic performance. According to the obtained results, the BalancedIDR-B model, which maintains similar CBSR ratios as the other models, exhibits similar behavior in both IDR and damage index distributions. The damage index

value of 0.34 obtained on the first floor indicates that the expected damage is concentrated on the first floor, as observed throughout the building height.

4   Conclusion

The key findings obtained are as follows:

- The minimum standards specified by regulations do not lead to the collapse of the structure; however, as evident from the IDR distribution, the damage concentrates in certain floors, rendering it inefficient. Nevertheless, the CBSR values are still higher than the minimum 1.2 set by the regulations.
- Structures with constant CBSR distributions throughout the building exhibited better seismic performance in terms of IDR and damage index compared to the code-based design.
- Triangular CBSR distribution resulted in weaker lower floors compared to upper floors, leading to concentrated damage in the lower floors and minimal damage in the upper floors.
- The CBSR distribution leading to a balanced IDR distribution yielded the best seismic performance as expected.
- Based on the results obtained from varying the column and beam reinforcement to change the CBSR ratio, it can be concluded that modifying the beam strengths has a greater influence on the seismic performance than modifying the column strengths. This can be attributed to a higher occurrence of plastic deformation in beams.

In conclusion, it is evident that different CBSR distributions play a significant role in the seismic performance of structures. However, it should be noted that the ratios specified in seismic design codes may not always be sufficient to achieve optimal performance. Furthermore, it is understood that achieving a uniform IDR distribution through an appropriate CBSR distribution helps enhance the seismic. The findings emphasize the need for careful consideration of CBSR distribution and appropriate detailing strategies to ensure adequate seismic performance and mitigate potential structural vulnerabilities.

References

1. Fardis, M.N.: Capacity design: early history. Earthq. Eng. Struct. Dyn. **47**, 2887–2896 (2018). https://doi.org/10.1002/eqe.3110
2. TBDY-2018. Turkish Earthquake Code for Building Structures: Specifications for Design of Buildings under Earthquake Forces; Presidency of Disaster and Emergency Management (2018)
3. Ghorbanzadeh, M., Khoshnoudian, F.: The effect of strong column-weak beam ratio on the collapse behaviour of reinforced concrete moment frames subjected to near-field earthquakes. J. Earthq. Eng. **26**, 4030–4053 (2022). https://doi.org/10.1080/13632469.2020.1822228
4. Building Code Requirements for Structural Concrete : (ACI 318-95) ; and Commentary (ACI 318R-95). American Concrete Institute, Farmington Hills (1995)
5. Eurocode 8: design provisions for earthquake resistance of structures. Author: British Standards Institution. Print Book, English (1996)

6. IS 13920 Ductile detailing of reinforced concrete structures subjected to seismic forces—code of practice. Bureau of Indian Standards, New Delhi (1993)
7. Surana, M., Singh, Y., Lang, D.H.: Effect of strong-column weak-beam design provision on the seismic fragility of RC frame buildings. Int. J. Adv. Struct. Eng. **10**, 131–141 (2018). https://doi.org/10.1007/s40091-018-0187-z
8. Turkish Standard Institute. Turkish Standard, TS498: The Calculation Values of Loads used in Designing Structural Elements. Ankara, Turkey, 21 p.(1997)
9. TS 500 Requirements for design and construction of reinforced concrete structures (2000)
10. McKenna, F.: OpenSees: a framework for earthquake engineering simulation. Comput. Sci. Eng. **13**(4), 58–66 (2011). https://doi.org/10.1109/mcse
11. CSI. SAP2000 Integrated Software for Structural Analysis and Design. Computers and Structures Inc., Berkeley, California
12. Kent, D.C., Park, R.: Flexural members with confined concrete. J. Struct. Div. (1971)
13. Fllippou, F.E., Popov, E.P., Bertero, V.V.: Effects of bond deterioration on hysteretic behavior of reinforced concrete joints by national technical informalion service (1983)
14. Ancheta, T.D., et al.: PEER NGA-West2 database; PEER report 2013/03, Pacific Earthquake Research Center: University of California, Berkeley, CA (20130
15. Kunnath, S.K., Reinhorn, A.M., Lobo, R.F.: IDARC version 3.0: inelastic damage analysis of reinforced concrete structures (1992)
16. Park, Y.J.; Ang, A.H.-S.: Mechanistic seismic damage model for reinforced concrete. J. Struct. Eng. (U.S.) **111**(4), 722–739 (1985)

Seismic Behaviour of Corrosion Damaged Reinforced Concrete Columns Under Combined Loadings

Elif Nazlı Akbas[✉] [iD], Serhan Sensoy [iD], and Ozgur Eren [iD]

Civil Engineering Department, Eastern Mediterranean University, Famagusta, Northern Cyprus, Türkiye

`{elif.akbas,serhan.sensoy,ozgur.eren}@emu.edu.tr`

Abstract. The corrosion of reinforcement is a major concern for the structural integrity and durability of reinforced concrete (RC) structures. In order to investigate the effect of reinforcement corrosion on bearing capacity and changes in the collapse mechanism, an experimental study on two identical square columns with a section size of 200×200 mm were designed, one column was kept sound and the other one was corroded by applying accelerated corrosion process. The two columns were tested under a constant axial compression and reversed cyclic torsional loading with variable drift amplitudes. In order to calibrate accelerated corrosion process for the columns, the results of preliminary corrosion tests, applied to bare steel bars and later on reinforced concrete beams with a section size of $600 \times 150 \times 150$ mm, were used. The results of the experiment on columns showed that the reinforcement corrosion in concrete structures can cause reduction of the strength and ductility up to 20.54% and 11.34% respectively, and also alters the failure modes from bending failure to a shear-bending mode. This could be a significant concern, particularly for buildings in earthquake-prone areas.

Keywords: Corroded RC Columns · Accelerated Corrosion · Combined Loadings · Cyclic Test

1 Introduction

Reinforced concrete structures, particularly those constructed with low-strength concrete, can experience a reduction in service life due to reinforcement corrosion, especially when insufficient concrete cover is provided. The corrosion of reinforcement in RC structures can have multiple structural consequences. One of the primary effects is the decrease in the effective cross-sectional area of the reinforcement, which weakens the structural capacity of the members [1]. Furthermore, the corrosion products tend to occupy the space between the reinforcement and the concrete, creating stresses from the expansion of the corrosion products, which exert pressure on the surrounding concrete [2]. The accumulation of high stresses can accelerate the development of cracks and further weaken the structure as well as reducing the bond strength and compromising the transfer of forces between the two materials [3]. Additionally, corrosion can lead to a reduction in the ductility of the reinforcement [4–6].

There are numerous articles in the literature addressing corrosion related problems including corrosion mechanisms, impact of corrosion on concrete structures, effectiveness of repair and strengthening techniques for corroded structures [1–10].

In recent years, there have been several studies in the literature that investigate the cyclic behaviour of corroded reinforced concrete columns [4–8], on the other hand, there is a limited amount of research available on the cyclic lateral torsional response of columns that incorporate corroded reinforcement [9, 10]. This study aims to understand how corrosion influences overall structural behaviour of corroded RC columns by subjecting them to cyclic lateral torsional loads, and investigating load-carrying capacity, deformation characteristics, energy dissipation, and failure modes.

The research begins with the first part dedicated to the calibration and optimization of the corrosion process. This is achieved through the use of electrolytic cells, which allow for controlled and accelerated corrosion of the steel rebars. The goal was to establish reliable and reproducible corrosion conditions that simulate different levels of corrosion. For this purpose, first of all, bare steel bars were subjected to accelerated corrosion and later embedded steel rebars in beam specimens of size 600 × 150 × 150 mm were corroded. Faraday's Law has been employed to calculate mass loss. Following the calibration and optimization of the accelerated corrosion process, experimental research was carried out with two column specimens. One column is kept as a reference specimen and the other column is subjected to accelerated corrosion of the rebars to simulate the effects of corrosion on the reduction of strength and ductility.

1.1   Calibration of the Rebar Corrosion

Accelerated Corrosion

Literature review on previous studies related with corrosion revealed that corrosion rate is either controlled by time [5, 8] or Faraday's law [4, 6] during experimental programmes. Some researchers applied current on specimens until they reached the targeted time period i.e. 60 days, 90 days or 120 days. However, it was not possible to set a target corrosion rate by this method. Hence, the researchers aimed to have same corrosion level for the specimens in the same group by keeping current application period same.

On the other hand, it is possible to set a target corrosion rate by employing Faraday's law. In this study, the designed (theoretical) mass loss of the reinforcement bars due to corrosion are calculated according to Faraday's law. First of all, it was aimed to apply corrosion procedure and use Faraday's Law successfully on bare steel bars as shown in Fig. 1(a). Later, it would be possible to obtain target mass loss and consequent corrosion levels for RC specimens Fig. 1(b).

Once the application of corrosion procedure is finished, all the rust from the surface of the reinforcement bars were cleaned by mechanically and chemically Fig. 2. Later, actual corrosion level or percentage mass loss of each specimen were calculated by reweighing all reinforcement bars. The theoretically calculated and experimentally obtained corrosion levels on bare reinforcement bars are given in Table 1.

It is clear from the experimentally obtained data that Faraday's Law is working efficiently and the project researcher can successfully manage the corrosion process. Once this result is obtained from bare steel bars, the next step was to apply corrosion on embedded bars. For this purpose, in total four different RC specimens were corroded.

(a)   (b)
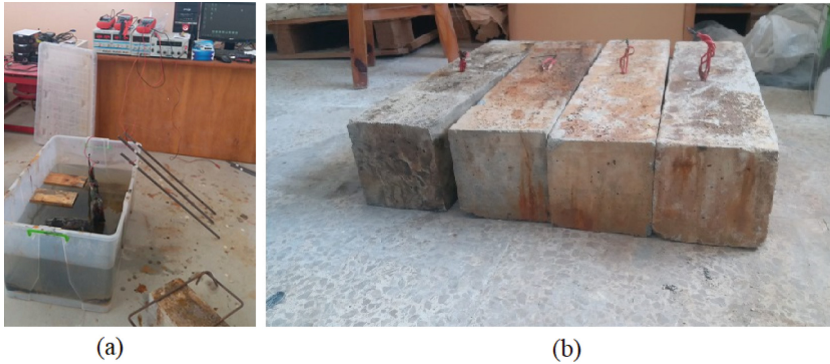
Fig. 1. Preliminary corrosion tests on (a) bare steel bars (b) reinforced concrete beams.

Table 1. The theoretically calculated and experimentally obtained corrosion levels on bare reinforcement bars.

Rebar No	Initial Mass (gr)	Final Mass (gr)	Calculated Mass Loss (gr)	Actual Mass Loss (gr)	Difference Between Experimental and Faraday's Law (gr)	Difference Between Experimental and Faraday's Law (%)
1	428.12	356.21	68.81	71.91	3.10	0.72
2	467.75	389.2	74.93	78.55	3.62	0.77
3	478.39	399.46	74.56	78.93	4.37	0.91

The corrosion rate at each RC specimen was calculated by using the recorded data. However, real corrosion levels can only be measured by reweighing all reinforcement bars extracted from test specimens when the corrosion process has completed. The four RC specimens were destroyed and each bar cleaned mechanically and chemically (see Fig. 2). The theoretically calculated and experimentally obtained corrosion levels on embedded bars are given in Table 2.

It is clear from the experimental data that the actual corrosion levels of embedded reinforcement could not reach to the calculated corrosion levels. For majority of the specimens, it can be concluded that the actual degree of corrosion for embedded steel is approximately 30–50% less than the calculated corrosion degree. Hence, column specimens should be subjected to accelerated corrosion according to the desired level of corrosion by considering the aforementioned difference.

(a) (b)
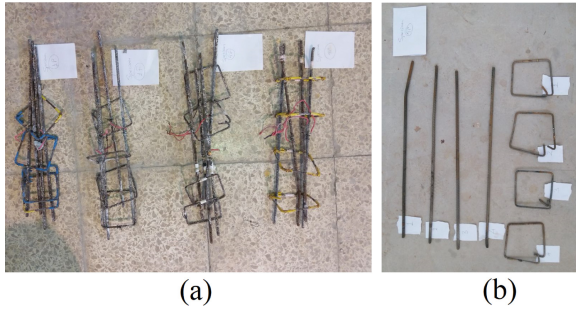
Fig. 2. Embedded rebars before (left) and after (right) cleaning.

Table 2. The theoretically calculated and experimentally obtained corrosion levels of specimens.

Specimen No	Reinforcement Detail	Initial Total Mass (gr)	Final Total Mass (gr)	Calculated Total Mass Loss (gr)	Total Actual Corrosion (gr)	Percent Difference (%)
S1	Stirrups	281.91	268.24	54.17	31.17	42.46
	Longitudinal	880.91	863.41			
S2	Stirrups	294.11	0	979.63	678.89	30.70
	Longitudinal	865.72	480.94			
S3	Stirrups	295.76	159.86	779.55	353.39	54.67
	Longitudinal	860.58	643.09			
S4	Stirrups	282.62	222.00	383.84	274.39	28.52
	Longitudinal	868.96	655.19			

2 Experimental Program

2.1 Column Specimen Details

Two column specimens were constructed (see Fig. 3) according to ACI 318-14 [11]. All the columns had a square cross-section of 200 mm by 200 mm and were reinforced with four longitudinal rebars with a diameter of 12 mm. This resulted in a steel ratio of 1.1%, which represents the reinforcement ratio commonly used in reinforced concrete (RC) building columns in the Mediterranean region.

The footings in all specimens were prismatic, with dimensions of 200 mm thickness, 350 mm width, and 1800 mm length. They were reinforced longitudinally with six rebars with a diameter of 14 mm, three rebars near the top face and three near the bottom face. Additionally, stirrup bars with 8 mm diameter were provided at a spacing of 80 mm both in the footing and in the body of the column specimens. Section details are given in Fig. 3 with the precise positioning of the reinforcing bars, as well as the concrete cover applied to both the column and the footing.
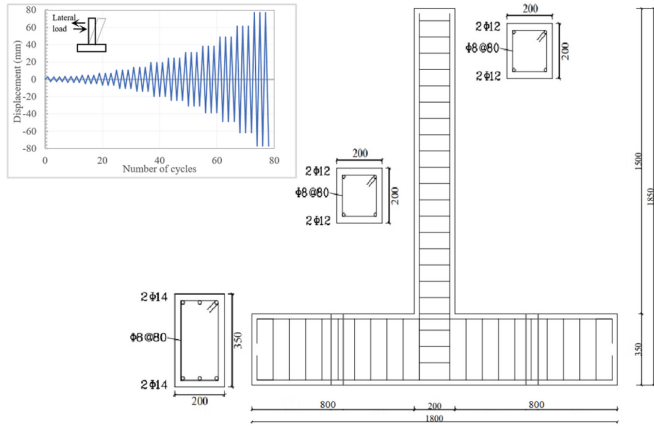
Fig. 3. Details of the test specimen and loading history (unit: mm).

2.2 Material Properties

For both test specimens, ready-mix concrete with strength class of C16 was used. The concrete mixture consisted of aggregate with a maximum size of 10 mm, and it had a slump value of 180 mm. The columns were cast in one continuous operation, preventing the formation of a cold joint between the column and the footing. The compressive strength of the concrete was evaluated using three standard concrete cubes with dimensions of 150 mm. The measured strengths of these cubes at 28 days were 16.1 MPa, 17 MPa, 17.3 MPa. The longitudinal and transverse reinforcing bars in the specimens were indicated to have a specified yield strength of 420 MPa. However, during mechanical testing, it was observed that the actual yield strengths (f_y) of the bars exhibited higher strength properties than what was initially anticipated. Table 3 shows mechanical properties of steel reinforcing bars.

Table 3. Mechanical properties of reinforcement.

Rebar type	Yield strength f_y (MPa)	Ultimate strength f_u (MPa)	Strain at ultimate stress ε_u (%)
φ8	507.1	616.45	0.18
φ12	457.55	551.3	0.2
φ14	468.8	582.45	0.19

2.3 Instrumentation and Procedure

The test setup and instrumentation details are shown in Fig. 3 and Fig. 4. The footing of the specimen was securely attached to the rigid laboratory floor with special studs,

providing a stable foundation. Lateral and axial loads were applied to the unfixed end of the column with two double acting hydraulic actuators having a maximum capacity of 1000 kN. The axial load was applied at the centre of cross-section on the top of the column, while a quasi-static lateral load was applied at the extending column end to create torsion in a displacement-controlled mode (Fig. 5). The specific displacement history is illustrated in Fig. 3. To measure the displacements at different locations, a total of six linear variable displacement transducers (LVDTs) were installed on each specimen (Fig. 4). Two LVDTs were positioned near the free end of the column. One of these LVDTs was used to measure top displacement and the other one is used to measure rotation of the column body. One LVDT was placed in the middle of the specimen, while another one at the lower end of the column, close to the foundation level. Additionally, two LVDTs were positioned at the foundation level to detect any potential slippage or movement of the footing itself.

(a)   (b)
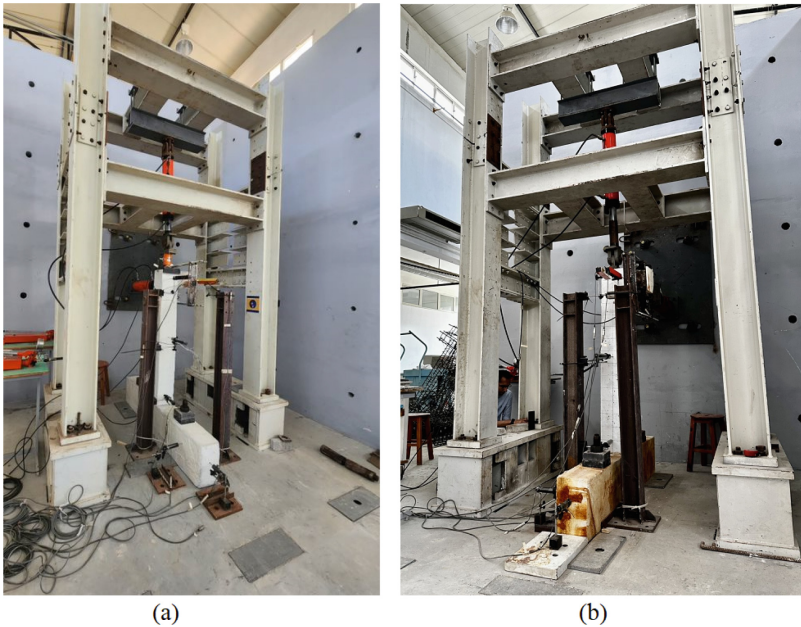
Fig. 4. Test set up for cyclic loading (a) sound column (b) corroded column.

3   Results and Discussion

3.1   Failure Modes

During the initial phase of the loading process, while the specimens were still within their elastic range, there were no major cracks detected on the exterior surface of the concrete. On the other hand, when the drift ratio reached 1.58% and 1.19% for the sound

and corroded columns respectively, cracks were observed horizontally starting from the edges of the column. These flexural cracks initiated on one face of the column and continued to propagate on the other faces with the increase in the lateral displacement. However, the cracks on the corroded column were wider and deeper. As the lateral load increased gradually, shear cracks were formed more intensely on the corroded column than those of the sound column. Furthermore, concrete on the bottom right and left of the footing started crushing from the edges followed by pieces of concrete to break away from the surface and fall down. The sound column exhibited bending failure mode where the corroded column failed under a shear-bending mode. Also, on the positive load application direction, large separation cracks have formed between the column body and the foundation. This result is also consistent with the studies reported by Goksu & Ilki [7]. The crack patterns at the end of testing of the sound specimen is shown in Fig. 6.
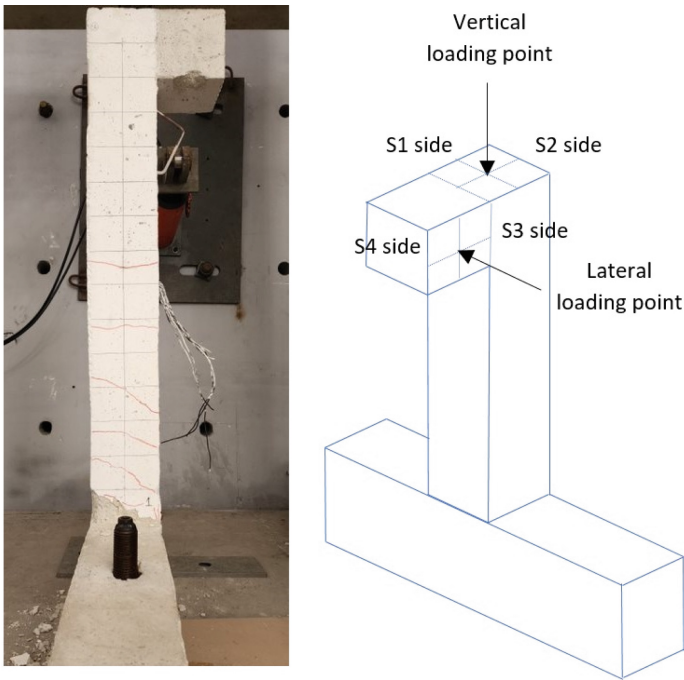
Fig. 5. The sound column specimen after the test and the loading method.
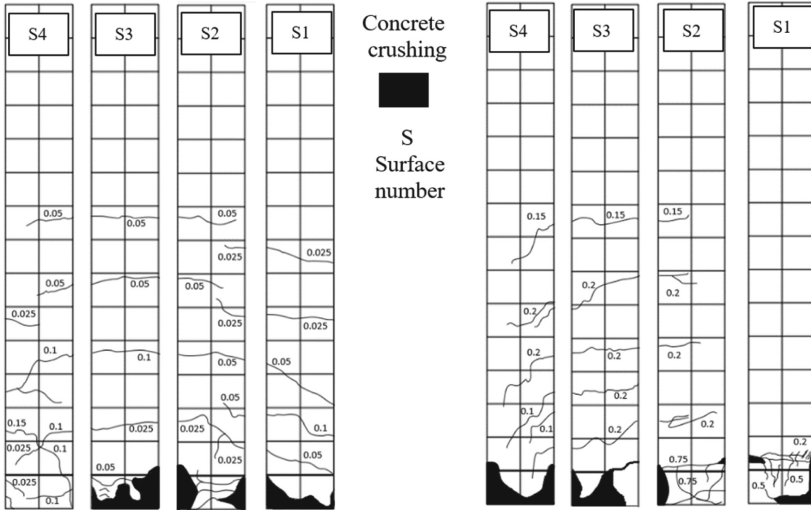
Fig. 6. Crack patterns of test specimens after the test; sound column on the left and the corroded column on the right (unit: mm).

3.2 Hysteresis Curves

Figure 7 illustrates the hysteresis curves for both the control specimen and the corroded specimen. From the hysteretic curves, two critical characteristic points, namely, the ultimate point (P_u, Δ_u) and the failure point (P_f, Δ_f) can be obtained.
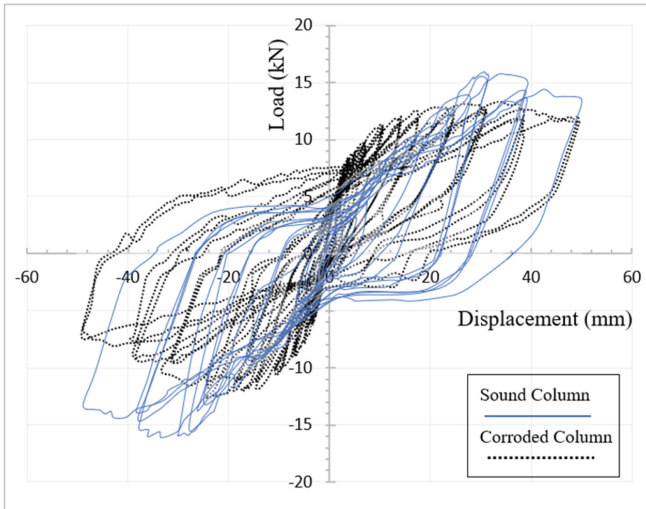
Fig. 7. Horizontal load- displacement curves of the sound column and the corroded column.
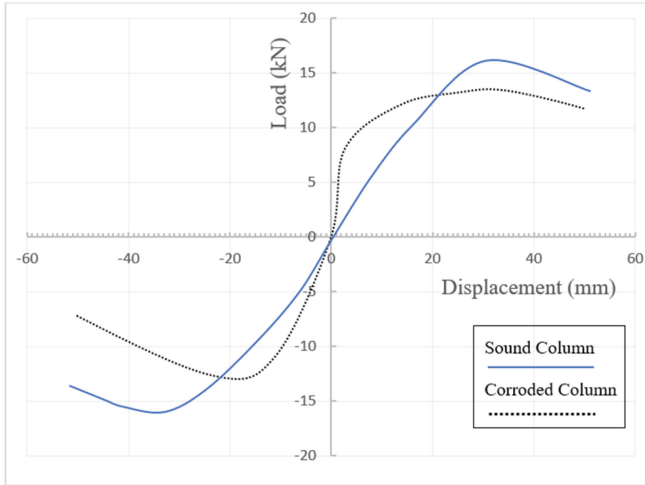
Fig. 8. The skeleton curves of the columns.

The corresponding load and displacement values for each specimen together with column torsions are summarized in Table 4. The ultimate point and failure point are designated as the maximum load and 85% of the maximum load respectively. The strength of sound column at the peak load is 20.54% higher than that of the corroded column. At the failure point this difference in strength drops to 17.16%. Similarly, the displacement of sound column at the peak load is 11.34% higher than that of the corroded column. On the other hand, displacements of two columns were close to each other at the failure load, 50.12 mm and 49.54 mm for the sound column and the corroded column respectively.

Table 4. Cyclic test results of the specimens.

Specimen	Peak Load and Corresponding Displacement & Rotation		
	Load, P_u (kN)	Displacement, Δ_u (mm)	Torsion, γ_u (rad)
Sound C.	16.06	30.52	0.022
Corroded C.	13.30	33.98	0.021
	Failure Load and Corresponding Displacement & Rotation		
	Load, P_f (kN)	Displacement, Δ_f (mm)	Torsion, γ_f (rad)
Sound C.	13.64	50.12	0.038
Corroded C.	11.30	49.54	0.033

Although, torsion angle, γ_u of both specimens at the peak load were slightly different from each other, there is a considerable difference at the failure load. This increment can be due to the loss of bond between the rebars and concrete.

3.3   Skeleton Curves

The skeleton curves of two specimens are given in Fig. 8. The corroded column exhibited a higher initial rigidity than that of the sound column, which can be associated with the well-established positive effect of rust and the confining effect on core concrete resulting from the expansion pressure of rebar corrosion. Additionally, the curve is not symmetrical for the corroded column in the positive and negative directions. This can be due to different corrosion rates of longitudinal steel bars as well as decrease in bond strength at the peak load [3]. Furthermore, the decrease in the load for the corroded specimen in the positive direction following the peak load is less significant compared to the decrease observed in the sound specimen which can be attributed to the complete yielding of the longitudinal bars in that direction.

3.4   Energy Dissipation

Figure 9 shows the energy absorption of column specimens calculated from the area under hysteresis curve, employing the trapezoidal rule, considering the product of horizontal load and horizontal deformation.
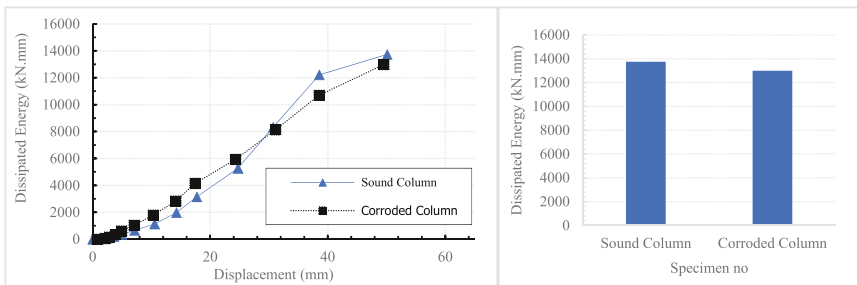
Fig. 9. Effect of corrosion on energy dissipation: cumulative energy dissipation (on the left); total energy dissipation (on the right).

Energy absorption of corroded column at the early stages of loading was higher than the sound column due to its higher lateral load capacity. This result is similar to the findings of Meda et al. [6] and it is associated with the pre-existing damage due to corrosion. However, energy absorption of the sound column became higher when the extent of deformation was larger. The total dissipated energy at the end of the test for two columns were very close to each other. This can be related to the applied corrosion level. A higher level of applied corrosion may result in a higher level of difference between the sound column and the corroded column.

4 Conclusions

The effect of reinforcement corrosion on seismic behaviour of RC columns under lateral torsional cyclic loading is presented in this paper. The following conclusions are obtained at the end of the tests:

- Faraday's law provides perfect results for bare rebars as the calculated mass losses and the actual mass losses are almost the same. However, when the rebars are embedded in concrete depending on many factors such as concentration of chloride ions, temperature, diffusion coefficient of concrete, calculated mass loss can be higher or lower than the actual mass loss.
- The sound column without corrosion reached 3.3% lateral drift ratio without a significant loss in strength, while the corroded column reached yielding load at much lower drift ratios. In the tested case, the percent difference between the ultimate loads was 20.54% for the sound and corroded column.
- Although, torsion angles of the two columns were very close to each other at the peak load, at the failure there was 13% difference.
- Energy dissipation of corroded column at the early stages of loading is slightly higher than that of the sound column. As the displacement amplitudes increased, the energy absorption of the two columns became equal, and towards the end of the loading, the energy absorption of the non-corroded column exceeded that of the corroded column.

It is clear from this limited test data that further research is necessary for introducing a concept for understanding the behaviour of corroded RC columns subjected to lateral torsional cyclic loads under constant axial loads.

References

1. Li, J., Gong, J., Wang, L.: Seismic behavior of corrosion damaged reinforced concrete columns strengthened using combined carbon fiber-reinforced polymer and steel jacket. Constr. Build. Mater. **23**, 2653–2663 (2009)
2. Tondolo, F.: Bond behavior with reinforcement corrosion. Constr. Build. Mater. **93**, 926–932 (2015)
3. Yalciner, H., Eren, O., Sensoy, S.: An experimental study on the bond strength between reinforcement bars and concrete as a function of concrete cover, strength and corrosion level. Cem. Concr. Res. **42**, 643–655 (2012)
4. Ma, Y., Che, M., Gong, J.: Behavior of corrosion damaged circular reinforced concrete columns under cyclic loading. Constr. Build. Mater. **29**, 548–556 (2012)
5. Lee, H.S., Kage, T., Noguchi, T., Tomosawa, F.: An experimental study on the retrofitting effects of reinforced concrete columns damaged by rebar corrosion strengthen with carbon fiber sheets. Cem. Concr. Res. **33**(4), 563–570 (2003)
6. Meda, A., Mostosi, S., Rinaldi, Z., Riva, P.: Experimental evaluation of the corrosion influence on the cyclic behavior of RC columns. Eng. Struct. **76**, 112–123 (2014)
7. Göksu, C., Ilki, A.: Seismic behavior of reinforced concrete columns with corroded deformed reinforcing bars. ACI Struct. J. **113**(5), 1053–1064 (2016)
8. Yang, S., Song, X., Jia, H., Chen, X., Liu, X.: Experimental research on hysteretic behaviors of corroded reinforced concrete columns with different maximum amounts of corrosion of rebar. Constr. Build. Mater. **121**, 319–327 (2016)

9. Wang, Y., et al.: Combined compression-bending-torsion behaviour of CFST columns confined by CFRP for marine structures. Compos. Struct. **242**, 112181 (2020)

10. Huang, H., Guo, M., Zhang, W., Huang, M.: Seismic behaviour of strengthened RC columns under combined loadings. J. Bridge Eng. **27**(6), 05022005 (2022)

11. ACI. ACI 318-14: Building code requirements for reinforced concrete. ACI, Farmington Hills (2014)

Seismic Performance of RC Frame with Different Types of Slabs Using Non-linear Time History

Mahmoud Eissa[(✉)] and Murude Celikag

Department of Civil Engineering, Faculty of Engineering, Eastern Mediterranean University, Famagusta, Mersin 10, Northern Cyprus, Turkey
mahmoud6cyprus@gmail.com, murude.celikag@emu.edu.tr

Abstract. The Composite slab made of galvanized steel deck and concrete has proven to be the most utilized slab in steel-framed structures. In this research, the seismic performance of a newly-introduced RC frame with a composite slab was analyzed and compared to the seismic performance of RC frames utilizing four other typical slabs. 23 separate ground motions were used with OpenSees to carry out nonlinear time history analysis that considered bar slip, shear deformation, and flexural deformation. The 3D building with composite slab achieved the lowest self-weight when compared to the buildings with other slab types. In addition, the base shear performance of 2D frames with composite slab was superior to those of the other cases. In accordance with Hazus-MH MR5 standards, the inter-story drift of composite slab frames and solid one-way slab frames demonstrated the best performance among the other cases. In the RC construction sector, however, composite slabs are a formidable rival to conventional slabs due to their lighter weight and superior seismic performance under NTHA, as well as their lower material consumption. Composite slabs, which consists of a concrete slab poured over a steel deck, have been demonstrated to enhance the seismic behavior of low-rise reinforced concrete building.

Keywords: Composite Slab · Seismic Performance · RC Frame · Slab Type

1 Introduction

The selection of different types of slabs for reinforced concrete (RC) structures depends on their intended use, as it affects the efficient transmission of vertical and horizontal loads, seismic performance, and construction costs [1]. Slabs, as horizontal elements within a structure, bear loads and transfer them to columns and beams. According to [2], RC slabs can be classified into solid slabs, flat slabs, and ribbed slabs based on how seismic forces convey loads in RC structures. In Turkey, ribbed slab systems are predominantly used in residential buildings, while flat slab systems are more common in parking facilities. [3] argue that the selection of a specific slab type is significantly influenced by floor loads and span lengths. Therefore, it is crucial to thoroughly evaluate all potential slab types to identify the most cost-effective option that ensures structural

integrity and satisfactory seismic performance. It is worth noting that slabs in tall RC structures generally require more building materials compared to other structural components [4]. Consequently, optimizing the cost of floor slabs becomes more important than optimizing the quantity and size of columns and beams. Considering that the amount of concrete used for columns is typically limited to 2.5% to 14% of that used for floor slabs [5], reducing the weight of floor slabs can lead to a decrease in concrete usage, positive environmental impact, and construction costs. [6] contend that incorporating a composite slab in an RC-framed building results in a lighter self-weight for the structure, thus reducing material usage. A composite slab with a galvanized steel deck can serve as an innovative alternative for RC structures. The use of composite slabs with galvanized decks and no props allows for a decrease in formwork usage, contributes to increased construction speed and reduced labor intensity for in-situ RC structures. One-way slabs are considered to be one of the simplest forms of solid slabs; nevertheless, their economic viability is limited to spans up to 4.6 m due to their low efficiency and weight [7]. Conversely, two-way slabs are commonly used for heavy loads and larger spans. The reinforcement in two-way slabs allows for the distribution of loads in both directions, enhancing their structural performance. Joist floor and waffle slab types offer several advantages owing to the presence of voids within the slabs, which effectively reduce both the self-weight of the slab and the amount of concrete below the neutral axis (Sacramento et al., 2018). However, it is important to note that these types of slabs exhibit poor stiffness and ductility, rendering them unsuitable for seismic regions [8].

Öztürk and Öztürk (2008) conducted a comprehensive investigation into the effects of different slab types, namely two-way slabs with beams, grid slabs, and flat slabs, on multistory buildings. Their study focused on assessing the structural performance under seismic conditions. The findings of their research indicated that flat slabs exhibited larger displacements, higher base shear forces, and longer periods compared to two-way slabs with beams. Consequently, the authors recommended the utilization of two-way slabs with beams in seismically active regions.

Similarly, [1] examined the seismic behavior of a five-story reinforced concrete (RC) building, analyzing various slab types including solid two-way slabs, joist floors, waffle slabs, flat slabs, and slabs with wide beams. Their investigation encompassed different span lengths and site classifications. The results demonstrated that solid two-way slabs exhibited superior robustness, characterized by minimal roof displacement and natural periods across all span lengths and site classifications. Accordingly, the authors suggested the adoption of solid two-way slabs for seismically active regions. Notably, it was found that flat slabs with high concrete volume and low stiffness were associated with higher vibrational periods. Consequently, it was advised against the use of flat slabs for spans exceeding 5 m. Furthermore, the study revealed that solid two-way slabs required a lesser amount of concrete compared to flat slabs.

After conducting an extensive review of the existing literature, it has been observed that majority of studies pertaining to the seismic performance of reinforced concrete (RC) buildings with different types of slabs predominantly employ push-over analysis, linear dynamic analysis, and linear static analysis. However, [9] asserts that non-linear dynamic time history analysis (NTHA) represents the most rigorous and reliable technique for investigating the seismic behavior of structures subjected to ground motion excitations.

It should be noted, however, that the response of the structure is highly sensitive to its structural characteristics and the input ground motion, necessitating multiple evaluations involving increased complexity, computational expenses, and time consumption. Hence, the objective of this study is to comparatively assess the performance of RC buildings featuring various slab types, specifically solid one-way, solid two-way, waffle, and joist floor systems, in comparison to slabs composed of galvanized metal deck. To achieve this aim, non-linear time history analysis is employed, offering a comprehensive evaluation of the seismic response of the structures.

2   Methodology

2.1   Case Study

The same building configuration, same floor area and floor heights, with three different story numbers (three, five, and seven stories) has been selected as a case study (Fig. 1). A typical floor height of 3.2 m was used for all buildings. Figure 2 presents the typical floor configuration of the chosen building used to assess the seismic performance of RC moment resisting frame with different slab types. Each building with one of the slab types has initially been designed as a 3D building using ETABS 16, under gravity load, equivalent static method for lateral load and considering the requirements of EN4 and ASCE/SEI 7-16 [10]. The building was assumed to be a residential building with an additional dead load of 1.2 kN/m^2 and an imposed load of 3 kN/m^2. The seismic parameters used in this study were taken from Kitayama and Constantinou [11]. The cross-section of the structural members with the rebar are given in Table 1.
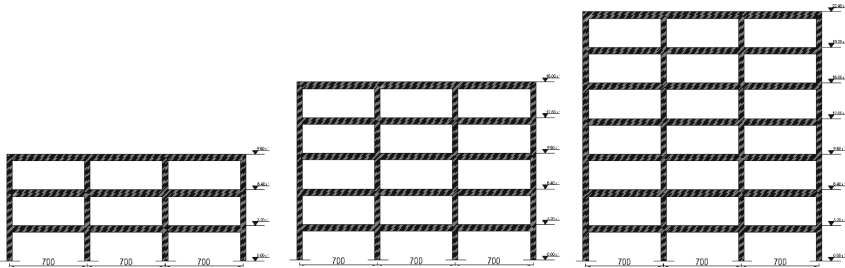
Fig. 1. Elevations of case study buildings.
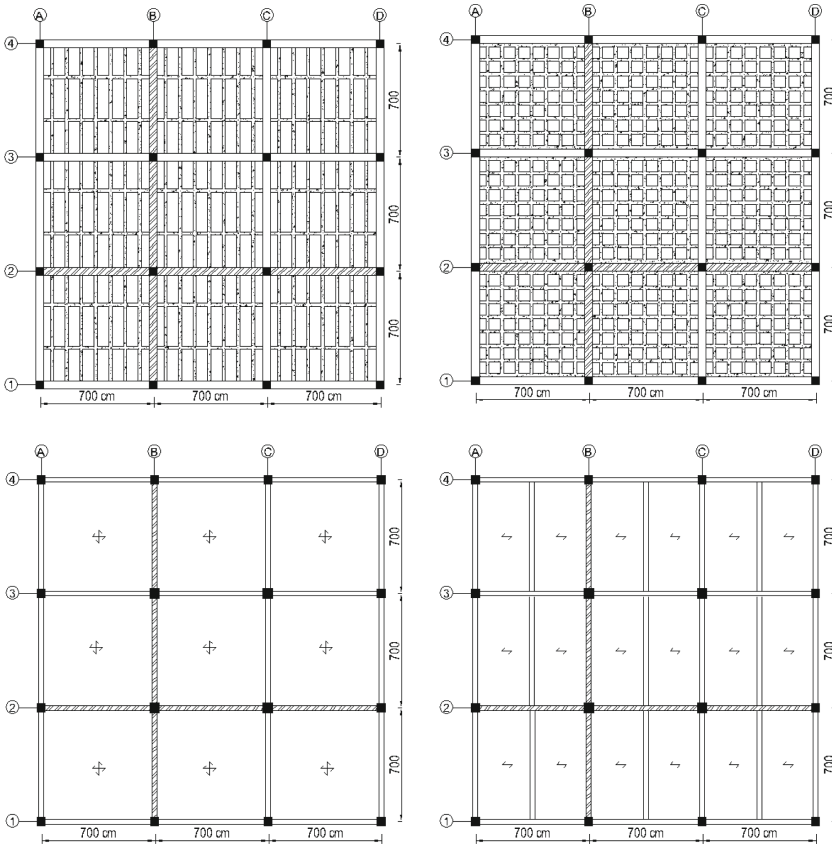
Fig. 2. Top view of the selected case study buildings with different slab types.

Table 1. Cross-sectional dimensions and rebar sizes for all analyzed frames.

	Axis B Three Story							Axis 2 Three Story					
Slab type	Thickness (cm)	Beams (cm)	Columns (cm)	Column rebar	Beam rebar B	Beam rebar T	Slab type	Thickness (cm)	Beams (cm)	Columns (cm)	Column rebar	Beam rebar B	Beam rebar T
Two-way solid	18	25/55	50/50	8Ø20	4Ø20	5Ø20	Two-way solid	18	25/55	50/50	8Ø20	4Ø20	5Ø20
One-way solid	12	25/50	50/50	8Ø20	3Ø20	5Ø20	One-way solid	12	25/60	50/50	8Ø20	7Ø20	6Ø20
Composite	12	25/45	50/50	8Ø20	3Ø20	4Ø20	Composite	12	25/55	50/50	8Ø20	6Ø20	4Ø20
One-way joist	28	50/28	50/50	8Ø20	3Ø20	4Ø20	One-way joist	28	50/28	50/50	8Ø20	4Ø20	6Ø20
Waffle	28	50/28	50/50	8Ø20	3Ø20	5Ø20	Waffle	28	50/28	50/50	8Ø20	3Ø20	5Ø20

	Axis B Five Story							Axis 2 Five Story					
Slab type	Thickness (cm)	Primary beam (cm)	Columns (cm)	Column rebar (%)	Beam rebar B (%)	Beam rebar T (%)	Slab type	Thickness (cm)	Primary beam (cm)	Columns (cm)	Column rebar (%)	Beam rebar B (%)	Beam rebar T (%)
Two-way solid	18	25/55	50/50	8Ø20	6Ø16	9Ø16	Two-way solid	18	25/55	50/50	8Ø20	6Ø16	9Ø16
One-way solid	12	25/50	50/50	8Ø20	5Ø16	7Ø16	One-way solid	12	25/60	50/50	8Ø20	7Ø20	7Ø20
Composite	12	25/45	45/45	8Ø20	5Ø16	7Ø16	Composite	12	25/55	45/45	8Ø20	7Ø20	5Ø20
One-way joist	28	50/28	50/50	8Ø20	4Ø16	7Ø16	One-way joist	28	50/28	50/50	8Ø20	5Ø20	8Ø20
Waffle	28	50/28	50/50	8Ø20	4Ø16	8Ø16	Waffle	28	50/28	50/50	8Ø20	4Ø16	8Ø16

	Axis B Seven Story							Axis 2 Seven Story					
Slab type	Thickness (cm)	Beams (cm)	Columns (cm)	Column rebar (%)	Beam rebar B (%)	Beam rebar T (%)	Slab type	Thickness (cm)	Beams (cm)	Columns (cm)	Column rebar (%)	Beam rebar B (%)	Beam rebar T (%)
Two-way solid	18	25/55	55/55	10Ø20	4Ø20	6Ø20	Two-way solid	18	25/55	55/55	10Ø20	4Ø20	6Ø20
One-way solid	12	25/50	55/55	10Ø20	4Ø16	7Ø16	One-way solid	12	25/60	55/55	10Ø20	6Ø20	6Ø20
Composite	12	25/50	50/50	8Ø20	4Ø16	7Ø16	Composite	12	25/60	50/50	8Ø20	5Ø20	5Ø20
One-way joist	28	55/28	55/55	10Ø20	4Ø16	8Ø16	One-way joist	28	55/28	55/55	10Ø20	5Ø20	7Ø20
Waffle	28	55/28	55/55	10Ø20	4Ø16	10Ø16	Waffle	28	55/28	55/55	10Ø20	4Ø16	10Ø16

Table 2. Selected ground motions with their properties.

Result ID	RSN	MSE	Scale Factor	T_p (s)	Event	Year	Mag	R_{jb} (km)	V_s30 (m/s)
					NF NP				
1	130	0.6	10.5	-	Friuli, Italy-02	1976	5.9	11.0	310.7
2	187	0.1	5.6	-	Imperial Valley-06	1979	6.5	12.7	348.7
3	236	0.5	5.7	-	Mammoth Lakes-03	1980	5.9	2.7	382.1
4	313	0.4	4.5	-	Corinth, Greece	1981	6.6	10.3	361.4
5	320	0.8	9.4	-	Mammoth Lakes-10	1983	5.3	6.5	382.1
6	391	0.6	10.0	-	Coalinga-03	1983	5.4	12.9	352.2
7	445	0.3	13.3	-	New Zealand-01	1984	5.5	3.8	356.4
8	457	0.5	7.6	-	Morgan Hill	1984	6.2	13.0	349.9
9	517	0.6	3.7	-	N. Palm Springs	1986	6.1	1.0	359.0
10	547	0.5	5.7	-	Chalfant Valley-01	1986	5.8	6.1	316.2
11	564	0.3	4.0	-	Kalamata, Greece-01	1986	6.2	6.5	382.2
12	613	0.7	12.6	-	Whittier Narrows-01	1987	6.0	9.5	324.8
13	725	0.4	3.2	-	Superstition Hills-02	1987	6.5	11.2	316.6
14	821	0.3	1.8	-	Erzican, Turkey	1992	6.7	0.0	352.1
15	864	0.3	3.7	-	Landers	1992	7.3	11.0	379.3
16	953	0.4	2.2	-	Northridge-01	1994	6.7	9.4	355.8
17	1615	0.1	8.7	-	Duzce, Turkey	1999	7.1	9.1	338.0
18	2628	0.4	4.5	-	Chi-Chi, Taiwan-03	1999	6.2	0.0	443.0
19	4130	0.3	4.0	-	Parkfield-02, CA	2004	6.0	1.6	381.3
20	4337	0.8	5.7	-	Umbria Marche (foreshock), Italy	1997	5.7	0.6	317.0
21	4349	0.6	7.3	-	Umbria Marche, Italy	1997	6.0	0.8	317.0
22	4457	0.2	4.6	-	Montenegro, Yugoslavia	1979	7.1	1.5	410.4
23	8157	0.7	1.3	-	Christchurch, New Zealand	2011	6.2	0.0	422.0

2.2 Record Selection and Scaling Method

23 near-fault non-pulse real ground motion data has been selected from Ground Motion Database - PEER Center website. The magnitude and soil type are the parameters used to select the ground motion given in Table 2. Mean squared error MSE scaling method was adopted to scale the selected ground motions. The aim was to achieve the average spectrum of the resulting scaled earthquake records that gives the finest match to the target spectrum for the concerned period.

2.3 Modeling Technology and the Material Used

The study employs a fiber section approach with fully distributed plasticity element models, combined with non-linear beam-column elements using Gauss-Lobatto integration and Geo-transfer of P-delta for columns, as well as linear beams. The fiber-section locations and integration weights are carefully selected to ensure optimal integration algorithms. OpenSees, a computational platform, allows the user to specify the precise location of the fiber section within the plastic hinge length [12] was used for the modelling. It is important to note that the fiber-section elements primarily account for flexural deformations by integrating moment-curvature relationships over the member length. Consequently, the inclusion of bar-slip and shear flexibilities was necessary for

fiber-section frame elements [12]. To consider the effects of the slab, a distributed mass from the floor to the adjacent beams was considered. The modeling technique is visually depicted in Figs. 4 and 5. Furthermore, the effectiveness of this modeling approach has been validated by [13] and recommended by [14] following a comparative analysis conducted among various non-linear modeling techniques. Yet the shear deformation effect together with the bar-slip has been added to the model as zero length element.

3   Results and Discussions

3.1   Story Shear

The average story shear of the analyzed building frames with various types of slabs and varying number of stories and for both axis 2 and B is presented in Fig. 3. It is evident from the figure that the composite slab configuration exhibited lower base shear compared to the other slab types across all three building heights in axis 2 and axis B. Moreover, the disparity in base shear between the two axis in the composite slab case was found to be the least when compared to the other slab types. Therefore, this observation substantiates the proposition that the reduction in slab mass in the composite slab configuration surpasses the reduction in stiffness, leading to an improved overall performance.

3.2   Story Displacement

The depicted diagram in Fig. 4 shows the average displacement of stories among the examined frames with various types of slabs and different building heights. The data presented clearly indicates that the composite slab configuration, when combined with the one-way solid slab, exhibited notably lower story displacement in comparison to the other slab variations across both axis 2 and axis B, irrespective of the building height. Additionally, it is noteworthy that the joist floor and waffle slab combinations displayed the highest story displacements in axis 2, whereas the waffle slab alone recorded the highest displacement in axis B. However, it is important to mention that in buildings with five and seven stories, slabs with wide beams demonstrated higher story displacements than slabs with drop beams, as depicted in Fig. 4.
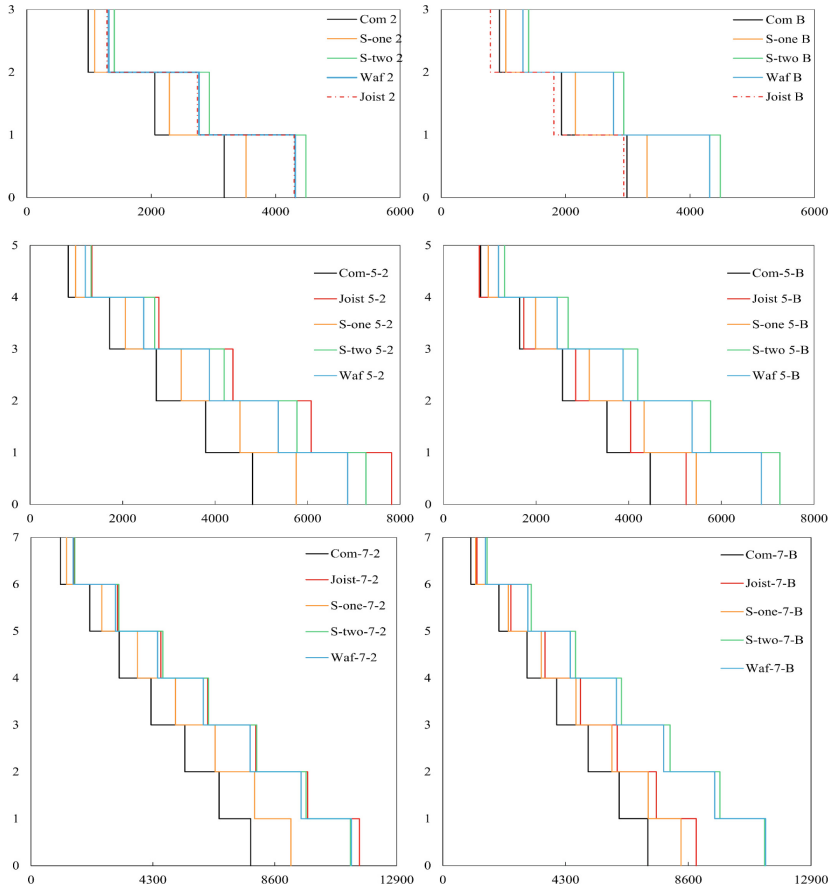
Fig. 3. Story number versus story shear of all analyzed frames.
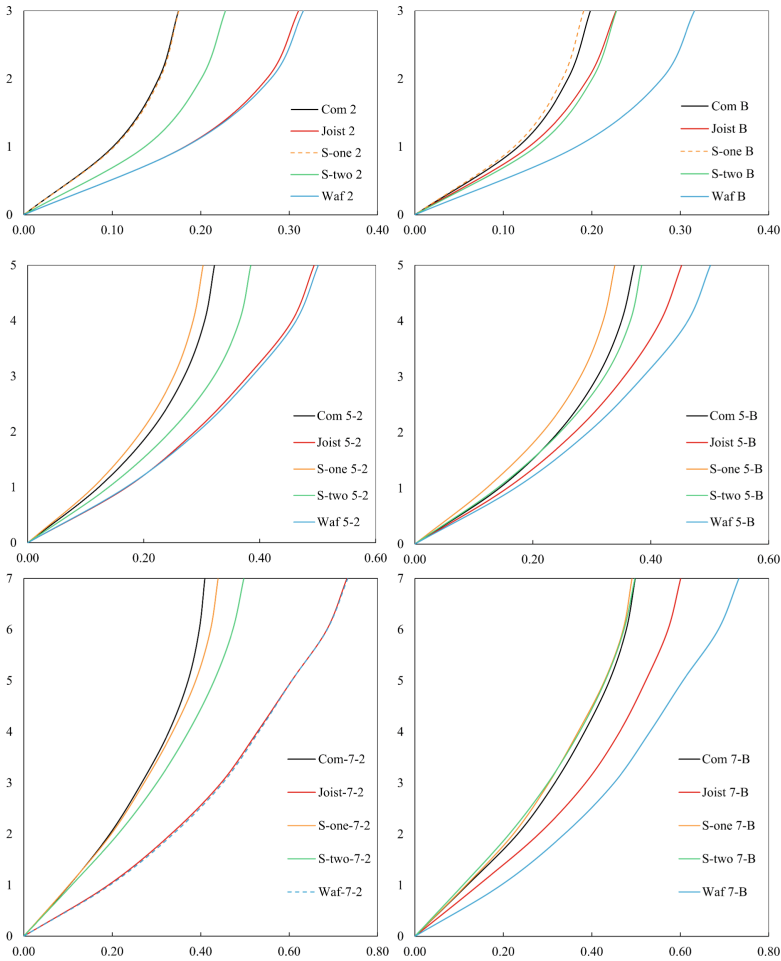
Fig. 4. Story number versus average story displacement for all analyzed frames.

3.3   Average Inter-Story Drift

Inter-story drift serves as a critical indicator for assessing the seismic performance of structures. Moreover, numerous national standards incorporate evaluation systems that consider inter-story drift when assessing building performance. In Fig. 5, the average inter-story drift of all examined building frames with varying number of stories is depicted. The results clearly indicate that the composite slab and solid one-way slab configurations exhibit superior inter-story drift performance in three and five-story buildings. However, in seven-story building frames, where frame behavior is predominantly influenced by stiffness rather than mass reduction, frames with drop beams outperformed those with wide beams in terms of inter-story drift.
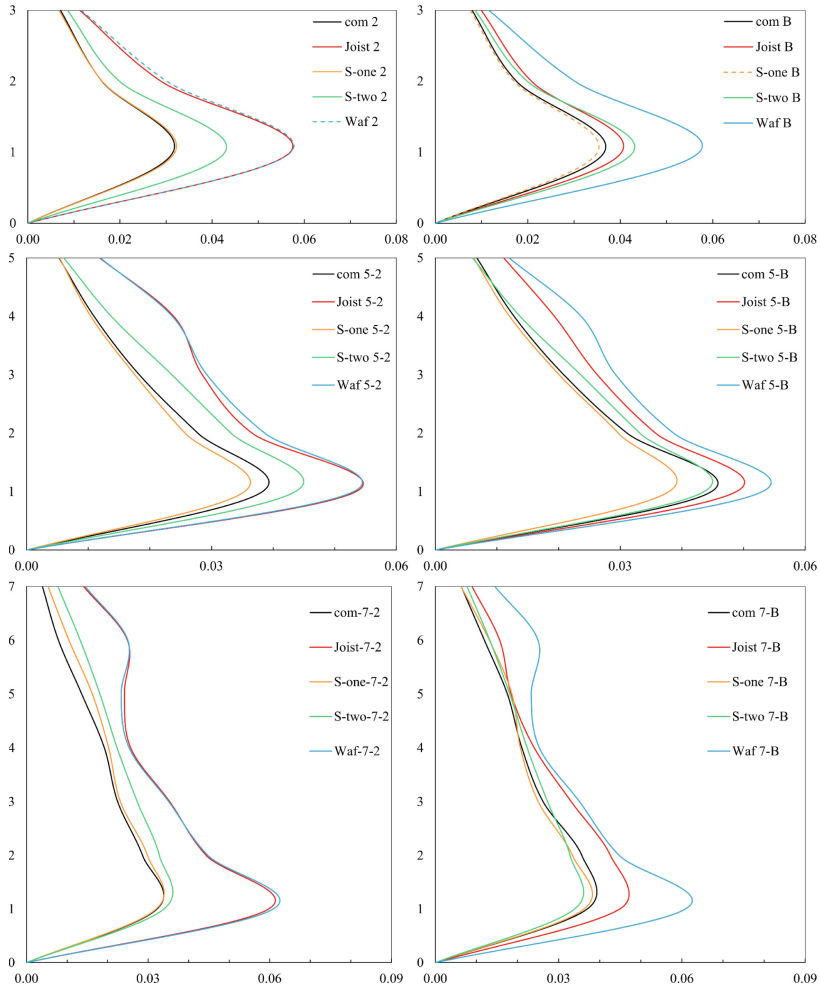
Fig. 5. Story number versus average inter-story drift of all analyzed frames.

4 Conclusions

In this study, a comprehensive set of 552 non-linear time history analyses was conducted to investigate the behavior of recently introduced reinforced concrete (RC) frame with composite slab in comparison to RC frames employing four other prevalent slab types. The analyses were performed using near fault non-pulse real earthquake records. The key findings of this study can be summarized as follows:

- The utilization of composite slabs in reinforced concrete (RC) structures offers a notable advantage in terms of reduced base shear compared to other configurations. This reduction in base shear represents a significant benefit associated with the incorporation of composite slabs in RC framed buildings.

- Despite the relatively lower weight of the composite slab frame, it exhibited superior roof displacement performance compared to the other cases. This finding suggests that the mass reduction of the composite slab outweighs the reduction in frame stiffness, leading to improved roof displacement characteristics.
- The inter-story drift of composite slab frames, along with the solid one-way slab frames, showed the best performance among the other cases.

References

1. Gürsoy, Ş, Uludağ, Ö.: Investigation of the effects on earthquake behavior and rough construction costs of the slab type in reinforced concrete buildings. Adv. Concr. Constr. **10**(4), 333–343 (2020)
2. Eşki, H., Sayın, B., Güneş, B.: The effect on structural behavior of different slab types for RC buildings. J. Struct. Eng. Appl. Mech. **3**(1), 41–48 (2020)
3. Gökhan, T., Azizi, A.B., Tanfener, T.: Effects of slab types on the seismic behavior and construction cost of RC buildings. Politekn. Dergisi. **1**(1), 1 (2021)
4. Schwetz, P.F., Gastal, F.P.S.L., Silva, F.L.: Numerical and experimental study of a waffle slab designed to serve as a tennis court floor. Rev. IBRACON de Estruturas Mater. **6**, 375–391 (2013)
5. Ženíšek, M., Pešta, J., Tipka, M., Kočí, V., Hájek, P.: Optimization of RC structures in terms of cost and environmental impact—case study. Sustainability **12**(20), 8532 (2020)
6. Eissa, M., Celikag, M.: Composite Behavior of reinforced concrete T-beam with composite slab. Arab. J. Sci. Eng. 1–21 (2022)
7. Tikka, T.K., Mirza, S.A.: Effective length of reinforced concrete columns in braced frames. Int. J. Concr. Struct. Mater. **8**(2), 99–116 (2014)
8. Benavent-Climent, A., Donaire-Ávila, J.: Moment transfer and influence of transverse beams in interior waffle flat plate–column connections under lateral loading. Eng. Struct. **49**, 146–155 (2013)
9. Teruna, D.: Comparison of seismic responses for reinforced concrete buildings with mass and stiffness irregularities using pushover and nonlinear time history analysis. In: IOP Conference Series: Materials Science and Engineering. IOP Publishing (2017)
10. Engineers ASoC, editor Minimum design loads and associated criteria for buildings and other structures. American Society of Civil Engineers (2017)
11. Kitayama, S., Constantinou, M.C.: Seismic performance of buildings with viscous damping systems designed by the procedures of ASCE/SEI 7–16. J. Struct. Eng. **144**(6), 04018050 (2018)
12. ATC, editor Guidelines for Nonlinear Structural Analysis for Design of Buildings. Part IIb–Reinforced Concrete Moment Frames (NIST GCR 17-917-46v3)2017: ATC Redwood City, CA, USA
13. Oinam, R.M., Sahoo, D.R.: Numerical evaluation of seismic response of soft-story RC frames retrofitted with passive devices. Bull. Earthq. Eng. **16**(2), 983–1006 (2018)
14. Huang, X., Kwon, O.S.: Numerical models of RC elements and their impacts on seismic performance assessment. Earthq. Eng. Struct. Dyn. **44**(2), 283–298 (2015)

Identification of the Tensile Properties of Concrete in Pre-stressed Elements Subjected to 4-Point-Bending Test

Gabriella Bolzon[1(✉)] , Mohammad Hajjar[1], and Emanuele Zappa[2]

[1] Department of Civil and Environmental Engineering, Politecnico di Milano, Milan, Italy
{gabriella.bolzon,mohammad.hajjar}@polimi.it
[2] Department of Mechanical Engineering, Politecnico di Milano, Milan, Italy
emanuele.zappa@polimi.it

Abstract. Data collected from 4-point bending tests can be exploited to determine, albeit indirectly, the tension properties of pre-stressed (actually, precompressed) concrete beams, which fail by fracture propagation. The overall result of these experiments depends on several factors. Cracks can vary in number and position even in nominally identical samples, and can close almost completely upon unloading. The onset and propagation of fracture in concrete elements can be detected during the loading process by high resolution cameras, which also provide input data to digital image correlation techniques. This rich experimental information can be interpreted with the support of numerical models of different realism and complexity. Their ability to obtain reliable results for parameter identification purposes, at reasonable computational costs, is discussed in this contribution.

Keywords: Pre-compressed concrete beams · Fracture properties · Digital image correlation · Numerical analysis

1 Introduction

The practical difficulties associated with the determination of the tensile properties of concrete by uniaxial loading [1, 2], favor the use of indirect identification procedures based on bending tests. In contrast to 3-point bending test (3PBT), the alternative 4-point bending test (4PBT) produces a region free of any shear contribution or local compressive damage, which can develop under the location where the load is applied [3–5].

Both 3PBT and 4PBT can induce complex fracture patterns. In pre-compressed (PC) elements, cracks can close almost completely upon unloading. Therefore, fracture position and extent can hardly be determined a-posteriori, unless the sample is lead to complete failure.

The onset and propagation of fracture can be monitored by optical means [5–10], which also provide quantitative data for the indirect calibration of the tensile properties of brittle and quasi-brittle materials.

Parameter identification procedures rely on the comparison between the available measurements, and the results of a realistic simulation of the experiment. Cohesive processes, typical of concrete-like materials, are commonly reproduced by either continuum-like smeared crack models, or by discrete crack approaches [5, 11–13]. The possible alternatives and their outcome are here compared to the measurements collected during 4PBT of PC sleepers.

2   Experimental Work

Three nominally identical PC sleepers are subjected to the 4PBT schematically represented in Fig. 1. The load is applied at the constant rate 120 kN/min by means of a 300 kN servo-hydraulic actuator. The element deformation and the fracture propagation during the test is monitored by two high resolution cameras in stereoscopic configuration, which take pictures at 1 Hz frequency focusing on the region of interest (ROI) visualized in the sketch. The 3D digital image correlation (DIC) software VIC 3D processes the sequence of the acquired pictures, and returns the displacement and strain distribution at each instant [14]. The experimental setup and the image acquisition system are illustrated in [15].
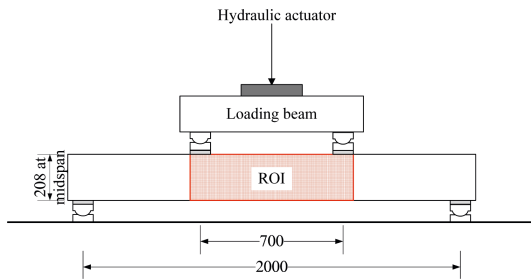
Fig. 1. Schematic of the performed 4PBTs and of the region of interest (ROI) monitored by DIC.

Figure 2 shows the orizontal strain maps of two loaded samples at the maximum applied force (120 kN). The graphs suggest the location and severity of the cracks, in a number that depends on each case.
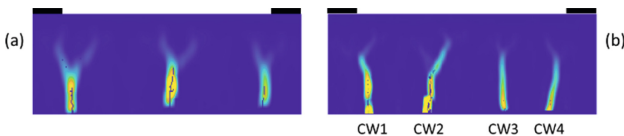
Fig. 2. Strain maps of two nominally identical samples at the maximum applied load (not in real scale).

The discontinuities produced at the material separation surfaces are represented in Fig. 2 by equivalent (albeit immaterial) strains. In fact, the main output of digital image

correlation (DIC) algorithms are displacements, while strains are obtained by finite differences. The graphs also show the crack branching that occurs as fracture propagates and a biaxial stress state develops [16].

Displacement discontinuities can also be extracted from DIC results. The opening displacements of two of the cracks developing in sample (b), Fig. 2, are visualized in Fig. 3. The fracture portion below the branching points is represented. Notice the different scales on the horizontal axes.
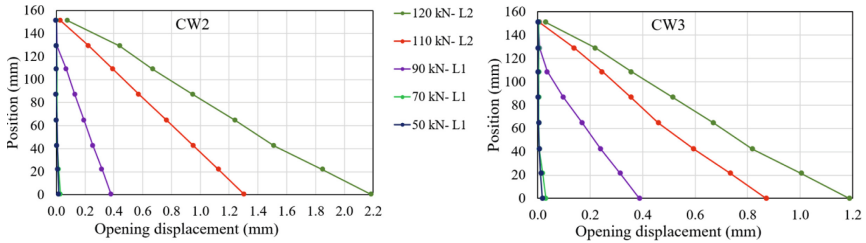
Fig. 3. Opening displacement distribution in CW2 and CW3cracks of sample (b) in Fig. 2, for increasing load levels.

3   Simulation Models

Fracture propagates in pure opening mode in quasi-brittle materials like concrete, in unconstrained conditions. The process is characterized by a tensile softening curve, which represents the relationship between the decaying cohesion stresses that are still transferred across the fracture surface and the corresponding displacement discontinuities, up to a critical threshold.

Linear, bi-linear or exponential traction-separation laws are mostly considered. The main parameters that characterize each material are the tensile strength and fracture energy. Their value can be estimated indirectly from the experimental results, by comparison with corresponding simulation output.

The finite element method is usually applied to non-linear problems. In the present work, the sample geometry is discretized into square elements of 10 mm characteristic size. Plane stress analyses are performed, introducing pre-compression as uniformly distributed initial stress.

3.1   Smeared Crack – Full Model

The continuum-like smeared crack model implemented in the commercial code Abaqus is employed first to simulate the 4PBT of the PC elements. The formulation details can be found in the theory manual [17].

Linear traction-separation relationship is assumed in this work. The critical displacement discontinuity at which the cohesive stresses vanishes is transformed into an equivalent strain through a length scale, which corresponds to the characteristic element size.

In the smeared crack approach, material separation is replaced by strain localization into some elements, as visualized in Fig. 4.
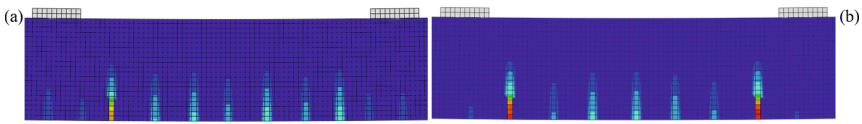
Fig. 4. Strain maps obtained from the simulation of the 4PBT, assuming tensile strength: (a) 3.5 MPa; (b) 5 MPa. The remaining parameters are assumed to be the same.

The strain maps returned by the smeared crack approach present a qualitative agreement with the DIC output. The crack pattern is however different. In fact, in real experiments fracture is initiated by material imperfections, while strain localization is driven by numerical round-off errors in the simulation models.

Figure 5 compares the experimental load-displacement curve with the corresponding numerical results, obtained by assuming tensile strength equal to either 3.5 MPa or 5 MPa while the critical strain is set to the values 0.05 and 0.5.
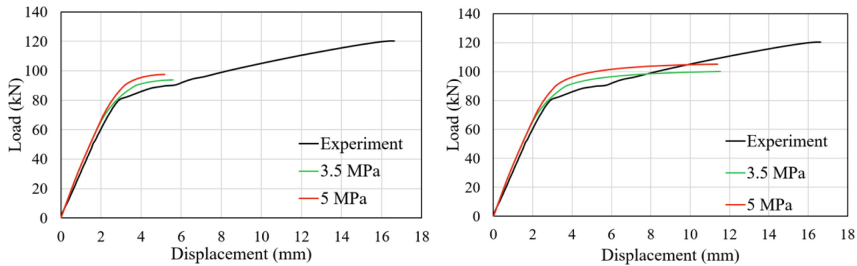
Fig. 5. Experimental and numerical load-displacement curves: tensile strength 3.5 MPa or 5 MPa; critical strain 0.05 (left) or 0.5 (right).

The FE analyses stop as the stress state at the tip of the localization zones becomes biaxial, i.e. at the threshold of crack branching, due to difficulties in numerical convergence. The maximum displacement achieved in the simulations depends on value of the critical strain, but the pronounced macroscopic hardening shown by the experimental output is never captured.

3.2 Discrete Crack – Reduced Model

In the discrete crack approach, the displacement discontinuities that arise in correspondence of the new forming surfaces are explicitly accounted for. In the traditional FE context, they are reproduced by couples of nodes placed along the fracture path, which is a priori known in the present case.

Quasi-brittle behavior is described by a traction-separation law attributed to the interfaces (usually of zero-thickness) across which cracks propagate, while the remaining

material is considered linear elastic. The last assumption permits to condense most of the degrees of freedom of the FE discretization and to retain the sole displacement discontinuities, generating effective computational models also in the field of mixed mode and hydraulic fracture [18, 19].

The computational burden can also be reduced by discretizing only the region enclosing each crack, as schematized in Fig. 6, and introducing the horizontal displacements measured by DIC as boundary conditions on the vertical sides of the investigated (sub)domain, as done in [6, 15].
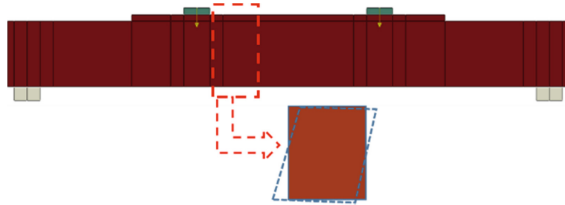
Fig. 6. Schematization of the region subjected to FE simulation in the reduced model.

The results of these fast simulations are fed into an optimization toolbox, which determines the most likely values of the fracture parameters while minimizing the discrepancy between the numerical and experimental output [20].

The measurements considered to identification purposes in the present work consist of the sequence of the crack opening profiles, e.g. represented in Fig. 3. The optimal parameter set, identified by a zero-th order genetic algorithm, highlights a rather brittle behavior of the concrete, characterized by tensile strength 1.7 MPa and critical opening displacement 0.194 mm.

The bending moments (and the corresponding forces applied during the 4PBT) are recovered from the distribution of the lateral reaction forces obtained from the reduced FE model.

The optimized simulation results are compared in Fig. 7 with the real load-displacement curve, which here represents an independent information source since these overall measurements are not fed into the discrepancy function. The agreement is fairly good, though.
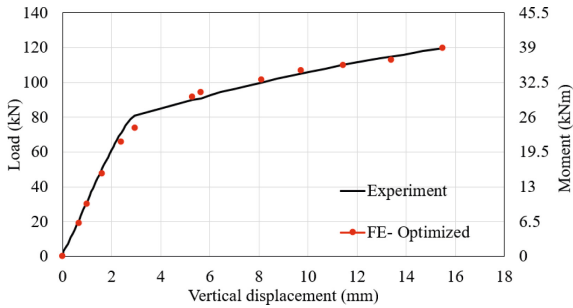
Fig. 7. Comparison between the experimental load-displacement curve and the output of the reduced FE model with cohesive parameters set to their optimized value.

4   Conclusion

The identification of the tensile properties of concrete-like materials can rely on the rich information provided by vision-based measurement techniques. Full-field data can be collected, and the structural response of the investigated samples can be interpreted with the aid of simulation models of the performed mechanical tests. Full-field measurements can also be exploited to define computationally effective numerical strategies.

The investigations summarized in the present work concern 4PBTs of PC elements simulated in a FE context by either the smeared-crack and the discrete crack approaches. The possibility of discretizing either the whole tested sample or a portion of it has been also considered.

The presented results show that the discrete crack approach combined with a reduced FE model performs better in terms of both computational effectiveness and overall realism.

References

1. Reinhardt, H.W., Hans, A.W., Cornelissen, H.A.W., Hordijk, D.A.: Tensile tests and failure analysis of concrete. ASCE J. Struct. Eng. **112**(11), 2462–2477 (1987)
2. Akita, H., Koide, H., Tomon, M., Sohn, D.: A practical method for uniaxial tension test of concrete. Mater. Struct. **36**, 365–371 (2003)
3. ASTM C78/C78M-18; Standard Test Method for Flexural Strength of Concrete (Using Simple Beam with Third-Point Loading). ASTM International, West Conshohocken (2018)
4. Rezaie, F., Farnam, S.: Fracture mechanics analysis of pre-stressed concrete sleepers via investigating crack initiation length. Eng. Fail. Anal. **58**, 267–280 (2015)
5. Silva, R., Silva, W., Farias, J., Santos, M., Neiva, L.: Experimental and numerical analyses of the failure of prestressed concrete railway sleepers. Materials **13**(1704), 1–20 (2020)
6. Bolzon, G., Buljak, V., Zappa, E.: Characterization of fracture properties of thin aluminium inclusions embedded in anisotropic laminate composites. Frattura Integr. Strutturale **19**, 20–28 (2012)
7. Yao, Y., Tung, S.-T.E., Glisic, B.: Crack detection and characterization techniques—an overview. Struct. Control. Health Monit. **21**, 1387–1413 (2014)
8. Liu, R., Zappa, E., Collina, A.: Vision-based measurement of crack generation and evolution during static testing of concrete sleepers. Eng. Fract. Mech. **224**(106715), 1–14 (2020)

9. Reagan, D., Sabato, A., Niezrecki, C.: Feasibility of using digital image correlation for unmanned aerial vehicle structural health monitoring of bridges. Struct. Health Monit. **17**(5), 1056–1072 (2018)
10. Dizaji, M.S., Harris, D.K., Kassner, B., Hill, J.C.: Full-field non-destructive image-based diagnostics of a structure using 3D digital image correlation and laser scanner techniques. J. Civ. Struct. Heal. Monit. **11**(5), 1415–1428 (2021). https://doi.org/10.1007/s13349-021-00516-6
11. Rots, J.G., Blaauwendraad, J.: Crack models for concrete: discrete or smeared? Fixed, multidirectional or rotating? Heron **34**(1), 1–59 (1989)
12. Bolzon, G., Fedele, R., Maier, G.: Parameter identification of a cohesive crack model by Kalman filter. Comput. Methods Appl. Mech. Eng. **191**, 2847–2871 (2002)
13. Maier, G., Bocciarelli, M., Bolzon, G., Fedele, R.: Inverse analyses in fracture mechanics. Int. J. Fract. **138**, 47–73 (2006)
14. VIC 3D. Correlated Solutions Inc., Irmo (2020)
15. Hajjar, M., Bolzon, G., Zappa, E.: Experimental and numerical analysis of fracture in prestressed concrete. Procedia Struct. Integr. (2023). In press
16. Bolzon, G., Cocchetti, G.: On a case of crack path bifurcation in cohesive materials. Arch. Appl. Mech. **68**, 513–523 (1998)
17. Abaqus Theory Manual, Version 6.11. Dassault Systèmes Simulia Corp., Providence (2011)
18. Bolzon, G., Cocchetti, G.: Direct assessment of structural resistance against pressurized fracture. Int. J. Numer. Anal. Meth. Geomech. **27**, 353–378 (2003)
19. Bolzon, G.: Collapse mechanisms at the foundation interface of geometrically similar concrete gravity dams. Eng. Struct. **32**, 1304–1311 (2010)
20. Matlab Optimization Toolbox, Release 2020b, The Math Works Inc., Natick (2020)

Machine Learning-Based Structural Health Monitoring of Dams

Gabriella Bolzon[(✉)] and Caterina Nogara

Department of Civil and Environmental Engineering, Politecnico di Milano, Milan, Italy
{gabriella.bolzon,caterina.nogara}@polimi.it

Abstract. Dams are an important asset of the European Countries in the Alpine region. Italy, for instance, hosts more than 500 large dams, initially conceived to support the development of the Country in the period between the two world wars, and in the years 1950–1970. Most of them are still in operation to produce electricity, supply water for drinking and irrigation, contribute to the mitigation of the often dramatic consequences of current climate change. The safety assessment of these strategic infrastructures, which are getting old, is supported by sensor networks that collect environmental data and response measures. The number of monitoring devices and the acquisition frequency have generally increased over time. The large amount of gathered information is usually processed through interpretation functions, while machine learning tools have recently been introduced as early recognition methods of possible anomalies in the structural response. This contribution summarizes the most recent results obtained in this context, illustrates the performance of the most promising approaches, even if not yet fully validated, discusses the still open issues and presents the latest trends.

Keywords: Structural health monitoring · Aging dams · Early recognition methods · Machine learning tools

1 Introduction

The safety assessment of existing dams represents a task of paramount importance due to the essential services these structures provide and the possible severe consequences of even local failure. The integrity of these infrastructures is continuously monitored during their service life by acquiring data concerning the environmental conditions (e.g., water levels, air and water temperature) and, possibly, material aging, as well as observation variables representing the structural response (for instance, measured displacements in some specific positions in the dam body) [1, 2].

Typical seasonal trends of the environmental factors are, for instance, represented in Fig. 1. These data were provided by the formulators of one of the problems proposed at the Benchmark Workshop recently organized by the International Committee on Large Dams (ICOLD) [3].

The large amount of data displayed in Fig. 1 and Fig. 2 can be handled through various approaches, mentioned in the following Sect. 2, with the purpose of providing
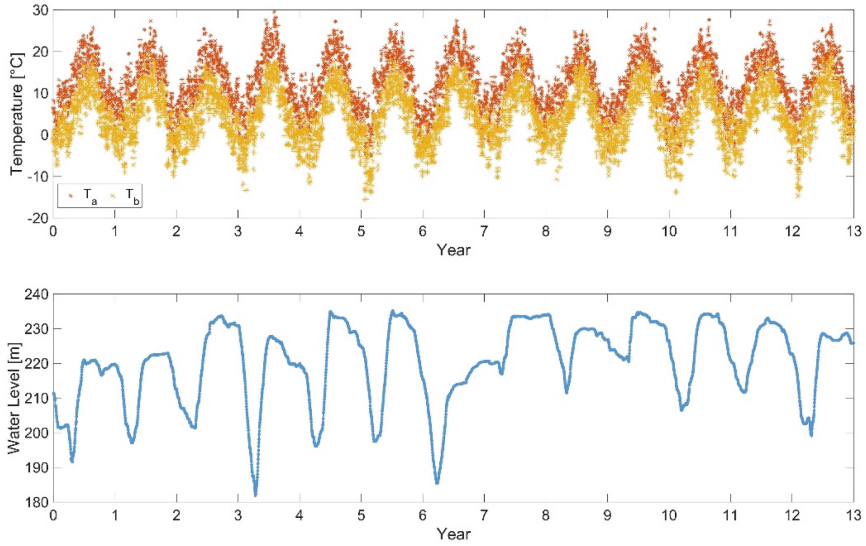
Fig. 1. Air temperatures (acquired by 2 sensors) and water level of the dam proposed as ICOLD benchmark problem [3]: daily measurements.
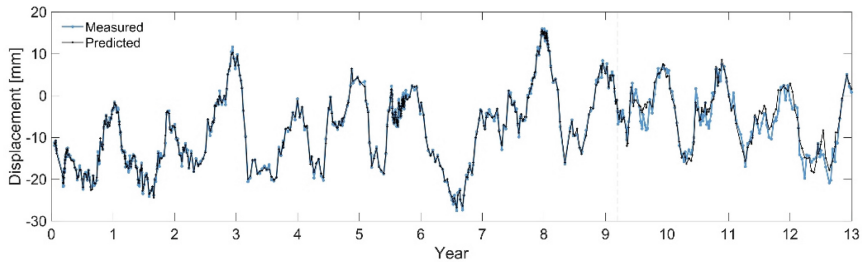
Fig. 2. Measured and predicted [4] displacement near the crest of the dam proposed as the ICOLD benchmark problem [3].

warnings in case of significant deviations of the examined structural variable from the expected trend and, possibly, identifying the anomaly source.

The observed differences may be due to faults in some measuring devices (easily solvable by recalibrating or replacing them), exceptional environmental conditions that have never occurred before, or actual structural damage, developed over time or resulting from sudden events, such as floods and earthquakes.

2 Interpretation Models

The large amount of data collected by monitoring systems operating on dams, as well as on other infrastructures [5], can be analyzed by:

– statistical approaches,

– physical simulation models and inverse analysis procedures,
– soft computing and machine learning (ML) tools.

Traditionally, the so-called statistical approach [6] has been mostly considered. It consists in the calibration of predefined fitting functions that relate the environmental variables with the observational quantities returned by the available measurement instruments. These methodologies are relatively simple to implement, and are validated by long-standing applications on various facilities. The statistical approach can be combined with data compression schemes and more advanced noise reduction procedures, which extract the essential features of the external action and structural response [7, 8]. However, validity is still to be confirmed in the case of atypical situations, either for extreme environmental conditions (that, unfortunately, more and more often occur) or for unique typological configurations.

In contrast, physical simulation models permit to customize the investigation to any dam characteristics. In this context, the main difficulties arise from the uncertainties that can affect the models, including the possible heterogeneity of the material distribution and/or the definition of the correct boundary conditions, such as the actual temperatures on the dam surface deduced from a few thermometers, and other environmental effects [9]. Calibrating the mechanical characteristics of natural or artificial joints, which can produce a non-linear system response, is also challenging.

The probabilistic distribution of the aforementioned factors can be analyzed within a stochastic framework [10, 11]. However, so far, this kind of investigation has mainly been applied to simplified models, due to the high cost of the related numerical analyses, while current research focuses on mitigating the computational burden by implementing surrogate analytical models trained on the results of a limited number of finite element simulations [12–14].

More recently, soft computing and ML tools have been explored to implement data-driven models directly based on monitored variables [15]. A variety of different algorithms have been tested, ranging from neural networks (NNs) and extreme learning machines (a type of feedforward NN with fewer parameters to calibrate and better generalizations capabilities) to regression trees and support vector machines, cast into a probabilistic context [16–22]. Usually, they are employed as regression models of the available data and are reasonably accurate in predicting the normal response of the considered structures under varying external actions [23, 24].

One major limitation of pure regression models is the impossibility of identifying the type and severity of local damages due to the lack of information about the corresponding structural responses. Hybrid models based on additional data collected from accurate finite element simulations of harmful scenarios, and on different types of pattern recognition algorithms, such as clustering or classification, are therefore almost inevitable.

3   Data Correlation and Sensitivity

Mostly, the regression analyses mentioned above are applied individually to the quantities returned by each measuring device. However, the physical response of a structural system to external actions must obey the governing equations of mechanics.

In some situations, the correlation between measured quantities (e.g., displacements) is as meaningful as the influence of environmental factors. This occurrence is, for instance, suggested by the relative importance indexes visualized in Fig. 3.
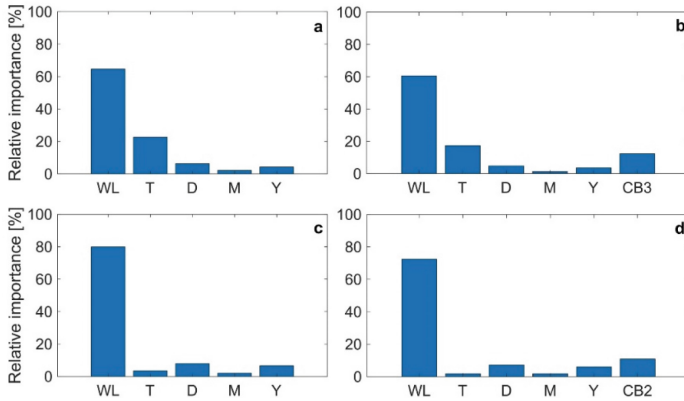
Fig. 3. Relative importance indexes of the input variables for two monitored points in the dam of the ICOLD benchmark problem [3]: point CB2 near the crest (a, b) and point CB3 at the foundation (c, d); un-correlated (a, c) and correlated (b, d) input. Influence of water level (WL), temperature (T), date (day: D; month: M; year: Y).

The graphs in Fig. 3 concern the response of the dam proposed as ICOLD benchmark problem [3], analyzed by boosted regression trees [4]. In this heuristic approach, the importance of predictors is evaluated according to Friedman's proposal [25], i.e. as the relative presence of every predictive variable, selected as the best partition during the training phase, and the error reduction achieved correspondingly.

Other methods, such as linear or logistic regression, consider quantifications based on the coefficients of the model. A methodology applicable to any algorithm, introduced by Breiman [26] for random forests, computes the increase in the prediction error after the permutation of the predictor variable whose relative importance is to be estimated. A significant increase in error indicates an important predictor.

Importance indexes can guide the variable selection and the reduction of the model complexity.

Response variables can be introduced in multi-target regression methodologies, analyzing and modeling all monitored quantities simultaneously [27]. Potentially, this approach allows to define the digital twin of a structure using the sole output of a large sensor network [28].

Alternatively, monitoring data can be added to the input set used in the training phase of ML algorithms, in order to improve their prediction performance. Conversely, changes in the expected spatial correlation degree might identify the location of ongoing damaging processes.

The joint analysis of all available information may also be exploited in multi-class classification methodologies to detect anomalies at an early stage, and to distinguish between different outliers, provided that an appropriate training is performed [29].

On the other hand, not all observation variables are affected to the same extent by the external action or by the internal evolution of the structural system, as sensitivity analyses show [30–32]. Predictions can then be improved by an adequate selection of the measurements to be considered. In long-existing dams, the number of sensors is often limited, and their placement may not be optimal for the detection of some anomalies. Further information may be occasionally or systematically acquired by radar monitoring, or through vision-based techniques, possibly mounting the appropriate equipment on drones [33, 34]. In this context, even digital images can be processed by neural networks and deep learning algorithms, to produce high-quality quantitative information [35].

4   Closing Remarks

Machine learning (ML) finds application in several engineering fields and supports the relevant technological advancements. The different methodologies developed in this context can be trained on actual data without introducing any a priori assumption on the input-output relationships.

In structural health monitoring applications, optimized algorithms perform well in predicting the normal response of even complex mechanical systems such as dams. Deviations of the observations from the expected trend highlight the malfunctioning of some measuring devices, or the occurrence of damaging phenomena.

In any case, the diagnostic analysis of dams cannot be based on ML approaches alone as training data for most potentially critical scenarios are usually not available. Therefore, the methodology must be complemented by defining first the most likely (or catastrophic, foremost to be prevented) failure modes. Corresponding (but artificial) monitoring records are then generated from numerical simulations performed on corrupted digital twins of the real facility. To be accurate, the models must be calibrated to the actual measurements. This process can involve considerable computing efforts, possibly mitigated by replacing traditional finite element analyses with analytical surrogates.

References

1. International Commission on Large Dams (ICOLD): Automated dam monitoring systems: guidelines and case histories. Technical Report B-118 (2000)
2. International Commission on Large Dams (ICOLD): Dam surveillance guide. Technical report B-158 (2012)
3. Malm, R., Hellgren, R., Klun, M., Simon, A., Salazar, F.: Theme A: Behaviour prediction of a concrete arch dam. In: 16th International Benchmark Workshop on Numerical Analysis of Dams, Ljubljana, Slovenia (2022)
4. Nogara, C., Bolzon, G.: Machine Learning tools applied to the prediction and interpretation of the structural behavior of existing dams. In: Procedia Structural Integrity, in press (2023)
5. Figueiredo, E., Brownjohn, J.: Three decades of statistical pattern recognition paradigm for SHM of bridges. Struct. Health Monit. **21**(6), 3018–3054 (2022)
6. Léger, P., Leclerc, M.: Hydrostatic, temperature, time-displacement model for concrete dams. ASCE J. Eng. Mech. **133**(3), 267–277 (2007)
7. Mata, J., Tavares de Castro, A., Sá da Costa, J.: Constructing statistical models for arch dam deformation. Struct. Control. Health Monit. **21**(3), 423–437 (2014)

8. Wei, B., Chen, L., Li, H., Yuan, D., Wang, G.: Optimized prediction model for concrete dam displacement based on signal residual amendment. Appl. Math. Model. **78**, 20–36 (2020)

9. Sivasuriyan, A., Vijayan, D.S., Munusami, R., Devarajan, P.: Health assessment of dams under various environmental conditions using structural health monitoring techniques: a state-of-art review. Environ. Sci. Pollut. Res. **29**, 86180–86191 (2022)

10. Hariri-Ardebili, M.A., Salazar, F.: Engaging soft computing in material and modeling uncertainty quantification of dam engineering problems. Soft. Comput. **24**, 11583–11604 (2020)

11. Hariri-Ardebili, M.A., Salazar, F.: Coupling machine learning and stochastic finite element to evaluate heterogeneous concrete infrastructure. Eng. Struct. **260**(114190), 1–13 (2022)

12. Fedele, R., Maier, G., Miller, B.: Health assessment of concrete dams by overall inverse analyses and neural networks. Int. J. Fract. **137**, 151–172 (2006)

13. Lin, C., Li, T., Chen, S., Yuan, L., van Gelder, P.H.A.J.M., Yorke-Smith, N.: Long-term vis-coelastic deformation monitoring of a concrete dam: A multi-output surrogate model approach for parameter identification. Eng. Struct. **266**(114553), 1–14 (2022)

14. Kang, F., Liu, X., Li, J., Li, H.: Multi-parameter inverse analysis of concrete dams using kernel extreme learning machines-based response surface model. Eng. Struct. **256**(113999), 1–17 (2022)

15. Hariri-Ardebili, M.A., Salazar, F., Pourkamali-Anaraki, F., Mazzà, G., Mata, J.: Soft computing and machine learning in dam engineering. Water **15**(917), 1–8 (2023)

16. Mata, J.: Interpretation of concrete dam behaviour with artificial neural network and multiple linear regression models. Eng. Struct. **33**(3), 903–910 (2011)

17. Xu, G.H.: Application of RBF neural network in dam deformation prediction. Appl. Mech. Mater. **675–677**, 261–264 (2014)

18. Chen, S., Gu, C., Lin, C., Zhao, E., Song, J.: Safety monitoring model of a super-high concrete dam by using RBF neural network coupled with kernel principal component analysis. Math. Probl. Eng. **2018**(1712653), 1–13 (2018)

19. Kang, F., Liu, X., Li, J., Li, H.: Concrete dam deformation prediction model for health monitoring based on extreme learning machine. Struct. Control. Health Monit. **24**(e1997), 1–11 (2017)

20. Cheng, J., Xiong, Y.: Application of extreme learning machine combination model for dam displacement prediction. Procedia Comput. Sci. **107**, 373–378 (2017)

21. Su, H., Chen, Z., Wen, Z.: Performance improvement method of support vector machine-based model monitoring dam safety. Struct. Control. Health Monit. **23**(2), 252–266 (2016)

22. Chen, S., Gu, C., Lin, C., Zhang, K., Zhu, Y.: Multi-kernel optimized relevance vector machine for probabilistic prediction of concrete dam displacement. Eng. Comput. **37**(3), 1943–1959 (2021)

23. Hellgren, R., Malm, R., Ansell, A.: Performance of data-based models for early detection of damage in concrete dams. Struct. Infrastruct. Eng. **17**(2), 275–289 (2020)

24. Mata, J., Salazar, F., Barateiro, J., Antunes, A.: Validation of machine learning models for structural dam behaviour interpretation and prediction. Water **13**(2717), 1–27 (2021)

25. Friedman, A.: Greedy function approximation: a gradient boosting machine. Ann. Stat. **29**(5), 1189–1232 (2001)

26. Breiman, B.: Random forests. Mach. Learn. **45**(1), 5–32 (2001)

27. Chen, S., Gu, C., Lin, C., Hariri-Ardebili, M.A.: Prediction of arch dam deformation via correlated multi-target stacking. Appl. Math. Model. **91**, 1175–1193 (2021)

28. Salazar, F., Toledo, M.Á., González, J.M., Oñate, E.: Early detection of anomalies in dam performance: a methodology based on boosted regression trees. Struct. Control. Health Monit. **24**(e2012), 1–16 (2017)

29. Salazar, F., Conde, A., Irazábal, J., Vicente, D.J.: Anomaly detection in dam behaviour with machine learning classification models. Water **13**(2387), 1–22 (2021)

30. Ardito, R., Bartolotta, P., Ceriani, L., Maier, G.: Diagnostic inverse analysis of concrete dams with statical excitation. J. Mech. Behav. Mater. **15**(6), 381–386 (2005)
31. Li, Z.: Global sensitivity analysis of the static performance of concrete gravity dam from the viewpoint of structural health monitoring. Arch. Comput. Methods Eng. **28**, 1611–1646 (2021)
32. Hariri-Ardebili, M.A., Mahdavi, G., Abdollahi, A., Amini, A.: An RF-PCE hybrid surrogate model for sensitivity analysis of dams. Water **13**(302), 1–21 (2021)
33. Niezrecki, C., Baqersad, J., Sabato, A.: Digital image correlation techniques for NDE and SHM. In: Ida, N., Meyendorf, N. (eds.) Handbook of Advanced Non-Destructive Evaluation, pp. 1–46. Springer, Cham (2018). https://doi.org/10.1007/978-3-319-30050-4_47-1
34. Reagan, D., Sabato, A., Niezrecki, C.: Feasibility of using digital image correlation for unmanned aerial vehicle structural health monitoring of bridges. Struct. Health Monit. **17**(5), 1056–1072 (2018)
35. Gonzales, R.C., Woods, R.E.: Digital Image Processing, 4th edn. Pearson, New York (2018)

A Study on the Safety Assessment of the Base Isolation System Regarding the Ductile Behavior of the Superstructure

Soheil Ramezani$^{(\boxtimes)}$ (iD)

International Institute of Earthquake Engineering and Seismology (IIEES), Tehran, Iran
s.ramezani@iiees.ac.ir

Abstract. In the code-based procedures such as the ones presented in the ASCE7 standard, the use of ductility resources is not allowed in the design of the super-structure in order to prevent structural damage and provide a high level of structural performance for all types of occupancies. But these code procedures suggest the use of ductility resources for design of the fixed-base systems is allowed even for the occupancy types which need high structural performance levels. The aim of this paper is to investigate the effect of seismic isolation on the ductility reduction factor of a structural system and comparing it between a fixed-base structure and an equivalent isolated superstructure. In this regard, a simplified method based on a single-degree-of-freedom system is proposed to assess the safety of the system considering a conditional probability of collapse as the safety measure. Then, a structural model corresponding to a low-rise frame with residential occupancy is constructed and the relationship between the ductility reduction factor and the design period of the system is extracted by applying a constant level of safety and performing a regression analysis. The results indicate that under the same safety level, the isolated superstructure can be designed with a higher ductility reduction factor compared with the corresponding fixed one. Moreover, the derived relationship shows that the ductility reduction factor follows a descending trend with increasing the selected design period of the superstructure.

Keywords: Base isolation · Ductility reduction factor · Safety

1 Introduction

The base isolation has been proved to be an efficient method in reducing seismic effects in structures. During the past decades, numerous researches have been done on the base isolation system to improve it from technical and practical aspects [1]. Owing to these researches, the design method for the base isolation system is well-established and is included in many modern seismic design codes such as ASCE7–22 standard [2].

In the current design codes, the use of ductility resources in design of base isolation system is prohibited or is strictly limited [3]; mainly because that the seismic codes intend to provide a high level of structural performance for the base isolation system. On the other hand, under the same importance category, these codes allow the use of

ductility resources in design of fixed-base structural systems. By applying the code provisions, there would be always a major discrepancy between the structural performance of a base-isolated structure with its fixed-base counterpart. This discrepancy may be more justifiable in case of important occupancies (e.g., hospitals), but it may be considered unnecessary in case of regular importance categories (e.g., residential or office occupancies). The unnecessary performance discrepancy between the fixed and isolated systems can be reduced by using higher ductility factors than the code-defined values. This leads to lower lateral design forces for the isolation system which brings benefits in reducing cost of isolation layer and construction cost of superstructure [4].

This paper aims to compare the design ductility reduction factor between a fixed-base system and its corresponding isolated one in which a constant safety constraint based on ASCE7-22 [2] is considered for both systems. In the study, through a parametric analysis, the ductility reduction factor is extracted as a function of fundamental period for a low-rise frame structure with a regular occupancy simulated by a single-degree-of-freedom model. The method of study and the obtained results are presented in the following sections.

2 Method of Study

2.1 Safety Measure

The conditional probability of collapse is considered as the safety measure in this study. For the design purpose, the safety is a more useful measure than the performance alone because it combines both the structural performance and the seismic hazard. To define the safety measure, simplified models for structural performance and the earthquake hazard are applied.

Figure 1 shows the probability of structural collapse as a function of earthquake return period (T_R) in which the collapse curve is simplified through the definition of collapse return period (T_c). By defining the simplified probability curve depicted in Fig. 1 and employing the Poisson model for distribution probability of the earthquake events, the conditional probability of collapse (P_c) can be expressed as Eq. 1. In this equation, $\delta(\cdot)$ is the Kronecker delta function and T_D is the design period of the structure. P_c can be derived in its simplest form as it is presented in Eq. 2.

$$P_c = \int_{T_{R,min}}^{T_{R,max}} \delta(T_R - T_c)\left(\sum_{n=1}^{\infty} \frac{\lambda^n e^{-\lambda}}{n!}\right)dT_R = 1 - e^{-\frac{T_D}{T_c}} \tag{1}$$

$$P_c \approx \frac{T_D}{T_c} \tag{2}$$

To determine the value of T_c, an incremental dynamic analysis (IDA) approach can be employed. To generate the different earthquake intensity levels required in the IDA analysis, the following relationship is selected [5].

$$S_{T_R} = \left(\frac{T_R}{475}\right)^n \tag{3}$$
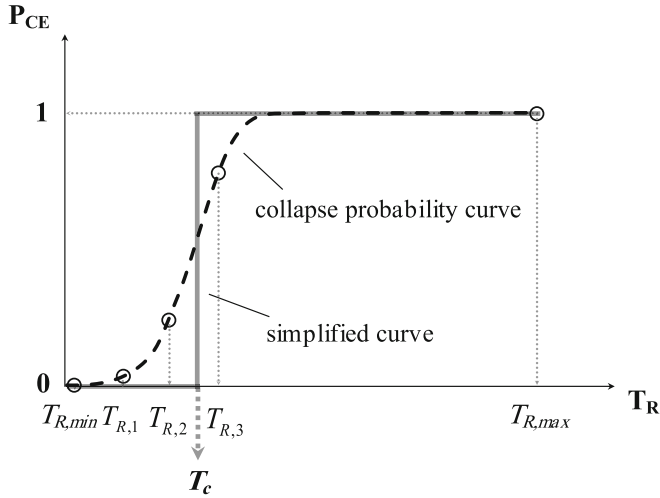
Fig. 1. A simplified model for probability of structural collapse.

2.2 Structural Modeling and Collapse Criterion

To simulate the seismic response of a fixed-base structure, a simple model based on a single-degree-of-freedom (SDOF) system is selected (Fig. 2a) incorporating the material nonlinearity by a rotational hinge at base. The hinge is able to model the softening behavior of the system by a negative post-yield stiffness. Using this hinge model, the force-displacement behavior of the fixed-base system under lateral loading is obtained as shown in Fig. 2(b) that is similar to the bilinear model employed in [6]. This figure presents the relationships between the model parameters and the design parameters such as ductility design factor (R_μ) and design base shear (V_d) defined by ASCE7 code. In order to model the base-isolated version of the structure, a link with linear behavior is inserted between the hinge and the ground representing the isolation layer (not shown for the sake of brevity). The stiffness of the link can be determined based on the mass and the isolation period of the system.

To determine T_c in Eq. 2 through the IDA analysis, a collapse criterion needs to be defined. To do so, a collapse criterion based on the equity of the resistant moment (i.e., M in Fig. 2a) and the destabilizing moment due to weight is selected for both fixed-base and base-isolated structures. In case of the isolated system, an additional criterion reflecting the failure of rubber isolator is considered. In the present study, it is assumed that the isolator fails if it reaches to a shear displacement which causes it to experience roll-out condition (i.e., roll-out instability).

It should be noted that the estimation of collapse drift (i.e., θ_c) in Fig. 2(a) needs a detailed structural model with member-by-member representation, but there is no such a model at the design stage, therefore another approach needs to be followed for the estimation of θ_c. In the current study, the θ_c value which gives the most compatible results with those suggested by the code is taken as the appropriate estimation of the collapse drift. This approach is more clarified through the case study presented in the next section.
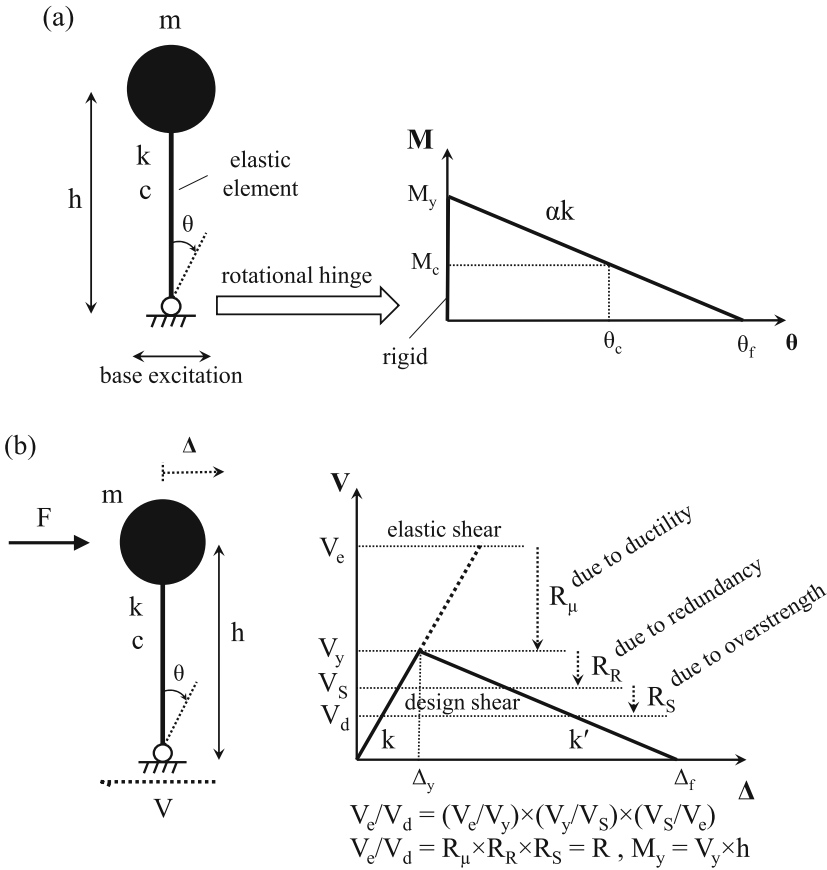
Fig. 2. Structural modeling of the fixed-base system.

3   Case Study

3.1   A Low-Rise Frame Structure

A four-story moment-resisting frame in two cases of fixed and isolated base is considered to be designed according to equivalent static force method suggested by ASCE7-05 [7]. The reason why ASCE7-05 code is employed is only because in the later versions of this code, a modification is made to the design spectrum to set the conditional probability of collapse equal to 1% in 50 years for regular occupancy types. In order to not to include the effects of this modification in the results, the older version of the design spectrum suggested by the ASCE7-05 is employed. The lateral load-resisting system of the frame is assumed to be of an intermediate moment-resisting type whose design and model parameters are given in Table 1.

The rotational hinge plays a key role in the behavior of the structural system. Figure 3 shows an example of hinge behavior with normalized force-displacement relationship using $F_y = 40 \, \text{kN}$, $\Delta_y = 0.01 \, \text{m}$ and $\alpha = -1\%$. A pinching model similar to that presented

Table 1. The design and model parameters of the fixed-base and isolated systems.

System type	Parameter	Value
Fixed-base /isolated	Importance factor	1.0
	Total mass - m (kg)	400,000
	Height - h (m)	14
	Spectrum parameters - S_{DS}, S_{D1}, T_L (s)	1.12, 0.60, 8
	$R_R \times R_S$	2.0
Isolated	Isolation period (s)	2.5
	Damping ratio of rubber isolator	0.1
	Roll-out shear strain	3

in this figure is applied in the case study. All the structural analyses are performed by the OpenSees program [8].
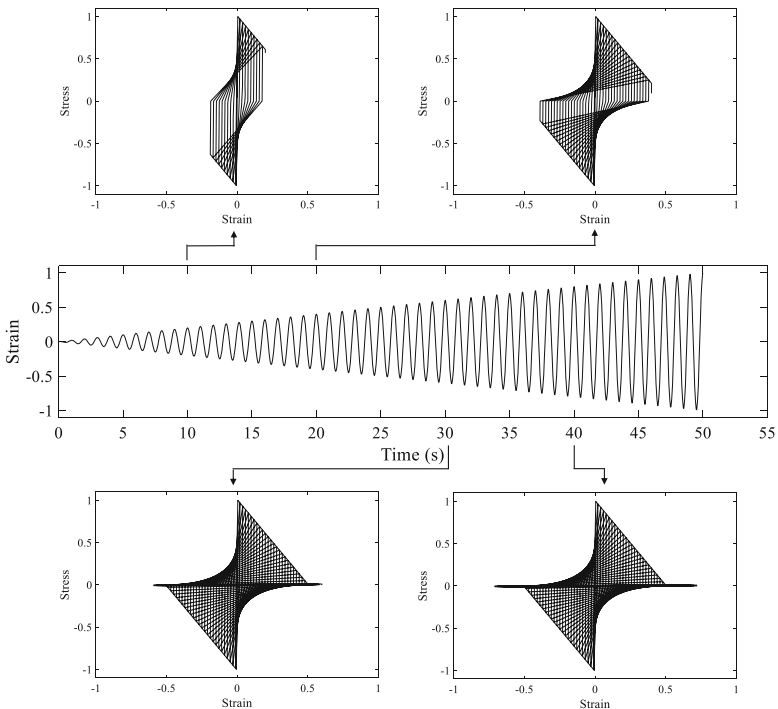
Fig. 3. An example of the hinge behavior.

By performing the IDA analysis with 15 spectrum-matched acceleration records, the values of T_c are estimated in terms of R_μ, T_n and θ_c as presented in Table 2. T_n is

the natural period of the system which is taken as the representative of the fundamental period of the structure defined in the equivalent static force method in ASCE7–05 [7]. In this table, R_μ and T_n are varied within the wide ranges to form the parametric space required for regression analysis. The three values for θ_c are chosen to later determine which of these values results in compatible R_μ and T_n with those defined by the code.

Table 2. The estimation of T_c in terms of R_μ, T_n and θ_c.

System type	R_μ	$T_n = 0.5$ s			$T_n = 0.75$ s			$T_n = 1.0$ s		
		$\theta_c =$ 5%	$\theta_c =$ 4.5%	$\theta_c =$ 4%	$\theta_c =$ 5%	$\theta_c =$ 4.5%	$\theta_c =$ 4%	$\theta_c =$ 5%	$\theta_c =$ 4.5%	$\theta_c =$ 4%
F	2	8875	6675	5275	6875	4475	3675	4075	3675	2275
F	3	5875	4475	2875	5475	2675	2075	3675	2675	1475
F	4	3675	3075	2475	3475	2275	1675	3275	2275	1675
F	5	3075	2075	1875	3075	1875	1475	2475	1675	1475
F	6	2275	1675	1275	2275	1475	1075	1475	1475	1075
I	2	22675	21875	21275	9675	8475	7675	7075	6275	4075
I	3	8475	7475	6475	4875	4675	3875	2875	2475	2275
I	4	6675	5475	4875	2875	2475	2275	2275	1875	1675
I	5	3675	3475	2875	2275	1675	1275	2075	1675	1075
I	6	2675	2275	1875	1875	1475	1075	1875	1475	1075

From Table 2, it is seen that the T_c values decrease with the increase of R_μ and T_n and θ_c. Besides, the table clearly shows the efficiency of the isolation system to shift the collapse period toward the higher ranges. However, as expected, this efficiency decreases with the softening of superstructure (i.e., increase of R_μ or T_n). It should be pointed that the softening of the superstructure due to R_μ refers to ability of the structural elements to deflect while maintaining the load-carrying capacity, whereas the softening due to T_n refers to the stiffness (i.e., dimensions) of the elements.

3.2   Regression Analysis

Having the collapse return periods in Table 2, a regression analysis is used to formulate the relationship between T_c, T_n and R_μ. The formula given in the following equation was found to be well-suited for efficient fitting in which a_1 to a_4 are constants. The fitting parameters obtained from the regression analysis are given in Table 3.

$$T_c \approx a_1 T_n^{a_2} R_\mu^{a_3} e^{a_4 T_n R_\mu} \tag{4}$$

Figure 4 and Fig. 5 illustrate the fitted surfaces for T_c using the different values of θ_cs in case of fixed-base and isolated structures, respectively. To extract the relationship between T_n and R_μ for the design purpose, a safety constraint is applied on each surface.

Table 3. The fitting parameters obtained from the regression analysis to formulate T_c.

Regression parameter	System type	$\theta_c = 5\%$	$\theta_c = 4.5\%$	$\theta_c = 4\%$	R-square ($\theta_c = 5\%$)	R-square ($\theta_c = 4.5\%$)	R-square ($\theta_c = 4\%$)
a_1	F	10180	7068	4625	0.9158	0.9787	0.9665
a_2	F	−0.8744	−1.123	−1.445			
a_3	F	−1.205	−1.459	−1.636			
a_4	F	0.09122	0.1816	0.2667			
a_1	I	16830	15440	12270	0.9908	0.9906	0.9922
a_2	I	−2.482	−2.707	−3.182			
a_3	I	−2.704	−2.944	−3.264			
a_4	I	0.4433	0.5008	0.5983			

To set the safety constraint, the target conditional probability of collapse suggested by ASCE7-22 [2] is applied in which the collapse probability of 1% in 50 years is defined as the acceptable level of safety for the buildings with ordinary risk category. To translate this probability to a safety constraint in the present work, the relationship given in Eq. 2 can be simply employed. By substituting $P_c = 0.01$ and $T_D = 50$ years in Eq. 2, T_c is obtained equal to 5000 years which this value is then intersected with each surface to extract the design relationships.

3.3 Results

The extracted design relationships between T_n and R_μ with different values of θ_c for each structural system are shown in Fig. 6. To choose which of the selected θ_cs is compatible with the code-defined values, the fundamental periods and the ductility reduction factors defined by ASCE7-05 [7] for intermediate steel and concrete moment-resisting frames are shown as two points in Fig. 6(a). This figure indicates that the obtained T_n-R_μ curve obtained by $\theta_c = 4.5\%$ have the most compatibility with the code design parameters. Therefore, the counterpart curves with $\theta_c = 4.5\%$ in Fig. 6(a) and Fig. 6(b) are selected as the accurate design relationship for both structural systems. Comparing the curves in Fig. 6(a) and Fig. 6(b) demonstrates that the T_n-R_μ relationship for the isolation system has less sensitivity to the variation of the collapse drift than the fixed-base system.

Finally in Fig. 7, the calculated T_n-R relationships for both structural systems are presented. This figure clearly shows that the isolated superstructure can be designed with higher R values than the ones for the fixed-base structure. On the contrary, in ASCE7–05 [7] and its later versions, the R value for the design of the isolation system is limited to a maximum value of 2 (i.e., $R_R \times R_S$) excluding the ductility (i.e., R_μ).
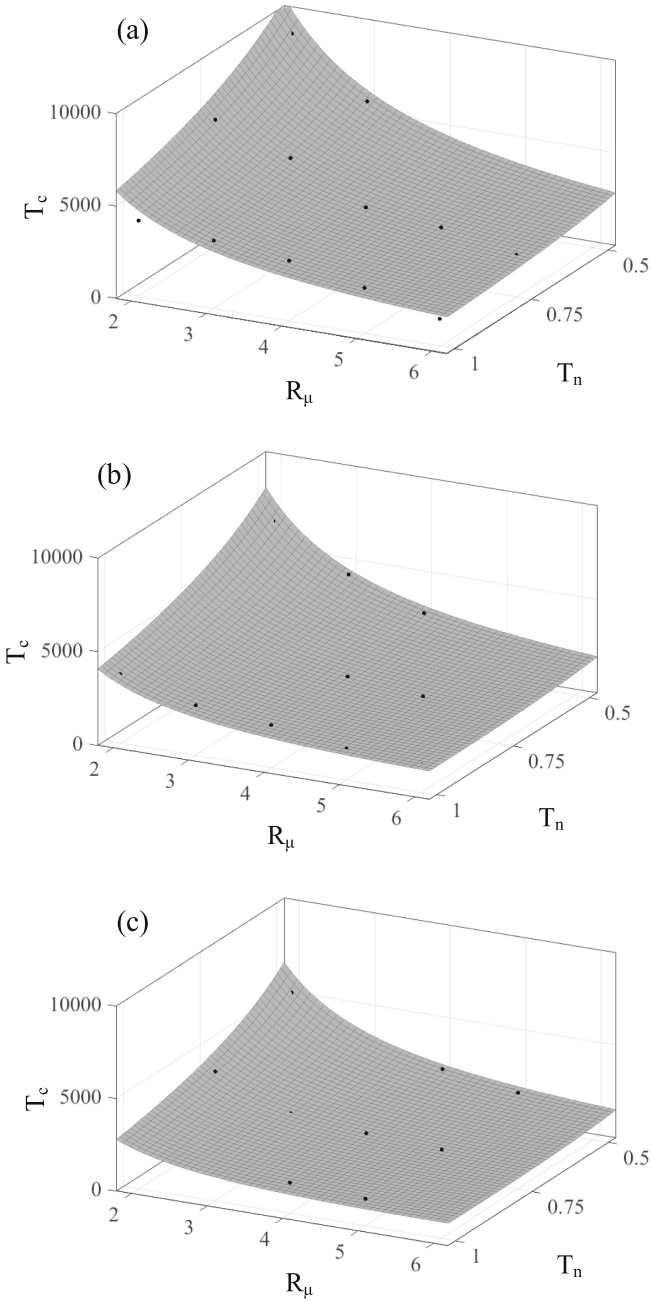
Fig. 4. The fitted surfaces for the collapse return periods of the fixed-base system obtained from: (a) $\theta_c = 5\%$, (b) $\theta_c = 4.5\%$, and (c) $\theta_c = 4\%$.
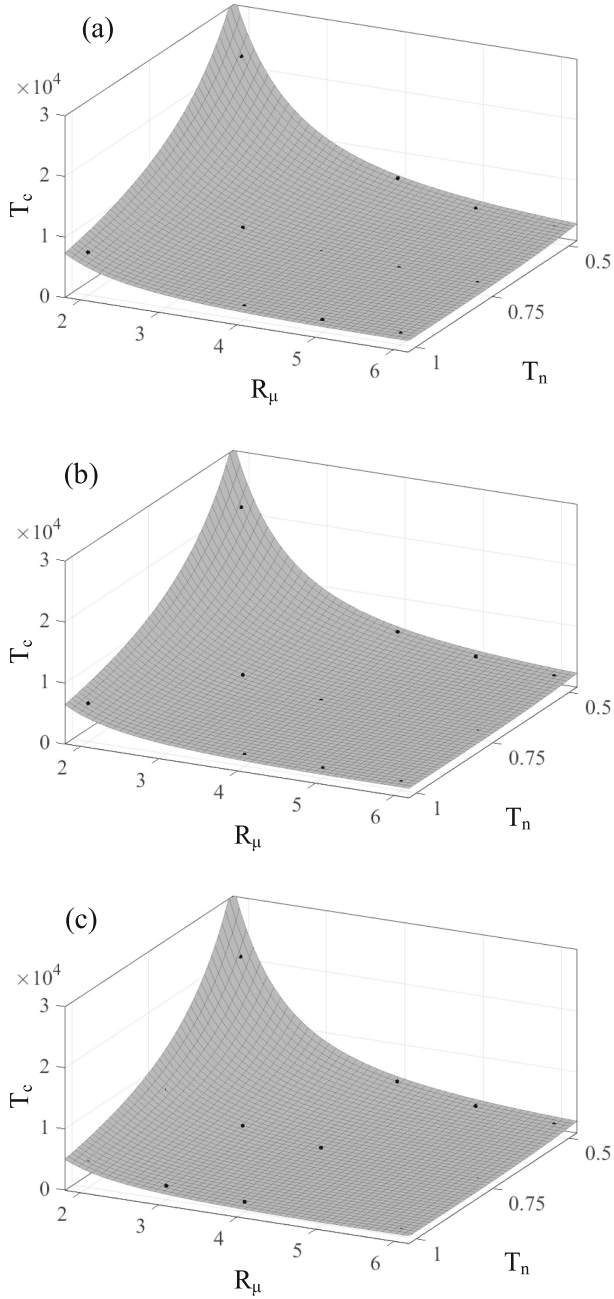
Fig. 5. The fitted surfaces for the collapse return periods of the base-isolated system obtained from: (a) $\theta_c = 5\%$, (b) $\theta_c = 4.5\%$, and (c) $\theta_c = 4\%$.

Fig. 6. The T_n-R_μ curves obtained from the different values of the collapse drift for: (a) the fixed-base system and (b) the base-isolated system.
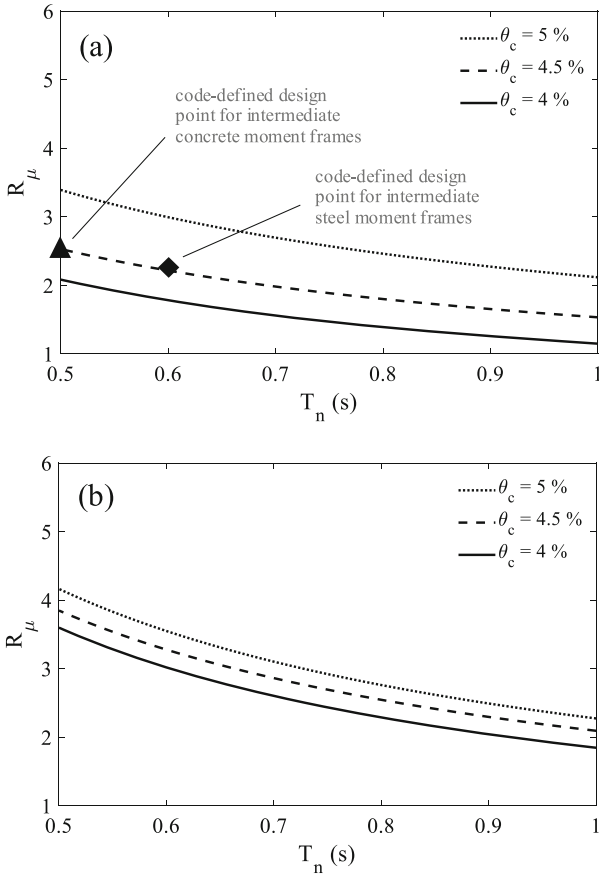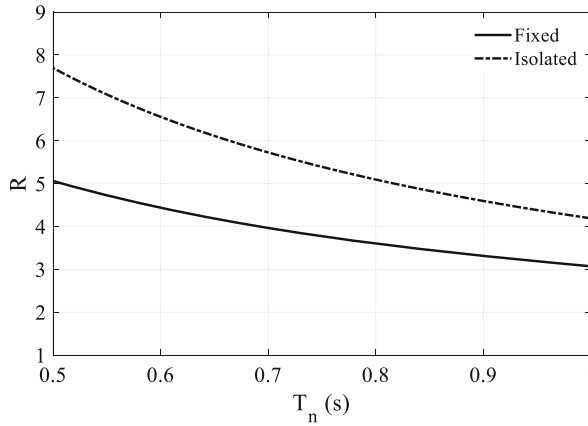
Fig. 7. The T_n-R curves obtained from $\theta_c = 4.5\%$ for the fixed-base and base-isolated systems.

4   Conclusion

In this paper, a simplified method based on a SDOF system was proposed to assess the safety of the system considering a conditional probability of collapse as the safety measure. Then, a structural model corresponding to a low-rise moment resisting frame with residential occupancy is constructed and the relationship between the ductility reduction factor and the design period of the system is extracted by applying an acceptable level of safety and performing a regression analysis. The results of the present study indicate that the ductility reduction factor follows a descending trend with increasing the selected design period of the superstructure under the same safety level. Moreover, the results demonstrate that the isolated superstructure can be designed with a higher ductility reduction factor compared with the corresponding fixed structure. Despite this, the design criteria in ASCE7 code do not allow to use the ductility resources for design of base-isolated structures even in case of building with ordinary risk category such as residential buildings. However, further investigation needs to be conducted on the acceptable amount of ductility use in design of base-isolated structures from the safety viewpoint.

References

1. De Luca, A., Guidi, L.G.: State of art in the worldwide evolution of base isolation design. Soil Dyn. Earthq. Eng. **125**, 105722 (2019)
2. American Society of Civil Engineers. (2022). Minimum design loads and associated criteria for buildings and other structures. American Society of Civil Engineers
3. Lopez-Almansa, F., Piscal, C. M., Carrillo, J., Leiva-Maldonado, S. L., & Moscoso, Y. F. (2022). Survey on Major Worldwide Regulations on Seismic Base Isolation of Buildings. Advances in Civil Engineering, 2022
4. Ramezani, S., Ziyaeifar, M.: A value-based design approach for base-isolated structural systems. Civ. Eng. Environ. Syst. **34**(1), 34–52 (2017)

5. Tsompanakis, Y.: Earthquake return period and its incorporation into seismic actions. Encyclopedia Earthq. Eng. 1–35 (2014)
6. Miranda, E., Akkar, S.D.: Dynamic instability of simple structural systems. J. Struct. Eng. **129**(12), 1722–1726 (2003)
7. American Society of Civil Engineers. (2005). Minimum Design Loads for Buildings and Other Structures-ASCE/SEI 7–05. American Society of Civil Engineers
8. McKenna, F., Fenves, G.L., Scott, M.H.: Open system for earthquake engineering simulation. University of California, Berkeley, CA (2000)

Analysis of Cable-Net Systems for Glass Facades

Vitalii Komlev$^{(\boxtimes)}$ and Josef Machacek

Faculty of Civil Engineering, Czech Technical University in Prague, Prague, Czech Republic
vitaliikomlev89@gmail.com, machacek@fsv.cvut.cz

Abstract. The paper deals with large glass facades using prestressed cable nets in exceptional buildings and halls in the recent decades, which has led to an intense investigations of the system. The facades typically use the laminated glass panes, point-fixed bolted or clamped systems and prestressed net of stainless steel cables. The paper describes numerical analyses of several finite element models concerning such cable-nets. The studied nets have 5 vertical and 4 horizontal cables and involve 4 principal elements: glass panes, point-fixed bolted fittings ("spiders"), the actual bolts and prestressed cables. The material of the glass panes is thermally strengthened and heat soaked thermally toughened safety glass, the "spiders" are typically of austenitic steel 1.4432, while cables are considered as Macalloy stainless steel strands. The proposed FE model using ANSYS software was submitted to a study of the mesh sensitivity, leading to a reasonable meshing and a successful validation based on published tests. The prestressing of the cables was applied as the initial tension. The façade wind loading was taken appropriately in accordance with EN 1991–1-4 as a corresponding pressure/suction and applied on the glass panes surfaces in the final loading step. The paper demonstrates the deflections and tension/stresses of the fractional parametrical study under the given prestressing and loading. The maximum deflections and tension/stresses found in the analyses are evaluated with the respect to acceptable values. The study provides a reasonable insight into the cable-net façade systems and specifies the orientation of the full follow-up parametrical study.

Keywords: Cable-net · Prestressing · Glass facade · Nonlinear Analysis

1 Introduction

Recent frequent design of large prestressed cable-net glass facades in exceptional buildings and halls (see Fig. 1) initiated the intensive investigations into the respective load carrying elements. Both experimental [1–3] and theoretical [4–6] studies are available. These facades are usually using laminated glass panes (typically from 2×6 mm to 2×12 mm, depending on pane sizes, with two or more 0.38 mm interlayer PVB sheets), point-fixed bolted (spider) or clamped system and prestressed nets from stainless steel cables with diameter of 19–36 [mm]. The cable-nets may be of various forms, e.g. as a single layer one-way cable system, double layer planar or double layer curved systems. Typical square meshes of the nets range from 1300–1500 [mm] or similar rectangular ones up to 2100×2400 [mm]. Some appraisal of the systems was described in the previous paper of the Authors.

Fig. 1. a: Sea-Tac Int. Airport Seattle (2005), **b:** Beijing New Poly Plaza (2007), **c:** China Maritime Museum Shanghai (2009), **d:** Mennica Tower Warsaw (2019).

The paper deals with numerical analyses of typical planar prestressed cable-net façade systems. Some details of the final element approach are described and the results of a preliminary parametrical study are presented.

2 Numerical Analysis

2.1 Description of Models and Used Data

Investigation of the planar prestressed cable façade behavior was concentrated on three deliberately chosen examples in accordance with Fig. 2. Model 1 with glass panes of 1.2×1.2 [m] and due to a gap between the adjacent glass panes of 5 mm (filled-in by a sealant) with the total size 7.22×6.015 [m], Model 2 with glass panes 1.5×1.5 [m] and the total size 9.02×7.515 [m], Model 3 with glass panes 1.8×1.8 [m] and the total size 10.82×9.015 [m]. The total and panes dimensions are presented in Table 1.
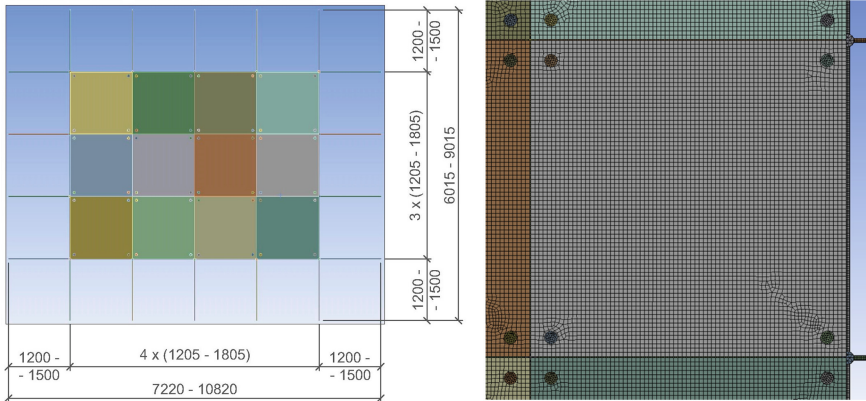
Fig. 2. Finite element model: General view and the example of one glass pane FE meshing.

Table 1. Models under investigation.

Model [mm]	Total dimensions [mm]	Glass pane size[mm]	Number of panes
1	7220 × 6015	1200 × 1200	12
2	9020 × 7515	1500 × 1500	12
3	10820 × 9015	1800 × 1800	12

Table 2. Laminated glass panes introduced in the study according to EN 16612.

Laminated panes [mm]	Equivalent thickness for deflections [mm]	Equivalent thickness for stress [mm]
4 + 0.76 + 4	6.63	7.32
6 + 0.76 + 6	9.75	10.74
8 + 0.76 + 8	12.86	14.15
10 + 0.76 + 10	15.98	17.57
12 + 0.76 + 12	19.10	20.98

The glass panes are attached to the net by point-fixed bolted (spider) fittings made of stainless steel. The spiders (e.g. of the grade 1.4404) have two holes for joining with horizontal and vertical cables of the façade net. The laminated glass is commonly used in the system, composed of two thermally toughened safety glass panes and interlayer of PVB (polyvinylbutyral) in accordance with prEN 16613 [7]. The equivalent thickness of laminated glass for calculating bending deflection in accordance with EN 16612 [8] and CEN/TS 19100-2 [9] is given by formula:

$$h_{ef,w} = \sqrt[3]{\sum_i h_i^3 + 12\omega\left(\sum_i h_i h_{m,i}^2\right)} \tag{1}$$

and the equivalent thickness for calculating the stress of the glass ply is

$$h_{ef,\sigma} = \sqrt{\frac{h_{ef,w}^3}{h_i + 2\omega h_{m,i}}} \tag{2}$$

where for the laminated glass with two plies of the same thickness h_i is the value of $h_{m,i}$ the distance between centroid of a ply and centroid of the laminated glass (incl. the PVB layer). The shear transfer coefficient due to the PVB interlayer is taken for wind gust load and family No. 1 as $\omega = 0.3$. The resulting equivalent thicknesses are presented in Table 2.

The mechanical and physical properties of the glass (thermally strengthened to EN 12150–1 [10] and heat soaked thermally toughened safety glass to EN 14179-1) in the following analyses were considered in accordance with EN 16612: modulus of elasticity

70 GPa, density 2500 kg/m3, compression strength of 1000 MPa and Poisson's ratio 0.23. The design bending strength for the thermally toughened safety glass to EN 14179-1[11] was taken accordingly to EN 16612 using formula:

$$f_{g,d} = \frac{k_{mod} k_{sp} f_{g,k}}{\gamma_{M,A}} + \frac{k_v \left(f_{b,k} - f_{g,k}\right)}{\gamma_{M,V}} \tag{3}$$

where for the analysis the load duration factor was taken as $k_{mod} = 1.0$, the glass surface profile factor $k_{sp} = 1.0$, characteristic bending stress for the prestressed glass $f_{bk} = 120$ MPa, the characteristic value of the bending strength of annealed glass $f_{gk} = 45$ MPa, the strengthening factor for the horizontal toughening $k_v = 1$ and partial factors for the annealed and surface prestressed glass for class CC2 consequences in accordance with EN 19100–1 [12] as $\gamma_{MA} = 1.8$ and $\gamma_{MV} = 1.2$, for class CC3 $\gamma_{MA} = 2.0$ and $\gamma_{MV} = 1.3$. The resulting design bending strength for the laminated glass was considered as $f_{gd} = 82.5$ MPa (for CC2 class) and $f_{gd} = 75.7$ MPa (CC3 class).

Cables were considered as Macalloy stainless steel strands 1×19 with diameters of 12, 14, 16 and 19 [mm], modulus of elasticity 107 GPa, breaking and design loads according to Table 3. The prestressing was assumed as 30% of the design loading in accordance with the published recommendations.

Table 3. Macalloy stainless steel 1×19 strands used in the study.

Diameter [mm]	Breaking load [kN]	Design load [kN]	Prestressing load [kN]
12	102.0	68.0	20.4
14	139.0	92.7	27.8
16	182.0	121.3	36.4
19	212.0	141.3	42.4

2.2 Numerical Modelling

ANSYS 2021/R2 software using Python code for a facilitation of the work with data was used throughout the numerical study.

In the finite element (FE) model the glass was applied as GLASS material type of ANSYS library. Cables were introduced as CABLE element type. The connection fitting (spiders) and bolts were modelled as SOLID element types.

All contact pairs of the principal elements mentioned above have a frictional connection between their contact surfaces with the appropriate friction coefficients (stainless steel - stainless steel 0.18, stainless steel - glass 0.12, fittings – cables are fixed). The cable ends on one side have movement restrictions in all axes. The prestressing of cables was applied on each cable and, therefore, the cable has a free movement on one end in the direction of the axis along which was applied the prestressing force.

A study of FE meshing was accomplished to find an optimal (economic and adequately faithful) mesh in all involved model elements. The mesh sensitivity test was

conducted on a simple finite elements model, which consisted of 2 × 2 cables only with one glass pane. The mesh sizes were reduced step by step until the response of the model didn't demonstrate significant changes. Finally the mesh shown in Fig. 3 was adopted in glass panes, while for cables the element length of 100 mm was used. Meshing of spiders and bolts is shown in Fig. 3.
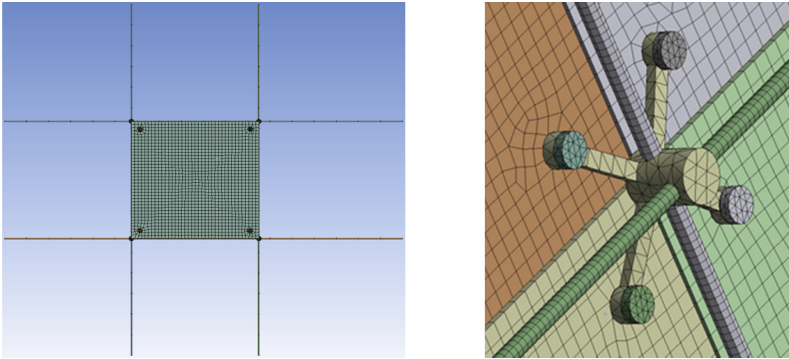
Fig. 3. Study of FE glass pane meshing and FE used in spiders and bolts.

The proposed numerical model was successfully validated based on experiments by Yussof (2015) in the previous paper by the Authors (2022). In this validation the clamped glass pane to cables connection was considered. The experiment had 7 × 7 cable-net with cable spacing of 305 mm, each with diameter of 4 mm and glass pane of 4 mm thickness. Three different prestresses were applied. Validation of deflections resulted in maximal differences of 6%. Another verification of the modelling was performed using numerical results by Shang (2014), based on point-fixed bolted (spider) connection. Here 4 × 6 cable-net was used with cables of diameter 22 mm and glass panes of 15 mm thickness, see Fig. 4. The cable prestress was considered as 50 kN. The comparison of results and current analysis for a wind loading of 1 kPa is shown in Fig. 4.
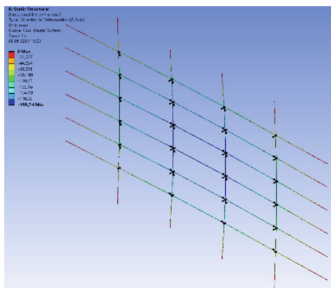
Deflections:
Shang: max. 208.7 mm
Current analysis: max 198.2 mm
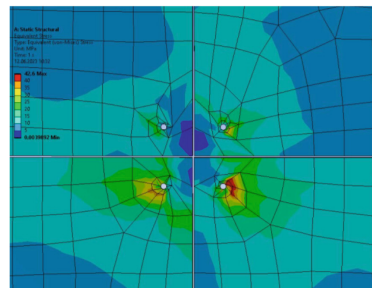
Stresses in glass under connection:
Shang: max 53.35 MPa
Current analysis: max 42.6 MPa

Fig. 4. Verification based on the cable-net presented by Shang with bolted attachment

The differences of both analyses are 5% in deflections and 20% in stresses of glass. Such variance is acceptable, taking into consideration the very local character of stresses under spider connections.

3 Parametrical Study

The study demonstrates a detailed deflections and stresses of the cable-net finite element models under the prestressing and given load.

The loading of the models respects the façade wind loads in accordance with EN 1991-1-4 [13] (region III, terrain III, force coefficients for suction -1.2) as a characteristic pressure of $F_{wk} = 1$ kPa (in case of the serviceability limit states, i.e. for deflections) and design pressure of $F_{wd} = 1.5$ kPa (in case of ultimate limit states, i.e. for stresses and cable loads). These loadings were applied as the uniform loadings following the cable prestress in the next, final loading step.

Deflections for the characteristic loading (to minimize stresses on the edge seal or ensure the proper fixings) are limited in accordance with EN 16612 to $L/65$ or 50 mm with L as the shorter span. Nevertheless, due to the large façade sizes the first requirement is taken into account only, which gives for Model 1 6015/65 = 92.5 mm, Model 2 7515/65 = 115.6 mm and Model 3 9015/65 = 138.7 mm.

Results of Model 1 analysis are presented in Table 4, while for other pane sizes are to be presented in the same format in the follow-up paper.

The results not meeting the required values (for glass $f_{gd} > 75.7$ MPa according to CC3 class and deflection greater than 92.5 mm) are highlighted in bold and indicate the necessity to use in this case cables with diameter at least 16 mm.

Table 4. Results of analysis for Model 1.

Glass panel size [mm]	Laminated glass [mm]	Cable diameter [mm]	Cable prestress [kN]	Max. cable load [kN]	Max. glass stress [MPa]	Max. deflection [mm]
1200 × 1200	4 + 0.76 + 4	12	20.4	28.8	**94.3**	**141.3**
	6 + 0.76 + 6		20.4	28.8	**79.7**	**134.5**
	10 + 0.76 + 10		20.4	30.0	65.9	**128.6**
	4 + 0.76 + 4	14	27.8	34.9	**81.4**	**112.5**
	6 + 0.76 + 6		27.8	34.9	64.4	**107.3**

(continued)

For an illustration, the deformed cable-net corresponding to glass panel 1200x1200 [mm] with laminated glass 6 + 0.76 + 6 [mm] and cable diameter 16 mm presented in

Table 4. (*continued*)

Glass panel size [mm]	Laminated glass [mm]	Cable diameter [mm]	Cable prestress [kN]	Max. cable load [kN]	Max. glass stress [MPa]	Max. deflection [mm]
	10 + 0.76 + 10		27.6	36.1	55.3	**102.5**
	4 + 0.76 + 4	16	36.4	42.2	75.7	91.5
	6 + 0.76 + 6		36.4	42.5	58.6	87.0
	10 + 0.76 + 10		36.4	43.9	51.8	83.6
	4 + 0.76 + 4	19	42.4	48.9	68.9	79.3
	6 + 0.76 + 6		42.4	48.0	40.3	74.9
	10 + 0.76 + 10		42.4	49.8	37.7	72.4
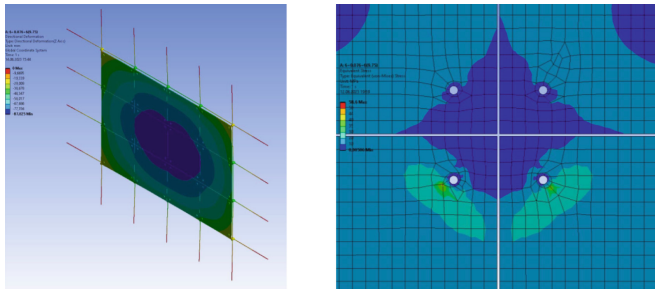
Fig. 5. Cable net with cables of diameter 16 mm and laminated glass 6 + 0.76 + 6 [mm]: Deformed cable-net under characteristic loading and stresses under design loading.

Table 1 is shown in Fig. 5. The stress distribution in the glass under point fixing is also shown in Fig. 5.

The table results demonstrate the increase of the final cable forces in comparison with given prestress. With greater cable diameters the local glass stress decrease significantly and with the glass pane thickness as well. The decisive parameter for a possible design is however the deflection and an appropriate diameter of cables need to comply with the limiting requirements.

4   Conclusions

Numerical modeling of the façade cable-net prestressed system is presented. Based on a survey of realized facades and published numerical and experimental analyses the investigation program was proposed, embracing a spectrum of cable-nets with various

parameters. The nets of prestressed stainless steel cables with point-fixed bolted (spider) fittings and laminated glass panes are analyzed using ANSYS software. The entry data respect the current European standards for glass, including relevant wind loading in serviceability and ultimate limit states.

The presented results cover the first part of the parametric studies concerning cable-nets with glass panes of size 1.2×1.2 [m], various cable diameters and various laminated glass panes thicknesses. The numerical model was validated and verified using published experiments and numerical results. The cable prestress was taken as 30% of their design capacity in accordance with common practice.

Results of the study in the Table 4 demonstrate the applicability of the analysed variants. From both serviceability limit states (limited by deflections of $L/65$) and ultimate limit states (limited by maximum glass stresses for CC3 class consequences) follows that the cables of diameter 12 and 14 are not suitable in the studied cable-net arrangement. Paradoxically under the given loading and size of the cable-net the cable capacities are not exhausted and their load surpass the prestress not much. Rather different situation occurs in larger sizes of cable-nets under continuing analyses.

References

1. Yussof, M.M.: Cable-net supported glass façade systems. PhD Thesis, University of Surrey, p. 279 (2015)
2. Yang, L., Shi, G., Yin, H., Shi, X., Guo, Z.: Full-scale experimental study on the influence of damages on the static behavior of the single-layer cable net structure. Structures **3**, 153–162 (2015)
3. Marzuki, N.A., Yussof, M.M., Keong, C.K., Min, Y.H.: Experimental performance of the cable-net structure supported glass systems with cable damages. In: Cecot, W., et al (eds.), 4th Polish Congress of Mechanics and the 23rd International Conference on Computer Methods in Mechanics, Conference Proceedings, vol. 2239, pp. 0200301–02003019, AIP Publishing, Krakow (2020)
4. Shang, C. D.: Numerical simulation and analysis of the mechanical behaviour of cable supported glass façades. PhD Thesis, UPC University of Barcelona, p. 171 (2014)
5. Piyasena, R.R.C., Thambiratnam, D.P., Chan, T.H.T., Perera, N.: Comparative analysis of blast response of cable truss and cable net façades. Eng. Failure Anal. **104**, 740–757 (2019)
6. Komlev V., Machaček, J.: Cable-net systems supporting glass facades. In: Fišer, C., Náprstek, J. (eds.), International Conference on Engineering Mechanics 2022, pp. 205–208, ITAM, Czech Academy of Sciences, Milovy (2022)
7. EN 16613 Glass in building — Laminated glass and laminated safety glass — Determination of interlayer mechanical properties, p. 22 (2019)
8. EN 16612 Glass in buildings - Determination of the lateral load resistance of glass panes by calculation, CEN, p. 52 (2019)
9. CEN/TS 19100–2 Design of glass structures - Part 2: Design of out-of-plane loaded glass components, EN-CENELEC, p. 35 (2021)
10. EN 12150–1+A1 Glass in building - Thermally toughened soda lime silicate safety glass - Part 1: Definition and description, p. 36 (2020)

11. EN 14179–1 Glass in building - Heat soaked thermally toughened soda lime silicate safety glass - Part 1: Definition and description, p. 44 (2005)
12. EN 19100–1 Design of glass structures - Part 1: Basis of design and materials, EN-CENELEC, p. 44 (2021)
13. EN 1991–1–4 Eurocode 1: Actions on structures – Part 1–4: General actions – Wind loads, p. 124 (2005)

Investigating the Inelastic Performance of a Seismic Code-Compliant Reinforced Concrete Hospital Under Long Sequence of Ground Motions Records

Sasan Babaei[✉] , Ahed Habib , Mahmood Hosseini , and Umut Yildirim

Civil Engineering Department, Eastern Mediterranean University, Famagusta, North Cyprus, Turkey

{22600309,ahed.habib,mahmood.hosseini,umut.yildirim}@emu.edu.tr

Abstract. In recent years, the seismic design of buildings has become an increasingly important issue due to the devastating earthquakes that have occurred around the world. In many regions, including North Cyprus, building codes have been developed to ensure that new constructions are designed to withstand seismic hazards. However, simply complying with building codes does not guarantee that a building will perform well during a seismic event. The inelastic behavior of a structure can significantly affect its seismic performance and may compromise its ability to remain functional and safe during and after an earthquake. Hospitals are critical facilities that must be designed to remain operational during and after a seismic event. The consequences of a hospital's failure during an earthquake can be severe, as it can impact the ability to provide medical care to those in need. This paper presents a case study on the inelastic performance of a seismic code-compliant reinforced concrete hospital designed according to the TNRC-SC2015 requirements under a long sequence of ground motions records. Within the study context, a nonlinear time-history analysis is conducted using SAP2000 software to simulate the seismic response of the hospital. In general, the study highlights the effectiveness of designing hospitals to meet the TNRC-SC2015 requirements under a strong and long sequence of earthquake loads taking the recent Turkey-Syria earthquake as the case study.

Keywords: Reinforced concrete · Hospital design · Sequence of ground motions · Nonlinear response history analysis

1 Introduction

Seismic events have shaped the narrative of structural engineering and urban planning globally. Several devastating earthquakes in the past years have drawn attention to the seismic vulnerability of built environments, revealing gaps in our understanding of seismic design and the resilience of structures under seismic loads (Shokrabadi & Burton, 2018; Mahat et al. 2022). This has generated increased interest in seismic design research,

particularly for reinforced concrete (RC) buildings that constitute a significant propor-
tion of the world's infrastructure. Modern building codes, such as the TSC2007, and the
Turkish Republic of Northern Cyprus Seismic Code (TNRC-SC2015) in North Cyprus,
reflect our understanding of the seismic performance of structures and are intended
to ensure that new constructions are designed to withstand seismic hazards (Jeong,
Mwafy, & Elnashai, 2012). However, compliance with these codes does not always
equate to good seismic performance (Huang, Qian, Zhuang, & Fu, 2012). The inelastic
behavior of a structure during an earthquake, defined by its ability to deform without
losing its strength, has a significant impact on its seismic performance (Iervolino, Chioc-
carelli, & Suzuki, 2020; Zhai, Zheng, Li, & Xie, 2015). When we turn our attention to
critical facilities such as hospitals, this issue becomes even more pressing. Hospitals
are vital structures that must remain functional during and after seismic events, as their
failure could have severe consequences on the delivery of emergency medical care (Jeon,
DesRoches, Lowes, & Brilakis, 2015). This necessitates a thorough understanding and
application of seismic design principles in the context of hospital construction. Recent
advancements in understanding seismic behavior and computer-aided design technolo-
gies have made it possible to conduct in-depth studies on the seismic performance of
structures. One such technology, the SAP2000 software, allows for nonlinear time-
history analysis to simulate the seismic response of a structure under a sequence of
ground motions (Qiao, Lu, & Yu, 2022). This computational approach has proved use-
ful in understanding the complex behavior of structures under earthquakes, especially
their response to mainshock-aftershock sequences, which can lead to cumulative dam-
age (Ruiz-García, Marín, & Terán-Gilmore, 2014). Ground motion records can exhibit
significant variations, and the long-term sequence of these records can have a profound
impact on the seismic performance of structures (Khatami, Gerami, Kheyroddin, & Siah-
polo, 2020). For RC structures, these sequences can lead to the progressive accumulation
of damage, especially if the structures are not designed and maintained appropriately
(Rajabi & Ghodrati Amiri, 2022; Afsar Dizaj, Salami, & Kashani, 2022). The goal of
this study is to assess the inelastic performance of a seismic code-compliant RC hospital
designed according to TNRC-SC2015 requirements under a long sequence of ground
motion records, using the real-world record of the 1997 Umbria-Marche earthquake in
Italy. Specifically, this study aims to evaluate the effectiveness of the TNRC-SC2015
requirements in ensuring that a hospital remains operational and safe under a strong and
long sequence of earthquake loads. The study employs a nonlinear time-history analysis
through SAP2000 software to simulate the seismic response of the hospital. The results
of this study are expected to contribute valuable insights to the field of seismic design,
particularly for critical facilities such as hospitals.

2   Materials and Methods

This research conducted a comprehensive analysis of a newly constructed hospital
located in Kyrenia, Cyprus, utilizing the advanced capabilities of the SAP2000 soft-
ware. The hospital is a three-dimensional structure designed in compliance with the
TNRC-SC2015 standard, constituting a basement and two stories above ground level.
As depicted in Fig. 1, the building is characterized by coupled reinforced concrete (RC)

frames integrated with shear walls in both X and Y directions, thus enhancing its seismic resistance.
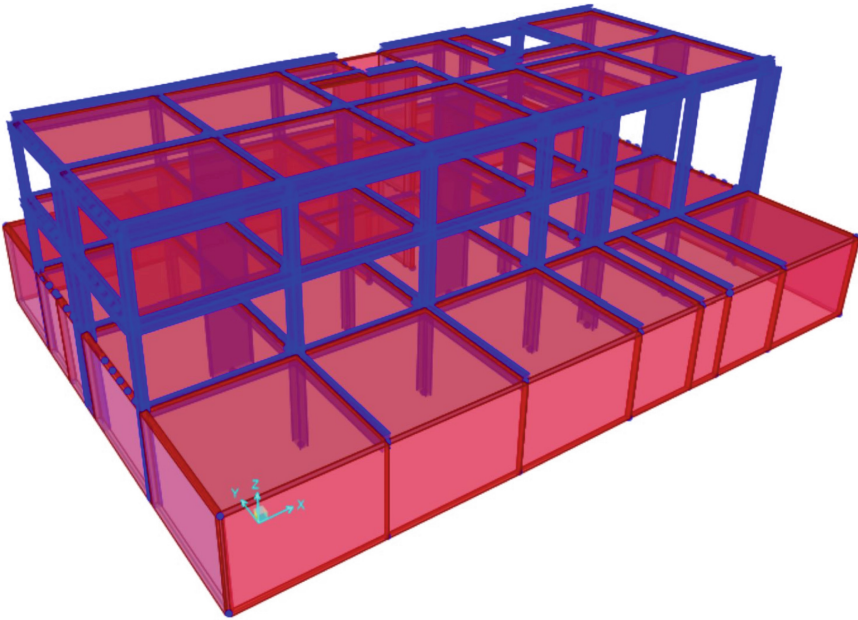
Fig. 1. Finite element model of the hospital structure developed in SAP2000.

The construction materials adopted for the building include concrete of two grades, C25 and C30, utilized for different components. The reinforcement type employed is S420, a high-strength steel variant commonly used in modern constructions. The choice of these materials aligns with the provisions of the TNRC-SC2015 standard and seeks to maximize the building's structural resilience. For the analysis, the Nonlinear Response History Analysis (NRHA) method was employed. The NRHA approach was chosen because of its capability to assess a structure's performance under sequential ground motions, including foreshocks, mainshocks, and aftershocks. This approach facilitates a detailed understanding of cumulative damage on a code-compliant structure subjected to repeated seismic loading. The seismic record chosen for the analysis is the real-world record of the 1997 Umbria-Marche earthquake in Italy, a seismic event with a considerable magnitude and extended sequence of ground motions. The earthquake record was sourced from the reliable PEER database, ensuring the accuracy and reliability of the seismic loading applied in this study. In the NRHA, the horizontal components of the earthquake record were applied to the X and Y directions of the model, while the upward component was applied in the Z direction. This simulates the multi-dimensional nature of real earthquake ground motions and captures the comprehensive seismic response of the structure. To incorporate the material nonlinearity in the analysis, a combination of Fiber and ASCE41–17 code-based hinges models were used for the shear walls and

the frame elements, respectively. This approach helps in modeling the complex, non-linear behavior of the RC members under seismic loading. The analysis also accounted for the P-delta effects, which refer to the changes in geometry and subsequent stresses that structures experience under lateral loads. These effects are crucial in capturing the structure's overall stability under the seismic load. However, this study did not consider soil-structure interactions, which could further influence the seismic response of the building. Despite this limitation, the adopted methodology provides a robust and comprehensive understanding of the building's seismic performance under a sequence of ground motions.

3 Results and Discussions

Figure 2 portrays the roof displacement of the investigated model in the X and Y directions, highlighting that both directions exhibit a similar trend of peak values with the maximum surpassing 0.04 m displacements. This result indicates the effect of the long sequence of ground motions records on the structural displacement, where the reinforced concrete hospital experiences similar displacement magnitudes in both the X and Y directions. The comparable trends suggest that the structure experiences fairly uniform inelastic performance under the impact of the seismic event. The base shear versus roof displacement of the investigated model for both X and Y directions, represented in Figs. 3 and 4, respectively, illustrate the interplay between the two variables. As the roof displacement increases, a corresponding increment in base shear is evident, pointing towards a progressive strain in the structure's inelastic state due to the ground motion's effects.
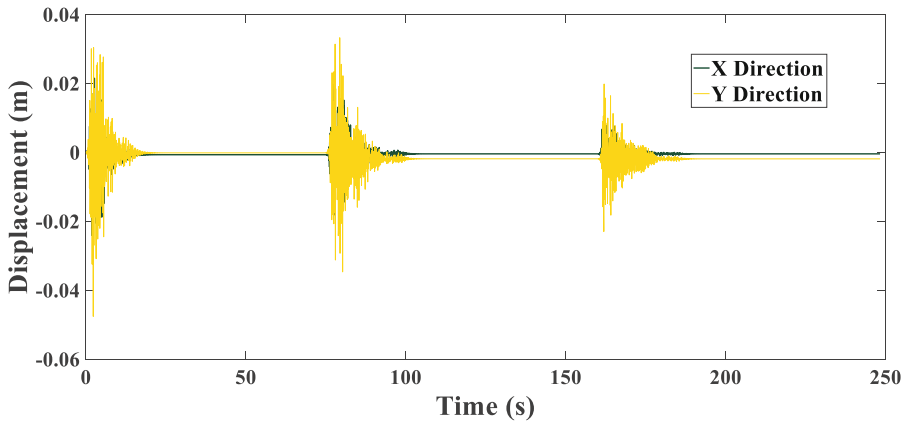
Fig. 2. Roof displacement of the investigated model in the X and Y directions.
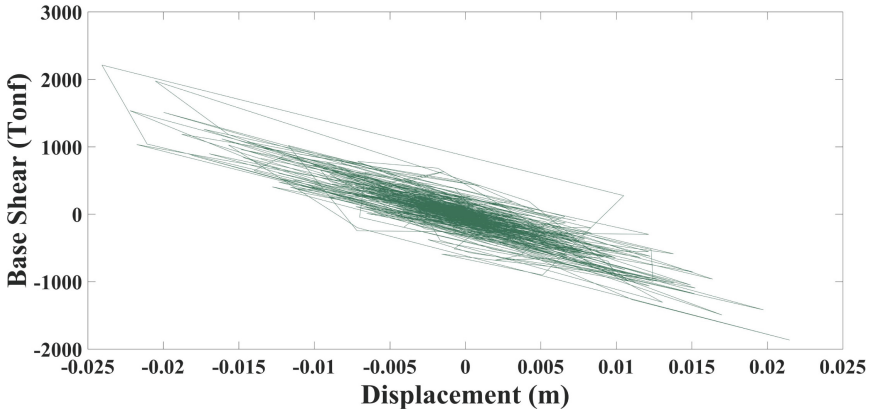
Fig. 3. Base shear versus roof displacement of the investigated model in the X direction.

The roof acceleration of the model, as visualized in Fig. 5, shows that both X and Y directions have similar peak values, with the maximum exceeding 40 m/s2. This trend reflects that the acceleration imposed on the building's roof due to the earthquake load is symmetrical in both directions, indicating a uniform distribution of forces on the structure.
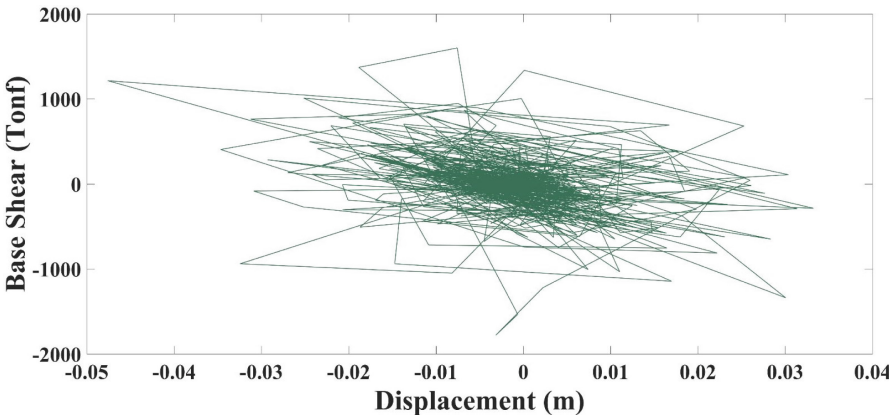
Fig. 4. Base shear versus roof displacement of the investigated model in the Y direction.
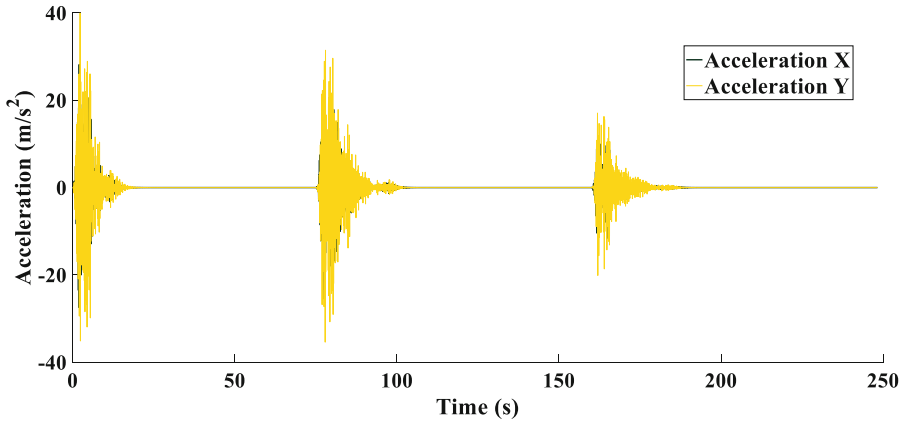
Fig. 5. Roof acceleration of the investigated model in the X and Y directions.

The study also looked at the formation of hinges under different conditions of seismic events, as depicted in Figs. 6, 7, and 8. Most of the hinges formed under the foreshock record only, as observed in Fig. 6. Interestingly, a few more hinges formed under both the foreshock and mainshock records, as demonstrated in Fig. 7. Notably, no new hinges were formed under the foreshock, mainshock, and aftershock records combined, as seen in Fig. 8. This might suggest that the structure's inelastic performance, characterized by the formation of hinges, reached its peak during the mainshock event and no additional structural deformation occurred during the aftershock.
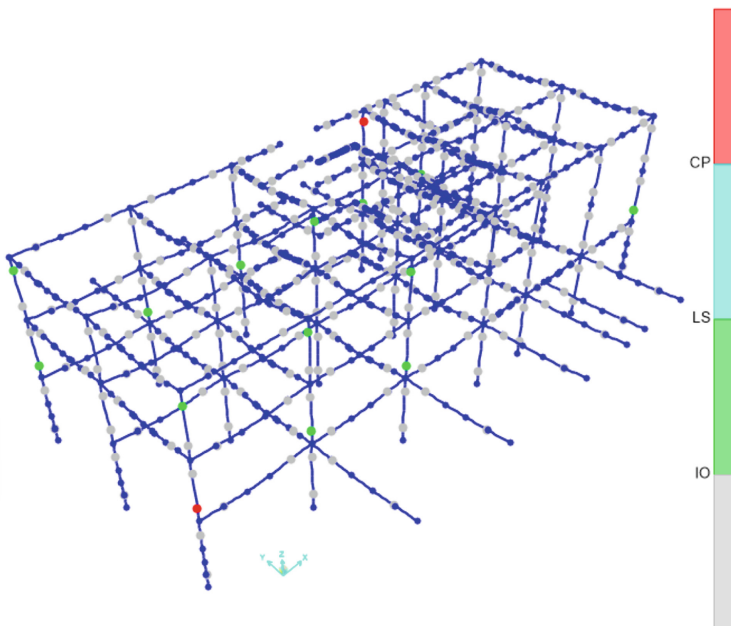
Fig. 6. Hinge formation in the frames under the foreshock record only.
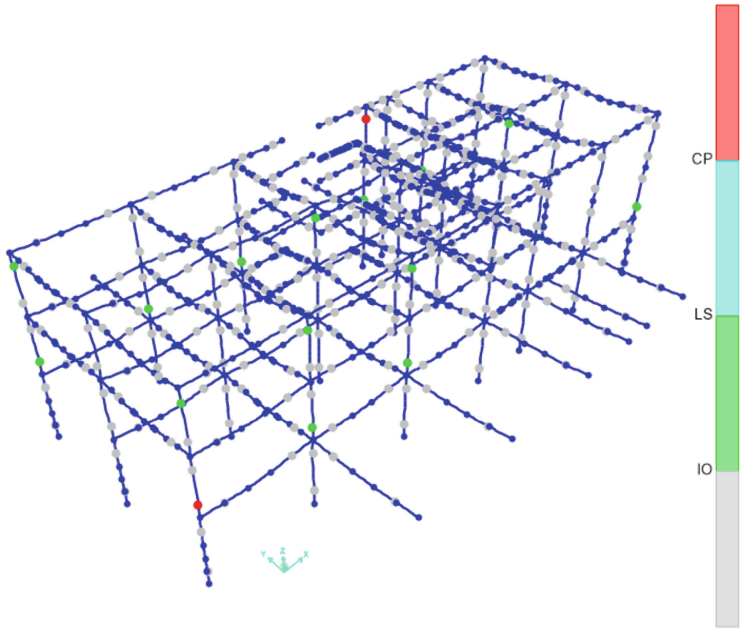
Fig. 7. Hinge formation in the frames under the foreshock and mainshock records.
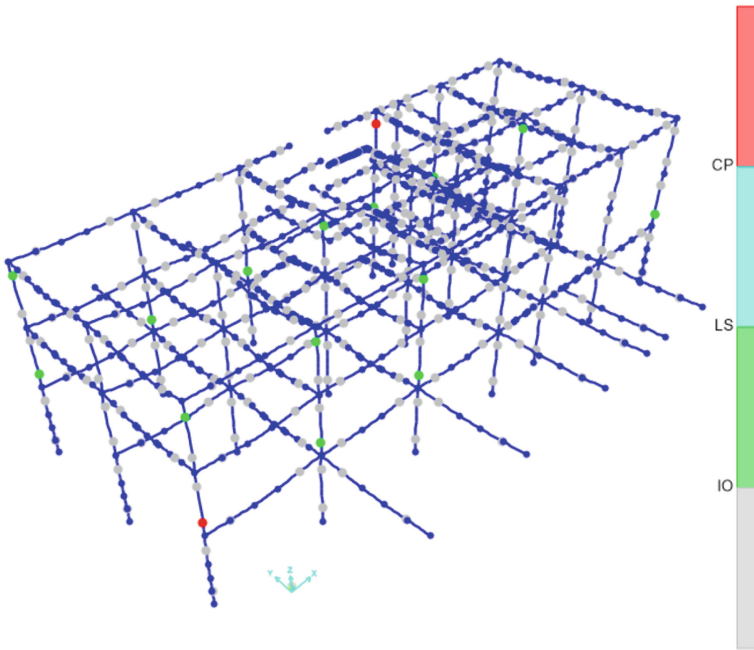
Fig. 8. Hinge formation in the frames under the foreshock, mainshock, and aftershock records.

    Table 1 presents a summary of the hinge formation in the structural elements of the investigated model under the sequences of the foreshock, mainshock, and aftershock records. The hinges are categorized based on their impact on the structural performance, including immediate occupancy, life safety, collapse prevention, and collapse. Upon analyzing the table, it can be observed that under the impact of the foreshock, mainshock, and aftershock records, the hinge formation in the beams remained consistent. There were 244 hinges formed under the "Immediate occupancy" category, with no hinges forming under the "Life safety," "Collapse prevention," or "Collapse" categories. This suggests that the beams' performance was confined to an elastic or immediate occupancy behavior during all stages of the earthquake sequence, indicating a high degree of resilience. In contrast, the columns demonstrated a slightly different pattern. Under the foreshock record, the columns exhibited 111 hinges under the "Immediate occupancy" category, 13 under the "Life safety" category, and 2 under the "Collapse" category. Notably, under the foreshock and mainshock records combined, the number of hinges formed under the "Immediate occupancy" category slightly decreased to 110, while there was an increase of one hinge in the "Life safety" category. The number of hinges under the "Collapse" category remained the same. The trend persisted even when the aftershock record was included, signifying the structure's behavior had reached a threshold during the mainshock and did not change significantly during the aftershock.

Table 1. Summary of the hinge formation in the frames under the foreshock, mainshock, and aftershock records.

Record	Element	Immediate occupancy	Life safety	Collapse prevention	Collapse
Foreshock	Beams	244	0	0	0
	Columns	111	13	0	2
Foreshock + Mainshock	Beams	244	0	0	0
	Columns	110	14	0	2
Foreshock + Mainshock + After shock	Beams	244	0	0	0
	Columns	110	14	0	2
Total	Beams	244	0	0	0
	Columns	110	14	0	2

    Overall, the results indicate that the reinforced concrete hospital, designed according to the TNRC-SC2015 requirements, exhibited considerable inelastic behavior under the long sequence of ground motion records. The structure's performance under the seismic conditions was marked by similar roof displacement and acceleration trends in both the X and Y directions, indicating a uniform inelastic response. Moreover, the formation of hinges, an essential feature of inelastic performance, was mostly limited to the foreshock and mainshock events, with no additional hinges formed during the aftershock, suggesting that the structure's capacity to absorb seismic energy was maximized during

these stages. These insights into the building's inelastic performance under seismic loads highlight the importance of accounting for such behavior in the design and evaluation of critical facilities, such as hospitals, to ensure their continued operation during and after seismic events.

4   Conclusions

In conclusion, this study illuminates the significant insights into the inelastic behavior of a seismic code-compliant reinforced concrete hospital under a prolonged sequence of ground motion records. First, the consistent roof displacement and acceleration trends in both the X and Y directions demonstrate a uniform inelastic response to the seismic events, underscoring the effectiveness of TNRC-SC2015 requirements in fostering uniform structural performance. Second, the investigation of hinge formation, an essential indicator of inelastic behavior, reveals that the structure reached its peak inelastic performance during the mainshock, with no new hinges formed during the aftershock. This finding signifies a strong resilience of the structural design under extreme conditions. Finally, the study draws attention to the necessity of considering inelastic behavior in the design and evaluation of critical facilities, particularly hospitals, to assure their continued functionality during and after seismic incidents. The in-depth understanding of these aspects, yielded by this case study, can contribute towards improving building codes and fostering safer and more resilient structures in seismic-prone regions.

References

Afsar Dizaj, E., Salami, M.R., Kashani, M.M.: Seismic vulnerability assessment of ageing reinforced concrete structures under real mainshock-aftershock ground motions. Struct. Infrastruct. Eng. **18**(12), 1674–1690 (2022)

Huang, W., Qian, J., Zhuang, B.B., Fu, Q.S.: Damage assessment of RC frame structures under multi-earthquake sequences. Adv. Mater. Res. **446**, 739–744 (2012)

Iervolino, I., Chioccarelli, E., Suzuki, A.: Seismic damage accumulation in multiple mainshock–aftershock sequences. Earthq. Eng. Struct. Dynam. **49**(10), 1007–1027 (2020)

Jeon, J.S., DesRoches, R., Lowes, L.N., Brilakis, I.: Framework of aftershock fragility assessment–case studies: older California reinforced concrete building frames. Earthq. Eng. Struct. Dynam. **44**(15), 2617–2636 (2015)

Jeong, S.H., Mwafy, A.M., Elnashai, A.S.: Probabilistic seismic performance assessment of code-compliant multi-story RC buildings. Eng. Struct. **34**, 527–537 (2012)

Khatami, M., Gerami, M., Kheyroddin, A., Siahpolo, N.: The effect of the mainshock–aftershock on the estimation of the separation gap of regular and irregular adjacent structures with the soft story. J. Earthq. Tsunami **14**(02), 2050008 (2020)

Mahat, P., Pradhan, P., Adhikari, R., Furtado, A., Gautam, D., Rupakhety, R.: Seismic sequence vulnerability of low-rise special moment-resisting frame buildings with brick infills. Appl. Sci. **12**(16), 8231 (2022)

Qiao, Y.M., Lu, D.G., Yu, X.H.: Shaking table tests of a reinforced concrete frame subjected to mainshock-aftershock sequences. J. Earthq. Eng. **26**(4), 1693–1722 (2022)

Rajabi, E., Ghodrati Amiri, G.: Behavior factor prediction equations for reinforced concrete frames under critical mainshock-aftershock sequences using artificial neural networks. Sustain. Resilient Infrastruct. **7**(5), 552–567 (2022)

Ruiz-García, J., Marín, M.V., Terán-Gilmore, A.: Effect of seismic sequences in reinforced concrete frame buildings located in soft-soil sites. Soil Dyn. Earthq. Eng. **63**, 56–68 (2014)

Shokrabadi, M., Burton, H.V.: Risk-based assessment of aftershock and mainshock-aftershock seismic performance of reinforced concrete frames. Struct. Saf. **73**, 64–74 (2018)

Zhai, C.H., Zheng, Z., Li, S., Xie, L.L.: Seismic analyses of a RCC building under mainshock–aftershock seismic sequences. Soil Dyn. Earthq. Eng. **74**, 46–55 (2015)

Seismic Performance Assessment of Reinforced Concrete Building Stock Using Artificial Neural Network and Linear Regression Analysis

Oğuz Karayel[(✉)] and Giray Özay

Civil Engineering Department, Eastern Mediterranean University, Famagusta, North Cyprus, Turkey
{19600125,giray.ozay}@emu.edu.tr

Abstract. In the last half century, Turkish earthquake codes for designing building under earthquake loads went through many modifications and editions (TEC1975, TEC1997, TEC2007 and TBEC2018). Hence, there are many buildings existing that has been built in accordance with old regulations since improvements in the recent earthquake code. Therefore, the need of a quick assessment method to identify the building seismic performance level in accordance with the latest seismic code is extremely vital. For this purpose, this research aimed to prepare a database for the quick estimation of building seismic performance by constructing an artificial neural network model and linear regression analysis. In order to meet these objectives, 540 reinforced concrete building models with various parameters such as building material properties, geometry, designed standard, site class, and peak ground acceleration were modeled with respect to TEC1975, TEC1997, TEC2007, TBEC2018 and seismic performance obtained from the pushover analysis in accordance with TBEC2018. Data obtained were used to perform multiple linear regression analysis (MVLRA). Also, data obtained from the pushover analysis were used to train and validate the constructed artificial neural network (ANN) model with several training algorithms performed with various number of hidden layers in order to figure out the optimum number of hidden layers and best train method which gives the highest accuracy of prediction for the performance assessment of the buildings as well. Results indicate that ANN can be a very profound technique in predicting the seismic performance levels. In addition, validity of the created model was checked by the application through the existing buildings as a case study with various parameters within the range of considerations according to the existing study. Furthermore, identification of the significance of the predictor variables according to their effect on seismic assessment have been done with several methods which are widely used in literature as well.

Keywords: ANN · MVLRA · TBEC2018 · Prediction · Performance · Pushover Analysis

1 Introduction

Reinforced concrete building structures that are subjected to earthquake are expected to dissipate high input energy without failure to assure controlled damage performance level. Errors of providing enough capacity leads to catastrophic failure and in most cases to disasters. Turkey as a country is prone to many earthquakes' excitations since it is hovering over multiple faults such as Anatolian Fault etc. [1–4].

A large part of Turkey is situated in an active earthquake zone which causes devastating consequences both on human lives and serious damage to structures due to earthquakes. Due to this, designing structures in a way safety and resisting against earthquake is revised during past years and researches will continue on. Therefore, it's important to update the performance of these old buildings continuous against most recent standards as a part of vulnerability assessment to prevent this disaster from happening [5–7].

The recent development achieved over the last few decades in the field of technology has indeed impacted our lives. Day by day new methods are being introduced to the literature trying to overcome certain difficulties and obstacles with the help of these improved technologies. Nowadays, many efforts are being spent on developing new interpolation techniques to improve their modeling capability and reduce their uncertainty represented in most cases by what so called "coefficient of determination" which is represented as R^2.

The aim herein is to find adapted this improved technology in the field of structural engineering by means of developing a quick performance assessment method based on the recent Turkish Building Earthquake Code 2018 by using Artificial Neural Network and Multiple Linear Regression Analysis. As a part of the study, about 540 case is to be considered to cover the most significant parameters that has effect on the performance of the buildings including Turkish Earthquake Code which is designed, peak ground acceleration (PGA), soil class, concrete grade, steel grade, several types of irregularities in plan and elevation. In general, this model is expected to help structural engineers who are trying to check the performance of the existing structures constructed with the guidelines of previous Turkish earthquake code and to assess their deficiency against the most recent one.

2 Methodology

Detailed descriptions of the selected cases in terms of their geometry and the modeling of the structural elements are presented in this section.

2.1 Structural Models

Reinforced concrete buildings with both regular and irregular plans are designed in accordance with the Turkish Earthquake Codes (TEC1975, TEC1997, TEC2007 and TBEC2018) under different ground acceleration and different ground types (various spectral acceleration from Istanbul region). The buildings are located at various location of Istanbul province in order to cover wide ranges of ground peak acceleration ranging
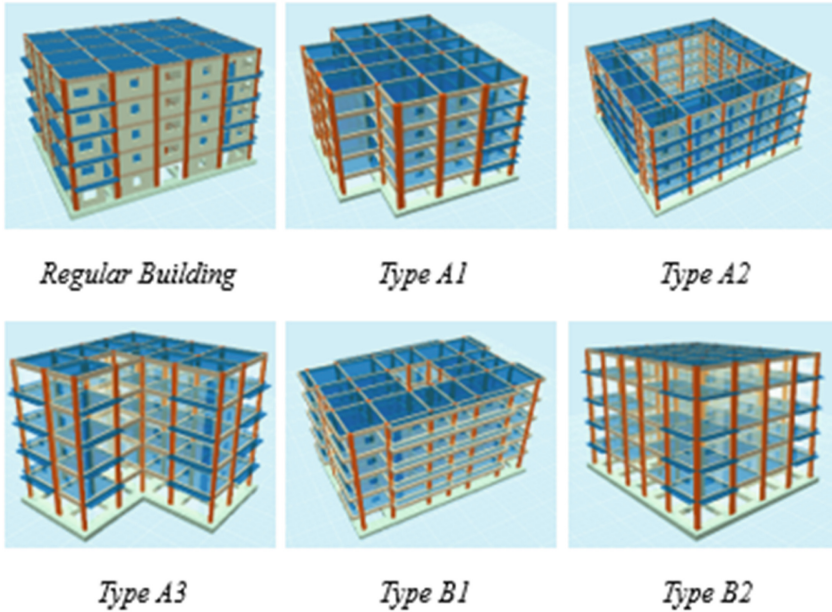
Fig. 1. Selected different types of the RC buildings analyzed in the study.

between 0.2 g–0.55 g (10% of exceedance within 50 years) in addition to various types of site classes Z_A, Z_B, Z_C, Z_D, and Z_E (TBEC 2018).

As shown in Fig. 1, the regular building is assumed to be symmetric along both axis with a typical span between the column of 5 m and it is regular along both plan (center of rigidity matches with the center of mass) and elevation where all floor height are 3 m. The building which is type A1 is considered to be torsional irregular when the ratio of max displacement to the minimum displacement of a given story is larger than 1.2 in accordance with TBEC 2018. Also, another building is considered to be irregular from type A2 (slab discontinuity) along the plans when the total area of the openings within a given floors exceeds one third of the total area. In addition, another building is considered to be irregular from type A3 when the discontinuity along the plan exceeds the 20% ratio of the tallest parallel length. Furthermore, in accordance with TBEC2018, a building is considered to be irregular (type B1) along elevation with weak story irregularities when the area of the lateral forces resistant (columns area, shear walls area, 0.15 of walls area) is reduced by 80% or more. Lastly, in accordance with TBEC2018 a building is consider to be irregular along elevation with soft story irregularities when the ratio of the floor drift ratio to either top or bottom ratio is larger than 2.

The structures with geometry identified in Fig. 1 are modeled, analyzed, and designed using STA4CAD software where buildings initially are designed (sections capacity and reinforcement) with respect to gravity loads and lateral loads of the considered earthquake code (TEC1975, TEC1997 and TEC2007). Then, the procedure is followed by seismic performance assessment in accordance with TBEC2018. The large collected

data are used as input and output for the training of the ANN where its prediction results are validated afterwards. Application of a case study with various parameters within the range limits of existing study is considered in order to check the validity of the created performance prediction method. In addition, multiple linear regression analysis is conducted by using the same data as an alternative method as well.

2.2 Performance Analysis

Non-linear static pushover analysis method is accounted to be one of the most applied techniques for determining the plastic behaviour of RC structure. In general, this method requires high computational effort unlike the linear static method, since the stiffness matrix of the structure varies with respect to the applied loads. It is an iterative method where forces are subdivided into multiple steps. At each step the stresses which are resulted within the primary elements are checked and the stiffness matrix is modified accordingly. This iterative approach continues until the limit state is reached (target displacement).

In this study the nonlinear static pushover analysis is conducted in accordance with TBEC2018. This analysis method is selected since it is widely used in the literature for the performance-based design. In this analysis method, step by step increment of lateral forces are analyzed by taking into consideration the domain of the structure modal vibration shape amplitude and the mass sources in both orthogonal directions. In addition, the secondary moment resulted from the P-Delta effect is also considered.

Performance of existing buildings are related to the expected damage that occurred within the building under seismic forces applied which are categorized as four main damage conditions.

Limited damage performance level is determined in a building when it is satisfying the given condition such that it is only allowed to have maximum 20% pronounced damage on beams after the calculation for each direction of earthquake applied in any storey of a building. In case there are brittle damaged elements, retrofitting is needed.

Controlled damage performance level is determined when given three conditions are satisfied and retrofitting is applied to the brittle damaged elements. First of all, it is only allowed to have maximum 35% advanced damage on beams (except secondary beams) and the regulation specified for vertical elements regarding advanced damage zone should be satisfied after the calculation for each direction of earthquake applied in any storey of a building. Another issue is that the ratio of the summation of shear forces carried by the vertical elements that are in advanced damage zone on the top storey to the summation of shear forces of all vertical elements at the same storey should not exceed 40%. Furthermore, the ratio of the summation of shear forces that are carried by the vertical elements in any storey which are exceeded pronounced damage zone at both top and bottom sections to the summation of shear forces of all vertical elements within the same storey should not exceed 30% while all other elements are within the limited damage zone or pronounced damage zone.

Regarding collapse prevention performance level, at most 20% of the beams (except secondary beams) can exceed collapse zone after the calculation for each direction of earthquake applied in any storey of a building. In addition, the ratio of the summation of shear forces that are carried by the vertical elements in any storey which are exceeded

pronounced damage zone at both top and bottom sections to the summation of shear forces of all vertical elements within the same storey should not exceed 30% while all other elements are within the limited damage zone, pronounced damage zone or advanced damage zone. The usage of building with its existing condition is threatened in terms of life safety.

If the building is not satisfying collapse prevention performance level conditions, then it is collapse case [8].
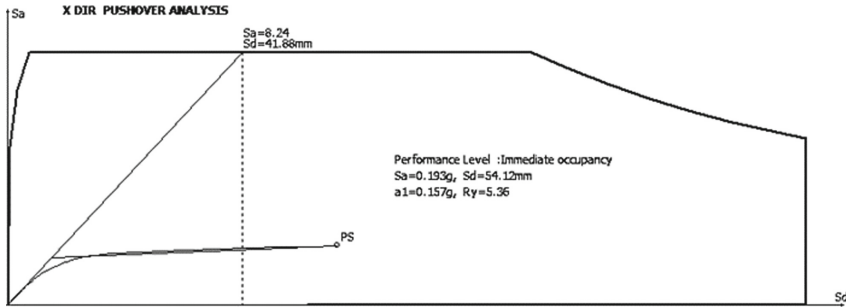
Fig. 2. Obtained Pushover Curve of Immediate Occupancy Performance Level.
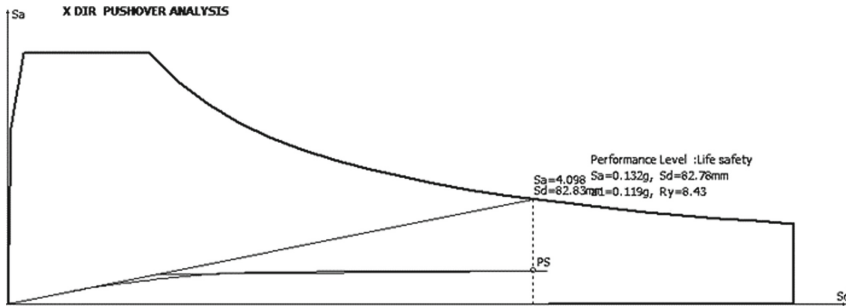
Fig. 3. Obtained Pushover Curve of Controlled Damage Performance Level.

In the current study, a nonlinear static pushover analysis was executed in compliance with the guidelines outlined in TBEC2018. The resulting base shear versus roof displacement curves have been illustrated in Fig. 2, 3, 4, and 5, each corresponding to selected specific performance levels such as Immediate Occupancy, Controlled Damage, Collapse Prevention, and Collapse Case, respectively. The graphical representations in Figs. 2 through 5 offer a visual depiction of the relationship between base shear and roof displacement for each designated performance level, contributing valuable insights into the structural behavior across different scenarios.
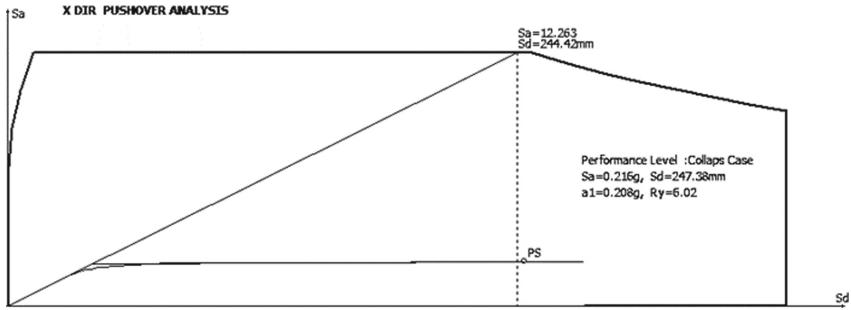
Fig. 4. Obtained Pushover Curve of Collapse Prevention Performance Level.
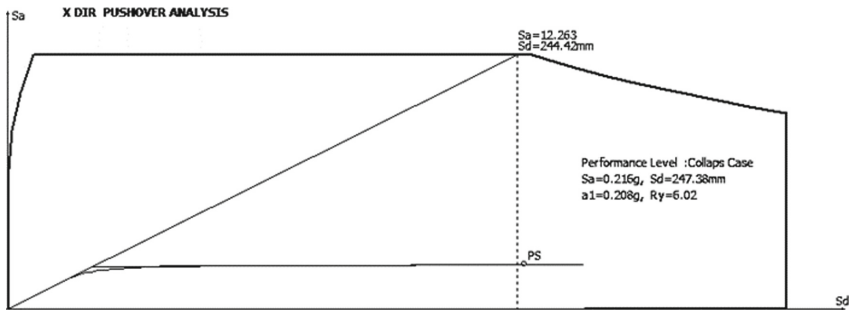
Fig. 5. Obtained Pushover Curve of Collapse Case Performance Level.

3   Multiple Linear Regression Analysis

Multiple linear regression analysis is widely used statistical methodology in many research fields in order to determine the relationship between one continuous dependent variable and a set of data which is made of two or more independent predictor variables for the predictions. There are several approaches to build regression model according to the aim of the study. Therefore, it is possible to build the best model to perform in accordance with the aim of the specified study due to the expectations. Moreover, two principles are applied to regression modelling in general. One is that, each and every variable should explain its own statistically significant amount of variance in the outcome variable. Another one is, it should be expected that some of the predictor variables will be correlated with one another as well as the dependent outcome variable in case of dealing with multiple predictors. Addition or removal of a variable to the model probably will affect the coefficients of all the variables in this case [9, 10].

$$y = \beta_0 + \beta_1 x_1 + \cdots + \beta_n x_n + \varepsilon \tag{1}$$

Equation given above represents a typical linear regression model equation where, 'y' is dependent outcome variable, 'β_0' is the intercept, 'x_1' is the first independent predictor variable, 'β_1' is the coefficient of first predictor variable and 'ε' is the error.

In this research, the data of the input parameters and the performance analysis results as output parameter are used to construct a prediction model through multiple variable

linear regression analysis. This is achieved by converting the input and output parameters to numerical values instead of their string values. Then, these numerical data are fed into EViews 10 software which evaluated the coefficients of the linear model.

4 Application of Artificial Neural Network

Due to the restricted properties of the traditional knowledge-based systems, Artificial Neural Networks started to be used as a complement and advanced applications since eighties especially in civil engineering. One of the most important properties of ANNs which makes it useful for engineers is to be able to learn from examples and generate solutions by trying to imitate human brain learning activities [11]. Artificial neural networks (ANNs) are networks of artificial neurons which in other words are processing elements. These artificial neurons are sets of three different types of layers such as input layer, hidden layer and output layers. The input layers have the input data and variable parameters. Hidden layers have the neurons which perform the computations and output layers which is the solution takes place. Furthermore, learning algorithm is needed in order to train the network. So, multilayer feedforward network is the most widely used popular network type among several types such as single layer feedforward networks, recurrent networks, lattice structures and so on. The main aim of training the network is to find out the weights (parameters) of the neural network model in order to minimize the output errors of the model. So, back propagation is the most widely used supervised learning method due to the nonlinearity of the model in the parameters and need of a nonlinear algorithm [12–14] (Fig. 6).
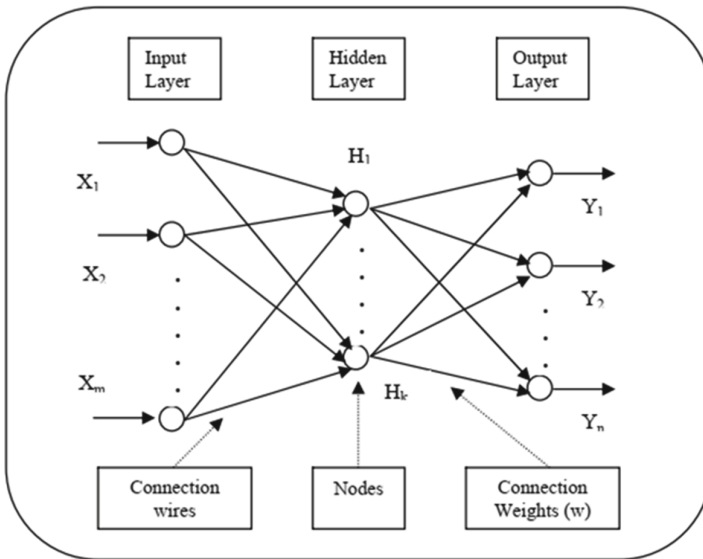
Fig. 6. A typical Artificial Neural Network modelling system.

A back-propagation neural network is simply defined as shown in Fig. 2 as a network with number of layers synthesized with processing elements called neurons. There are input layers consists of input data or parameters of a problem, hidden layers which the information is processed by trial and error due to the complexity of the problem and output layers which gives the solution of the problem. Each neuron receives inputs, processes and generates an output [15].

In this research, MATLAB 2018 neural network module is used in this study to construct and train the network. Feed forward artificial neural network composed of three layers structure is adopted. The general structure of the network is composed of multiple input cells followed by multiple hidden layers defined by the user and an output layer, where all of which are interconnected. The input layers are determined to be the variety of considered parameters which are; designed earthquake standard (TEC1975, TEC1997, TEC2007, or TBEC2018), type of the building (regular, A1, A2, A3, B1, B2, or week column strong beam), designed peak ground acceleration (0.1, 0.2, 0.3, or 0.4), performance check peak ground acceleration (0.2, 0.3, 0.4, or 0.55), designed soil type (Z_A, Z_B, Z_C, or Z_D), performance check soil type (Z_A, Z_B, Z_C, Z_D, or Z_E), designed concrete grade (C16, C20, or C25) and designed reinforcing steel grade (S220, or S420). Meanwhile, the output layer is composed of 4 main results which are; Immediate occupancy (KK), Controlled damage (KH), Collapse prevention (GO) and Collapse case (GD).

Back propagation technique is adopted to train the network which is derived through the chain rule presented in calculus theory. The considered multiple back propagation algorithm methods are given as follow; BFGS Quasi-Newton Backpropagation, Bayesian regularization backpropagation, Conjugate Gradient Backpropagation with Powell-Beale Restarts, Conjugate gradient backpropagation with Fletcher-Reeves updates, Conjugate gradient backpropagation with Polak-Ribiére updates, Gradient descent backpropagation, Gradient descent with momentum backpropagation, Gradient descent with adaptive learning rate backpropagation, Levenberg-Marquardt backpropagation, One-step secant backpropagation, Resilient backpropagation and Scaled conjugate gradient backpropagation.

5   Results and Discussions

This part represents the construction and results of the created Artificial Neural Network and Multiple Variable Linear Regression Analysis models. In addition, comparison in between the two approaches as well.

Linear regression analysis is conducted using multiple variables. The fitting function is developed on the basis of the sum of square root error method. The obtained results are displayed in Fig. 3 where 1, 2, 3, and 4 represents KK, KH, GO, and GD performance levels respectively. The fitting function is presented in Eq. (2) where, PER: Performance level (KK, KH, GO, and GD), EQ: Earthquake standard (TS1975, TS1997, TS2007, and TS2018), IR: Irregularity type (Regular, A1, A2, A3, B1, and B2), AD: Designed peak ground acceleration (0.1 g, 0.2 g, 0.3 g, and 0.4 g), AC: Checked peak ground acceleration (0.2 g, 0.3 g, 0.4 g, and 0.55 g), SD: Designed soil type (Za, Zb, Zc, and Zd), SC: Checked soil type (Za, Zb, Zc, Zd, and Ze), CG: Grade of concrete (C16, C20,

and C25), SG: Grade of steel, (S220 and S420), and $\alpha_{(1-9)}$: Fitting coefficients (Fig. 7).

$$PER = \alpha_1 + \alpha_2 EQ + \alpha_3 IR + \alpha_4 AD + \alpha_5 AC + \alpha_6 SD + \alpha_7 SC + \alpha_8 CG + \alpha_9 SG \quad (2)$$
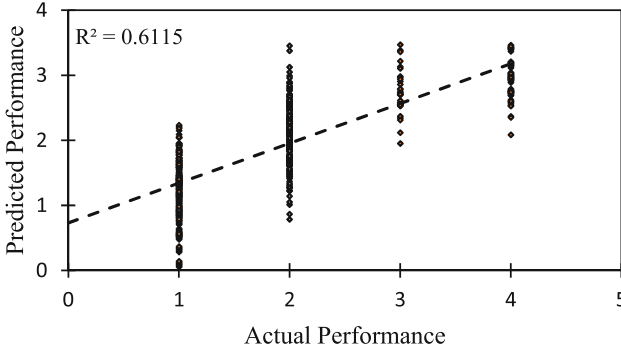
Fig. 7. Predicted performance using the linear regression analysis versus the actual performance.

The selected input parameters of the case study are fed into an ANN model that uses the feed-forward back propagation method where multiple training algorithms and multiple number of hidden layers are applied. In this part, the performance of the training algorithms and the optimum number of hidden layers for each and every training algorithm is presented (Fig. 8).
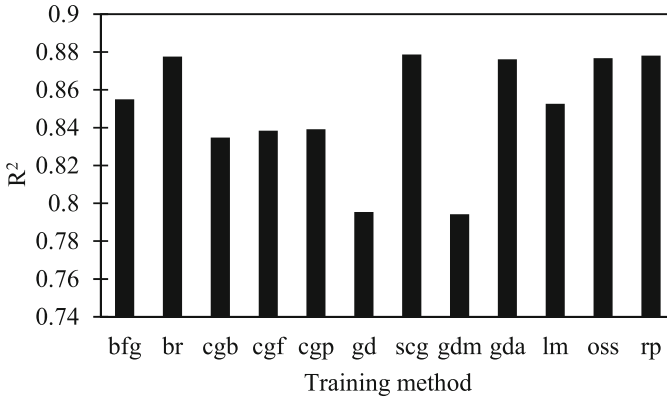
Fig. 8. Accuracy of training algorithms at their optimum number of hidden layers.

The results of the training algorithms using their optimum number of hidden layers is presented in Fig. 4. As observed, the optimum training algorithm is Scaled conjugate gradient backpropagation method with an accuracy of 0.8786. On the other hand, the least accurate training algorithm is Gradient descent with momentum and adaptive learning rate backpropagation where it has an accuracy of 0.79 (Fig. 9).
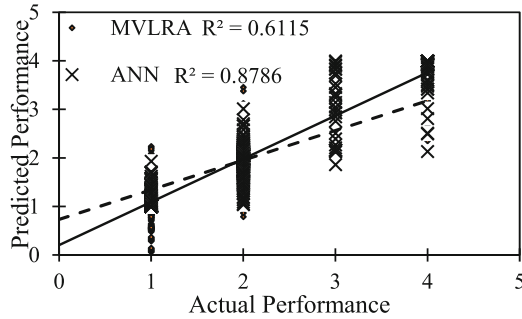
Fig. 9. Comparison between performances obtained by ANN model and MVLRA.

The obtained performance from the optimum trained Artificial Neural Network model and the Multiple Variable Linear Regression Analysis are presented in Fig. 5 where 1, 2, 3, and 4 represents KK, KH, GO, and GD performance levels respectively. Results show that artificial neural network is more accurate in predicting the actual performance than the multiple variable linear regression analysis. However, it is worth to mention that both methods predict the building performances with KH level in extreme high accuracy. On the other hand, MVLRA accuracy is dramatically reduced for the GO and GD performance levels.

In addition, validity of the created model is checked by the application through the existing buildings as a case study with various parameters within the range of considerations according to the existing study. Table 1 shows the predicted performance level of a case study as an application of the existing buildings with various parameters. Since the created ANN model with the optimum method of training algorithm has the accuracy of prediction of 88%, it is clearly seen from the application as well that nine out of ten building performance levels are predicted in a way correctly by using the created ANN model when compared to the actual performance levels.

Furthermore, identification of the significance of the predictor variables according to their effect on seismic assessment have been done with several methods which are widely used in literature as well. Multiple linear regression analysis coefficients are standardized to assess the importance and order of the input variables on the prediction results. Results of the parameters according to their significance from top to bottom respectively for each of the given methods are presented in Table 2.

Table 1. Application of the created ANN model to a case study.

	1	2	3	4	5	6	7	8	9	10
EQ	TEC 1997	TEC 1975	TEC 2007	TEC 2007	TBEC 2018	TEC 1997	TEC 1975	TEC 2007	TEC 2007	TBEC 2018
IR	Reg	A1	A3	B1	B2	Reg	A1	A3	B1	B2
AD	0.4	0.3	0.2	0.1	0.55	0.4	0.3	0.2	0.1	0.55
AC	0.55	0.4	0.3	0.2	0.55	0.55	0.4	0.3	0.2	0.55
SD	Zc	Za	Zb	Za	Zd	Zd	Za	Zc	Zb	Ze
SC	Zd	Za	Zc	Zb	Zd	Ze	Zb	Zd	Zc	Ze
CG	C20	C16	C25	C25	C25	C20	C16	C25	C25	C25
SG	S220	S220	S420	S420	S420	S220	S220	S420	S420	S420
Act. Per	GO	KH	KH	KK	KH	GO	KH	KH	KK	KH
Pred. Per	GO	KH	KK	KK	KH	GO	KH	KH	KK	KH

Table 2. Order of the predictor variable significance in accordance with applied methods.

Order	Standardized regression coefficients	Zero-order correlation method	Product measure	P-value	Variable elimination method
1	EQ	SC	EQ	SG	SG
2	CG	SD	CG	SC	SC
3	SC	AC	SC	EQ	EQ
4	SG	AD	SG	CG	CG
5	AD	SG	SD	SD	SD
6	SD	CG	AD	IR	IR
7	AC	IR	AC	AD	AD
8	IR	EQ	IR	AC	AC

6　Conclusion

In this research, quick estimation methods of buildings seismic performance under different properties and conditions are created by developing an artificial neural network model and by linear regression analysis as an alternative method as well in accordance with the latest Turkish earthquake code (TBEC2018). Hence, 540 analysis have been done regarding reinforced concrete buildings with various plan geometries, material grades, irregularities, seismic design codes, peak ground accelerations and site classes. Followings are the conclusive remarks based on the statements given.

- Number of hidden layers used in the structure of the constructed neural network influences the results of the predicted performance dramatically and every training method has its unique optimal number of hidden layers.
- Scaled conjugate gradient backpropagation training method resulted the highest accuracy ($R^2 = 0.8786$) compared with the other training methods at their optimal number of hidden layers.
- It can be seen from the application that nine out of ten building performance levels are predicted correctly by using the created ANN model when compared to the actual performance levels since the created ANN model with the optimum method of training algorithm has the accuracy of prediction of 88%.
- Multivariable linear regression analysis prediction of accuracy for the building performances levels obtained as ($R^2 = 0.6115$).
- The predictor variables are sorted according to their significance by using standardized coefficient regression, zero-order correlation methods, product measure of these two methods, P-value and variable elimination method which are widely used in literature.
- Finally, it can be concluded that artificial neural network performs better than multiple linear regression analysis in terms of prediction of the building seismic performance in accordance with TBEC2018.

References

1. Soyluk, A., Harmankaya, Z.: The history of development in Turkish seismic design codes. Int. J. Civ. Environ. Eng. **12**(1), 25–29 (2012)
2. Ozcebe, G., Yucemen, M.S., Aydogan, V.: Statistical seismic vulnerability assessment of existing reinforced concrete buildings in Turkey on a regional scale. J. Earthq. Eng. **8**(05), 749–773 (2004)
3. Yakut, A.: Preliminary seismic performance assessment procedure for existing RC buildings. Eng. Struct. **26**(10), 1447–1461 (2004)
4. Hassan, A.F., Sozen, M.A.: Seismic vulnerability assessment of low-rise buildings in regions with infrequent earthquakes. ACI Struct. J. **94**(1), 31–39 (1997)
5. Arslan, M.H.: An evaluation of effective design parameters on earthquake performance of RC buildings using neural networks. Eng. Struct. **32**(7), 1888–1898 (2010)
6. Arslan, M.H., Ceylan, M., Koyuncu, T.: Determining earthquake performances of existing reinforced concrete buildings by using ANN. World Acad. Sci. Eng. Technol. Int. J. Civ. Environ. Struct. Constr. Archit. Eng. **9**(8), 921–925 (2015)
7. Hakan Arslan, M.: Application of ANN to evaluate effective parameters affecting failure load and displacement of RC buildings. Nat. Hazard. **9**(3), 967–977 (2009)
8. Code, T.B.E.: Ministry of public works and settlement. specification for structures to be built in disaster areas. Government of Republic of Turkey (2018)
9. Uyanık, G.K., Güler, N.: A study on multiple linear regression analysis. Procedia Soc. Behav. Sci. **106**, 234–240 (2013)
10. Nathans, L.L., Oswald, F.L., Nimon, K.: Interpreting multiple linear regression: a guidebook of variable importance. Pract. Assess. Res. Eval. **17**(9), n9 (2012)
11. Rafiq, M.Y., Bugmann, G., Easterbrook, D.J.: Neural network design for engineering applications. Comput. Struct. **79**(17), 1541–1552 (2001)
12. Setyawati, B.R., Sahirman, S. Creese, R.C.: Neural networks for cost estimation. AACE Int. Trans. (2002)

13. Riedmiller, M.: Advanced supervised learning in multi-layer perceptrons—from back-propagation to adaptive learning algorithms. Comput. Stan. Interfaces **16**(3), 265–278 (1994)
14. Sapna, S., Tamilarasi, A., Kumar, M.P.: Backpropagation learning algorithm based on Levenberg Marquardt algorithm. Comp. Sci. Inform. Technol. (CS IT) **2**, 393–398 (2012)
15. Elhag, T.M.S. Boussabaine, A.H.: An artificial neural system for cost estimation of construction projects. In: Proceedings of the 14th ARCOM Annual Conference, pp. 219–245 (1998)

3D Soil-Structure-Pile Interaction Analysis for Heterogeneous Soil Medium

Yasin Fahjan[1] and Fatma İlknur Kara[2(✉)]

[1] Civil Engineering Department, Istanbul Technical University, Istanbul, Turkey
fahjan@itu.edu.tr

[2] Architecture Department, Gebze Technical University, Kocaeli, Turkey
figokce@gtu.edu.tr

Abstract. Soil-Pile-Structure Interaction (SSI) analysis plays a crucial role in the design of structures aimed at withstanding various external loads, including seismic events. SSI is a complex process that manifests when the response of the soil, pile, and structure influence each other reciprocally under seismic activities or other dynamic loads. This interaction can precipitate significant changes in the dynamic characteristics of the system, consequently affecting the responses of the structure and soil. The initial and most critical step for a successful analysis is the accurate modeling of the soil profile, pile elements, and interaction springs to represent their real behaviors. Even in a project area with homogeneous structure, the modeling of all static and dynamic characteristics of the soil profile poses substantial challenges. These challenges intensify when considering a heterogeneous soil profile. In the context of this study, a comprehensive soil-structure-pile interaction analysis has been conducted on a project site possessing a heterogeneous structure. At the core of the research, a meticulous 3D modeling of the complex geological constitution of the site and the associated pile elements of varying dimensions and lengths has been carried out. The study's approach towards 3D modeling not only elucidates the intricate relationship between the soil, structure, and piles, but also enhances the understanding of their dynamic behavior under various load conditions.

Keywords: Soil-pile-structure interaction analysis · Heterogeneous Soil Profile · 3D Modeling and Analysis

1 Introduction

The way a structure reacts to earthquake tremors is influenced by the interplay between three interconnected systems: the structure itself, the foundation upon which it stands, and the soil that underlies and surrounds this foundation [1]. Soil-structure interaction (SSI) analysis assesses the joint response of these systems to a given ground motion. Over the past three decades, several methods have been developed to incorporate Soil-Structure Interaction (SSI) analysis (Wolf, 1985 ([2]); Park and Antin, 2004 [3]; Zerfa and Loret, 2004 [4]; Wang et al., 2006 [5]; Kausel, 2010 [6]) [7]. This analysis represents a multifaceted occurrence, where the soil and structure reciprocally affect their respective responses under specific load conditions [8]. The complexity of this analysis escalates particularly in heterogeneous soil profiles, due to the diverse properties of the soil.

Within heterogeneous soils, properties such as shear modulus, density, damping ratio, and Poisson's ratio, are not uniformly distributed and can fluctuate from one location to another. The complex spatial configuration of the soil-foundation interface or the distribution of the soil medium is often simplified by using flat-layered soil profiles, while the nonlinearity of the soil medium is commonly accounted for using an equivalent linear model [7]. This spatial variability introduces an additional level of intricacy to the SSI analysis. The procedure to conduct a soil-structure interaction analysis on a heterogeneous soil profile can be organized in the following manner: site characterization, modeling the heterogeneous soil profile and pile elements, including soil-structure interaction effects, conducting dynamic analysis, and interpreting results to guide design.

Site Characterization: This initial step is of paramount importance and necessitates geotechnical investigations along with in-situ tests to identify soil layers, their depths, and physical properties, such as density, stiffness, shear strength, among others. Site characterization may involve the utilization of Standard Penetration Tests (SPT), Cone Penetration Tests (CPT), or shear wave velocity tests [9]. Soil profiles are typically represented based on stratigraphy and geotechnical properties.

Modeling The Soil Profile, Foundation System, and Pile Elements: Post data collection, a numerical model should be established. This step becomes more challenging within a heterogeneous soil profile due to the variable properties across soil layers, which complicates the accurate modeling and analysis of wave propagation. The model is intended to accurately represent soil property variations. It significantly influences the precision of predictions concerning structural response and performance under dynamic loads, including seismic activities. The determination of free field motion characteristics, vital for dynamic soil-structure interaction analysis, is further complicated by the presence of diverse soil properties within a heterogeneous soil profile. The Finite Element Method (FEM) or Finite Difference Method (FDM) can be applied for this purpose [10]. It is imperative to accurately model soil layers with their distinct properties. These property variations should be included in the model to mirror soil heterogeneity. Depending upon soil behavior, various constitutive models may be employed. Another significant issue is the accurate definition of the material properties of the foundation systems, dimensions, and lengths of the pile elements.

Incorporating Soil-Structure Interaction Effects: The structure under analysis is also modeled, and the boundary conditions at the soil-structure interface are determined. These boundary conditions should closely mirror real-world scenarios. The interaction between the soil and structure is modeled using interface elements that can capture potential slippage or separation at the interface.

Conducting Dynamic Analysis: Dynamic analysis is performed on the combined model of the structure and the soil considering suitable loading conditions. These loading conditions could include seismic loads or structure weight, among others. The analysis could be linear or non-linear, contingent on the anticipated behavior of the structure and soil. It is also crucial to account for the dynamic properties of the soil, such as damping, which may vary with depth, in the analysis.

Interpreting Results and Designing: The results of the SSI analysis are interpreted and utilized for the design of the structure or to assess its safety [8]. The interpretation encompasses understanding how the SSI has influenced the structural responses and ensuring the structure's ability to withstand the forces generated during the event. If the analysis

reveals potential unsatisfactory performance of the structure, design modifications may be warranted.

These steps, however, are not linear and often necessitate multiple iterations, particularly in complex or large-scale projects. Due to the complexity of SSI analysis in a heterogeneous soil profile, advanced computational tools like PLAXIS, FLAC, ABAQUS are commonly deployed for such analyses.

2   Soil Structure Analysis in Turkish Seismic Code

In accordance with Article 16.10 of Turkish Seismic Code (TBDY 2018) [10], for projects to be executed on relatively weak soils, it is necessary to conduct soil-structure-pile interaction analyses considering the influence of the soil. This is essential for the design of pile foundations, which function as load-bearing system components alongside the superstructure, under the impact of an earthquake. In weak soils, determining the potential deformations and internal forces in pile elements, which work in conjunction with the superstructure under earthquake impact, is crucial for the system to demonstrate the expected performance.

The Regulation outlines three different analysis methods as detailed in Table 1, which vary according to the Earthquake Design Class (DTS), Building Height Class (BYS), and Local Soil Class. DTS is detailed in the regulations based on seismicity and the intended use of the structure, while BYS is determined considering DTS and the building height range. The seismic code categorizes soil into five different classes from ZA to ZE, with an additional class ZF, based on various parameters that influence seismic wave propagation, such as the upper average shear wave velocity (Vs30), average Standard Penetration Test-N (SPT-N) values, and shear strength. According to Table 1, for tall structures (BYS = 1) with local soil classes ZD, ZE, and ZF, Method I should be used for Soil-Structure-Pile Interaction analyses if DTS = 1, 1a, 2, 2a. Method II is suitable for systems with DTS = 1a, 2a and BYS = 2, 3, as well as those with DTS = 3, 3a, 4, 4a and BYS = 1. Method III is applicable in systems where DTS = 1a, 2a and BYS ≥ 4, and those with DTS = 1, 2, 3, 3a and BYS ≥ 2.

In Method I, the soil environment should be modeled three-dimensionally, taking into account the piles to be analyzed with finite elements or finite differences methods. The analyses of the created model should be completed under at least eleven pairs of earthquake records, defined at the determined engineering bedrock level. In Method II,

Table 1. Turkish Seismic Code Application Areas of Interaction Analysis Methods.

Analysis Method	Earthquake Design Class (DTS)	Building Height Class (BYS)	Local Soil Class
Method I	DTS = 1, 1a, 2, 2a	BYS = 1	ZD, ZE, ZF
Method II	DTS = 1a, 2a	BYS = 2, 3	ZD, ZE, ZF
	DTS = 3, 3a, 4, 4a	BYS = 1	
Method III	DTS = 1a, 2a	BYS ≥ 4	ZD, ZE, ZF
	DTS = 1, 2, 3, 3a	BYS ≥ 2	

the time-dependent changes of total displacements obtained at pile node points along the soil profile, as a result of soil behavior analyses under dynamic loading, are utilized.

In Method III, the envelope of maximum displacements over time, obtained at the alignment of pile node points along the soil profile as a result of free soil behavior analyses performed with eleven earthquake records, is used as loading. Additionally, the average of the spectra obtained at the foundation base is used as the design spectrum. According to the regulation, Method I and Method II require a DD-1 earthquake level (with a return period of 2475 years), while Method III requires a minimum of DD-2 earthquake level (with a return period of 475 years).

Soil-pile-structure interaction analyses can be solved using either a direct analysis or a substructure approach [11] (see Fig. 1). The substructure approach consists of three main steps: (i) computation of kinematic interaction, (ii) calculation of inertial interaction, and (iii) combining the internal forces obtained by the two methods. Method III is based on static kinematic interaction calculation; therefore, the average of the spectra obtained from site response analysis can be used as the design spectrum in inertial interaction calculation.

Direct Analysis Approach   **Substructure Approach**
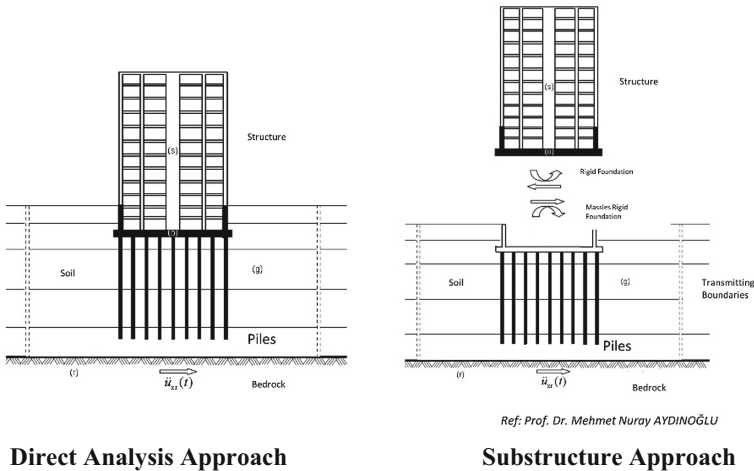
Fig. 1. SSI analysis approachs (Aydınoğlu, 2011)

3 Case Study

Within the scope of this study, soil-structure-pile interaction analyses will be conducted for a project site possessing a heterogeneous profile (see Fig. 2). The superstructure under consideration is planned to be used for residential and commercial purposes. The structure has a height of 83.0 m above the foundation upper level. The building usage class (BKS) of the structure within the project scope has been determined to be 3, the building importance factor is 1, the Building Height Class (BYS) is 1, and the Earthquake Design Classes (DTS) is 1.

The project site exhibits a variable soil and shear wave profile. Considering the geotechnical properties of the project site, the height class of the building, and the

seismicity of the project site, soil-structure-pile interaction analyses were carried out with Method I in accordance with TBDY 2018. A substructure approach was used in the analyses.To determine the geological properties of the soil section on which the planned construction project will be located, and to reveal the underground section, 37 soil borings, 10 seismic measurements, and pressuremeter tests in 16 wells were carried out. The locations of the borings are indicated with Fig. 3. As a result of the drilling studies conducted within the examined parcel boundaries, four different units have been observed: Artificial Fill, Clay, Clay (Alluvium), and Sandstone. Additionally, it has been determined that there are four different shear wave velocity values for the project site.
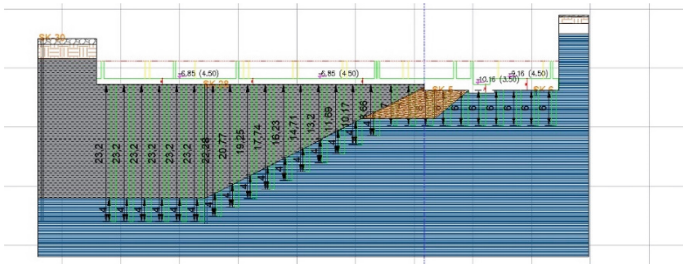
Fig. 2. Project site -cross-sectional view
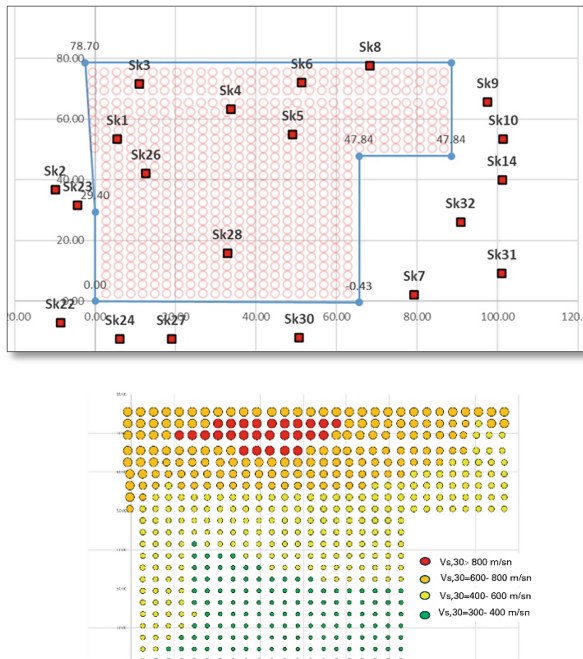
Fig. 3. The locations of the borings (Sk) and shear wave velocity ($V_{s,30}$) map

As part of this study, the soil environment, building foundation, and pile elements have been modeled in 3D. It is planned to use pile elements of 80 cm diameter and lengths of 6 m, 10 m, 14 m, and 20 m within the project scope. The 3D geometry of the soil environment used in the analyses, as well as the raft foundation and pile placement plan, are presented (see Fig. 4). In accordance with TBDY 16C.2.2.1 (c), the building foundation and basement perimeters (up to the ground floor level) have been modeled as massless, infinitely rigid elements.
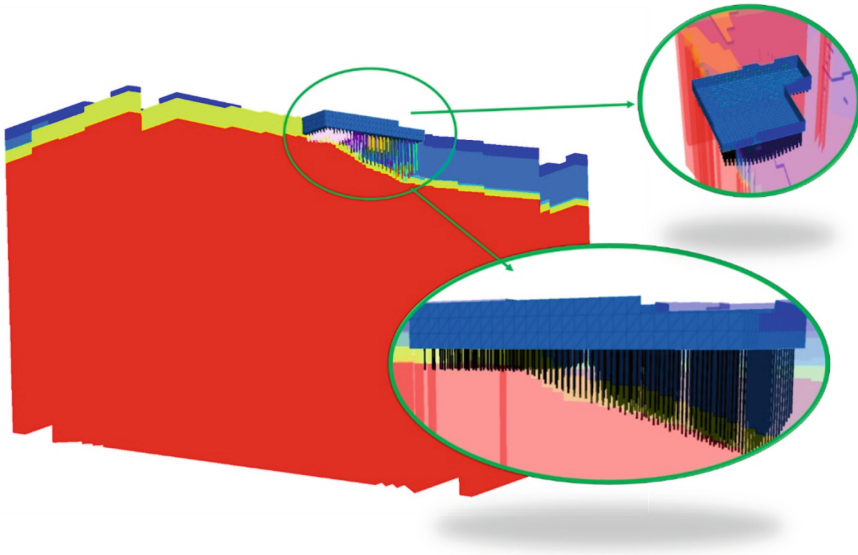
Fig. 4. The 3D geometry of the soil environment raft foundation and pile placement plan,

The non-linear behavior of the soil has been considered using the hysteretic behavior model in FLAC3D 3.0 [12], and due to the software's low damping ratio at low unit deformation levels for each soil layer, an additional 2% damping has been considered in layers behaving elastically at the engineering base level. A viscous boundary, proposed by Lysmer and Kuhlemeyer [13] as a transmitting boundary, has been utilized. FLAC3D 3.0 forms the viscous boundary by placing independent damping elements parallel and perpendicular to the boundary at the limits of the model.

In the analyses, pile elements have been modeled using built-in applications in Flac3D. Interactions between the piles and the surrounding soil are considered using springs perpendicular and parallel to the pile axis. These springs are elastoplastic, function of cohesion, and their yield strengths are dependent on effective normal stress.

According to provision TBDY 16C.2.2.1 (b), appropriate interface elements will be used between the piles and the soil medium. To calculate the stiffness of these interface elements in horizontal and vertical directions, the p-y, t-z, and Q-Z curves specified in TBDY 16C.3.2.1(b) will be employed. In the formation of the p-y, t-z, and Q-Z curves, nonlinear relationships developed for static and cyclic loads by Matlock [14] for soft clay (water < 50 kPa), by Reese and others [15] for dense clay below the water level,

by Welch and Reese [16] for dense clay above the water level, and by Reese and others [17]for sand, have been used. These references were used as indicated in the regulations for generating p-y curves for soft clay (water < 50 kPa), dense clay below water level, dense clay above water level, and sand.

The calculation model was finalized with a soil layer at a depth of 180 m, having a shear wave velocity Vs = 878 m/s, considering the geotechnical studies conducted for the project site. Probabilistic seismic hazard analyses have been carried out for the project site, and design spectra have been obtained for the DD-1 earthquake level (see Fig. 5). Considering this spectrum, 11 earthquake records have been selected as required by the regulations. The selected records have been modified to ensure spectral match with the design spectrum, and subsequently, the Soil-Structure Interaction (SSI) analyses have been conducted.
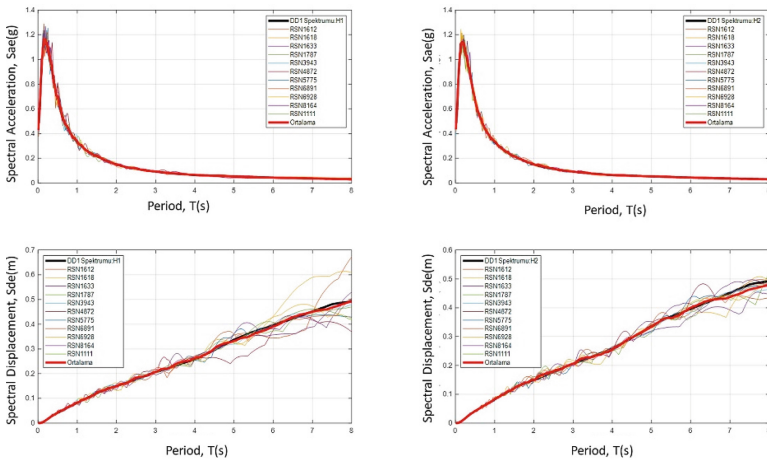
Fig. 5. Design spectrum of the project site

4   Analysis Results

Within the scope of the study, the structure–pile–soil interaction analysis has been performed. The results of the kinematicinteraction and inertia interaction analyses are presented.

4.1   Kinematic Interaction Analysis and its Results

For the DD-1 earthquake ground motion level, three-dimensional foundation-pile-soil interaction analyses were carried out using the 11 earthquake ground motion records defined at the lower boundary of the established soil calculation model (Vs = 878 m/s). In these analyses, the inertial characteristics of the superstructure are not considered, hence the term kinematic interaction is used to describe this formation in the foundation-pile-soil system. The largest pile internal forces were calculated for the 11 earthquake

ground motions used in the analyses. The diagrams of the average maximum pile moment and shear force obtained are presented with Fig. 6 for pile elements of 6 m and 14 m in length.
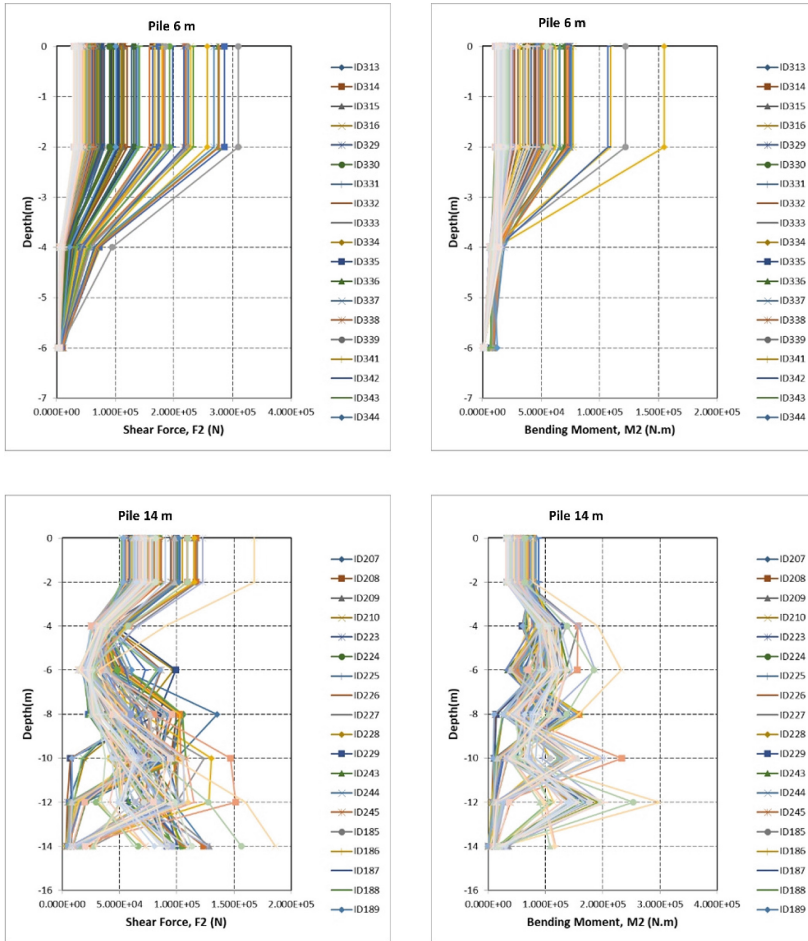
Fig. 6. Kinematic interaction analysis results

4.2 Inertial Interaction Analysis and its Results

The second step of the interaction analysis with the Subsystem Method is called "Inertial Interaction". Inertial interaction analyses allow for consideration of the additional strains caused by earthquake waves returning from the vibrating superstructure to the pile-soil medium in pile elements. The analysis results are given with Fig. 7. The internal forces and displacements obtained in the piles as a result of the inertial interaction calculation must be combined with those obtained from the kinematic interaction calculation.
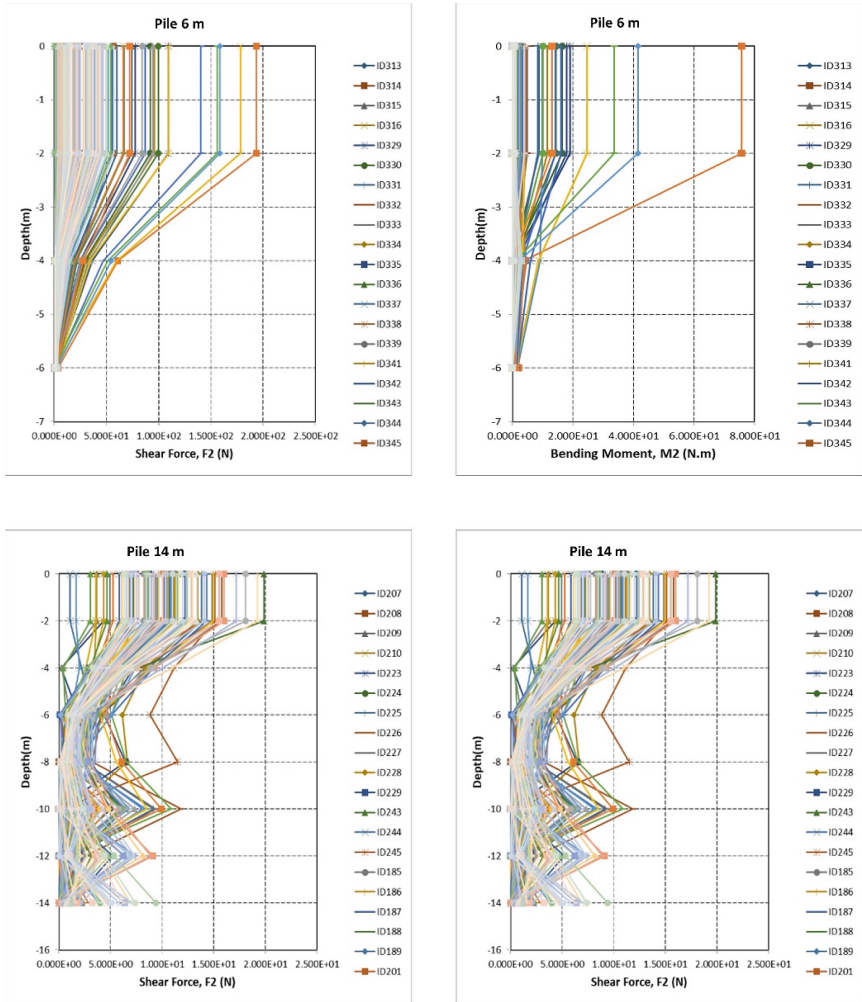
Fig. 7. Inertial interaction analysis results

4.3   Combination of Kinematic and Inertial Interactions

According to TBDY 2018, Article 16.c.5, the displacements and internal forces in the piles to be considered for evaluation/design must be calculated as the sum of the absolute values of the results of kinematic and inertial interaction.

5   Conclusion

This study involves conducting three-dimensional structure-pile-soil analyses in a project area with heterogeneous characteristics. Firstly, the geology and local soil conditions of the region were investigated. The available data, along with the results of seismic surveys, were thoroughly reviewed to obtain the profile of the project site.

The analyses were conducted following Method I as required by the Turkish Earthquake Design Code of 2018 (TBDY 2018). Probabilistic seismic hazard analyses were performed for the site, and the design-based spectrum was obtained for the DD-1 earthquake level. Eleven earthquake ground motion records, compatible with the regional seismicity, were selected and modified to match the design-based spectrum. The soil medium, structure foundation, and pile elements were modeled in three dimensions, and dynamic structure-pile-soil analyses were performed.

When the results of kinetic interaction and inertial interaction analyses conducted in a heterogeneous soil medium were investigated, it was determined that both approaches exhibit significant discrepancies and variations in the internal forces (shear and moment) of the piles.

The simplification of the soil medium as infinite layer soil profiles in structure-pile-soil interaction analyses can lead to non-negligible effects on the results of the SSI analysis. Therefore, it is crucial to avoid such simplifications, especially in engineering applications.

References

1. FEMA.gov | Federal Emergency Management Agency - FEMA.gov is experiencing technical difficulties. https://www.fema.gov/disaster/2009. Accessed 30 July 2023
2. Wolf, J.P., Obernhuber, P.: Non-linear soil-structure-interaction analysis using dynamic stiffness or flexibility of soil in the time domain. Earthq. Eng. Struct. Dyn. Eng. Struct. Dyn. **13**, 195–212 (1985). https://doi.org/10.1002/EQE.4290130205
3. Park, S.H., Antin, N.: A discontinuous Galerkin method for seismic soil–structure interaction analysis in the time domain. Earthq. Eng. Struct. Dyn. **33**(2), 285–293 (2004). https://doi.org/10.1002/eqe.353
4. Zerfa, Z., Loret, B.: A viscous boundary for transient analyses of saturated porous media. Earthq. Eng. Struct. Dyn. **33**(1), 89–110 (2004). https://doi.org/10.1002/eqe.339
5. Wang, G., Chen, L., Song, C.: Finite–infinite element for dynamic analysis of axisymmetrically saturated composite foundations. Int. J. Numer. Methods Eng. **67**(7), 916–932 (2006). https://doi.org/10.1002/nme.1654
6. Kausel, E.: Early history of soil–structure interaction. Soil Dyn. Earthq. Eng. **30**(9), 822–832 (2010)
7. Park, J.H., Choo, J.F., Cho, J.R.: Dynamic soil-structure interaction analysis for complex soil profiles using unaligned mesh generation and nonlinear modeling approach. KSCE J. Civ. Eng. **17**, 753–762 (2013). https://doi.org/10.1007/S12205-013-0135-1
8. Kramer, S.L.: Geotechnical Earthquake Engineering. Prentice Hall (1996)
9. Braja, M.: Das Principles of Geotechnical Engineering (2011)
10. TBDY-2018 (2018) Türkiye Deprem Bölgelerinde Yapılacak Binalar Hakkında Yönetmelik
11. Aydınoğlu, M.N.: Zayıf Zeminlerde Yapılan Binalarda Dinamik Yapı-KazıkZemin Etkileşimi İçin Uygulamaya Yönelik Bir Hesap Yöntemi. Boğaziçi Üniversitesi Kandilli Rasathanesi ve Deprem Araştırma Enstitüsü Rapor No. 2011/1, İstanbul (2011)
12. FLAC 8 Basics | US Minneapolis - Itasca Consulting Group, Inc. https://www.itascacg.com/software/flac-8-basics. Accessed 30 July 2023
13. Lysmer, J., Kuhlemeyer, R.L.: Finite dynamic model for infinite media. J .Eng. Mech. Div. **95**, 859–877 (1969). https://doi.org/10.1061/JMCEA3.0001144
14. Matlock, H.: Correlation for design of laterally loaded piles in soft clay. In: Proceedings of the Annual Offshore Technology Conference 1970-April (1970). https://doi.org/10.4043/1204-MS

15. Reese, L.C., Welch, R.C.: Lateral loading of deep foundations in stiff clay. J. Geotech. Eng. Div. **101**, 633–649 (1975). https://doi.org/10.1061/AJGEB6.0000177
16. 3–5–65–89 RW-RR n., 1972 undefined Laterally loaded behaviour of drilled shafts. cir.nii.ac.jp
17. Reese, L., Cox, W.: Conference FK-OT, 1974 undefined Analysis of laterally loaded piles in sand. onepetro.orgLC Reese, WR Cox, FD KoopOffshore Technology Conference (1974). onepetro.org

Transportation

Interactions Between Automated Shuttle and Vulnerable Road Users: A Case Study

Stefano Coropulis(✉) , Nicola Berloco , Roberta Gentile , Paolo Intini ,
Paola Longo, and Vittorio Ranieri

Department of Civil, Environmental, Land, Construction and Chemistry, Politecnico di Bari,
Bari, Italy
{stefano.coropulis,nicola.berloco,roberta.gentile,paolo.intini,
paola.longo,vittorio.ranieri}@poliba.it

Abstract. The evermore introduction of automated systems in driving operations opens the possibility of an upcoming traffic scenario with automated vehicles. Research about automated vehicles in traffic has been run with automated shuttles mainly for two reasons: to provide a wide idea about users' acceptance (more users can get on a bus than on a private vehicle) and valuable simulation of interactions with other vehicles, but on a fixed and limited route. The main concern in this sense is a quantitative estimation (speed, acceleration, and deceleration) of the automated shuttle while interacting with vulnerable road users (VRUs) and regular vehicles. This specific analysis about the interactions was the main focus of this study. The proposed study was a real-world simulation set in Bari (Italy), with a partially automated shuttle bus provided by Navya. Data about the vehicle interacting with pedestrians, e-scooters, and regular vehicles were collected and then processed. The automated vehicle behaved in a safe way in all the tested interactions, keeping its speed very low (below 15 km/h), to ensure comfort also during the emergency braking (with a maximum deceleration of 1.5 m/s^2). The most outstanding result of the tests was to verify that the automated shuttle behaves in the same way for all the different interactions, regardless of the type of user interacting and the modality (crossing, overtaking, following). This result means a lot because it suggests that the vehicle can safely deal also with unpredictable decisions by VRUs, that otherwise could have constituted a big issue for the implementation of such types of vehicles.

Keywords: Vulnerable Road Users · automated shuttle bus · interactions · road safety

1 Introduction

The vehicles circulating in traffic, nowadays, are evermore equipped with Advanced Driving Assistant Systems (ADAS) which reduce the driving complexity for human drivers. The rate of help that technology can provide to the driver strictly depends on the level of automation reached by the vehicle [1].

Currently, in the world, just vehicles with a rate of automation corresponding to the 3 and 4 of [1] are widely tested in several scenarios [2]. There are several testbeds deployed to understand simultaneously the reliability of automation in real-world situations and the human acceptance of such devices. This twofold scope is generally got by relying on automated shuttle buses that, at the same time, can get the perceptions from several different users per trip (the passengers), and driving on a fixed route, reducing the possible uncontrolled and unpredictable situations, especially while interacting with other road users.

The tests using automated shuttle buses were deployed especially in the United States [3] all aimed at understanding the human acceptance and safety perception of automated vehicles. For reason of uniformity, the tests had some characteristics in common related to the automated shuttle, like the restricted number of available seats (ranging from 6 to 12), low travel speeds (never greater than 25 km/h), traveling on short routes with few stops, free fares (to enhance the use), and at least one onboard human driver ready to take over the automated vehicle. During these tests, retrieving data by the circulating vehicle can provide useful insights about the motion of the vehicle. While considering the motion, being aware of the mechanisms of interactions between the automated shuttle bus and pedestrians, other vehicles, bicycles, and so forth, becomes a crucial output [4], especially because these data are not openly available. Thus, the highlighted outcomes from previous studies in this field with automated shuttle bus were mostly related to the human perceptions of automation rather than on interactions. In fact, from the analysis conducted by [5] emerged that 30% of users after the first automated ride were confident in using the driverless shuttle bus. This result was in accordance with other studies, concluding that the rate of onboard security and safety perceived by users is extremely high, more than the one on regular buses [6, 7].

Despite this perception of extreme onboard safety, it is debatable whether the users are trustful enough towards the automation to drastically change their driving behaviors. In fact, most users seemed to be uncomfortable about the chance of performing other secondary tasks (working or watching movies) while traveling even if on board of an automated vehicle. They prefer to be alert. This behavior is justified by the fact that users' expectations about the automation were greater by far than what they experienced [8]. Under this light, the automated bus was considered just a good feeder for public transport [9], not as a relevant means of transport for long private journeys. Hypothesized countermeasures thought to overcome human reluctance are the development of mobile apps or videos which inform the travelers about the vehicle maneuvers, in real-time [7], and the equipment of the vehicle with more advanced and human-friendly control systems for taking over [10]. Moreover, designing shuttle buses with comfortable sizes seemed to be crucial for increasing the attractivity of the vehicle, in fact it is perceived safer by passengers [11, 12], making possible to create more interactions among passengers [13]. On the other side, small sized buses can reduce the inclusivity [14], and the chance of sharing the vehicle with just a few unknown people can create unpleasant situations.

All the above-mentioned considerations about the human acceptance of automation create a solid base for the massive introduction of such technologies. Under this light, testing in real-world scenarios how the automated shuttle bus can behave in a complex

urban scenario seems a good chance to deeply understand how effective its implementation can be. When tested with other vehicles, the automated shuttle buses provided promising results at intersections [15]. However, it is still unknown how these vehicles can interact with vulnerable road users (VRUs) in an urban environment, but it is supposed to be a problematic coexistence [16], despite the implementation of advanced VRU detection systems in the vehicles [17]. The aim of this research is to fill this gap, simulating the interactions of the automated shuttle bus with VRUs and vehicles. The testbed for the proposed research was Fiera del Levante, located in Bari, Italy. The main scope of the research is to transform all the qualitative results provided by literature into quantitative outputs about how the automated shuttle behaves in presence of VRUs and complex urban scenarios. The automated shuttle bus, by Navya, was categorized as a SAE level 3 vehicle. It travelled in the Fiera del Levante in Bari, on a fixed route with few stops. The test was composed of three sub-categories, as follows:

- The interaction between the shuttle bus and one pedestrian crossing the road (on crossing walk or outside), in different ways;
- The interaction between the shuttle bus and one e-scooter/bicycle overtaking, following, and leading the automated shuttle bus;
- The interaction between the shuttle bus and one regular vehicle overtaking the automated shuttle bus.

The three sub categories of the text will be detailed in the following chapter, that also provide the characteristics of the simulated scenarios. Then the results will be shown and discussed, before summarizing all the main outcomes and considerations in the conclusion.

2   Methodology

The case study was set in the Fiera del Levante in Bari (an area with regulated access), Italy, on a predetermined route (marked by a red sign in Fig. 1) as shown in Fig. 1. The shuttle travelled by its own settings on the largest road sections in the Fiera del Levante, to allow comfortable spaces and pick-up spots. The presence of pick-up spots implied the absence of parking slots on the roadside. Among all the roads travelled in the Fiera del Levante, the test was conducted on Viale Pisa, because it showed a segment of about 80 m without pick-up spots that enables the shuttle bus to reach its greatest speeds and not to stop. The absence of stops allowed to run the tests at condition of free-flow speed regime.

The automated shuttle always keep a spatial headway of 2 m ahead and 1 m on the side before the emergency stop, considering these values as safety thresholds for its motion. The shuttle bus tried always to pursue comfortable travelling conditions for all the passengers; thus, it slows down when the sensors perceived something and then it performs the regular braking maneuvers to ensure the passenger safety. The emergency braking is usually performed when something unexpected happens and the vehicle can not do anything else.

Being a SAE level 3, the shuttle requires the presence of a human driver to take over in case of failure or to drive in a different operational domain from the designed ones (the operational domain is the red route in Fig. 2).

Fig. 1. Investigated area, Fiera del Levante, in Bari (BA), Italy.
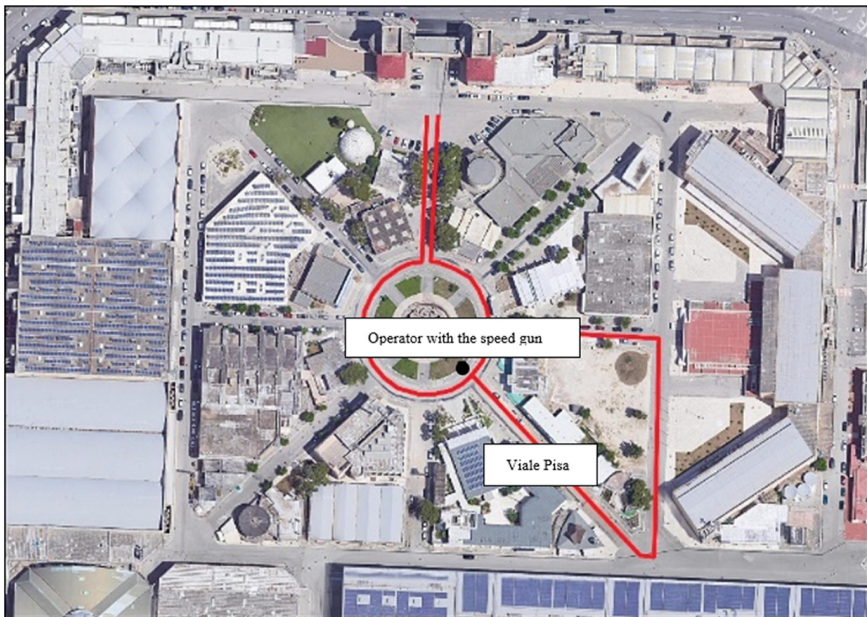
Fig. 2. Focus on the investigated road (Viale Pisa) and the position of the operator with the laser speed gun (black circle).

To run the experiment in a precise way, the chosen road, Viale Pisa, was marked with horizontal signs with an interval of 5 m. This marking was crucial to precisely set all the phases of the tests and to have reproducibility of them every time.

All the measurements were taken by two operators, one outside the shuttle, and the other inside. The operator outside was equipped with a speed laser gun (LaserTech TruSpeed®) placed on a tripod to collect the shuttle speed and position every second. The operator was placed in front of the shuttle, at the centerline of the lane, in the main square (the rounded area in Fig. 2), far 15 m (the sensitivity of the instrument) from the end of the road, Viale Pisa, to collect all the data from the beginning to the end of the test (Fig. 2). On the other side, another operator was inside the vehicle to record how the shuttle perceive the external environment through sensors thanks to a desktop that enables this operation (Fig. 3).

Fig. 3. Automated shuttle by Navya (external view) and focus on the desktop showing how the shuttle perceive the external environment through its sensors (in blue the predetermined route, in yellow the detected obstacles as point clouds).

The test was composed, as mentioned before, of three different sub categories of tests, investigating the possible interactions that could happen at urban level:

- automated shuttle-pedestrians;
- automated shuttle-micromobility devices/bicycles;
- automated shuttle-vehicles.

Each of the subcategories tried to simulate the most probable situations that could happen during these interactions; thus, they consisted in multiple tests for each subcategory.

2.1 Automated Shuttle-Pedestrians

Two tests were performed for this category of experiment: pedestrian crossing outside the crosswalk (Experiment 1) and stopping on the crosswalk while crossing (Experiment 2). The automated shuttle (AV) was monitored by the operators in order to collect its data about speed, acceleration, deceleration, time gap, and vehicle behavior.

The Experiment 1 was performed as follows: the shuttle runs in presence of crosswalk on its route, but one pedestrian regularly crosses the street around 10 m before the crosswalk with an unexpected maneuver. The pedestrian starts its action when the shuttle is 15 m distant from the crossing (calculated stop distance plus a safety margin for redundancy).

The Experiment 2 followed this instruction: the shuttle runs in presence of crosswalk where a pedestrian regularly crosses the street. The pedestrian starts its action when the shuttle is 15 m distant from the crossing (calculated stop distance plus 5 m, for redundancy) and stands on the crosswalk in the middle of the street for 5 s, watching his mobile phone.

2.2 Automated Shuttle-Micromobility Device (e-Scooter)

This category was investigated by running three different tests. Two car-following situations were tested with the shuttle being also the follower of a micromobility device. And another situation, a crossing maneuver by the device was studied. In this set of tests, either an electric scooter or a bicycle could be used, depending on the availability of the means, since, although the two vehicles are different, the maneuvers they perform are the same, as well as their vulnerability. For convenience, the tests are explained below using the e-scooter as tested vehicle, considering that the procedure is identical for the bicycle.

The collected data about the AV motion for this set of tests were speed, acceleration, deceleration, and headway (lateral or longitudinal, according to the test).

Experiment 3: the automated shuttle following the e-scooter. As soon as the shuttle enters Viale Pisa after a right-side turn, it faces an e-scooter already travelling on Viale Pisa. Thus, the AV is forced to follow the e-scooter that travels at 10–15 km/h and to adapt its behavior accordingly (it can overtake or follow).

Experiment 4: e-scooter overtaking the automated shuttle. This experiment starts from a condition of AV leading and ends in a condition of AV following. In fact, the shuttle travels along Viale Pisa leading an electric scooter. The e-scooter overtakes on the left the shuttle at 75 m from the operator with the speed gun. The maximum speed reached by the e-scooter is 25 km/h. Completed the overtaking, the e-scooter performs the cut-in on the desired lane on its right, with aggressive behavior. In this moment the e-scooter becomes leader, and the shuttle follower. The analysis was made on the behavior that the AV keeps in this switch from leader to follower and on the reaction to an aggressive cut-in.

Experiment 5: e-scooter crossing the road section as a pedestrian, outside and at the crosswalk. The shuttle travels along Viale Pisa where there is a crosswalk, that the e-scooter regularly crosses (crossing maneuver number 2). Before the crosswalk, the e-scooter performs an irregular crossing (crossing maneuver number 1). Both these maneuvers happen when the shuttle is 15 m from the e-scooter (stop distance is a safety margin for redundancy). The e-scooter starts from a standstill position and crosses the road reaching its possible maximum speed in the available space.

2.3 Automated Shuttle-Cars

Even if cars are not VRUs, the interactions among shuttle bus and cars can lead to risky situations, especially in urban environment where the driving behavior is highly unpredictable. The tests run for this category were two. The importance of the tests for the interaction AV-car was also for modelling purposes. In fact, studying the car-following behavior of the automated shuttle, it was possible to carve out useful data for

the parameters to use while simulating automated vehicles in simulators. In this sense, two situations were tested, the regular vehicle as the leader, and the regular vehicle overtaking the shuttle with an aggressive maneuver. The collected data about AV for this experiment were the speed, deceleration, acceleration, time gap, spatial headway from the vehicle, acceptance of the leader's speed. The car driver behavior was also monitored to understand the behavior related to AV.

The Experiment 6, automated shuttle as follower, was run according to the following procedures: the shuttle turns on Viale Pisa and immediately after the turn, meets the private vehicle, which begins to be followed by the AV. The private vehicle travels at 10–20 km/h decelerating frequently, forcing the AV to maintain adaptive behavior or to overtake the private vehicle.

The Experiment 7, regular vehicle overtaking the automated shuttle, was performed as follows: the shuttle travels along Viale Pisa leading the regular vehicle behind. The private car followed the shuttle and, when 75 m far from the speed gun, the private vehicle began the overtaking maneuver. The maximum speed reached by the car during the overtaking was set equal to the posted speed limit, 50 km/h. After completing the maneuver, the car completes the cut-in with aggressive behavior.

3 Results and Discussions

The following graph shows the behavior of the automated shuttle bus during a pedestrian crossing. The graph trend shows the two distinct phases of the experiment, as highlighted in Fig. 4. In the first phase the pedestrian starts the crossing phase, the automated shuttle recognizes the pedestrian at a distance of at least 4 m (as stated by the onboard desktop) and slows down from a speed of 10 km/h to 8 km/h. The pedestrian finishes the crossing,
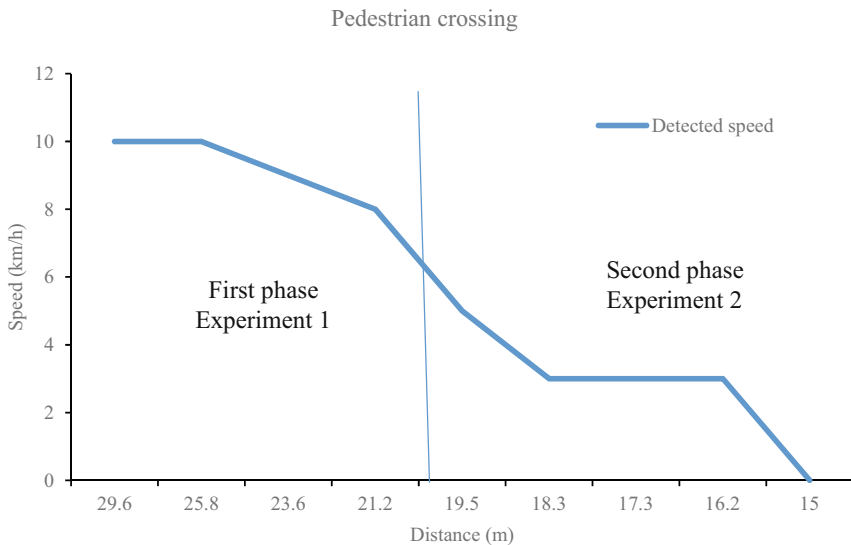
Fig. 4. Graph showing shuttle reactions to pedestrian crossing.

and the vehicle continues its way, without braking because it recognizes the obstacle before the 2 m and the pedestrian ends its task before being 2 m or less far from the shuttle (Experiment 1).

In the second phase (Experiment 2), the pedestrian is stationary along the lane on the crosswalk, the automated shuttle recognizes the obstacle at 4 m and then stops with a regular brake when the distance between the pedestrian and the automated vehicle is greater than 2 m. The deceleration and the acceleration are always below 1 m/s^2. This is due to the low traveling speeds kept by the shuttle in presence of obstacles, or possibly dangerous situations, like the presence of a crosswalk. After the first interaction with the pedestrian, the shuttle does not speed up since the crosswalk is close to its position, so it just starts again its motion and is ready for a possible imminent stop due to a probable pedestrian crossing at the crosswalk. The shuttle keeps always safe conditions towards the pedestrian. While the pedestrian is on the crosswalk, waiting and not walking, the shuttle is stopped, and it is ready to start again its travel after 3 s that the route is free. Unless the obstacle stays in its route (with a side margin of 1 m on both sides) the shuttle stays still (Fig. 5).

Fig. 5. Experiment 2: the pedestrian is crossing on the crosswalks and the shuttle bus stops.

The following graphs show the behavior of the automated shuttle bus when the e-scooter leads, overtakes, and crosses the automated shuttle bus (Experiment 3-4-5).

In the case of Experiment 3, e-scooter leading, the second graph shows a variable trend in dependence of the e-scooter speed: the speed of the automated shuttle decreases when the distance between the shuttle and the e-scooter is less than 4 m and when the scooter speeds up increasing the headway (greater than 4 m) the shuttle speeds up too, reaching its maximum speed of 10 km/h. During the rest of the experiment, when the distance between the two vehicles is in the range of 4 m, the speed kept by the shuttle is always ranging between 8 km/h and 4 km/h according to the speed of the e-scooter and the calculated stop safety distance by the algorithm of the shuttle. The decelerations

are always lower than 0.3 m/s^2. The maximum recorded acceleration is 0.75 m/s^2 going from 5 km/h to 8 km/h when the headway between the two vehicles started to increase.

The shuttle bus travels at a constant speed of 13 km/h when the e-scooter overtakes it, during the Experiment 4. Once overtaken, the automated vehicle stops because the distance between the two involved elements is less than 2 m. In this situation, the e-scooter keeps a lateral safety distance of 1.5 m from the shuttle, and after completing the overtake, with a speed of 25 km/h, it executes the aggressive cut-in. The shuttle does emergency braking since the e-scooter appears on its path at a distance lower than 2 m and it cannot keep a safety margin except for braking and stopping. The value of the emergency braking is lower than the maximum allowed emergency braking (equal to 6 m/s^2), since the traveling speed is always low, and the sensors start perceiving the moving obstacle (the e-scooter) thanks to 360° view before the e-scooter is already on the same path of the shuttle itself.

The last experiment, Experiment 5, was conducted in two distinct phases. In the first phase the e-scooter starts the crossing phase not on the crosswalk, the automated shuttle recognizes the presence of a moving obstacle and gradually stops (with a maximum deceleration of 0.6 m/s^2). In the second phase, the shuttle is traveling again at 13 km/h, but the e-scooter unexpectedly crosses at the crosswalk and the shuttle slows down to 3 km/h (maximum deceleration of 1.5 m/s^2). The shuttle does not stop at all because the e-scooter ends its maneuver before being in a 2-m-range from the shuttle. When the e-scooter completed the crossing, the automated vehicle continues along the path and then started again to slow downs being at the end of its route on the segment and approaching an intersection (deceleration equal to 0.4 m/s^2). During this experiment, the maximum achieved acceleration was 0.8 m/s^2, the designed deceleration and acceleration according to Italian regulations for the speed diagram [18] (Figs. 6 and 7).

The following graphs show the behavior of the automated shuttle bus when the regular vehicle is the leader and when it overtakes the automated vehicle. In the case of the car leading, Experiment 6, the first graph shows a variable trend dependent on the speed of the car: the speed of the automated vehicle decreases when the distance between the shuttle and the car is less than 4 m, and the automated vehicle stops when the distance is smaller than 2 m. According to this behavior, the acceleration and the deceleration of the automated vehicle are always below 0.5 m/s^2, because it keeps the safety distance and the necessary speed to avoid emergency braking.

In the second experiment, the shuttle bus travels, starting from a still position, reaching its maximum speed of 9 km/h. When the car starts overtaking, the shuttle slows down to 8 km/h, perceiving thanks to the sensor the modified external conditions. Once overtaken, the vehicle executes an aggressive cut-in on the desired lane on the right, where the shuttle is traveling. The vehicle appears on the lane within the 2-m-range and so the automated vehicle stops with an emergency braking of 1.6 m/s^2. During the experiment, before the aggressive cut-in, the maximum acceleration and deceleration were always below 0.5 m/s^2, providing comfortable travels to the shuttle users (Figs. 8 and 9).
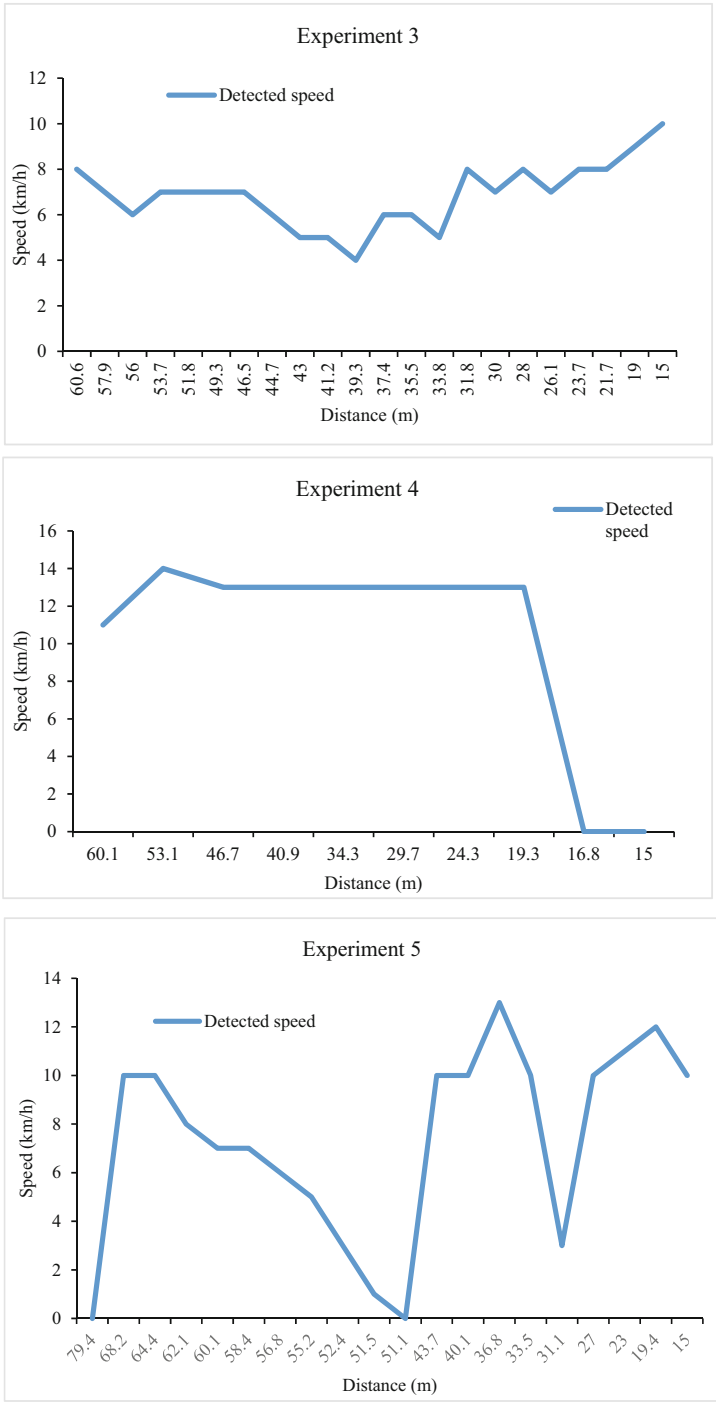
Fig. 6. Graphs about the shuttle behaviors in presence of an e-scooter.

Fig. 7. Experiment 5: E-scooter crosses the road in front of the shuttle bus, in an unexpected way.

4 Conclusions

This study aims at highlighting the automated shuttle (SAE level 3 automated vehicle) behavior in presence of VRUs and regular vehicles, in the urban context. This study was run in a protected environment like the Fiera del Levante in Bari, with a limited number of vehicles and pedestrians, for a predetermined operation domain of the automated vehicle [19]. Moreover, the outcome of this study could have provided important insight into the parameters to set for the partially automated vehicle in a simulation environment (traffic simulation and driving simulation) for making road safety assessments in future scenarios. The three tested interactions of the automated vehicle were with a pedestrian crossing regularly and irregularly, with an e-scooter leading, overtaking, and crossing, and with a regular vehicle leading and overtaking.

In all the aforementioned tests the vehicle keeps a safety margin of 2 m from the vehicles traveling behind or in front of it. In this sense, the automated shuttle is designed to behave in the same way no matter the type of vehicle or user interacting with it, but just considering physical parameters, like the safety distance and the maximum acceleration and deceleration. The safety margin of 2 m to stop the vehicle is always ensured. To always ensure safe and comfortable travel, whenever something happens in the 4-m-range the vehicle starts to decrease its speed or stop if something abnormal is happening. It stops also when there is an obstacle (fixed or in motion) within the 2-m-range. Then it starts again its travel after waiting for 3 s. If anything happens it stays for another 3 s still. Hence, the time margin to start again the travel after stopping is 3 s. This time is also the time that the vehicle will stop at an intersection before crossing it, in absence of obstacles. This vehicle is designed to be always safe within its operational domain, which is limited. But in this domain, it cannot fail. The presence of the human driver is requested in case of technological failure or in case of route changing for some reasons [19]. In fact, this SAE level 3 automated vehicle is capable of autonomous driving and behavior only on its predetermined route and only for car-following. If there
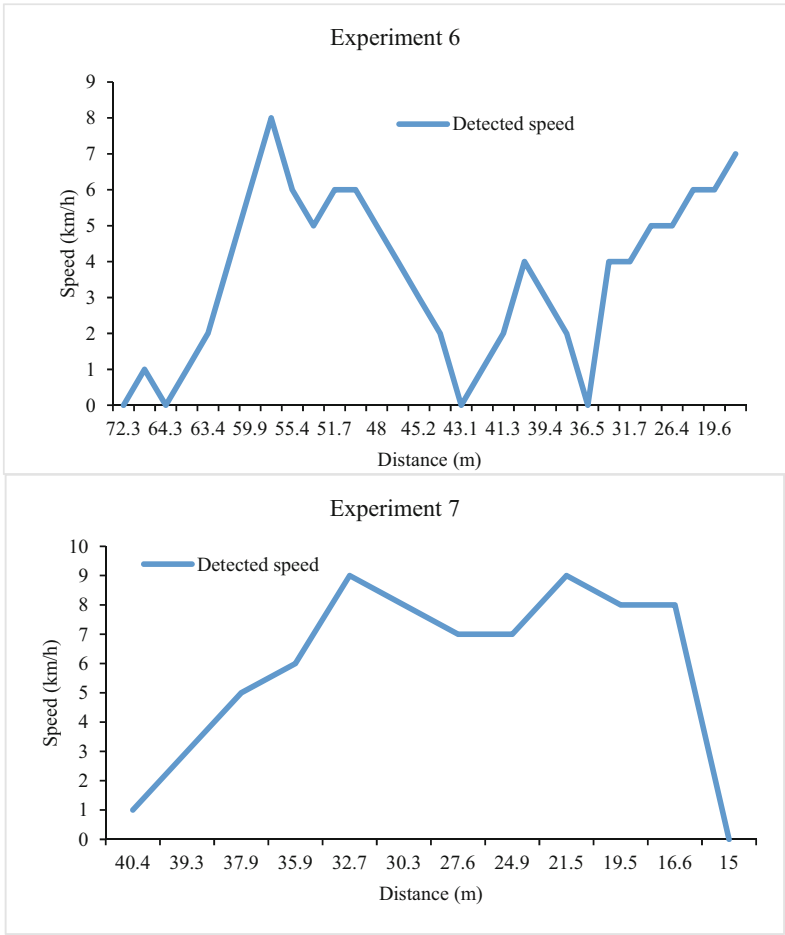
Fig. 8. Graphs about the shuttle behaviors in presence of a regular vehicle.

is an obstacle it will not execute any lane-changing behavior considering this kind of maneuver too risky. The human driver, in this case, must take over and execute the lane-changing with a manual controller.

The automated vehicle can react in the same way to regular and irregular actions from other users. This is a crucial outcome, as well as the standardized behavior of the automated vehicle regardless of the type of user interacting with it. This fact enables a great safety margin for the vehicle. Moreover, the fact that the vehicle tries always to keep travel comfortable for the users is another important aspect to consider. In fact, this point goes toward the acceptance of automation by the users.

One crucial aspect, but in a negative sense, is the fact that the vehicle cannot work well under bad weather conditions because the sensors cannot perceive well the external environment. Hence, currently, the use of automated vehicles can be restricted to sunny

Fig. 9. Experiment 7: the car is overtaking the shuttle bus in an aggressive way.

or cloudy weather and restricted/controlled environments (as also stated by Italian and European regulations).

Despite the promising results of the tests, the performance of the automated vehicle in terms of speed and acceleration, and deceleration cannot be translated into parameters to use in the simulators, due to the limited operational domain and the restricted numbers of experiments not considering all the possible shades of automated behavior. Moreover, in a limited and controlled domain, like the tested one, the vehicle did not have the chance of expressing all its motion features. It must also be noted that the vehicle is a public means of transport, that must ensure the comfort of the users; thus, its travel will always be safer and at a lower speed than a private automated vehicle. Hence, the characteristics of an automated shuttle bus cannot be applied to all the automated vehicles, especially the private ones, in the simulators.

References

1. SAE International. https://www.sae.org/standards/content/j3016_201806/. Accessed 30 Apr 2021
2. Iclodean, C., Cordos, N., Varga, B.O.: Autonomous shuttle bus for public transportation: a review. Energies **13**(11), 2917 (2020)
3. Haque, A.M., Brakewood, C.: A synthesis and comparison of American automated shuttle pilot projects. Case Stud. Transp. Policy **8**(3), 928–937 (2020)
4. Mcity. https://mcity.umich.edu/wp-content/uploads/2018/09/mcity-driverless-shuttle-case-study.pdf. Mcity driverless shuttle: A case study. University of Michigan (2018)
5. Akers, M.: How does downtown's autonomous bus work? Las Vegas Sun (2018)

6. Soe, R.M., Müür, J.: Mobility acceptance factors of an automated shuttle bus last-mile service. Sustainability **12**(13), 5469 (2020)

7. Nordhoff, S., Malmsten, V., van Arem, B., Liu, P., Happee, R.: A structural equation modeling approach for the acceptance of driverless automated shuttles based on constructs from the Unified Theory of Acceptance and Use of Technology and the Diffusion of Innovation Theory. Transport. Res. F: Traffic Psychol. Behav. **78**, 58–73 (2021)

8. Nordhoff, S., de Winter, J., Madigan, R., Merat, N., van Arem, B., Happee, R.: User acceptance of automated shuttles in Berlin-Schöneberg: a questionnaire study. Transport. Res. F: Traffic Psychol. Behav. **58**, 843–854 (2018)

9. Nordhoff, S., de Winter, J., Payre, W., Van Arem, B., Happee, R.: What impressions do users have after a ride in an automated shuttle? An interview study. Transport. Res. F: Traffic Psychol. Behav. **63**, 252–269 (2019)

10. Brell, T., Philipsen, R., Ziefle, M.: Suspicious minds? Users' perceptions of autonomous and connected driving. Theor. Issues Ergon. Sci. **20**(3), 301–331 (2019)

11. Sovacool, B.K., Axsen, J.: Functional, symbolic and societal frames for automobility: implications for sustainability transitions. Transp. Res. Part A: Policy Pract. **118**, 730–746 (2018)

12. Pudāne, B., Rataj, M., Molin, E.J., Mouter, N., van Cranenburgh, S., Chorus, C.G.: How will automated vehicles shape users' daily activities? Insights from focus groups with commuters in the Netherlands. Transp. Res. Part D: Transp. Environ. **71**, 222–235 (2019)

13. Gurumurthy, K.M., Kockelman, K.M.: Modeling Americans' autonomous vehicle preferences: a focus on dynamic ride-sharing, privacy & long-distance mode choices. Technol. Forecast. Soc. Chang. **150**, 119792 (2020)

14. Mirnig, A.G., Gärtner, M., Wallner, V., Trösterer, S., Meschtscherjakov, A., Tscheligi, M.: Where does it go? A study on visual on-screen designs for exit management in an automated shuttle bus. In: Proceedings of the 11th International Conference on Automotive User Interfaces and Interactive Vehicular Applications, Utrecht, Netherlands, pp. 233–243 (2019)

15. Beauchamp, É., Saunier, N., Cloutier, M.S.: Study of automated shuttle interactions in city traffic using surrogate measures of safety. Transp. Res. Part C: Emerg. Technol. **135**, 103465 (2022)

16. Kaye, S.A., Buckley, L., Rakotonirainy, A., Delhomme, P.: An adaptive approach for trialling fully automated vehicles in Queensland Australia: a brief report. Transp. Policy **81**, 275–281 (2019)

17. Ahmed, S., Huda, M.N., Rajbhandari, S., Saha, C., Elshaw, M., Kanarachos, S.: Pedestrian and cyclist detection and intent estimation for autonomous vehicles: a survey. Appl. Sci. **9**(11), 2335 (2019)

18. Ministerial decree 5th of November 2001, n. 6792: Functional and geometric standards for road design, Italy

19. Ministerial decree 28th of February 2018, GU Serie Generale n. 90: Methods and instruments to run experiments on roads for Smart Roads and Connected and Automated Vehicles

Use of Synthetic Fibers in Asphalt Pavements-Mini Review

Halime Solak[1](✉) ⬥, Erol İskender[1] ⬥, Atakan Aksoy[2] ⬥, and Cansu İskender[3] ⬥

[1] Civil Engineering Department, Karadeniz Technical University, Trabzon, Türkiye
{halimesolak,eiskender}@ktu.edu.tr
[2] Engineering Faculty, Karadeniz Technical University, Trabzon, Türkiye
aaksoy@ktu.edu.tr
[3] Civil Engineering Department, Avrasya University, Trabzon, Türkiye
cansu.iskender@avrasya.edu.tr

Abstract. Asphalt pavements are the most widely used pavement type due to their comfort, fast construction and various advantages over other pavements. Although the visco-elastic and thermo-plastic behavior of the bituminous binder, which is one of the asphalt pavement materials, provides advantages such as the elasticity of the asphalt pavement against small deformations, it can cause the formation of rutting problems at high temperatures. On the other hand, high tensile stresses may occur due to the plastic behavior of the bituminous mixture and cracks may occur in the asphalt pavement in cold climates and regions where temperature changes are rapid and high. Various additives can be used against major problems such as rutting, water damage and cracking problems in asphalt pavements. Despite the positive effects of these additives at medium and high temperatures, a high effect is generally not achieved in terms of low temperature cracking problem. Fiber additives come to the fore in this sense. Synthetic fibers can increase the crack resistance of asphalt pavements at low temperatures and increase the life of the pavement with their adhesion and high tensile strength with bitumen. In this study, a general evaluation will be made on the use of synthetic fiber in asphalt pavements. Synthetic fibers used in asphalt pavements and their properties, the effect of fiber diameter and length, proportional addition amounts and addition techniques will be investigated.

Keywords: Asphalt Pavement · Synthetic Fiber · Deformation

1 Introduction

The rapidly growing transportation industry and the resulting traffic loads have led to an intensification of deformation in asphalt pavements. Therefore, the use of sustainable and durable asphalt pavement materials has become mandatory to address the problems caused by the constantly increasing traffic volume and repeated loads [1]. Increasing the structural capacity of the asphalt pavement and improving the durability of the layers are seen as effective approaches to meet sustainability and increasing capacity demands [2].

Asphalt concrete that is prepared using aggregates, bituminous binders, and, when necessary, additives, is widely used as a road pavement worldwide [1, 3–5]. Known for their strong stability, advanced mechanical properties, and good service performance, these materials are typically used in the construction of the top layers of flexible pavements due to their ability to form strong adhesive bonds [6–10].

Asphalt pavement modifiers have been used for many years to improve the pavement's resistance to deformations such as rutting, low-temperature cracking, water damage, and load-related fatigue cracking. Fibers are one of the additives used for this purpose [4]. Based on the existing literature, it can be said that synthetic fibers increase the resistance to rutting, freeze-thaw resistance, and tensile strength at low temperatures, and reduce the life cycle cost of the pavement [9].

Gallo (2017) documented the effectiveness of fibers obtained from renewable sources in improving pavement performance and ensuring sustainability. In his study, he demonstrated the effect of fibers on asphalt pavements. Fibers were first used in the early 1920s in the United States to prevent segregation in open and gap-graded asphalt mixes, improve the mechanical properties of dense-graded asphalt concrete, and minimize deformations such as rutting and cracking [5–7].

Ahmet I (2012) conducted a study to investigate the effects of different densities of polypropylene fibers on weight percent changes, mechanical and volumetric properties, vertical stress, and indirect tensile strength modulus of asphalt mixture. In the study, high-performance 19 mm short polypropylene fibers were used. The results showed that the use of polypropylene fibers in different types of aggregates improved Marshall stability by 7–9%, increased resistance to plastic flow by 13%, and reduced air voids by 26–42% compared to traditional dense mixtures without fibers. Additionally, when adding 0.2–0.3% polypropylene to the mixture by total mixture weight, the modified mixture showed higher tensile strength compared to the control mixtures and reduced low-temperature cracking [8].

Kumar et al. (2004) investigated the applicability of natural and synthetic fibers in bitumen in stone mastic asphalt and showed that the addition of synthetic fibers improved many mechanical properties, including stiffness and shear modulus, as well as wheel track and moisture sensitivity. Furthermore, the use of 0.3% synthetic fibers was found to significantly reduce permanent deformation in stone mastic asphalt.

2   Synthetic Fibers

There are various studies in the literature for the application of different fiber types to improve the physical and mechanical properties of asphalt mixtures [6, 11–13]. In these studies, fibers from different classes have been tested in terms of mixture performance. Fibers are generally separated into two main groups: synthetic and natural fibers, based on their methods of production [14]. Due to weaknesses such as decrease tensile strength due to moisture, homogeneity issues, and fungal formation, natural fibers are not preferred in the asphalt industry, while synthetic fibers are in the forefront. Another drawback of natural fibers are the high absorption rate, resulting in high optimum bitumen content in the asphalt mixture, which increases the cost of the mixture. Synthetic fibers are preferred as performance enhancers in asphalt pavements due to their more homogeneous structure,

higher resistance to moisture, and high tensile strength [12, 13, 15]. Synthetic fibers are typically categorized into three primary groups: natural fibers, man-made fibers, and miscellaneous fibers, and they are additionally classified into various subcategories depending on their sources, as shown in Fig. 1.
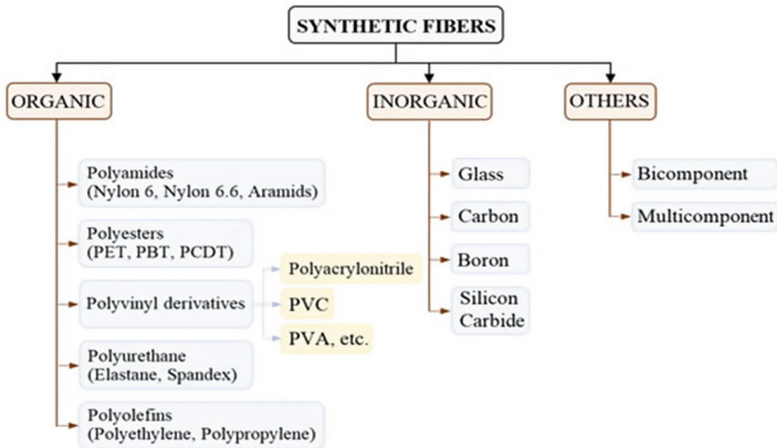
Fig. 1. Classification of synthetic fibers [16]

Unlike natural fibers, synthetic fibers are generally produced in the laboratory by processing polymers, which are often by-products of petroleum. Synthetic fibers are processed using spinning, polymerization, and filament techniques. In addition, the spinning process that is required to produce filaments from synthetic polymers is divided into three subcategories: melt spinning, wet spinning, and dry spinning [17].

Polyester, polypropylene, and aramid fibers are commonly used synthetic fibers in asphalt mixtures. The round and smooth microstructure of polypropylene fibers allow them to have a higher softening point and tendency to interlock with each other. When polypropylene fibers are used in porous asphalt mixtures, it has been observed that they can reduce the mixture's draindown up to 49% and increase the mixture's strength up to 50% [18]. The performance of synthetic fiber-modified asphalt mixtures depends on the type and characteristics of the fiber as well as the type of asphalt binder. The diameter, length, and texture of the fiber are also important factors. In a study comparing the performance of polyolefin and aramid fibers in asphalt mixtures, it was observed that these fibers were more effective in virgin (unmodified) bitumen than in SBS modified bitumen [19].

2.1 Methods of Adding Fibers to the Asphalt Binders

In order to achieve high performance from fiber-modified asphalt mixtures, it is understood that fiber bundles should show a good (homogeneous) distribution in the mixture [20]. For this reason, before adding fibers to bitumen or aggregates, they should be mixed to become random. Randomized fibers show better distribution in the mixture [21].

Fibers can be added to asphalt mixtures using two methods: wet process and dry process, also known as the "wet" and "dry" methods. In the wet method, the fiber-bitumen bond is formed before mixing the aggregate and bitumen. After ensuring the fibers are well distributed in the bitumen, the aggregate-fiber modified bitumen mixture is prepared. In the dry method, the fibers are first mixed with the aggregate, and then the fiber-aggregate mixture is combined with the bitumen.

In a study investigating the most effective mixing method for polypropylene (PP), visual evaluations were conducted, and it was found that a dry method provided a more homogeneous distribution compared to the wet method [22]. In some studies, fibers have been added after the asphalt mixture has been prepared, that is, after the bitumen-aggregate cohesion has been achieved [23].

In another study that was conducted with PP fibers, wet and dry processes were compared. It was reported that in the wet method, the fibers shrunk and did not mix well with other materials, while in the dry method, the fibers tended to clump together due to absorbing bitumen. Therefore, both methods were deemed unsuitable for adding fibers to the asphalt mixture. However, the study found that gradually adding the fibers to the asphalt mixture after the bitumen and aggregate were mixed for 5–10 s, provided a uniform distribution and thus the modified method was deemed ideal [24].

Each different fiber used in asphalt mixtures has its unique properties. Since the mixing process is dependent on these properties, the distribution method should be carefully executed in order to provide a homogeneous distribution. Furthermore, since it is known that the performance of fibers in asphalt mixtures is inconsistent, evaluation of the distribution through methods such as X-ray computed tomography or electron microscopy is suggested. Attention should be paid to the vertical or horizontal orientation of the fibers to understand their reinforcement mechanisms in asphalt pavements [3].

2.2 Effect of Fiber Diameter and Content on Mixture Performance

Theoretically, it has been demonstrated that the stresses developed within the pavement can be transmitted to strong fibers, thereby alleviating the stresses within the relatively weaker mixture. In this context, the adhesion between fibers and asphalt binder plays a critical role. Effective stress transfer is accomplished through a strong bonding between the mixture and the fiber. The larger surface area of the fiber facilitates this adhesive bond [11]. However, the use of excessively long fibers can give rise to balling issues, resulting in an unsuitable asphalt concrete mixture, whereas very short fibers may not provide sufficient reinforcement effects within the mixture [25].

Therefore, the fiber length significantly affects the distribution of the mixture and can greatly change its performance. The utilization of shorter fibers may not yield significant improvements in the performance of the asphalt mixture, whereas longer fibers tend to enhance the adhesion between the components of the asphalt mixture, resulting in notable improvements in performance properties [12, 26]. However, it is important to note that once the optimum fiber content in the asphalt mixture is achieved, adding more fibers can have adverse effects on the performance of the mixture [27].

Indeed, an extremely low fiber content in the asphalt mixture raises the risk of creating a weak section that facilitates crack propagation on the surface. Conversely, an excessively high fiber content can diminish the adhesion strength between aggregates and

lead to shrinkage issues [22]. Therefore, it is imperative to carefully select the appropriate quantity of fibers in the asphalt mixture while also enhancing their characteristics. This ensures an optimal balance that promotes the desired performance and durability of the mixture.

The use of bitumen-fiber mastics can make the binder more brittle by increasing its stiffness, which can lead to damage on the road surface and disintegration and detachment under the effect of traffic and load climate. Therefore, understanding the properties of bitumen-fiber mastics is important, as they are currently scientifically classified as insufficient to provide better control over the performance of asphalt roads [18].

Badeli et al. [28] conducted an experiment where they incorporated aramid pulp fiber (APF) into the asphalt control mixture at a dosage of 0.3% of the total mixture weight. The APF had a specific surface area ranging from 7–11 m2/g. Their findings revealed an enhancement in the fatigue life of the fiber-reinforced mixture. Specifically, under high-stress conditions such as heavy truck loads, the fiber-reinforced mixture demonstrated an improvement in fatigue life of up to 70%.

Similarly, Wang et al. [18] investigated the fatigue life of asphalt mixtures reinforced with polyacrylonitrile (PAN) fibers using the central point bending fatigue test. The PAN fibers utilized in the study had a length of 6 mm and a diameter of 3 μm. The fibers were added to the asphalt mixture in amounts of 0.15%, 0.3%, and 0.45% of the total mixture weight. It was observed that the PAN-reinforced asphalt mixture showed greater fatigue resistance than the control mixture, and this increase was four times greater in the mixture with a 0.3% fiber content compared to the control mixture, although the test showed different results at different stress levels [29].

In their study, Chen et al. [18] investigated the operational mechanism of mineral, cellulose, and polyester fibers in asphalt mixtures. They observed that mineral fibers exhibited greater stiffness compared to polyester fibers, attributed to their smaller diameter and increased interfacial area. On the other hand, polyester fibers demonstrated higher tensile strength when compared to mineral fibers. Most studies have reported that all fibers increase the resistance to flow and fracture of PAM. However, it was found that the only fibers that were observed to increase the abrasion resistance and ITS of the mixtures were the synthetic fibers and the steel fibers.

2.3 Effects on Mechanical Properties

Xu et al. [13] conducted an analytical study to compare the performance of four dissimilar fibers, including polyester, PAN, lignin, and asbestos. The study showed that the fatigue performance of hot-mix asphalt was significantly improved by the addition of polymer fibers (polyester and PAN) at room temperature using a three-point bending fatigue test. Motamedi et al. [30] conducted a study to assess the fracture resistance properties of asphalt mixtures reinforced with aramid-polyolefin fibers. They employed the ENDB (Energy Normalized Fracture Direct Tension) method and observed a substantial improvement in the fracture resistance of the reinforced asphalt mixtures.

In separate studies, Stempihar et al. [31] and Mateos and Harvey [32] investigated the performance of various Stone Matrix Asphalt (SMA) and Hot Mix Asphalt (HMA) mixtures that incorporated aramid fibers. They conducted a four-point beam fatigue test and observed significant effects of the fibers on the fatigue performance of the original

mixture, particularly at high stress levels. When the cost situation of fiber application in asphalt mixtures was examined, it was revealed that fiber materials should be added at a minimum level to provide the desired performance [18], and the improvements were positive and economical. The initial cost increase due to fiber application decreases to zero and provides profit with the increase in road service life and the decrease in long-term maintenance costs [31]. The effects of fibers on thermal cracking in asphalt pavements have not been sufficiently studied, but clarifying this issue would be useful for regions where temperatures are very low. Comparison of performance of synthetic fibers in both conditions is given in Table 1.

Table 1. Comparison of performance of synthetic fibers in dry and wet conditions.

Fiber	Length (mm)	Diameter (μm)	Adding method	Content (%)	ITS	TSR	Rutting
Cellulose [21]	6	–	dry	0.3 (mix)	X	0	0
Cellulose [33]	1.1	45	wet	0–0.5	X	X	0
Cellulose [34]	1.1	45	wet	0.25, 0.5, 0.75	X	X	–
Mineral (basalt) [35]	24	18	wet	0,2	0	X	–
Polyester [36]	6	20	wet	0.1, 0.3, 0.5	–	0	0
Polyethylene Terephthalate [37]	2	30	dry	0.5, 1.0, 1.5, 2.0	0	–	0
Aramid-Polyalphaolefin [27]	19	–	dry	0.05	–	–	0
Glass [19]	10-14-20	–	dry	0.15, 0.25, 0.35, 0.45, 0.55	0	X	0
Polypropylene [38]	2.36	–	dry	0.5, 1.0	–	X	0
Polyproplylene [20]	–	–	wet	2–4	0	–	0

The utilization of various synthetic fiber types have demonstrated favorable outcomes in enhancing properties like elastic modulus and tensile strength (ITS) [12]. Mixtures incorporating polypropylene and polyester fibers exhibit beneficial effects on rutting by serving as three-dimensional reinforcements and promoting binder stability. The combination of additives and modifiers have been found to yield synergistic advantages, such as augmenting the mechanical strength of fibers and enhancing the adhesion strength, stability, and abrasion resistance of PAM (polymer-modified asphalt) through the introduction of nanosilica [39].

In a study conducted by Ma et al. [25], the impact of polyester, mineral, and cellulose fibers (at a weight of 2.5% of the aggregate) in mixtures with modified bitumen were examined. The mixtures incorporating polyester fibers exhibited favorable performance in the wet Cantabro test, indicating improved resistance to abrasion and reduced sensitivity to moisture. It should be noted that the immersion time during the wet Cantabro test is a crucial parameter for obtaining accurate measurements of mass loss. Longer immersion times result in higher mass loss. Therefore, the successful performance of mixtures utilizing polyester fibers with extended immersion time suggests that the fibers significantly enhance the moisture resistance of the mixtures [40].

3   Conclusion

This paper serves as a review that explores the potential advantages of employing synthetic fibers as reinforcement in flexible pavements, with a specific focus on asphalt concrete. It discusses how the utilization of synthetic fibers has resulted in performance enhancements in asphalt mixtures, specifically in terms of mitigating fatigue cracking and reducing rutting. Additionally, the paper examines two potential methods for incorporating fibers into asphalt concrete: the wet process and the dry process. These methods are explored in relation to their effectiveness in introducing fibers into the asphalt mixture and improving its properties. The authors emphasize the importance of carefully dispersing the fibers to ensure a homogeneous distribution, as different fibers have different properties that affect the mixing process.

The research recommends conducting detailed investigations into the reinforcing mechanisms of synthetic fibers, as well as determining the optimum fiber content in asphalt concrete. The authors acknowledge that the performance of synthetic fibers in asphalt mixtures can be inconsistent and suggest using scanning electron microscopy or x-ray computed tomography scans to evaluate the fiber distribution and orientation within the mixture. Understanding the orientation of the fibers, whether vertically or horizontally, is crucial for understanding the reinforcing mechanism of the fibers in the asphalt mixture.

In these continuations, this paper discusses how fibers can change the viscoelasticity of asphalt mixtures and improve various properties such as moisture susceptibility, creep compliance, dynamic modulus, freeze-thaw resistance and rutting resistance while also reducing reflective cracking. The paper also examines these properties separately for different types of fibers including polyester, polypropylene, cellulose, carbon, asbestos, glass, and nylon. The methods of sample preparation and the issues related to implementation were also discussed, and it was found that the dry process is generally preferred over the wet process due to various reasons.

There is a potential for research in the field of modeling the mechanical properties of fiber-reinforced asphalt concrete mixtures using composite science principles. The paper recommends that the orientation of fibers within the mixture should be examined using optical and/or scanning electron microscopy, as this is an area that has not been fully explored.

Overall, this paper provides further detail on the potential benefits and methods of using synthetic fibers in asphalt concrete, as well as potential areas for further research.

References

1. Hamdar, Y., Kassem, H., Srour, I., Chehab, G.: Performance-based specifications for sustainable pavements: a lean engineering analysis. Energy Procedia **74**, 453–461 (2015)
2. Kassem, H.A., Saleh, N.F., Zalghout, A.A., Chehab, G.R.: Advanced characterization of asphalt concrete mixtures reinforced with synthetic fibers. J. Mater. Civ. Eng. **30**(11), 04018307 (2018)
3. Musa, N.F.A.A., Aman, M.Y., Shahadan, Z., Taher, M.N., Noranai, Z.: Utilization of synthetic reinforced fiber in asphalt concrete—a review. Int. J. Civ. Eng. Technol **10**(5), 678–694 (2019)
4. White, T.D., Huang, H.: Effect of Fibers on HMA Performance. TRB, National Research Council, Washington, DC (1999)
5. Serfass, J.P., Samanos, J.: Fiber-modified asphalt concrete characteristics, applications and behavior. Asphalt Paving Technol. **65**, 193–230 (1996)
6. Abtahi, S.M., Sheikhzadeh, M., Hejazi, S.M.: Fiber-reinforced asphalt-concrete–a review. Constr. Build. Mater. **24**(6), 871–877 (2010)
7. Brown, E., Mallick, R.B., Haddock, J.E., Bukowski, J.: Performance of stone matrix asphalt (SMA) mixtures in the United States (No. Report No: NCAT Report No. 97–1). National Center for Asphalt Technology (1997)
8. Ahmed, A.I.: Laboratory investigation into the impact of polypropylene fiber content on temperature susceptibility of dense graded mixtures. Al-Qadisiya J. Eng. Sci. **5**(4), 424–438 (2012)
9. Aliha, M.R.M., Razmi, A., Mansourian, A.: The influence of natural and synthetic fibers on low temperature mixed mode I+II fracture behavior of warm mix asphalt (WMA) materials. Eng. Fract. Mech. **182**, 322–336 (2017)
10. Kumar, P., Sikdar, P.K., Bose, S., Chandra, S.: Use of jute fibre in stone matrix asphalt. Road Mater. Pavement Des. **5**(2), 239–249 (2004)
11. McDaniel, R.S.: Fiber additives in asphalt mixtures (No. Project 20-05 (Topic 45-15)) (2015)
12. Slebi-Acevedo, C.J., Lastra-González, P., Pascual-Muñoz, P., Castro-Fresno, D.: Mechanical performance of fibers in hot mix asphalt: a review. Constr. Build. Mater. **200**, 756–769 (2019)
13. Xu, Q., Chen, H., Prozzi, J.A.: Performance of fiber reinforced asphalt concrete under environmental temperature and water effects. Constr. Build. Mater. **24**(10) (2010)
14. Ziari, H., Aliha, M.R.M., Moniri, A., Saghafi, Y.: Crack resistance of hot mix asphalt containing different percentages of reclaimed asphalt pavement and glass fiber. Constr. Build. Mater. **230**, 117015 (2020)
15. Perca Callomamani, L.A., Hashemian, L., Sha, K.: Laboratory investigation of the performance evaluation of fiber-modified asphalt mixes in cold regions. Transp. Res. Rec. **2674**(7), 323–335 (2020)
16. Rajak, D.K., Wagh, P.H., Linul, E.: A review on synthetic fibers for polymer matrix composites: performance, failure modes and applications. Materials **15**(14), 4790 (2022)
17. Begum, S., Fawzia, S., Hashmi, M.S.J.: Polymer matrix composite with natural and synthetic fibres. Adv. Mater. Process. Technol. **6**(3), 547–564 (2020)
18. Chen, J.S., Lin, K.Y.: Mechanism and behavior of bitumen strength reinforcement using fibers. J. Mater. Sci. **40**, 87–95 (2005)
19. Muftah, A., Bahadori, A., Bayomy, F., Kassem, E.: Fiber-reinforced hot-mix asphalt: Idaho case study. Transp. Res. Rec. **2633**(1), 98–107 (2017)
20. Vasconcelos, K.L., Bernucci, L.B., Chaves, J.M.: Effect of temperature on the indirect tensile strength test of asphalt mixtures. In: 5th Eurasphalt & Eurobitume Congress, pp. 344–352 (2012)
21. Callomamani, L.A.P., Bala, N., Hashemian, L.: Comparative analysis of the impact of synthetic fibers on cracking resistance of asphalt mixes. Int. J. Pavement Res. Technol. 1–17 (2022)

22. Khabiri, M.M., Alidadi, M.: The experimental study of the effect of glass and carbon fiber on physical and micro-structure behavior of asphalt. Int. J. Integrated Eng. **8**(3) (2016)
23. Modarres, A., Hamedi, H.: Effect of waste plastic bottles on the stiffness and fatigue properties of modified asphalt mixes. Mater. Des. **61**, 8–15 (2014)
24. Zahedi, M., Bayat, R., Jalal, M.N.: The most appropriate mixing method of polypropylene fiber with aggregates and bitumen based on binder mix design. Int. J. Eng. Technol. **3**(3), 333 (2014)
25. Jaskuła, P., Stienss, M., Szydłowski, C.: Effect of polymer fibres reinforcement on selected properties of asphalt mixtures. Procedia Eng. **172**, 441–448 (2017)
26. Park, P., El-Tawil, S., Park, S.Y., Naaman, A.E.: Cracking resistance of fiber reinforced asphalt concrete at− 20 C. Constr. Build. Mater. **81**, 47–57 (2015)
27. Jahromi, S.G.: Effect of carbon nanofiber on mechanical behavior of asphalt concrete. Int. J. Sustain. Constr. Eng. Technol. **6**(2), 57–66 (2015)
28. Badeli, S., Carter, A., Doré, G., Saliani, S.: Evaluation of the durability and the performance of an asphalt mix involving Aramid Pulp Fiber (APF): complex modulus before and after freeze-thaw cycles, fatigue, and TSRST tests. Constr. Build. Mater. **174**, 60–71 (2018)
29. Wang, H., Yang, Z., Zhan, S., Ding, L., Jin, K.: Fatigue performance and model of polyacrylonitrile fiber reinforced asphalt mixture. Appl. Sci. **8**(10), 1818 (2018)
30. Motamedi, H., Fazaeli, H., Aliha, M.R.M., Amiri, H.R.: Evaluation of temperature and loading rate effect on fracture toughness of fiber reinforced asphalt mixture using edge notched disc bend (ENDB) specimen. Constr. Build. Mater. **234**, 117365 (2020)
31. Barman, M., Ghabchi, R., Singh, D., Zaman, M., Commuri, S.: An alternative analysis of indirect tensile test results for evaluating fatigue characteristics of asphalt mixes. Constr. Build. Mater. **166**, 204–213 (2018)
32. Mateos, A., Harvey, J.: Laboratory evaluation of the mechanical properties of asphalt concrete reinforced with aramid synthetic fibers (2019)
33. Wu, M.M., Li, R., Zhang, Y.Z., Fan, L., Lv, Y.C., Wei, J.M.: Stabilizing and reinforcing effects of different fibers on asphalt mortar performance. Pet. Sci. **12**, 189–196 (2015)
34. Kietzman, J.H.: Effect of short asbestos fibers on basic physical properties of asphalt pavement mixes. Highway Res. Board Bull. (270) (1960)
35. Soltani, M., Moghaddam, T.B., Karim, M.R., Baaj, H.: Analysis of fatigue properties of unmodified and polyethylene terephthalate modified asphalt mixtures using response surface methodology. Eng. Fail. Anal. **58**, 238–248 (2015)
36. Wu, S., Ye, Q., Li, N.: Investigation of rheological and fatigue properties of asphalt mixtures containing polyester fibers. Constr. Build. Mater. **22**(10), 2111–2115 (2008)
37. Dehghan, Z., Modarres, A.: Evaluating the fatigue properties of hot mix asphalt reinforced by recycled PET fibers using 4-point bending test. Constr. Build. Mater. **139**, 384–393 (2017)
38. Ye, Q., Wu, S.: Rheological properties of fiber reinforced asphalt binders (2009)
39. Klinsky, L.M.G., Kaloush, K.E., Faria, V.C., Bardini, V.S.S.: Performance characteristics of fiber modified hot mix asphalt. Constr. Build. Mater. **176**, 747–752 (2018)
40. Ma, X., Li, Q., Cui, Y.C., Ni, A.Q.: Performance of porous asphalt mixture with various additives. Int. J. Pavement Eng. **19**(4), 355–361 (2018)

Tracing Back the Energy Use in Transportation Systems and Modes: An Energy-Balance Methodology for Turkey

Hediye Tuydes-Yaman[1] , Gulcin Dalkic-Melek[1]([✉]) , Ege Cem Saltik[1] ,
and Kemal Sarica[2]

[1] Civil Engineering Department, Middle East Technical University, Ankara, Turkey
{htuydes,dalkic,e153105}@metu.edu.tr
[2] Engineering Faculty, Gebze Technical University, Gebze, Kocaeli, Turkey
kemalsarica@gtu.edu.tr

Abstract. Transportation is a major contributor to global greenhouse gas emissions, accounting for nearly a quarter of the total. The sector heavily relies on fossil fuels, necessitating the development of effective mitigation policies. Monitoring total fuel consumption alone is insufficient because different transportation modes serve distinct travel segments and use various fuel types, requiring tailored mitigation actions. Additionally, transportation activity measured in vehicle-km travelled (VKT) can vary significantly within the same vehicle category, with low truck freight activity in short-haul and intense activity in long-haul. Fuel types are often shared across multiple transportation systems and modes, such as diesel usage in PCs, buses, and trains. Therefore, a comprehensive analysis framework is essential to track energy use in different modes, technologies, and travel segments.

This study presents an approach for collecting and processing data to estimate travel demand and energy consumption in the transportation sector. Validation of energy consumption values is performed by comparing them to published total energy consumption values by the Ministry of Energy and Natural Resources. The estimation of total fuel consumption involves multiplying VKTs with assumed fuel consumption factors (FCFs) for each subsector. An iterative process is employed to balance the estimated and observed energy use, adjusting FCF and VKT values within acceptable ranges. This proposed approach serves as a foundation for future emission and energy models, providing detailed input to support national climate change action plans. It enables policymakers to develop effective strategies for reducing greenhouse gas emissions in the transportation sector.

Keywords: Transportation · Demand · Energy Consumption ·
Vehicle-Km-Travelled (VKT)

1 Introduction

Transportation is a critical sector causing almost a quarter of global greenhouse gas (GHG) emissions and plays an important role in reaching climate change mitigation targets. GHG emission mitigation studies can be grouped as aggregate and disaggregate modelling approaches. Aggregate modelling covers the bottom-up or top-bottom

approaches such as path analyses, energy models or system dynamics models [1–4]. In the disaggregate models, majority of the studies include survey data and investigated travel behaviors or used historical data to investigate statistical patterns as in Activity, modal share, energy intensity, fuel/carbon intensity (ASIF) modeling [5–7]. More recently, simpler calculations are performed via programs, i.e. COPERT and EMISIA [8], which use average fuel consumption factors (FCFs) varying for vehicle types and travel demand measure of vehicle-km traveled (VKT), as in the simple ASIF approach [5, 9].

As countries strictly monitor annual fuel consumption (i.e. gasoline, diesel, LPG, CNG); using FCFs enables calculation of total national transportation emissions. Total VKT can be also published at a national level. But, such total values are not for developing detailed mitigation policies addressing different modes and technologies. The complex multi-system (road, railway, airway, and maritime) and multi-modal (i.e., private car, bus, truck, metro, etc.) structure of the transportation sector requires detailed mode/technology datasets for complex energy system models or emission calculation models. For example, all passenger cars (PCs) and light duty vehicles use mostly gasoline, whereas heavy and large road vehicles (trucks, buses, etc.) use diesel as well as some of the trains. Furthermore, PCs can serve intercity as well as urban travel demand, and have different VKT levels, which are necessary in development of proper mitigation policy tools.

In the absence of detailed mode/technology-based VKT values, as in the case of Turkey, we can estimate the VKT for some transportation subsectors, by balancing the total energy use (by fuel type) and available VKT statistics creating the "energy-balance" scenario, which is the main focus of this study. Based on the available national transportation statistics published by relevant institutions including TurkStat, the General Directorate of Highways (GDH), the Turkish State Railways (TSR) and energy statistics by the Ministry of Energy and Natural Resources (MoENR), the transportation sector was first divided into 4 systems (road, rail, air and maritime), while the road transportation was further divided into 17 subsegments considering vehicle technologies (i.e. PC, truck, HGV, bus, etc.) and fuel type (i.e. gasoline, diesel, LPG, etc.) as well as travel distance (short-haul, long-haul, etc.). Energy balance is obtained using FCFs within the acceptable values employed in an iterative process. The main output is the estimated VKTs for a larger set of subsectors for which more specific mitigation policies can be developed in the future.

2 Transportation Sector in Turkey

Turkish transportation sector relies heavily on roads for both passenger and freight. In 2021, the share of road and air transport was 92.7% and 6.3%, respectively, while the share of rail decreased to 0.6% [10]. Turkey, as a developing country with continuing economic growth, has experienced a significant increase in vehicle ownership, resulting in 25.2 million vehicles (13.7 million PCs) [11]. The share of gasoline vehicles has decreased from 54.4% to 28.9%, while diesel-fueled vehicles has risen from 32.7% to 50.3% between 2004 and 2021. Today, among PCs, the shares of gasoline, diesel, and LPG are recorded as 25.5%, 37.6% and 35.9%, respectively. Commercial vehicles such as minibuses, buses, small trucks, and trucks primarily use diesel fuel.

The national VKT statistics by TurkStat showed that commercial vehicles have much higher average annual traveled distances (AATD) compared to PCs (see Table 1), whereas total PC VKTs are higher due to their large share in the national fleet. Diesel cars have higher AATD than gasoline and LPG ones, possibly due to their higher commercial use as taxis or intercity travels. Total national VKT values reached 300.6 billion vehicle-km (BVKm) [11]. Intercity road VKT values published by the GDH showed recently a three-fold growth (see Table 2), reaching up to 142.5 BVKm in 2021 [12]. Most of the total VKT was accounted for by PCs, with a 54.3% share, followed by small trucks (included in LDVs) at 21.4% (Table 1).

Table 1. Road Transportation Statistics for 2021 [11]

Vehicle Type	Number of Vehicles%		VKT		AATD
	N (*1000)	%	BVKm	%	
Total	23145.6	100.0	329.6	100.0	14 240
PC	13706.1	59.2	178.8	54.3	13 048
Gasoline	*3495.2*	*25.5*	*34.2*	*19.1*	*9 790*
Diesel	*5287.6*	*38.6*	*89.4*	*50.0*	*16 900*
LPG	*4923.3*	*35.9*	*55.3*	*30.9*	*11 223*
Minibus	484.8	2.1	13.6	4.1	28 142
Bus	208.9	0.9	10.7	3.3	51 459
Small truck	4115.2	17.8	70.6	21.4	17 161
Truck	886.3	3.8	41.3	12.5	46 643
Motorcycle	3744.4	16.2	14.4	4.4	3 847

Due to the large investments and introduction of High Speed Rail (HSR), the railway network has 13,022 km (including 1,213 km HSR lines) [13]. The share of electrified lines is increased to 46%. In 2021, electrified trains accounted for 44.2 million train-km (42% passenger, 58% freight), while diesel trains accounted for 23.2 million train-km (24% passenger, 76% freight). Air passenger traffic reached 68.5 million in 2021 [14]. The total amount of maritime freight, including domestic and international, was 460.15 million ton-km in 2018. Domestic cargo accounted for 13% (59.56 million ton-km) of the total freight. The number of passengers increased to 139.56 million, and passenger-mile reached 1134.35 [15].

According to the latest data published by MoENR, the total energy consumption in 2020 was 105.5 Mtoe, with the transportation sector accounting for 27 Mtoe, making it the second-highest contributor. Distribution of the transportation energy use among modes and fuel types is presented in Table 3 [16] showing a considerable diesel consumption, primarily due to road transportation. While gasoline and LPG fuels have consumption levels that are similar to each other, electricity consumption has been increasing due to the expansion of railway electrification.

Table 2. Intercity Road Transportation Statistics [12]

Years	2015				2018				2021			
	H	S	P	T	H	S	P	T	H	S	P	T
PC	14.1	55.5	12.0	**81.6**	17.0	65.5	14.4	**96.9**	19.6	70.0	15.4	**105.1**
Bus	1.0	2.8	0.4	**4.2**	1.0	3.7	0.8	**5.5**	1.1	3.5	0.8	**5.4**
Truck	5.5	19.0	3.0	**27.5**	5.7	19.9	3.7	**29.3**	6.6	21.7	3.7	**32.0**
T	**20.6**	**77.3**	**15.4**	**113.3**	**23.6**	**89.0**	**19.0**	**131.6**	**27.3**	**95.2**	**20.0**	**142.5**

Note: H: Highways, S: State Roads, P: Provincial Roads, T: Total

Table 3. Energy Balance Statistics [16]

	Die (MT)	Gas (MT)	LPG (MT)	Jetfuel (MT)	CNG (10^6S)	Elec (GWh)
2018	**19.8**	**2.2**	**3.3**	**1.2**	**92.3**	**1023.7**
Road	*19.3*	*2.2*	*3.3*		*92.3*	
Rail	*0.1*					*1023.7*
Maritime	*0.3*					
Air				*1.2*		

3   Methodology

Thr proposed method focuses on a) data collection and processing for VKT estimation and energy consumption; and b) validation by the total energy consumption values published by the MoENR. To calculate the FCF (Ω) of a mode (i) using a fuel type (j), VKTs are by the assumed FCF value and the fuel density factor (FDF) for each subsector. The summation of fuel consumption values for each fuel type resulted in total FCF values for gasoline, diesel, LPG, CNG, and electricity).

$$\sum_{i}^{n} \Omega = VKT_{i,j} * FCF_{ij} * FDF_{ij} \tag{1}$$

where

Ω is the fuel consumption and **FDF** is the fuel density factor. An example calculation is given below for total gasoline (Gas) fuel consumption that includes the summation of gasoline consumption (Eq. 2d) for PCs in long-haul (LH), short-haul (SH) as well as motorcycles (2-Wh) running on only SH.

$$\Omega_{PC\_LH\_Gas} = VKT_{PC\_LH\_Gas} * FCF_{PC\_LH\_Gas} * FDF_{Gas} \tag{2a}$$

$$\Omega_{PC\_SH\_Gas} = VKT_{PC\_SH\_Gas} * FCF_{PC\_SH\_Gas} * FDF_{Gas} \tag{2b}$$

$$\Omega_{2-Wh\_SH\_Gas} = VKT_{2-Wh\_SH\_Gas} * FCF_{2-Wh\_SH\_Gas} * FDF_{Gas} \tag{2c}$$

$$\Omega_{Gas} = \Omega_{PC\_LH\_Gas} * \Omega_{PC\_SH\_Gas} * \Omega_{2-Wh\_Gas} \tag{2d}$$

Fuel consumption was calculated for each mode and fuel type, considering the travel scale. An iterative process balanced estimated and observed energy use, adjusting FCF and VKT values within an acceptable range. This maintained consistency with published total travel statistics while meeting literature-recommended ranges.

3.1 Transportation Sector Mode and Technology Brake-Down for VKT Estimation

Fuel consumption values were determined using Eq. (1) and Eq. (2a–d). Not all transportation modes use all fuel types (see Fig. 1). For instance, buses run on diesel or CNG, while minibuses and small trucks exclusively use diesel. Road transportation modes differ in travel scale, with minibuses in short-haul (SH) and buses in both SH and long-haul (LH). The figure depicts the division of road and rail mode-technology sets. Railway transportation was modeled separately for passenger and freight using annual TSR statistics [13], distinguishing between electric and diesel trains. The maritime and airway sectors were also modeled, encompassing freight and passenger VKT values based on diesel and jet fuel correspondingly.
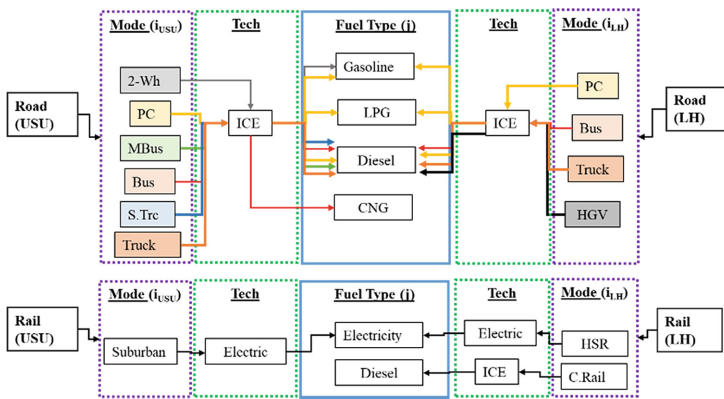
Fig. 1. Framework of the Road and Railway Mode and Technology Breakdowns

3.2 Determination of Fuel Consumption Factors (FCFs)

For road transportation, minimum (FCF_{min}) and average (FCF_{avg}) values were compiled for both short-haul (SH) and long-haul (LH) distances (Table 4). For PC, the five top-selling car brands in C-segment in Turkey over the past 15 years were identified using annual statistics on new car sales published by the Automotive Distributors' Association [17]. Note: the FCF for LPG-fueled PCs was assumed to be 1.2 times that of gasoline consumption, as suggested by the literature. Buses were categorized as i) LH coaches, ii) SH shuttle coaches, iii) public transit buses, and iv) SH other buses. While LH buses are mostly new vehicles compliant with Euro 5 or Euro 6 standards, shuttle bus fleets and public transit bus fleets may include older vehicles. To determine the FCFs for buses,

commonly used bus brands and models were evaluated by examining the bus fleets [18–20]. A similar approach was applied to determine the FCFs for trucks. Minibuses (including both *dolmuş* and service shuttles) and small trucks are classified as light-duty vehicles (LDVs), and it is assumed that all of them run on diesel fuel for short-haul distances (urban and suburban). For motorcycles (2-Wh), the Motorcycle Industry Association (MOTED) statistics showed that 70% of motorcycles in Turkey have engine capacities under 250cc for some brands such as Yamaha, Honda [21].

Table 4. Summary of Road FCFs (lt/100km)

Vehicle Fleet	Fuel Type	FCF_min	FCF_avg
LDV_PC_LH	Gasoline	6.0	6.9
LDV_PC_LH	Diesel	7.0	6.9
LDV_PC_LH	LPG	8.4	8.2
LDV_PC_SH	Gasoline	8.0	9.3
LDV_PC_SH	Diesel	9.0	9.5
LDV_PC_SH	LPG	10.8	11.4
Bus_LH	Diesel	25.0	28.3
Bus_SH_coach	Diesel	25.0	28.0
Bus_SH_pt	Diesel	30.0	42.0
Bus_SH	CNG	23.0	30.0
Truck_Med_LH	Diesel	16.0	24.0
Truck_Med_SH	Diesel	17.0	26.0
Truck_LH	Diesel	21.0	25.0
Truck_SH	Diesel	25.0	28.0
HGV_LH	Diesel	25.0	32.0
LDV-MB_SH	Diesel	6.6	14.5
LDV-STrc_SH	Diesel	6.6	14.5
2-Wh (Motorcycle)	Gasoline	2.0	3.0

For railway transportation, VKT statistics by train and fuel type were directly obtained from TSR statistics [13]. For the maritime sector, FCFs were calculated by examining the fleet of Istanbul Deniz Otobusleri [22]. Considering 31 types of vehicles and their numbers in the fleet, the average FCF was determined to be 5000 lt/100 km. For airway transportation, the most popular brands for Turkish Airlines and Pegasus are Airbus and Boeing. The minimum FCF value was 257 lt/100 km, while the maximum was 519 lt/100 km [23].

3.3   Estimation of Transportation Demand

Estimating transportation demand (VKT) is challenging due to the fragmented structure of the transportation sector, as discussed before (Fig. 1). In the scope of this study, each transportation sub-sector (road, railway, airway, and maritime) was first investigated by data availability. Road transportation mode-technology set was first divided into 12 categories to estimate their VKTs by travel scale (Table 10). VKT values were calculated from the comparison of TurkStat [11] and GDH annual travel statistics [12]. As SH means the total VKT values of urban and suburban travel segments, provincial road VKT values published by GDH were also considered as they represent the suburban roads within the city borders. Even though it was available for 2019 year, an adjustment factor was applied for 2018. For fuel-based VKT estimation, road transportation was divided by fuel type, which resulted in 17 categories (Table 5). As seen in the table, there is a need for distributing the calculated LH or SH VKT values into different fuel types for PC and Bus. Adjustment of VKTs based on the total fuel consumption values were also necessary.

Table 5. VKT Data Availability for Road Transportation Vehicle Fleet

Vehicle Type	VKT Data Source	VKT (BVKm)	VKT by fuel type (BVKm)
LDV_PC_LH	GDH	82.42	Gasoline, Diesel, LPG**
LDV_PC_SH	TurkStat-GDH	234.16–82.42	Gasoline, Diesel, LPG**
Bus_LH	GDH	2.05	Diesel
Bus_SH	TurkStat-GDH	10.67–2.05	Diesel, CNG***
Truck_Med_LH	GDH	8.66	Diesel
Truck_Med_SH	*		Diesel
Truck_LH	GDH	7.80	Diesel
Truck_SH	*		Diesel
HGV_LH	GDH	11.69	Diesel
LDV-MB_SH	TurkStat	13.20	Diesel
LDV-STrc_SH	TurkStat	63.36	Diesel
2-Wh_SH	TurkStat	12.75	Gasoline
Total	*12 categories*		*17 categories*

*VKT values are presented at an aggregate level in TurkStat thus, they are estimated

**VKT data by fuel type is only available in TurkStat for total (SH+LH) PC mode. Thus, these values should be distributed as SH and LH by an assumption

***As there is no information regarding the share of CNG in busses, an assumption is needed to distribute the total Bus_SH VKT value

Railway transportation was separately modeled for passenger and freight, differentiating between electric and diesel trains. VKT data for diesel and electric trains were

available in TSR Annual Statistics including both suburban railways (passenger), conventional railways (passenger, freight) and HSR (passenger). Thus, these values were directly used in the energy balance model without need for any estimation.

4 Energy Balance for Transportation Sector

Total fuel consumption by each mode was presented in Table 6. The estimated breakdown of transportation energy use in Turkey for 2018 suggested that PC had a considerable share in gasoline consumption and LPG consumption while the majority of diesel was consumed by commercial vehicles such as PT, trucks, HGVs and small trucks. While road transportation was responsible from the 19328 Kton diesel consumption, railway sector consumed 122.8 Kton diesel. Metro and tramway systems operating as urban rail transit had the biggest electric consumption having 76% share, it was followed by freight trains (10%) and HSR (9%). The differences between the published energy consumption values by MoENR and estimated values were given in Table 7 showing the difference lower than 5% that can be negligible in such a national energy balance model.

Table 6. Energy Balance for the year 2018

2018	Fuel Type	VKT (BVKm)	FCF	Ω_Gasoline (Kton)	Ω_Diesel (Kton)	Ω_LPG (Kton)	Ω_CNG (MSm3)	Ω_Elekt (KWh)	Ω_Jet (Kton)
LDV_PC_LH	Gasoline	19.700	7.0	1075.6					
LDV_PC_LH	Diesel	52.650	6.0		2764.1				
LDV_PC_LH	LPG	10.000	8.4			487.2			
LDV_PC_SH	Gasoline	12.400	8.6	831.8					
LDV_PC_SH	Diesel	28.954	7.6		1925.4				
LDV_PC_SH	LPG	47.067	10.3			2817.2			
Bus_LH	Diesel	2.047	26.0		465.7				
Bus_SH_coach	Diesel	2.416	27.0		570.7				
Bus_SH_pt	Diesel	5.947	33.0		1717.3				
Bus_SH	CNG	0.260	35.4				92.0		
Truck_Med_LH	Diesel	8.658	15.0		1136.4				
Truck_Med_SH	Diesel	4.198	19.0		697.9				
Truck_LH	Diesel	7.803	25.0		1706.9				
Truck_SH	Diesel	3.830	27.0		904.8				
HGV_LH	Diesel	11.689	26.0		2659.2				
LDV-MB_SH	Diesel	13.201	8.0		924.1				
LDV-STr_SH	Diesel	63.360	8.0		4435.2				
2-Wheeler	Gasoline	12.746	3.7	367.8					
Road Total		306.926		2275.3	19907.8	3304.4	92.0		
Rail_Pax_SH	Electric	0.230	3.3					773897476.3	
Rail_pax_SUR	Electric	0.003	10.0					26760000.0	
Rail_pax_HSR	Electric	0.007	13.0					92534000.0	
Rail_pax_Con	Electric	0.002	11.0					21285000.0	
Rail_pax_Con	Diesel	0.011	360.0		34.5				
Rail_fr	Electric	0.005	21.0					102564000.0	
Rail_fr	Diesel	0.018	560.0		88.3				
Railway_total		0.275			122.8			1017040476.3	
Maritime Total	Diesel	0.008	5000.0		345.6				
Airway Total	Jetfuel	0.298	393.3						1171.0

Table 7. Comparison of Energy Balance for the year 2018

2018	Ω_Gasoline (Kton)	Ω_Diesel (Kton)	Ω_LPG (Kton)	Ω_CNG (MSm3)	Ω_Elekt (KWh)	Ω_Jet (Kton)
Road_MoENR	2184.0	19328.0	3283.0	92.0		
Road_Balanced	2275.3	19907.8	3304.4	92.0		
Road Difference (%)	-4.2	-3.0	-0.7	0.0		
Railway_MoENR		124.0			1023658559.9	
Railway_Balanced		122.8			1017040476.3	
Railway_Difference (%)		1.0			0.6	
Maritime_MoENR		349.0				
Maritime_Balanced		345.6				
Maritime_Difference (%)		3.4				
Airway Total (MoENR)						1171.0
Airway Total						1171.0
Airway_Difference (%)						0.0

5 Conclusion

Transportation sector plays a vital role in reducing GHG emissions, if realistic policies are developed by accurate sector statistics. Current aggregate travel statistics by the TurkStat and the GDH are not enough to describe the structure of the complex structure of national transport sector (with many subsectors at vehicle technology and travel distance levels). When total energy consumption (which is simply a function of "fuel consumption factors x fuel density factor x VKT") values published by the MoENR is combined with the travel statistics to satisfy the national "transportation energy-balance", it is possible to estimate VKTs for transport technology/modes unmonitored by either the TurkStat or the GDH. The results of the energy balance for a 17-subsegment road sector and 5-subsegment rail sector, in addition to air and maritime sectors were reached that are consistent with published values with a tolerance of <5% errors. The energy balance results revealed a high VKT values for the small trucks and minibuses as 63.36 BVKm and 13.20 BVKm. Most of the diesel used by trucks was estimated to be in the LH, whereas truck activities in the SH are estimated to be lower (8.0 BVKm). These results provide base values to calculate potential reductions in GHG emission if electric vehicles (PCs, minibuses and buses) are promoted in SH distances, even though their current travel ranges still prevent intercity usage.

References

1. Wang, C., Cai, W., Lu, X., Chen, J.: CO_2 mitigation scenarios in China's road transport sector. Energy Convers. Manag. **48**, 2110–2218 (2007)
2. Song, H., Ou, X., Yuan, J., Yu, M., Wang, C.: Energy consumption and greenhouse gas emissions of diesel/LNG heavy-duty vehicle fleets in China based on a bottom-up model analysis. Energy **140**, 966–978 (2017)
3. Jing-Li, F., Jia-Xing, W., Fengyu, L., Hao, Y., Xian, Z.: Energy demand and greenhouse gas emissions of urban passenger transport in the Internet era: a case study of Beijing. J. Clean. Prod. **165**, 177–189 (2017)

4. Liu, F., Zhao, F., Liu, Z., Hao, H.: China's electric vehicle deployment: energy and greenhouse gas emission impacts. Energies **11**, 3353 (2018)

5. Jain, D., Tiwari, G.: How the present would have looked like? Impact of non-motorized transport and public transport infrastructure on travel behavior, energy consumption and CO_2 emissions – Delhi Pune and Patna. Sustain. Cities Soc. **22**, 1–10 (2016)

6. Zeng, Y., Tan, X., Gu, B., Wang, Y., Xu, B.: Greenhouse gas emissions of motor vehicles in Chinese cities and the implication for China's mitigation targets. Appl. Energy **184**, 1016–1025 (2016)

7. Li, X., Yu, B.: Peaking CO_2 emissions for China's urban passenger transport sector. Energy Policy **133** (2019)

8. Sun, S., et al.: Past and future trends of vehicle emissions in Tianjin, China, from 2000 to 2030. Atmos. Environ. **209**, 182–191 (2019)

9. Li, P., Zhao, P., Brand, C.: Future energy use and CO_2 emissions of urban passenger transport in China: a travel behavior and urban form based approach. Appl. Energy **211**, 820–842 (2018)

10. Ministry of Transportation and Infrastructure: National Transportation and Communication Strategy. Ankara, Türkiye (2022)

11. Turkish Statistical Institute. VKT Statistics. https://data.tuik.gov.tr/Bulten/Index?p=Vehicle-kilometer-Statistics-2018-33627#:~:text=Toplam%20ta%C5%9F%C4%B1t%2Dkm%20306%20milyar,926%20milyon%20kilometre%20yol%20katedildi. Accessed 05 June 2023

12. General Directorate of Highways, Traffic and Transportation Statistics. https://www.kgm.gov.tr/Sayfalar/KGM/SiteTr/Istatistikler/TrafikveUlasim.aspx. Accessed 05 June 2023

13. Turkish State Railways-TSR, 2022. Traffic and Transportation Statistics. https://www.kgm.gov.tr/Sayfalar/KGM/SiteTr/Istatistikler/TrafikveUlasim.aspx. Accessed 05 June 2023

14. TurkStat statistics, Airway statistics. https://data.tuik.gov.tr/Kategori/GetKategori?p=Ulastirma-ve-Haberlesme-112. Accessed 05 June 2023

15. TurkStat statistics, Maritime statistics. https://data.tuik.gov.tr/Kategori/GetKategori?p=Ulastirma-ve-Haberlesme-112. Accessed 05 June 2024

16. Ministry of Energy and Natural Resources - MoENR. Energy Balance Tables. https://enerji.gov.tr/eigm-raporlari. Accessed 05 June 2023

17. Automotive Distributors Association (2023). https://www.odmd.org.tr/web_2837_1/neural network.aspx?type=26. Accessed 10 June 2023

18. Aydin, R.: Toplu Ulaşımda Ticari Hız ve Hızın Yakıt Tüketimine Etkisi. Bahcesehir University, Master thesis (2013)

19. Topal, O., Nakir, İ.: Total cost of ownership based economic analysis of diesel, CNG and electric bus concepts for the public transport in Istanbul City. Energies **11**, 2369 (2018)

20. Elektrik Mühendisleri Odası Dergisi (2017)

21. Motorcycle Industry Association. https://www.moted.org.tr/IDS-Media/Haberler/2021-Mart-TUIK-Verileri-Moted-M23.pdf. Accessed 15 June 2023

22. Ülgen, H., Altuntaş, G.: İstanbul Deniz Otobüsleri. İstanbul Üniversitesi İşletme Fakültesi İktisadı Enstitüsü Yönetim Dergisi **21**(66), 119–148 (2010)

23. Open Airlines. https://blog.openairlines.com/how-much-fuel-per-passenger-an-aircraft-is-consuming. Accessed 15 June 2023

Author Index